Title
Mixing and Structural Characteristics of Unforced and Forced Jets in Crossflow

Author
Shoji, Takeshi

Publication Date
2017

Peer reviewed|Thesis/dissertation

UNIVERSITY OF CALIFORNIA

Los Angeles

Mixing and Structural Characteristics of Unforced and Forced Jets in Crossflow

A dissertation submitted in partial satisfaction

of the requirements for the degree

Doctor of Philosophy in Aerospace Engineering

by

Takeshi Shoji

2017

ABSTRACT OF THE DISSERTATION

Mixing and Structural Characteristics of Unforced and Forced Jets in Crossflow

by

Takeshi Shoji
Doctor of Philosophy in Aerospace Engineering
University of California, Los Angeles, 2017
Professor Ann R. Karagozian, Chair

This dissertation describes an experimental exploration of structural and mixing characteristics of unforced as well as forced jets in crossflow (JICF). A jet comprised of mixtures of helium and nitrogen, as well as tracer materials for laser diagnostics, perpendicularly issues into air crossflow. For unforced jet experiments, variable jet-to-crossflow density ratios ($0.35 \leq S \leq 1.00$) and momentum flux ratios ($5 \leq J \leq 41$) were explored, for three alternative injectors with the same exit diameters ($D \cong 4$ mm) and in all cases with a fixed jet Reynolds number $Re_j = 1900$. These injectors included circular nozzles which were flush as well as elevated with respect to the floor of a wind tunnel, in addition to a flush-mounted round straight pipe. For forcing experiments, an equidensity ($S = 1.00$) jet emanating from the flush nozzle ($Re_j = 1900$) as well as a larger-diameter flush nozzle ($D \approx 7.6$ mm and $Re_j = 1500$) were explored. Hotwire anemometry, planar laser-induced fluorescence (PLIF) imaging of acetone seeded in the jet, and stereo particle image velocimetry (PIV) were utilized for JICF characterization in the centerplane and cross-sectional planes.

The interplay between scalar and velocity fields for the non-reactive JICF was studied using simultaneous PLIF/PIV measurements in the centerplane. Proper orthogonal decomposition analysis of scalar and velocity fields generally showed a clear transition from convective to absolutely instability in the jet's upstream shear layer as J values were reduced. The strained dissipation and reaction layer model, with the Howarth transformation for the $S = 0.35$ cases, was applied to extract strain rates from PLIF images, which were compared

with PIV-extracted strain rates. For all flow conditions, strain rates on the upstream mixing layer generally became higher than those for the downstream mixing layer, suggesting easier ignition on the lee-side of the jet for the equivalent reactive flowfield, consistent with reactive flow observations (Wagner et al., 2015).

Mixing characterization based on a new approach, accounting for variable scale lengths, was studied based on centerplane PLIF images for the variable density ($0.35 \leq S \leq 1.00$), flush nozzle-, elevated nozzle-, and flush pipe-injected JICF at a range of J values ($5 \leq J \leq 41$). The new algorithm successfully captured different mixing characteristics associated with stirring as well as molecular mixing, with differences that were apparent especially for the flush pipe injection case. For the equidensity flush pipe-injected JICF, an increase in the Unmixedness and thus worsening mixing was observed for relatively large scale lengths, but not for smaller scale lengths. These mixing trends were likely to be caused by stirring in rolled-up vortical flow structures on the upstream shear layer, capturing relatively high concentrations of jet fluid inside themselves, preventing uniform fluid mixing over the entire flowfield.

For external, axisymmetric forcing of jet fluid, three temporal waveform types were applied: sine wave forcing, and controlled single- as well as double-pulse square wave forcing. These excitations were created with matched root-mean-square (RMS) values of the jet velocity perturbation $U'_{j,rms}$ to achieve effectively the same forcing amplitude (and impulse) among all forcing conditions. Mean and instantaneous metrics were utilized to characterize mixing for the forced JICF. While mean metrics involved jet penetration and spread only in the centerplane view, instantaneous metrics involved the Unmixedness and the probability density function for scalar concentrations in both centerplane and cross-sectional views.

Sinusoidal forcing of the equidensity flush nozzle-injected convectively unstable JICF (e.g., $J = 41$) demonstrated that relatively low forcing amplitudes significantly affected jet structures and mixing, especially for forcing frequencies f_f fairly close to a natural fundamental frequency of the upstream shear layer f_o. For the equidensity absolutely unstable JICF at $J = 5$, a much higher forcing amplitude was required to alter jet's structural and mixing characteristics with f_f in the vicinity of f_o. The effect of sine wave forcing on absolutely unstable JICF characteristics appeared to suggest that lock-in of the upstream shear layer to an imposed forcing frequency f_f enhanced molecular mixing.

Single-pulse square wave forcing significantly altered jet structural characteristics, even for the absolutely unstable JICF, with deeply-penetrating puff-like vortical flow structures being created. The stroke ratio L/D associated with a universal time scale for optimum vortex ring formation (Gharib et al., 1998), was utilized to characterize square wave pulsation of the JICF. Interestingly, the best jet spread and penetration did not necessarily correspond to the best molecular mixing. At a given forcing frequency f_f and amplitude $U'_{j,rms}$, while an optimal stroke ratio L/D for the best jet spread and penetration decreased as J values were reduced, qualitatively consistent with computational studies by Sau and Mahesh (2010), an optimal L/D for the best molecular mixing did not vary for variable J values ($L/D \approx 3{-}3.5$).

Double-pulse square wave excitation consisted of two pulses within each temporal period with different amplitudes and temporal pulse widths, creating successive vortex rings and thus enabling the jet's nearfield vortex rings to interact and collide. Such vortex ring interactions and collisions could enhance JICF molecular mixing as compared with that for the unforced case, although molecular mixing was more significantly enhanced with moderate nearfield vortex interactions rather than nearfield vortex collisions.

The dissertation of Takeshi Shoji is approved.

Jeffrey D. Eldredge

Robert Thomas M'Closkey

Luminita Aura Vese

Ann R. Karagozian, Committee Chair

University of California, Los Angeles

2017

To my parents, brother, fiancée Miri and everybody who has supported me.

Fiat lux

Table of Contents

List of Figures

List of Tables

Nomenclature

Roman Symbols

A Area, with the following particular subscripts:

A_{jet} – cross-sectional area of the jet

A_{tot} – total domain of the interrogation area

C Concentration, with the following particular notations:

C_o – concentration of jet fluid inside the potential core region

$\overline{C/C_o}$ – mean concentration of jet fluid over all instantaneous images

C_{rms} – Root-mean-square of concentration values

D Diameter or diffusivity, with the following particular subscripts:

D – (unsubscripted) jet nozzle diameter

$\hat{D}$ – molecular mass diffusivity

f Frequency, with the following particular subscripts or superscripts:

f_c – corner frequency of a low-pass filter

f_f – forcing frequency

$f_{f,cr}$ – critical forcing frequency associated with the start of lock-in

f_h – horseshoe vortex instability frequency

f_n or f_o – natural (fundamental) frequency of jet's upstream shear layer instability

f_n^* – natural frequency modified by forcing

J Momentum flux ratio, with the following particular subscripts:

J – (unsubscripted) jet-to-crossflow momentum flux ratio, $\rho_j {U_j}^2/\rho_\infty {U_\infty}^2$

J_{cr} – critical jet-to-crossflow momentum flux ratio at which bifurcation to a global mode occurs

K Perturbation matrix

K_n Norm perturbation matrix

L/D Non-dimensional stroke ratio related to vortex ring formation, or length to diameter ratio

L_y, L_z dimensions of an interrogation area

M Molecular mass, with the following particular subscripts:
M_j − jet molecular mass
M_∞ − crossflow molecular mass

$\langle M \rangle$ Mixing criterion

m Mode number

$\dot{m}$ Mass flow rate

N_e the number of fluid elements

n Spatial coordinate or number density, with the following particular subscripts:
n − (unsubscripted) normal to the jet fluid concentration centerline trajectory, or the number density of acetone
n_l − parallel to the scalar gradient vector direction

p'_{crit} Critical acoustic pressure perturbation amplitude for lock-in

Q Q-criterion

$\dot{Q}$ Volume flow rate

R Jet-to-crossflow velocity ratio, U_j/U_∞

Re Reynolds number, with the following particular subscripts:
Re_j − jet Reynolds number, based on mean jet velocity U_j and nozzle diameter D, $Re_j = \rho_j U_j D/\mu_j$
Re_∞ − crossflow Reynolds number, based on freestream crossflow velocity U_∞ and nozzle diameter D, $Re_\infty = \rho_\infty U_\infty D/\mu_\infty$

R_{fit} Pearson correlation or correlation coefficient

r_{ring} Ring velocity ratio, $\Delta U_j/U_\infty$

S Jet-to-crossflow density ratio ρ_j/ρ_∞

S_{ij} Symmetric tensor

St Strouhal number based on diameter, fD/U_j

s Spatial coordinate, with the following particular subscripts:

s – (unsubscripted) along the center of the upstream shear layer

s_c – along the jet fluid concentration centerline trajectory in question

$s_{c,unforced}$ – along the unforced jet fluid concentration centerline trajectory

T Period of acoustic forcing, or temperature

t Time

U Unmixedness or mean velocity, with the following particular subscripts:

U_j – mean jet velocity

U_∞ – mean freestream crossflow velocity

U_{yz} – cross-section-based Unmixedness along horizontal coordinate, x/D

$U_{c,sn}$ – centerplane-based Unmixedness along jet centerline trajectory s_c/D or $s_{c,unforced}/D$

$U_{c,xz}$ – centerplane-based Unmixedness along horizontal coordinate, x/D

ΔU_j – peak-to-peak jet velocity amplitude of temporal pulse

$U_{j,wire}$ – mean jet velocity over the hotwire length

$U_{5\%}$ – jet velocity associated with "5 % points" for stroke ratio calculation

$U'_{j,rms}$ Root mean square (RMS) of the jet velocity perturbation

u_j Temporal jet velocity variation

V_{hw} Hotwire voltage

x, y, z Downstream, spanwise, and axial coordinates measured from jet orifice (see Fig. 1.1)

z_p Jet penetration

Greek Symbols

α Duty cycle of square wave forcing or absorption coefficient, with the following particular subscripts:

α – (unsubscripted) an arbitrary duty cycle or absorption coefficient

α_{actual} – actual duty cycle acquired from temporal data, τ_{actual}/T

α_{input} – input or prescribed duty cycle, τ_{input}/T

Δ Δ-criterion

δ Jet spread, boundary layer thickness, or scale length, with the following particular subscripts:

δ_n – jet spread normal to each jet trajectory in question

$\delta_{n,unforced}$ – jet spread normal to the unforced jet trajectory

δ_p – pixel size in PLIF images

δ_s – scale length ($\delta_p \leq \delta_s \leq \delta_{s,max}$)

$\delta_{s,max}$ – maximum scale length

δ_z – vertical jet spread

$\delta_{99\&}$ – boundary layer thickness defined by 0.99 % of free stream velocity

ϵ Strain rate, with the following particular

ϵ_{SDRL} or ϵ_{PLIF} – strain rate extracted from PLIF data via SDRL model

ϵ_{PIV} – strain rate extracted from PIV data

ϵ_{ij} – strain rate tensor

ζ Mixture fraction, with the following particular superscripts:

ζ – (unsuperscripted) mixture fraction in flowfield

ζ^+ – boundary of the mixture fraction value as $n \to +\infty$

ζ^- – boundary of the mixture fraction value as $n \to -\infty$

θ Momentum thickness, with the following particular superscripts:

θ_j – momentum thickness of jet

θ_{infty} – momentum thickness of crossflow

λ_D Scalar diffusion scale

μ Viscosity, with the following particular superscripts:

μ_j – jet viscosity

μ_∞ – crossflow viscosity

ρ Density, with the following particular subscripts:

ρ_j – jet density

ρ_∞ – crossflow density

σ Absorption cross-section

τ Temporal pulse width of square wave forcing,

with the following particular notations:

τ_{actual} – actual temporal pulse width from temporal data

τ_{input} – input or prescribed temporal pulse width

$\Delta\tau$ – temporal interval of two pulses

χ Scalar dissipation rate

ψ Molecular fraction of acetone vapor within the jet fluid

Ω_{ij} Antisymmetric tensor

ω_y Vorticity in the y direction

Acronyms

CVP	Counter-rotating vortex pair
DAQ	Data Acquisition
DEHS	Di-Ethyl-Hexyl-Sebacat
DMD	Dynamical mode decomposition
DML	Downstream mixing layer
DNS	Direct numerical simulation
FFT	Fast Fourier Transformation
FOV	Field of view
FWHM	Full width at half maximum
IRO	Intensified Relay Optics
JICF	Jet in crossflow
K-H	Kelvin-Helmholtz
PCA	Principal Component Analysis
PDF	Probability density function
PIV	Particle image velocimetry
PLIF	Planar laser-induced fluorescence
POD	Proper orthogonal decomposition
PSD	Power spectral density
PVC	Polyvinyl chloride
RMS	Root-mean-square
SDRL	Strained dissipation and reaction layer
SE	Scalar fluctuation energy
SMD	Spatial mixing deficiency
UML	Upstream mixing layer
UV	Ultra violet
VE	Velocity fluctuation energy

Acknowledgments

I would fist and foremost like to thank my advisor Professor Ann Karagozian for her guidance, and patience throughout my life as a graduate student. My invaluable experience at UCLA would have never existed without her support. Her guidance encompasses not only our research but also my personal growth and career as an international researcher by showing desirable researcher's attitude with enthusiasm, as well as even teaching technical English presentation and writing skills. All of her consistent, patient supports enabled me to complete this work. I am unbelievably happy that I have been able to work under her.

I want to thank my committee members Professors Jeffrey Eldredge, Robert M'Closkey and Luminita Vese for their constructive comments and helpful suggestion for this study. In particular, Professor M'Closkey greatly helped me to develop a feedback control system for forced JICF experiments, which I was not so familiar with. Without his guidance and consistent support, I could not complete the majority of my work in this dissertation. I extend special thanks to Professor Owen Smith at UCLA, who has supported me to conduct thorough experiments by his extensive knowledge of experimental studies.

I am grateful to Professor Luca Cortelezzi at Politecnico di Milano for his dedication to experimental studies of JICF mixing characterization with variable scale lengths and double-pulse forcing. His enthusiasm in research always inspired me, and his assistance in any way possible is very appreciated. I am also indebted to Professor Igor Mezić at UC Santa Barbara, who provided me with constructive suggestion for the study on variable mixing scale lengths. Discussion with him played an important role in me administering the mixing study.

I have been always surrounded by the bright individuals at the UCLA Energy and Propulsion Research Laboratory. I would like to first offer special thanks to Dr. Levon Gevorkyan, who showed me everything he knew with enthusiasm and persistence. I believe he definitely established a foundation of my experimental skills and the beginning of the "JICF world". I do not know how to express my large gratitude to all of my current and past labmates including Richard Abrantes, Cristian Sevilla, Dr. Dan Getsinger, Ari Ekmekji, Wen Yu (Terry) Peng, Phuoc Hai Tran, Dr. Dario Valentini, Andres Vargas, Ayaboe Edoh, Andrea

Besnard, Miguel Plascencia, Dr. John Bennewitz, Elijah Harris, Dr. Hyung Sub Sim, and Stephen Schein. They have been greatly supporting me during the past five years. Their helps, encouragements, discussions, friendships both inside and outside the lab. These are the treasures in my life. I will not forget the time I have spent with all of them.

I cannot forget to offer gratitude to my previous advisor Professor Tetsuya Sato at Waseda University in Japan. He sincerely helped me to come to the United States and study aerospace engineering. Not only did he taught how to do research, but also he showed how to have a happy life as a Ph.D. student. I still vividly remember his unique, interesting story, which has been supporting my life at UCLA and will permanently remain in my mind.

I would like to express my deepest gratitude to my parents and brother for their unconditional love and just always being there for me. They have never forced me to do anything, and they always trust me, respect what I decide to do, and keep providing irreplaceable support for me pursuing my goal. Although I do not think I can return all the favor they have given to me, I look forward to being there for them and supporting them whenever they need me.

I would like to greatly thank my fiancée, Miri, for her consistent support, encouragement and persistence for five years from Japan. Despite the fact that we could only see once a year, she always respects my research and supports my career as a researcher with her beloved smiles. I want to also express my appreciation to her parents, who also respect my work at UCLA.

Finally, I would like to thank my friends outside of the lab in Japan and the United States, as well as everybody who has supported me throughout my entire life. My personality and ability are all affected and created by their irreplaceable relationship with me. Without anyone, I would not be standing here and even the same person as I am today. This work is dedicated to all of them.

This research has been supported by the National Science Foundation under grants CBET-1133015 and CBET-1437014, by the Air Force Office of Scientific Research under grants FA9550-11-1-0128 and FA9550-15-1-0261, and by DURIP grant FA9550-10-1-0461.

Vita

2010-2012	Undergraduate Student Researcher, Waseda University, Department of Applied Mechanics and Aerospace Engineering, Tokyo, Japan
2012	B.S. (Aerospace Engineering), Summa Cum Laude, Waseda University, Tokyo, Japan Japan Society of Mechanical Engineers Hatakeyama Award
2013	Graduate Teaching Assistant, UCLA. MAE 157 - Basic Mechanical Engineering Laboratory
2014	Graduate Teaching Assistant, UCLA. MAE 157S - Basic Aerospace Engineering Laboratory
2014	M.S. (Aerospace Engineering), UCLA MAE Department Outstanding M.S. in Aerospace Engineering Award, UCLA
2014	Graduate Teaching Assistant, UCLA. MAE C150/250R - Rocket Propulsion Systems
2014	Graduate Teaching Assistant, UCLA. MAE C150/250P - Aircraft Propulsion Systems
2016	The U.S. USNC/TAM Travel Fellowship to attend the 24th International Congress of Theoretical and Applied Mechanics in Montréal
2013-2017	Graduate Student Researcher, UCLA Energy and Propulsion Research Laboratory, Los Angeles, CA

Publications and Presentations

L. Gevorkyan, T. Shoji, W. Y. Peng, and A. R. Karagozian, *Influence of the Velocity Field on Scalar Transport in Gaseous Transverse Jets*, submitted to The Journal of Fluid Mechanics.

L. Gevorkyan, T. Shoji, D. R. Getsinger, O. I. Smith, and A. R. Karagozian, *Transverse Jet Mixing Characteristics*, Journal of Fluid Mechanics, 790, pp. 237-274, 2016.

T. Shoji, A. Besnard, E. W. Harris, S. G. Schein, R. T. MCloskey, A. R. Karagozian, and L. Cortelezzi, *Structural and mixing characteristics in actively controlled transverse jets*, 69th Annual Meeting of the American Physical Society Division of Fluid Dynamics, Portland, OR, November 2016.

T. Shoji, A. Besnard, E. W. Harris, R. T. M'Closkey, and A. R. Karagozian, *Effects of External Forcing on Transverse Jet Structure and Mixing*, 24th International Congress of Theoretical and Applied Mechanics, Montréal, Canada, August 2016.

T. Shoji, A. Besnard, E. W. Harris, R. T. M'Closkey, and A. R. Karagozian, *Effects of Axisymmetric Forcing on Transverse Jet Structure and Mixing*, 10th Southern California Flow Physics Symposium, UC Irvine, CA, April 2016.

T. Shoji, L. Gevorkyan, A. Besnard, O. I. Smith, and A. R. Karagozian, *Strain Rates and Scalar Dissipation Rates in Gaseous Transverse Jets*, 68th Annual Meeting of the American Physical Society Division of Fluid Dynamics, Boston, MA, November 2015.

T. Shoji, L. Gevorkyan, A. Besnard, O. I. Smith, and A. R. Karagozian, *Scalar Dissipation Rates and Strain Rates for Gaseous Transverse Jets*, 9th Southern California Flow Physics Symposium, San Diego State University, CA, April 2015.

CHAPTER 1

Introduction and Background

1.1 Transverse Jet and Its Applications

The jet in crossflow (JICF) or transverse jet typically consists of the round jet perpendicularly issuing into crossflow. This canonical yet complicated three-dimensional flowfield has been studied for many decades, mainly because of its extensive applications in engineering propulsion systems (Margason, 1993; Karagozian, 2010). There are many variations of the basic JICF, involving variable flow phases (e.g., gaseous/liquid jet into gaseous/liquid crossflow) and injection systems (e.g., coaxial, triplet or impinging injection, air blast or pressure-swirl atomizers for liquid fuel injection, circular or rectangular jets, and flush or elevated injection with respect to a wall), as well as having a non-reactive or reactive flowfiled. Many early studies associated with the JICF explored chimneys and smokestacks injecting into the effluent atmosphere. Here mixing rates are important primarily for the environment (Margason, 1993). Yet most JICF studies are relevant to propulsion systems, and are discussed below.

Dilution air jets injected perpendicularly into a primary or secondary zone of a combustion chamber in air-breathing gas turbine combustors are a typical JICF configuration (Kamotani and Greber, 1972; Fearn and Weston, 1974; Vermeulen et al., 1982). The cooling air jets, if injected downstream of the combustion zone, result in a change in the temperature distribution, which can be characterized by the temperature pattern factor (PF) at the turbine inlet:

$$PF = \frac{T_{4,peak} - T_3}{T_{4,mean} - T_3} \tag{1.1}$$

where T_3, $T_{4,peak}$ and $T_{4,mean}$ stand for the combustion chamber inlet temperature, and the peak and mean temperatures at the turbine inlet, respectively. Transverse dilution jets can reduce the PF or, equivalently, decrease the peak temperature of the hot crossflow entering the turbine section (Vermeulen et al., 1982, 1992; Karagozian, 2010), which is desirable from a robustness and efficiency perspective. The appropriate dilution and cooing of combustor gases by dilution air jets also reduces the fuel-air equivalence ratio in the combustion chamber, which can lower NO_x and/or CO emissions via careful control of the mixture (Bowman, 1992). For instance, lean premixed combustion and/or staged combustion can contribute to the reduction of NO_x emissions, which are lowered at lean conditions. Such reduction can be successfully achieved by applying transverse air jets in the combustion zone (Priere et al., 2005). More recently, the reduction of NO_x emission associated with the JICF has been practically achieved in the GE Twin Annular Premixed Swirler (TAPS) (Foust et al., 2012) as well as Rich Burn, Quick-Quench, Lean Burn (RQL) combustors (Samuelsen, 2016).

The JICF can also be found in turbine-blade film cooling systems, where arrays of cooling air jets typically using high-pressure air from the compressor are injected along blade rows through small holes on the blade surface. Such jets generate vortices from the surface of turbine blades to passively or actively control separation of the crossflow boundary layer on the blades. This system enables the crossflow boundary layer to be attached to the blades longer than that without the vortex generation, which in turn creates gaseous layers on the blades and prevents overheating of the blades by hot crossflow (approximately $1600-1900$ K) from the combustion chamber (Bons et al., 2002; Bogard and Thole, 2005; Ekkad et al., 2006). The improved effectiveness of film cooling as well as reduced heat load over a leading edge model can be potentially achieved using actively pulsed jets in comparison with those in the absence of external forcing (Ekkad et al., 2006).

Thrust vectoring jets also utilize the JICF configuration. Thrust vectoring enables control of rocket and missile flight trajectories and attitudes (e.g., vehicle's roll, yaw and pitch) using single or multiple injections in the nozzle to asymmetrically distort the exhausting gas. The JICF is also used in thrust vectoring for takeoff/landing transition for V/STOL aircraft from hovering to regular flight. Oh and Schetz (1990) used single circular and rectangular jets to investigate the surface pressure distribution on a V/STOL aircraft model caused by the transition, observing considerable benefits. In high speed nozzles, thrust vectoring also requires the precise control of the JICF system typically utilizing a shock vector control or fluidic throat skewing. A fluidic nozzle throat skewing method for thrust vectoring can decrease the weight of the nozzle or other associating mechanical components, and thus enhance the control of the vehicle (Miller et al., 1999; Yagle et al., 2001).

The transverse jet can be applied in supersonic crossflows, especially for applications to supersonic combustion in scramjet engine combustors. Transverse injection of fuel into supersonic crossflow behind a rearward-facing step or within or upstream of a cavity can improve the configuration's flame-holding ability as well as fuel-air mixing, resulting in a more complete and efficient combustion system (Karagozian et al., 1996; Ben-Yakar et al., 1998; Gruber et al., 2004).

1.2 Flow Parameters and Vortex System in JICF

The interaction of a jet perpendicularly issuing into crossflow from a flush injector with respect to a wall generates diverse vortical structures as schematically shown in Figure 1.1. The coordinate system in Figure 1.1 will be consistent throughout the present study. The jet has a mean velocity of U_j at the exit plane, exhausting perpendicularly into crossflow with a freestream velocity U_∞ (outside of the injection wall boundary layer) in the positive x direction. The trajectory of the transverse jet's upstream shear layer is parameterized by the coordinate s, while the trajectory of transverse jet's centerline is characterize by the coordinate s_c. The coordinate s_c is defined from a power-law fit to the maximum concentration loci acquired in a mean concentration field (Gevorkyan et al., 2016).

The parameters typically characterizing the JICF are defined as follows. The jet-to-crossflow density ratio, $S = \rho_j/\rho_\infty$, velocity ratio, $R = U_j/U_\infty$, and momentum flux ratio, $J = \rho_j U_j^2/\rho_\infty U_\infty^2 = SR^2$, are parameters generally used to characterize JICF behavior (Kamotani and Greber, 1972). The Reynolds number of the jet, $Re_j = \rho_j U_j D/\mu_j$, is based on jet diameter, D, as well as other jet properties, although the crossflow-based Reynolds

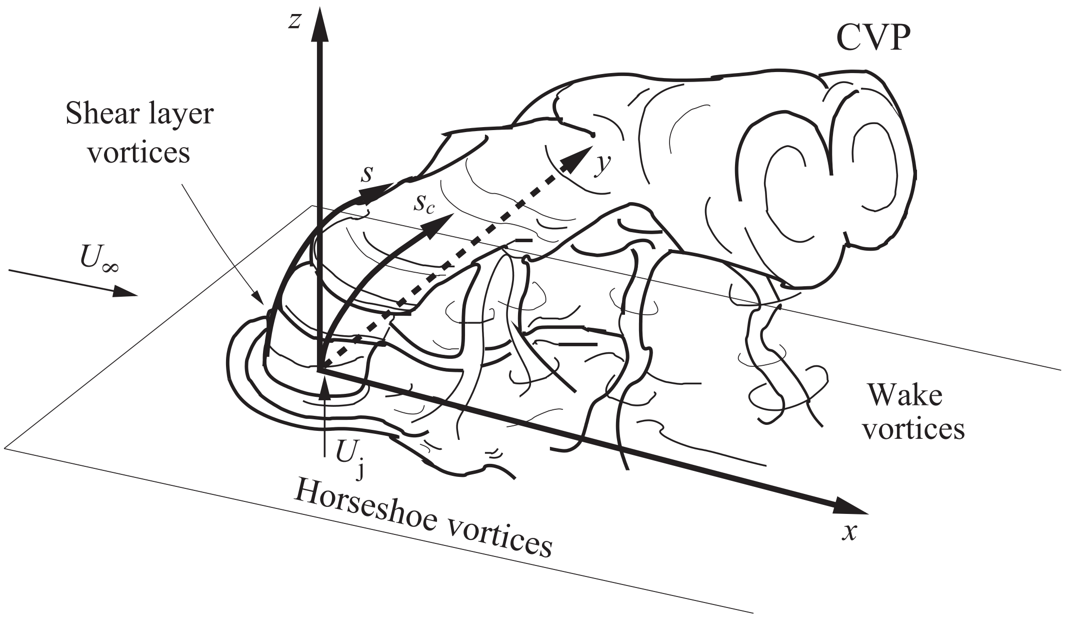

Figure 1.1: Schematic of the jet in crossflow and associated vortical flow structures such as the jet upstream shear layer vortices and counter-rotating vortex pair (CVP). Orientation of coordinate axes x, y, z, jet upstream shear layer trajectory s and jet centerline trajectory defined by a power-law fitting to the loci of the maximum scalar concentration values on mean centerplane acetone PLIF images s_c are shown. Adapted from Fric and Roshko (1994).

number, Re_∞, is also often cited (Fric and Roshko, 1994; Narayanan et al., 2003). Other relevant parameters for transverse jets are the momentum thickness of the jet at its exit plane, θ_j, and that of the crossflow boundary layer, θ_∞. The jet momentum thickness θ_j may be separately quantified on the windward-side (negative x region) and lee-side (positive x region) of the jet in the centerplane ($y = 0$ plane) (Megerian et al., 2007). The Strouhal number, $St = fD/U_j$, usually pertains here to the initial instability mode or frequency f associated with vortex rollup in the upstream shear layer in the absence of external forcing.

Four dominant vortical structures for the JICF are identified for flush-injected jets in crossflow, as shown in Figure 1.1: (1) the counter-rotating vortex pair (CVP), (2) jet shear layer vortices or roll-up vortices, (3) wake vortices and (4) horseshoe vortices. The CVP has long been understood to be a fundamental dominant feature of the transverse jet's cross-sectional structure. Various aspects of the CVP have been identified over the years

(Kamotani and Greber, 1972; Moussa et al., 1977; Broadwell and Breidenthal, 1984; Andreopoulos, 1985; Karagozian, 1986; Kuzo, 1995; Kelso et al., 1996; Yuan and Street, 1998; Smith and Mungal, 1998; Yuan et al., 1999; Cortelezzi and Karagozian, 2001; Muppidi and Mahesh, 2007; Mahesh, 2013; Getsinger et al., 2014). One main interest in the study of the CVP has been the suggestion that it increases entrainment of the crossflow into the jet, in comparison to that for the free jet in quiescent surroundings, hence the CVP is considered to contribute to better mixing for the JICF (Margason, 1993; Karagozian, 2010). The experimental study of Kelso et al. (1996) concluded that the formation of CVP is initiated very close to the jet exit, with distortion of vortex ring structures forming in the jet shear layer to create a cross-sectional CVP structure. The shear layer vortices result from jet shear layer stabilities in the JICF, as will be described in Section 1.3. The computational study of Cortelezzi and Karagozian (2001) involves three-dimensional transient vorticity evolution, suggesting that the near-field interaction of vortex rings at the jet exit with the crossflow lead to the predicted folding and tilting of the windward- and leeside- shear layer vortices, indeed leasing to the formation of the CVP structure, as suggested by Kelso et al. (1996). The CVP is also known to significantly affect the penetration and trajectory of the jet, related to mixing enhancement suggested to be induced by the CVP structure's evolution, sustenance and eventual breakdown of the jet in crossflow as compared with the free jet (Kamotani and Greber, 1972; Moussa et al., 1977; Broadwell and Breidenthal, 1984; Karagozian, 1986; Margason, 1993). A separate experimental study by Peterson and Plesniak (2004) utilizing particle image velocimetry (PIV) suggests that asymmetry in the jet supply channel (feeding the jet thorough its injector) creates vortical structures within the jet orifice, which interact with the CVP in a constructive or destructive manner, hence affecting the strength and coherence of the CVP.

While the generation of wake vortices shown in Figure 1.1 originally was thought to be associated with the vortex shedding process, as one sees for flow around a solid cylinder, known as the Kármán vortex sheet, the formation mechanism for wake vortices in transverse jets originates from different dynamics. Fric and Roshko (1994) investigated wake vortical structures and their characteristics in detail by utilizing smoke visualization and hotwire anemometry. Fric and Roshko (1994) observed the tornado-like upright vortical structures to originate from the separation of the crossflow boundary layer, beginning just downstream and to either side of the jet, because of the adverse pressure gradient. The upright vortices can draw fluid from the wall boundary layer into the jets, which also affects jet structure. In addition, Fric and Roshko (1994) suggest that the wake vortices are often non-periodic and intermittent. Yet the experimental study of Smith and Mungal (1998) suggests that the periodicity of the wake vortices depends upon R, Re_∞ and θ_j/D.

Horseshoe vortices can be created close to the injection wall ($z = 0$ plane) upstream of the jet, wrapping around the potential core region of the jet and evolving downstream. The oscillating frequency for horseshoe vortices is similar to that for interactions between crossflow and a wall-mounted circular cylinder, as described by Kelso and Smits (1995). Kelso and Smits (1995) indicate that horseshoe vortices operate in three regimes: steady, oscillating and coalescing, depending upon the values of R and Re_∞. The horseshoe vortices are quite periodic and repeatable in three regimes, unlike the characteristics of the wake vortices. If the wake vortices are periodic with a relatively close phase to that of the horseshoe vortices, the coupling of the horseshoe vortices with the wake vortices occurs, per Kelso and Smits (1995), although such coupling has not been extensively documented. Similar oscillation frequencies between the horseshoe vortices and wake vortices are observed using a rectangular jet into crossflow by Krothapalli et al. (1990). The jet velocity profile close to the jet exit can be significantly altered by the interaction with the horseshoe vortices in the vicinity of the upstream edge of the jet (Andreopoulos, 1985). The jet velocity profile is responsible for the nature of shear layer instabilities as documented in experiments by Megerian et al. (2007), analysis by Alves et al. (2008), and simulation by Iyer and Mahesh (2016).

1.3 JICF Structure and Instability

In general, a linear stability theory classifies a shear flow instability into three main types (Huerre, 2000): (1) a convectively unstable flow, (2) a marginally convectively/absolutely unstable flow and (3) an absolutely unstable flow. The linear impulse response for these instability types is shown in Fig 1.2 from Li (2011), where a flow takes place in the positive x direction (horizontal axis), and the vertical axis represents the elapsed time. In a temporally and/or spatially growing flow for an open shear layer (here, "open" means that fluid particles contained in a flowfield can enter or leave in the domain of interest), a perturbation source creates a "perturbation wavepacket" that travels in time. The perturbation source can be considered to be initiated at $x = 0$ in Figure 1.2, and the source generates the wavepacket at $t = 0$, shown to evolve in time as confined within the dotted lines. In the case where a shear flow is linearly stable, the wavepacket decays in time everywhere in the flowfield (not shown in Figure 1.2). When the wavepacket grows in amplitude and is convected in the streamwise direction from the source in time, the shear flow is said to be convectively unstable (Figure 1.2(a)). For an absolutely unstable shear flow, the growing wave packet increases in amplitude and travels upstream as well as downstream over the entire flowfield in time, as shown in Figure 1.2(c). If a flowfield contains a sufficient number of absolutely unstable regions, the flow is called globally unstable (Li, 2011). Flows known to undergo absolute instability, based on specific flow conditions, include bluff-body wakes (Provansal et al., 1987) as well as low density or heated free jets (Monkewitz et al., 1990; Kyle and Sreenivasan, 1993). Because of the dynamics of these instabilities shown here, the convective and absolute instabilities are sometimes called an "amplifier" and "oscillator", respectively. A marginally convective/absolute instability possesses characteristics of both instabilities, that is, the wavepacket grows and expands into the flowfield, but only downstream, in the positive x direction (Figure 1.2(b)). The impulse is characterized by a Green's function obtained in the linear stability theory associated with spatial and temporal approaches (Huerre and Monkewitz, 1990; Huerre, 2000; Li, 2011).

Shear layer vortices for the JICF were previously considered to be attributed to a Kelvin-Helmholtz (K-H) type of shear instability, initiated in the jet's nearfield (Fric and Roshko, 1994; Kelso et al., 1996; Yuan and Street, 1998). However, Blanchard et al. (1999) suggest that the near-field vortex generation and its evolution for the JICF are better explained by the Landman and Saffman theory associated with a global elliptic instability of 3D vortices (Landman and Saffman, 1987) rather than the classical K-H type instability. Camussi et al.

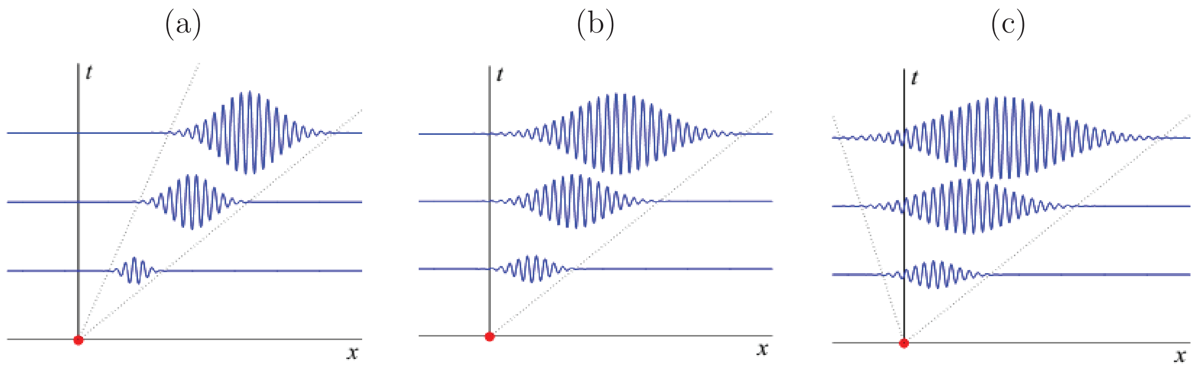

Figure 1.2: The wavepacket loci in time for the different types of instability: (a) convectively unstable flow, (b) marginally convectively/absolutely unstable flow, and (c) absolutely unstable flow. Taken from Li (2011).

(2002) also argue that dominant near-field vortical dynamics for the JICF at relatively low jet Reynolds number ($Re_j = 100$) are wake-like structures coupled to the CVP ($R < 3$) or jet-like rings relevant to the coupling between positive and negative vorticity ($R > 3$), and hence the shear layer instability of JICF is not driven by the K-H type mechanism but more by "waving of the jet flow".

Recent in-depth studies of the JICF by our group at UCLA have focused on the stability and structural characteristics of transverse jets. Experimental studies of stability characteristics have mainly focused on the upstream shear layer instability associated with rollups on the upstream shear layer as well as their response to external perturbation (Megerian et al., 2007; Davitian et al., 2010a; Getsinger et al., 2012, 2014). These studies have shown that the mechanism of the instability for JICF is more complex than the K-H type instability for a planar shear layer, involving different types of instabilities (see Figure 1.2) depending on flow conditions. Corresponding linear stability analyses for this flowfield provide confirmation and additional insights.

Using hotwire anemometry, Megerian et al. (2007) experimentally investigated the stability characteristics of the jet's upstream shear layers (Figure 1.3) at $S = 1$ for $1.15 \leq R \leq \infty$, with a flush nozzle as described in the previous section. Figures 1.3(a), (c) and (e) represent the power spectra of the shear layer at various trajectory locations scaled by the nozzle exit diameter, D, and the figures in the right column are the corresponding color contour plots, showing the strength and Strouhal number, $St = f_o D/U_j$, of the instabilities on a finer spatial scale. f_o in these figures represents the initial natural frequency of the shear layer for the transverse jet. In Figures 1.3(a-b) for $R \to \infty$ (the free jet), the upstream shear layer shows a very weak amplitude. Beyond approximately $s/D \approx 3$, the growth of the instability increases, especially at $St \approx 0.5$ and 0.7, although the amplitude is still weaker than that of the other two velocity ratio cases at the same s/D location. For the $R = 6.4$ case, shown in Figures 1.3(c-d), the shear layer mode ($St \approx 0.7$) and its subharmonics ($St \approx 0.35$) start to grow stronger at $s/D \approx 2$. The growth of power spectra peaks begins at a similar location of s/D than that of the free jet, hence closer to the jet exit, and then the instability convects in the streamwise direction. Subharmonic growth further downstream suggests vortex pairing and merger. These and additional flow features indicate that this jet shear layer is considered to be convectively unstable. In addition, a mode shift in the Strouhal number approximately between $St = 0.6$ and 0.7 is present in the spectra and is more obvious in the contour plot (Figure 1.3(d)) beyond $s/D = 2$. The mode shifting/hopping is revealed as 2-3 multiple peaks in the corresponding power-spectra plot, Figure 1.3(c). Getsinger et al. (2012) later determined this frequency shifting to arise from tonal interactions between the strengthened shear layer instability and the hotwire probe. Characteristic contour plots as seen in Figure 1.3(d) are only observed for the transverse jet's shear layer under convectively unstable conditions, and not for the free jet or for the case with absolute instability. Finally, Figures 1.3(e-f) exhibit a strong pure tone instability in the shear layer at f_0 and with higher harmonics almost right from the beginning, at the jet exit. The instability modes grow in amplitude immediately, and are dominant over the entire flowfield, without formation of subharmonics which are common to convective instability. This shear flow has been demonstrated to be absolutely unstable, consistent with Figure 1.2(c). The transition in stability is demonstrated in Megerian et al. (2007) and in further study in Davitian et al. (2010a) to occur at approximately $R = 3.1$ for the equidensity ($S = 1.00$) JICF. Substantial additional evidence for this transition is provided in these references.

Megerian et al. (2007) used an acoustic loud speaker to study the nature of the shear

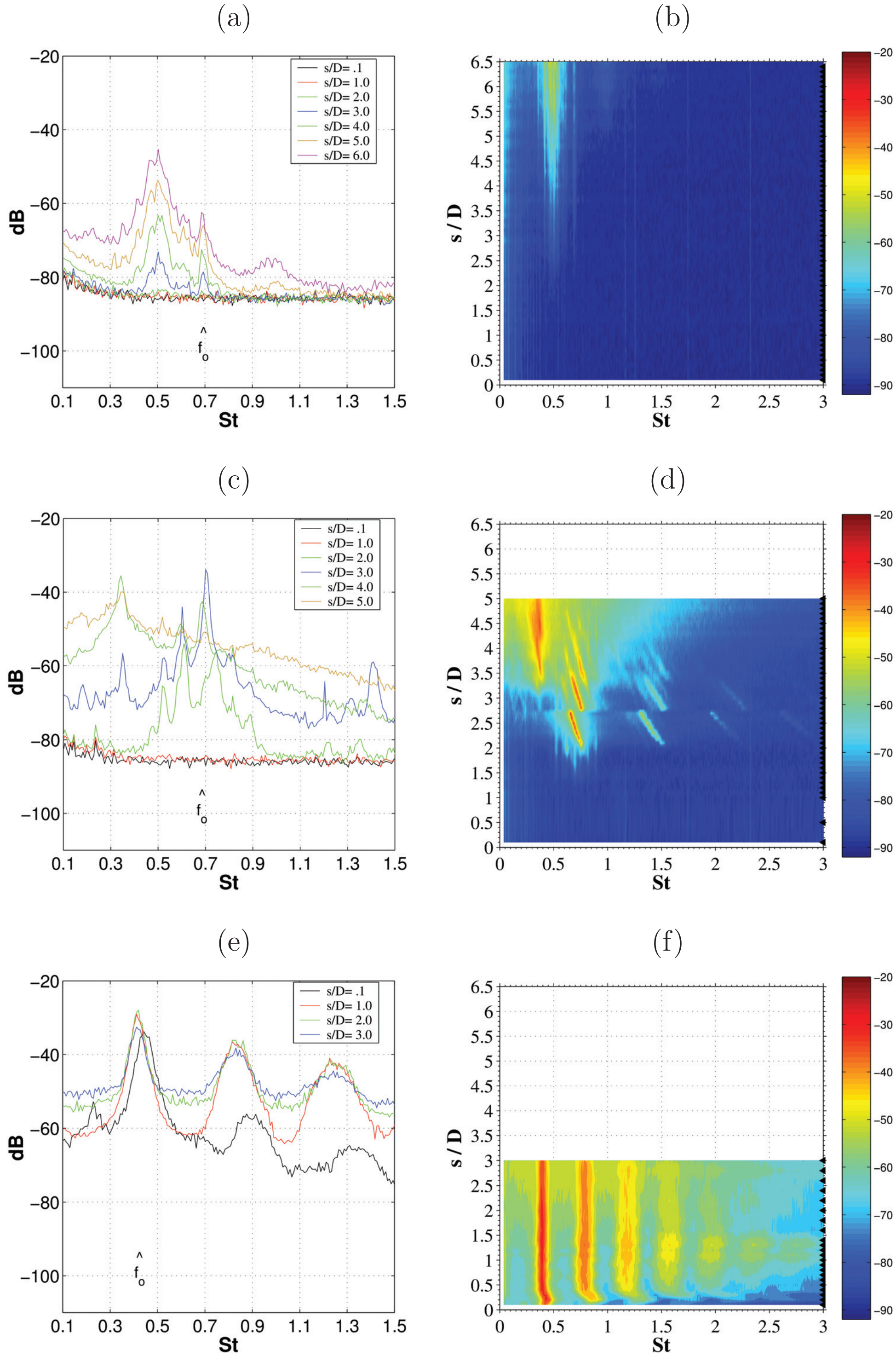

Figure 1.3: Power spectra plots and the corresponding contour plots for the upstream shear layer from the flush nozzle at $R = \infty$ for (a) and (b), $R = 6.4$ for (c) and (d), and $R = 1.15$ for (e) and (f), from Megerian et al. (2007).

layer instabilities by imposing a low-level acoustic excitation, less than 1 % of the mean jet velocity, within the jet injection apparatus for a range of velocity ratios ($1.15 < R < \infty$). For the relatively higher velocity ratios ($4.1 < R < \infty$), the spectral measurements of the shear layer for the forced transverse jets show a strong peak at the Strouhal number, St_f, corresponding to the forcing frequency, f_f, and a diminished peak at the shear-layer mode, f_0, corresponding to the unforced transverse or free jet. For relatively low velocity ratios ($1.15 < R < 4.1$), however, the low-level forcing does not affect shear layer spectral characteristics very significantly, and the amplitude of the peak at f_0 remains high. Megerian et al. (2007) thus demonstrated that absolutely unstable transverse jets are little affected by low-level sinusoidal-wave excitation, another characteristic of a shear layer transition to absolute instability. Further evidence for this transition for the equidensity transverse jet may be found in Megerian et al. (2007) and Davitian et al. (2010a), while for low density transverse jets, with $0.25 \leq S \leq 1.00$, the transition to absolute instability is documented in Getsinger et al. (2012) to occur at a momentum flux ratio $J \cong 10$ or for density ratio $S \lesssim 0.40$. This critical density ratio S to create an absolutely unstable shear layer agrees well with $0.27 \lesssim S \lesssim 0.5$ experimentally obtained by Hallberg and Strykowski (2006) for the Reynolds numbers in question.

Getsinger et al. (2014) performed the spectral measurements along the transverse jet shear layer for several different injectors, the flush nozzle, elevated nozzle and flush pipe (See Figure 2.2), with varying J values, to study the relationship between instabilities and jet structures via optical diagnostics. The specifications of these injectors are explained in Section 2.1. Spectral measurements for all three injectors at the same flow conditions ($2 \leq J \leq 41$) are shown in Figure 1.4, represented in terms of contour plots. Getsinger et al. (2014) note that the shear layer instability transitions for both the flush nozzle and flush pipe from convective to absolute instability at approximately $J \approx 10$. For $J \lesssim 10$, strong shear layer instability is initiated very close to the exit for both flush injectors, with strong higher harmonics as well. However, the jet shear layer from the elevated nozzle reveals a relatively weak amplitude in the contour plots and, as the J value is lowered, is considered convectively unstable for all flow conditions examined in Getsinger et al. (2014). This weakening is found

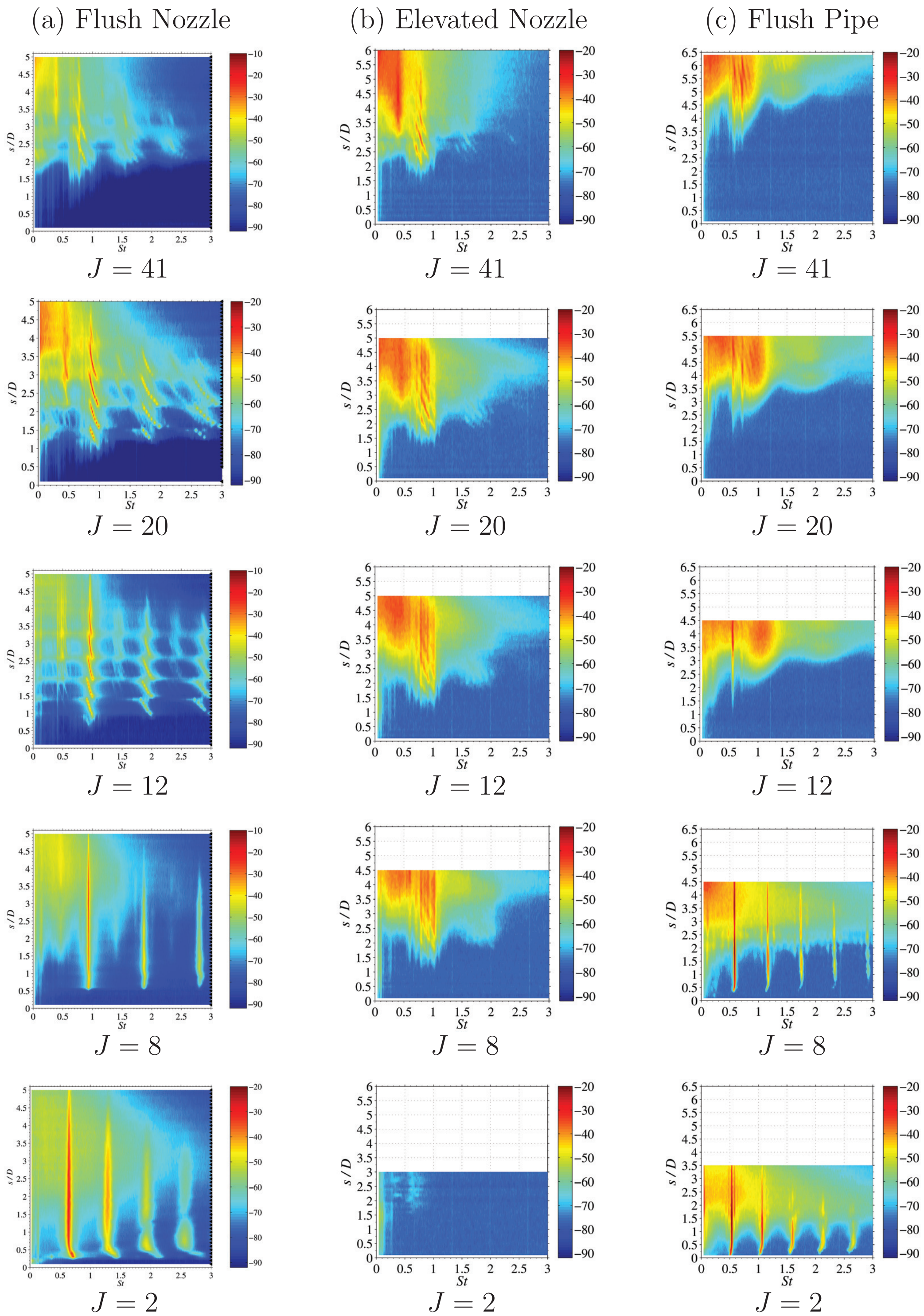

Figure 1.4: Spectral contour plots of the upstream shear layers for three different injectors with various jet-to-crossflow momentum flux ratio, J. Taken from Getsinger et al. (2014).

to be due to vertical coflow upstream of the elevated nozzle (Megerian et al., 2007). At very low values of J or R, Megerian et al. (2007) documented a transition from a convective to an absolutely shear layer for the elevated jet at $J \approx 0.93$, where J is based on the mean jet velocity. The results and observations in Figure 1.4 overall agree with previous experimental studies (Megerian et al., 2007; Davitian et al., 2010a; Getsinger, 2012).

Iyer and Mahesh (2016) applied direct numerical simulation (DNS) and dynamical mode decomposition (DMD) to explore JICF characteristics at $R = 4$ and 2, corresponding to convectively and absolutely unstable upstream shear layers, using the same flow conditions as well as the same nozzle configuration as in Megerian et al. (2007). Spectral characteristics based on point-wise temporal vertical velocity on the upstream shear layer at $R = 2$ and 4 extracted from DNS simulation showed qualitatively and quantitatively good agreement with those in Megerian et al. (2007) by including the flow inside the nozzle in the simulation. DMD analysis extracted the same dominant frequency as in Megerian et al. (2007) pertaining to the shear mode initiated close to the jet exit at $R = 2$ and further from the exit at $R = 4$, again consistent with the observations by Megerian et al. (2007). Also, the same dominant frequency was observed even inside the nozzle for both $R = 2$ and 4, with a decay of the vertical velocity fluctuation magnitude in proportion to z^{-2} (distance from the jet exit). The dominance of the shear layer instability inside the nozzle was observed more strongly at $R = 4$ than $R = 2$. Interestingly, despite the instability arising even inside the nozzle, Iyer and Mahesh (2016) also acquired qualitatively and quantitatively similar spectra to those in Megerian et al. (2007) even without the nozzle in the simulation, but by imposing the same mean velocity profile at the jet exit as determined from DNS within the nozzle. This suggests that the existence of the nozzle itself in the simulation does not directly affect the JICF instability characteristics, but contributes to imposing the instability by a given mean flow at the jet exit.

Investigation of JICF structural characteristics has also been pursued recently by our group in relation to stability characteristics (Getsinger et al., 2014), in part because of the potential contribution of the vortical structures described in Section 1.1 to improving mixing as compared to free jets (Karagozian, 2010). Over many years structural studies have focused on the qualitative and quantitative characteristics of transverse jet centerplane structures (Fric and Roshko, 1994; Narayanan et al., 2003; Su and Mungal, 2004; Muppidi and Mahesh, 2005; Getsinger, 2012) and cross-sectional structures (Kamotani and Greber, 1972; Smith and Mungal, 1998; Cortelezzi and Karagozian, 2001; Narayanan et al., 2003; Getsinger, 2012), equivalent to the x-z plane ($y = 0$) and y-z plane (different x values), respectively, in Figure 1.1.

Getsinger et al. (2014) conducted acetone PLIF imaging to visualize the centerplanes (Figure 1.5) and cross sections (Figure 1.6) in the farfield ($x/D \cong 10.5$) of the JICF, using the three different injectors indicated above, for varying jet-to-crossflow momentum flux ratios, J, ranging from convective to absolute instability in the shear layers. Results for the flush nozzle, elevated nozzle, and flush round pipe are shown for $2 \leq J \leq 41$.From Figures 1.5(a) and (c), it appears that the formation of the rolled-up vortical structures on the upstream jet shear layer occurs closer to the jet exit as J decreases, especially for $J \leq 8$, although the flush pipe generates less well organized vortical structures at lower J values, and has more delayed rollup at higher J. These structural centerplane trends are consistent with the power spectra in Figures 1.3. Similarly, the first rolled-up structure from the elevated nozzle moves toward the jet exit as J decreases for $12 \leq J \leq 41$, with similarly to the flush nozzle of the same interior shape. Yet the shear layer at $J = 2$ and even $J = 8$ for the elevated jet seems not to create much vortex rollup, and in fact, the shear layer stabilities for $J \leq 8$, are in agreement with spectral measurements. This stabilized upstream shear layer at lower J values, observed in the spectral measurements and in PLIF imaging for the elevated nozzle (Figure 1.5(b)), is attributed to the interaction of the jet with the vertical co-flow along the upstream side of the nozzle, with relatively higher magnitude of the vertical velocity component, which can stabilize a shear layer (Jendoubi and Strykowski, 1994). While the centerplane PLIF images in Figure 1.5 enable one to examine the rolled-up shear layer vortical structures, those images cannot capture the out-of-plane fluid components in the y direction, which are considered to be important to the mixing quantification. Hence, Getsinger et al. (2014) also investigated the mean cross-sectional PLIF images as shown in Figure 1.6. Interestingly, asymmetric cross-sections are observed at $J = 41$ for all three

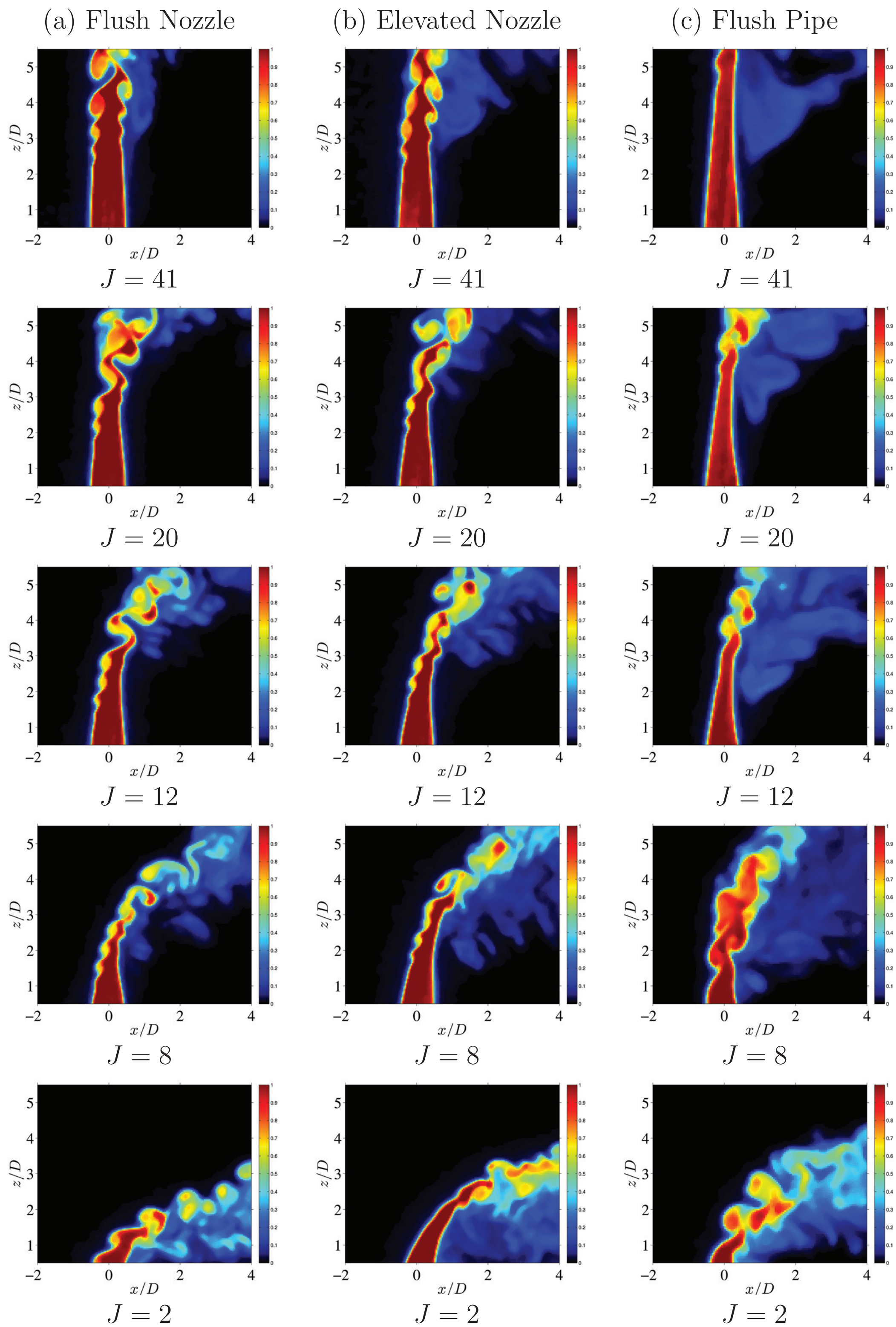

Figure 1.5: Instantaneous centerplane PLIF images for three different injectors with various jet-to-crossflow momentum flux ratio, J. From Getsinger et al. (2014).

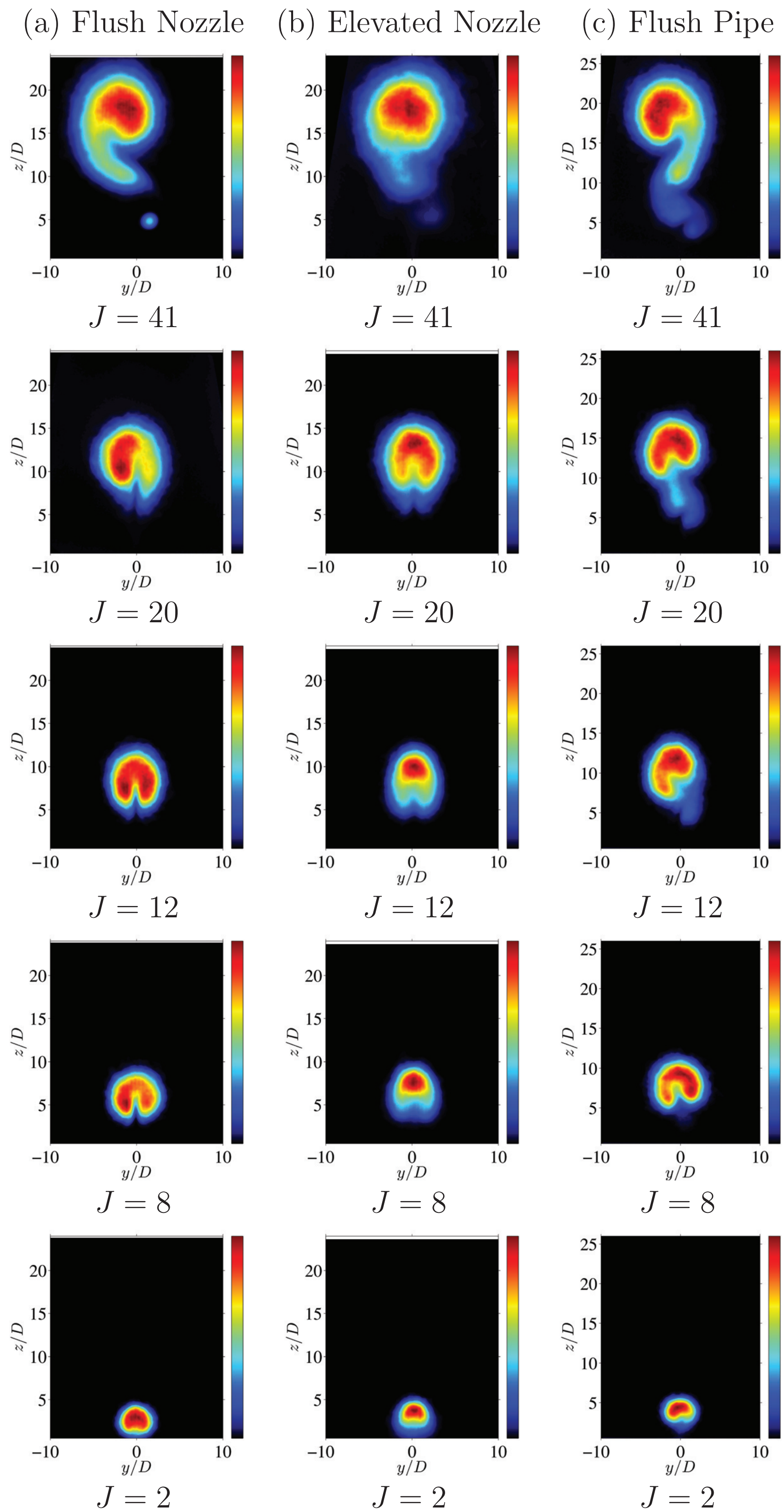

Figure 1.6: Mean cross-sectional PLIF images for three different injectors with various jet-to-crossflow momentum flux ratio, J. Each image was obtained by averaging over 300 instantaneous images. From Getsinger et al. (2014).

injectors, at $J = 20$ and 12 for the flush pipe and at $J = 20$ for the flush nozzle. The jet cross-section from the flush nozzle contains tail-like flow structures approximately below $z/D = 10$ at $J = 41$ and below $z/D = 6$ at $J = 20$, with lower scalar concentrations than those of the main flow/vortical structures. Such asymmetric cross-sectional structures are observed by the earlier experimental study by Kuzo (1995), especially at $R = 10$ and relatively higher jet Reynolds number of $Re_j \approx 2100 - 7300$ utilizing digital particle image velocimetry (DPIV). A similar asymmetric cross-section created by the JICF at $R = 10-20$ and $Re_j = 33000 - 16000$, utilizing nozzle injection, as well as $J = 36$ and $Re_j = 5000$, using the parabolic velocity profile at the jet exit, was also seen in the experimental study by Smith and Mungal (1998) and the computational study by Muldoon and Acharya (2010). Muldoon and Acharya (2010) also showed that sine wave excitation could reduce the level of asymmetry of or symmetrize the cross-sections. The other cross-sections in Figure 1.6, except at higher J for flush injected-asymmetric cases, are relatively symmetric, and CVP structures can be observed depending on the flow conditions e.g. $J \leq 12$ for the flush nozzle.

The theoretical study by Alves et al. (2007) suggested that asymmetric transverse jet structures at higher momentum flux ratio might be associated with the azimuthal modes of the JICF. They conducted an inviscid linear stability analysis to conduct the coupling of the different multiple azimuthal modes, especially an axisymmetric mode ($m = 0$) and helical modes ($m = \pm 1$ and ± 2, where the positive and negative signs respectively correspond to the conunterclockwise and the clockwise directions). Alves et al. (2007) detected that the jet in crossflow behaves differently from the free jet even at very high jet-to-crossflow velocity ratio, above around $R \approx 278$. In addition, they described that the helical mode becomes stronger than the axisymmetric mode with a certain value of jet shear layer Strouhal number St and R value, resulting in the destabilization of the jets by crossflow. Moreover, the growth rates of the helical modes might be slightly different depending on the signs, plus or minus, which could be associating with the weakly asymmetric jet or the lack of symmetry for Kelvin-Helmholtz like instability. Corke et al. (1991) experimentally observed asymmetric flow structures induced by the helical mode ($m = \pm 1$) for the free jet, although the instability mode or phase of the jet in crossflow is locked and mode switching between the axisymmetric and helical modes occurs.

Alves et al. (2008) advanced their linear stability analysis from Alves et al. (2007) to examine the stability characteristics for the equidensity transverse jets in crossflow in the near-field using a continuous (i.e. viscous) base flow. They suggested that the most unstable disturbance at $R > 4$ correspond to the nominally axisymmetric mode ($m = 0$) with the weaker magnitude of the helical modes, and the growth rate of the axisymmetric mode increase as R decreases. In addition, they demonstrated that the convective instability is dominant at $R > 4$, which agrees with the experimental study of Megerian et al. (2007).

1.4 Excitation of Transverse Jets

External excitation of a jet in a quiescent surroundings or crossflow is known to have a significant ability to change the structural characteristics of the jet and/or penetration and spread of the jet (Crow and Champagne, 1971; Reynolds et al., 2003). Some typical forcing methods involve sinusoidal and square wave forcing of the jet fluid (Johari et al., 1999; Eroglu and Breidenthal, 2001; M'Closkey et al., 2002; Narayanan et al., 2003; Shapiro et al., 2006; Johari, 2006; Davitian et al., 2010b). Most free jet excitation involves sine wave forcing of the jet into quiescent surroundings (Crow and Champagne, 1971). More recent studies are summarized as follows.

Juniper et al. (2009) experimentally and numerically explored a non-reacting helium free jet ($Re_j = 1100$ and $S = 0.14$) and buoyant jet diffusion flame ($Re_j = 1100$ and $S = 0.5$ of unburnt fluid CH_4 or H_2/N_2), both of which are self-excited or absolutely unstable. Forcing studies involved sine wave forcing created by a loudspeaker situated upstream of the nozzle exit. The power spectral density (PSD) of velocity fluctuations for a non-reacting, low density free jet were acquired via hotwire anemometry 1.5 jet diameter downstream of the exit along the jet centerline. These demonstrated that there was a critical input voltage to the loudspeaker at which the global mode of the jet at frequency f_n in the absence of external forcing disappears and thus is locked-in to a forcing frequency f_f. This forcing condition creates "lock-in". Juniper et al. (2009) then created a lock-in diagram, showing critical input voltages over a range of forcing frequencies to generate lock-in of the jet. The lock-in diagram typically takes a V shape with respect to the natural mode of the jet in the absence of external forcing f_n because of the linear relation of critical input voltages and $|f_f - f_n|$. Based on the PSD of jet velocity fluctuations and the lock-in diagram, they concluded that a non-reacting jet was relatively easily locked-in to external forcing, especially for f_f close to f_n, with non-linear interactions between the natural and forcing modes. On the other hand, the PSD of heat release oscillations for a diffusion flame in quiescent surroundings acquired via shlieren and OH* chemiluminescence imaging showed that a reactive jet requires higher forcing amplitudes, due to heat release, to be locked-in to the forcing. There is less non-linear frequency interactions as well, although the natural mode becomes dominant again over the forcing frequency in the jet's farfield (vertical coordinate $z/D \sim 16 - 18$).

Li and Juniper (2013a,b) experimentally studied the quasiperiodicity of a self-excited non-reacting helium free jet and a buoyant diffusion flame, respectively, created by mixtures of methane and nitrogen, using the same loudspeaker configuration as in Juniper et al. (2009) to impose sine wave forcing. For the non-reactive case, Li and Juniper (2013a) found a range of non-linear dynamics at a given forcing frequency f_f fairly close to the natural frequency of the jet f_n in the absence of forcing, depending on input voltage to the loudspeaker, where the dominant mode can be the natural frequency (at zero or very low voltage amplitude), the forcing frequency f_f in addition to a natural frequency modified by the forcing, f_n^*, with/without several nearby frequencies (at an intermediate voltage amplitude), or the forcing frequency f_f itself (at a fairly high voltage amplitude). This is called a 1:1 lock-in. Such a transition with an increasing input voltage to the loudspeaker is defined mainly based on the PSD of jet velocity perturbations and a Poincaré map as the following transitions: (1) from periodicity to $\mathbb{T}^2$ quasiperiodicity via a torus-birth bifurcation and (2) from $\mathbb{T}^2$ quasiperiodicity to 1:1 lock-in via either a saddle-node or a torus-death bifurcation. Interestingly, the non-linear V-shape in the lock-in diagram is observed at fairly high input voltage amplitude, as shown in Figure 1.7(a). In this Figure 1.7(a) the lock-in diagrams from several previous studies for the transverse jet (Davitian et al., 2010a; Getsinger et al., 2012) and the non-reactive and reactive jet (Li and Juniper, 2013a,b) are shown for comparison. Figure 1.7(a) suggests a break of the linearity with relatively strong external perturbation of the jet. Also, the non-reactive jet is more readily locked in if forcing frequency is below natural mode, as one can see in Figure 1.7(a), with a larger magnitude of PSD at the forcing frequency, equivalently stronger jet flow oscillations. In contrast, Li and Juniper (2013b) for a reacting jet demonstrated that the diffusion flame was more resistance to lock-in at forcing frequency below the natural one, as shown in Figure 1.7(b). However, the diffusion flame oscillates stronger at a forcing frequency below the natural mode f_n, with similar quasiperiodicity, consistent with the behavior of the non-reacting jet. The quasiperiodicity extracted from the experimental results was also similarly predicted by a van der Pol oscillator model, although there were slight differences in trends between the data. For both non-reacting and reactive free jet flows, slightly asymmetric lock-in diagrams with respect to f_f/f_n were thus observed, as shown in Figures 1.7(a) and (b).

For transverse jet excitation, Narayanan et al. (2003) utilized a spinning mechanical valve to modulate a gaseous jet at a jet-to-crossflow velocity ratio of $R = 6$. Although the input signal was a square wave, the actual output resulted in sinusoidal forcing at a prescribed forcing frequency. Their study demonstrates that even low level forcing affects the jet penetration, spread and wake region structures, although since $R = 6$ in their study, as discussed in Section 1.3, the shear layer instability mode was likely in the convectively unstable regime. This could explain the jet's response to such low level excitation. Narayanan et al. (2003) experimentally obtained an entrainment enhancement of 30-40 % and higher turbulence intensity during such sinusoidal forcing.

The effect of sinusoidal wave forcing on gaseous, non-reactive flush-injected JICF characteristics was investigated at UCLA for a range of S and J values. As documented in Section 1.3, to study stability characteristics, Megerian et al. (2007) imposed fairly weak acoustic excitation to the equidensity jet, less than 1 % of the mean jet velocity. When there is an absolutely unstable upstream shear layer, there is little effect of the weak external forcing, although if the JICF is convectively unstable, there is an alteration in the spectra. Davitian et al. (2010a) more extensively explored the effect of sine wave excitation of the equidensity JICF on instability characteristics when there is an absolutely upstream shear layer. They

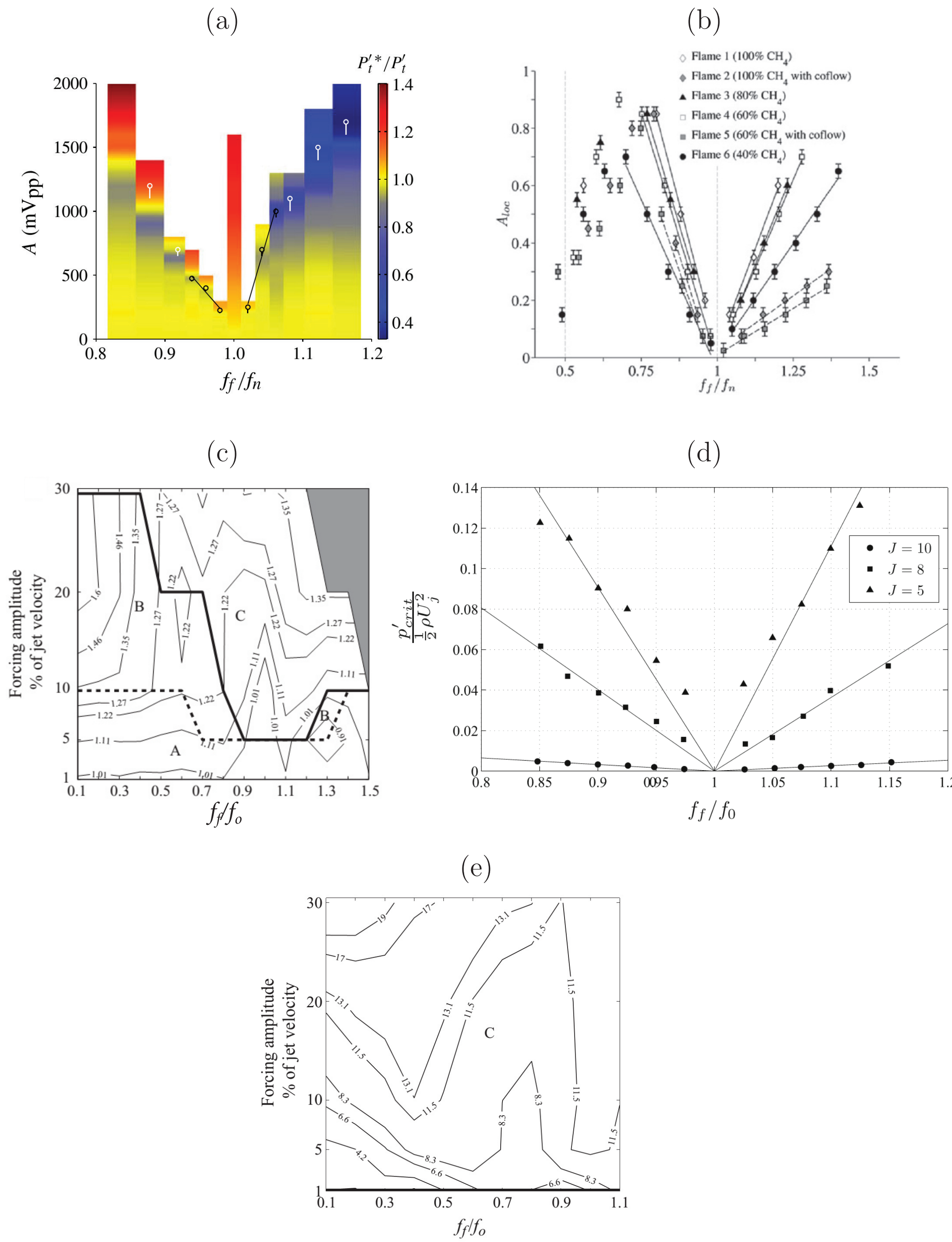

Figure 1.7: Lock-in diagrams taken from (a) Li and Juniper (2013a) for the non-reactive free jet, (b) Li and Juniper (2013b) for the reactive free jet, (c) Davitian et al. (2010a) for the equidensity transverse jet at $R = 1.5$ ($J = 2.25$), (d) Getsinger et al. (2012) for the low density transverse jet with $S = 0.55$ and (e) Davitian et al. (2010a) for the equidensity transverse jet at $R = 6.4$ ($J \approx 41$).

observed a lock-in response of the absolutely unstable upstream shear layer depending on forcing frequency, as in Juniper et al. (2009) and Li and Juniper (2013a). The lock-in diagram associated with percentage of mean jet velocity by Davitian et al. (2010a) (Figure 1.7(c)) showed fairly coarse linearity and a slight asymmetry with respect to the natural frequency, suggesting that the upstream shear layer is more resistant to lower frequency excitation, which is opposite to the non-reactive low density free jet experimental study by Li and Juniper (2013a). There are important differences between Davitian et al. (2010a) and Li and Juniper (2013a), e.g., a free jet vs. JICF, $S = 0.14$ vs. $S = 1.00$, and jet response at the jet centerline vs. on the upstream shear layer. For the JICF, the lock-in diagram for the convectively unstable shear layer was observed to be completely flat, which means that the convectively unstable upstream shear layer is locked-in to any forcing frequency, at even fairly weak amplitudes (Davitian et al., 2010a), as shown in Figure 1.7(e).

Getsinger et al. (2012) also explored transverse jet response to sine wave forcing using a gaseous, variable density ratio ($0.14 \leq S \leq 1.00$) flush nozzle-injected JICF. Again, the lock-in response of the jet to sine wave forcing was observed for the absolutely unstable upstream shear layer with respect to the amplitude of acoustic pressure perturbation, as shown for the $S = 0.55$ case in Figure 1.7(d). The asymmetry in the lock-in diagram was confirmed at $J = 5$, suggesting higher resistance to the higher frequencies than to the lower frequencies, as seen by Li and Juniper (2013a), although the other plots in Figure 1.7(d) for the JICF at $J = 8$ and 10 are fairly symmetric.

For square wave forcing, it has been suggested by several previous experimental (Johari et al., 1999; Eroglu and Breidenthal, 2001; M'Closkey et al., 2002; Narayanan et al., 2003; Shapiro et al., 2006; Johari, 2006; Davitian et al., 2010b; Hendrickson and M'Closkey, 2012) and computational studies (Sau and Mahesh, 2007, 2008, 2010; Muldoon and Acharya, 2010; Coussement et al., 2012) that square wave-like pulsed transverse jet flow initiates the formation of a vortex ring or turbulent puff-like vortical structures, with or without a trailing flow, depending upon the forcing conditions, which control jet spread and penetration. Several fundamental parameters characterize this pulsed jet flow that is fully- or partially- modulated in time by square wave excitation. The excited flowfield with a temporally varying jet exit velocity u_j can be typically characterized by a temporal square wave forcing frequency, f_f, the square wave's duty cycle, α, and a root mean square (RMS) of the jet perturbation, $U'_{j,rms}$. The duty cycle α is related to the period of excitation, $T = 1/f_f$, and the temporal pulse width τ, through the relation $\alpha = \tau/T$. An expression for $U'_{j,rms}$ can be defined as follows:

$$U'_{j,rms} = \sqrt{\frac{1}{T}\int_{t_1}^{t_1+T}(u_j - U_j)^2 dt} \tag{1.2}$$

where u_j and U_j are the temporally varying jet velocity and the mean jet velocity at the jet exit, respectively.

Excitation of the jet in crossflow can affect the jet's mixing length for non-isothermal, non-reactive conditions. Vermeulen et al. (1992) studied an acoustically pulsed cool air jet in hot crossflow and measured the resulting temperature profile. They obtained a 70 % decrease in the length required to achieve a given mixed state as well as a significant increase in the jet penetration and temperature profile.

For the single vortex ring, Gharib et al. (1998) investigated the relation between flow structures for a single pulse of fluid in quiescent surroundings and a variable stroke ratio, L/D, which characterizes the formation of a vortex ring. The stroke ratio represents the ratio of the distance traveled by a notional piston, L, to the jet orifice diameter, D. When a vortex ring is created by a single pulsation, a critical stroke ratio exists, below which there is an absence of the trailing flow behind the vortex ring and an incomplete filling of fluid in the vortex ring, but above which there is trailing flow exceeding the filled vortex ring. Gharib et al. (1998) found that this critical stroke ratio ($L/D \sim 4$) is a universal time-scale for optimum vortex ring formation, that is, optimum propagation and impulse, under single pulsation.

Johari et al. (1999) experimentally studied in liquid the fully modulated, square wave-like pulsed turbulent jet in crossflow by varying excitation frequency (0.5-5 Hz range), temporal pulse width, and hence duty cycle α. Their study demonstrated that, depending on L/D, long pulse-width excitation creates vertically elongated vortical structures that resemble the unforced JICF, while short-pulse, lower α modulation generates turbulent puff-like vortical structures with trailing flow, producing deeply penetrating jet structures. For the liquid reacting flow (acid-base) studied in Johari et al. (1999), as well as in Eroglu and Breidenthal (2001), a shorter pulse width excitation also reduced the mixing or reaction length (or "flame length") as compared with the unforced JICF.

Effects of a solenoidal valves creating square wave forcing on the characteristics of liquid jets in liquid crossflow were also explored by Eroglu and Breidenthal (2001). The partially or fully modulated transverse jets created turbulent vortical flow structures with or without the trailing flow, depending on the forcing Strouhal number, although the amplitude of excitation was not quantified in this study. At relatively high St, a flow bifurcation is also observed, where there is a bulk jet flow that penetrates close to the unforced trajectory, and a "wake" flow lying closer to the wall, in the same plane as the jet exit. In this research, a maximum 70 % increase of the jet penetration is observed, and in the presence of an acid-base reaction, a 50 % reduction in "flame length" is measured during forcing.

Johari (2006) re-defined the stroke ratio for JICF under square wave excitation of the jet to effectively account for the pulsation effect as for the jet in the absence of crossflow. The stroke ratio L/D for the JICF with a temporal jet exit velocity u_j (Johari, 2006) can be evaluated based on the square wave's temporal pulse width τ, the jet orifice diameter D, as well as the jet's cross-sectional area A_{jet} through the relation:

$$\frac{L}{D} = \frac{1}{A_{jet}D}\int_0^{\tau}\int_A u_j(dA)(dt) \cong \frac{\overline{U_j}\tau}{D} \tag{1.3}$$

where $\overline{U_j}$ is a mean jet velocity during the pulse. Based on these and others' studies, Johari (2006) proposed that stroke ratio L/D (or the temporal pulse width) and the duty cycle govern the forced jet's structural characteristics, which may be independent of velocity ratio R (Figure 1.8). For the various R or J values in Figure 1.8, the critical stroke ratio L/D at which distinct vortex rings form for transverse jet asymptotically approaches 4, again corresponding to the universal time scale of Gharib et al. (1998). Johari (2006) proposes two fundamental flow patterns governing the excited jet: (1) slug flow length, i.e., the vortex ring and its trailing column and (2) the spatial separation of the slug flow structures, creating distinct vortex rings. The slug length is mainly determined by the pulse width which governs

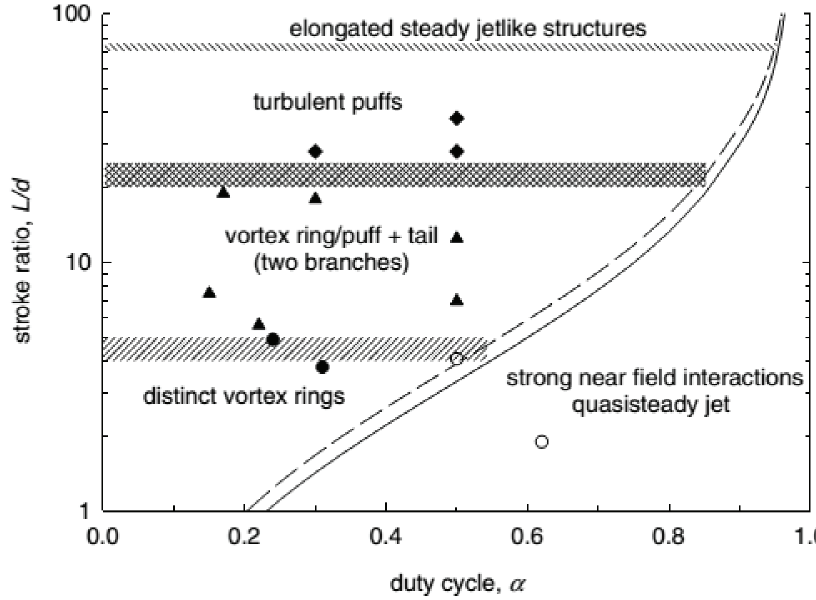

Figure 1.8: Flow regime map associating with the vortical and flow structures of the fully pulsed jets in crossflow as a function of the stroke ratio L/D and duty cycle α. Each dot respectively stands for the experimentally obtained jet's structures such as the distinct vortex rings (●), vortex rings followed by trailing flow (▲), turbulent puff (♦) and strongly interacting quasi steady-like jet structures (○). The solid and dashed curves represent the numerical definition which distinguishes the pulsed jet's structures at velocity ratio $R = 3$ and 10 respectively. From Johari (2006).

the initial flow structures.

Computational studies have shown the same trend as the experimental results summarized above and described further below (for UCLA experiments). Sau and Mahesh studied the correlation between vortex ring and transverse jet excitation and mixing by direct numerical simulation (DNS). In Sau and Mahesh (2007), they laid emphasis on the passive scalar mixing of a vortex ring in the absence of crossflow, created by a single pulse with a prescribed stroke ratio L/D. The study demonstrates that the flow structures, consisting of the vortex ring and the trailing flow of the ring, and the mixing characteristics, are relevant to the stroke ratio and critical formation number, $L/D \cong$ 3.6-4.0. They also find that the trailing column following the ring actually causes a deterioration in the mixing, where mixing is quantified by the time evolution of scalar concentration in the vortex ring cores and by the rate of change in the volume of scalar containing fluid, where the latter is defined for concentrations exceeding 1 % of the maximum concentration, C_o. This study on a vortex ring in crossflow confirms optimal vortex mixing at a formation number near $L/D \cong 4$. However, with the existence of crossflow, the single vortex ring with a certain length of the trailing column, in contrast, can enhance the mixing (Sau and Mahesh, 2008). Additionally, they find that there is no coherent vortex ring formation for an effective $R < 2$, but that at larger effective velocity ratios, there can be asymmetric vortex ring formation with or without a trailing column. Much like the UCLA-based experiments of M'Closkey et al. (2002) and Shapiro et al. (2006), Sau and Mahesh (2010) numerically obtained convecting vortical structures with or without the trailing columns and hairpin vortices at the lee-side of the transverse jet, depending upon flow conditions. The computational results shown in Figure 1.9 agree with previous experimental work (Eroglu and Breidenthal, 2001; Tomar et al., 2004; Shapiro et al., 2006). They also note that imperfections in the square wave shapes on jet characteristics, e.g. as in Shapiro et al. (2006), as compared with a perfect square wave, were less important than the effect of the actual stroke ratio or the duty cycle. Sau and Mahesh (2010) also demonstrate in their flow regime map (Figure 1.9) the optimal square-wave forcing conditions for the best jet spread and penetration using stroke ratio L/D and a vortex speed-to-crossflow velocity ratio, called a ring velocity ratio, r_{ring} defined for the transverse jet as follows:

$$r_{ring} = \frac{\Delta U_j}{U_\infty} \tag{1.4}$$

where ΔU_j represents a peak-to-peak velocity amplitude of a pulse in square wave forcing. Figure 1.9 suggests that (1) the optimal stroke ratio for the best transverse jet spread and penetration decreases as the ring velocity ratio decreases and (2) the optimal stroke ratio from their computation as well as some experimental results (Eroglu and Breidenthal, 2001; Shapiro et al., 2006) collapse well on to a so-called "optimal line" in the regime map.

Coussement et al. (2012) computationally studied the same forcing conditions as the experimental work of M'Closkey et al. (2002) using large-eddy simulation (LES). Their computation shows the temporal growth of the vortices around the jet exit, with similar puff-like

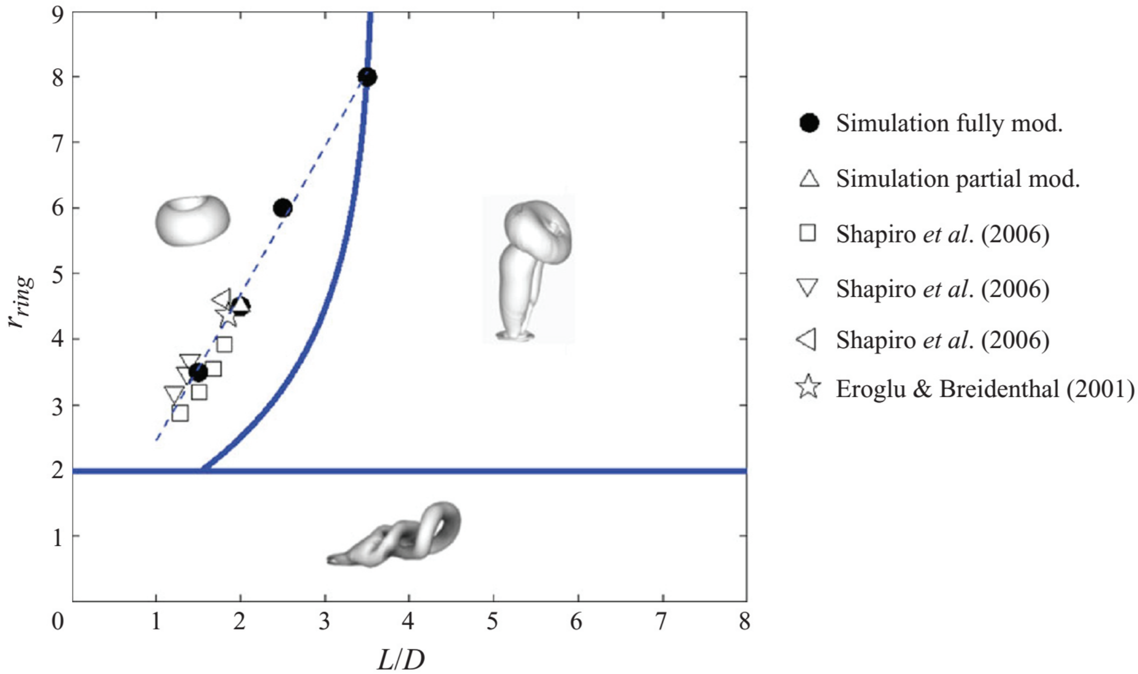

Figure 1.9: Flow regime map associated with the optimal forcing conditions for the best jet spread and penetration from some experimental studies (Eroglu and Breidenthal, 2001; Shapiro et al., 2006). Taken from Sau and Mahesh (2010).

turbulent structures and jet flow bifurcation to those in experiments for some cases. These flow structures appear more commonly at relatively lower duty cycles, $\alpha = 0.15$, of the excitation wave, which agrees with experimental studies (Johari et al., 1999; M'Closkey et al., 2002; Shapiro et al., 2006).

At UCLA, transverse jet square wave excitation studies at $R = 2.58$ by M'Closkey et al. (2002), to be discussed in more detail below, suggested that square wave forcing at frequencies which are the subharmonics of the preferred frequency associated with the jet's shear layer improved the penetration and the spread of the jets more than forcing at other frequencies. Using the same configuration, Shapiro et al. (2006) examined the effects of duty cycle, α, and excitation frequency of the prescribed square wave, for two different velocity ratios, $R = 2.58$ and 4.0, although at the time it was not appreciated that the unforced jets have had different shear layer stability characteristics for $R = 2.58$ and 4.0. They found that the optimum stroke ratio L/D which maximized transverse jet penetration and the jet's deeply-penetrating vortical structures, occurred at $L/D \approx 4$, near the universal time scale of Gharib et al. (1998).

Actually creating temporal square waves with distinct pulse widths is challenging in an experiment, however. A jet compensator with feedforward (and later, feedback) control has demonstrated an ability to more successfully prescribe a desired temporal jet velocity profile and specified RMS of the jet perturbation at the jet exit in our UCLA-based transverse jet experiments (M'Closkey et al., 2002; Shapiro et al., 2006; Davitian et al., 2010b; Hendrickson and M'Closkey, 2012). M'Closkey et al. (2002) developed a jet compensator or a feedforward flow controller, enabled by an eight-state dynamical model, to represent the dynamical response of the actuation system. The model was then inverted and applied as forcing input to the actuation system to achieve a flatter frequency response. This model inversion enabled creation of more precise square waveforms. To actuate the transverse jets, an acoustic loudspeaker was utilized in these earlier experiments (see details in Sections 2.1 and 2.4). Shaping filter and Bessel filters also enable acquiring the desired RMS of the jet perturbation. This overall feedforward controller or jet compensator system sufficiently matched the RMS amplitudes for all forcing conditions, a sinusoidal or a square wave, so that the true effect of forcing parameters could be compared. These studies (M'Closkey et al., 2002; Shapiro et al., 2006; Davitian et al., 2010b) used a nozzle mounted flush to the bottom floor of the wind tunnel's test section. While sine wave excitation seems to have little impact on transverse jet penetration as well as a spread, both for uncompensated and compensated (controlled) jets, controlled square wave excitation significantly enhanced the penetration and the spread seen in smoke-visualized images of the jets (M'Closkey et al., 2002). The smoke visualization of these unforced and forced transverse jets at $R = 2.58$ is shown in Figure 1.10, where the natural frequency of the shear layer was 220 Hz. Figure 1.10(a) shows the unforced JICF, Figures 1.10(b) and (d) show uncompensated sine and square wave excitation effects, Figure 1.10(c) shows jet response to compensated sine wave excitation, and the rest show jet response to compensated square wave excitation at various frequencies. The distinct, deeply penetrating vortical puff-like structures can be observed clearly in Figures 1.10(e), (f) and (g), corresponding to square wave forcing at subharmonics of the fundamental shear layer frequency. Square wave forcing at the fundamental frequency

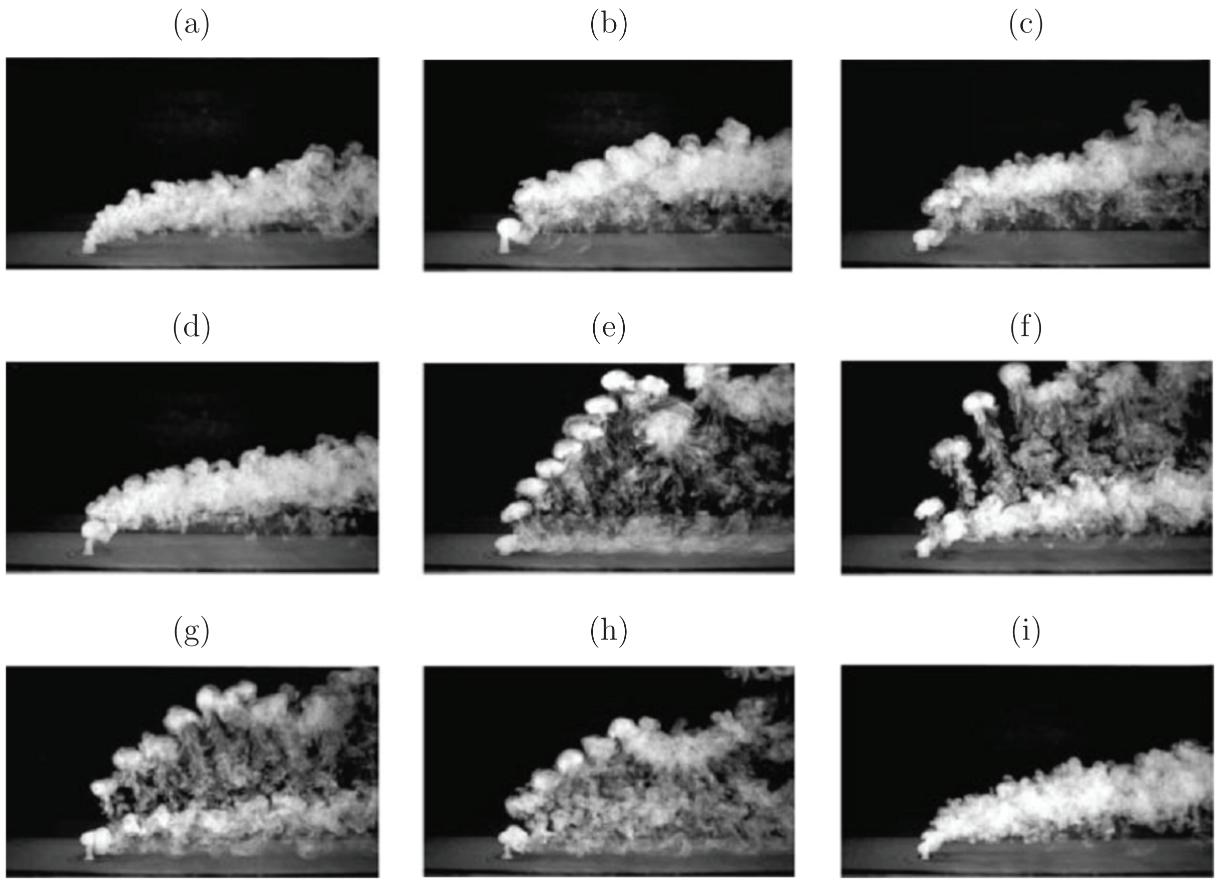

Figure 1.10: Instantaneous smoke visualization of unforced and forced jets in crossflow at jet-to-crossflow velocity ratio of $R = 2.58$, and the matched root-mean-squared of jet velocity perturbation of $U'_{j,rms} = 1.7\ m/s$ amongst all excitation cases. Each image represents: (a) unforced jet, (b) uncompensated forced jet by sine wave at forcing frequency of $f_f = 73.5\ Hz$, (c) compensated forced jet by sine wave at $f_f = 73.5\ Hz$, (d) uncompensated forced jet by square wave at $f_f = 110\ Hz$ and duty cycle of $\alpha = 31\ \%$, (e) compensated forced jet by square wave at $f_f = 110\ Hz$ and $\alpha = 31\ \%$, (f) compensated forced jet by square wave at $f_f = 55\ Hz$ and $\alpha = 15\ \%$, (g) compensated forced jet by square wave at $f_f = 73.5\ Hz$ and $\alpha = 22\ \%$, (h) compensated forced jet by square wave at $f_f = 85\ Hz$ and $\alpha = 24\ \%$, and (i) compensated forced jet by square wave at $f_f = 220\ Hz$ and $\alpha = 62\ \%$. Taken from M'Closkey et al. (2002).

(Figure 1.10(i)) or at a random frequency (Figure 1.10(h)) yielded lesser jet response. The convecting vortex rings in Figures 1.10(e), (f) and (g) improve the penetration and spread of the jets in comparison with those for the unforced jet (Figure 1.10(a)), resulting potentially in better mixing, although this was not quantified due to the diagnostic used. Interestingly, M'Closkey et al. (2002) find that sinusoidal excitation at the same $U'_{j,rms}$ as for square wave forcing does not seem to show noticeable differences from the unforced jet image, although the sinusoidal forcing frequency, 73.5 Hz, is fairly lower than the fundamental shear layer mode at 220 Hz.

Controlled transverse jet excitation studies by Shapiro et al. (2006) utilize the same feedforward controller system as in M'Closkey et al. (2002), and demonstrated for both $R = 2.58$ and 4.0 that square wave forcing at subharmonic frequencies and with temporal pulse widths corresponding to $L/D \approx 4.0$ produce the most deeply penetrating vortical structures. Note that Shapiro et al. (2006) matched the initial peak-to-peak velocity amplitude of a square-wave pulse ΔU_j among different forcing conditions, rather than $U'_{j,rms}$ used by M'Closkey et al. (2002). Shapiro et al. (2006) also approximated the stroke ratio L/D for a partially modulated JICF as $L/D \cong \Delta U_j \tau / D$ to effectively account only for the effect of pulsation of square wave forcing.

Later, Davitian et al. (2010b) applied the feedforward jet control developed in M'Closkey et al. (2002) and Shapiro et al. (2006) to an elevated nozzle, with its exit plane protruding above the test section's floor, as well as a flush nozzle with a smaller diameter matched to that of the elevated nozzle. The study by Davitian et al. (2010b) sought to explore forcing effects for the JICF under clearly absolutely unstable and convectively unstable conditions. For a range of excitation conditions, they quantify the jet penetration and spread from smoke-visualized images via the Canny edge detection method. Sample images for the response of the elevated jet to sinusoidal and square wave excitation are shown in Figure 1.11. This experimental study observed an enhancement of the jet penetration and spread under the effect of either low-to-moderate amplitude sinusoidal excitation or square wave excitation if $R > 3.3$ for the flush nozzle and $R > 1.2$ for the elevated nozzle, corresponding to the convectively unstable regime for the jet's shear layer instability mode (see Section 1.3). But

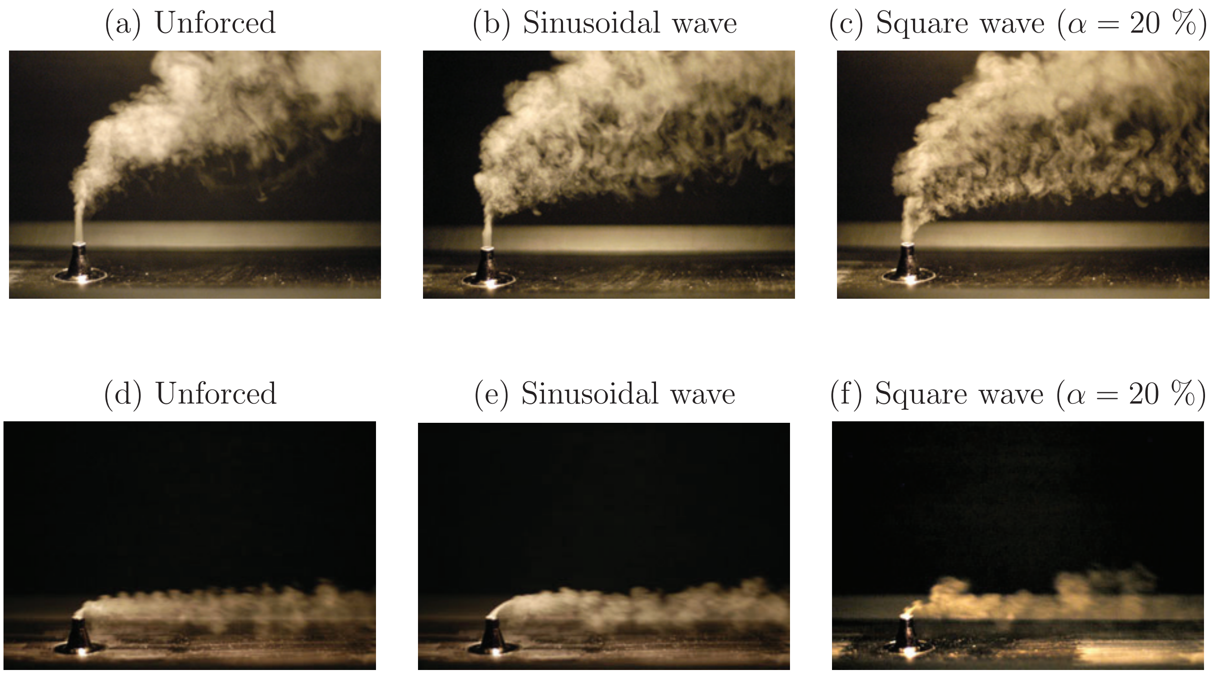

Figure 1.11: Smoke visualization of the unforced and forced jets in crossflow from the elevated nozzle with matching $U'_{j,rms} = 1.7\ m/s$ amongst all excitation cases, the jet-to-crossflow velocity ratio of $R = 10$ (a-c) and $R = 1.15$ (d-f), and jet Reynolds number $Re_j = 2000$. Forcing frequencies of the excitation are $f_f = 0.10 f_o$, where f_o is the dominant shear layer frequency at the corresponding R values, for all forcing cases. Each image displays: (a) unforced jet, (b) forced jet by sine wave at $f_f = 0.10 f_o = 147.2\ Hz$, (c) forced jet by square wave at duty cycle $\alpha = 20$ % and stroke ratio $L/D = 4.9$, (d) unforced jet, (e) forced jet by sine wave at $f_f = 0.10 f_o = 88\ Hz$, and (f) forced jet by square wave at duty cycle $\alpha = 20$ % and stroke ratio $L/D = 7.3$. Data from Davitian et al. (2010b).

such low-to-moderate sinusoidal wave excitation has little impact on the penetration and spread of the jets for $R < 3.3$ for the flush jet or $R < 1.2$ for the elevated jet. For these low velocity ratio jets, the upstream shear layer is in the absolutely unstable regime, as discussed in Section 1.3. But square wave excitation of such jets at lower duty cycle does affect the jet characteristics, as shown in Figure 1.11(f). The periodic vortical structures are pulsed at a frequency that is 1/10 of the frequency associated with the upstream side of the shear layer, resulting in the deeper penetration and wider jet spread.

1.5 Mixing Metrics

Molecular mixing of fluid flows is an important factor to be able to quantify for various applications of jets in propulsion systems. However, there are many different mixing metrics which can be used to quantify diverse flow fields comprising different length- and time-scales. Hence, many studies have been focusing on defining or estimating these different mixing metrics and characteristics. Danckwerts (1952) indicates that the level of mixing in flow fields can be characterized mainly by two elements: (1) a scale of segregation and (2) an intensity of segregation. Danckwerts (1952) describes that the mixing process includes the breaking-up of a clump of fluid from a large scale to a smaller scale, which changes the size of the clump and the molecular interdiffusion, and creates differences in scalar concentration values. The former phenomenon is associated with the scale of segregation and the latter is relevant to the intensity of segregation, examined in the variance of the scalar concentration fields. Kukukova et al. (2009) advance the concept of the segregation proposed by Danckwerts (1952). In addition to the scale and intensity of segregation, Kukukova et al. (2009) propose an "exposure" to quantify mixing in flow fields. The exposure expresses the interaction of a specific scalar concentration with the other concentration values, analogous to the rate of mass transfer across the interfaces of the scalar field. Hence, a higher exposure indicates the higher potential to diffuse and increase the intensity of segregation the molecular interdiffusion.

In the jet's centerplane (x-z plane in Figure 1.1) where $y = 0$, mixing of transverse jet flow has been quantified historically in several different ways. A centerline scalar concentration decay along the jet trajectory (locus of concentration maximum, usually), is sometimes used to quantify downstream mixing for transverse jets (Smith and Mungal, 1998; Su and Mungal, 2004; Getsinger, 2012). For the gaseous JICF, Smith and Mungal (1998) experimentally examined the concentration decay as a function of distance along the jet trajectory s, where s is scaled by velocity ratio and the jet diameter, s/RD, in a logarithmically scaled plot. Smith and Mungal (1998) found that the slopes of the decay curves for various R values were relatively parallel to the line of $(s/D)^{-1.3}$ in the near-field and of $(s/D)^{-2/3}$ in the farfield. Interestingly, as compared to the decay rate of the free jet, s^{-1}, the jets in crossflow exhibit faster decay rate in the near-field but a slower decay rate in the far-field. Smith and Mungal (1998) suggest that this transition occurred approximately around $s = 0.3R^2D$ for $10 \leq R \leq 25$. However, this transitional trend was not observed in the studies of Su and Mungal (2004) for lower R values, e.g., $Re_j = 5000$ and $R = 5.7$. Getsinger (2012) explored lower velocity ratios and density ratios below unity ($Re_j = 1800$, $0.35 \leq S \leq 1.00$ and $5 \leq J \leq 41$ with a flush nozzle), but saw slightly different decay trends. It should be noted that the velocity at the jet exit had a top-hat profile for Smith and Mungal (1998) and Getsinger (2012) but a parabolic profile for the studies in Su and Mungal (2004).

Other mixing metrics that have been widely utilized are jet spread, δ, and jet penetration, P. The spread of the jet is often measured in the direction normal to the jet trajectory direction, s, and the penetration represents the vertical distance between the bottom floor and the upper edge of the jet in z direction, defined in terms of a threshold cutoff in scalar concentration. Both metrics are estimated based on such threshold values of the experimentally or computationally obtained scalar field, which determine the "minimum" jet fluid concentration in the flowfield. For instance, Getsinger (2012) sets 5 % of the maximum concentration value in the centerplane scalar field as the threshold to evaluate the penetration and spread, while Su and Mungal (2004) used 20 % of the maximum concentration value. Getsinger (2012) demonstrated that the equidensity jet in crossflow penetrates more deeply at higher J values, even when the jet velocity is fixed. Getsinger (2012) also suggested that the jet at lower S values less penetrates at $J = 41, 20, 8$ and 5. However, the spread at $S = 0.35$ was greater than that at $S = 1.00$, which is the opposite trend to the penetration and thus unexpected.

Even though the mixing metrics on the centerplane seem to produce useful information on mixing characteristics for the jet in crossflow, one must note that the centerplane jet image only contains the in-plane (x-z plane) components of the jet, but not the cross-sectional or out-of-plane (positive or negative y direction) components of the scalar field. As mentioned in Section 1.1, since the JICF is basically a complex three-dimensional flow field, the out-of-plane scalar field is critical to the mixing characterization. Therefore, Shan and

Dimotakis (2006) and Getsinger (2012) utilized the cross-sectional scalar fields (y-z plane) to evaluate the level of mixing, using the spatial Probability Density Function (PDF) (Shan and Dimotakis, 2006), and Unmixedness and Spatial Mixing Deficiency (SMD) (Getsinger, 2012; Gevorkyan, 2015).

The spatial Probability Density Function (PDF) (Smith and Mungal, 1998; Shan and Dimotakis, 2006) in two-dimensional flow fields can be defined as

$$f(C) = \frac{1}{A_{tot}} \left| \frac{dA(C)}{dC} \right| \tag{1.5}$$

where the area, $A(C)$, is the function representing the area of fluid containing a specific scalar concentration value, and A_{tot} is the total domain of the interrogation scalar field. The PDF theoretically becomes the Dirac delta function at a mean concentration value if the fluids are completely mixed. Thus, more uniform or homogeneous flow fields reveal strong peaks adjacent to the "preferred" mean value. Smith and Mungal (1998) quantified the PDF from the centerplane jet images and categorized the transitions in the PDF plots in the normal direction to the jet trajectory. Shan and Dimotakis (2006) evaluated the PDF from cross-sectional PLIF images of the jet in crossflow, which showed that the scalar field becomes spatially more homogeneous as Re_j increases, associated with the growth of the peak in PDF plots. The peak represents the uniformity of the scalar concentration field. However, the PDF peak diminishes for the free jets as Re_j increases. Shan and Dimotakis (2006) investigated the anisotropy of the jet cross-sections, arising from the turbulence, between in the vertical direction (z direction) and in the horizontal direction (y direction) by using the PDF.

Unmixedness (Danckwerts, 1952; Dimotakis and Miller, 1990; Smith et al., 1997; Getsinger, 2012; Gevorkyan et al., 2016), associated with the intensity of segregation defined by Danckwerts (1952) and Kukukova et al. (2009), basically expresses the variances of the scalar concentrations as compared to the mean concentration values (or the second moment of scalar concentrations) over the entire interrogation area, $L_y \times L_z$. Unmixedness can be defined as follows:

$$U = \frac{1}{L_y L_z} \int \int \frac{(C - \overline{C})^2}{\overline{C}(1 - \overline{C})} dydz \tag{1.6}$$

where C and $\overline{C}$ stand for local and mean scalar concentration values in the scalar field of the interest. Another mixing metric related to the variances of the scalar concentrations is spatial mixing deficiency (SMD),

$$SMD = \left[\frac{1}{L_y L_z} \int \int \left\{ \frac{C - \overline{C}}{\overline{C}} \right\}^2 dydz \right]^{\frac{1}{2}} \tag{1.7}$$

The Unmixedness and SMD are the basically similar metrics except that the normalization factors make a difference, $\overline{C}(1 - \overline{C})$ for Unmixedness and $\overline{C}$ for SMD. This normalization causes Unmixedness to vary between 0 and 1 (or 0 and 100 %). Getsinger (2012) estimates Unmixedness and SMD using the mean cross-sectional concentration fields for jets in crossflow at $x/D = 2.5, 5.5, 10.5$ and 15.5 with the flush nozzle for the range of momentum flux ratios, $2 \leq J \leq 12$. For the fixed S value $S = 1.00$, Unmixedness shows that the $J = 2$ case is the "worst" mixer at $x/D = 2.5$ but the "best" mixer at $x/D = 15.5$. However, SMD suggests that the $J = 2$ case is the "best" mixer for all cases. This quantitatively different result indicates that the normalization factors for Unmixedness and SMD can contribute to a significant change in the mixing characterization and trends, depending upon the flow conditions. Here, it should be mentioned that the mixing quantification based on mean scalar fields could be ambiguous or even incorrect due to the inability to account for structural characteristics. Coussement et al. (2012) proposed that the temporal or spatial averaging of the flowfield can change the mixing trends from their computational study of the pulsed jets in crossflow (details on this issue are described later).

Unmixedness and SMD are useful mixing metrics for a diffusion-dominant flowfield but not for the flowfield in which there is no diffusion, just fluid mechanical stirring. In the case of fluid stirring with or without diffusion, the mean value of the scalar field does not vary in time. But in the case of stirring without diffusion, one needs to use a mixing metric that takes into account the variable scale of segregation of the fluid scalars. Both Unmixedness and SMD neglect the effect of the stirring process occurring at both small and large scales in flow structures.

In a chaotic dynamical system, the quality or efficiency of mixing may indeed depend not only on molecular diffusion but also pure "stirring" of fluid, which is difficult to be evaluated in an open-boundary flow system. Aref (1984) first introduced the concept of chaotic advection based on numerical analysis of a circular stirred tank with two agitators. The study illustrated different stirring effect depending on agitator control parameters even from the same initial flow configuration. The study shows critical points and bifurcations based on integrability of particle trajectories in Lagrangian representation or Hamiltonian system of incompressible, inviscid flow, suggesting the three types of stirring: (1) integrable, (2) transitional and (3) chaotic stirring, where chaotic stirring is the most efficient for the fluid stirring. This study also observed an "island" (or a stable fixed point) even within the chaotic region where particles do not exist and an open region is created. After this pioneering study, many studies associated with chaotic advection or the quality of mixing in closed-boundary or volume preserving dynamical systems were conducted (Rothstein et al., 1999; D'Alessandro et al., 1999; Mathew et al., 2003, 2004, 2005; Gouillart et al., 2006; Mathew et al., 2007; Gubanov and Cortelezzi, 2010). Some of the recent studies are summarized as follows, although basic concepts and theory are well summarized in the works of Ottino (1989) and Aref (2002).

Rothstein et al. (1999) explored persistent flow spatial patterns in a closed-boundary system (an electromagnetically-driven two-dimensional fluid at Reynolds number lower than 100 under time-periodic perturbations) using the intensity variance, that is, the second moment of intensity, which is a L^2-norm mixing metric. They observed the convergence of the variance after a certain number of periods associated with periodic perturbation, which accounts for only intensity but not "stirring" efficiency of mixing. Although Rothstein et al. (1999) applied a L^2-norm mixing metric without accounting for fluid stirring, the main focus was on the persistent flow pattern associated with chaotic advection with fluid stirring, which is not commonly observed even in weakly turbulent flow at lower viscosity. D'Alessandro et al. (1999) utilized a periodic mixing protocol and find the best mixing which maximized the entropy of a dynamical system, or a randomness of the mixing, which is a potential indicator of the effectiveness of mixing if the same initial flow configuration is compared. D'Alessandro et al. (1999) mentioned that the maximum entropy approach does not account for different initial fluid configurations and hence was not appropriate if optimal mixing or mixing efficiency was explored among flowfield containing different initial configurations.

Although the studies summarized above explored stirring effect of fluid in volume-preserving dynamical systems, Mathew et al. (2005) clearly mentioned that maximum entropy approach as well as L^p-norm mixing metrics fail to quantify pure "stirring" effect of fluid or the efficiency of mixing in the absence of diffusion as well as with different initial flow configurations. Hence, the Mix-Norm and Mix-Variance parameters were introduced by Mathew et al. (2003, 2005) as a indicator of the quality of mixing that could be universally applicable for flowfield involving diffusion and stirring. The Mix-Norm can be implemented not only to capture the effects of diffusion, which can be also detected by the L^p norm, but also to capture the stirring process, which cannot be estimated by the L^p norm. The Mix-Norm is based on a variance calculation, similar to that for Unmixedness and SMD, but the Mix-Norm also varies the integration areas throughout its calculation to estimate the level of mixing at one instant of time, to allow capturing small and large length-scales in the flow structures as well as the diffusive processes. The Mix-Norm actually integrates the square of the mean of a spatially- or temporally- averaged function over various length scales contained in the entire interrogation space.

The computational study by Mathew et al. (2004) successfully implemented the Mix-Norm to an active micromixer under time-dependent pressure-driven perturbation of the fluid where fluid stretching and folding associated with the concept of chaotic advection are more dominant than molecular diffusion mainly due to fairly low Reynolds number. They ignored diffusion effects in the simulation for the optimization of perturbation amplitudes and phases to only account for the "stirring" effect of fluid, which cannot be administered by L^2-norm or classic mixing metrics.

Gubanov and Cortelezzi (2010) successfully applied this mixing metric to an advection-dominated flowfield driven by sinusoidal velocity disturbances in the absence of the diffusive effect, with variable operating conditions and mixture configuration. Gubanov and Cortelezzi (2010) indicate that the application of Mix-Norm to the realistic flow fields consisting of inherently three-dimensional concentration fields is quite promising.

Fluid mechanical strain is also relevant to mixing process. Based on the fact that the instantaneous scalar dissipation rate field can be considered as locally one-dimensional shear-like structures, consistent with flamelet modeling in reactive flows, Bish and Dahm (1995) established the so-called strained dissipation and reaction layer (SDRL) model to quantify the local scalar dissipation rate and the strain rate in a non-equilibrium combustion field. While the scalar dissipation rate is related to diffusive and mixing processes, it is readily applicable to chemical reactions as well. This formulation is also confirmed by Buch and Dahm (1996, 1998) suggesting that the dynamics of scalar mixing sustains the sheet-like flow structures, similar to the vorticity fields consisting of the sheet-like and line-like flow structures at unity Schmidt number $Sc \approx 1$, as discussed by Bish and Dahm (1995). Scalar dissipation rate (Bish and Dahm, 1995; Buch and Dahm, 1996; Smith et al., 1997; Buch and Dahm, 1998; Su and Clemens, 1999), χ, in a scalar mixture fraction field, $\zeta(\boldsymbol{x}, t)$, is represented by

$$\chi \equiv \hat{D} \left(\frac{\partial \zeta}{\partial x_i} \right)^2 \tag{1.8}$$

where $\hat{D}$ represents binary mass diffusivity. Next, the local strain rate (Marble and Broadwell, 1977; Bish and Dahm, 1995; Smith et al., 1997), $\epsilon(n)$, can be defined in the layer-normal direction, n, in terms of the scalar dissipation rate χ:

$$\epsilon_{SDRL}(n) \equiv \frac{2\pi\chi(n)}{(\zeta^+ - \zeta^-)^2} exp \left\{ 2 \left[erf^{-1} \left(\frac{\zeta(n) - \frac{1}{2}(\zeta^+ + \zeta^-)}{\frac{1}{2}(\zeta^+ - \zeta^-)} \right) \right]^2 \right\} \tag{1.9}$$

In Equation (1.9), ζ^+ and ζ^- correspond to the "boundary" mixture fraction values as $n \to \pm\infty$, respectively, in the one-dimensional layer-like structures. The strain rate field, ϵ_{ij}, can be also characterized by the symmetric part of the velocity gradient tensor as follows:

$$\epsilon_{ij} = \frac{1}{2} \left(\frac{\partial u_i}{\partial x_j} + \frac{\partial u_j}{\partial x_i} \right) \tag{1.10}$$

It should be noted that the orientations of the strain rates from Equations (1.9) and (1.10) are different. In a combusting flow, there is a critical strain rate at which the diffusive transportation between the fuel and oxidizer cannot be achieved at the interface of a flame sufficiently to sustain the flame. If the thickening effect of the flame, associating with the fuel/oxidizer reaction and diffusion, does not balance or overcome the stretching at the flame interface, the flame extinguishes. Hence, higher strain rate fields decrease the possibility of preserving the combustion process. Bish and Dahm (1995) applied this formulation to the experimentally obtained OH planar laser-induced fluorescence (PLIF) images of turbulent flows to estimate the strain rate field. Bish and Dahm (1995) concluded that the above formulation is applicable to non-reactive scalar field measurements to predict whether or not flame extinction would occur in a reactive flowfields. At UCLA, Smith et al. (1997) used this formulation (Equations (1.8) and (1.9)) for a non-reactive flow field, involving a flow from a lobed injector issuing parallel into crossflow, to calculate the local scalar dissipation rate and strain rate downstream of injection. The results were comparable to corresponding reactive experiments by Mitchell et al. (1998, 2004).

The experimental studies of non-reactive gaseous JICF by Gevorkyan (2015) and Gevorkyan et al. (2017) primarily explored the interplay between velocity- and scalar-field dynamics utilizing simultaneous acetone PLIF and stereo PIV measurements. Proper orthogonal decomposition (POD) was applied to both PLIF and PIV data in order to extract the most dominant mode flow structure. Both PLIF- and PIV-extracted POD showed clear periodicity on the upstream shear layer for the equidensity JICF at $J = 5$ (absolutely unstable upstream shear layer), but only PIV-based POD provided periodicity at $J = 12$ (transitional upstream shear layer), suggesting different periodic behaviors between velocity and scalar fields, as noted by Kothnur and Clemens (2005). This discrepancy was also observed in the comparison between scalar dissipation rate χ from PLIF data and PIV-extracted strain rate in the mixing layer-normal direction (or equivalently the scalar gradient direction), especially for the $S = 1.00$ and 0.35 flush nozzle-injected JICF at $J = 5$ on the downstream mixing layer because of strong three-dimensional effect. They also applied Equation (1.9) to estimate local strain rates on upstream and downstream mixing layers for the JICF in the layer-normal direction based on acetone PLIF scalar data. Strain rate in the same layer-normal direction was also calculated based on PIV data for comparison. Remarkably, for the equidensity flush nozzle- and flush pipe-injected JICF at $J = 41$, 12 and 5, PLIF- and PIV-based strain rates suggest a qualitatively good agreement, in general, although considerable quantitative difference was observed. In addition, lower strain rates are generally observed on the lee side of the jet than that on the windward side, suggesting that a flame is more easily ignited or less often extinguished on the lee side if reactive flow is used, which is consistent with reactive flow experiments by Sullivan et al. (2014); Wagner et al. (2015). For the $S = 0.35$ JICF, Gevorkyan et al. (2017) applied Howarth transformation to make flowfields effectively incompressible and enabled strain rate evaluations. More details on works by Gevorkyan (2015) and Gevorkyan et al. (2017) are discussed in this dissertation as well (see Chapter 3).

Coussement et al. (2012) introduced another mixing metric, so-called $\langle M \rangle$ mixing criterion defined as

$$M(Y_1, Y_2, t) = \frac{\int_{Y_1}^{Y_2} \dot{m}_Y dY}{< \dot{m}_{tot} >} \tag{1.11}$$

where

$$\dot{m}_{Y^*} = \int\int (\rho Y V_n|_{Y=Y^*}) dS \tag{1.12}$$

stands for the instantaneous mass flow rate longitudinally passing through a cross-section S of a flowfield, with a given mass fraction Y^*. $\langle M \rangle$ physically represents, at a given location, the temporally averaged mass flow rate of fluid with mass fractions lying between Y_1 and Y_2, normalized by the total mass flow rate. If the $\langle M(0, Y) \rangle$ mixing criterion, as a function of an arbitrary mass fraction, Y, reaches unity quickly, better mixing has been accomplished since most of the flow constituents possess lower mass fractions, equivalent to a lower intensity of segregation. One can also interpret the criterion by noting that there is a maximum existing mass fraction at a given location, Y_{max}, for $\langle M(0, Y) \rangle$ at which $\langle M(0, Y_{max}) \rangle = 1$. This formulation suggests that the $\langle M \rangle$ mixing metric could be effective for the JICF configuration, since one could associate $\langle M \rangle$ with the mass flow rate of the jet as well as crossflow. Coussement et al. (2012) also indicate that SMD estimation based on temporally-averaged scalar fields might be erroneous from a comparison study between the $\langle M \rangle$ criterion and SMD, because the mean scalar fields are disregarded in the instantaneous vortex structures convecting the flowfield, which is considered crucial for mixing processes as mentioned in Section 1.1.

Although many mixing metrics are described here, the mixing quantification generally involves challenges, especially in non-volume-preserving systems or equivalently open-boundary systems. First, as mentioned in the Mix-Norm description, the interrogation area where mixing metrics are estimated is related to the quantitative measure of mixing, that is, if the size or location of the interrogation area changes, the quantitative values or the trends of the mixing metrics can vary. The same thing applies to Unmixedness and SMD. Second, Unmixedness and SMD estimations are based on the fact that the concentration values in the flowfield finally approach the mean value, if the fluids are eventually perfectly mixed. However, the eventual concentration value for the "perfect" mixing in the specified interrogation area may not necessarily be its mean value. Moreover, one can apply a desired concentration value, instead of the mean value of the entire interrogation area, to Unmixedness and SMD formula to evaluate the degree of mixing for real application systems by choosing an alternate interrogation area, and thus to analyze how well the systems are designed to satisfy the requirements of the mixing conditions. Hence, in determining the appropriate mixing calculation, one has to determine the mean value or the desired mixture value for the flowfield, depending on the application. This difficulty in determining the mixing criterion causes the secondary issue that if the mean values differ among the same fundamental flowfield with varying the flow conditions, each flowfield might not be comparable because the required mixing conditions could be significantly different.

The experimental study by Gevorkyan et al. (2016) utilizing acetone PLIF imaging sheds light on the molecular mixing evaluation for the JICF, relevant to open-boundary systems. Gevorkyan et al. (2016) developed a new algorithm to evaluate molecular mixing of the JICF based on the Unmixedness and PDF of scalar values, which is potentially applicable to a wide range of open-boundary flow configurations. The basic concept of the newly developed

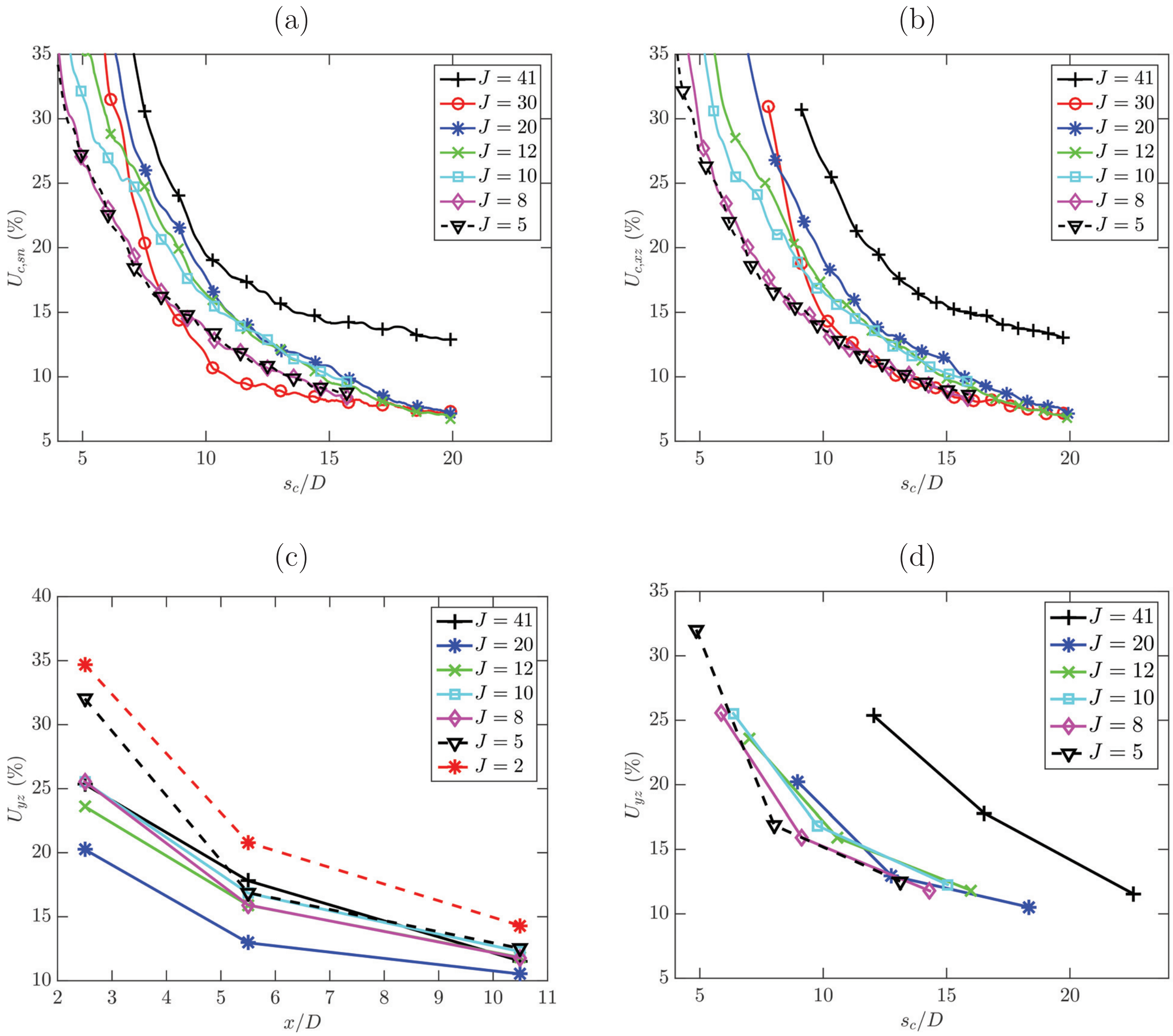

Figure 1.12: Mixing evaluation using centerplane- and cross-section-based Unmixedness. Taken from Gevorkyan et al. (2016): (a) centerplane-based Unmixedness $U_{c,sn}$ evaluated in a transformed plane ($s_c - n$ plane) along the jet centerline trajectories s_c/D, (b) centerplane-based Unmixedness $U_{c,xz}$ evaluated in a regular plane ($x - z$ plane) along the jet centerline trajectories s_c/D, (c) cross-section-based Unmixedness U_{yz} evaluated in a regular plane ($y - z$ plane) along the horizontal coordinate x/D, (d) U_{yz} along the jet centerline trajectories s_c/D.

algorithm encompasses variable sizes of an interrogation area, by adding or removing zero scalers, to match the mean value of scalar among different flow conditions for direct comparison. Such variable interrogation area enables one to apply mass conservation to each interrogation area, as demonstrated in the work of Shan and Dimotakis (2006). Based on the Unmixedness and PDF with the new algorithm employed in centerplanes and cross sections, as well as classic centerplane-based mean mixing metrics (e.g., maximum concentration decay), the degree of molecular mixing for the JICF was extensively explored for a range of $S = 0.35 - 1.00$, $J = 2 - 41$ and injections (see Section 2.1) at a fixed jet Reynolds number of $Re_j = 1900$. Some of their mixing evaluations for the equidensity ($S = 1.00$) flush nozzle-injected JICF at $J = 2 - 41$ in centerplanes and cross sections are shown in Figure 1.12 with two different coordinates, horizontal coordinate x/D and jet centerline trajectory coordinate s_c/D defined as a power-law fit to maximum concentration loci in mean PLIF images over all instantaneous images. Gevorkyan et al. (2016) indicated that the decay of Unmixedness is more rapid for the $S = 1.00$ flush pipe-injected JICF than the $S = 1.00$ flush nozzle-injected JICF. Among the flow conditions for the $S = 1.00$ flush nozzle-injected JICF ($5 \leq J \leq 41$), the decay of the Unmixedness is more vigorous at $J = 20$ and 30 than the other conditions. Also, for the flush nozzle-injected JICF at relatively high J (e.g., $J = 41$), molecular mixing at a given s_c location is enhanced, corresponding to lower Unmixedness, as S decreases from $S = 1.00$ to $S = 0.35$ mainly due to higher crossflow entrainment within the rollups on the upstream shear layer. In contrast, for the absolutely unstable flush nozzle-injected JICF at $J = 5$, lowering S worsens molecular mixing because of the nature of entrainment of high-density fluid into shear layer vortices by lower S jets. More details about mixing metrics, their application of the algorithm, and mixing characteristics of the JICF are described in Gevorkyan et al. (2016).

1.6 Current Study

Gevorkyan (2015) and Gevorkyan et al. (2016, 2017) extensively studied the influence of velocity fields on scalar transport of the JICF for a range of S, J and injections (flush nozzle and pipe, see Section 2.1), as summarized in Section 1.5, although alterations in the algorithm for the PLIF-based strain rate calculation and its quantification for the $S = 0.35$ flush nozzle-injected JICF, as well as further exploration of the effect of spatial resolutions (equivalently pixel resolution here) on POD analyses were done as part of the present study. Therefore, further in-depth exploration of strain rate characterization for the JICF via simultaneous PLIF/PIV measurements is one of the objectives in this study.

Secondly, as described in Section 1.5, Gevorkyan et al. (2016) explored molecular mixing of the unforced JICF for widely varying flow conditions with a length scale of the size of a pixel in PLIF images. However, such a L^2-norm mixing metric is not capable of quantifying the effect of fluid mechanical stirring as well as mixing occurring with different length scales. The Mix-Norm, for example, has been successfully applied to volume-preserving systems even without diffusion to quantify the efficiency of mixing for various length scales, although it is highly challenging to implement the Mix-Norm in open-boundary flow systems. Hence, this study develops a new algorithm based on both the Unmixedness and Mix-Norm to quantify mixing in open-boundary systems (e.g., the JICF) but with various length scales, which may provide different insights into mixing dynamics associated not only with molecular diffusion but also with fluid mechanical stirring, a phenomenon particularly relevant to vortical structures.

Prior sections of this chapter (Sections 1.1 to 1.5) have discussed studies which have focused on the stability, structural and mixing characteristics of the unforced jet in crossflow, as well as (separately) JICF excitation using sine and square wave forcing. As summarized, the stability, structural and mixing characteristics have recently been examined both qualitatively and quantitatively via laser-based optical diagnostics in the absence of forcing. However, the quantitative structural and mixing evaluation for the forced JICF for centerplanes and cross sections has not been conducted in a detailed manner via such diagnostics, at least, enough to conclude or determine which flow or forcing conditions actually yield the best molecular mixing in a given application system. Even though the previous studies (M'Closkey et al., 2002; Shapiro et al., 2006; Davitian et al., 2010b) explored structural and mixing characteristics for the forced JICF based on the jet spread and penetration in the centerplanes using smoke visualization, more in-depth exploration is required, using more appropriate experimental techniques for the quantification of molecular mixing (i.e., acetone PLIF imaging in this study). Moreover, only a few studies have focused on forcing the

JICF and quantifying the actual degree of mixing and its enhancement (or not). If mixing enhancement of the forced JICF as compared to the unforced JICF can be quantitatively determined, the research could significantly contribute to a true optimization of the flow-field for various energy and propulsion system applications. Hence in this study, our main emphasis is on exploration of the instability, structural and mixing characteristics for the equidensity ($S = 1.00$) forced jets in crossflow with various J values, which alters the type of instability in the upstream shear layer. Forcing methods applied in this study are sine wave forcing, single-pulse square wave forcing as well as double-pulse square wave forcing, which triggers near-field vortex interactions or collisions. Scalar concentration fields in the centerplane and cross-sectional planes are obtained via acetone-PLIF imaging, which is used for structural investigations as well as mixing quantification.

This dissertation is organized as follows. Chapter 2 describes the experimental configuration associated with our wind tunnel facility, hotwire anemometry, laser diagnostics and the actuation system designed to create external forcing of the jet. A newly developed image processing method for PLIF images (i.e., for laser energy absorption correction) is also documented. Chapter 3 discusses the strain rate quantification for the low density JICF based on simultaneous PLIF/PIV measurements. The main focus there lies in the detailed explanation of an algorithm to calculate PLIF- and PIV-based strain rates, and further POD analysis with variable spatial resolution in PLIF images and the strain rate evaluation for the $S = 0.35$ flush nozzle-injected JICF at $J = 5 - 41$ by applying the Howarth transformation. Chapter 4 explores mixing quantification for the JICF accounting for mixing length scale, in contrast to that previously explored using the Unmixedness with a single length scale (Gevorkyan et al., 2016). A new algorithm taking into account mixing length scale is developed based on the Unmixedness for open-boundary systems (Gevorkyan et al., 2016) as well as the Mix-Norm developed by Mathew et al. (2003, 2005). Chapters 5-7 investigate the effect of sine, single-pulse square, and double-pulse square wave excitation of the jet, respectively, on instability, structural and mixing characteristics for the equidensity JICF with variable J ($5 \leq J \leq 41$). Mixing characteristics are examined using mean and instantaneous mixing metrics with the same algorithm as in (Gevorkyan et al., 2016). Finally, Chapter 8 summarizes our findings, conclusions, and implications of the present study and future directions.

CHAPTER 2

Experimental Configuration

2.1 Wind Tunnel Configuration for Jet in Crossflow

This experimental study utilized a low-velocity wind tunnel to measure jet in crossflow (JICF) characteristics. A schematic of the wind tunnel and associated diagnostics is shown in Figure 2.1. A crossflow of air in the downstream (positive x) direction was created by a centrifugal blower (Baldor M3546-T) placed upstream of the test section through a flexible duct which decreased a oscillatory effect of the blower on the test section. A frequency controller was connected to the blower and was capable of adjusting the rotational frequency, and hence the volume flow rate of crossflow in the tunnel or crossflow velocity, U_∞, calibrated in the tunnel using a pitot tube (see Section 2.2).

The flow from the blower issued into the test section through a 9 : 1 area ratio contraction section with honeycomb and screens with decreasing cell and mesh sizes to straighten the crossflow (Barlow et al., 1999). The maximum achievable flow velocity in the test section was approximately 7.00 m/s, at which a maximum turbulence intensity was less than 1.5 % in the freestream. In this experimental study, two test sections were used. The first primary test section, fitted flush with the contraction section, was used for all experiments in this study including hotwire anemometry (see Section 2.2) as well as laser diagnostics (see Section 2.3), e.g., planar laser-induced fluorescence (PLIF) imaging, particle image velocimetry (PIV) measurements and simultaneous PLIF/PIV measurements, with/without axisymmetric excitation. The size of the test section was 30 cm $\times$ 12 cm $\times$ 12 cm. Black paint was sprayed on the tunnel floor to lessen the reflection of the laser sheet coming from the top of the test section through a quartz window. The quartz window did not reflect or significantly

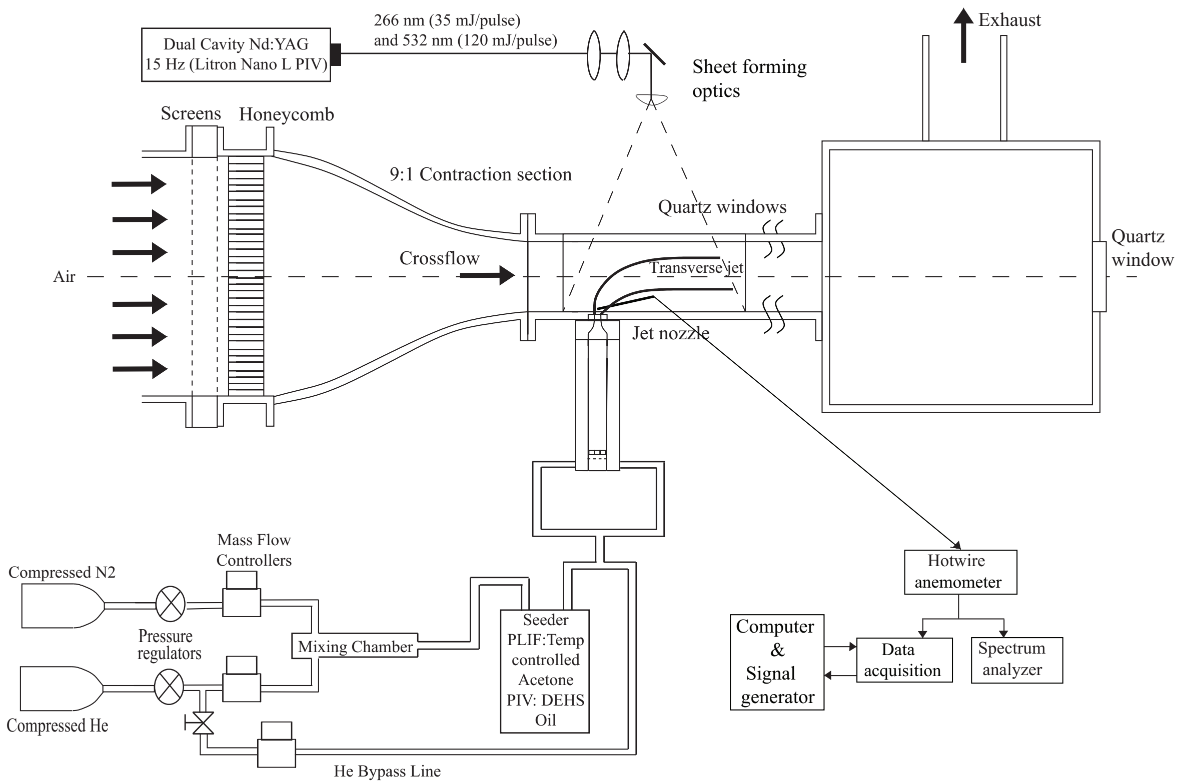

Figure 2.1: Experimental configuration associated with low-velocity wind tunnel, laser optical alignment, hotwire anemometry and jet flow lines.

attenuate incident ultra-violet light applied PLIF imaging as compared with plexiglass. A plexiglass window was fitted into the side of the test section to enable optical device access (e.g. camera) and sealing of the fluid inside the test section. A black panel was also used instead of the side plexiglass window in case without camera operation to confine the fluid inside the test section. Hotwire anemometry required a cut-out in the black panel to employ traversal of the hotwire mechanism.

Another tunnel section with the same size was placed downstream of the primary one, not shown in Figure 2.1. The secondary tunnel section consisted of ceramic heat-resistant walls without optical access which can be potentially used for reactive JICF experimentation, although the present experiments were non-reactive. The purpose of the second tunnel section was to have a distance between the jet and ventilation system, resulting in removing the effect of the pressure change on the jet due to the gas exhaustion. The second tunnel section was followed by a wood cubic box with dimension of 30 cm $\times$ 30 cm $\times$ 30 cm. The

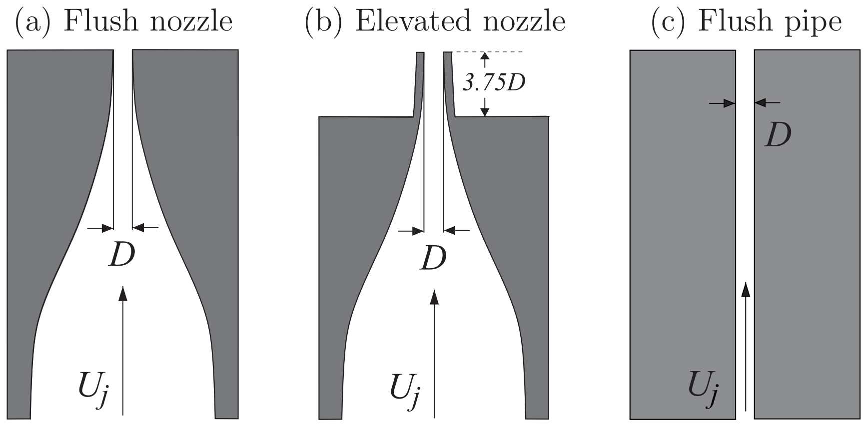

Figure 2.2: Injector designs utilized in transverse jet experiments.

box allowed optical access from the downstream end of the tunnel through 90 mm × 90 mm quartz window. Cross-sectional PLIF data in the $y - z$ plane were taken through this end window, with the camera oriented in the negative x direction. The wooden box exhausted the fluid via a flexible tube mounted on the top into the ventilation system of the lab.

Jet flow issued perpendicularly into the test section through an injection system connected to the primary test section's floor. The injection system mainly consists of an injector as well as a longitudinal straight PVC pipe with a length of $L = 0.9$ m attached to the injector to eliminate swirl or other asymmetries via internally attached honeycomb flow straighteners with a 2.5 cm length and 0.3 cm cell size. The length-to-diameter ratio L/D of the PVC pipe is large enough to create a fully developed laminar velocity profile at its exit, which contributes to the uniformity of flow issuing into the injector. Yet the PVC pipe can be removed from the injection system, depending on the aim of experiments.

To explore various flow fields, four types of injectors were implemented in this study, three of which were designed to have the same exit diameter (although minor machining errors created slight sizing discrepancies). The three with the same exit diameter are shown in Figure 2.2. The flush nozzle (Figure 2.2(a)) had a $D = 4.04$ mm exit diameter mounted flush to the bottom floor of the test section. The inner surface of the flush nozzle was formed as a 5^{th} order polynomial contraction, creating a top-hat velocity-like distribution with a fairly thin jet boundary layer in the absence of crossflow, as documented in Megerian et al. (2007).

The elevated nozzle (Figure 2.2(b)), whose exit diameter was $D = 3.94$ mm, possessed an identically designed inner configuration to that of the flush nozzle, but its exit plane protruded above the test section's floor by 3.75 jet diameters. Therefore, the elevated jet fluid issued into the crossflow outside of or above the crossflow (wall) boundary layer, which had a maximum value of $\delta_{99\%}/D \approx 2.3$ for the lowest crossflow velocity condition explored here, $U_\infty = 1.01$ m/s. The protrusion of the jet results in different velocity profiles at the jet exit with crossflow between the flush and elevated nozzles despite the same inner design, especially at fairly low jet-to-crossflow velocity ratio R, as documented in Megerian et al. (2007). The flush straight pipe (Figure 2.2(c)) was mounted flush to the tunnel wall with an exit diameter $D = 3.77$ mm and a length $L = 0.6$ m, and hence $L/D \approx 159$, large enough to achieve a fully-developed laminar parabolic velocity distribution at the exit in the absence of crossflow, which was confirmed via hotwire anemometry at the jet Reynolds number explored in this study, as shown in Figure 2.3. Hence, the flush pipe was utilized without the PVC pipe situated upstream of the injector. Lastly, a fourth flush nozzle was also utilized here but only for the study of double-pulse square wave forcing described in Chapter 7. This nozzle had a diameter of $D = 7.59$ mm emanating from a 5^{th} order polynomial contraction; it had the same kind of design as the flush nozzle with $D = 4.04$ mm but with a different exit. This larger-diameter flush nozzle was used in our group's earliest studies (M'Closkey et al., 2002; Shapiro et al., 2006), and created larger length-scales in flow structures e.g. the size of vortices in the upstream jet shear layer, than for the nozzle in Figure 2.2(a). This larger nozzle enabled visualization of clear vortical structures explored with the double-pulse square wave excitation. All injectors were mounted to the same downstream location in the test section floor, 9.5 cm downstream of the end of the tunnel contraction.

The jet fluid was comprised of mixtures of He, N_2 and tracers for laser diagnostics, enabling densities to be at or below that of the crossflow air. Mass flow controllers manufactured by Tylan (Model FC-260, (1) 0-5 NLPM N_2 and (1) 0-5 NLPM He, 1 % calibration accuracy, 0.2 % repeatability) and MKS Instruments (Model GM50A, 0-70 NLPM He, 1 % calibration accuracy, 0.3 % repeatability) were used to vary the He and N_2 mass flow rates that controlled the jet flow, consequently affecting the jet Reynolds number Re_j and jet-to-crossflow

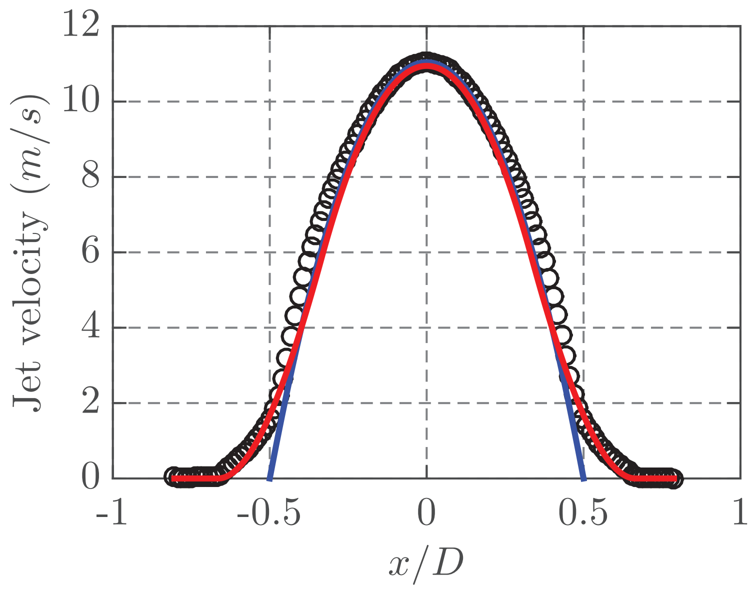

Figure 2.3: Parabolic jet velocity distribution in the $y = 0$ plane for the nitrogen flush pipe-injected free jet in quiescent surroundings at the jet Reynolds number $Re_j = 1900$. Data points (∘) are acquired via hotwire anemometry $0.1D$ above the jet exit plane. Two lines are theoretical fully-developed laminar parabolic velocity distributions without (—) and with (—) the hotwire length (1.25 mm or $0.33D$) effect in the x/D direction, respectively.

density ratio S. A dSPACE 1104 digital signal processing with ControlDesk software, configured by Matlab Simulink, controlled the Tylan mass flow controller according to voltage inputs. The voltage at the Tylan flow controller was also monitored by a multimeter (Fluke model 77 series II) to confirm whether or not the voltage input was correctly assigned to the controller. For the MKS mass flow controller, an internet connection between the controller and a computer established the ability to utilize MKS network-based control via an assigned IP address to the controller. The Tylan controller was used for all density ratios explored here, $S = 1.00$, 0.55 and 0.35, but the MKS controller was only applied for the $S = 0.35$ condition because the low density ratio experimentation required bypass (by the Tylan flow controller) and seeding (by the MKS flow controller) lines separately in order to simultaneously regulate the mole fraction of acetone (see Section 2.3.1) and the density ratio for the jet.

A flow filter to eliminate impurities from the N_2 and He flow was employed between pressurized gas cylinders and the flow controllers. Jet flows composed of the mixture of He and N_2 were mixed in a long, cylindrical chamber placed downstream of the flow controllers to passively remove non-uniformity of the gases. The mixed fluid flowed into a temperature-controlled acetone seeder for PLIF measurements or into a particle seeder for PIV measurements, as will be described below. The seeded mixture then entered four symmetrically center-oriented injectors attached to an 8 mm plexiglass pipe beneath the injection system (the injector and PVC pipe).

Axisymmetric excitation for the JICF can be applied from the bottom of the plexiglass pipe by two different methods. In one method, an acoustic loudspeaker (RadioShack 40-1022B, 4″ woofer) oriented toward the injector exit can create a sinusoidal oscillation or, with control, single- and double-pulse square wave excitation (M'Closkey et al., 2002; Shapiro et al., 2006; Davitian et al., 2010b) of the jet fluid in time. This speaker is enclosed by a plexiglass plenum housing attached to the bottom of the plexiglass pipe even for unforced transverse jet experimentation. The loudspeaker can be utilized either with or without the PVC pipe in between the plexiglass pipe and the injection system, which will be described in Section 2.4. The other method can generate sinusoidal or square waves via feedback control (Hendrickson and M'Closkey, 2012) by an aluminum piston attached to a modal shaker (Ling LVS-100). These excitation methods were applied successfully in previous work to create an axisymmetrically excited JICF, although this method was eventually not applied in the present study.

The Reynolds number of the jet was based on the mean jet velocity at the injector exit, U_j, injector exit diameter, D, jet density, ρ_j, and viscosity, μ_j. The jet Reynolds number was kept constant at $Re_j = 1900$ for the three injectors with a diameter $D \approx 4$ mm, as shown in Figure 2.2, and at $Re_j = 1500$ with the larger-diameter flush nozzle, while jet-to-crossflow density ratio ($0.35 \leq S \leq 1.00$) and momentum flux ratio ($5 \leq J \leq 41$) were independently varied to explore the effect of these parameters on JICF characteristics. Yet only the equidensity case ($S = 1.00$) was explored with forcing. The desired density ratio S was achieved by controlling the amount of N_2, He and acetone for PLIF imaging in the jet, and J was altered for a given S by varying the crossflow velocity. The mean jet velocity was determined by averaging the velocity distribution at the nozzle exit over its diameter. Jet flow consisted of N_2, He and acetone (utilized for PLIF); hence, jet density and viscosity were calculated considering all constituents in the jet depending on experimental conditions. The viscosity of the jet was determined by the Wilke formulation without acetone in the jet (Bird et al., 1960) and the Reichenberg method with acetone (Poling et al., 2001). Details on the methods for determining jet density and transport properties for these mixtures may be found in Getsinger (2012).

2.2 Hotwire Anemometry

This experimental study applied constant temperature anemometry (CTA) with and without forcing, and with and without seeding acetone in the jet. A single-component, boundary-layer type hotwire probe (Dantec 55P15) was used for measurements of crossflow boundary layer (Getsinger et al., 2014), jet flow velocity profiles (Megerian et al., 2007), and in spectral measurements of the jet's upstream shear layer (Megerian et al., 2007; Davitian et al., 2010a; Getsinger et al., 2012, 2014) as well as temporal jet velocity measurements in the vicinity of the jet exit with axisymmetric forcing (M'Closkey et al., 2002; Shapiro et al., 2006; Davitian et al., 2010b). The latter were specifically conducted 0.2 jet diameter above the center of the jet exit plane with seeding acetone in the jet in the current study. The hotwire was inserted through a cut-out in the black side wall of the test section and was three-dimensionally movable, with 1 μm accuracy, using a triple-axis linearly-staged platform. The data taken by the hotwire were delivered first to a 90C10 constant temperature anemometer module in a Dantec StreamLine 90N10 frame and then to an AC/DC signal splitter with signal conditioning developed by Hendrickson (2012). The conditioned AC and DC signals were combined and analyzed by a dSPACE 1104 DSP data acquisition (DAQ) board with ControlDesk software established by Matlab's Simulink program at a sampling frequency of 20 kHz. Spectral data were fed to a dual channel dynamic signal analyzer (HP Model 35665A) instead of the DAQ board and averaged over 40 instantaneous frequency distributions. The spectral measurements were applied over a 6.4 kHz range and with 8 Hz resolution. For

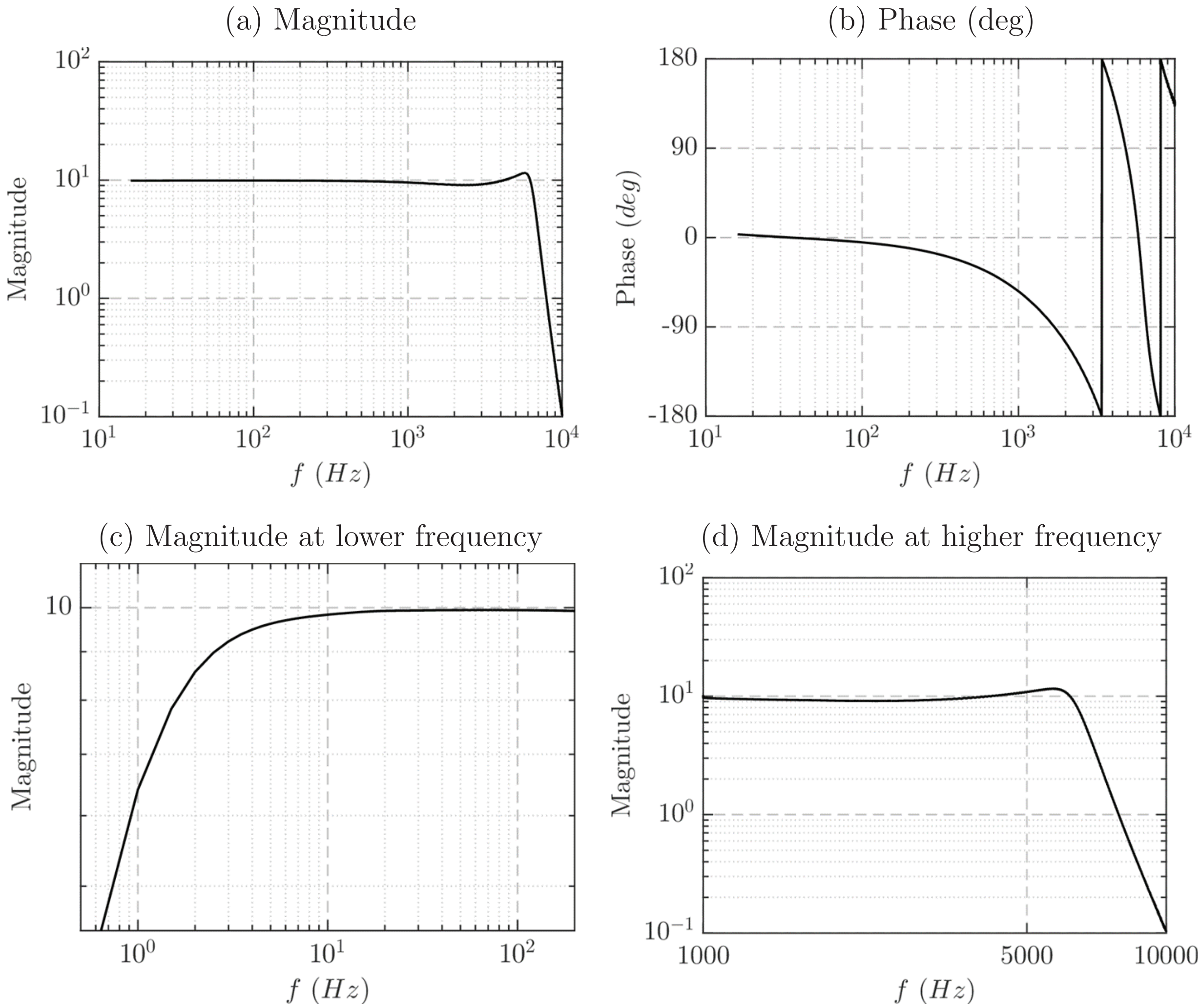

Figure 2.4: Frequency response measurement of the AC component of a signal splitter utilized for hotwire anemometry: (a) magnitude, (b) phase (deg), both of which are taken with a frequency sweep from 10 Hz to 10 kHz, (c) magnitude with frequency sweep in a lower range (0 to 200 Hz), and (d) magnitude with frequency sweep in a higher range (1 to 10 kHz).

thorough details on spectral measurements, see Getsinger (2012) and Gevorkyan (2015).

The signal splitter consisted of a gain and phase delay separately for AC and DC components, as shown in Figures 2.4 and 2.5. The frequency response data of the signal splitter were acquired via the dynamic signal analyzer by averaging 60 instantaneous frequency distributions. Figures 2.4(a) and 2.5(a) associated with a gain demonstrate that AC and DC signals were amplified by a factor of 10 and 2, respectively. These gains contributed to better

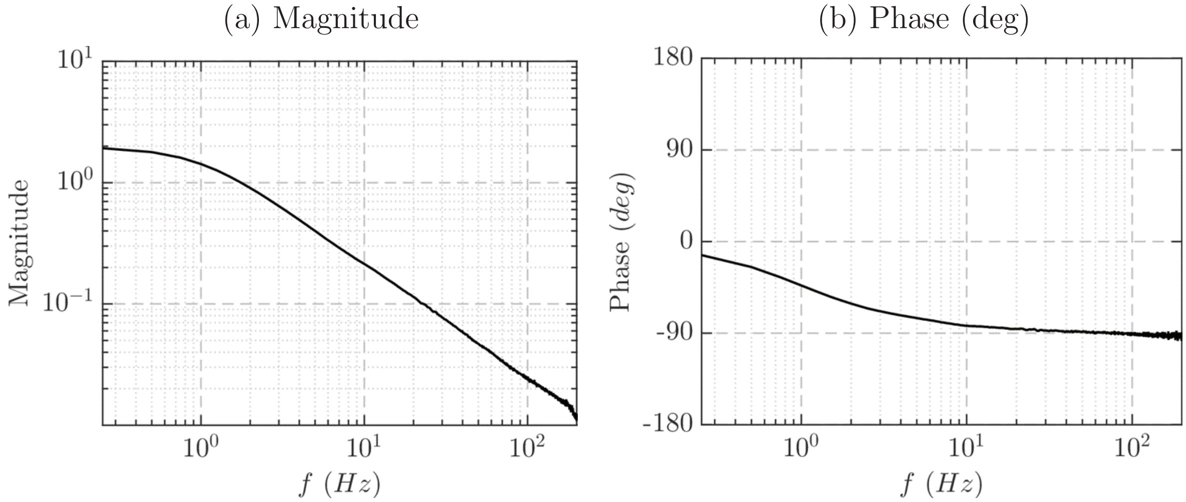

Figure 2.5: Frequency response measurement of the DC component of a signal splitter utilized for hotwire anemometry: (a) magnitude and (b) phase (deg). Frequency sweep was administrated from 0 to 200 Hz.

sensitivity of signals by the DAQ board. The amplified AC and DC signals were multiplied by a factor of 1/10 and 1/2 in the DAQ board, respectively, as compensation when the original signal was reconstructed. The AC component in the signal splitter consisted of a phase lag clearly after 100 Hz (Figure 2.4(b)), as well as a high- and low-pass filtering effects at a corner frequency of approximately 10 Hz and 6 kHz, respectively (Figures 2.4(c) and (d)). The frequency response data associated with DC magnitude (Figure 2.5(a)) revealed a roll-off after 0.5 Hz to eliminate AC components in a signal.

For the hotwire calibration, a pitot tube and crossflow from the blower (see Section 2.1) were utilized with air flow. The pitot tube was placed at the middle of the test section and connected to a 0-3″ H_2O differential pressure transducer (Omega PX653-03D5V) for higher-velocity range calibration, and a 0-0.25″ H_2O transducer (Omega PX653-0.25D5V) for lower-velocity range calibration. Since the calibration was based on air flow, the fluid properties applied in experiments had to be relatively similar to those of air, hence the calibration did not apply to low density jets or jets with acetone seeded for laser diagnostics. As mentioned in Section 2.1, this method also calibrated the blower by correlating its rotational frequency with voltage at pitot tube, namely crossflow velocity. The blower calibration utilizes a 0-

$0.25''$ H_2O pressure transducer, which is used in the hotwire calibration for lower-velocity range.

The hotwire anemometry was implemented in experiments with sine wave jet forcing, as well as single- and double-pulse square wave excitation to measure root-mean-square (RMS) of the jet velocity $U'_{j,rms}$. For the exploration of JICF characteristics under these forcing conditions, PLIF imaging was the primary diagnostic. To correlate the PLIF data and $U'_{j,rms}$, hotwire anemometry had to be implemented with acetone in the jet for accurate quantification. Hence, a different method was applied to calibrate the hotwire with acetone from that without acetone.

For calibration of the hotwire with acetone, we use a fully-developed laminar parabolic velocity distribution at the injector exit created by the flush pipe-injected jet but in the absence of crossflow. Since the velocity profile clearly followed the Hagen-Poiseuille relation in the laminar regime, and knowing the mass flow rates and bulk velocity of the jet, a correlation between hotwire voltage and jet velocity enabled hotwire calibration. This calibration is called the laminar pipe-flow method, as documented in Lee and Budwig (1991). The hotwire was situated at the center of the flush pipe exit plane during the calibration to acquire temporally averaged hotwire output voltage over 20 seconds for statistical convergence. The hotwire voltage was correlated to a mean jet velocity over the hotwire length of 1.25 mm, $U_{j,wire}$, calculated from the Hagen-Poiseuille formulation within the hotwire length. The effect of the hotwire diameter of 5 μm, which was significantly smaller than the hotwire length, was neglected to calculate $U_{j,wire}$. This calibration was performed at constant $S = 1.00$ but with a variable jet Reynolds number for the range of $300 \leq Re_j \leq 2300$, keeping the mole fraction of acetone in the jet within ± 1 % of the actual value during PLIF imaging. The maximum jet Reynolds number was verified to still create a fully-developed laminar parabolic velocity distribution via hotwire anemometry. The calibration data points were fitted to a modified King's law suggested by Lee and Budwig (1991) as follows:

$$V_{hw} = A + BU^n_{j,wire} \tag{2.1}$$

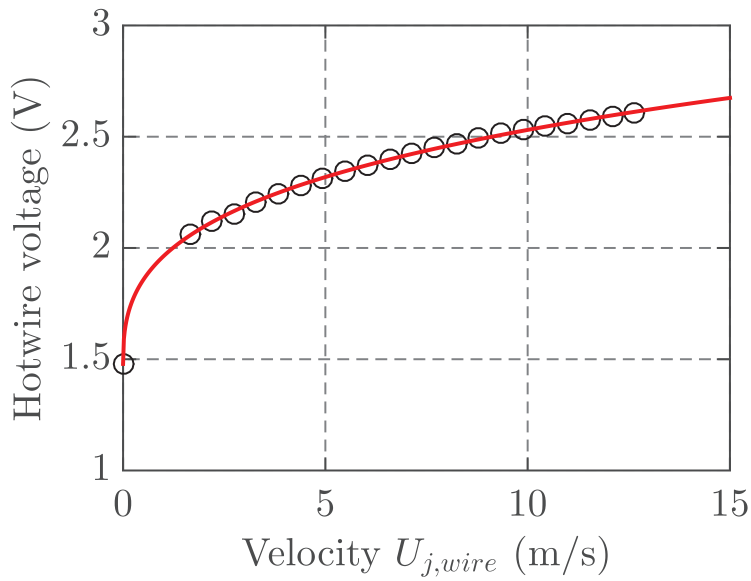

Figure 2.6: Typical hotwire calibration curve with seeded acetone in the jet for PLIF imaging generated using the laminar pipe-flow method. Black circles and the red line represent raw data points ($1.6 \leq U_{j,wire} \leq 13$ m/s or equivalently $300 \leq Re_j \leq 2300$) and a fitting based on a modified King's law (Lee and Budwig, 1991), respectively, as shown in Equation (2.1), where $A = 2.19$, $B = 1.67$ and $n = 0.40$ in this case.

where V_{hw} is the mean hotwire output voltage, and A, B, and n are constants for the best fit, respectively. This process yielded a hotwire calibration curve as shown in Figure 2.6. Due to the limited range of the jet Reynolds numbers in the calibration, the reliable velocity range was also limited, although the calibration curve was plotted for a wider range of velocity. For instance, the valid velocity in experiments ranged from $1.6 \leq U_{j,wire} \leq 13$ m/s in Figure 2.6. Note that because the maximum hotwire temperature (300 °C) is lower than the autoignition temperature of acetone (465 °C), the hotwire anemometry was able to be safely implemented. Additionally, the maximum obtainable frequency via CTA was 400kHz, which was significantly higher than the maximum forcing frequency of 6000 Hz imposed in the experiments.

2.3 Laser Diagnostics

Laser diagnostics were utilized to study the JICF flowfield in a non-intrusive manner, focusing on structural and mixing characteristics using planar laser-induced fluorescence (PLIF) imaging of seeded acetone, and velocity and vorticity fields, as well as strain field quantification utilizing stereo particle image velocimetry (PIV) measurements. The typical optical configuration for laser diagnostics is shown in Figure 2.1 and with additional details in Figure 2.7. A dual cavity Q-switched Nd:YAG laser (Litron Nano L PIV) was employed for all laser diagnostics experiments. This laser initially created monochromatic 1064 nm wavelength infrared light in both cavities. The cavities were followed by second- and fourth- harmonic generators to generate concentric 532 nm and 266 nm wavelength light, respectively. The former consisted basically of the green range of visible light, used for PIV measurements, and the latter light was mainly in the ultra-violet (UV) range for PLIF imaging of acetone. Each cavity was able to produce 8 ns full width at half maximum (FWHM) pulse with 30 mJ at 266 nm and 120 mJ at 532 mJ at the maximum repetition rate of 15 Hz, although the repetition rate in actual measurements was lower (1-7.5 Hz). The operation of the laser with synchronizing to imaging (e.g., cameras) was conducted by an external programmable timing unit and LaVision's DaVis 8.2 software.

The light emitted by the laser passed through two spherical lenses (LaVision 1108406: wavelengths 220-800 nm) to be focused at a desired location, a turning mirror for a 90 degree viewing direction (LaVision 1108407), a $f = -10$ mm cylindrical lens (LaVision 1108406: wavelengths 220-800 nm, divergence angle of 20 degree) and through the quartz window at the top of the test section, and was formed into a divergent sheet oriented at the desired configuration within the test section. Note that the focal point of the laser light should be right at or beneath the test section lower wall so that the laser light absorption correction could be successfully administrated (see Section 2.3.1). For the PLIF measurement setup, two 266 nm dichroic mirrors and a 3 mm thick uncoated UV grade fused silica window (Edmund optics 65865) were present prior to the spherical lenses. The dichroic mirrors diminished the green light energy and transmitted the 266 nm UV beam for acetone PLIF

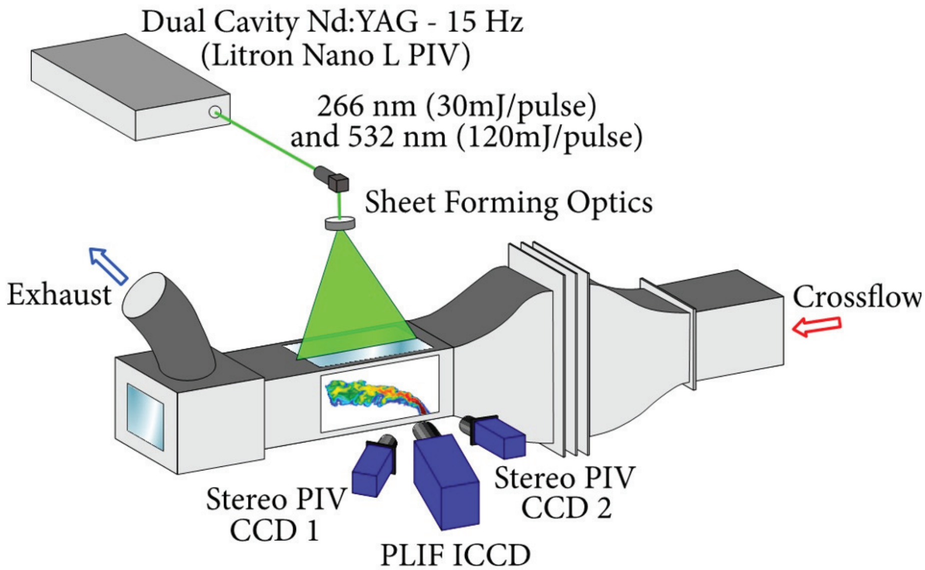

Figure 2.7: Typical laser and camera optical configuration for PLIF and PIV measurements.

measurement mainly to improve the signal-to-noise ratio (SNR) in PLIF images. The UV fused silica window after the dichroic mirrors reflected approximately 7 % of the 266 nm beam energy to measure partial laser energy using a pyroelectric energy detector (Newport 818E-10-50-S, 500 Hz maximum repetition rate). The output signal from the pyroelectric detector was transferred to an optical power/energy meter (Newport 842-PE) to convert the signal from the pyroelectric detector into an actual energy value based on a wavelength correction factor. The energy meter automatically configured the wavelength correction factor depending on the setting. The reflected laser light passed through two optics before the pyroelectric detector: (1) an optical quality synthetic fused silica beamsplitter (CVI Melles Griot BTQ-250-320-2503M-UV, 50/50 nominal reflection/transmission ratio) to orient the laser light path into the detector and (2) a UV grade fused silica plano-concave lens (Newport SPC034) to make the incident laser light diverged and hence to prevent the energy meter from being damaged by high laser intensity. The laser energy meter was connected to a PC through a USB port to save the laser pulse energy data. This monitored laser energy was eventually applied for PLIF image processing, in particular for background subtraction and an laser absorption correction, as a scaling factor (see Section 2.3.1). The laser energy was not measured in simultaneous PLIF/PIV measurements because the pyroelectric detector was not capable of separately capturing two laser pulses at a short temporal interval of approximately 6-17.5 μs, which was shorter than the maximum repetition rate of the detector. Hence, PLIF images as a part of simultaneous PLIF/PIV measurements were not corrected with respect to laser energy.

2.3.1 PLIF

Planar laser-induced fluorescence (PLIF) imaging is an optical measurement which visualizes and qualitatively and quantitatively analyzes flows by capturing fluorescence of tracers mixed with the flow. The fluorescence is generated when the tracer is excited to a higher energy state by the laser light, then returns to the ground state, emitting fluorescence which can be measured by an optical recording tool. This research utilized acetone ($CH_3 - CO - CH_3$), whose fluorescence is not quenched by the presence of oxygen, as a tracer for several reasons. First of all, acetone can be obtained at low cost, and its level of toxicity is relatively low to mild. Second, the high vapor pressure of acetone contributes to a high concentration of tracer in the jet flow. Third, acetone that is excited by UV light fluoresces in the range of 300-500 nm visible light, which leads to a good separation between excitation and emission bands. Furthermore, the low fluorescence lifetime of acetone (4 ns) enables short time-scale measurements. The use of acetone as a molecular tracer in PLIF is an extensively utilized technique for concentration, temperature and pressure measurements in gaseous flows (Lozano et al., 1992; Smith and Mungal, 1998; Thurber et al., 1998; Su and Mungal, 2004). For isothermal flows in which the excited fluid medium is optically thin, fluorescence intensity is proportional to both the laser fluence (assuming absorption saturation is not reached) and the acetone concentration (Lozano et al., 1992; Lozano, 1992). More details on the photophysics of acetone and its application as a seeder may be found in several references (van Cruyningen, 1990; Lozano et al., 1992; Lozano, 1992).

Two acetone seeder chambers placed upstream of the injector and vertical PVC pipe were capable of seeding acetone tracer into the jet fluid in the gas phase. The jet mixture first passed through a 0.25 m tall $\times$ 0.13 m diameter steel chamber with liquid acetone filled to approximately three-fourth. A 0.18 m tall $\times$ 0.19 m diameter steel chamber additionally seeded liquid acetone to achieve the desired acetone molar fraction in the jet fluid, shown in Figure 2.1. Only the second acetone seeder's chamber pressure and temperature were continuously monitored by the dSPACE 1104 DSP with ControlDesk during the entire experiment. These parameters were measured by a pressure transducer (Omega PX409-015G5V, 0-15 PSIG, 0.08 % BSL calibration accuracy) and a Type T thermocouple (Omega, with Analog Devices 2B50A Isolated Thermocouple Conditioner, 1°C max uncertainty). The second chamber temperature was controlled by a refrigerant recirculator combined with a copper coil ($\pm$0.2 % accuracy of set temperature) approximately within the range of 12-18°C, depending on the desired S, equivalent to 11-22 % by volume or mole of acetone in the mixture. The acetone seeder temperature was kept lower than the room temperature during the entire experiment to avoid acetone condensation.

For PLIF imaging without simultaneous stereo PIV measurement, a 14-bit CCD camera (LaVision Imager proX) with 1600 $\times$ 1200 pixel resolution recorded the acetone seeder concentrations in JICF. An external intensifier (LaVision IRO) was mounted to the camera to increase the fluorescence from acetone since the intensity of the fluorescence was not strong enough for the camera. The circular aperture of the intensifier is approximately 1500 pixels in diameter at the center of the CCD array. For PLIF imaging as a part of simultaneous PLIF/PIV measurement, a 12-bit internally-intensified CCD camera (LaVision NanoStar) with 1280 $\times$ 1040 pixel resolution was used. Unlike the externally intensified camera, there is no circular aperture imposed on images with the internally intensified camera. Different lenses were utilized depending on aimed field of view and direction of interest. For cross-sectional PLIF images, a Nikon 200 mm lens at f/4.0 was mounted on the camera. Note that simultaneous PLIF/PIV measurements in the cross-sectional view was not conducted in this study, although it is feasible. Without a simultaneous stereo PIV measurement, centerplane PLIF images were taken with relatively larger and smaller fields of view (FOV), corresponding to lower- and higher-resolution data, respectively. This smaller-FOV or locally focused data were utilized to estimate local scalar dissipation rate χ and strain rate ϵ, which require higher resolution images to enable spatial gradients in the flowfield to be calculated more

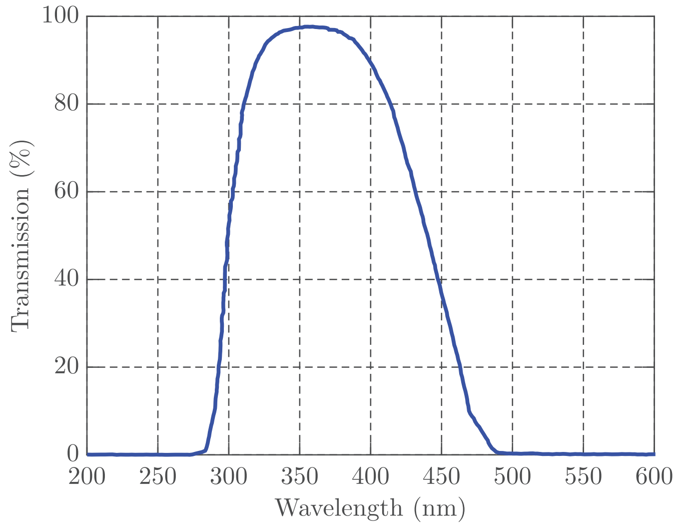

Figure 2.8: Transmission curve of a bandpass filter for acetone PLIF imaging (LaVision 1108562).

accurately. The smaller-FOV image has an approximately three times smaller FOV than that of the larger-FOV image.

The following calculation procedure was implemented for the $S = 1.00$ and 0.35 JICF for the various injectors. Larger-FOV centerplane images were recorded with a Nikon 50 mm lens at f/2.0, attached to a Vivitar +2 dioptre close-up lens to zoom in and capture the desired FOV. For smaller-FOV centerplane images, without simultaneous stereo PIV measurement, a Nikon 60 mm lens at f/2.8 was utilized. PLIF data as a part of the simultaneous PLIF/PIV measurement were taken with a Sigma 90 mm AF at f/2.8 equipped with a Vivitar +2 dioptre close-up lens. Since the signals from the test section included not only the fluorescence from the acetone seeder but also background light (e.g., residual green light in the laser sheet), a bandpass filter for acetone LIF was equipped for all configurations above to acquire only light at the desired wavelength range. The transmission curve for the bandpass filter is shown in Figure 2.8. The gate time of both the internal and external intensifiers was 200 ns, 1 % of the phosphorescence lifetime of acetone. Within the gate time, each laser cavity was operated with a 50 ns temporal interval. The temporal separation for the cavities was short enough to effectively increase in the incident laser sheet energy in the FOV but sufficiently long enough to avoid nonlinear interaction arising in the laser firing process.

The 266 nm laser sheet thickness was measured using the pyroelectric energy meter and a razor blade. The razor blade was traversed normal through the laser sheet utilizing the hotwire traversal mechanism, as documented in Section 2.2. The razor blade partially blocked the laser sheet when traversed and produced data points fairly close to an error function laser energy profile as a function of the position of the razor blade. The data points were then fitted to an theoretical error function profile defined as follows.

$$E = a\left[erf\left(\frac{X-b}{c}\right)+1\right] \tag{2.2}$$

where E and X are the laser intensity captured by the energy meter and the razor blade location with respect to the laser sheet, and a, b, as well as c are the best-fit constants. The raw data points and fitting are plotted in Figure 2.9(a). The spatial derivative of the error function fitting, as represented in Equation (2.2), with respect to X provided a Gaussian profile, coinciding with laser intensity profile of the sheet, as shown in Figure 2.9(b). The laser sheet thickness was quantified based on the Gaussian laser intensity profile using the $1/e^2$ criterion. That is, the sheet thickness was defined between two points (e.g., the two blue circles in Figure 2.9(b)) at which the maximum laser intensity, approximately at the center of the sheet, was reduced by a factor of $1/e^2$. This widely used method to measure the laser sheet thickness is called the scanning knife-edge technique. For more information about the laser sheet thickness measurement, refer to Clemens (2002) and Wang and Clemens (2004). The laser sheet thickness determined by this technique was approximately 400-900 μm within the optical field of view when only cross-sectional or centerplane PLIF imaging with the larger FOV was performed. For the smaller-FOV centerplane PLIF imaging, the laser sheet was created to be thinner, approximately 360-450 μm. The 266 nm laser sheet thickness in simultaneous PLIF/PIV measurements was approximately 1.4-1.9 mm. The laser sheet in simultaneous PLIF/PIV measurement was set to be thicker on purpose, for reasonable correlation in PIV data processing (see Section 2.3.2). These laser thicknesses were the dominant factor in determining the actual resolution of the PLIF images, because the pixel resolution for the camera's CCD array was typically much smaller than the sheet thickness, although the pixel size in images was a good indicator for in-plane spatial resolution.

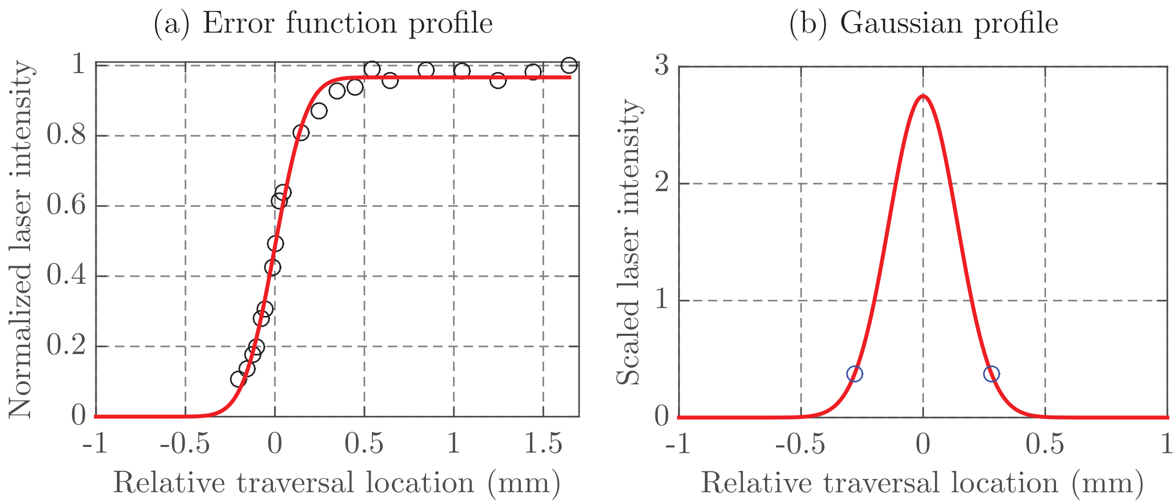

Figure 2.9: (a) Raw data (○) and error function fitting to the data (—, Pearson correlation coefficient of $R = 0.997$) using Equation (2.2) associated with the partial blockage of the laser sheet intensity by the scanning knife-edge technique and (b) Gaussian laser intensity profile (—) produced by the derivative of the error function fitting and $1/e^2$ thickness points (○), suggesting the laser sheet thickness of approximately 560 μm at $z/D = 3.0$.

The in-plane spatial resolution or pixel size of centerplane PLIF images with a larger FOV, and hence lower resolution, was 80 μm per pixel without binning to clearly visualize small flow structures (e.g., vortical structures on the upstream shear layer), and ranged from 140 μm to 170 μm per pixel with 2×2 hardware binning to increase the signal-to-noise ratio (SNR) in images. The spatial resolution of the smaller FOV centerplane images was 34 μm per pixel without binning, while the resolution of the PLIF images acquired via simultaneous PLIF/PIV measurements was 65 μm per pixel with 2×2 hardware binning. For the cross-sectional PLIF images, the spatial resolution ranged from 60 μm to 90 μm without binning and from 120 μm to 160 μm with 2×2 hardware binning. The comparison of instantaneous centerplane PLIF images with the different spatial resolutions is shown in Figure 2.10. The number of instantaneous PLIF images was typically 200-500 in order to have statistical significance in mixing evaluation, as discussed in Chapters 3-7. In Chapter 3, PLIF images with the in-plane spatial resolution in Figures 2.10(b) and (c) are utilized for the unforced JICF local strain rate evaluation. In Chapter 4, PLIF images with the

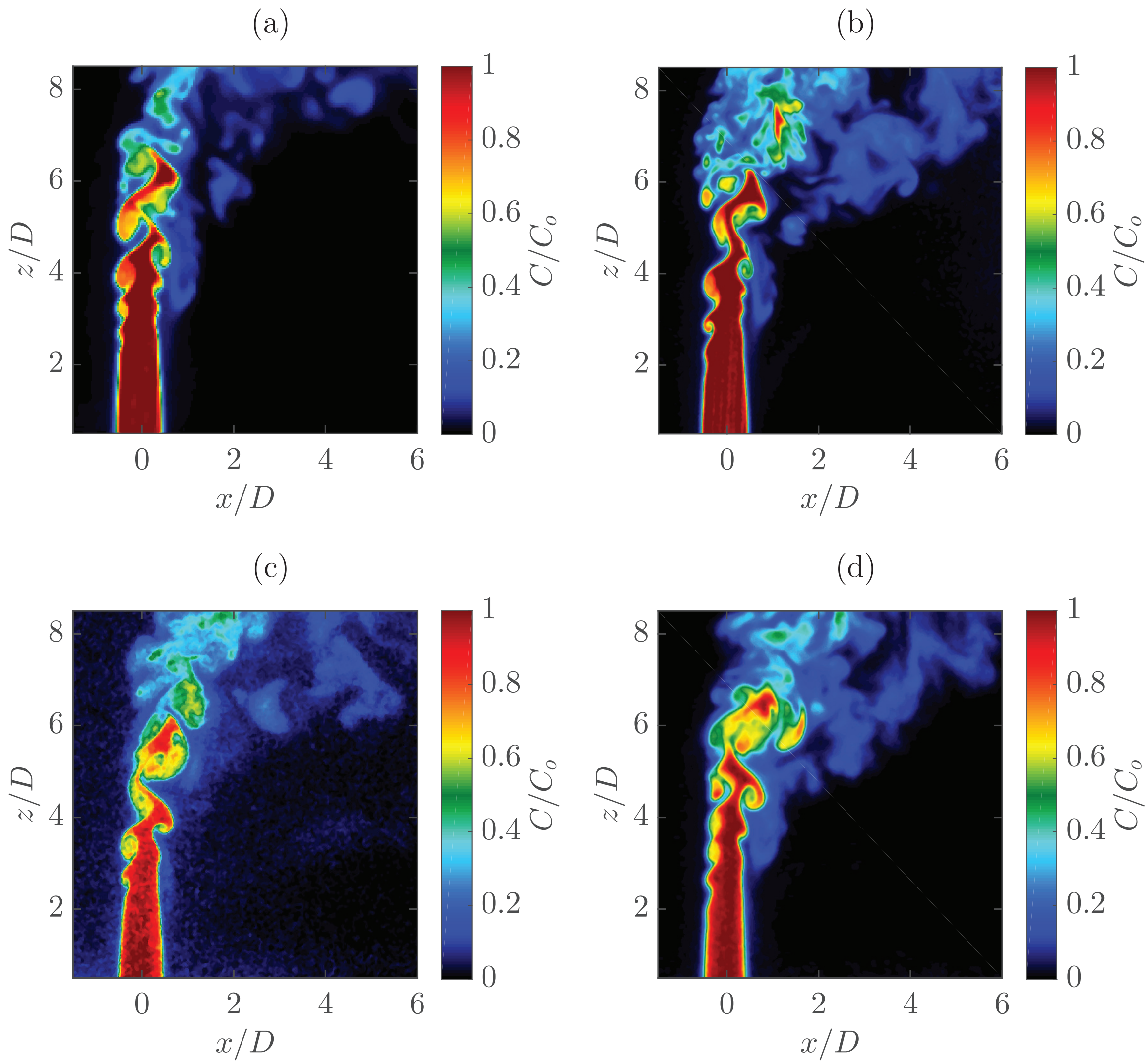

Figure 2.10: Comparison of PLIF centerplane instantaneous images for the equidensity flush nozzle-injected JICF at $J = 41$ amongst (a) larger FOV image with 2×2 hardware binning, (b) smaller FOV image without binning, (c) image as a portion of simultaneous PLIF/PIV measurement with 2×2 hardware binning, and (d) larger FOV image without binning.

in-plane spatial resolution in Figure 2.10(a) are used for the JICF mixing quantification with variable scale lengths in the absence of external forcing of the jet fluid. In Chapters 5 and 6, PLIF images with the spatial resolution in Figure 2.10(d) are used for the forced JICF studies with sinusoidal and single-pulse square wave excitation of the jet. In Chapter 7, PLIF images with the spatial resolution in Figure 2.10(a) are used for the forced JICF studies with double-pulse square wave excitation.

Before the experiments were conducted, the camera was calibrated with a two-plane calibration plate (LaVision Type 7). This calibration transformed the coordinate of recorder images into the lab reference frame. After the measurement, image processing was done to produce the results which could be analyzed. To accomplish image processing, several types of images had to be taken in the experiments, in addition to the JICF images themselves.

First, because the optical recording contained bias errors or background noise on a given image, bias noise correction with a so-called dark image had to be subtracted from the original jet images. In addition, camera recordings yielded non-uniform images regardless of the uniformity of incident light due to optical warping. This effect was taken into account as a flat-field correction with a so-called white image. Moreover, all images included background light which was not from acetone fluorescence but purely from the laser light and its reflection from the test section floor. Hence, a background image was taken in the absence of the jet, and subtracted from the acetone PLIF jet images. But before the background light effect was removed from the jet images, shot-to-shot fluctuation of the laser sheet intensity had to be taken into account. The concentration scale on each jet image was thus changed by multiplying a scaling factor from the mean laser energy, measured by the joulemeter, before background subtraction. These image processing was performed by LaVision's DaVis 8.2 software.

After the image processing, the laser energy absorption correction was applied to the processed images. The laser energy through the jet images diminished from the top of the tunnel to the test section floor because of significant laser light absorption by the acetone. This well-known phenomenon resulted in, for example, lower concentration values appearing to occur at the bottom of the jet's potential core than concentrations at the middle of the jet's centerplane PLIF images. This energy deviation was corrected by a laser energy absorption correction using a so-called source image with a small obstacle on top of the quartz window to block a part of the laser sheet to form a radial shade, as well as a laser sheet image and its background to be subtract from the laser sheet image. The laser energy absorption correction was implemented using Matlab, unlike the image processing in LaVision's DaVis 8.2 software, which is described in detail below. Additional details on the image processing may be found in Getsinger (2012) and Gevorkyan (2015).

After the absorption correction, mean concentration values in the potential core from jet centerplane images were used to normalize the concentration values for each pixel in the entire image. To determine the normalization factor, interrogation boxes were set inside the potential cores for each instantaneous jet image. The boxes were required to be small so as not to exceed the potential core region for all images. Averaging concentration values inside the box yielded the normalization factor for each centerplane image by which all pixels were then divided. Hence overall, PLIF imaging required the following images to be acquired: (a) JICF acetone PLIF images, (b) background images for the JICF images, (c) laser sheet images, (d) laser sheet source images, (e), background images for the laser sheet (correction) images, (e) white images, (f) background images for the white images, and (g) dark (noise) images.

As mentioned, the laser energy absorption correction required source images with a radially shaped shade by the small obstacle, as well as laser sheet and its background images. The shade in the source images formed a concentration contrast in the magnitude of pixel values, and thus enabled a line trace from the tunnel to the imaginary source of the laser using edge detection algorithm, as shown in Figure 2.11(a). The edge detection provided the angle of sheet expansion. Based on the imaginary source and the angle of sheet expansion, several radial lines from the source toward the tunnel floor were plotted, like spokes of a wheel. The laser energy decay along the series of radial lines was traced for the absorption correction. However, as previously utilized in Getsinger (2012) and Gevorkyan (2015), directly tracking laser energy decay along the radial lines angled with respect to coordinate systems was complicated because the lines did not necessarily cross exactly at each pixel, which required a marching, weighted scheme documented by Smith (1996) to account for pixels located around the lines. But applying this scheme at each radial line provided somewhat erroneous evaluation of laser energy decay due to the weighting. Hence, the present study applied a coordinate transformation based on the radial lines using a Matlab built-in function associated with 2D interpolation. The transformation yielded a collimated laser sheet along the radial lines, as shown in Figure 2.11(c) (to be compared with the original

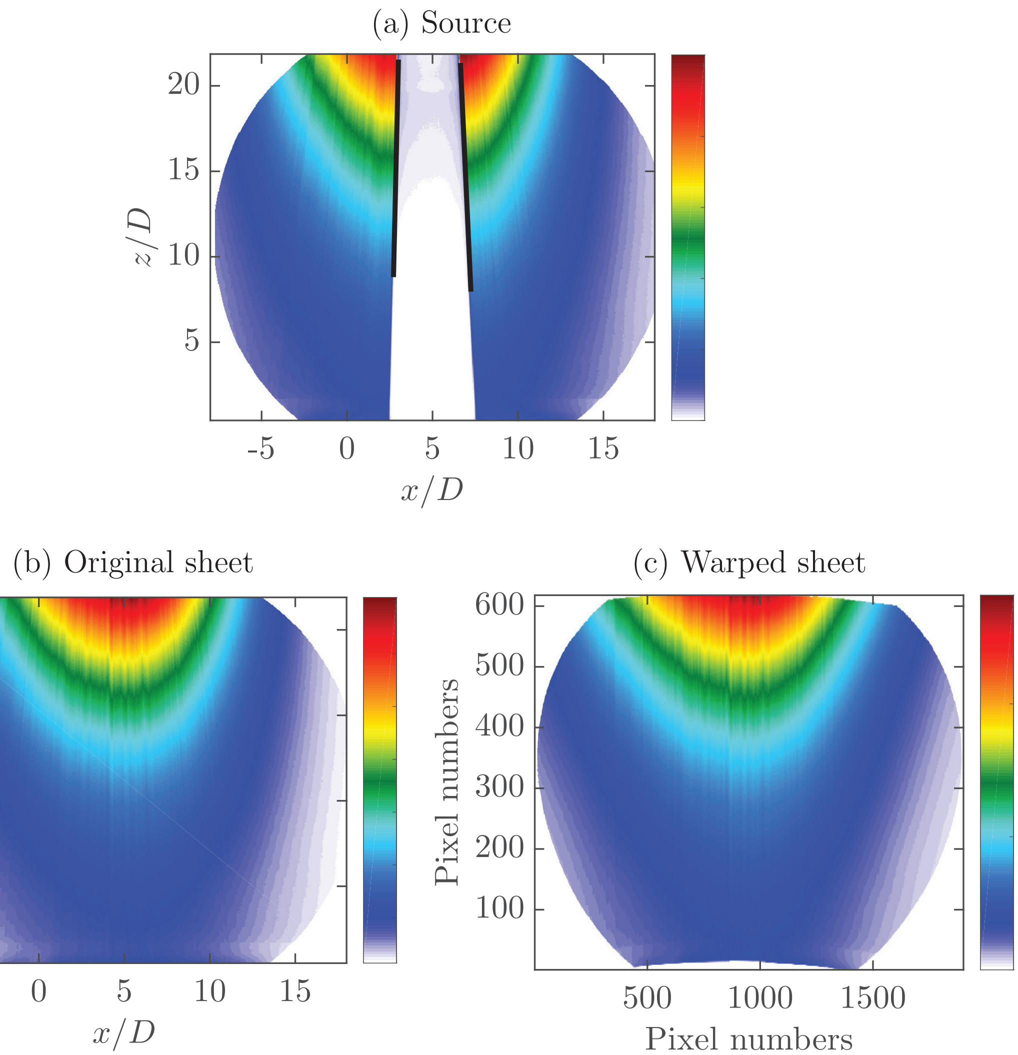

Figure 2.11: Mean laser sheet PLIF images for absorption correction: (a) source image with a radially shaped shade, where two black lines are tracking the edge of the shade to define an imaginary source, (b) laser sheet image in x-z plane without warping, and (c) warped laser sheet image based on a series of radial lines.

laser sheet image in Figure 2.11(b)). With this transformation, the laser energy decay was simply tracked into the vertical direction at each column in Figure 2.11(c) and then fitted to the Beer-Lambert law (Modest, 2013) as follows:

$$E(x) = E_o e^{-\sigma n x} = E_o e^{-\alpha x} \tag{2.3}$$

where σ is the absorption cross-section, n is the number density of acetone, and $\alpha = \sigma n$

is the absorption coefficient, respectively. α can be estimated directly by averaging all α values determined in each column in Figure 2.11(c) using the fitting. The estimated mean α corrected for the laser energy decrease toward the test section floor (Smith, 1996). The absorption coefficient was estimated as $\alpha = 0.022\ mm^{-1}$ using this new method, which was considerably different from that estimated by the previous method (Getsinger, 2012; Gevorkyan, 2015), $\alpha = 0.004\ mm^{-1}$.

After this estimation, an iterative method was also applied to obtain an improved α compared with one calculated from the fitting, by taking into account the uniformity of concentration inside the potential core region. First, several α values slightly smaller and larger than the estimated α from fitting were applied sequentially to correct an instantaneous centerplane image. Then, after the normalization by the multiplicative factor inside the potential core, the root-mean-square of concentration values C_{rms} relative to $C/C_o = 1$ was calculated for each α. Here, α providing the lowest C_{rms} produced the most uniform concentration distribution inside the potential core for the range of explored α. This process was applied again using the detected α as an initial condition in order to obtain more uniform potential core, although narrower range of α than that in the first iteration was utilized. The iteration was performed for 10 instantaneous images, and then a mean α was calculated. This iterative method provided $\alpha = 0.017\ mm^{-1}$, reduced from the initial $\alpha = 0.022\ mm^{-1}$. Using this estimated mean α, the laser sheet image was modified to effectively in the absence of laser energy absorption. The "modified" laser sheet without absorption was used for correcting each JICF PLIF image.

Finally, after the absorption correction as well as the normalization of concentration values were performed, image filtering was needed to remove some remaining noise in the images. The filtering typically includes two types of processes: a 5×5 median filter and a 3×3 thresholding or smoothing filter. The former filter calculated median values within an extracted, local 5×5 pixel region, and replaced the median value with the previous value of a middle pixel in the region. This filter basically removed the extremely high or low values compared to the surrounding pixel values, called spike noise, from the images. The latter process summed up the 3×3 local pixel values and employed thresholding to the sum. The

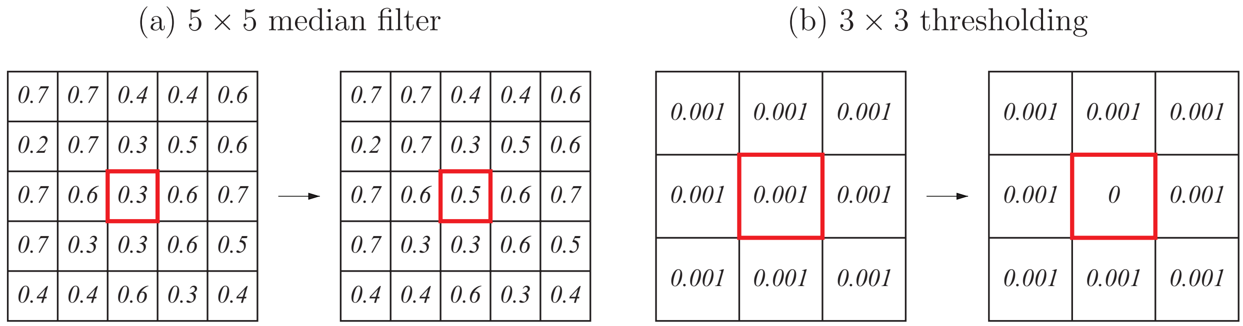

Figure 2.12: Diagrams associated with filtering process to remove noises from PLIF images.

threshold value was set as 0.05; namely, if the sum was less than 0.05, middle pixel value was replaced with 0, which removed noise having small concentration values mainly in the crossflow region without jet fluid. These filters are schematically illustrated in Figure 2.12. These processes were applied to the entire field of each image. All of the results from PLIF imaging without PIV were created through the filtering processes described above. For PLIF data as a portion of the simultaneous PLIF/PIV measurement, which were noisier than the PLIF-only data due to the different camera setup, a 5-pass 3×3 median filter was applied to strongly reduce noise, although another smoothing filter was not applied to minimize the smoothing effect on local scalar gradient calculations, e.g., for local scalar dissipation rate and strain rate quantification.

Examples of instantaneous centerplane jet images after the absorption correction with different α, the normalization, as well as filtering are applied are displayed in Figure 2.13. The comparison between Figures 2.13(b) and (c), with α estimated by the previous and new methods, clearly shows that the new absorption correction generated a more uniform concentration inside the potential core region without any evident laser energy absorption effect. The previous absorption correction created an inappropriate higher concentration value, for example, at $(x/D, z/D) \approx (0.5, 6.0)$ than that inside the potential core, resulting from laser absorption effects. More details on the previous laser sheet correction method are described in Smith (1996), Getsinger (2012) and Gevorkyan (2015).

Because the intensity in the laser sheet image was a product of acetone fluorescence within the laser sheet thickness, the trend of laser energy decay within the FOV could be

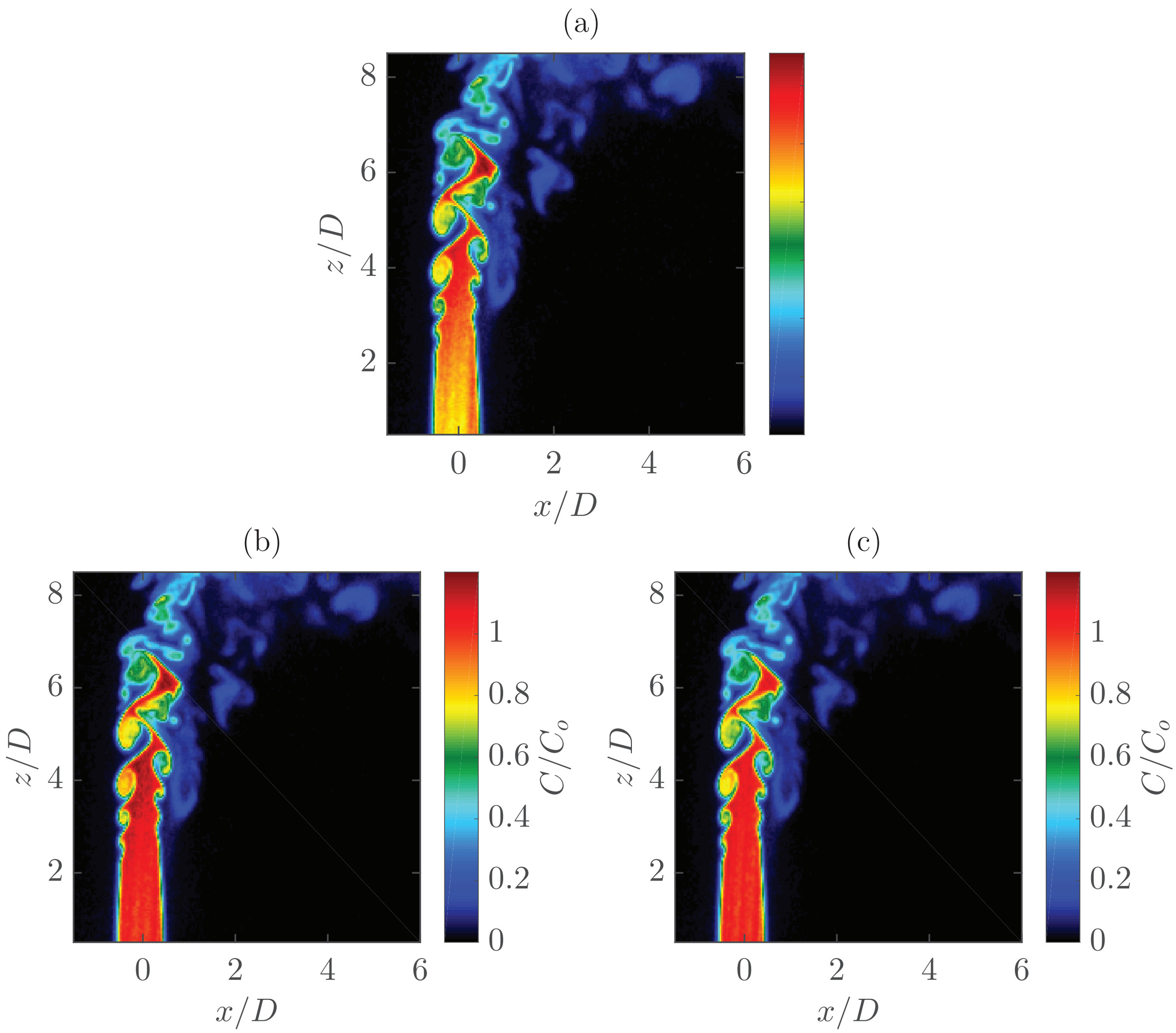

Figure 2.13: Instantaneous centerplane images for the equidensity ($S = 1.00$) flush nozzle-injected JICF at $J = 41$ after (a) image processing in LaVision's DaVis 8.2 software but without absorption correction, normalization and filtering, (b) previous absorption correction with $\alpha = 0.004\ mm^{-1}$, normalization and filtering, as well as (c) new absorption correction with $\alpha = 0.017\ mm^{-1}$ using iterative method, normalization and filtering.

altered if the focal point of the laser is made to be situated inside the FOV. Because the trend in laser energy decay before and after the focal point is slightly different, the Beer-Lambert law fitting does not effectively work throughout the FOV. Hence, as described in Section 2.3, the focal point was situated right at or below the test section floor by adjusting the spherical lenses.

For calibration of concentration values in cross-sectional images, the normalized mean centerplane image was utilized for determination of the multiplication factor. The pixel values or vertical concentration profile (z direction) for mean centerplane images at a specific x/D location can then be correlated with those in the mean cross-sectional image, thus enabling calibration of cross-sectional data. The concentration profiles in the mean centerplane and cross-sectional images are supposed to match for the same location in the same direction. Magnitude differences between the two concentration profiles produced the multiplication factor for normalization of cross-sectional images. This normalization procedure, however, included two special treatments. First, the vertical concentration profile was calculated by horizontally averaging pixel values, in the x direction for centerplane images and in the y direction for cross-sectional images, approximately corresponding to the region within the laser sheet thickness measured by the scanning knife-edge technique. Because pixel values in PLIF images were a sum of acetone fluorescence within the laser sheet thickness, there was a direct, reasonable mechanism for comparison of centerplane- and cross-section-derived profiles. Second, to account for slight spatial displacement of the laser sheet with respect to the target location (e.g., the $y = 0$ plane for the acetone centerplane), possibly arising both in centerplane and cross-sectional measurements, the horizontally-averaged vertical concentration profiles were evaluated at several different positions in the vicinity of a target location, both in mean centerplane and cross-sectional images, and the best correlation was detected among all combinations of the concentration profiles to produce the multiplicative factor. However, as will be shown later, the cross-section of the transverse jet was significantly asymmetric in some cases, especially at high momentum flux ratios, J. This cross-sectional asymmetry was not captured by centerplane images at $y = 0$, and thus the out-of plane components in the y direction in centerplane images (x-z plane) actually prevented a good correlation for mean concentration profiles. Hence, there were a few jet cross-sectional images which were not able to be normalized correctly. While the results for these asymmetric cross-section cases can be used for an understanding or jet structures, in some cases mixing quantification was not possible due to lack of quantitative accuracy.

After the processing and filtering, the SNR for the centerplane PLIF images with different spatial resolutions was estimated by dividing the average concentration inside an interrogation area inside the potential core region by the standard deviation of the concentration inside the area. Because the SNR varied from shot to shot for each instantaneous image, as Gevorkyan (2015) mentioned, this process was applied to all instantaneous images, and then averaged over all values to provides the mean SNR. The mean SNR for three different spatial resolutions shown in Figures 2.10(a)-(c) are approximately 55, 40, and 25, respectively, which are documented in detail in Gevorkyan (2015). The other condition shown in Figure 2.10(d) had an mean SNR of approximately 50, which was slightly lower than that with the binned data (Figure 2.10(a)) because binning increased the SNR by reducing the noise level or intensity fluctuations, hence data without binning were taken in this study to focus on small flow structures.

2.3.2 PIV

Particle image velocimetry is a method which indirectly examines flow fields by imaging the motion of tracer particles seeded in the flows and determining velocity, vorticity, and other important flowfield parameters. Flow motions or directions are determined by spatially cross-correlating the locations of the tracer particles or the most probable displacement of the particles in interrogation windows within a short time increment, based on Mie scattering of the tracer particles. Fast Fourier Transformation (FFT) algorithms are commonly used to estimate the correlation at a known time increment, providing the average displacement of all particles in the interrogation window as well as velocity components and other parameters for given data sets. To achieve this method, PIV measurements need to satisfy the requirements that tracer particles (1) reasonably follow the objective flowfield, (2) do not generally change the fluid properties, and (3) do not interact with each other and change the flowfield characteristics (Westerweel, 1997). To satisfy some of these assumptions, the size of the tracer particles must be sufficiently small enough to accurately follow the flow but large enough to scatter the incident light and hence enable accurate recording. For a comprehensive review of PIV measurement and its development, as well as explanation on its requirement, refer to Adrian and Westerweel (2011).

PIV measurements in our experiments employed the same Nd:YAG laser as in the PLIF measurements and the same optical configuration for the laser-sheet formation. But the laser light used in the PIV measurement has to be 532nm in wavelength, dominant mainly within the green visible light range. Hence, the dichroic mirrors isolating the 266 nm wavelength from the laser beam for PLIF and the UV grade fused silica window used as the beamsplitter, as well as the joulemeter measuring the laser energy, were removed. It should be noted that the beamsplitter and the joulemeter can be removed because our PIV measurements do not require laser energy information for normalization post-processing using the laser energy, unlike the PLIF measurements. The thickness of the laser sheet formed by the optical alignment was approximately 1.4-1.6 mm measured using the scanning knife-edge technique as for the PLIF imaging by Gevorkyan (2015). This thickness was sufficiently thin enough to yield a planar measurement for PIV, but thick enough to successfully acquire stereo PIV data by capturing out-of-plane motion of tracer particles. For simultaneous PLIF/PIV measurements, a thicker 266 nm laser sheet than that for single PLIF imaging was utilized, as documented in Section 2.3.1, to achieve an appropriate laser sheet thickness for both diagnostics. The temporal interval of two laser pulses Δt was chosen to be 17.5 μs for the equidensity flush-nozzle injected JICF data, 15 μs for the equidensity flush-pipe injected JICF data, and 6 μs for the $S = 0.35$ flush-nozzle injected JICF data. Adrian and Westerweel (2011) note that particle in-plane displacement within the Δt should be less than or equal to one-fourth of the initial interrogation window size in vector calculation (one-fourth of 32 pixels, so 8-pixel size in this study) over the entire FOV to obtain a good correlation in the vector calculation. In addition, this criterion should be satisfied for the out-of-plane flow component in stereo PIV measurements. Because the out-of-plane motion of tracer particles was not able to be monitored in experiments, to be conservative, this study used particle motions in the crossflow region away from the jet, with the crossflow velocity faster than the actual out-plane velocity, to estimate a reasonable Δt for out-of-plane components.

As one tracer species for the PIV, Di-Ethyl-Hexyl-Sebacat or DEHS ($C_{26}H_{50}O_4$, LaVision 1108951) oil was utilized for seeding the jet flow. For the crossflow, a commercial fog machine (Pea Soup Rocket) atomized and then injected glycol-based smoke fluid particles of 0.2 μm mass-median diameter into the crossflow blower inlet. The jet fluid was seeded by diverting part of the injection line through a TSI particle generator containing the DEHS oil, which allowed for fine-tuning the seeding density via a needle valve controlling the amount of jet fluid is diverted into the seeding line. The seeding density was visually determined based on raw PIV images in such a way that uniform seeding density in entire flowfield, both jet and crossflow, is achieved.

Our experiments adopted a stereoscopic PIV system comprising two 14-bit cross-correlation CCD cameras (LaVision Imager proX, 1600×1200 pixel resolution) with the same specifications given in Section 2.3.1. Note that the external intensifier utilized in PLIF imaging was not used in PIV measurement. A stereo PIV simultaneously records flow fields illuminated by a light source or sheet in the same region of interest, but in the different planes, by two separate cameras. The two different views of the same flowfield are capable of capturing the out-of-plane motion of particles, resulting in the reduction of perspective errors for in-plane measurements (Prasad, 2000). This configuration for two-dimensional three-component-PIV is called the 2D3C technique. In our experimental configuration, the two cameras were separated approximately by a 60° angle with respect to the z axis (see Figure 2.7). Each camera was equipped with a Nikon 60 mm lens at f/11.0, a 532.5 nm narrowband filter, and a Scheimpflug lens mount (LaVision 1108196 version 1) which was used to tilt the lens plane with respect to the CCD array plane so as to reinforce the inherent small depth of field in our optical configuration and hence to retain focus over the entire image domain. The transmission curve of the narrowband filter used in PIV measurements is shown in Figure 2.14.

The calibration of the PIV imaging exploited a two-plane calibration plate (LaVision Type 7), the same as one used in the PLIF measurement, placed sufficiently close to the plane of the laser sheet. The calibration method projected the acquired raw image data into real-world coordinates using a 3^{rd} order polynomial model. A self-calibration method (Wieneke, 2005) was also applied to the recorded images to alleviate the effect of the slight misalignment of the calibration plate. All image processing, vector calculations and vector post-processing were administrated using LaVision's DaVis 8.2 software. Before the processing, raw data

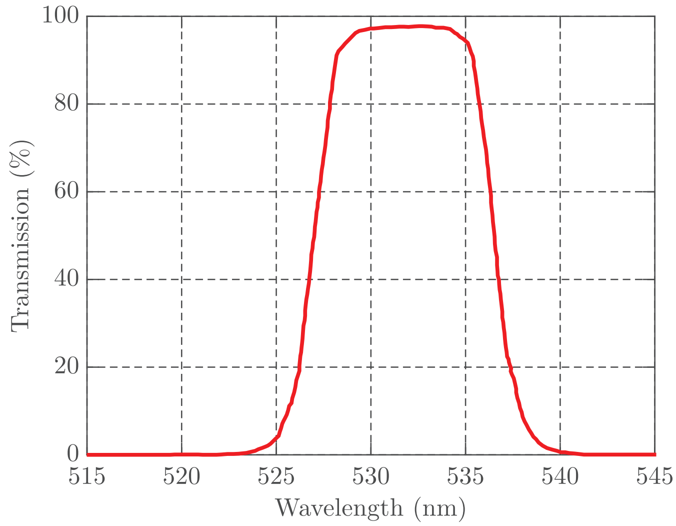

Figure 2.14: Transmission curve of narrowband filter in PIV measurement (LaVision 1108560: 10 nm bandwidth at 50 %, 95 % max transmission).

were transformed from the coordinate of recorder images into the lab reference frame by applying the calibration information. After the mapping, image processing was implemented, which mainly included 3 processes: (1) the global background subtraction to eliminate the background lighting, (2) the background subtraction with local 8-pixel sliding for further removal of the background effect, and (3) the min/max filter for the contrast normalization of particle intensity in each frame. Then, vector calculations were conducted, mainly the multi-pass stereo cross-correlation with a decreasing interrogation window size (2 passes at 32×32 pixel interrogation window size with 50 % overlap, and 4 passes at 24×24 interrogation window size with 75 % overlap). Finally, the resultant vector fields were post-processed to acquire cleaner data, mainly by removing vectors with low correlations, filling up spaces by interpolation, and smoothing vector fields utilizing average vectors from 3×3 pixel neighborhood. The final pixel size in PIV data after this processing was 120 μm, although this pixel size does not accurately represent the actual spatial resolution of the PIV data. For example, Westerweel (1997) evaluated how many vectors are extracted from a single image with a given pixel dimension, in order to approximate and compare the "effective spatial resolution" of PIV-based vector fields, which varies depending on the vector post-processing, e.g., the size of an interrogation window and the amount of an overlap between adjacent interrogations. In this study, approximately 58100 vectors were extracted from a 1600×1200 pixel image, corresponding to approximately 0.03 vectors per pixel (7.4 μm) in a raw image. For comparison, the "effective spatial resolution", the number of vectors per pixel in a raw image, in several different experimental studies is approximately 0.014 in Westerweel (1997), 0.01 in Su and Mungal (2004), and 0.036 in Kothnur and Clemens (2005). Because the effective vector resolution in Kothnur and Clemens (2005), associated with strain rate calculation in a finer flow structure than that in this thesis, is fairly close to that for our PIV images, the effective vector resolution of the present PIV data is reasonable for local strain rate evaluation, as discussed in Chapter 3. Note that the laser sheet thickness also affects the actual spatial resolution PIV data, although the effect of the laser sheet thickness is difficult to be incorporated into the quantification of the PIV spatial resolution. More details about the post-processing of the data, including the reconstruction of the velocity fields, are described by Getsinger (2012) and Gevorkyan (2015).

2.4 Forced Transverse JICF Experimentation

For this experiment, three different types of axisymmetric, temporally evolving forcing of jet fluid were imposed on the jet: sine wave, and single- as well as double-pulse square wave forcing. The forcing was created by a loudspeaker situated inside the plexiglass plenum housing beneath the injection system, as described in Section 2.1 and shown in Figure 2.1. For sine wave forcing, an initial sinusoidal signal was created by a function generator at a desired forcing frequency f_f and an amplitude. The initial signal was delivered to an amplifier (Adcom GFA-7300 high current 5-channel power amplifier) with a constant gain of 30 for all forcing frequencies in this study. The amplified sinusoidal signal drove the loudspeaker to create sine wave excitation of the jet. The jet excitation was measured via hotwire anemometry at a location 0.2 jet diameters above the center of the jet exit plane, as described in Section 2.2. The RMS of the velocity perturbation, $U'_{j,rms}$, was matched as an amplitude amongst different forcing conditions. The RMS values explored were in the range $0.07 \leq U'_{j,rms} \leq 1.00$ m/s, as compared with a mean jet velocity of $U_j \approx 6.5$ m/s. The RMS

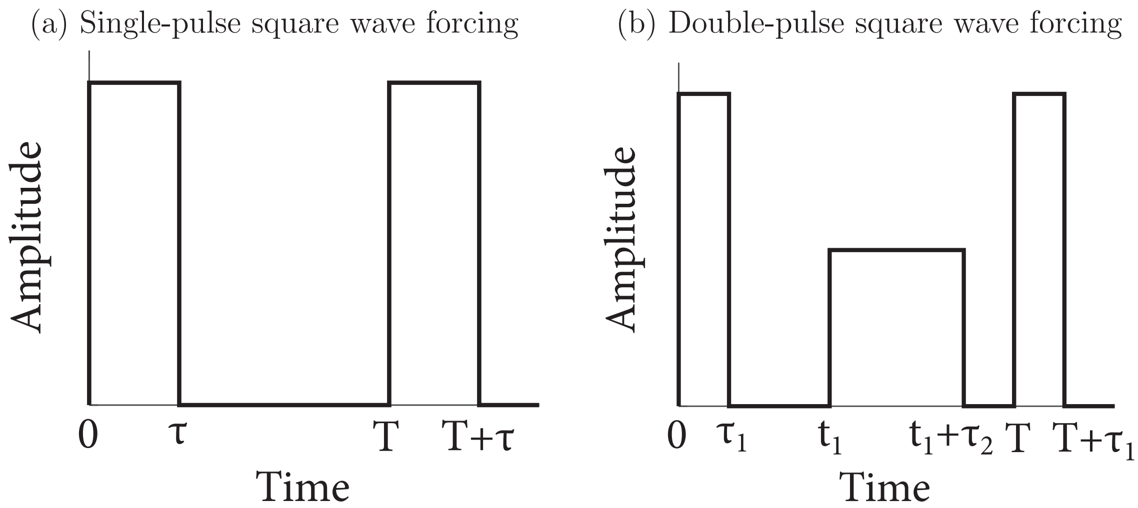

Figure 2.15: Pulse forcing types applied in jet-forcing experiment: (a) single-pulse square wave forcing and (b) double-pulse square wave forcing. Root mean squared of jet velocity $U'_{j,rms}$ was kept constant among all forcing conditions for each type of forcing.

jet exit values were carefully matched by adjusting the amplitude of the initial sinusoidal signal from the function generator. The matching of RMS values creates effectively the same level of forcing, or introduction of impulse to the jet fluid, and hence enables appropriate comparison among the different forcing conditions to be made. Thus, the matching of the RMS values was implemented for all types of forcing in this study. The forcing frequency of sine wave forcing explored in this study ranged from $200 \leq f_f \leq 6000$ Hz, depending on the required level of forcing, equivalent to $U'_{j,rms}$. Under sine wave forcing, only the equidensity ($S = 1.00$) flush nozzle-injected JICF at $Re_j = 1900$ could be explored with variable jet-to-crossflow momentum flux ratio of $5 \leq J \leq 41$. Re_j and J were based on the mean velocity of the unforced jet, so the actual flow parameters during the forcing could temporarily vary, although $U'_{j,rms}$ at the center of the jet exit was matched among all forcing conditions. More details on the application of sine wave forcing in experiments is documented in Chapter 5.

Single-pulse square wave forcing was defined as a single pulse within each temporal period $T = 1/f_f$ at the same amplitude and temporal pulse width τ. The diagram representing pulsation amplitude as a function of time for the forcing is schematically shown in Figure 2.15(a). As documented in M'Closkey et al. (2002), Shapiro et al. (2006), and Davitian et al.

(2010b), simply applying square wave signal to the loudspeaker without control creates a distorted square-wave vertical jet velocity distribution at the jet exit. Hence, a feedback control system was developed to achieve cleaner square-wave velocity profile at the jet exit. A feedback control system was initially developed by Hendrickson (2012) and Hendrickson and M'Closkey (2012), yet the present experimental study established a simpler control system compared with those in previous studies. The square-wave velocity profile was basically created by superposing 10 sinusoidal harmonics at frequencies of $100 \leq f \leq 1000$ Hz, corresponding to $f_f \leq f \leq 10f_f$, and by independently adjusting each phase and amplitude, although non-linear interactions among all harmonics made the control very difficult. More details on the control system for single-pulse square wave forcing will be described in Chapter 6. For this forcing, f_f and $U'_{j,rms}$ explored in this study were different from the sine wave forcing cases, which was $f_f = 100$ Hz and ranged $1.0 \leq U'_{j,rms} \leq 3.0$ m/s. As with sine wave forcing cases, the equidensity flush nozzle-injected JICF at $Re_j = 1900$ was explored with a range of J ($5 \leq J \leq 41$).

Additional forced transverse jet experiments were conducted during the summer of 2016 with Prof. Luca Cortelezzi of McGill University/Politecnico di Milano and Prof. Robert M'Closkey of UCLA using double-pulse square wave forcing to the equidensity larger-diameter flush nozzle-injected JICF at $Re_j = 1500$ and $J \approx 6.7$ ($R = 2.58$) in the absence of forcing. The same loudspeaker configuration was employed to create the forcing in the experiments. The additional forcing here is double-pulse forcing, as described below.

Double-pulse square wave forcing in this study consisted of two pulses within each temporal period T with different amplitudes and temporal pulse widths τ_1 and τ_2 for each pulse, which was generated using the same feedback control system as for single-pulse square wave forcing but with slight improvements. Since shaping a clean, double-pulse square wave required a larger number of harmonics or relatively high-frequency harmonics than the single-pulse square wave, 15 sinusoidal harmonics were superposed at frequencies of $55 \leq f \leq 825$ Hz, coinciding to $f_f \leq f \leq 15f_f$. The waveform associated with forcing amplitude as a function of time for double pulsing is shown in Figure 2.15(b). The two pulses created deeply penetrating puff-like flow structures twice within a temporal period but with different penetrating velocities, potentially triggering near-field vortex interactions or collisions, which could potentially enhance molecular mixing of the JICF. As with the previous two forcing cases, $U'_{j,rms}$ was matched among different forcing and flow conditions to achieve effectively the same-level forcing. Because $U'_{j,rms}$ was matched, the near-field flow interaction was considered to mainly depend on the different temporal pulse widths, τ_1 and τ_2, as well as the temporal interval of two pulses $\Delta\tau$ and forcing frequency f_f. τ_1, τ_2 and $\Delta\tau$ were systematically varied in experiments to investigate the effect of these parameters on structural and mixing characteristics for the JICF, while the forcing frequency was fixed at a constant, $f_f = 55$ Hz for all forcing conditions. For double-pulse square wave forcing, unlike the previous two types of sinusoidal and square wave excitation, the equidensity larger-diameter ($D = 7.59$ mm) flush nozzle-injected JICF at $Re_j = 1500$ as well as at $J = 6.7$ ($R = 2.58$) was explored, as examined in M'Closkey et al. (2002) and Shapiro et al. (2006).

For both single- and double-pulse square wave forcing, the PCV pipe in between the injector and the plexiglass housing was removed from the injection system because the longitudinal space with a relatively small diameter inside the PVC pipe caused acoustic wave amplitudes to decay, especially at higher frequencies. The pipe also generated resonant effects, which made the control of forcing considerably more difficult. The absence of the PVC pipe was confirmed not to alter the basic instability and structural characteristics of the JICF without forcing as explored in this study, as compared with flow characteristics with the pipe.

As noted, this jet forcing study emphasized PLIF imaging of the jet's centerplane and cross-section. The same optical configuration for the forced jets was used for unforced jets (see Section 2.3.1). Although the image post-processing was basically the same for forced jets as described in Section 2.3.1, the method to normalize the scalar concentration values from the PLIF images was somewhat different from that for the unforced jets. The reason for this difference is that the jet's potential core, used to obtain multiplication factors for the unforced jets' PLIF images, is not always distinct or definable in a forced jet's instantaneous PLIF image, due to the strong pulsations in the jet fluid. Therefore, the normalization method in the forced jet experiments extracted the first ten maxima inside an interrogation box inside the potential core region, as used in the unforced case, from each instantaneous image, and then averaged the extracted values to desire the core concentration and relevant pixel intensity. The mean normalization factors were then used to scale each instantaneous image by multiplication. The normalized mean jet image was then obtained by averaging over 500 scaled instantaneous images; this was done for the all unforced and forced cases.

CHAPTER 3

Scalar and Velocity Field Characteristics for JICF

Portions of this chapter are modified sections from Gevorkyan et al. (2017)

Strain rates and/or scalar dissipation rates are important parameters pertaining to reacting flowfields, as a means of characterizing ignition and extinction. Although the flowfields in the present study are non-reactive, the quantification of scalar dissipation rates (related to the spatial gradient of the scalar field), χ, related to the local strain rate, ϵ, in a non-reactive flowfield are potentially very useful indicators to be able to predict flame extinction/ignition locations for the equivalent reactive flowfield. They are also relevant to diffusion/mixing processes.

Gevorkyan (2015) and Gevorkyan et al. (2017) describe the interplay between velocity- and scalar-field dynamics for the variable density ($S = 0.35$ and 1.00) JICF for a range of J values ($5 \leq J \leq 41$) as well as different injectors (flush nozzle and flush pipe), using data acquired via simultaneous PLIF/PIV measurements, as summarized in Section 1.5. This chapter focuses on three additional subjects which are not described in detail in the previous studies: (1) proper orthogonal decomposition (POD) analyses using simultaneous PLIF/PIV data as well as high resolution PLIF data acquired via PLIF-only imaging (see Section 2.3.1) to investigate the effect of spatial resolution in PLIF images on POD analyses, (2) the in-depth validation of the present algorithm to extract local strain rates from PLIF data by Equation (1.9), including a study of the validity of the minimum number of data points in the averaging process, and (3) strain rate evaluation in the variable density ($S = 1.00$ and 0.35) JICF on the Upstream Mixing Layer (UML) as well as the Downstream Mixing Layer (DML) defined by loci of the local maximum scalar dissipation rates (see Section 3.2). All analyses here are conducted using the same data as in Gevorkyan (2015) and Gevorkyan et al. (2017).

However, it should be noted that the newly developed image processing described in Section 2.3.1 was applied to reduce the PLIF data shown in Gevorkyan et al. (2017) as a part of this thesis but was not used in the thesis of Gevorkyan (2015), although the different image processing method had little effect on the qualitative characteristics.

As documented in Section 2.1, the jet Reynolds number was fixed at $Re_j = 1900$ throughout the experiments, both for simultaneous PLIF/PIV measurements as well as PLIF-only imaging with a higher spatial resolution, determined by the mean (profile-averaged) bulk jet velocity, U_j. The variable density ($S = 1.00$ and 0.35) flush nozzle-injected JICF, as well as the equidensity flush pipe-injected JICF were explored in this chapter. Again, in the simultaneous PLIF/PIV measurements, laser pulse energy is measured for image processing because laser energy meter is unable to distinguish the first and second laser pulses during a fast temporal interval (see Section 2.3).

3.1 POD Analysis for the JICF

Proper Orthogonal Decomposition (POD), also known as Principal Component Analysis (PCA), has been used for decades as a method to extract the most dominant mode structures in a field of data obtained from a turbulent flow (Berkooz et al., 1993). One of the main advantages of POD analysis is that the structures extracted from the calculation are ordered according to fluctuation energy content, thus revealing important flow features from data that could otherwise be noisy or highly chaotic. Snapshot-POD (Sirovich, 1987) may be used to extract mode structures from instantaneous snapshots of the flow, and thus was used in the present JICF study. While several groups have utilized POD to analyze JICF velocity data (Meyer et al., 2007; Vernet et al., 2009; Schlatter et al., 2011), application of POD analysis need not be restricted to velocity components. Thus, a comparison between the POD mode structures and fluctuation energy distribution extracted from the PIV-based velocity field data, in addition to that extracted from PLIF-based scalar field data, can provide additional insights into the correlation between the scalar field and the velocity field as well as dominant instabilities in the flowfield. POD analysis thus was applied to 500 snapshots of the simultaneous PLIF/PIV data, for example, for the cases shown in Figures 3.1, 3.2, and 3.3 from Gevorkyan et al. (2017), with a resolution of 65 μm per pixel. To explore the effect of the spatial resolution of PLIF images, POD analysis was also applied separately to 300 snapshots of the higher resolution PLIF data, with a resolution of 34 μm per pixel.

Figure 3.4 highlights the first four velocity mode structures and their corresponding portion of the total velocity fluctuation energy of the flow extracted from the PIV data for the equidensity, flush nozzle cases, for which vorticity fields are shown in Figure 3.1. Figure 3.5 shows the first four scalar mode structures and their corresponding portion of the total scalar energy fluctuation of the flow extracted from the PLIF concentration data for the same conditions. As expected, both the velocity and scalar fields were dominated by shear layer structures, and the jet's upstream shear layer structures became more dominant and were initiated closer to injection as the momentum flux ratio was reduced and absolute instability was approached. The $J = 5$ case in particular showed strongly periodic upstream shear layer rollup initiated immediately at injection, especially visible in both PIV and PLIF-based POD modes 1 and 2. Wake structures were more visible in the velocity field POD modes since both crossflow and jet fluids were seeded with particles. Jet wake structures were especially strong for lower momentum flux ratios ($J \leq 12$), as evidenced by the out-of-plane velocity fluctuation on the lee-side of the jet for $J = 12$ and $J = 5$ in Modes 3 and 4 (third and fourth rows of Figure 3.4(b,c)). Some evidence for the effect of these wake structures on the scalar fluctuation can be seen in the PLIF POD as well (e.g., see Modes 3 and 4 for $J = 5$ in Figure 3.5(c)), suggesting the somewhat lesser relevance of the jet fluid in wake structures, yet with increasing influence as J was lowered. It should be noted that the dominance of the upstream shear layer in the most energetic modes from the PIV-based POD was similar to simulation results by Iyer and Mahesh (2016), examined via Dynamic Mode Decomposition (DMD). For both convectively and absolutely unstable conditions, the upstream shear layer was the dominant instability, although at low J conditions ($J = 2$) there were strong oscillations in the downstream wake region as well.

The effect of spatial resolution in PLIF images on the POD analysis is now investigated.

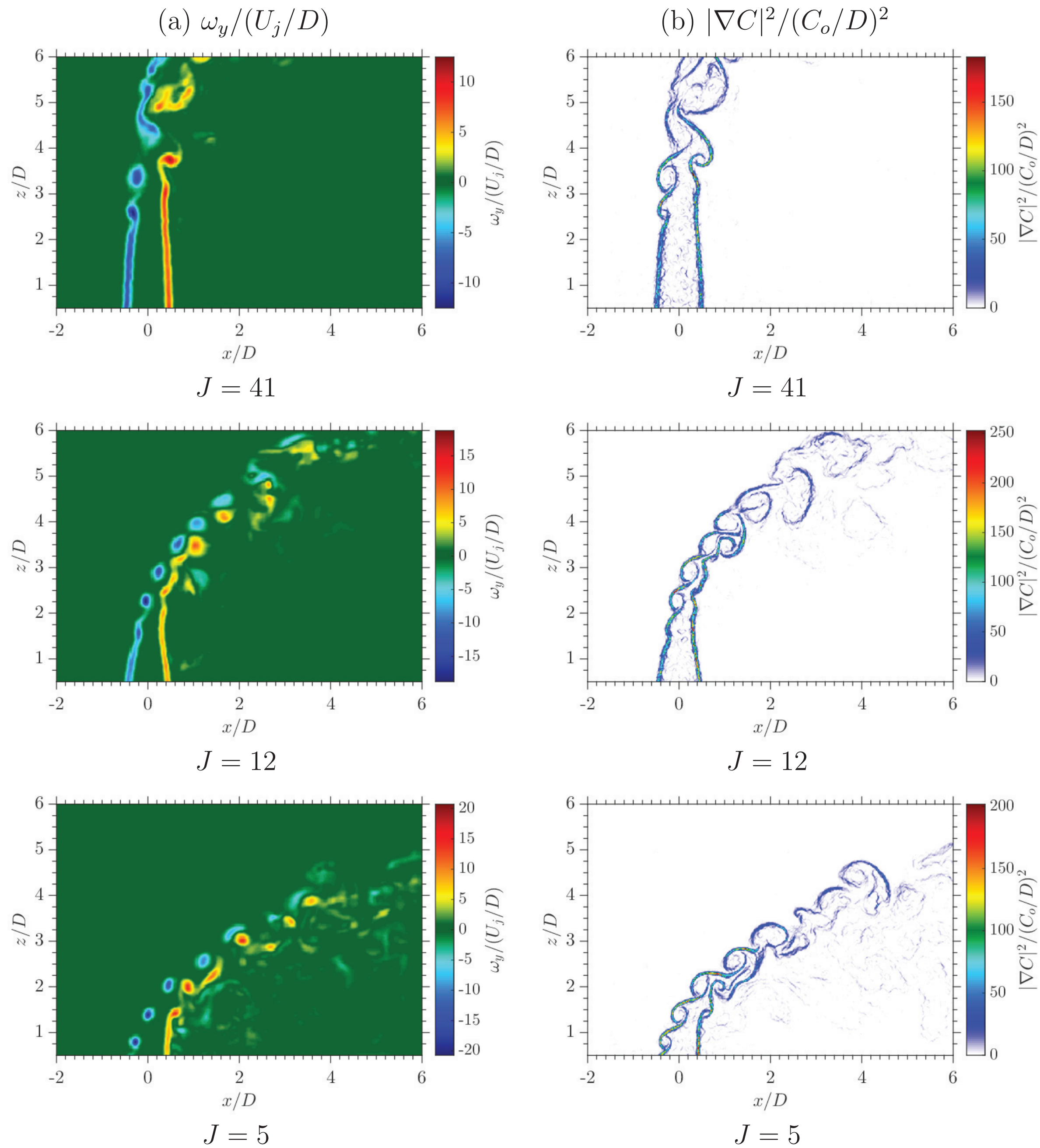

Figure 3.1: Instantaneous centerplane (side view) simultaneous PLIF/PIV imaging of the $S = 1.00$, flush nozzle-generated JICF with varying momentum flux ratios: $J = 41$ (top row), $J = 12$ (middle row), $J = 5$ (bottom row). Data shown for (a) scaled vorticity $\omega_y/(U_j/D)$ and (b) scaled jet fluid concentration gradient magnitude $|\nabla C|^2/(C_o/D)^2$, from Gevorkyan et al. (2017).

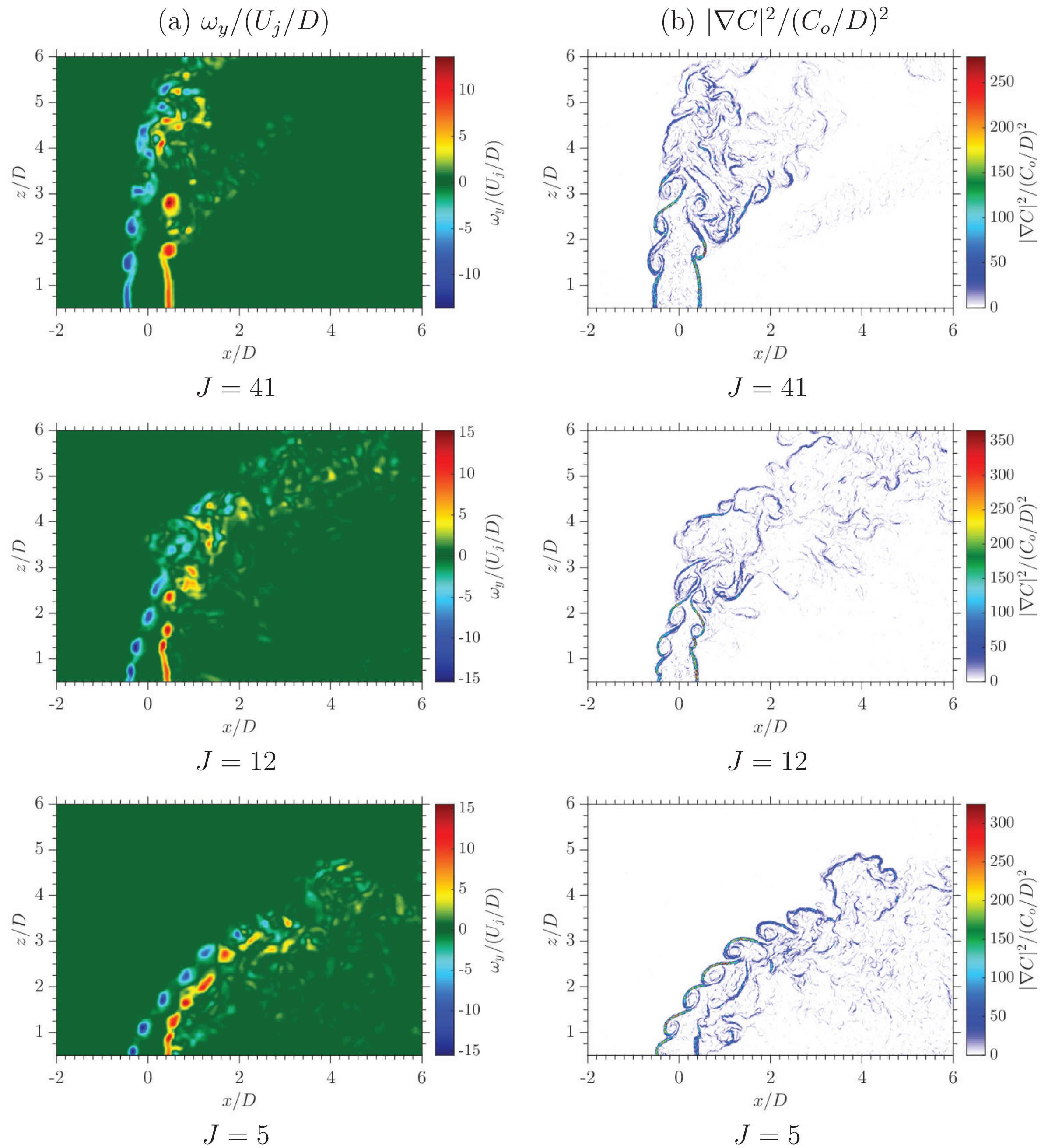

Figure 3.2: Instantaneous centerplane (side view) simultaneous PLIF/PIV imaging of the $S = 0.35$, flush nozzle-generated JICF with varying momentum flux ratios: $J = 41$ (top row), $J = 12$ (middle row), $J = 5$ (bottom row). Data shown for (a) scaled vorticity $\omega_y/(U_j/D)$ and (b) scaled jet fluid concentration gradient magnitude $|\nabla C|^2/(C_o/D)^2$, from Gevorkyan et al. (2017).

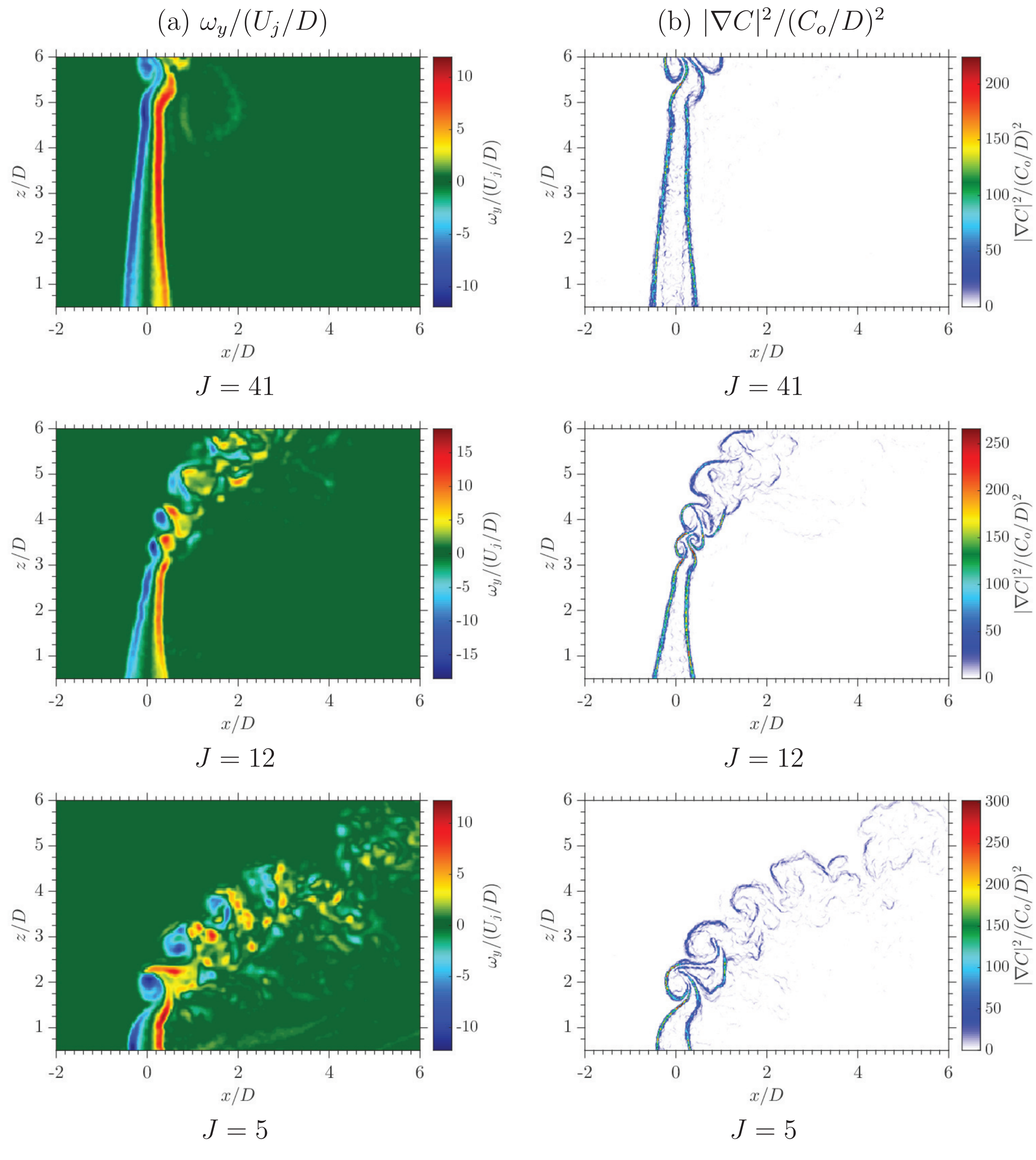

Figure 3.3: Instantaneous centerplane (side view) simultaneous PLIF/PIV imaging of the $S = 1.00$, flush pipe-generated JICF with varying momentum flux ratios: $J = 41$ (top row), $J = 12$ (middle row), $J = 5$ (bottom row). Data shown for (a) scaled vorticity $\omega_y/(U_j/D)$ and (b) scaled jet fluid concentration gradient magnitude $|\nabla C|^2/(C_o/D)^2$, from Gevorkyan et al. (2017).

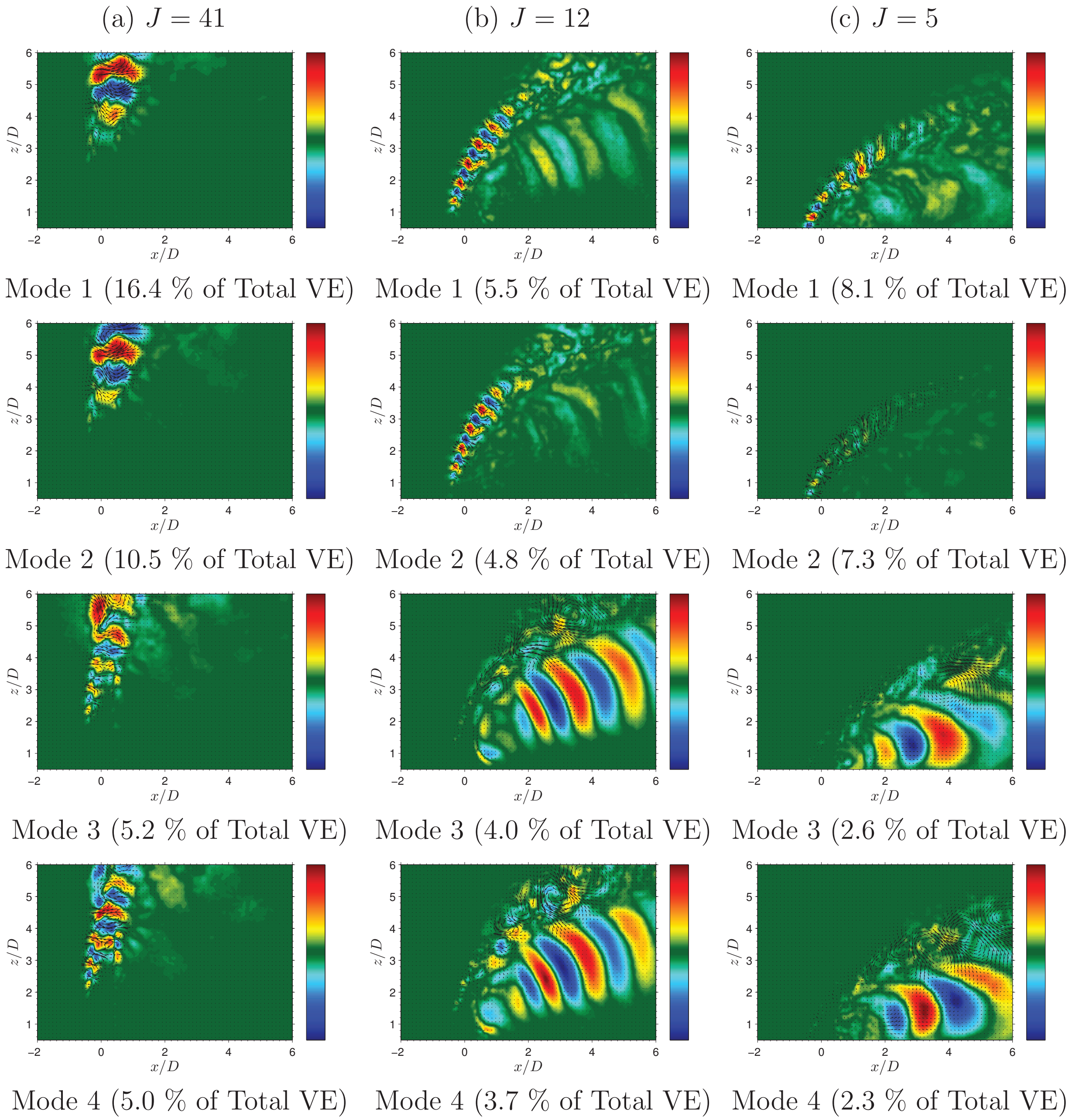

Figure 3.4: PIV POD mode structures extracted from instantaneous centerplane (side view) simultaneous PLIF/PIV imaging of the $S = 1.00$, flush nozzle-generated JICF with varying momentum flux ratios: (a) $J = 41$, (b) $J = 12$, (c) $J = 5$, from Gevorkyan et al. (2017). Data shown for Mode 1 (first row), Mode 2 (second row), Mode 3 (third row), Mode 4 (fourth row). Arrows in images indicate in-plane velocity component structure contribution, while colormap indicates out-of-plane velocity component structure contribution. Percent of total velocity fluctuation energy (VE) contributed by each mode is indicated below each image. (The color bar represents each mode scaled by its own norm and the mean jet velocity at the jet exit U_j.)

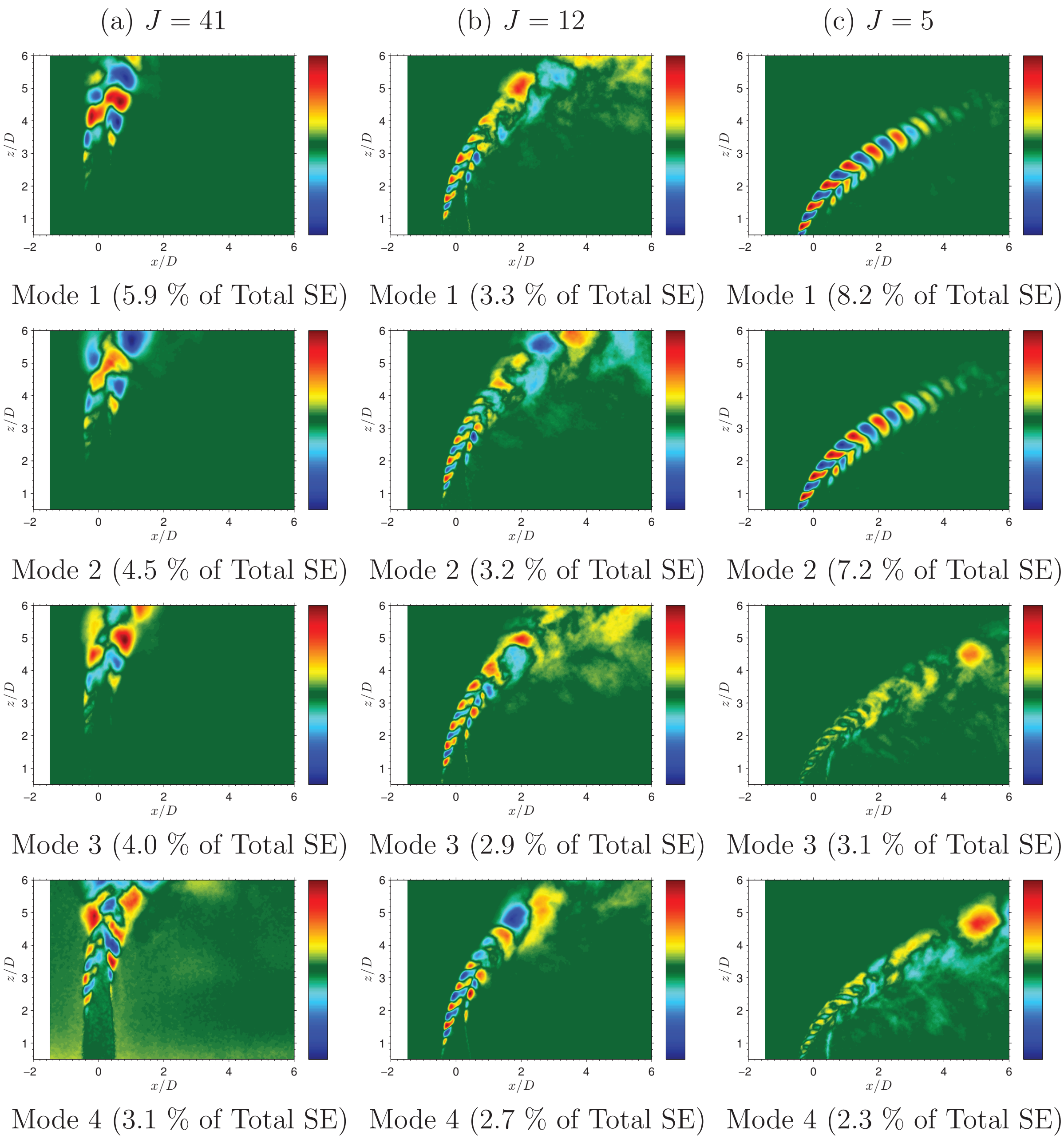

Figure 3.5: PLIF POD mode structures extracted from instantaneous centerplane (side view) simultaneous PLIF/PIV imaging of the $S = 1.00$, flush nozzle-generated JICF with varying momentum flux ratios: (a) $J = 41$, (b) $J = 12$, (c) $J = 5$, from Gevorkyan et al. (2017). Data shown for Mode 1 (first row), Mode 2 (second row), Mode 3 (third row), Mode 4 (fourth row). Percent of total scalar fluctuation energy (SE) contributed by each mode is indicated below each image. (The color bar represents each mode scaled by its own norm and the mean jet velocity at the jet exit U_j.)

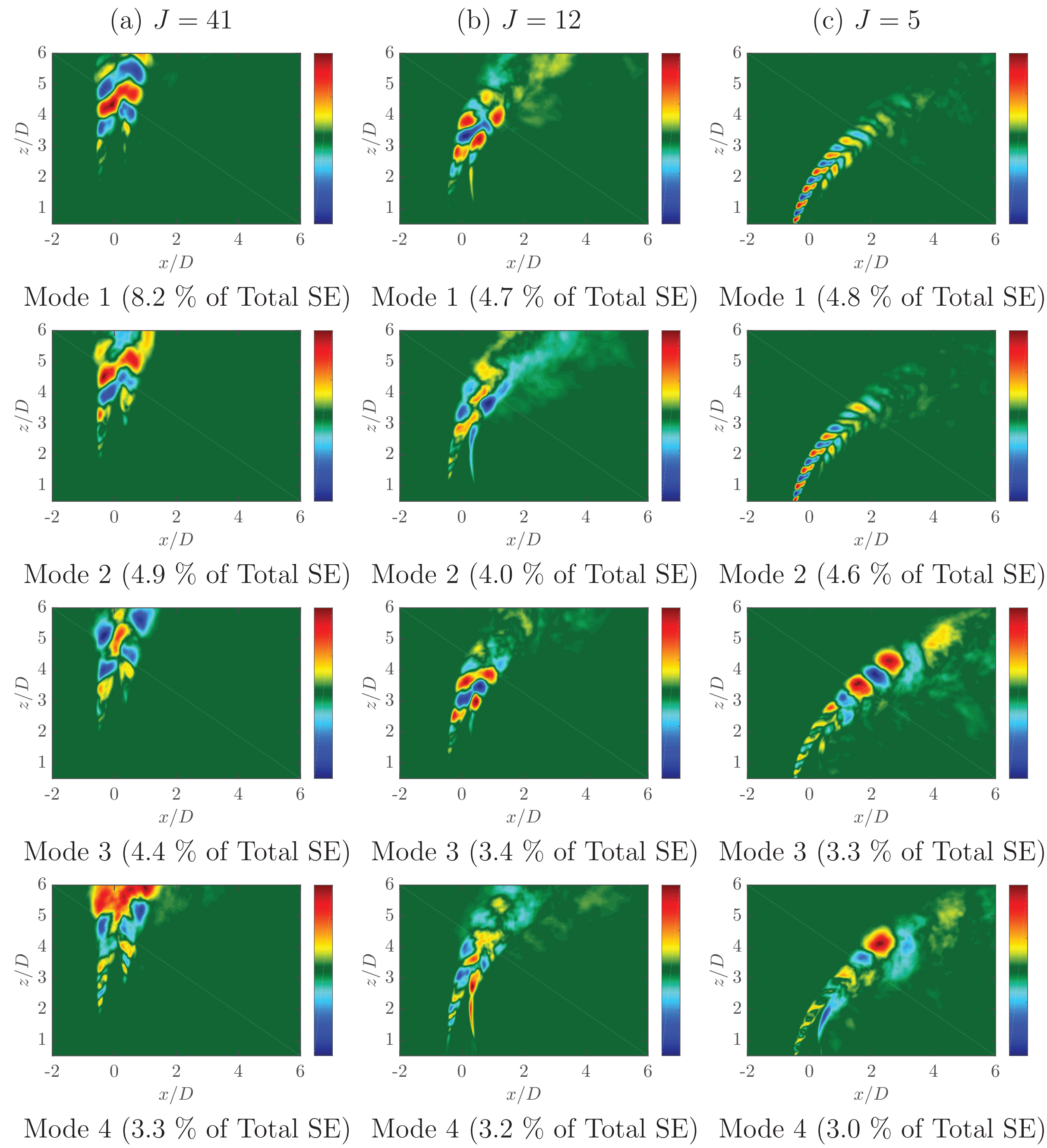

Figure 3.6: PLIF POD mode structures extracted from instantaneous centerplane (side view) higher resolution PLIF imaging of the $S = 1.00$, flush nozzle-generated JICF with varying momentum flux ratios: (a) $J = 41$, (b) $J = 12$, (c) $J = 5$. Data shown for Mode 1 (first row), Mode 2 (second row), Mode 3 (third row), Mode 4 (fourth row). Percent of total scalar fluctuation energy (SE) contributed by each mode is indicated below each image. (The color bar represents each mode scaled by its own norm and the mean jet velocity at the jet exit U_j.)

Figure 3.6 shows the first four scalar mode structures and their corresponding portion of the total scalar energy fluctuation of the flow based on 300 realizations of higher resolution centerplane PLIF images, for comparison with PLIF POD data involving 500 realizations at the present standard PLIF/PIV resolution. First of all, all mode structures in Figure 3.6 are less noisy than those extracted by PLIF data portion of the simultaneous measurements in Figure 3.5 due to the higher spatial resolution as well as the larger signal-to-noise ratio as reported by Gevorkyan (2015). These scalar mode structures reasonably well corresponded to those in Figure 3.5, although there were slight differences in dominant shear layer structures at the transitional case of $J = 12$. While the dominant upstream shear layer structures were initiated fairly close to the jet exit as shown in Figure 3.5(b), the mode structures began to be present further from the jet exit in Figure 3.6. Nevertheless, there appeared to be little effect of the spatial resolution of PLIF images on the qualitative trends in the POD analyses for this case.

It is worthwhile to explore the similarity between Mode 1 and Mode 2 for the data shown in Figures 3.4, 3.5 and 3.6. Following the work of Meyer et al. (2007), one can plot the POD coefficients of the first and second modes for all snapshots analyzed. If the coefficients of the first two modes plotted against each other yields a circle, then the structure in question is a periodic traveling wave that is characterized by linear combinations of the two modes. Figures 3.7(a) and (b) plot the coefficients of the first 2 modes (a_1 and a_2), extracted from the PIV and PLIF POD analyses, respectively, via Figures 3.4 and 3.5. As expected, as the momentum flux ratio was lowered and the flow transitioned to absolute instability (as noted before, yielding strongly periodic upstream shear layer vortex rollup), the coefficients of the first two modes plotted against each other for the PIV-based POD began to form a circular shape. For $J = 5$, the coefficient plot showed strong periodicity for both PLIF and PIV POD analyses, suggesting that the upstream shear layer absolute instability dominated the evolution of both scalar and velocity fields for this flow condition. For clearly convectively unstable conditions, as for $J = 41$, the shear layer instabilities were weaker and broadband in nature, without strong downstream periodic convection, and this yielded a more random pattern in the top row of Fig. 3.7. While the periodicity was not apparent in the PLIF POD

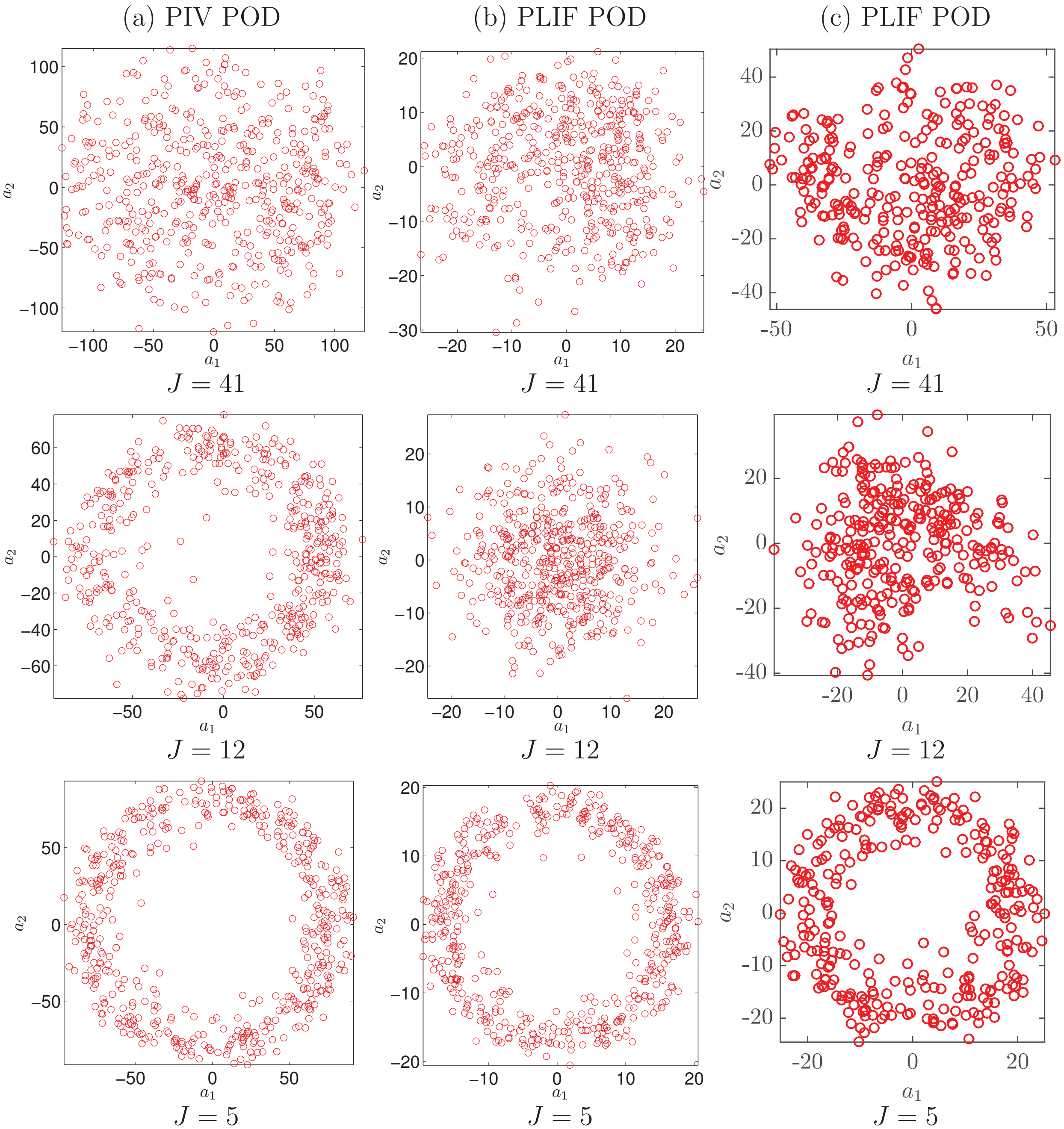

Figure 3.7: (a) PIV POD and (b) PLIF POD based on a portion of simultaneous PLIF/PIV data coefficients as well as (c) higher resolution PLIF data for the first two modes plotted against each other. POD analysis extracted from PLIF imaging of the $S = 1.00$, flush nozzle-generated JICF with varying momentum flux ratios: $J = 41$ (top row), $J = 12$ (middle row), $J = 5$ (bottom row). (a) and (b) are from Gevorkyan et al. (2017).

coefficient plot for $J = 12$ (see middle row of Figure 3.7(b)), this transitional flow condition did produce periodicity in the coefficients derived from the velocity data (middle row of Figure 3.7(a)). While it was not expected that the $J = 12$ case would yield different results between PLIF- and PIV-based coefficients, clearly, as noted by Kothnur and Clemens (2005), the velocity field and scalar field can respond differently to flow perturbations in a transitional flow. This would be true even for unity Schmidt number flows. As the JICF shear layer undergoes a transition in its nature, as occurs near the $J = 10$ transition, such differences in velocity and scalar response could become more pronounced. Figure 3.6, associated with higher resolution PLIF data, shows results which are consistent with Figure 3.5, extracted from the PLIF data portion of the simultaneous PLIF/PIV data sets, with little periodicity at $J = 41$ and 12 and clear periodicity at $J = 5$. Hence, the absence of the periodicity at $J = 12$ in the PLIF-based POD was not caused by the different spatial resolution in the PLIF images, but more likely due to different responses of the velocity and scalar fields to flow perturbations.

Figures 3.8, 3.9 and 3.10 show visualizations of the first four modes extracted from the PIV and PLIF (portion of the simultaneous PLIF/PIV measurements) POD analyses, as well as high resolution PLIF POD analyses applied to the low density ($S = 0.35$), flush nozzle-injected transverse jets for $J = 41$, $J = 12$, and $J = 5$, which all involved absolutely unstable upstream shear layers (Getsinger et al., 2012). Compared to the equidensity modes in Figures 3.4, 3.5 and 3.6, the PIV and PLIF POD modes for the $S = 0.35$ case shown in Figures 3.8, 3.9 and 3.10 had somewhat more chaotic and irregular-appearing structures. It is worthwhile to note that although the first two $S = 0.35$, $J = 41$ PIV POD modes were clearly shear layer modes (first and second rows of Figure 3.8(a)), the first two PLIF POD modes were actually associated with structures on the lee side of the jet (first and second row of Figures 3.9(a) and 3.10(a)). Thus, the lee-side jet stabilities of the $S = 0.35$, $J = 41$ jet had a more significant impact on the scalar field distribution and fluctuation content than on the velocity field. As the momentum flux ratio J was lowered for $S = 0.35$, the first two PLIF POD modes transitioned to becoming shear layer modes (e.g., compare $J = 41$ to $J = 5$ in Figures 3.9 and 3.10). In particular, clear periodicity for the first two modes is

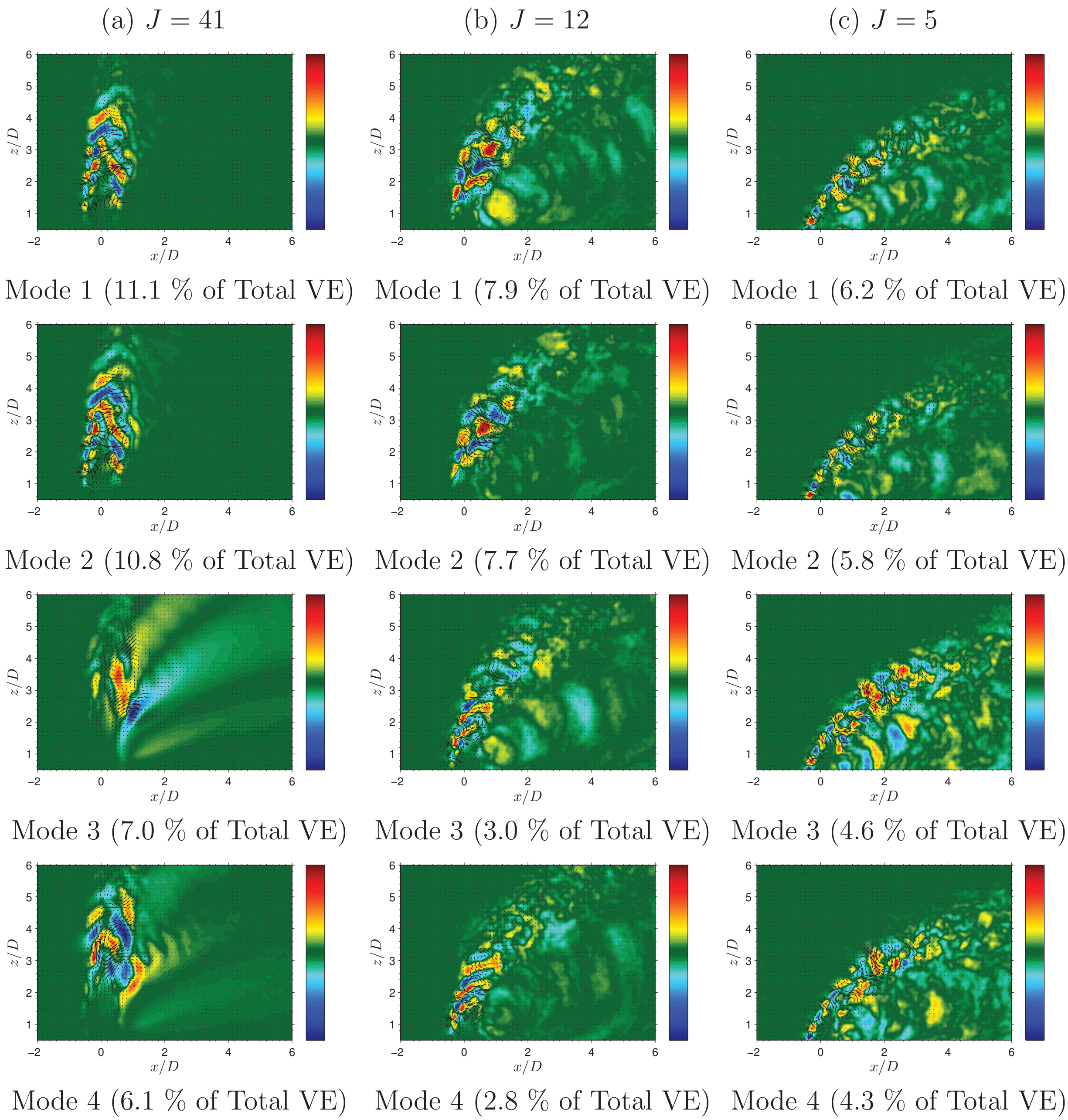

Figure 3.8: PIV POD mode structures extracted from instantaneous centerplane (side view) simultaneous PLIF/PIV imaging of the $S = 0.35$, flush nozzle-generated JICF with varying momentum flux ratios: (a) $J = 41$, (b) $J = 12$, (c) $J = 5$, from Gevorkyan et al. (2017). Data shown for Mode 1 (first row), Mode 2 (second row), Mode 3 (third row), Mode 4 (fourth row). Arrows in images indicate in-plane velocity component structure contribution, while colormap indicates out-of-plane velocity component structure contribution. Percent of total velocity fluctuation energy (VE) contributed by each mode is indicated below each image. (The color bar represents each mode scaled by its own norm and the mean jet velocity at the jet exit U_j.)

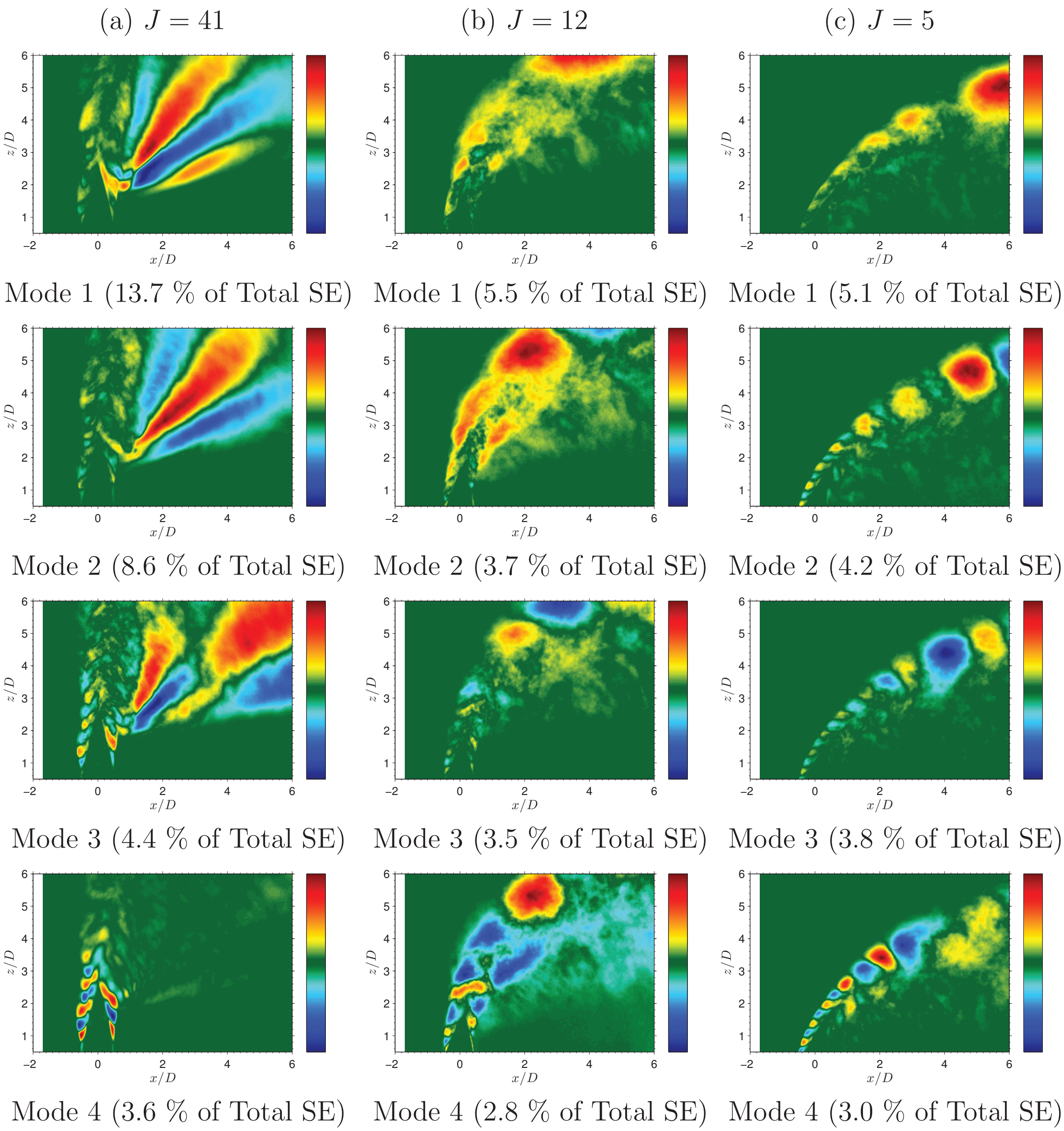

Figure 3.9: PLIF POD mode structures extracted from instantaneous centerplane (side view) simultaneous PLIF/PIV imaging of the $S = 0.35$, flush nozzle-generated JICF with varying momentum flux ratios: (a) $J = 41$, (b) $J = 12$, (c) $J = 5$, from Gevorkyan et al. (2017). Data shown for Mode 1 (first row), Mode 2 (second row), Mode 3 (third row), Mode 4 (fourth row). Percent of total scalar fluctuation energy (SE) contributed by each mode is indicated below each image. (The color bar represents each mode scaled by its own norm and the mean jet velocity at the jet exit U_j.)

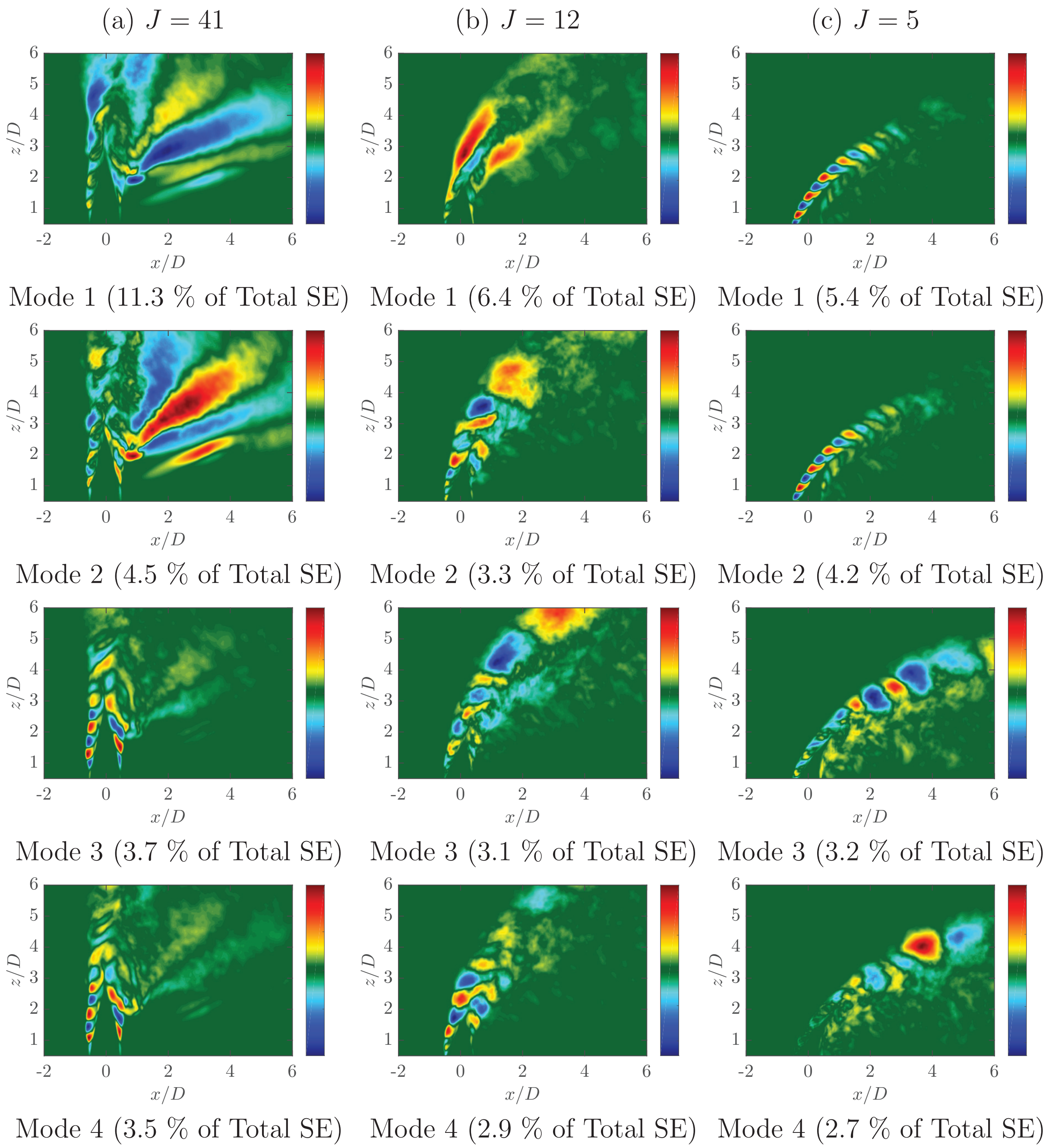

Figure 3.10: PLIF POD mode structures extracted from instantaneous centerplane (side view) higher resolution PLIF imaging of the $S = 0.35$, flush nozzle-generated JICF with varying momentum flux ratios: (a) $J = 41$, (b) $J = 12$, (c) $J = 5$. Data shown for Mode 1 (first row), Mode 2 (second row), Mode 3 (third row), Mode 4 (fourth row). Percent of total scalar fluctuation energy (SE) contributed by each mode is indicated below each image. (The color bar represents each mode scaled by its own norm and the mean jet velocity at the jet exit U_j.)

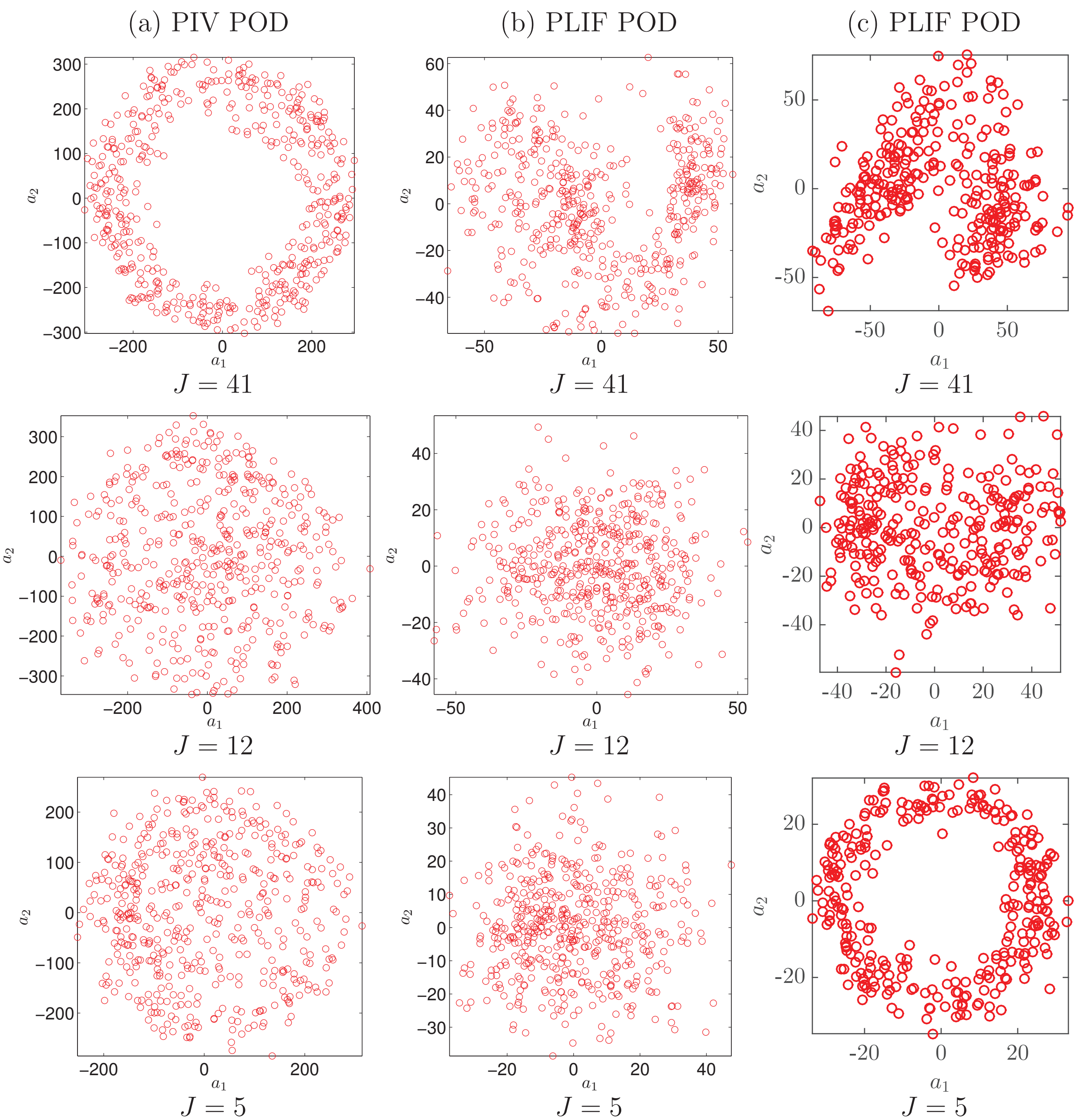

Figure 3.11: (a) PIV POD and (b) PLIF POD based on a portion of simultaneous PLIF/PIV data coefficients as well as (c) higher resolution PLIF data for the first two modes plotted against each other. POD analysis extracted from PLIF imaging of the $S = 0.35$, flush nozzle-generated JICF with varying momentum flux ratios: $J = 41$ (top row), $J = 12$ (middle row), $J = 5$ (bottom row). (a) and (b) are from Gevorkyan et al. (2017).

revealed in Figure 3.10(c) at $J = 5$. This transition from lee-side instability dominance to upstream shear layer-behavior dominance in the scalar field for these low density jets could in part be responsible for the reduction in mixing observed when one lowers J at a fixed density ratio below the critical value of $S \cong 0.40$, although differences in crossflow entrainment into variable density vortical structures are also important (Gevorkyan et al., 2016).

The first and second mode coefficients for these $S = 0.35$ jets, shown in Figure 3.11, showed strong periodicity in the upstream shear layer for PIV-based POD at $J = 41$, but with greater irregularity as momentum flux ratio was reduced, even though such a reduction in J still produced an absolutely unstable upstream shear layer. Clearly, the differences in the dynamics captured by the velocity and scalar fields in a density variable flow affected the relative energy content in the modes and their relationships that would suggest traveling wave behavior, although it was apparent that the first two modes for $J = 12$ and $J = 5$ in Figures 3.8(b) and 3.8(c) contained significant kinetic energy from wake vortices as well as shear layer vortices. These observations also could be related to the altered nature of crossflow entrainment by upstream shear layer vortices for the low density JICF with a reduction in J, as documented in Gevorkyan et al. (2016). Additionally, the comparison between PLIF POD results at differing spatial resolutions in Figures 3.11(b) and (c) at $J = 5$ illustrates that there can be a difference in periodicity, which is consistent with the first and second mode structure differences in Figures 3.9 and 3.10, the latter being at higher resolution. This qualitative discrepancy may be produced by both the higher spatial resolution and lower noise in higher resolution PLIF data, although the stronger periodicity did corroborate the existence of a transition from a lee-side instability dominance to an upstream shear layer-behavior dominance in the scalar field.

Figures 3.12, 3.13 and 3.14 show visualizations of the first four modes extracted from the PIV POD and PLIF (portion of the simultaneous PLIF/PIV measurements) POD analyses extracted from data in Figure 3.3, as well as high resolution PLIF POD analyses, respectively, for the equidensity, flush pipe-injected transverse jets at $J = 41$, $J = 12$, and $J = 5$. Similar to the modes for the equidensity flush nozzle cases shown in Figures 3.4, 3.5 and 3.6, the first two PLIF and PIV POD modes for the flush pipe-injected jets shown in Figures

3.12, 3.13 and 3.14 were composed primarily of shear layer structures, although they were comparatively weaker than for the nozzle-generated jets. Also as seen for the equidensity flush nozzle-injected jets, the first and second mode coefficients for the flush-pipe injected jets, shown in Figure 3.15, demonstrated increasing periodicity as J was reduced and the upstream shear layer transitioned to becoming absolutely unstable for $J = 5$. As also seen in hotwire spectral measurements (Getsinger et al., 2014), the transition to strong periodic behavior as J was reduced from $J = 12$ to $J = 5$ was more abrupt for the flush pipe than for the flush nozzle. The spatial resolution of the PLIF imaging did not appear to alter the qualitative characteristics of the POD analyses for the equidensity flush pipe-injected JICF, seen in comparing Figures 3.13 and 3.14, and also Figures 3.15(b) and 3.15(c), as occurred in the equidensity flush nozzle-injected JICF.

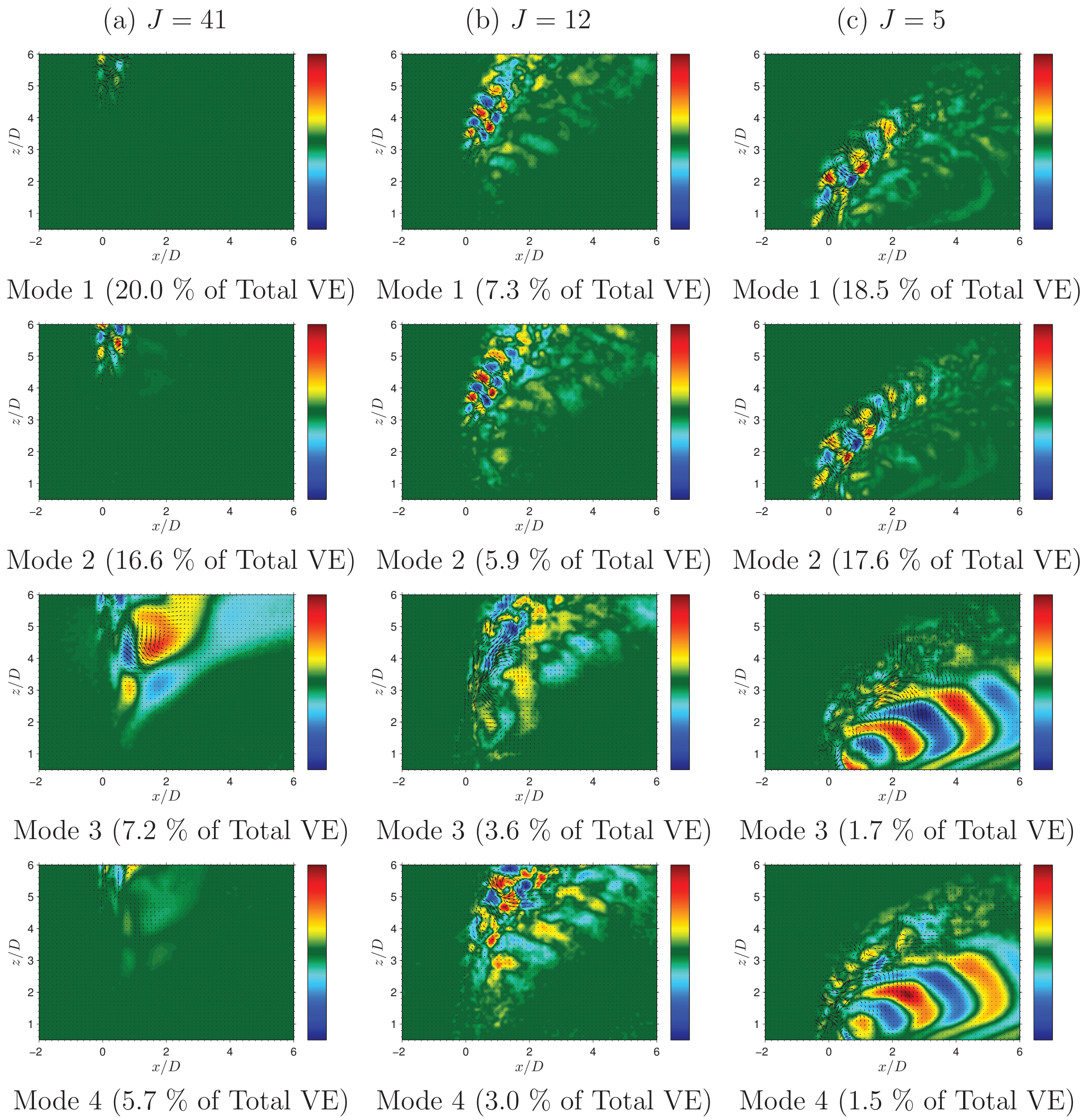

Figure 3.12: PIV POD mode structures extracted from instantaneous centerplane (side view) simultaneous PLIF/PIV imaging of the $S = 1.00$, flush pipe-generated JICF with varying momentum flux ratios: (a) $J = 41$, (b) $J = 12$, (c) $J = 5$, from Gevorkyan et al. (2017). Data shown for Mode 1 (first row), Mode 2 (second row), Mode 3 (third row), Mode 4 (fourth row). Arrows indicate in-plane velocity component structure contribution, while colormap indicates out-of-plane velocity component structure contribution. Percent of total velocity fluctuation energy (VE) contributed by each mode is indicated below each image. (The color bar represents each mode scaled by its own norm and the mean jet velocity U_j.)

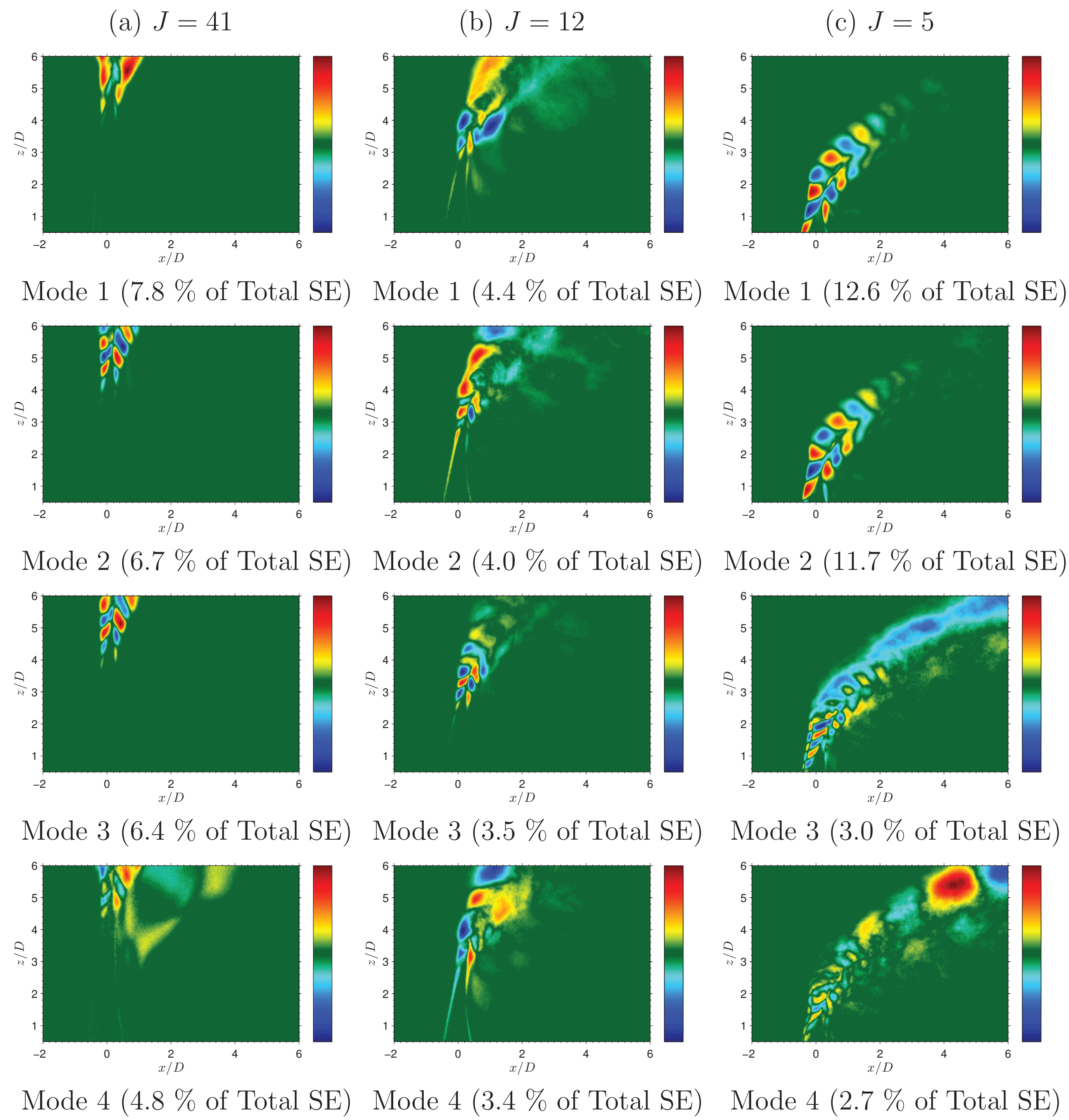

Figure 3.13: PLIF POD mode structures extracted from instantaneous centerplane (side view) simultaneous PLIF/PIV imaging of the $S = 1.00$, flush pipe-generated JICF with varying momentum flux ratios: (a) $J = 41$, (b) $J = 12$, (c) $J = 5$, from Gevorkyan et al. (2017). Data shown for Mode 1 (first row), Mode 2 (second row), Mode 3 (third row), Mode 4 (fourth row). Percent of total scalar fluctuation energy (SE) contributed by each mode is indicated below each image. (The color bar represents each mode scaled by its own norm and the mean jet velocity at the jet exit U_j.)

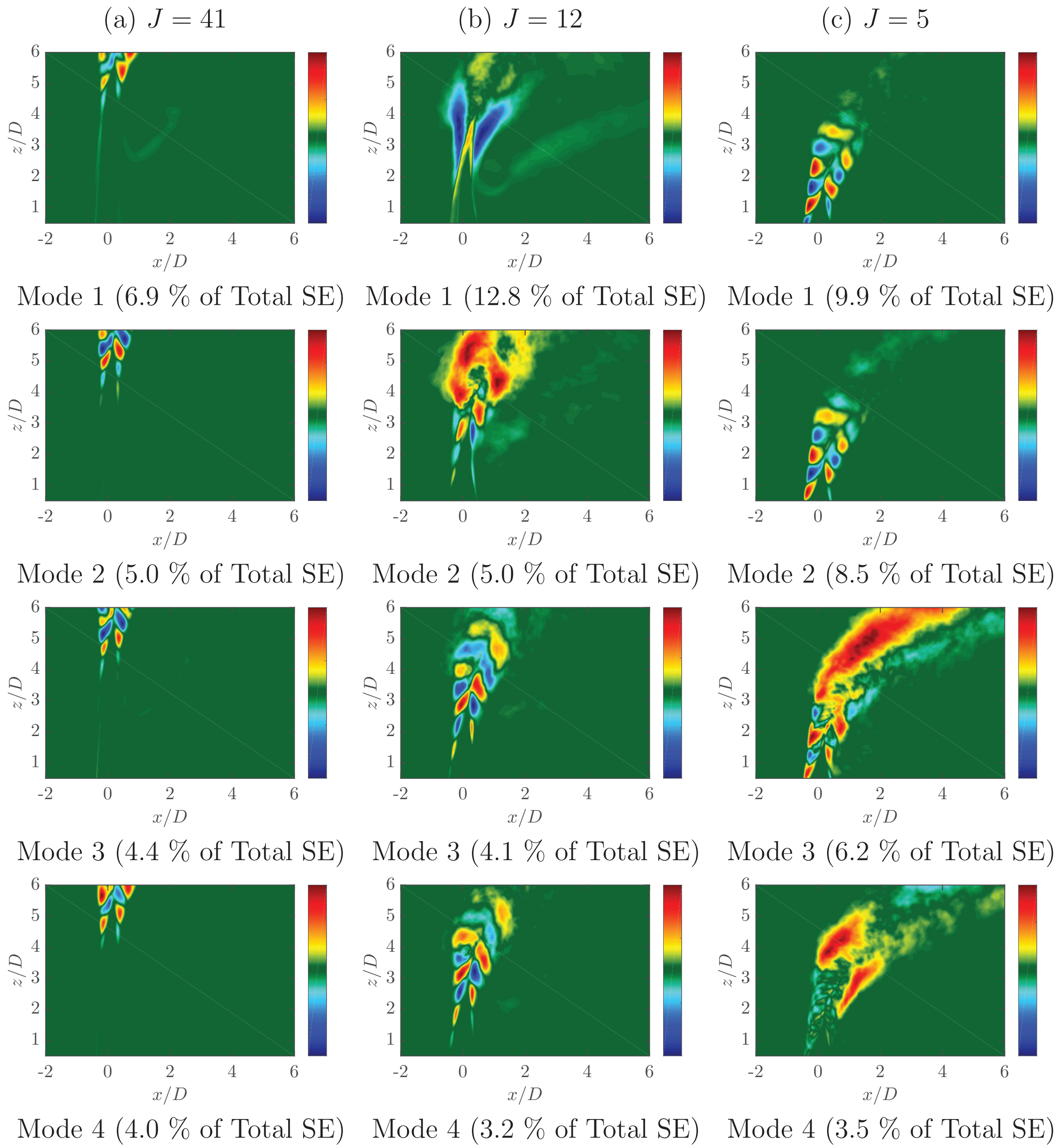

Figure 3.14: PLIF POD mode structures extracted from instantaneous centerplane (side view) higher resolution PLIF imaging of the $S = 1.00$, flush pipe-generated JICF with varying momentum flux ratios: (a) $J = 41$, (b) $J = 12$, (c) $J = 5$. Data shown for Mode 1 (first row), Mode 2 (second row), Mode 3 (third row), Mode 4 (fourth row). Percent of total scalar fluctuation energy (SE) contributed by each mode is indicated below each image. (The color bar represents each mode scaled by its own norm and the mean jet velocity at the jet exit U_j.)

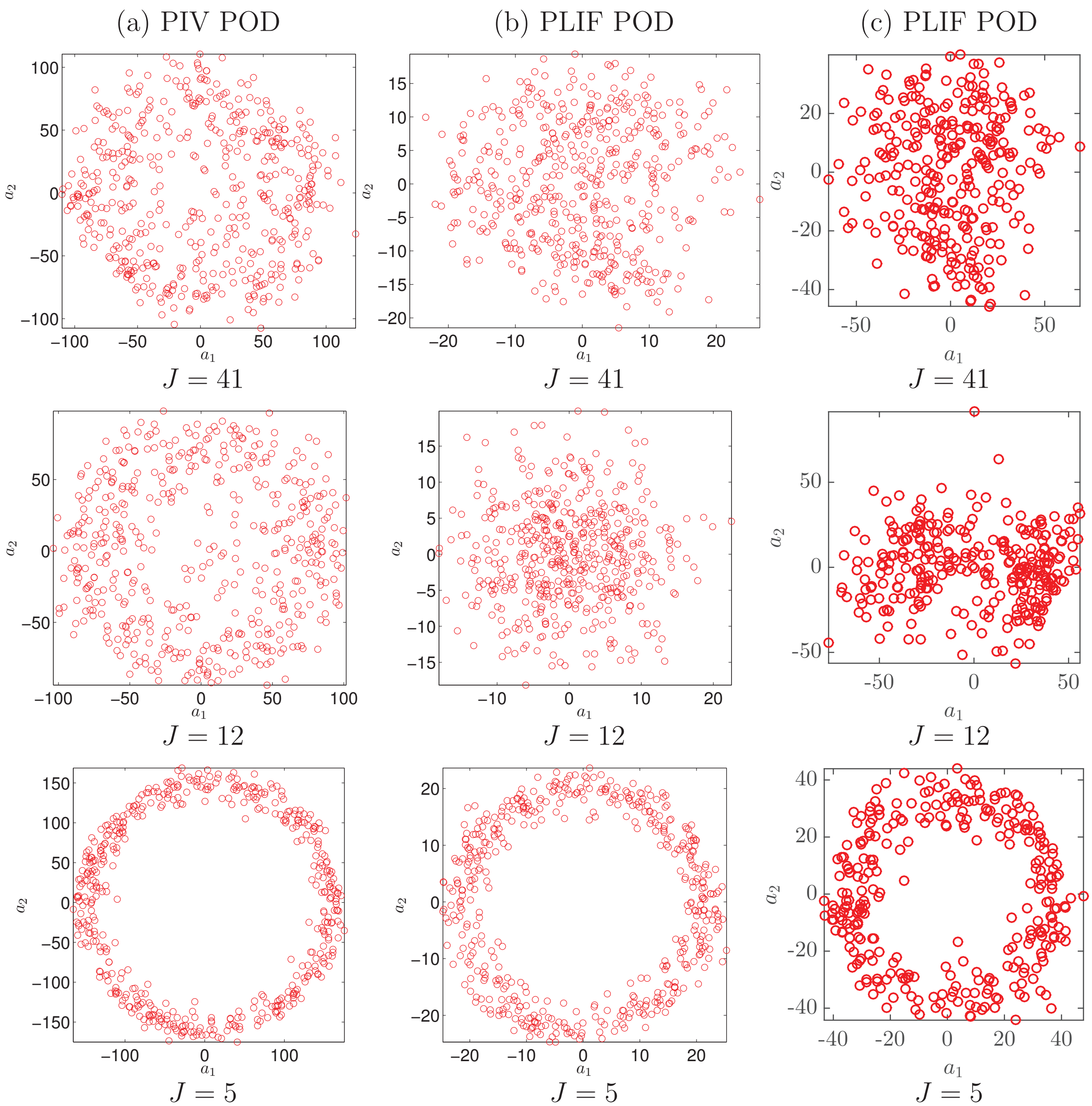

Figure 3.15: (a) PIV POD and (b) PLIF POD based on a portion of simultaneous PLIF/PIV data coefficients as well as (c) higher resolution PLIF data for the first two modes plotted against each other. POD analysis extracted from PLIF imaging of the $S = 1.00$, flush pipe-generated JICF with varying momentum flux ratios: $J = 41$ (top row), $J = 12$ (middle row), $J = 5$ (bottom row). (a) and (b) are from Gevorkyan et al. (2017).

3.2 Shear Layer Determination

In order to compare the velocity and scalar gradient quantities utilizing simultaneous acetone PLIF and stereo PIV measurements, a method for determining the location of the dominant upstream and downstream shear layers between jet and crossflow fluid was developed. Utilizing the mean jet trajectory based on concentration maxima from the PLIF data, a transformation from the $x-z$ coordinate system (shown in Figure 1.1) to the s_c-n (centerline-jet normal) coordinate system was implemented, similar to the method utilized for JICF mixing studies (see Gevorkyan et al. (2016) for details on the transformation method). After the transformation was implemented, the shear layer location was determined as the locus with the maximum scalar dissipation rate along a ray normal to each s_c/D position. This analysis yielded the local shear layer coordinate s_l and its local layer-normal direction n_l. An average shear layer trajectory coordinate s, used in prior JICF instability studies (Megerian et al., 2007; Davitian et al., 2010a) is shown in Figure 1.1. A similar method was utilized to track the downstream (lee-side) shear layer location. All average scalar dissipation rates and strain rates shown in this study were calculated at the instantaneous shear/mixing layer location determined from this method, and then averaged over the set of images for the coordinate location s_c.

3.3 SDRL Model Applied to the Equidensity JICF

In order to directly compare the strain rates extracted from the scalar field and from the velocity field in the JICF, the Strained Dissipation and Reaction Layer (SDRL) model (Equation (1.9)) was employed (Marble and Broadwell, 1977; Bish and Dahm, 1995; Smith et al., 1997). The SDRL model suggests that local quasi-steady strain rate can be extracted from error-function profile of mass fraction observed within the layer-like structures in its normal direction. This enabled the PLIF-based scalar data (and thus scalar dissipation rate χ and strain rate ϵ) to be compared directly to the strain rate extracted from the PIV-based velocity field data. The strain rate was calculated from PLIF concentration measurements utilizing an automated method of error function fitting, formulated and applied to each instantaneous scalar mixing layer location; such fitting was required in order to determine the boundary scalar values ζ^{+} and ζ^{-} in Equation (1.9). If one solves the 1D scalar advection-diffusion equation, assuming quasi-steady behavior and a locally uniform strain rate, the scalar distribution (normalized concentration C/C_o or ζ) takes the form shown in Equation (3.1):

$$\zeta = \frac{1}{2}\left(\zeta^{+} + \zeta^{-}\right) + \frac{1}{2}\left(\zeta^{+} - \zeta^{-}\right) erf\left(\frac{n_l}{\lambda_D}\right) \tag{3.1}$$

In this equation, n_l is the layer-normal coordinate direction, which is assumed to be the two-dimensional scalar gradient direction determined from the PLIF measurements for each mixing layer location, and λ_D is the length scale that results from the competition between strain and diffusion, so-called a strain-limited molecular diffusion length scale ($\lambda_D = \sqrt{\hat{D}/\epsilon}$ in the quasi-steady state limit, where $\hat{D}$ is the binary diffusivity). In practice, an error function fit of the form shown in Equation (3.2) was applied to the $\zeta = C/C_o$ data in the layer-normal direction n_l.

$$\zeta = a + b \times erf\left(\frac{n_l - c}{d}\right) \tag{3.2}$$

The coefficient c in Equation (3.2) represents the offset of the fit from the center location. The boundary conditions, $\zeta^{+} = C^{+}/C_o$ and $\zeta^{-} = C^{-}/C_o$, were determined by comparing Equation (3.1) to experimental concentration data. To ensure accuracy and applicability of the fit, besides requiring that the strain rate normal to the layer determined from comparative PIV data was compressive, another qualifier in the averaging process was applied based on the Pearson correlation coefficient or correlation coefficient of the fit ($R_{fit} > 0.99$) calculated as follows.

$$R_{fit} = \frac{\displaystyle\sum_{i=1}^{n}(A_i - \bar{A})(B_i - \bar{B})}{\sqrt{\left\{\displaystyle\sum_{i=1}^{n}(A_i - \bar{A})^2\right\}\left\{\displaystyle\sum_{i=1}^{n}(B_i - \bar{B})^2\right\}}} \tag{3.3}$$

where A_i and B_i are arbitrary data sets to be compared, and an overline stands for a mean value of a data set. R_{fit} is a commonly used parameter to evaluate the quality of fitting to data points, which takes a value between 0 (poor fitting) and 1 (good fitting). If R_{fit} for a fit was below the threshold of 0.99, the data point associated with the fit was removed from the averaging process to evaluate local mean strain rates. Additionally, error function fits assumed the magnitude of the coefficient $|c|$ in Equation (3.2) to be smaller than the two-pixel width in PLIF images in order to have a more precise representation of the layer-center location, corresponding to locations of maximum scalar dissipation rates in layer-like structures; points outside of this criterion were removed from the strain-rate evaluation. As with the comparison between local maximum scalar dissipation rate and layer-normal strain rate extracted from PIV shown in Gevorkyan (2015) and Gevorkyan et al. (2017), at least 200 data points (40 % of total instantaneous data) for each jet centerline trajectory location s_c/D were required in the averaging process in order to consider the average to be statistically significant. An example fit for the flush nozzle-injected, equidensity $J = 5$ jet is shown in Figure 3.16(a) for the spatial resolution associated with PLIF measurements during simultaneous PLIF/PIV experiments. For a comparison, an error function fit based on high resolution PLIF data is shown in Figure 3.16(b). These fits are reasonably good because each has $R_{fit} > 0.99$.

Before local strain rates in the equidensity JICF are compared, the validity of the qualifiers (e.g., R_{fit}, $|c|$, and the minimum number of data points in the averaging process) utilized in the strain rate calculation is required to be confirmed. The convergence of the strain rate calculation with the number of total instantaneous images is also investigated to verify that 500 instantaneous data sets were sufficient for statistical convergence. Figure 3.17 represents the local mean strain rates on the UML for the equidensity flush nozzle-injected JICF at $J = 41$, based on a minimum of 200 data points for averaging, with various thresholds of R_{fit} ($0.80 < R_{fit} < 0.99$). When the threshold is $R_{fit} > 0.80$, many data points are scattered downstream of $s_c \approx 4.0$. These sporadic data points were caused by poor error function fits, especially in the vicinity of the location where vortex rollup on the upstream shear layer were initiated. Because a good error function fit is less accurate around these rollups due to the

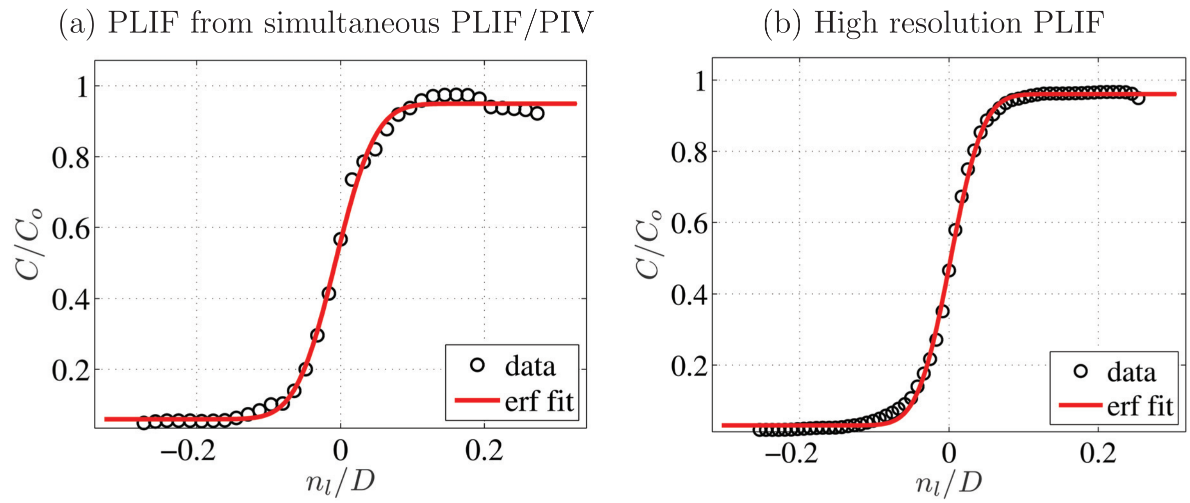

Figure 3.16: Example error function fits for flush-nozzle injected, $S = 1.00$, $J = 5$ transverse jets. Data shown for (a) PLIF portion of simultaneous PLIF/PIV experiments, and (b) high-resolution PLIF measurements, from Gevorkyan et al. (2017).

complex curvature of the shear layer as compared with that in the potential core region, the plots in Figures 3.17(a)-(c) become noisier downstream of the jet exit, beyond $s_c/D \approx 4.0$, with a lower threshold value of R_{fit}. As the threshold of R_{fit} increases, the plot becomes cleaner and less sporadic. For $R_{fit} > 0.99$ in Figure 3.17(e), data points did not become scattered due to an improved error function fit with this stricter threshold in R_{fit}. Hence, this study determined to utilize $R_{fit} > 0.99$ in the analysis in order produce fewer scattered local strain rates, and thus to obtain a better representation of the SDRL model.

Next, the effects of the magnitude of the coefficient in Equation (3.2), $|c|$, as well as the minimum number of data points in averaging process are investigated, as shown in Figures 3.18(a) and (b), respectively. Again, the local mean strain rates on the UML for the equidensity flush nozzle-injected JICF at $J = 41$ are plotted using $R_{fit} > 0.99$. In Figure 3.18(a), the local strain rates with various threshold values of $|c|$ ($1 \leq |c| \leq 3$) are evaluated, with a minimum of 200 data points for averaging. At $|c| = 3$, corresponding to a three-pixel width in PLIF images, one data point at $s_c/D \approx 4.9$ deviated from the other data points because of the error function fit from the layer-center location. However, even at $|c| = 3$, the strain rate evaluation was fairly consistent with those at $|c| = 1$, 1.5, and 2, as shown in Figure 3.18(a). This consistency among different $|c|$ values suggests that R_{fit} has a more

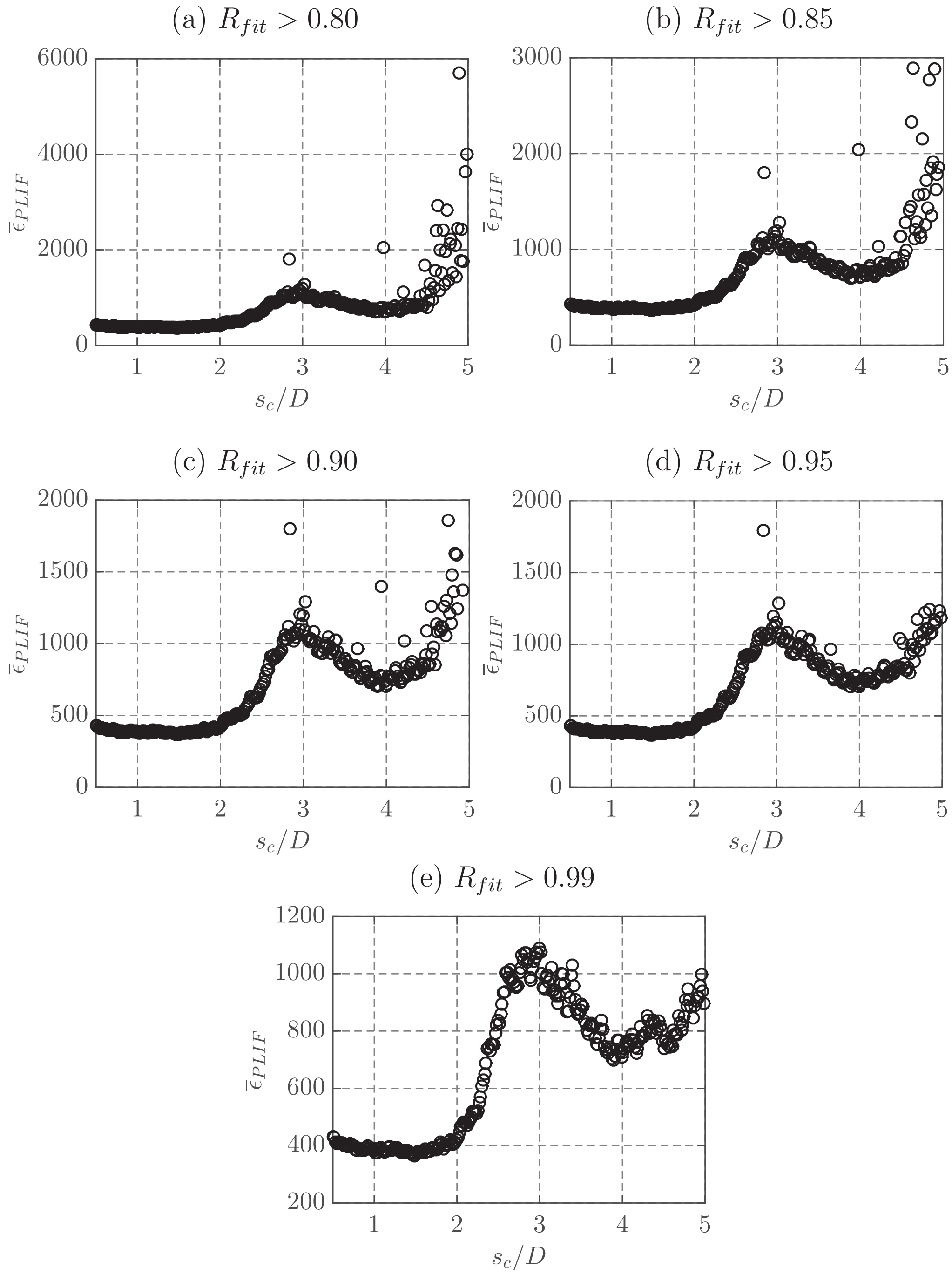

Figure 3.17: PLIF-extracted local strain rates on the upstream mixing layer for the equidensity flush nozzle-injected JICF at $J = 41$ with various thresholds of R_{fit}. The strain rate evaluation is performed using the PLIF data portion of the simultaneous PLIF/PIV measurements.

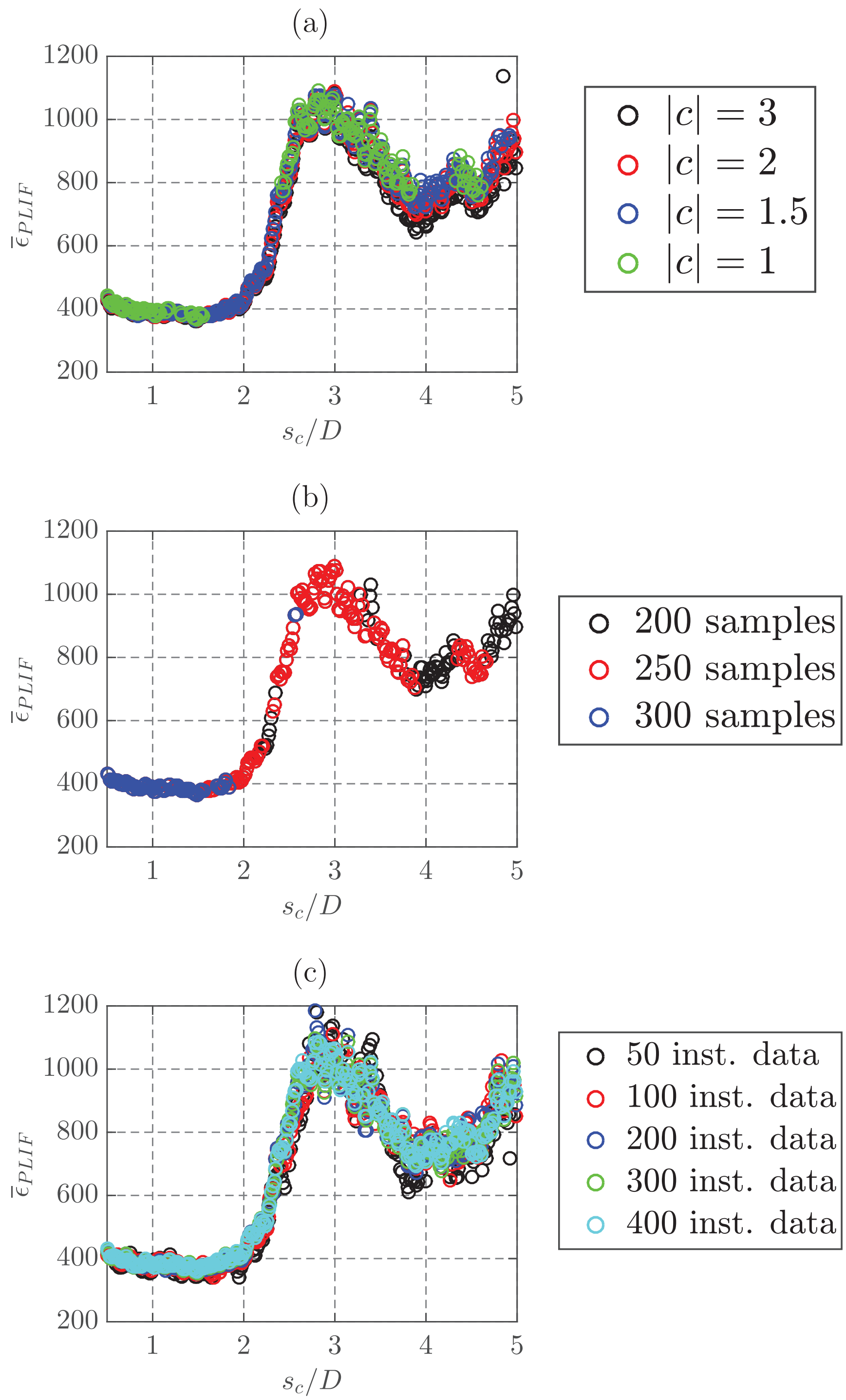

Figure 3.18: PLIF-extracted local strain rates on the upstream mixing layer for the equidensity flush nozzle-injected JICF at $J = 41$ with various (a) $|c|$, (b) minimum numbers of data points used in the averaging process, and (c) total numbers of instantaneous data. The strain rate evaluation is performed using the PLIF data portion of the simultaneous PLIF/PIV measurements.

significant effect on the strain rate evaluation than does $|c|$. As $|c|$ was decreased to $|c| = 1$, corresponding to one-pixel width in the PLIF images, some data points began to be missed due to the stricter criterion, although local strain rates were qualitatively and quantitatively consistent with results for higher $|c|$.

In Figure 3.18(b), the effect of minimum number of data points in the averaging process is shown based on the availability of 500 total instantaneous data with $R_{fit} > 0.99$ and $|c| = 2$. Utilizing 200, then 250, then 300 minimum samples ($40 - 60$ % of the total instantaneous data), the number of data points associated with local strain rates gradually decreased because of the stricter criterion, although all local strain rates were qualitatively and quantitatively similar to one another with various minimum numbers of data points used in the averaging process. This result also suggested that R_{fit} was more responsible for obtaining a sufficiently accurate strain rate evaluation. Hence, $|c| = 2$ and the minimum number of data points of 200 (or equivalently, 40 % of total instantaneous data) in the averaging process were utilized in this study.

Finally, the effect of the number of total instantaneous images (ranging from 50 to 400) on statistical convergence was also explored, as shown in Figure 3.18(c) for $R_{fit} > 0.99$, $|c| = 2$ and a minimum number of data points in the averaging process of 40 % of total instantaneous data (200 points). Here, even with only 50 total instantaneous data sets (20 minimum instantaneous data for the purpose of averaging), the local strain rates were qualitatively and quantitatively consistent with those based on a larger number of total instantaneous data sets. This consistency suggested that since all thresholds explored in this study (R_{fit}, $|c|$, and the minimum number of data points of 40 % of the total available instantaneous data) ensured a high quality determination of strain rate, where even a relatively low number of total instantaneous images provided consistent results with respect to larger numbers of instantaneous data sets. Beyond 300 instantaneous data sets, the quantitative difference in local strain rates was not recognizable because of this statistical convergence. Therefore, 500 instantaneous data in this study was deemed to be more than sufficient to obtain local mean strain rates for the JICF. From these investigations, the thresholds of $R_{fit} > 0.99$, $|c| = 2$ and a minimum number of data points of 200 in the averaging process were utilized, based on 500 total instantaneous image realizations for the strain rate evaluation.

Local strain rates from PIV data can be represented by principal strain rates, two strain components in a diagonalized strain rate tensor from Equation (1.10). However, as Gevorkyan (2015) notes, the directions of principal axes are not necessarily the same as the layer-normal directions, which must include the same direction as the strain extracted from PLIF data by definition in the SDRL model. Therefore, local strain rates from PIV data were calculated in the layer-normal directions determined from PLIF images, to directly compare the strain rates from PLIF and PIV measurements in the same directions.

First, one can decompose velocity into layer-normal directions and layer-parallel directions. Based on the layer-normal velocity $v_{n,l}$, local strain rates are calculated using the equation as follows.

$$\epsilon_{PIV} = -\frac{\partial v_{n,l}}{\partial n_l} \tag{3.4}$$

Because strain rates extracted from the SDRL model were assumed to be in layer-compressive (positive ϵ_{PIV} in Equation (3.4)) directions, strain rates in the layer-extensive (negative ϵ_{PIV} in Equation (3.4)) directions were removed from the calculation for the direct comparison. This algorithm was implemented for all instantaneous images and calculation of mean strain rates, provided by local averaging over the 500 instantaneous data. As described above, the minimum number of data points in averaging process was set to be 200 out of 500 total instantaneous data sets; otherwise, the data points were removed from the final results. More details on the algorithm involving the strain rate calculation from PLIF and PIV data may be found in Gevorkyan (2015) and Gevorkyan et al. (2017).

Figure 3.19 compares the computed mixing layer strain rate calculated from PLIF-based scalar measurements (Equation (3.1)), to the average layer-normal strain rate extracted from simultaneous PIV measurements, for the equidensity flush nozzle-injected transverse jets for J = 41, 12, and 5. This comparison is administered for both upstream (Figure 3.19(a)) and downstream (Figure 3.19(b)) shear layers. For J = 41, there was remarkable qualitative correspondence between the PIV- and PLIF-based strain rates on both upstream and downstream mixing layers (top row of Figure 3.19). As the momentum flux ratio was lowered to $J = 12$ and $J = 5$, the correlation between the PLIF- and PIV-based strain rate trends became poorer, especially in the UML for $J = 5$. It is difficult to definitively determine the exact cause of this qualitative discrepancy without time-resolved, fully three dimensional measurements of the scalar and velocity fields, but one explanation for the lack of correspondence on the downstream side of the jet for $J = 12$ and 5 must be associated with the increase in three-dimensional and transient effects on the lee side of the jet as momentum flux ratio is lowered, as evidenced by the transient wake vortices that appear in the structures of Mode 3 and Mode 4 seen in the PIV POD (third and fourth rows in Figure 3.4(b,c)). Another possible contributor to a lack of correspondence in trends for all cases studied here is the finite response time of the scalar dissipation layer to changes in strain rate. As summarized in the work of Kothnur and Clemens (2005), the scalar dissipation layer response time is dependent on both amplitude and frequency of strain rate fluctuations, and it is also dependent on whether the strain rate is temporally increasing or decreasing. It should be noted, however, that the lower magnitude in downstream PIV-based strain rates as compared with upstream PIV-based strain rates at $J = 12$ and $J = 5$ was consistent with trends for ignition of reactive jets in crossflow on the lee side of the jet (Sullivan et al., 2014; Wagner et al., 2015). Lowered strain rates suggest the propensity for more robust ignition, and for the transverse jet, this often occurs on the lee-side of the jet.

Despite qualitatively similar trends in PLIF- and PIV-based strain rates for $J = 41$, the quantitative differences were considerable. The peak strain rate value for $J = 41$ along the upstream shear layer in Figure 3.19, determined from the PLIF data was approximately 1100 s^{-1}, about half of the peak value extracted from the PIV data (approximately 2100 s^{-1}). Even larger quantitative differences were apparent for the downstream shear layer. Further exploration suggested that spatial resolution significantly affected the PLIF-based strain rates, as discussed in detail in Gevorkyan (2015) and Gevorkyan et al. (2017). Local strain rates extracted from high resolution PLIF data were significantly larger than those from relatively low resolution PLIF data portion of the simultaneous PLIF/PIV data, and hence the PLIF-extracted strain rates became closer to the PIV-extracted strain rates.

Figure 3.20 shows the trends in upstream and downstream mixing layer PIV and PLIF strain rates for equidensity, flush pipe-injected transverse jets for $J = 41$, 12, and 5. As with the flush nozzle data, the best correspondence in strain rates was observed for upstream mixing layers for convectively unstable conditions ($J = 41$ and 12) and downstream shear layers at $J = 41$, although all other conditions displayed some similarity in trends. Quantitative correspondence between the PLIF-calculated strain rate and the strain rate extracted from PIV was rare among the cases analyzed, however, despite these qualitative correspondences.

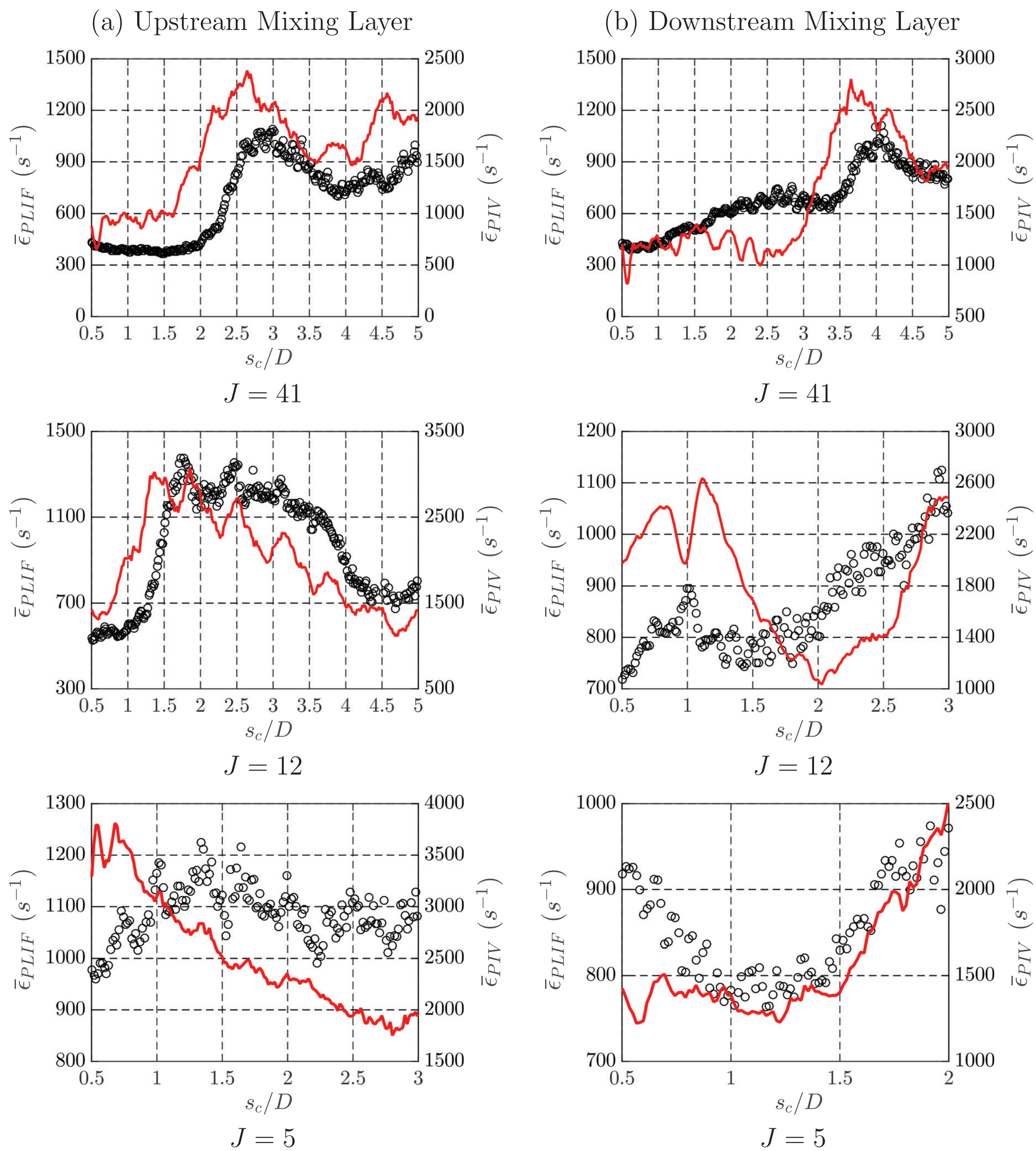

Figure 3.19: Average strain rate on the mixing layer calculated from scalar measurements using Equation (1.9) (○), and average strain rate extracted from PIV in the direction normal to the scalar gradient direction (—), of $S = 1.00$, flush nozzle-injected transverse jets with $J = 41$, $J = 12$, and $J = 5$ as indicated below each plot, from Gevorkyan et al. (2017). Data shown for (a) upstream mixing layer, and (b) downstream mixing layer. Data points with extensive strain in the scalar gradient direction are removed from averaging process.

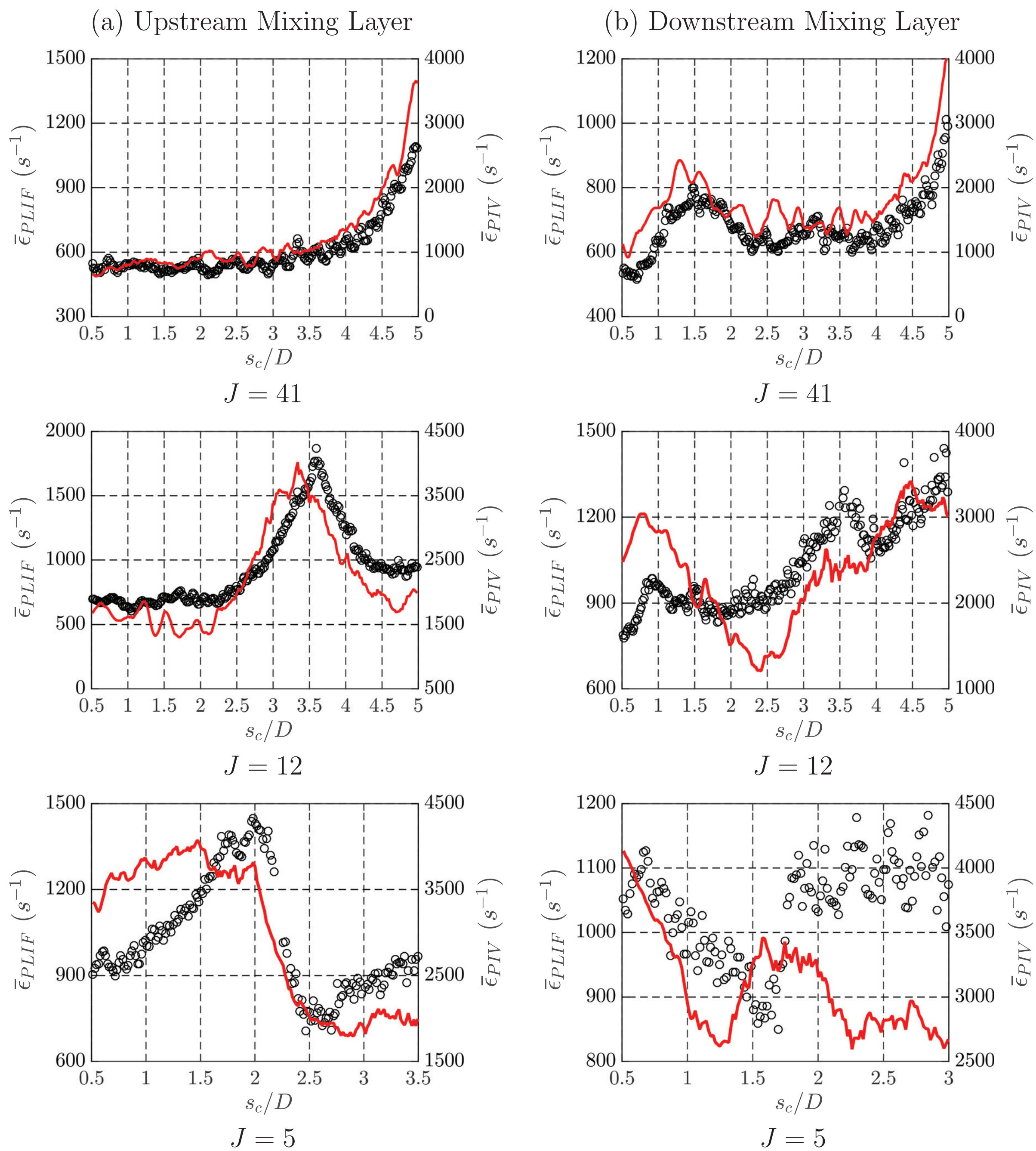

Figure 3.20: Average strain rate on the mixing layer calculated from scalar measurements using Equation (1.9) (**O**), and average strain rate extracted from PIV in the direction normal to the scalar gradient direction (—), of $S = 1.00$, flush nozzle-injected transverse jets with $J = 41$, $J = 12$, and $J = 5$ as indicated below each plot, from Gevorkyan et al. (2017). Data shown for (a) upstream mixing layer, and (b) downstream mixing layer. Data points with extensive strain in the scalar gradient direction are removed from averaging process.

3.4 Strain Rates in Lower Density Transverse Jets

In this section, strain rates associated with upstream and downstream mixing layers at a lowered density ratio, $S = 0.35$ for the flush nozzle-generated JICF, are discussed. For a non-unity density ratio in the flowfield, a coordinate transformation is required to account for the density variation across the jet and crossflow. The variation in density in the classical reaction-diffusion equation can be dealt with via the Howarth transformation (Howarth, 1948), which transforms a density-variable reference frame (y) to an effectively incompressible frame (normal coordinate n_l) via:

$$n_l = \int_0^y \left(\frac{\rho(\hat{y}, t)}{\rho_\infty} \right) d\hat{y} \tag{3.5}$$

where ρ_∞ is the density of the crossflow far from the jet, and ρ is the local density. Applying the Howarth transformation makes the density-variable flowfield effectively incompressible, and hence strain rates for the JICF shear layers with $S = 0.35$ can be calculated in the same manner as for those at $S = 1.00$, using the Howarth-transformed layer-normal coordinate, n_l.

To apply the Howarth transformation, the density or normalized density field is required, according to Equation (3.5). In this study, a density field was approximated based on acetone concentration fields acquired from PLIF imaging under the assumptions of: (1) the validity of the ideal gas law throughout the entire flowfield and (2) the assumption that the flowfield in this study was isothermal and isobaric, i.e., that the pressure and temperature did not dramatically change over the course of the experiments throughout the entire flowfield. To obtain jet temperature, it was noted that nitrogen and helium used to create the jet were stored at laboratory conditions (21°C), and crossflow was generated by a blower drawing the air from inside the laboratory. While the acetone temperature in the cooling chamber was controlled to be at a lower temperature than room temperature (approximately 12°C), the isothermal assumption was nevertheless valid because of the relatively small molecular fraction of acetone vapor within the jet fluid, $\psi \approx 0.1$, and the length of time the acetone had to heat up to room temperature after seeding but before injection into the test section. The pressure monitored inside the acetone cooling chamber for the entire experiments was only $4-5$ kPa higher than the room pressure, suggesting the validity of the isobaric assumption. As a consequence of isobaric, isothermal flow, the normalized acetone concentration, ζ, in PLIF images could be used to determine the local density ratio. The local molecular mass in the flowfield can be estimated from concentration ratio via the relation

$$M = \zeta M_j + (1 - \zeta)\, M_\infty \tag{3.6}$$

where M_j and M_∞ are the molecular masses of pure jet and pure crossflow fluid, respectively, which were constant during the experiments. Because jet-to-crossflow density ratio, S, can be expressed in terms of the ratio of molecular masses, $S = M_j/M_\infty$, one can obtain the local density ratio

$$\frac{\rho}{\rho_\infty} = 1 - \zeta(1 - S) \tag{3.7}$$

Hence, because crossflow density, ρ_∞, and jet-to-crossflow density ratio, S, were known and ζ was obtained from PLIF images, the density field could be determined using Equation (3.7). Figure 3.21 shows examples of instantaneous centerplane density ratio fields at $J = 41$ and $J = 5$ for the $S = 0.35$ flush nozzle-injected JICF. Clear evidence of density increases as the jet interacted with crossflow, especially after vortex breakdown and in the wake region, were apparent.

These instantaneous density ratio fields could be determined from each instantaneous PLIF image and incorporated into the Howarth transformation. As done in Section 3.3, for these non-unity density-ratio conditions, the Howarth transformation was applied in the layer-normal direction at each instantaneous scalar mixing layer location, based on the instantaneous density ratio fields, to generate a new Howarth-transformed layer-normal coordinate, n_l. After this, as before (Section 3.3), the error function was fit to concentration profiles with respect to the Howarth-transformed coordinate, then strain rates were determined via Equation (1.9). The Howarth transformation was only applied to the strain-rate calculation for PLIF data, of course, because strain rates from PIV data were explicitly derived from the velocity derivative in the layer-normal coordinate.

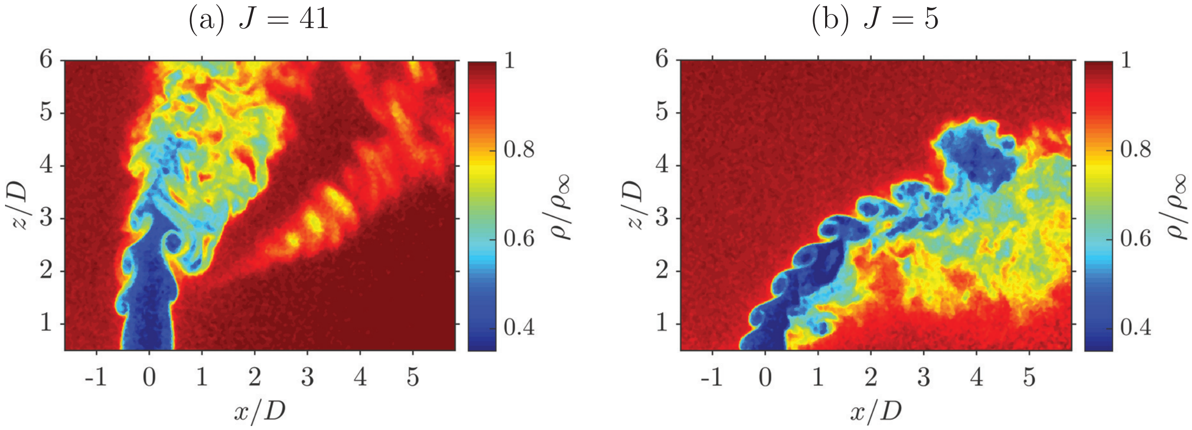

Figure 3.21: Instantaneous density ratio (ρ/ρ_∞) field images for flush nozzle-injected transverse jets at $S = 0.35$ and (a) $J = 41$ and (b) $J = 5$, from Gevorkyan et al. (2017). The density field is approximated from the instantaneous acetone concentration images from PLIF imaging. The density is normalized by the crossflow density, ρ_∞.

Strain rates for the flush nozzle-injected low-density ($S = 0.35$) transverse jets, derived from both PLIF and PIV data for the upstream and downstream mixing layers, are shown in Figure 3.22. Here, the jet-to-crossflow momentum flux ratios explored were $J = 41$ and 5, both of which are known to have an absolutely unstable upstream shear layer (Getsinger et al., 2012). Strain rates extracted from PLIF and PIV data at both $J = 41$ and 5 showed fairly good qualitative agreement in the upstream as well as downstream mixing layer, yet quantitative discrepancies between the strain rates was still significant in both regions, similar to discrepancies for the equidensity cases. Besides the effect of spatial resolution in the PLIF-derived strain rates as well as uncertainties in PIV measurements, the approximations in determining density fields here may have resulted in errors associated with application of the Howarth transformation and hence the strain rate calculation from PLIF data. Despite the significant quantitative discrepancies between the strain rates derived from PLIF and PIV data, it is interesting that applying the Howarth transformation to PLIF data for the lower-density jets provides comparable qualitative trends to those from PIV data. The similar qualitative trends between PLIF and PIV data further indicate that the SDRL model appears to be applicable to scalar fields with variable density conditions via the Howarth transformation.

As with equidensity jets, for the low density JICF, strain rates in the upstream mixing layer were considerably larger in the nearfield, closer to the jet exit, than for downstream mixing layer. The maximum strain rates for $J = 41$, for example, were located around $s_c/D \approx 2.7$ for the upstream mixing layer and $s_c/D \approx 1.8$ for the downstream mixing layer; for $J = 5$, maxima in strain rate were located at $s_c/D \approx 0.9$ for the upstream mixing layer and at $s_c/D \approx 1.3$ for the downstream mixing layer. Quantitatively, for the $S = 0.35$ data in Figure 3.22, strain rates were considerably lower in the DML close to the jet exit than in the UML in the same region. As noted earlier, these types of findings were consistent with the experimentally observed, ignition of the reactive JICF, where ignition tends to occur on the lee side of the jet (Wagner et al., 2015).

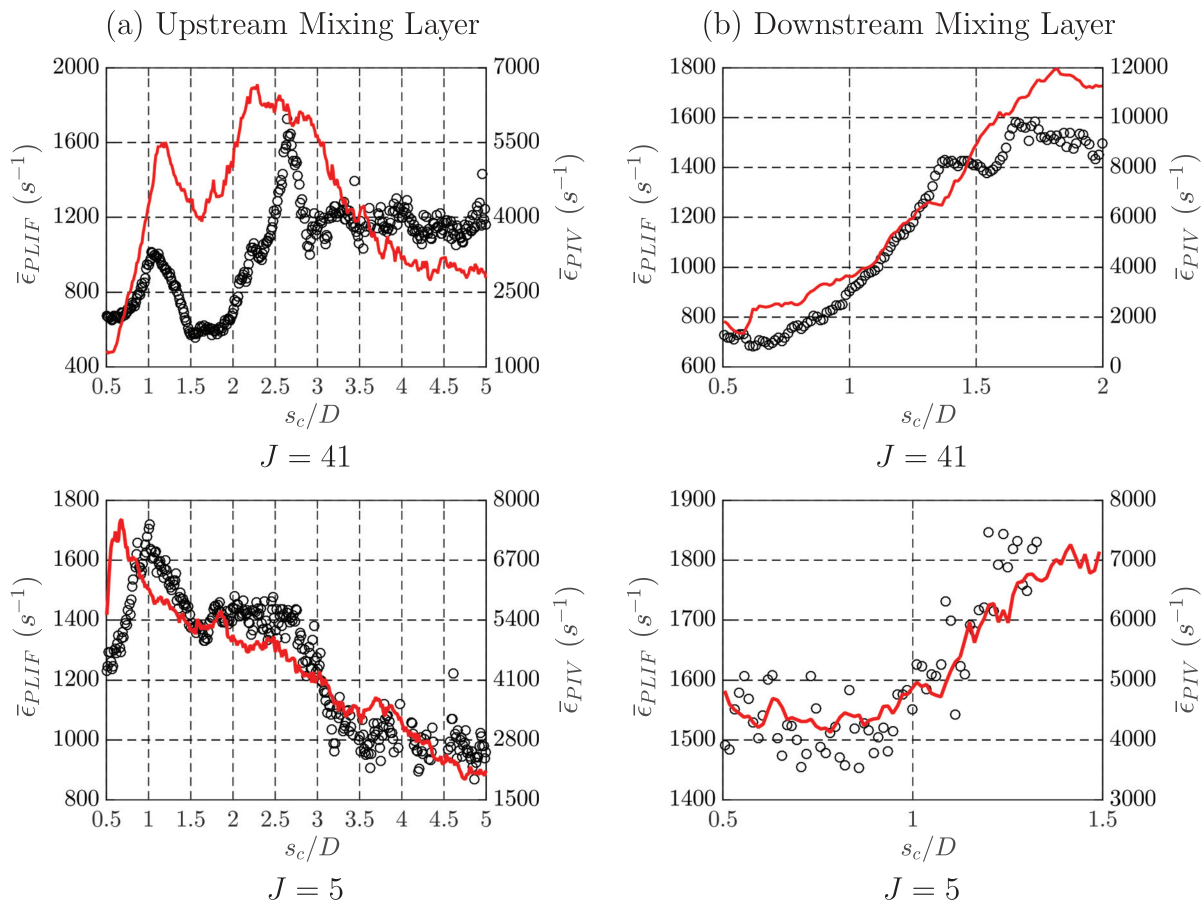

Figure 3.22: Mean strain rate on the mixing layer calculated from scalar measurements using Equation (1.9) with Howarth transformation on the left-hand side y axis (○), and mean strain rate extracted from PIV in the direction normal to the scalar gradient direction on the right-hand side y axis (—), of $S = 0.35$, flush nozzle-injected transverse jets with $J = 41$ and $J = 5$ as indicated below each plot, from Gevorkyan et al. (2017). Data shown for (a) upstream mixing layer, and (b) downstream mixing layer. Data points with extensive strain in the scalar gradient direction are removed from averaging process.

CHAPTER 4

Mixing Characterization with Variable Scale Lengths

Our group has extensively explored mixing characteristics for jets in crossflow over a wide range of jet-to-crossflow momentum flux ratios J and density ratios S with three different injectors: flush nozzle, elevated nozzle, and flush straight pipe (see schematics of injectors in Figure 2.2). Gevorkyan et al. (2016) discussed many types of mean-based and instantaneous-based mixing metrics that can be quantified from acetone PLIF experiments. These include maximum jet centerline concentration decay, and Unmixedness and Probability Density Function (PDF), using both centerplane and cross-sectional acetone concentration fields. In this earlier experimental study, the length scale of interest associated with mixing evaluation was the size of a pixel (approximately 0.4 mm widths) in the concentration images, which is the minimum possible length scale associated with the PLIF images. This relatively small length scale is used to quantify mixing metrics that relate more to molecular diffusion than to fluid stirring, which are associated with larger length scales (Aref, 1984; D'Alessandro et al., 1999; Mathew et al., 2003, 2004, 2005; Gouillart et al., 2006; Mathew et al., 2007; Gubanov and Cortelezzi, 2010). While the study by Gevorkyan et al. (2016) showed interesting mixing characteristics for the JICF with a relatively small length scale $\delta_s \approx 0.4$ mm, it is also worth exploring mixing characteristics related to larger length scales and thus relevant to stirring and related phenomena.

To characterize mixing with various length scales, an alternative mixing metric to the Unmixedness, which only incorporates a single small length scale (Gevorkyan et al., 2016), is required. An example of an alternative mixing metric is the Mix-Norm, introduced by Mathew et al. (2005). The Mix-Norm can estimate the efficiency of mixing over a range of length scales in the flowfield. An important feature of the Mix-Norm is the capability of sensing the effect of different fluid flow configurations with the same mean scalar property, enabling a distinction between the effects of molecular diffusion and fluid mechanical stirring, for example. As a consequence, the feature, the Mix-Norm can be successfully applied to capture the effect of various length scales on the mixing characteristics in a flowfield even in the absence of molecular diffusion. In contrast mixing metrics based upon the L^2 norm such as the Unmixedness, with a single length scale fail to evaluate mixing characteristics in a flow system without diffusion. In other words, the L^2 norm-based mixing metrics are unable to characterize the pure "stirring" effect in a mixing process as discussed in Mathew et al. (2005). The Mix-Norm application to closed-boundary systems by Mathew et al. (2005) implies that vortex flow structures do not necessarily enhance the degree of mixing for all length scales and can even worsen the mixing for certain length scales due to highly-concentrated portions of the flow captured by vortex structures. Gubanov and Cortelezzi (2010) applied the Mix-Norm to computationally-generated closed-boundary domains with different initial fluid geometrical configurations, but with the same mean scalar concentration, with variable forcing methods, resulting in the observation of different mixing characteristics for the different flows, despite their having the same mean scalar property. For a certain forcing condition where the same amount of sinusoidal shear is applied at the same location through the entire time, mixing becomes worse than the other cases because fluid pockets in flowfields analogous to vortical structures enclose highly-concentrated fluids inside themselves and prevent efficient mixing. These mixing characteristics cannot be captured by the Unmixedness metric, if it was a single fixed length scale, or it will even show the exactly same values due to the lack of ability to sense various length scales. Interestingly, Gubanov and Cortelezzi (2010), relevant to the Mix-Norm application, also suggest that vortical structures can enhance/deteriorate the overall mixing characteristics in flowfields, depending on how flow structures contribute to mixing process at different length scales, e.g., molecular diffusion and flow stirring. Hence, these previous studies (Aref, 1984; D'Alessandro et al., 1999; Mathew et al., 2003, 2004, 2005, 2007; Gubanov and Cortelezzi, 2010) indicate that mixing evaluation in a complicated flow system, where many different types of flow structures with different flow length scales coexist requires mixing metrics which account for various length scales to enable an in-depth study in the nature of mixing.

Now, as mentioned in Chapter 1, the JICF is known to be a very complicated flowfield which consists of many vortex systems (Margason, 1993; Karagozian, 2010). The JICF is typically considered to involve diffusion-limited transport process (Smith and Mungal, 1998; Gevorkyan et al., 2016), so applying mixing metrics related to the L^2 norm such as the Unmixedness, incorporating small fixed length scale, successfully estimates the degree of molecular mixing. The Unmixedness, in addition to more standard metrics such as centerline concentration decay and PDFs, is quantified very successfully in Gevorkyan et al. (2016). However, various flow structures in the JICF such as a potential core region, coherent vortex rollup on the upstream shear layer, or fluid in the wake region can contribute differently to mixing processes for the jet. The present mixing evaluation with a range of length scales, will provide a different interpretation of mixing characteristics for the JICF as compared with a mixing evaluation only with a single length scale (Gevorkyan et al., 2016). In this chapter, the centerplane-based Unmixedness with varying scale lengths, whose concept is analogous to the Mix-Norm or Mix-Variance (Mathew et al., 2005), will be developed based on the methods for Unmixedness computation in Gevorkyan et al. (2016) and analyzed using centerplane acetone concentration images acquired via PLIF imaging. The present results make used of the same PLIF-based scalar fields for the transverse jet used in Getsinger et al. (2014) and Gevorkyan et al. (2016).

4.1 Algorithm of Unmixedness Evaluation with Variable Scale Lengths

Although a new method to characterize mixing with various scale lengths described in this section is derived from the concept of the Mix-Norm, the basic algorithm and formulation are similar to the mean centerplane-based Unmixedness with a single length scale as described and implemented by Gevorkyan (2015) and Gevorkyan et al. (2016). However, accounting for various length scales in an open-boundary, complicated flow system such as the JICF is very challenging, mainly due to inflow and outflow from boundaries of a control volume enclosing the jet as well as out-of-plane components, which alter the local and global mean scalar properties. This contrasts closed-boundary systems studied in Mathew et al. (2005) and Gubanov and Cortelezzi (2010). To the best of our knowledge, mixing metrics accounting for variable scale lengths in an open-boundary, complex flowfield have not been extensively studied or even developed to date. In this section, an algorithm for applying the centerplane-based Unmixedness with different length scales is described.

To transform a transverse jet to its own centerline trajectory as for a free jet, a coordinate transformation from the x-z (horizontal - vertical) plane into the s_c-n plane (jet centerline trajectory coordinate - the normal direction to the trajectory) was applied to each instantaneous centerplane image. The jet centerline trajectory is defined as the best power-law fit to maximum concentration loci obtained from the mean concentration PLIF images. This coordinate transformation is successfully utilized in previous studies by our group on mixing and strain rate evaluation for the JICF (Gevorkyan, 2015; Gevorkyan et al., 2016, 2017) to enable comparison of such metrics along jet's centerline trajectory. In these studies, the centerplane-based Unmixedness $U_{c,sn}$ can be evaluated in the transformed planes within an interrogation area at a given location along jet's centerline trajectory, s_c/D. The interrogation area is oriented in the trajectory-normal direction n/D. For studies on Unmixedness (Gevorkyan et al., 2016), the length of the interrogation area was varied so as to match the mean concentration at all locations s_c/D and for a range of flow conditions, thus enabling consistency in comparisons. In the present studies on scale length effects, however, we used a fixed length of the interrogation area of 20 jet diameters ($-10 \leq n/D \leq 10$) and a fixed width of a single pixel δ_p in the s_c/D direction. This enables a systematic study of the effect of scale length, per Mathew et al. (2005) and Gubanov and Cortelezzi (2010). The single pixel size δ_p in PLIF images in this study is typically $\delta_p \approx 0.4$ mm. Figure 4.1(a) illustrates an instantaneous, transformed centerplane concentration image for the equidensity ($S = 1.00$) flush nozzle-generated JICF at $J = 12$ with an interrogation area located at $s_c/D = 5$ as shown. A zoomed-in interrogation area is shown in Figure 4.1(b), which will be used to explain the algorithm used in the present studies later. The size of the interrogation area is fixed through the entire mixing evaluation in the present studies in order to keep

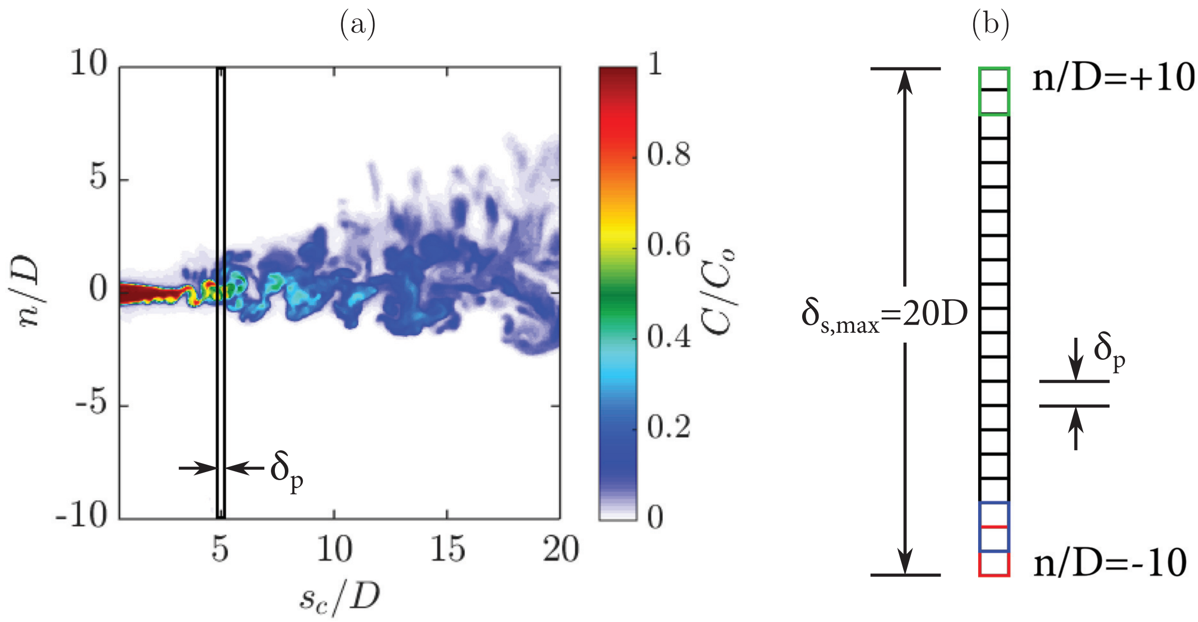

Figure 4.1: (a) An instantaneous centerplane PLIF jet image in the transformed plane (s_c/D-n/D) for the equidensity flush nozzle-injected JICF at $J = 12$, with a one-pixel-width (δ_p) interrogation area shown as a black box. (b) An interrogation area explaining about how to create a fluid element at two-pixel length scale ($\delta_s = 2\delta_p$) at the negative end of the interrogation area in n/D direction (red box), one-pixel away from the red box (blue box) and the positive end of the interrogation area (green box).

the range of mixing length scales constant over the entire set of s_c/D locations and for all instantaneous images.The procedure was as follows.

First, Unmixedness, whose original form was defined in Equation (1.6) in Section 1.5, was evaluated using the smallest length scale δ_p (the pixel length) in the n-direction in the interrogation area, shown by the black squares in Figure 4.1(b). This evaluation is basically the same as the method in Gevorkyan et al. (2016) but with a single pixel-width interrogation area instead of a seven-pixel-width interrogation area. In addition, there was no matching of mean concentration values inside each interrogation area to a reference value. Next, a 2-pixel length element (in the n-direction) is used, so $\delta_s = 2\delta_p$. We take the mean of the concentration values in two pixels next to each other in the n/D direction at $n/D = -10$, at the negative end of the interrogation area. The two pixels are shown in Figure 4.1(b) as a red box. This averaging process essentially creates a "single fluid element" with a half-spatial resolution (or doubled scale length) in the n/D direction. Then, the two-pixel long fluid element and its mean are determined at the next location, a single pixel away in the positive n/D direction from the $n/D = -10$ location, shown as a blue-lined rectangular area in Figure 4.1(b). Note that there is a one-pixel overlap between the two fluid elements, seen in the red and blue boxes in Figure 4.1(b). This process of shifting the element by one pixel and calculating the mean concentration continues to be implemented from the negative side ($n/D = -10$) to the positive end ($n/D = 10$) of the interrogation area. Figure 4.1(b) shows as a green-lined area as the last two-pixel long element of length $\delta_s = 2\delta_p$. Based on the two-pixel-sized fluid elements and their mean concentrations, the Unmixedness at this length scale is then evaluated. This process of evaluating the Unmixedness continues to be applied with varied length scales, ranging from $\delta_s = \delta_p$ to the length of the entire interrogation area in the n/D direction, $\delta_s = \delta_{s,max} = 20D$ ($\delta_p \leq \delta_s \leq \delta_{s,max}$ or $20D$). For this latter case, there is a single element in the n-direction and hence by definition the Unmixedness becomes 0 %, because the mean concentration value in the interrogation area is equal to the concentration value of the maximum-size single fluid element, observed in Equation (1.6). After the Unmixedness is calculated over all length scales at a given s_c/D location, the interrogation area is moved to the next s_c/D location, a single pixel away from the original location, and the same procedure is applied. This process is continuously applied pixel by pixel in the s_c/D direction, and the instantaneous centerplane-based Unmixedness is then evaluated for all possible length scales δ_s and over all s_c/D locations ($0.5 \leq s_c/D \leq 10$) in each instantaneous, transformed PLIF image. This relation determining the instantaneous centerplane-based Unmixedness at a given s_c/D location can be formulated as a function of a mixing length scale δ_s/D as follows:

$$U_{c,sn}(\delta_s) = \frac{1}{N_e(\delta_p)} \sum_{i=1}^{N_e(\delta_s)} \frac{(C_i(\delta_s)/C_o - \overline{C}/C_o)^2}{\overline{C}/C_o(1 - \overline{C}/C_o)} \tag{4.1}$$

In Equation (4.1), $N_e(\delta_s)$ represents the number of fluid elements with a length scale δ_s, $C_i(\delta_s)$ is mean concentration value of the i-th fluid element, counted from the fluid element at $n/D = -10$ ($i = 1$), with the length scale of δ_s, C_o is the mean concentration value extracted from the potential core region to normalize the concentration, and $\overline{C}$ is the mean concentration value inside the entire interrogation area. The denominator in Equation (4.1), $\overline{C}/C_o(1-\overline{C}/C_o)$, normalizes the Unmixedness, and hence the range of the Unmixedness extends between 0 and 1. Note that the main interest in this study lies in evaluating mixing at each length scale δ_s. The Unmixedness is typically not averaged over all length scales in contrast to the Mix-Norm (Mathew et al., 2005), which is defined as the efficiency of mixing over the entire range of length scales. Yet Unmixedness can be used to study mixing efficiency over variable length scale, as will be shown.

The number of fluid elements with a length scale δ_s in an interrogation area as shown in Figure 4.1 is calculated as follows:

$$N_e(\delta_s) = N_e(\delta_p) - \frac{\delta_s}{\delta_p} + 1 \tag{4.2}$$

The averaging procedure to create fluid elements in this algorithm is similar to that for the Mix-Norm in accounting for different length scales. For the Mix-Norm evaluation, one can first calculate $d(c, p, s)$, the mean value of a function c in the interval $[p - s/2, p + s/2]$ as follows:

$$d(c, p, s) = \frac{\int_{p-s/2}^{p+s/2} c(x)\mu(dx)}{s} \tag{4.3}$$

where c represents a scalar function with a non-dimensional distance x, p is a normalized spatial position, μ is the Lebesgue measure, and s is a normalized length scale (Mathew et al., 2005). Equation (4.3) integrates concentration values at the center spatial location of p within the spatial interval of $[p - s/2, p + s/2]$, corresponding to a spatial interval of a normalized length scale s. This operation is essentially analogous to the process of creating fluid elements in the current algorithm. Hence, $d(c, p, s)$ can be integrated at all locations p as follows:

$$\phi(c, s) = \left(\int_0^1 d^2(c, p, s)\mu(dp) \right)^{1/2} \tag{4.4}$$

where $\phi(c, s)$ is the L^2 norm of the averaged d for a fixed scale s. The Mix-Norm of the function c is obtained by the integral of these measures over all possible normalized scales $s \in (0, 1)$:

$$\phi(c) = \left(\int_0^1 \phi^2(c, s)\mu(ds) \right)^{1/2} \tag{4.5}$$

While the current algorithm for Unmixedness does not integrate the normalized scalar field over all length scales (in Equations (1.6) and (4.1)), the form of Equation (4.4) in the Mix-Norm evaluation is analogous to Equation (4.1). The instantaneous centerplane-based Unmixedness can be evaluated at a range of values of δ_s, and then averaged over $200 - 300$ instantaneous images at each s_c/D location and at each length scale δ_s to produce the mean centerplane-based Unmixedness as a function of various length scales δ_s.

In previous studies on the nature of multiscale mixing (Mathew et al., 2003, 2004, 2005, 2007; Gubanov and Cortelezzi, 2010), the Mix-Norm was applied in flowfields surrounded by closed boundaries. In closed-boundary systems, applying the Mix-Norm or any mixing metric is relatively simple because the interrogation area as well as the mean scalar properties inside the flow system are inherently constant, consistent with mass conservation. However, the present study implements the analogous mixing metric to open-boundary flow systems, so a valid application of the mixing metric as a variable dependent on length scales is highly challenging and often requires special treatment. Gevorkyan et al. (2016) also note that even applying metrics such as Unmixedness and Probability Density Function (PDF), using the smallest length scales from PLIF images, to an open-boundary flow system requires care to obtain results that may be compared among widely variable flow conditions. Gevorkyan et al. (2016) determine the Unmixedness and PDF of concentration fields by matching mean acetone concentration values inside each seven-pixel-width interrogation area over the entire flowfield (in the centerplane) and in cross-sectional jet slices. This is accomplished by changing the size of the interrogation area, adding or removing zero-valued pixels for the interrogation area, thus maintaining mass conservation. This special treatment successfully enables a study which appropriately compares mixing characteristics for jets in crossflow operating under various flow conditions. This approach of matching mean concentrations in interrogation areas to a fixed value is more appropriate when the mixing characteristics are compared among different flow conditions, as discussed in detail in Gevorkyan et al. (2016). But this approach is not precisely accurate when exploring the influence of length scales on mixing process.

In addition to the the Unmixedness evaluation introduced above, with a fixed interrogation area but without matching mean concentration values inside interrogation areas in order to explore the same range of length scales ($\delta_p \leq \delta_s \leq \delta_{s,max}$ or $20D$) over the entire range of s_c/D locations ($0.5 \leq s_c/D \leq 10$), we apply the alternative Unmixedness evaluation with matching mean concentration values inside variable-sized interrogation areas, as in Gevorkyan et al. (2016), in order to still explore the effect of variable mixing scale lengths. Note that when mean values are matched to a fixed reference value in each interrogation area, the range of length scales at each s_c/D location necessarily becomes different due to a variable size of the interrogation area (or maximum length $\delta_{s,max}$ in Figure 4.1). In the study by Gevorkyan et al. (2016), the reference value typically is the spatial mean concentration value of the temporally averaged concentration at a fairly far downstream location ($s_c/D = 15$) for the equidensity flush nozzle-injected JICF at $J = 5$ in the plane normal to the jet. Interestingly, Gevorkyan et al. (2016) confirm that the Unmixedness calculation with matched mean values is fairly insensitive to the selected reference value. In the present study, for the alternative Unmixedness evaluation with matching mean concentration values, the same reference value used in the study by Gevorkyan et al. (2016) is implemented, for the $J = 5$ case at $s_c/D = 15$. Because the same PLIF data sets are utilized in this study as in Gevorkyan et al. (2016), the choice of the reference value is considered to be reasonable.

As mentioned, matching the mean concentration value for the alternative Unmixedness evaluation produces different sizes of the interrogation areas at each s_c/D location, and hence different maximum length scales ($\delta_{s,max}$ in Figure 4.1). Thus, the process of averaging at each s_c/D location and at each length scale δ_s requires special consideration, especially at relatively larger length scales. In the alternative scheme with the matched mean concentration values, after the process of evaluating the instantaneous Unmixedness for all length scales over the entire set of s_c/D locations for a given condition is accomplished, the minimum length scale within all of the maximum length scales, $\delta_{s,threshold}$, is determined for all instantaneous images and s_c/D locations. Then the instantaneous Unmixedness data with length scales larger than $\delta_{s,threshold}$ are removed from the calculation to guarantee that the mean Unmixedness is evaluated based on all instantaneous images, $200-300$ samples. This treatment is especially important in this study to ensure statistical convergence because the number of pixels in each interrogation area is already small due to the use of a relatively narrow, one-pixel-width interrogation area as compared with the seven-pixel-width interrogation area in Gevorkyan et al. (2016). When zeros are added/removed to match mean concentration values in interrogation areas with the smallest length scale δ_p, equivalently to the evaluation administered in Gevorkyan et al. (2016), the direction of adding/removing zeros does not affect the mixing metric results because the Unmixedness with a single length scale is unable to capture the segregation of fluid. However, the process of adding/removing zeros with larger length scales δ_s is direction-sensitive because the added/removed zero-valued pixels play an important role in the process of creating fluid elements along the interrogation area and hence change the scale of fluid segregation or clustering. Hence, in the present study, if necessary, zeros are added/removed evenly from both sides (positive and negative n/D) of an interrogation area so that the zeros are not weighted on one of the sides. A variation in the maximum length scales in each interrogation area to match the mean concentration values generates a slight qualitative discrepancy as compared with the trends acquired by the scheme with fixed-size interrogation areas but without matching mean concentration values, as expected. Yet mixing characteristics of interest are sufficiently captured by both methods in the same manner, and with the same trend, which will be discussed in detail in Section 4.3.

To verify the validity of the algorithm with a fixed interrogation area but without matching mean concentration values, a test calculation is conducted based on the discussion of mixing characteristics by Kukukova et al. (2009). Kukukova et al. (2009) indicate that the scale of segregation pertaining to clustering of flow structures is important to characterize mixing, particularly turbulent mixing process. The concept of the scale of segregation is deeply related to mixing length scales, the main interest in this part of our study. Hence, the Unmixedness metric, yet applied with variable length scales, has to be capable of capturing the scale of segregation in flowfields if the mixing metric is to work successfully. That is, the Unmixedness should become lower, corresponding to better mixing, for a lower scale of segregation and higher, for worse mixing, with a higher scale of segregation at a given length scale. Figure 4.2(a) shows a 15×15 test fluid configuration with closed boundaries, where a black and white pixels correspond to concentration values of 1 and 0, respectively. The mean concentration value in each column, at all x_1 locations ($1 \leq x_1 \leq 15$), is set to be identical. At $1 \leq x_1 \leq 3$, fluid elements with black pixels are separated from each other with a length scale of one pixel, so the scale of segregation in this region is low. However, at $13 \leq x_1 \leq 15$, fluid elements with black pixels are all concentrated in one region, so the scale of segregation is high. The scale of segregation is set to be gradually higher every three columns, from the region at $1 \leq x_1 \leq 3$ through that for $13 \leq x_1 \leq 15$, where a fluid configuration for every group of three columns is identical. Although each column consists of the same number of black and white pixels, the flowfield at $1 \leq x_1 \leq 3$ is obviously better mixed than that at $12 \leq x_1 \leq 15$ due to its lower scale of segregation. Then, the Unmixedness metric with various length scales with a fixed interrogation area is applied to this configuration to validate the capability of the metric in sensing the scale of segregation. As noted earlier, the size of the interrogation area is fixed throughout the entire process at a 15-pixel length ($\delta_{s,max}$) in the x_2 direction and a 1-pixel width (δ_p) in the x_1 direction, resulting in the same range of variable length scales, $1 \leq \delta_s \leq 15$, over all x_1 locations. The same algorithm is applied over all length scales δ_s as well as at all x_1 locations.

The results are shown in Figure 4.2(b) and (c), which represent the concentration-based Unmixedness U_{c,x_1x_2} as a function of length scale δ_s, for different ranges of horizontal pixel location x_1 and as a function of x_1 for different δ_s values, respectively. As observed in the plot in Figure 4.2(c) shown as a black line and circle markers, the Unmixedness with the smallest length scale at $\delta_s = 1$ along x_1 is 100 % over the entire region, corresponding to completely unmixed fluid, even though the scale of segregation every three columns is significantly different. The same thing is shown in Figure 4.2(b) for $\delta_s = 1$. While this makes sense for the smallest δ_s, this equivalent Unmixedness for different fluid configurations suggests a lack of the ability to quantify the scale of segregation if the Unmixedness or any L^2 norm-based

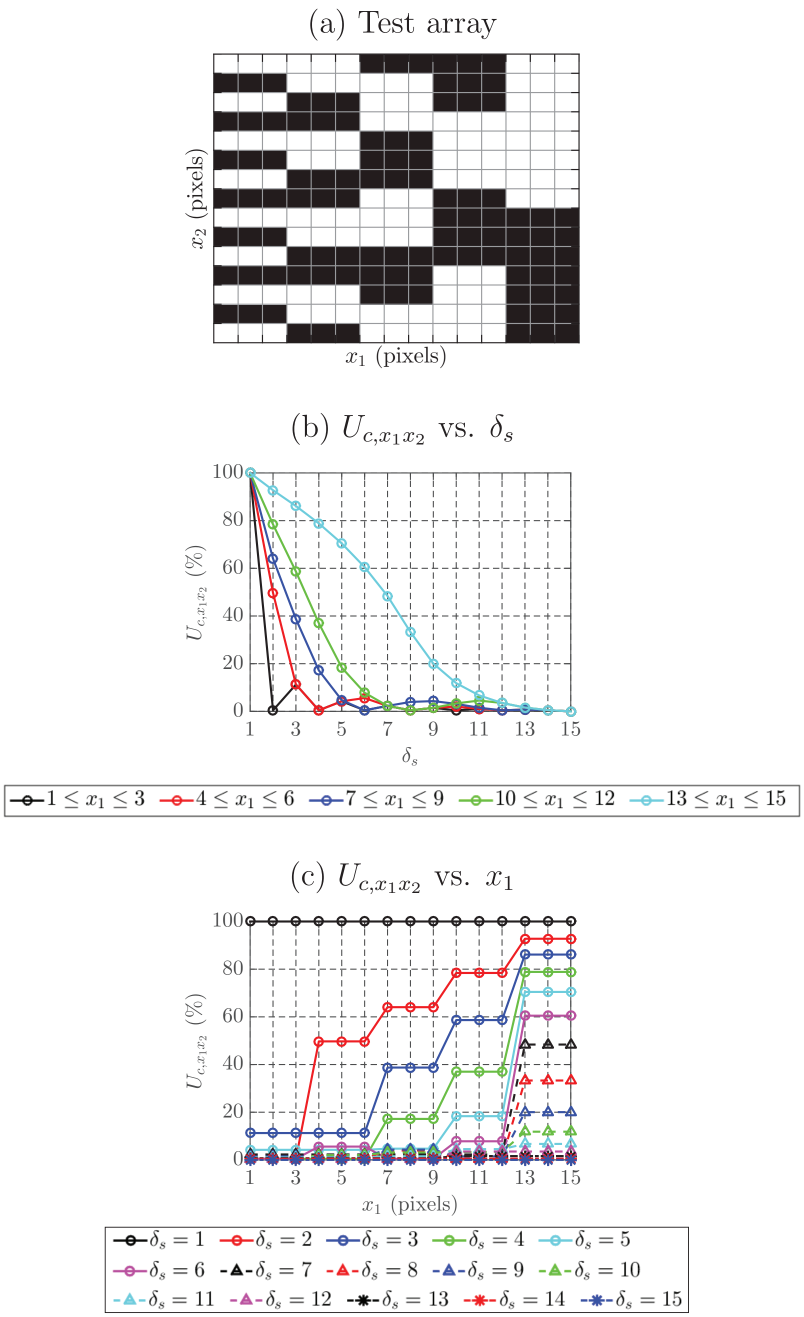

Figure 4.2: (a) Example of a scalar fluid configuration in a closed 15×15-pixel array used to validate the evaluation of Unmixedness for various length scales. Black and white pixels correspond to 1 and 0, respectively. Each column (x_1) has the same mean scalar value of approximately 0.47, but with various scales of segregation. (b) Unmixedness of the fluid configuration U_{c,x_1x_2} as a function of length scales δ_s for an one-pixel-width interrogation area and a length of 15 pixels in the x_2 direction. (c) The same Unmixedness for various length scales as a function of the x_1 coordinate location.

mixing metric is applied without special treatment. The Unmixedness evaluation at larger length scales, δ_s, however, does capture differences in the scale of segregation because larger scale lengths can capture regions of mixed fluid, i.e., pixels with both 0 and 1 values. Figure 4.2(b) generally reveals a lower Unmixedness, corresponding to better mixing, most length scales δ_s when the fluid configuration has a lower scale of segregation as at the left side of Figure 4.2(a). The same trend is observed in Figure 4.2(c); the Unmixedness is generally lower in the region $1 \leq x_1 \leq 3$, with a lower scale of segregation, and U_{c,x_1x_2} gradually becomes higher toward the region $13 \leq x_1 \leq 15$ with a higher scale or degree of segregation, strongly depending on the value of δ_s. At $\delta_s = 15$ (the maximum length scale $\delta_{s,max}$), for all flow configurations, the Unmixedness is 0 %, as expected, indicating completely mixed fluid in each large interrogation area.

The results of the test case indicate that this algorithm successfully captures varying degrees of mixing with variable length scales δ_s and thus distinguishes higher and lower scales of segregation. In actual flowfields, one can expect an increase in the Unmixedness if the degree of fluid segregation becomes larger in the flowfield at a certain length scale. This increase could be associated with actual flow structures, such as vortices in the upstream shear layer of the JICF or flow structures in the wake region with a relatively higher degree of out-of-plane component.

4.2 Unmixedness with Variable Scale Lengths without Matching Mean Values

In the previous study associated with mixing characteristics for the JICF by our group (Gevorkyan et al., 2016), the mean centerplane-based Unmixedness in the transformed plane ($n/D - s_c/D$) is evaluated using a seven-pixel-width interrogation area, approximately corresponding to a scale length of $s_c/D \approx 0.25$. This width is carefully determined to be sufficiently thin to be fairly close to the experimentally-measured $1/e^2$ laser sheet thickness (approximately $400 - 900$ μm) at the wavelength of 266 nm for acetone PLIF imaging (see Section 2.3.1), and sufficiently thick to achieve statistical convergence. In the present study, on the other hand, a one-pixel-width interrogation area, approximately corresponding to $s_c/D \approx 0.04$, was applied to study the effect of varying length scales in the n/D direction, normal to the jet's centerline trajectory, on Unmixedness and flow segregation. Therefore, it has to be verified that one-pixel width for the interrogation area is sufficient for statistical convergence or to properly capture the mixing characteristics at each s_c/D location.

For this verification, the values of Unmixedness with the smallest length scale $\delta_s = \delta_p$ (approximately $0.04D$) are evaluated and compared using one- and seven-pixel-width interrogation areas. With the one-pixel-width interrogation area, because the Unmixedness can be evaluated with/without matching the mean concentration value in each interrogation area to the reference value, the results acquired by both methods are also compared. The Unmixedness with the seven-pixel-width interrogation area is taken from the study by Gevorkyan et al. (2016). Note that the same set of PLIF data is utilized to evaluate the Unmixedness, so the results should be qualitatively as well as quantitatively highly similar.

Figure 4.3 shows the mean centerplane-based Unmixedness with the smallest length scale, $\delta_s/D = \delta_p/D \approx 0.04$, along s_c/D calculated with the seven-pixel-width interrogation area with matching mean values (Gevorkyan et al., 2016), as well as with the one-pixel-width interrogation area without and with matching mean values. The equidensity flush nozzle-, elevated nozzle- and flush pipe-injected transverse jets are considered here at $J = 41$, 12 and 5. Sample instantaneous PLIF images for these cases are shown in Figure 1.5. As one can see, all three results in Figure 4.3 show qualitatively and quantitatively good agreement, with consistent reduction in Unmixedness (increase in mixing) as one moves downstream. There is a very slight quantitative discrepancy between $U_{c,sn}$ from Gevorkyan et al. (2016) and this study without matching mean values, especially fairly far downstream and at higher J values. This small quantitative difference is likely caused by the process of matching mean values; without matching mean values, each interrogation area clearly has a different spatial mean concentration value. The mean values may fluctuate even more at downstream locations and/or higher J values because the jet is more turbulent and chaotic, possibly resulting in more significant out-of-plane concentration fluctuations. One does not see any significant differences between the results from Gevorkyan et al. (2016) and those from the present study with a one-pixel-width interrogation area when there is mean matching in Figure 4.3.

To explore a possible culprit for the quantitative difference in the Unmixedness in more detail, the PDF of mean spatial concentration values inside a one-pixel-width interrogation area with the smallest length scale ($\delta_s/D \approx 0.04$) is calculated at various s_c/D locations, in order to estimate the significance of the mean value fluctuations. To evaluate the PDF, samples are collected from all instantaneous images at each s_c/D location. Figure 4.4 shows PDFs for various nozzles and flow conditions, where the PDF represents a histogram of the instantaneous scalar data, normalized such that the area under the curve is unity (Dimotakis and Miller, 1990). Increased levels of mixing here result in the appearance of a preferred (or most probably) value of the scalar concentration. The variation in mean concentration values becomes higher (broader distributions) at downstream locations than upstream locations as well as higher J values. As one can see, the PDF shows steeper, narrower peaks in the nearfield at all J cases but wider mean concentration distributions in the relatively farfield. As seen in Figure 1.5, in the nearfield, the main dominant flow structures are a potential core and coherent rolled-up vortices on the upstream shear layer. These nearfield structures are very repetitive over all instantaneous images, and are considered to have lower mean concentration fluctuations than in the farfield. Strong peaks in the PDF in the nearfield suggest strong potential for rapid mixing associated with the vortices. Clearly, in the farfield, the flow is more turbulent and considered to have more out-of-plane components, which causes larger fluctuations in mean concentration values. This results indicate that the small quantitative difference is mainly due to the mean concentration fluctuations at relatively far downstream locations and higher J values. The mean values in each interrogation area do not change with matching mean values, resulting in almost identical results between the Unmixedness with a different size of the interrogation area (one- vs. seven-pixel width). Although the slight quantitative difference is observed, the general mixing trend based on the Unmixedness is sufficiently captured. In addition, the purpose of this study is to evaluate the Unmixedness with various length scales and interpret the relationship between the degree of mixing and flow structures associated with dominant mixing process, not to quantitatively compare the results among all flow conditions as done in Gevorkyan et al. (2016). The

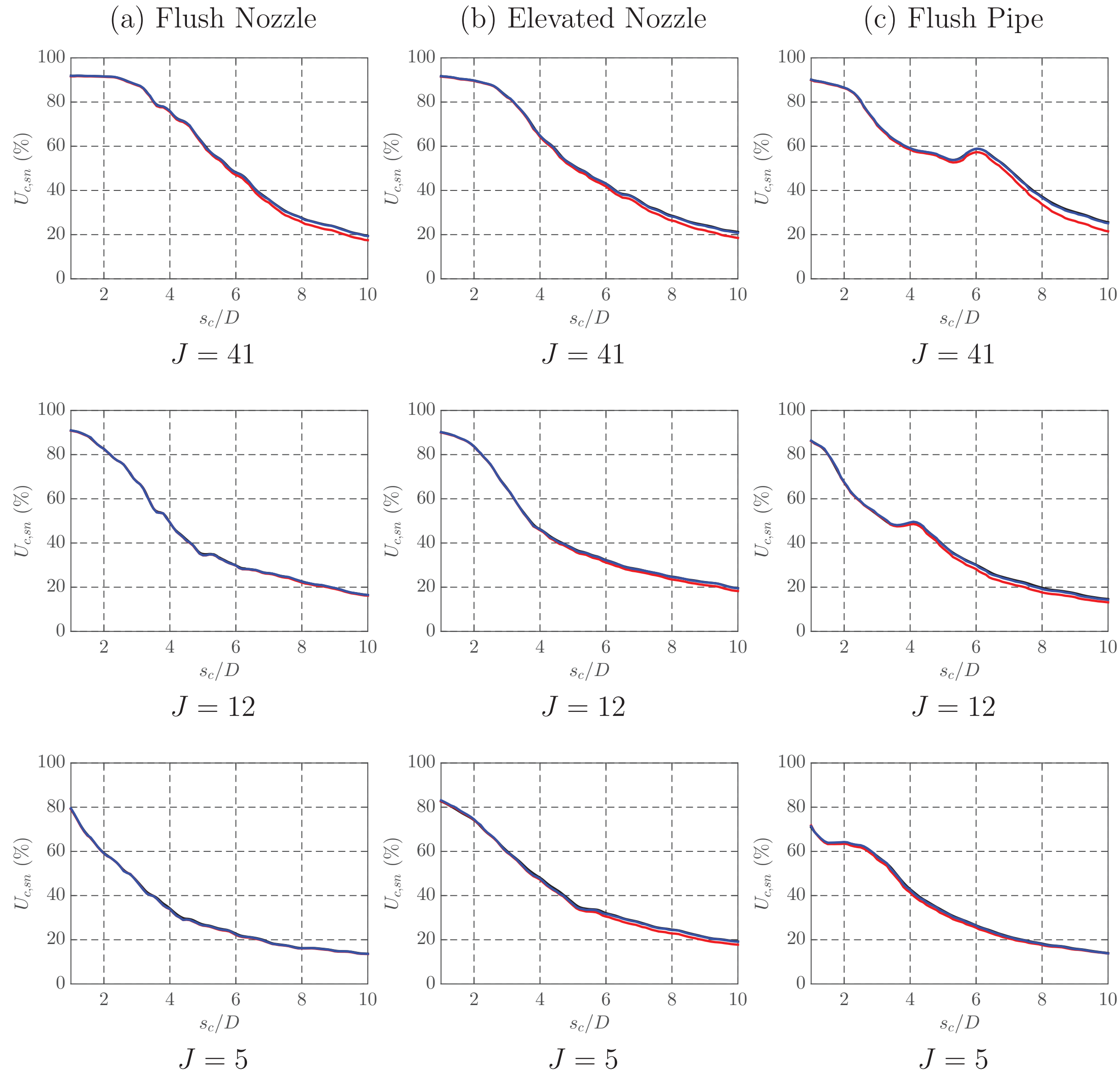

Figure 4.3: Comparison of mean centerplane-based Unmixedness $U_{c,sn}$ evaluated in the transformed plane ($s_c/D - n/D$) along the jet centerline trajectory s_c/D with the smallest length scale $\delta_s = \delta_p$ in PLIF images for the equidensity (a) flush nozzle-, (b) elevated nozzle- and (c) flush pipe-injected JICF at $J = 41$ (top row), 12 (middle row) and 5 (bottom row). Each plot corresponds to $U_{c,sn}$ with: a seven-pixel-width interrogation area with matching mean values by Gevorkyan et al. (2016) (—), a one-pixel-width interrogation area without matching mean values (—), as well as with matching mean values (—).

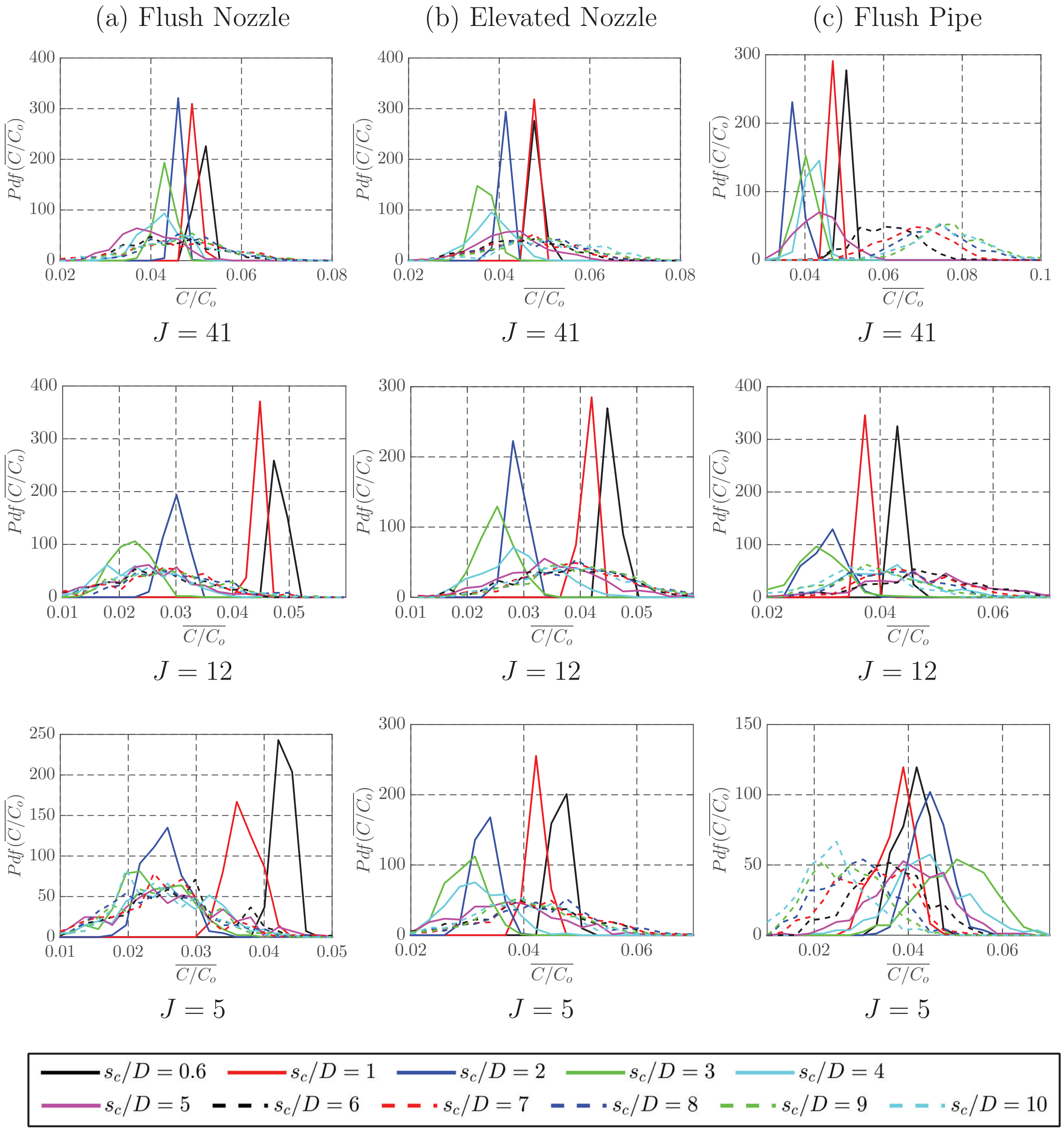

Figure 4.4: Probability Density Function (PDF) evaluated in the transformed plane ($s_c/D - n/D$) for the range of mean concentration values $\overline{C/C_o}$ over 200 instantaneous images at a given jet centerline trajectory coordinate s_c/D for the equidensity (a) flush nozzle-, (b) elevated nozzle- and (c) flush pipe-injected JICF at $J = 41$ (top row), 12 (middle row) and 5 (bottom row).

good quantitative and qualitative agreements among three types of $U_{c,sn}$ in Figure 4.3 are also observed for the lowered density ($S = 0.35$ and 0.55) flush nozzle-generated transverse jets, which are shown in Appendix A. This exploration clearly demonstrates the validity of applying the one-pixel-width interrogation area to sufficiently capture general mixing characteristics using the present algorithm, both with and without matching mean values.

The results of the Unmixedness evaluation with various length scales are now considered without matching mean concentration values. Figures 4.5 and 4.6 show the Unmixedness for various length scales δ_s/D at a given jet centerline trajectory location s_c/D, and with s_c/D at a given δ_s/D, respectively, for the equidensity JICF at $J = 41$, 12 and 5 for the three different injectors. As previously mentioned, a transition from convective to absolute instability occurs at a critical jet-to-crossflow momentum flux ratio $J_{cr} \approx 10$ for flush injection and $J_{cr} \approx 0.93$ for elevated injection (Megerian et al., 2007; Davitian et al., 2010a; Getsinger et al., 2014). Hence, the upstream shear layers for the flush nozzle- and flush pipe-generated JICF at $J = 41$, 12 and 5 are convectively unstable, transitioning from convectively to absolutely unstable, and absolutely unstable, respectively, while the upstream shear layers for the elevated nozzle-injected JICF at these J values are all convectively unstable. For the flush nozzle- and elevated nozzle-injected JICF, as one can see in Figures 4.5(a) and (b), the Unmixedness gradually decreases at a given s_c/D location ($0.6 \leq s_c/D \leq 10$) as δ_s/D becomes larger. The Unmixedness asymptotically converges to zero at the largest length scale $\delta_s/D = 20$ although the Unmixedness is plotted up to $\delta_s/D = 15$ to easily focus on mixing characteristics in a range of smaller scales. As s_c/D becomes larger and one moves downstream from 0.6 to 10 over the entire set of length scales δ_s, the Unmixedness gradually and monotonically decreases in general. The general, monotonic decrease in the Unmixedness means that the jet is mixed better for all length scales at further downstream locations. This trend in the Unmixedness with various length scales is clearly seen in Figure 4.6(a) and (b) as well.

For the flush pipe-injected JICF in Figures 4.5(c) and 4.6(c), however, one can clearly observe a different mixing trend from those for the flush and elevated nozzles. In Figure 4.5(c), crossover between plots begins to be observed as s_c/D becomes larger: $s_c/D \approx 5-6$

for $\delta_s/D \approx 1$ at $J = 41$, $s_c/D \approx 3-4$ for $\delta_s/D \approx 0.35$ at $J = 12$, and $s_c/D \approx 1-2$ for $\delta_s/D \approx 1.3$ at $J = 5$, for example. These crossovers suggest that the degree of mixing of the JICF actually lessens at a certain length scale δ_s as s_c/D increases, which is not observed for the flush nozzle- and elevated nozzle-generated transverse jets at any of the J values shown in Figure 4.5(a) and (b). This alteration in the trend in mixing, with an increase in $U_{c,sn}$ at specific s_c/D locations before returning to a reduction, is shown in Figure 4.6(c) for the flush pipe at all three J values. For smaller length scales (approximately $0 \leq \delta_s/D \leq 0.2$), a slight increase in the Unmixedness is observed, while for larger length scales (approximately $0.5 \leq \delta_s/D$), a more significant increase or clear local minima and maxima of the Unmixedness begin to be observed at specific downstream locations instead of the monotonic decrease in the Unmixedness. The local minima, corresponding to the initial point of the increase in the Unmixedness, are located at $s_c/D \approx 5.1$ at $J = 41$, $s_c/D \approx 3.2$ at $J = 12$, and $s_c/D \approx 1.3$ at $J = 5$, respectively, which is within the spatial range of the crossovers determined in Figure 4.5(c). It should be noted that such local minima and maxima are also observed for the flush nozzle at $J = 12$ in Figure 4.6(a), and for the elevated nozzle at $J = 12$ and 5 in Figure 4.6(b), although the increase rate from the local minima to maxima is lower and less steep than that for the flush pipe.

Both Figures 4.5 and 4.6 can be plotted together as a contour map as shown in Figure 4.7, representing the Unmixedness as an function of δ_s/D on the x axis and s_c/D on the y axis. Again, in the contour maps, one can clearly observe the increase in the Unmixedness for the flush pipe as wavy contours, especially at relatively larger δ_s/D. This is not as clearly seen for the flush and elevated nozzles in Figures 4.7 (a) and (b), although there appears to be a small amount of waviness for the nozzle flows at the transitional $J = 12$ condition, and for the elevated nozzle flows as the $J = 12$ and 5 conditions. These observations are relevant to conjectures by earlier researchers.

Mathew et al. (2005) suggests, for example, that vortex structures contribute to better molecular mixing at relatively smaller fluid mechanical length scales. However, vortices possibly capture fluid locally inside themselves, e.g., in their cores, resulting in locally uniform but overall nonuniform fluid concentrations and hence worse mixing in the flowfield with

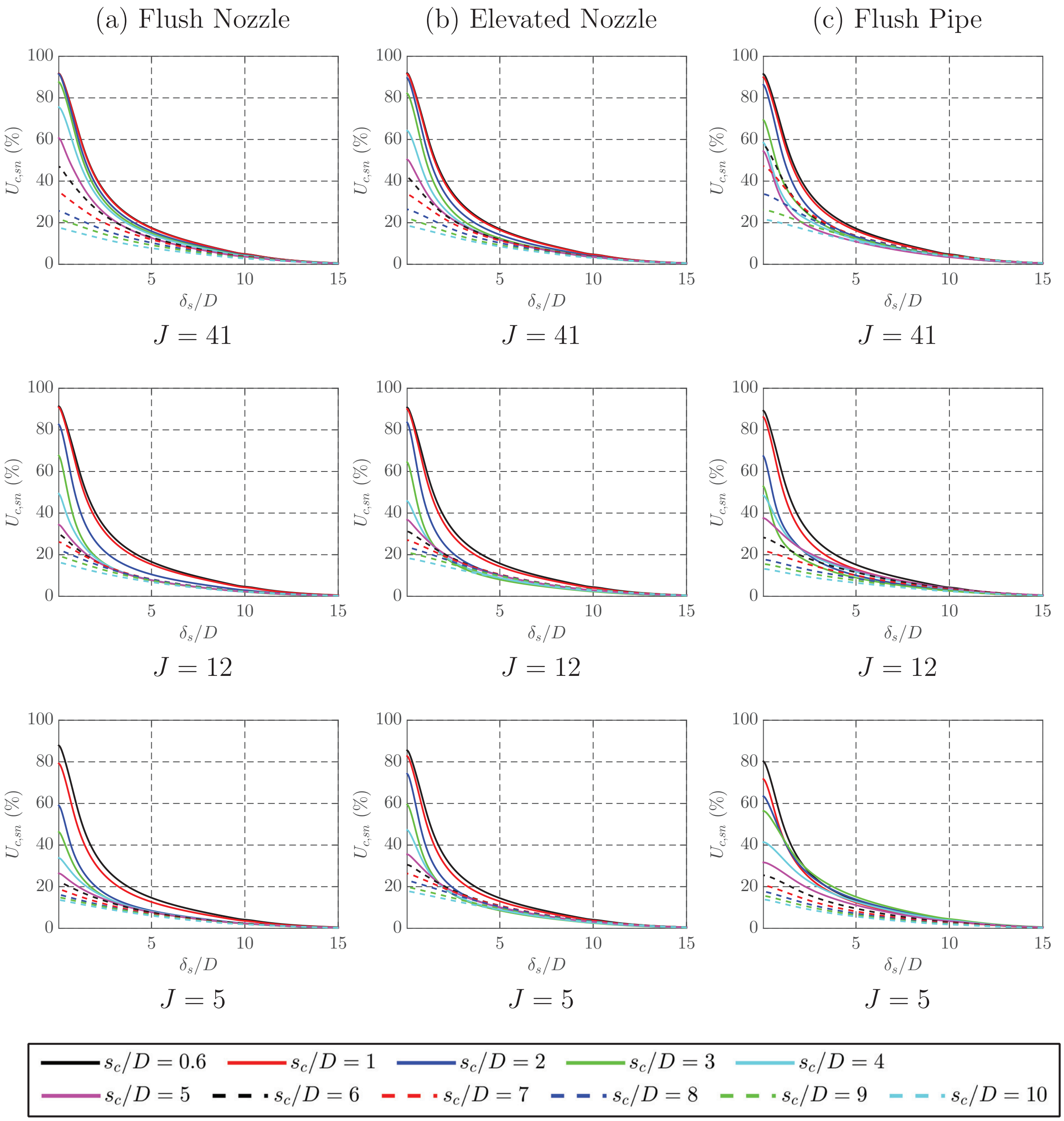

Figure 4.5: Mean centerplane-based Unmixedness $U_{c,sn}$ evaluated in the transformed plane ($s_c/D-n/D$) as a function of various length scales normalized by the jet diameter δ_s/D at a given jet centerline trajectory coordinate s_c/D for the equidensity (a) flush nozzle-, (b) elevated nozzle- and (c) flush pipe-injected JICF at $J = 41$ (top row), 12 (middle row) and 5 (bottom row). Mean concentration values in each interrogation area are not matched to the reference value here.

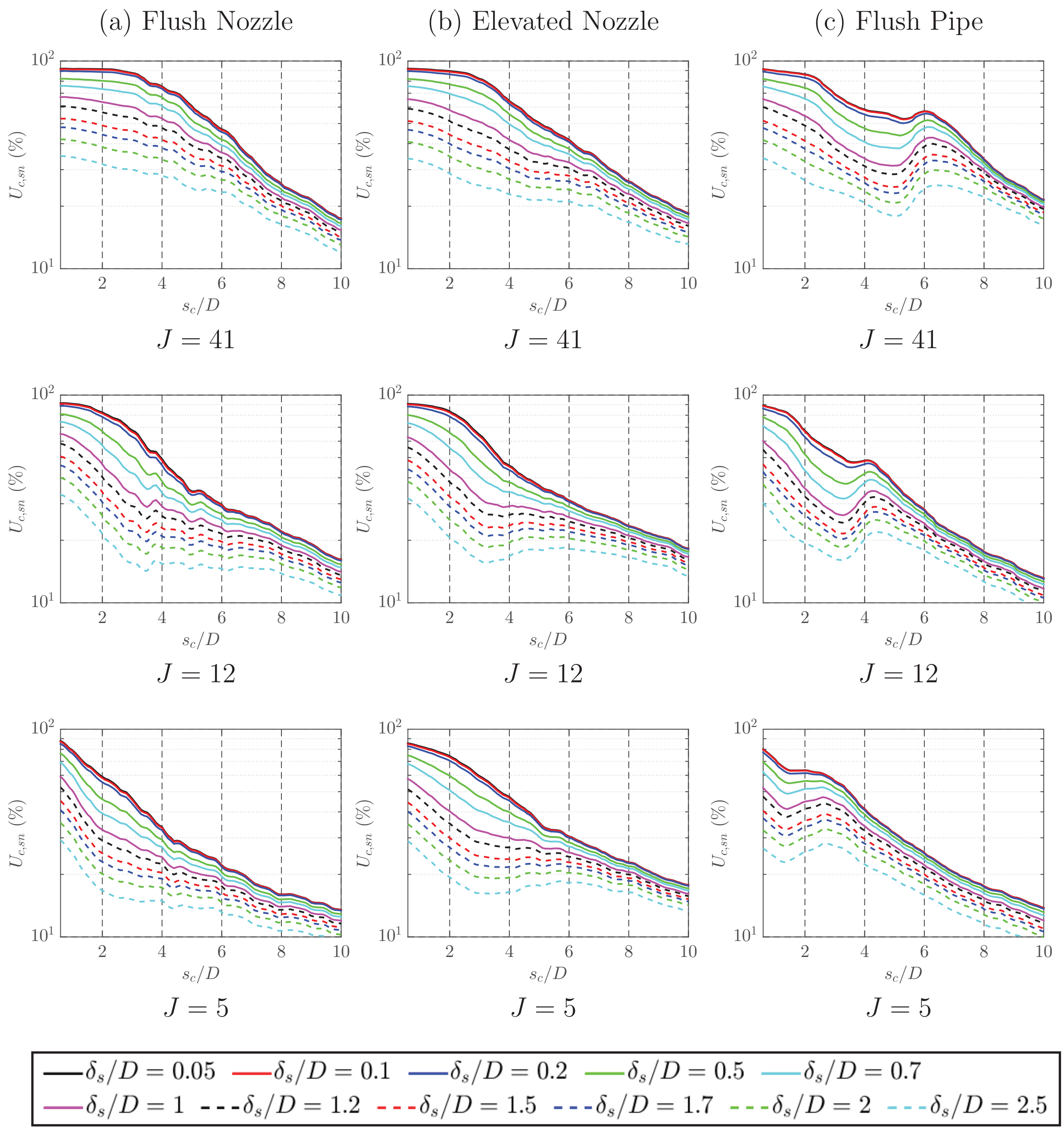

Figure 4.6: Mean centerplane-based Unmixedness $U_{c,sn}$ evaluated in the transformed plane (s_c/D–n/D) as a function of jet centerline trajectory coordinate s_c/D with a given length scale δ_s/D for the equidensity (a) flush nozzle-, (b) elevated nozzle- and (c) flush pipe-injected JICF at $J = 41$ (top row), 12 (middle row) and 5 (bottom row). Mean concentration values in each interrogation area are not matched to the reference value here.

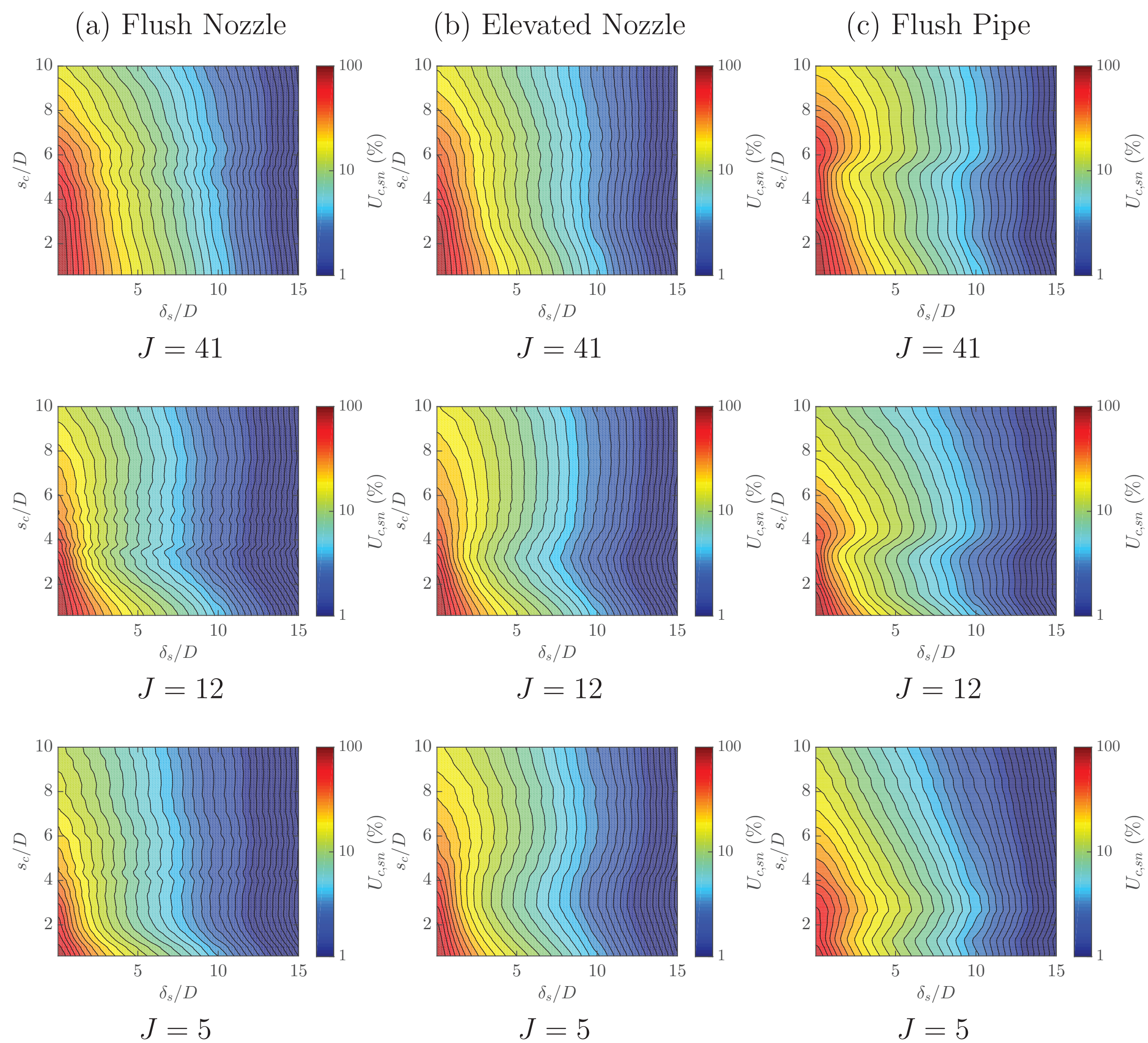

Figure 4.7: Contour maps of the mean centerplane-based Unmixedness $U_{c,sn}$ evaluated in the transformed plane ($s_c/D{-}n/D$) as a function of various length scales normalized by the jet diameter δ_s/D (x axis) and jet centerline trajectory coordinate s_c/D (y axis) for the equidensity (a) flush nozzle-, (b) elevated nozzle- and (c) flush pipe-injected JICF at $J = 41$ (top row), 12 (middle row) and 5 (bottom row). Mean concentration values in each interrogation area are not matched to the reference value here.

vortex evolution. It is interesting to investigate such a relationship between mixing length scales and vortical structures, especially vortex rollups that appear in the upstream shear layer in this study which may be a dominant factor in nearfield mixing. For the equidensity flush nozzle- and elevated nozzle-injected JICF, one can see a monotonic decrease in the Unmixedness towards 0 % as mixing length scale increases for all J values in Figures 4.5(a) and (b). This tendency is generally expected because $U_{c,sn}$ decreases mainly due to the less fine spatial resolution and averaging effect of concentration values as the length scale δ_s increases. Hence, any vortical flow structures for the nozzle injection captured in our PLIF imaging do not worsen the degree of molecular mixing at larger mixing length scales, at least, based on the current spatial resolution (a pixel size of δ_p) in the PLIF images. However, for the equidensity flush pipe-injected JICF, e.g., in Figure 4.5(c), an increase in the Unmixedness was observed via the "crossover" shown as length scale was increased, which may be ascribed to differences in flow structures from those for the flush injection. An in-depth study of flow structures helps to investigate the relationship between such structures and mixing characteristics for these different injections.

We can examine instantaneous centerplane acetone concentration images in the transformed plane ($s_c/D - n/D$) for these three injectors as shown in Figure 4.8 to investigate the effect of flow structures on mixing characteristics, especially in the increase in the Unmixedness for the equidensity flush pipe-injected JICF. Here, our main focus is on rolled-up vortical structures on the upstream shear layer and fluid in the wake region, which are signature nearfield flow structures in the centerplane view. For the equidensity flush and elevated nozzle-injected JICF, coherent rolled-up vortices on the upstream shear layer are clearly observed, which are initiated closer to the jet exit as J values decrease. The rollups generally contain fluid with concentration values $C/C_o \approx 0.5 - 0.7$, while potential core regions contain fluid with $C/C_o \approx 1.0$, corresponding to pure jet fluid. For the equidensity flush pipe-injected JICF, the structural characteristics of rolled-up vortices are different from those for the other two injectors. The vortical rollups on the upstream shear layer here contain higher-concentration fluid with $C/C_o \approx 0.8 - 0.9$, closer to the unity concentration in the potential core region. These highly concentrated rollups for the flush pipe are likely to be caused by a lowered degree of crossflow entrainment into the jets. In addition, shear layer vortices seem to be more closely engaged with the potential core region for the flush pipe, while vortices on the upstream shear layer for the nozzle-injected JICF are more distinguishable from the potential core region based on structural and concentration differences. The initial rollup locations on the upstream shear layer for the equidensity flush pipe-injected JICF can be visually determined from the instantaneous images in Figure 4.8 to lie approximately at $s_c/D \approx 4.9$ for $J = 41$, $s_c/D \approx 3.2$ for $J = 12$, and $s_c/D \approx 1.5$ for $J = 5$. These locations are very close to the locations where the local increase in the Unmixedness with $s_c/D$was observed in Figures 4.5-4.7.

Another interesting flow structure is observed in the wake region for these jets. More jet fluid in the wake region is observed for the flush pipe-injected JICF than that for the nozzle-injected JICF, especially for the elevated nozzle. The wake region for the flush pipe is likely to be initiated relatively closer to the jet exit than the locations of initial upstream shear layer rolled-up vortices, visually determined for the wake at $s_c/D \approx 2.5$ at $J = 41$, $s_c/D \approx 1.5$ at $J = 12$ and $s_c/D \approx 1.0$ at $J = 5$ from Figure 4.8(c). These nearfield locations associated with the initiation of the wake flow are fairly repetitive over all instantaneous images for each flow condition. Therefore, from these observations of flow structures in the instantaneous images, it is conjectured that, for the flush pipe, the initial locations of the rolled-up vortices on the upstream shear layer are more closely associated with the locations at which there is an increase in the Unmixedness at relatively large length scales. This increase does not appear to be associated with initiation of structures in the wake region.

To confirm this conjecture on the effect of the flow structures on an increase in the Unmixedness for the equidensity flush pipe-injected JICF, the instantaneous centerplane-based Unmixedness for variable length scales is investigated, in contrast to the mean Unmixedness over all instantaneous images as explored in Figures 4.3-4.7. The purpose of this additional examination is to see if the clear correspondence between specific instantaneous flow structures and mixing characteristics can be observed in an instantaneous metric. The same algorithm as the mean Unmixedness evaluation is applied to the instantaneous calculation; the only difference is that there is no average over $200-300$ instantaneous images computed.

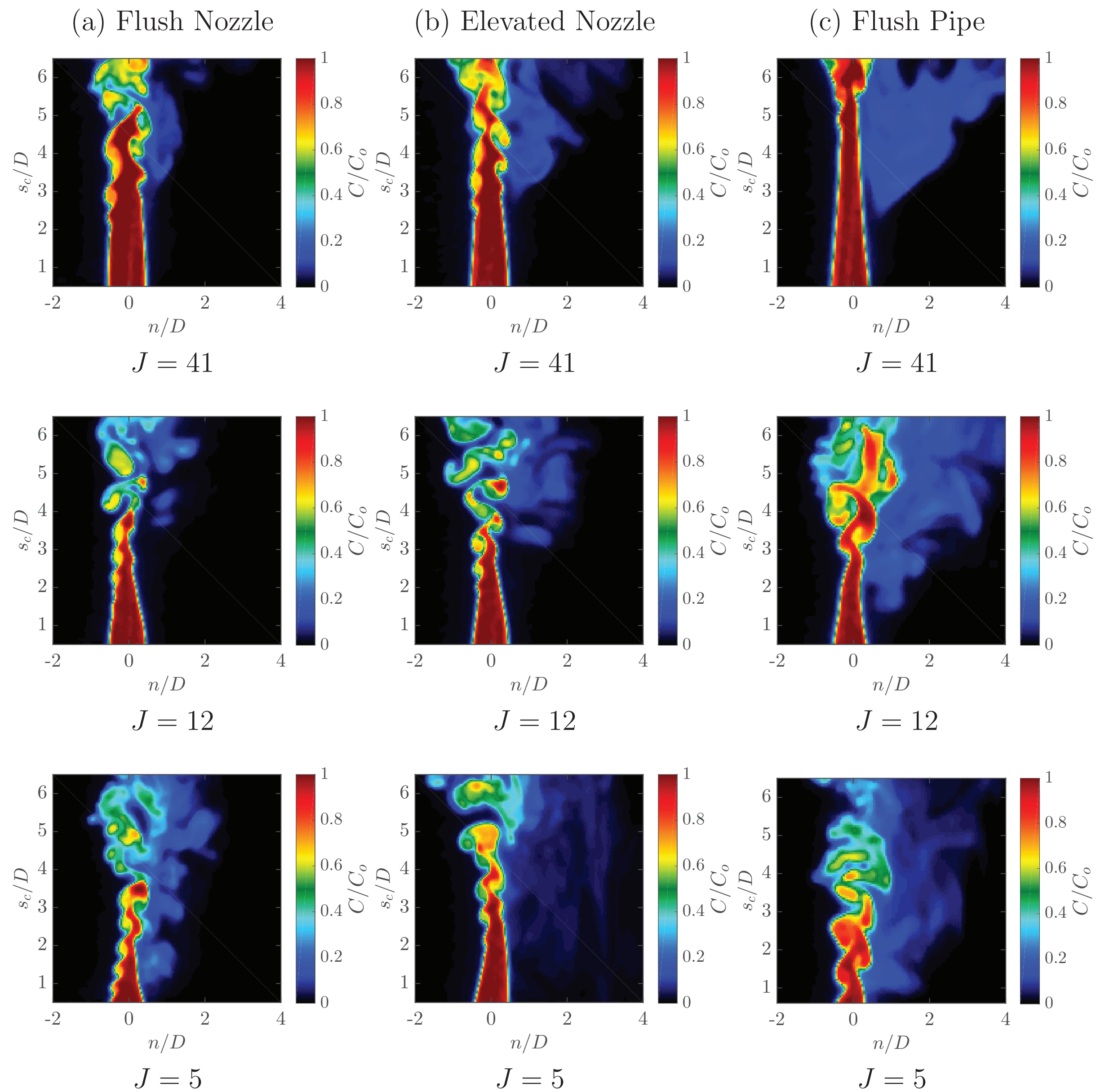

Figure 4.8: Instantaneous centerplane acetone concentration images in the transformed plane ($n/D - s_c/D$) for the equidensity (a) flush nozzle-, (b) elevated nozzle- and (c) flush pipe-injected JICF at $J = 41$ (top row), 12 (middle row) and 5 (bottom row). Acetone concentration C is normalized by the mean concentration value inside the potential core C_o in each instantaneous image.

Figures 4.9, 4.10 and 4.11 represent the centerplane-based Unmixedness evaluated on the instantaneous images in Figure 4.8. Note that these results have much greater fluctuations than the mean Unmixedness shown previously due to the instantaneous evaluation of the metrics. Yet these results are useful in understanding the relationship between instantaneous flow structures and mixing characteristics. In Figures 4.9(c) and 4.10(c) for the flush pipe, one can still observe the crossovers initiated at $s_c/D \approx 5-6$ for $\delta_s/D \approx 0.88$ ($J = 41$), $s_c/D \approx 3-4$ for $\delta_s/D \approx 0.78$ ($J = 12$), and $s_c/D \approx 1-2$ for $\delta_s/D \approx 0.72$ ($J = 5$), as well as an increase in the Unmixedness for relatively larger length scales starting at $s_c/D \approx 5.7$ for $J = 41$, $s_c/D \approx 3.3$ for $J = 12$, and $s_c/D \approx 1.3$ for $J = 5$. Interestingly, the locations at which the crossovers and the increase in the Unmixedness are observed are close to the visually-determined initial rollup locations on the upstream shear layer in Figure 4.8(c) and not to the appearance of fluids in the wake region. Again, one could attribute the increase in the Unmixedness for the equidensity flush pipe-injected JICF to be related to rollups on the upstream shear layer rather than to flow structures in the wake region.

Based on results in Figures 4.8 to 4.11, and the correlation of even instantaneous vortical structures with alterations in mixing trends, further conjectures may be made. Upstream shear layer rollups could contribute to enhancing smaller-scale mixing (e.g., molecular diffusion) at small length scales, but there may not significantly enhance or even worsen larger-scale mixing (e.g., mechanical stirring) at larger scales due to the highly concentrated fluid captured by the vortices, as mentioned in previous studies (Mathew et al., 2005; Gubanov and Cortelezzi, 2010). This appears to be consistent with instantaneous images and metrics for all injectors. Because this trend is only observed for the straight pipe injection for mean metrics, however, an overall reduction in crossflow entrainment might be associated with some inherent mean characteristic of pipe injection, such as a thicker jet boundary layer or momentum thickness at the jet exit than for the nozzle injection. Another feature could involve lowered crossflow entrainment into the flush pipe itself, or into its upstream shear layer, creating higher-concentrated vortices on the upstream shear layer than for nozzle injection. An in-depth exploration pertaining to the entrainment mechanism for the pipe injection or the effects of flow structures on the mixing characteristics is not covered in this study, but

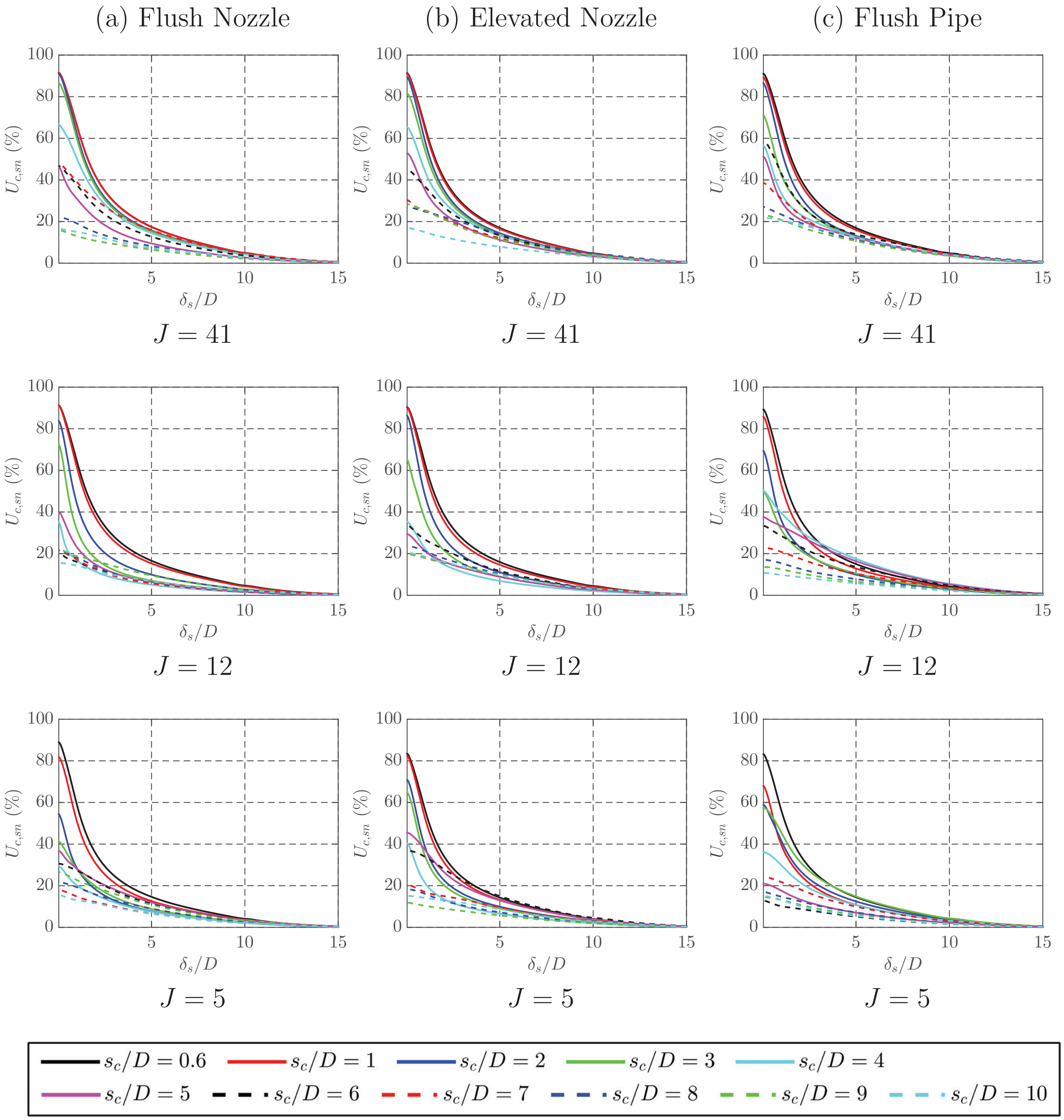

Figure 4.9: Instantaneous centerplane-based Unmixedness $U_{c,sn}$ evaluated in the transformed plane ($s_c/D - n/D$) shown in Figure 4.8 as a function of various length scales normalized by the jet diameter δ_s/D at a given jet centerline trajectory location s_c/D for the equidensity (a) flush nozzle-, (b) elevated nozzle- and (c) flush pipe-injected JICF at $J = 41$ (top row), 12 (middle row) and 5 (bottom row). Mean concentration values in each interrogation area are not matched to the reference value here.

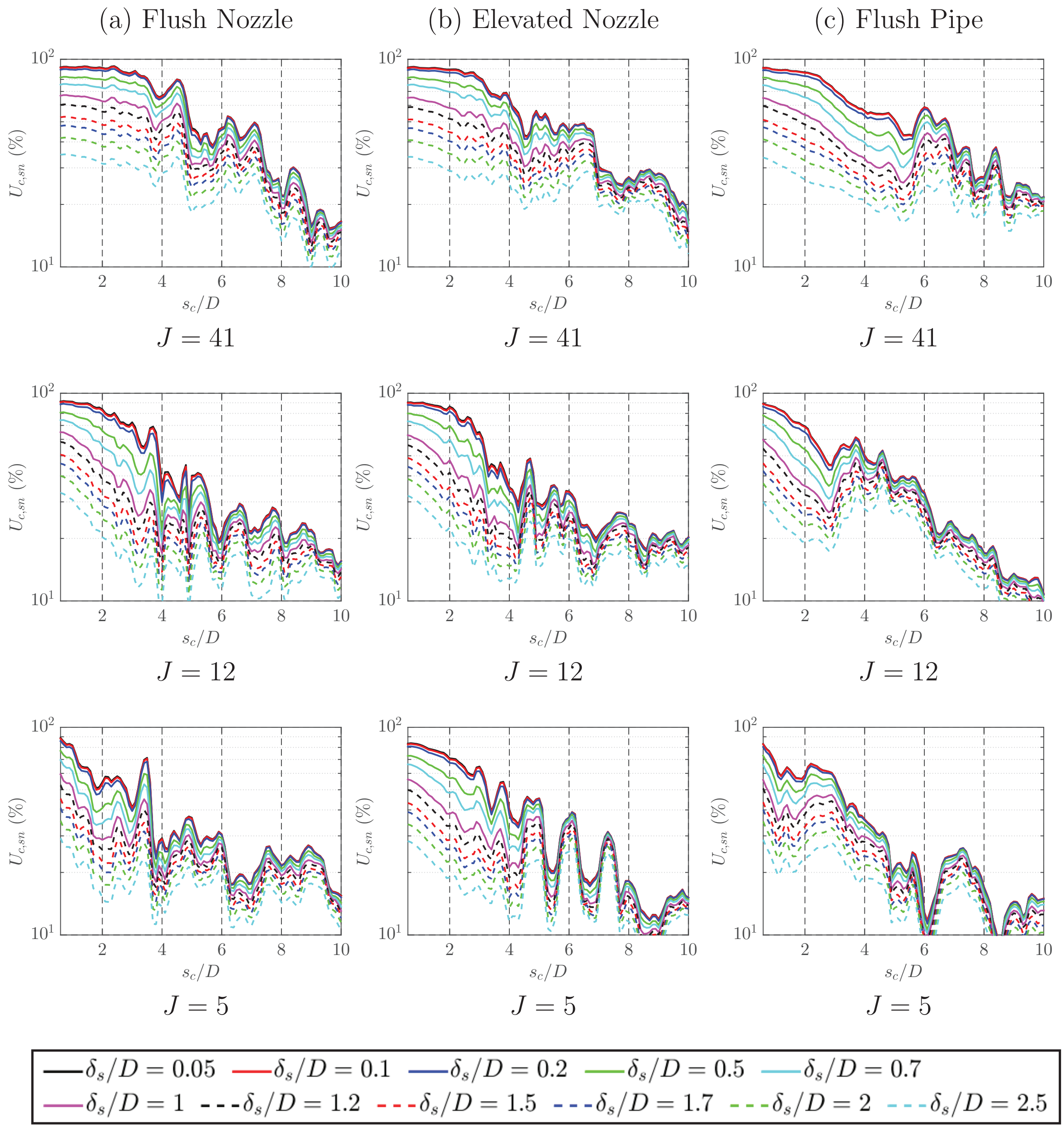

Figure 4.10: Instantaneous centerplane-based Unmixedness $U_{c,sn}$ evaluated in the transformed plane $(s_c/D - n/D)$ shown in Figure 4.8 as a function of jet centerline trajectory coordinate s_c/D with a given length scale δ_s/D for the equidensity (a) flush nozzle-, (b) elevated nozzle- and (c) flush pipe-injected JICF at $J = 41$ (top row), 12 (middle row) and 5 (bottom row). Mean concentration values in each interrogation area are not matched to the reference value here.

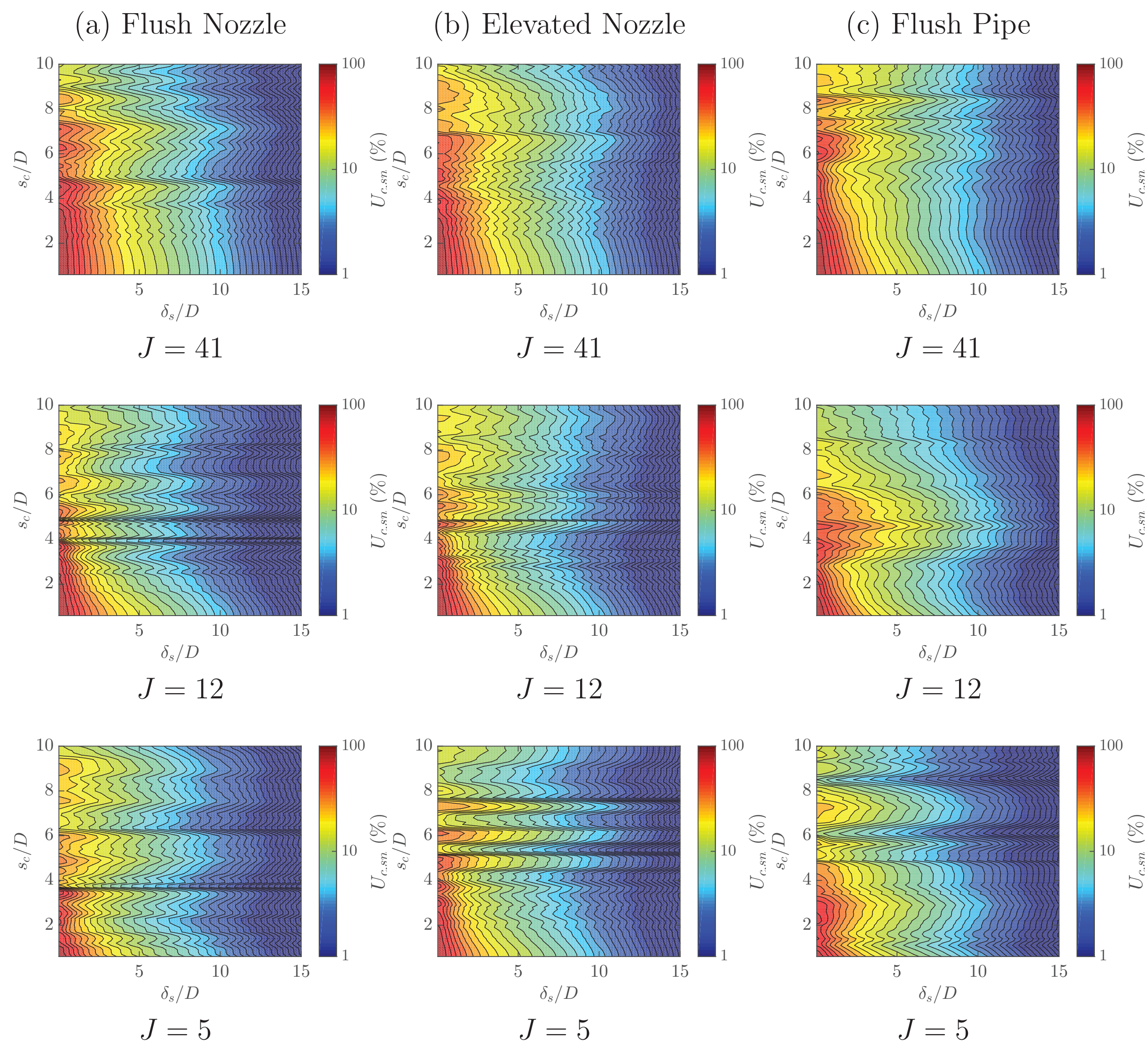

Figure 4.11: Contour maps of the instantaneous centerplane-based Unmixedness $U_{c,sn}$ evaluated in the transformed plane ($s_c/D - n/D$) shown in Figure 4.8 as a function of various length scales normalized by the jet diameter δ_s/D (x axis) and jet centerline trajectory coordinate s_c/D (y axis) for the equidensity (a) flush nozzle-, (b) elevated nozzle- and (c) flush pipe-injected JICF at $J = 41$ (top row), 12 (middle row) and 5 (bottom row). Mean concentration values in each interrogation area are not matched to the reference value here.

could be an interesting direction for future examination.

The observation of an increase in the Unmixedness, i.e., reduced mixing, with larger length scales as compared with smaller length scales may also be associated with the mechanism of vortex initiation and breakdown. Due to the velocity-induction effect of the Biot-Savart law (Lamb, 1895; Batchelor, 1967), a vortex structure in the shear layer entrains some fluid from both the jet and the crossflow. This engulfment of fluid is related to the creation of rolled-up vortices on the JICF upstream shear layer, and occurs at large length scales or, equivalently, low wavenumbers. Once vortices are created, they extend the surface area of the upstream shear layer, which enhances molecular diffusion. When vortex breakdown occurs further downstream along the shear layer, smaller length scales are generated in the flowfield. This evolution in scales suggests that the mixing mechanism is different along the jet and amongst various flow length scales, depending on how the entrainment process or vortex breakdown occurs, i.e., with better mixing at smaller length scales but worse mixing at larger length scales. The present mixing metric is able to capture these differences in mixing characteristics related to the different length scales, in contrast to metrics with a single minimum flow scale. A detailed investigation in terms of the relationship between flow length scales and mixing mechanisms is outside of the main focus of this study, although such as exploration would be worthwhile.

Figures 4.12 and 4.13 represent the corresponding results to Figures 4.5 and 4.6 for mean centerplane-based Unmixedness for the lowered density ratio ($S = 0.55$ and 0.35), flush nozzle-generated JICF at $J = 41$, 12 and 5. Here, the upstream shear layer becomes absolutely unstable when S is brought below approximately $S_{cr} \approx 0.40 - 0.45$ (Getsinger et al., 2012). As discussed for the equidensity JICF, crossovers in $U_{c,sn}$ observed in Figure 4.5 are related to the increase or dramatic change in the mixing trend for the Unmixedness, especially for $S = 0.35$ and $J = 41$, and for $S = 0.55$ and $J = 12$. Hence, similar phenomena for lowered density ratio cases occur as for equidensity conditions, though for different injection. Figure 4.12 show that there are no clear crossovers except for the $S = 0.35$ flush nozzle-injected JICF at $J = 41$ and for $S = 0.55$ and $J = 12$. In most of the cases for the flush nozzle injection for both S values, as observed for the equidensity cases, the crossovers are not as clearly observed as for equidensity straight pipe injection. For the $S = 0.35$ flush injection case at $J = 41$, however, the crossover starts to be observed at $s_c/D \approx 1 - 2$ with $\delta_s/D \approx 2.0$. In Figure 4.13(b) at $J = 41$, one can observe the slight but abrupt increase in the Unmixedness at $s_c/D \approx 2.0$, while the other cases in Figure 4.13 generally show monotonic decrease in the Unmixedness along s_c/D coordinate at all length scales, with a minor exception for $S = 0.55$ and $J = 12$. The abrupt increase in the Unmixedness can be more clearly observed in the contour map plots in Figure 4.14. For the $S = 0.35$ jet at $J = 41$, $\delta_s/D \geq 2$ and $s_c/D \approx 2.0$, we observe the increase in the Unmixedness becomes more significant than for smaller length scales, which correspond to the crossover location determined in Figure 4.12(b) at $J = 41$. Interestingly, the increase in the Unmixedness observed for the equidensity pipe injection and this low density nozzle case behaves differently. For the pipe injection, the Unmixedness increases and then decreases moderately, while the Unmixedness abruptly increases and then monotonically decreases for the $S = 0.35$ flush nozzle-injected JICF at $J = 41$. This difference may indicate that different flow structures contribute to the behavior of the Unmixedness for these two cases.

Figure 4.15 shows the transformed instantaneous centerplane PLIF images for the lowered density, flush nozzle-injected JICF, corresponding to Figure 4.8 for the equidensity cases. For all cases shown here, clear, coherent rolled-up vortices are observed on the upstream shear layer, consistent with absolute instability. The concentration values inside the vortices are slightly higher than those for the equidensity flush nozzle injection cases, approximately $C/C_o \approx 0.8 - 0.9$ for all cases in Figure 4.15, although the sizes of the vortices are visually very similar to those of the equidensity flush nozzle cases. Gevorkyan et al. (2016) suggest that this more highly-concentrated vortices on the upstream shear layer than those for the equidensity flush nozzle-injected JICF produced higher Unmixedness and lower molecular mixing for the lowered S cases. Similarly to the flush pipe-injected JICF cases, the initiation of the rollups on the upstream shear layer may contribute to the abrupt increase in the Unmixedness, although the behavior of the Unmixedness is clearly different. The initial vortex location visually appears for $S = 0.35$ and $J = 41$ at $s_c/D \approx 1.2$, which is slightly closer to the jet exit than the location of the increase in the Unmixedness in Figures 4.12-

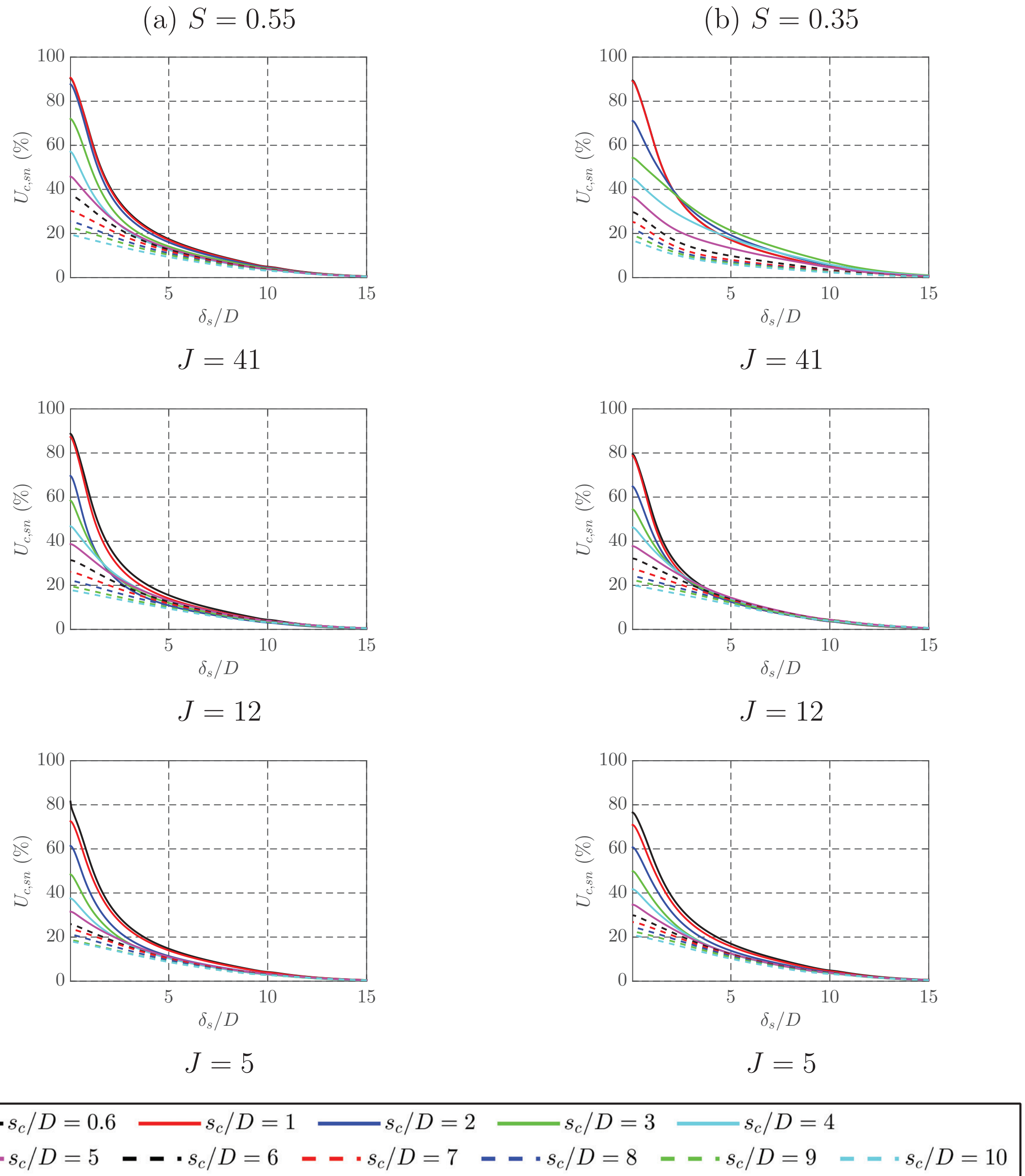

Figure 4.12: Mean centerplane-based Unmixedness $U_{c,sn}$ evaluated in the transformed plane $(s_c/D - n/D)$ as a function of various length scales normalized by the jet diameter δ_s/D at a given jet centerline trajectory location s_c/D for the (a) $S = 0.55$ and (b) $S = 0.35$, flush nozzle-injected JICF at $J = 41$ (top row), 12 (middle row) and 5 (bottom row). Mean concentration values in each interrogation area are not matched to the reference value here.

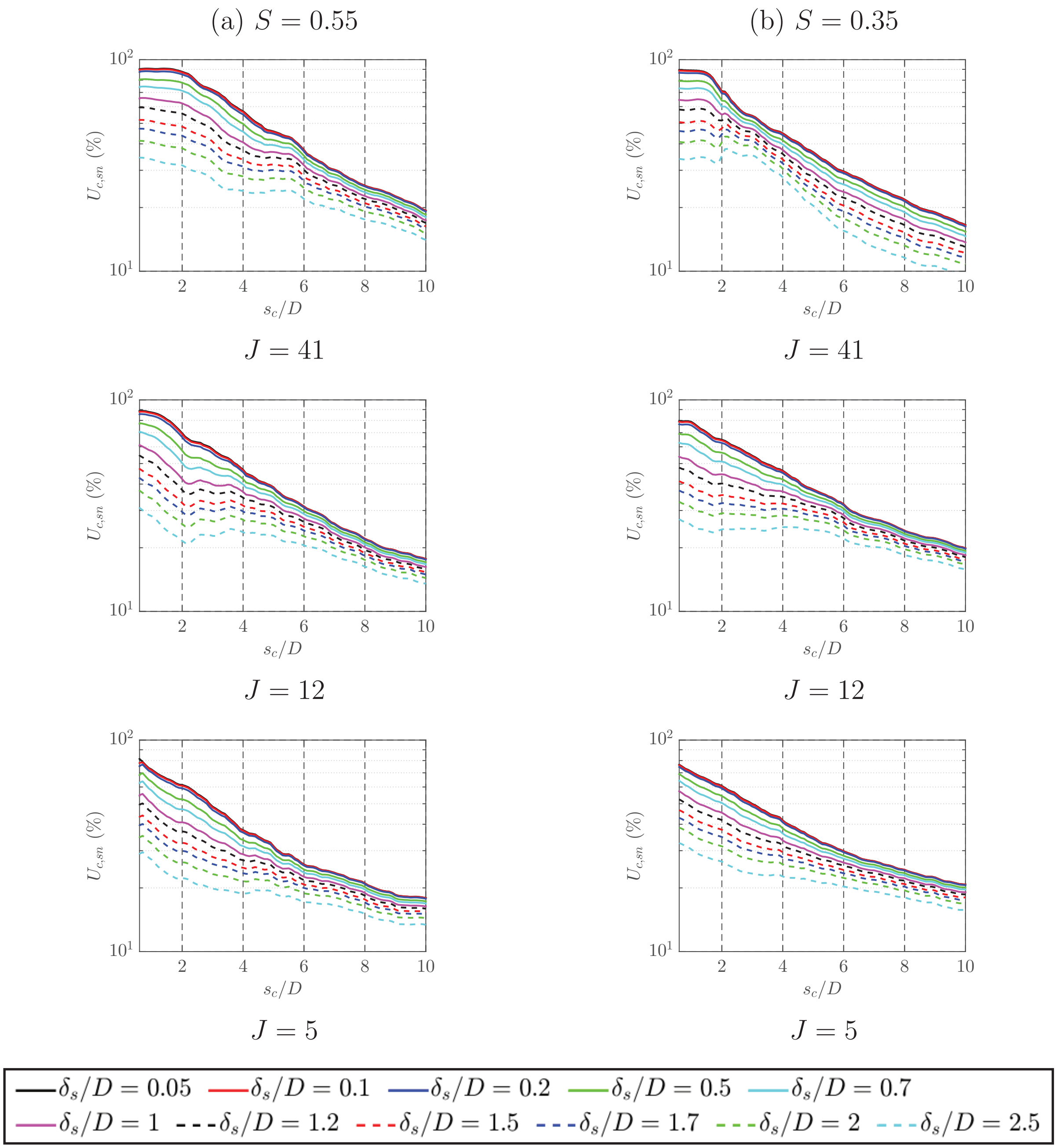

Figure 4.13: Mean centerplane-based Unmixedness $U_{c,sn}$ evaluated in the transformed plane ($s_c/D - n/D$) as a function of jet centerline trajectory coordinate s_c/D with a given length scale δ_s/D for the (a) $S = 0.55$ and (b) $S = 0.35$, flush nozzle-injected JICF at $J = 41$ (top row), 12 (middle row) and 5 (bottom row). Mean concentration values in each interrogation area are not matched to the reference value here.

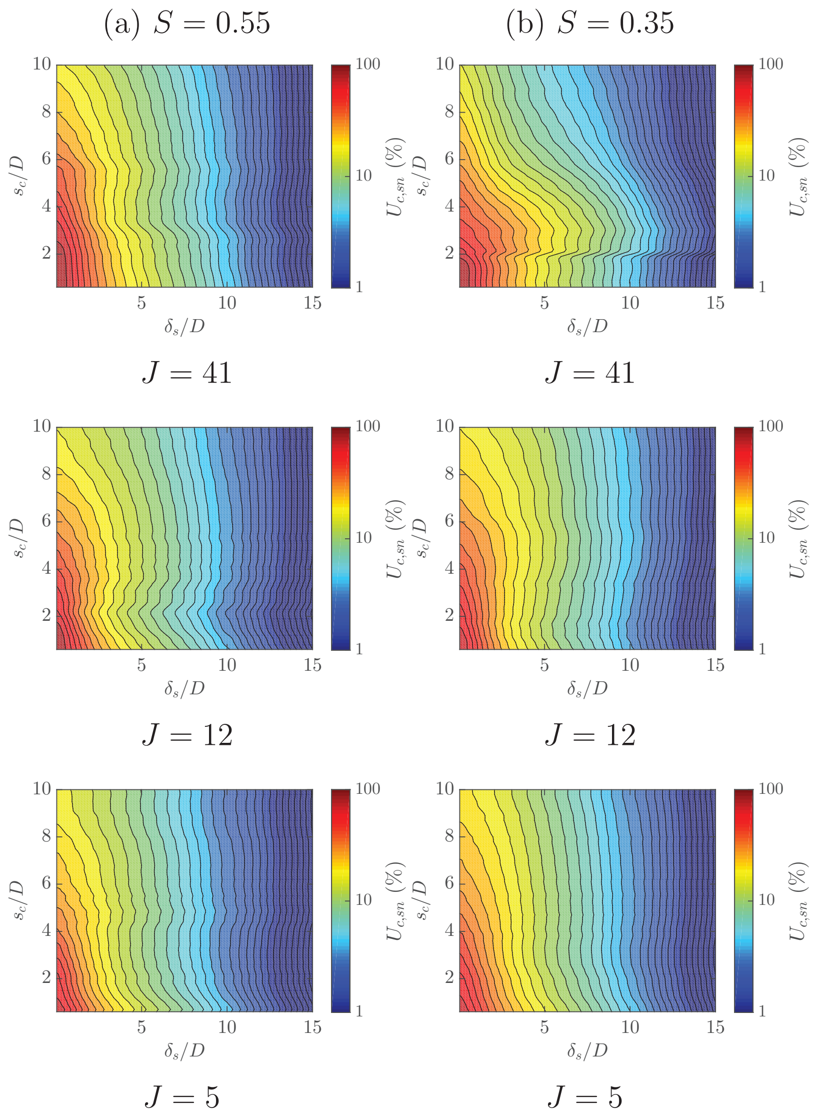

Figure 4.14: Contour maps of the mean centerplane-based Unmixedness $U_{c,sn}$ evaluated in the transformed plane (s_c/D–n/D) as a function of various length scales normalized by the jet diameter δ_s/D (x axis) and jet centerline trajectory coordinate s_c/D (y axis) for the (a) $S = 0.55$ and (b) $S = 0.35$, flush nozzle-injected JICF at $J = 41$ (top row), 12 (middle row) and 5 (bottom row). Mean concentration values in each interrogation area are not matched to the reference value here.

4.14. For the $S = 0.35$ flush nozzle-injected JICF at $J = 41$ (Figure 4.15(b)), unlike the other lowered S cases, there is widely spread wake region initiated approximately from $s_c/D \approx 2.0$ on the positive n/D side, very close to the location where the increase in the Unmixedness was observed. The fluid in the wake region consists of relatively higher concentration fluid than for other flow conditions, and its length scale appears to be larger than the upstream shear layer vortical rollup. After the wake region is created at $s_c/D \cong 2.0$, the concentration seems to monotonically decrease without any clearly visible vortices capturing highly-concentrated fluid. This structural trend agrees with the mixing trends in Figure 4.14(b). The rather abrupt increase in the Unmixedness may correspond more to the initiation of the relatively large, moderately-concentrated wake region than to the vortical rollup on the upstream shear layer, but after this the fluid in the wake region behaves as a regular jet showing monotonic concentration decay. Hence, based on this observation, the lowered density flush nozzle-injected JICF generally does not show the increase in the Unmixedness like the pipe injection, but the presence of a relatively large wake region may influence abrupt changes in mixing characteristics. Consequently, the application of the Unmixedness with various length scales to JICF for widely varied flow conditions suggests the capability of capturing the effect of flow structures with different length scales on mixing process, both molecular mixing as well as fluid mechanical stirring.

4.3 Unmixedness with Variable Scale Lengths with Matching Mean Values

As mentioned previously, Gevorkyan et al. (2016) utilized the Unmixedness in the JICF fields with matched mean concentration values in each interrogation area to reasonably compare all results among widely varied flow conditions with various injectors. Although the current study does not directly and quantitatively compare the Unmixedness amongst various flow conditions, it is worthwhile to apply the Unmixedness calculation for various scale lengths with matched mean concentration values in each interrogation area to see how the results compare with those in Section 4.2. Again, the width of an interrogation area is fixed at a

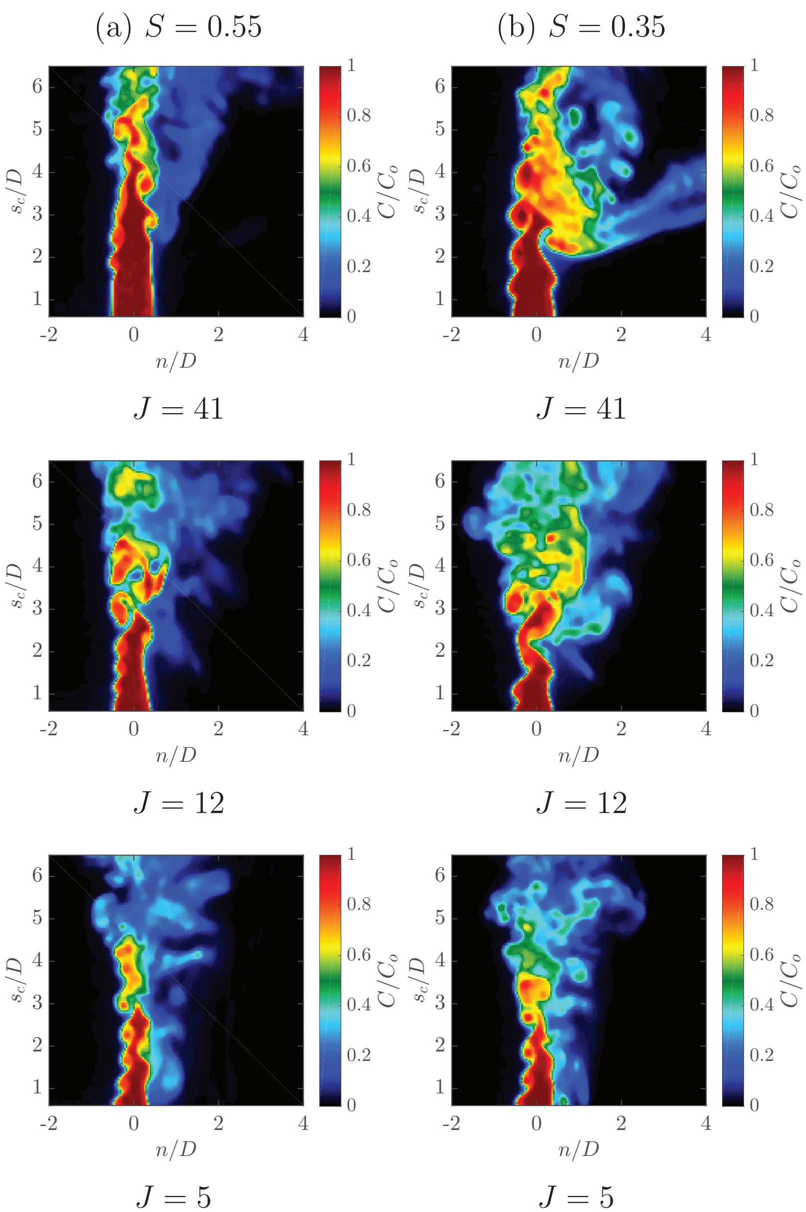

Figure 4.15: Instantaneous centerplane acetone concentration images in the transformed plane ($n/D - s_c/D$) for the (a) $S = 0.55$ and (b) $S = 0.35$, flush nozzle-injected JICF at $J = 41$ (top row), 12 (middle row) and 5 (bottom row). Acetone concentration C is normalized by the mean concentration value inside the potential core C_o in each instantaneous image.

single pixel in the s_c/D direction, but the length in the n/D direction is varied at each s_c/D location and for each instantaneous image due to the necessity to match mean values by adding/removing zeros.

Figures 4.16, 4.17 and 4.18 are the results of the Unmixedness evaluation with matching mean values for the equidensity flush nozzle-, elevated nozzle-, and flush pipe-injected JICF, corresponding to Figures 4.5, 4.6 and 4.7 which were analyzed without matching mean values. Additionally, Figures 4.19, 4.20 and 4.21 are the same mixing evaluation for the lowered density, flush nozzle-injected JICF with means matched, corresponding to Figures 4.12, 4.13 and 4.14 without matching mean values. Note that because the maximum length scales $\delta_{s,max}$ are varied due to the process of matching the mean values by adding/removing zeros, each figure has a different range of δ_s/D. In Figure 4.16, one can observe fairly close mixing characteristics to those without matching mean values (Figure 4.5). For the equidensity flush nozzle- and elevated nozzle-injected JICF cases in Figures 4.16(a) and (b), clear crossovers in the plots are not observed, while for the equidensity flush pipe-injected JICF, Figure 4.16(c)), clear crossovers, which implies a worsening in mixing at a certain length scale as s_c/D becomes larger, are initiated approximately at $s_c/D \approx 5-6$ for $\delta_s/D \approx 0.84$ ($J = 41$), $s_c/D \approx 3-4$ for $\delta_s/D \approx 0.31$ ($J = 12$), and $s_c/D \approx 1-2$ for $\delta_s/D \approx 1.1$ ($J = 5$). The crossover locations extracted with matching mean values agree well with those without matching means in the interrogation areas. From Figures 4.17(a) and (b) for the equidensity flush nozzle- and elevated nozzle-injected JICF, a monotonic decrease in the Unmixedness at various length scales is generally shown, as observed for plots in Figure 4.6 without matching mean values. Again, for the equidensity flush pipe-injected JICF in Figure 4.17(c), the increase in the Unmixedness is clearly observed at $s_c/D \approx 5.1$ at $J = 41$, $s_c/D \approx 3.2$ at $J = 12$, and $s_c/D \approx 1.3$ at $J = 5$, which show surprisingly good agreement with the locations extracted from data in Figure 4.6(c)without matching mean values.

Very similar mixing characteristics extracted for the cases with matching mean values are observed in Figures 4.19-4.21 for the lowered S flush nozzle-injected JICF, as compared with those without matching mean values (Figures 4.12-4.14). From these investigations, this mixing metric basically captures qualitatively similar mixing characteristics with/without

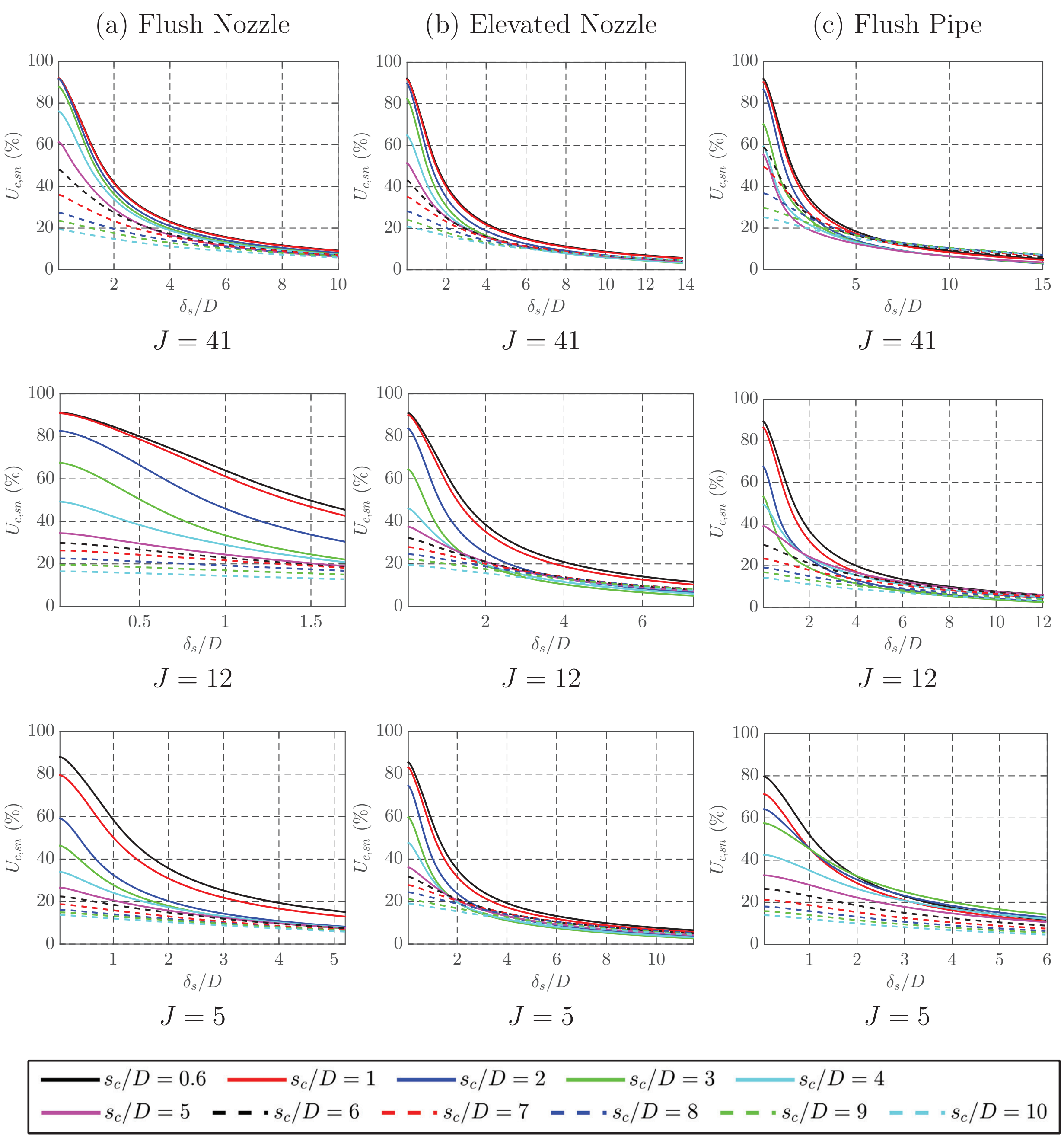

Figure 4.16: Mean centerplane-based Unmixedness $U_{c,sn}$ evaluated in the transformed plane ($s_c/D - n/D$) as a function of various length scales normalized by the jet diameter δ_s/D at a given jet centerline trajectory location s_c/D for the equidensity (a) flush nozzle-, (b) elevated nozzle- and (c) flush pipe-injected JICF at $J = 41$ (top row), 12 (middle row) and 5 (bottom row). Mean concentration values in each interrogation area are matched to the reference value.

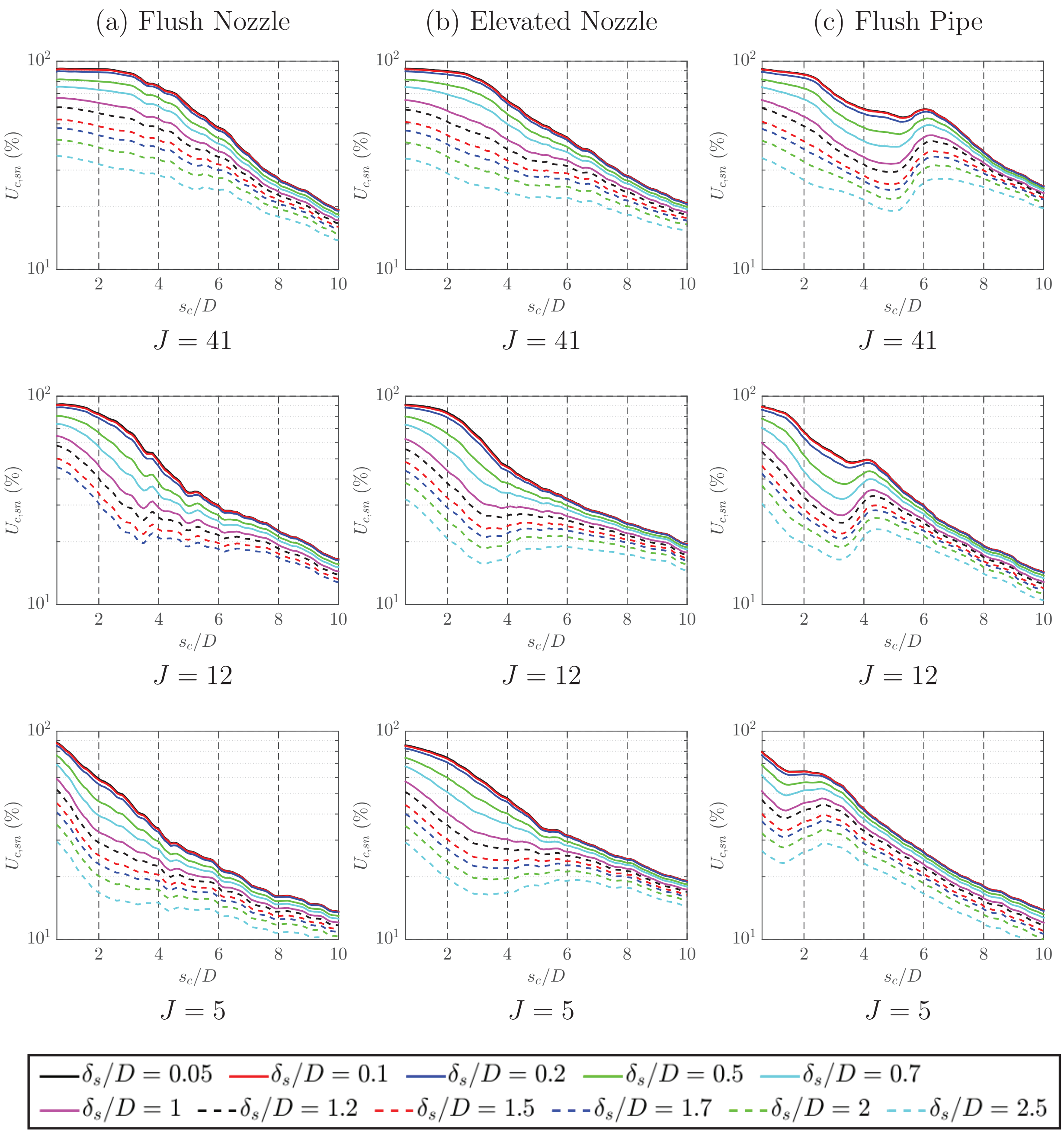

Figure 4.17: Mean centerplane-based Unmixedness $U_{c,sn}$ evaluated in the transformed plane ($s_c/D - n/D$) as a function of various length scales normalized by the jet diameter δ_s/D at a given jet centerline trajectory location s_c/D for the equidensity (a) flush nozzle-, (b) elevated nozzle- and (c) flush pipe-injected JICF at $J = 41$ (top row), 12 (middle row) and 5 (bottom row). Mean concentration values in each interrogation area are matched to the reference value.

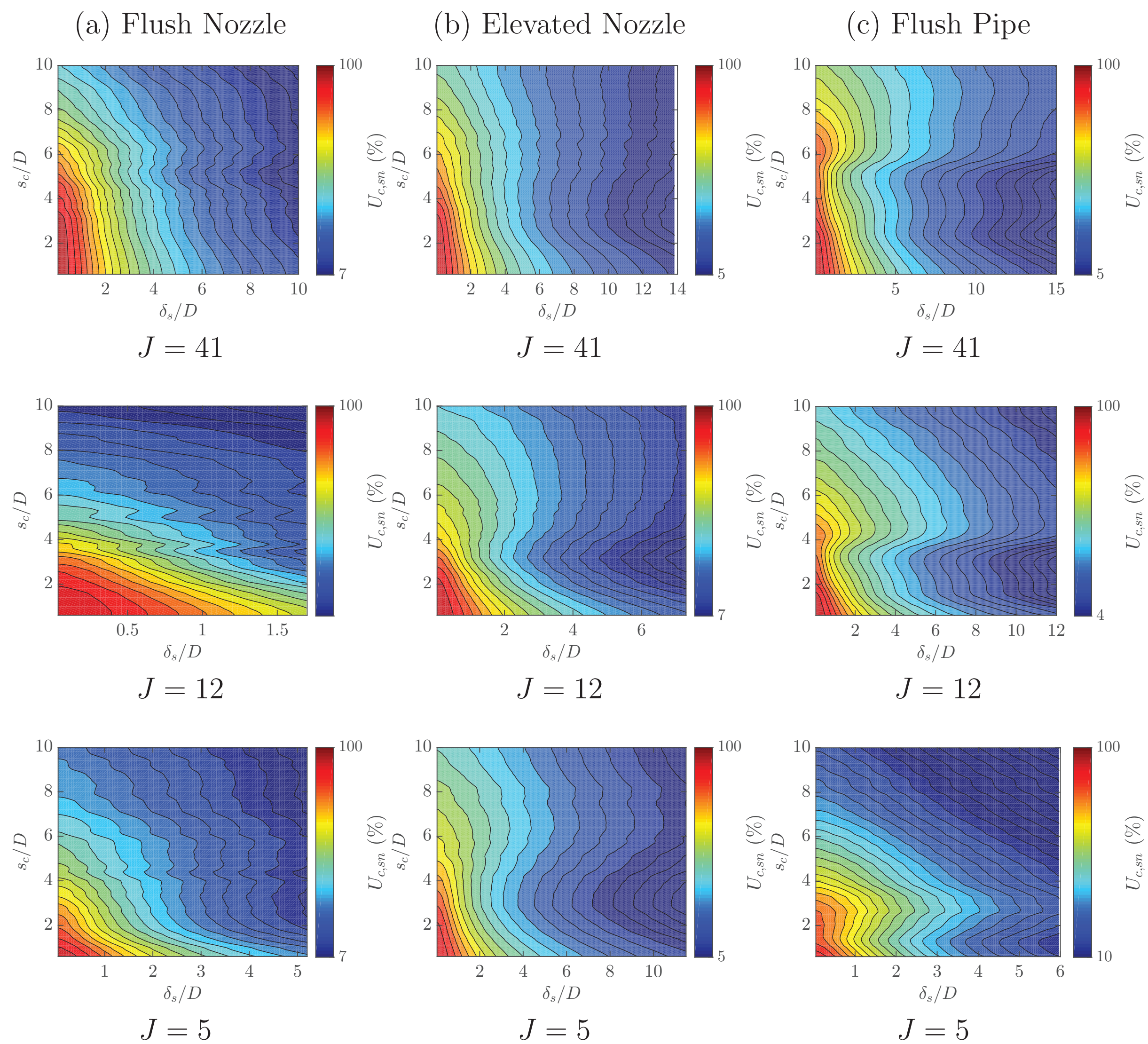

Figure 4.18: Contour maps of the mean centerplane-based Unmixedness $U_{c,sn}$ evaluated in the transformed plane ($s_c/D - n/D$) as a function of various length scales normalized by the jet diameter δ_s/D (x axis) and jet centerline trajectory coordinate s_c/D (y axis) for the equidensity (a) flush nozzle-, (b) elevated nozzle- and (c) flush pipe-injected JICF at $J = 41$ (top row), 12 (middle row) and 5 (bottom row). Mean concentration values in each interrogation area are matched to the reference value.

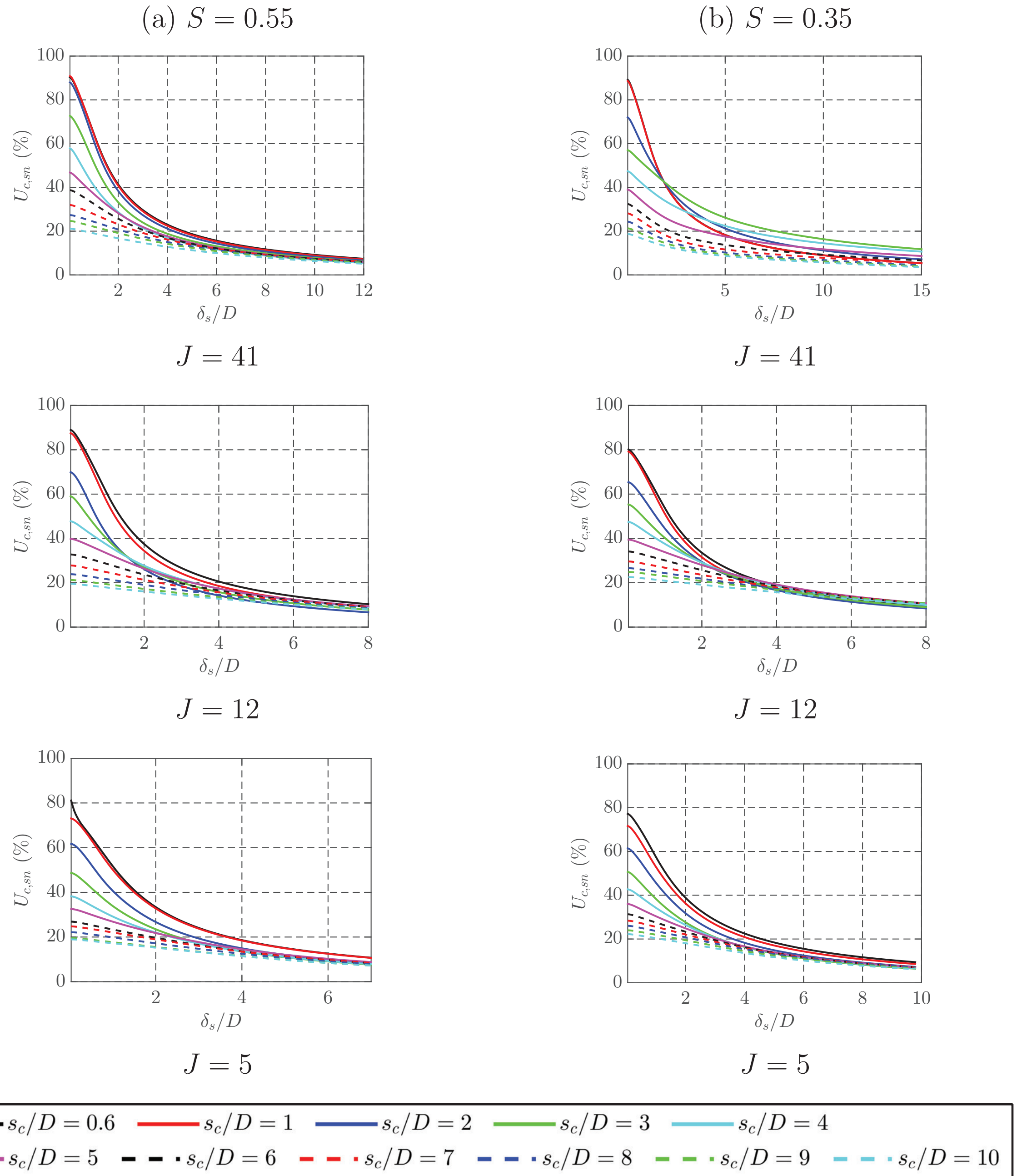

Figure 4.19: Mean centerplane-based Unmixedness $U_{c,sn}$ evaluated in the transformed plane $(s_c/D - n/D)$ as a function of various length scales normalized by the jet diameter δ_s/D at a given jet centerline trajectory location s_c/D for the (a) $S = 0.55$ and (b) $S = 0.35$, flush nozzle-injected JICF at $J = 41$ (top row), 12 (middle row) and 5 (bottom row). Mean concentration values in each interrogation area are matched to the reference value.

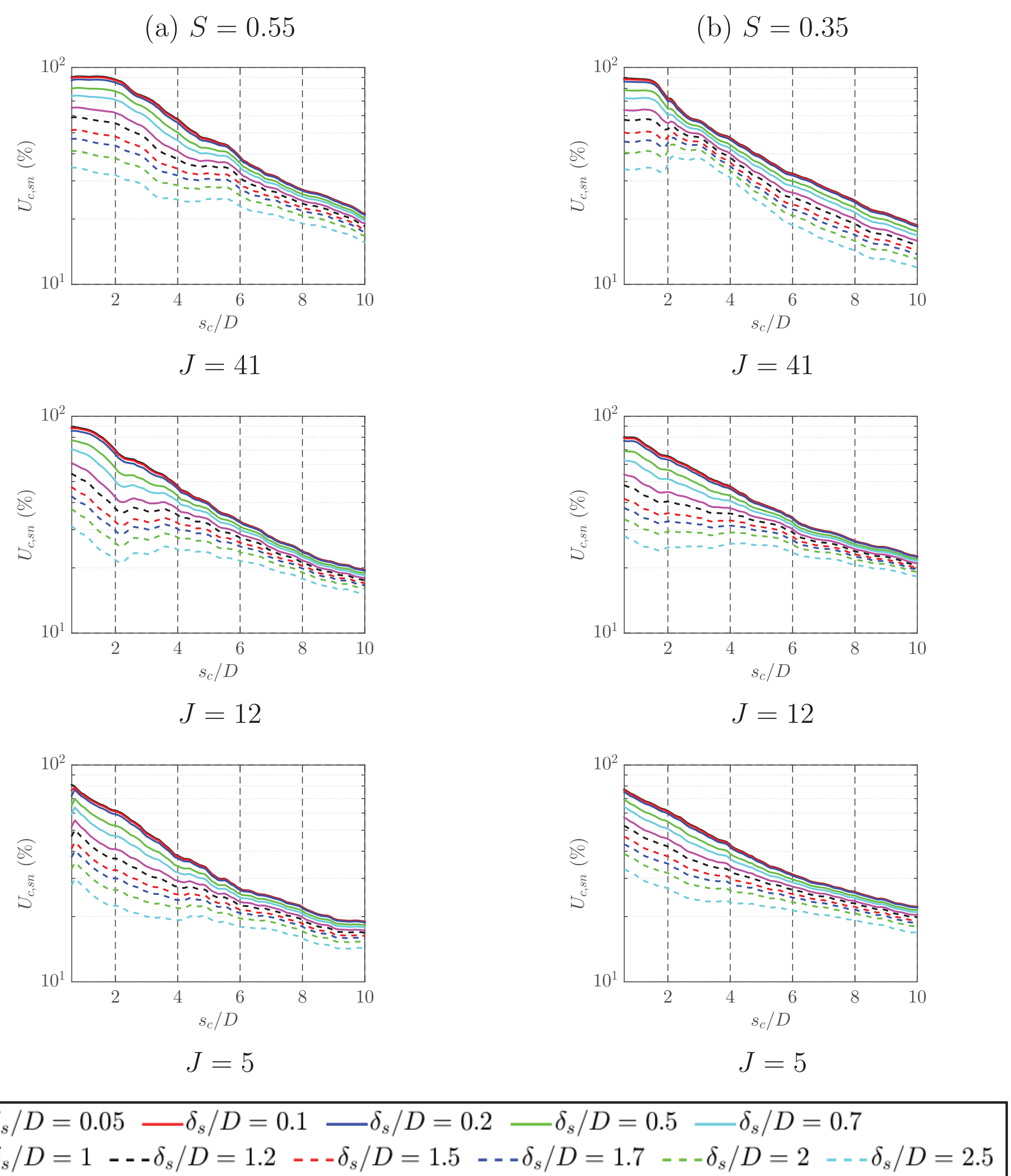

Figure 4.20: Mean centerplane-based Unmixedness $U_{c,sn}$ evaluated in the transformed plane ($s_c/D - n/D$) as a function of various length scales normalized by the jet diameter δ_s/D at a given jet centerline trajectory location s_c/D for the (a) $S = 0.55$ and (b) $S = 0.35$, flush nozzle-injected JICF at $J = 41$ (top row), 12 (middle row) and 5 (bottom row). Mean concentration values in each interrogation area are matched to the reference value.

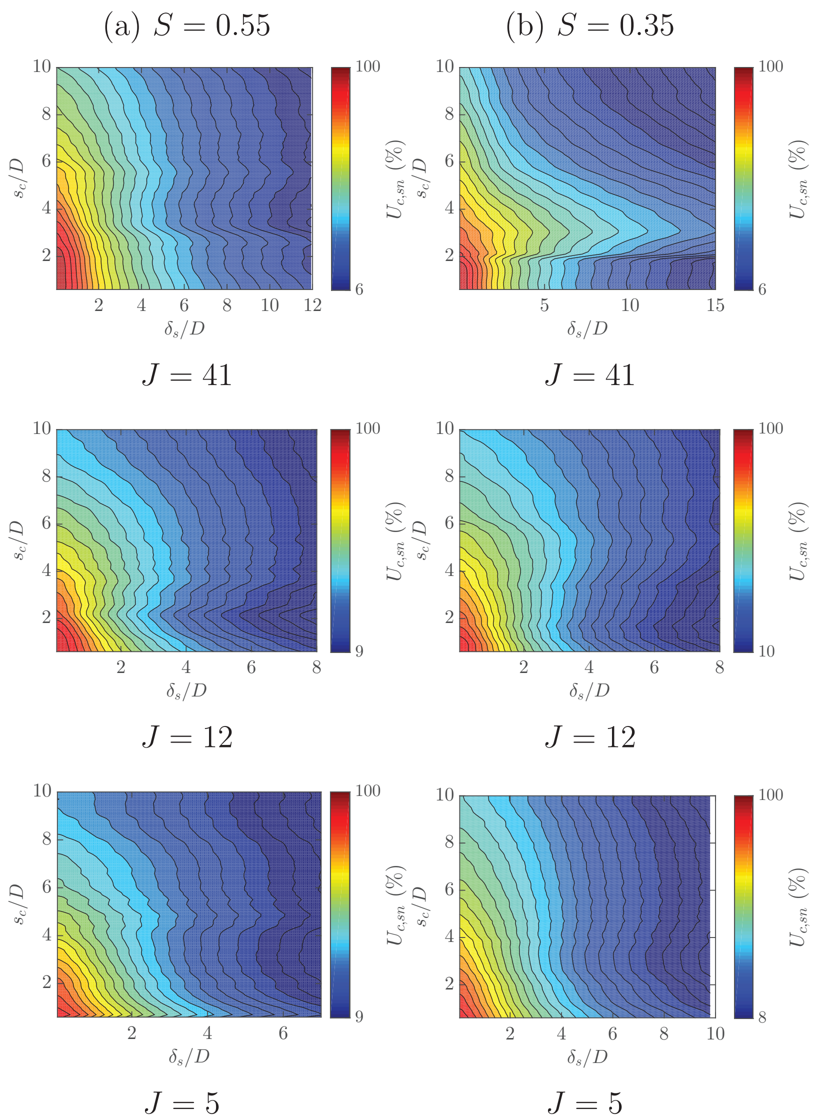

Figure 4.21: Contour maps of the mean centerplane-based Unmixedness $U_{c,sn}$ evaluated in the transformed plane (s_c/D–n/D) as a function of various length scales normalized by the jet diameter δ_s/D (x axis) and jet centerline trajectory coordinate s_c/D (y axis) for the (a) $S = 0.55$ and (b) $S = 0.35$, flush nozzle-injected JICF at $J = 41$ (top row), 12 (middle row) and 5 (bottom row). Mean concentration values in each interrogation area are matched to the reference value.

matching mean values, although the range of mixing length scales becomes quite different among all flow conditions with matching mean values, as noted above. Although similar mixing characteristics are observed with and without matching mean values, the current mixing metric inherently consists of different features when one accounts for matched means. The Unmixedness with matched mean values provides a smaller range of length scales δ_s in which the mean Unmixedness can achieve improved statistical convergence. The smaller range of δ_s could be problematic if a wide range of length scales needs to be investigated based on the nature of the flow. Matching mean values, however, enables mixing metrics to be compared over widely varying flow conditions. Therefore, the mixing metric and how it is evaluated should be carefully chosen, depending on applications. In this study, the results obtained using the mean centerplane-based Unmixedness without matching mean values are mainly analyzed because a wider range of length scales is preferred for the purpose of this study, where scale lengths provide insights into molecular mixing as compared with stirring.

4.4 Initial Locations of Rolled-up Vortices on Upstream Shear Layer

The investigations in Sections 4.2 and 4.3 suggests a possible relationship between the initiation of vortex rollup on the upstream shear layer and the local increase in the Unmixedness for larger length scales, depending on injectors and flow conditions. Further exploration of the relationship is considered in this section. The interest here is the initial locations of the rollup, which not only could correspond to the increase in the Unmixedness, but also is related to the determination of absolute vs. convective instability in the shear layer. From the instantaneous PLIF images shown in Figures 4.8 and 4.15, it is difficult to determine the initial locations of the rollups because one can hardly distinguish vortices from other flow structures via concentration scalar fields. To define locations of vortices, velocity fields are more appropriate to be used. Hence, PIV results from a part of prior simultaneous PLIF/PIV measurements (Gevorkyan, 2015; Gevorkyan et al., 2017) are used to track vortices. Although DEHS oil particles and fog are seeded into jet and crossflow, respectively for these PIV measurements, the existence of acetone vapors in the jet fluid for the PLIF will cause fairly similar behavior to the JICF as in PLIF-only measurements, providing comparable results to those in the present study. Velocity/Vorticity and scalar concentration fields have been verified in the PLIF/PIV studies to be well aligned (Gevorkyan, 2015). Note that we cannot utilize the PLIF results from part of the simultaneous PLIF/PIV measurements to quantify the Unmixedness for variable length scales, which would provide more directly comparable results, because: (1) the laser sheet is aligned not only for PLIF imaging but also for PIV measurements in the simultaneous imaging, so the laser sheet thickness is relatively thick ($1.4 - 1.9$ mm) for PLIF imaging (see Section 2.3.1), which worsens the spatial resolution in PLIF images; and (2) addition of DEHS oil particles and fog in flowfield generates noisier acetone concentration images which also affects resolution and image quality. The mixing evaluation is inherently sensitive to the level of noise and the variation in spatial resolution, so the PLIF data via single PLIF imaging with less noise and higher spatial resolution were utilized to avoid erroneous mixing evaluations and comparison. The PIV data from simultaneous PLIF/PIV measurements were utilized to determine the locations of the initiation of rolled-up vortices on the upstream shear layer. Due to the good correlation between scalar and velocity fields (Gevorkyan, 2015), the PIV data can be validly used for purposes of this study. There are three relevant cases in the PIV data: the equidensity flush nozzle-, equidensity flush pipe-, and $S = 0.35$ flush nozzle-injected JICF.

It has been noted earlier that vorticity itself is not appropriate for the identification of a vortex because vorticity characterizes not only swirling motion of the fluid but also shearing motions (Jeong and Hussain, 1995; Kida and Miura, 1998). In particular, vorticity is not suitable for vortex identification if the magnitude of background shear is comparable to the magnitude of vorticity in the vortex regions. Figure 4.22 shows vorticity fields ω_y in the transformed plane ($n/D - s_c/D$) extracted from the PIV data in Gevorkyan (2015). The PIV data are transformed based on the jet centerline trajectory coordinate s_c/D and its normal direction n/D defined from mean PLIF images acquired via PLIF imaging as a part of the simultaneous PLIF/PIV measurements. This transformation is successfully used in Gevorkyan (2015) and Gevorkyan et al. (2017) for quantifying local strain rates on the upstream and downstream mixing layers along s_c/D coordinate. As one can observe in Figure 4.22, vorticity clearly captures vortex as well as shear layer components, especially at higher J values such as $J = 41$, with a longer potential core region than at lower J values. This trend is often observed in transverse jets because the magnitude of the background shear is comparable to that of the vorticity, especially adjacent to the potential core region. Hence, other methods are required to identify vortices. Many definitions to identify the location of vortices in the Eulerian coordinate system have been developed over the years, such as Q-criterion (Hunt et al., 1988), Δ-criterion (Dallmann, 1983; Vollmers et al., 1983; Chong et al., 1990), or λ_2-criterion (Jeong and Hussain, 1995). In the present study, Q- and Δ-criterion are applied to determine vortex locations, or more specifically, initial vortex locations on the upstream shear layer.

The Q-criterion is a commonly used parameter to identify vortices defined by Hunt et al. (1988) as connected fluid regions with a positive second invariant of ∇u. That is, the Q-criterion identifies regions where the magnitude of swirling motion prevails over the degree of shearing motions. Additionally, the pressure in the vortex region is required to be lower than the ambient pressure. For an incompressible flow, the Q-criterion is defined as follows:

$$Q = \frac{1}{2}\left(||\Omega||^2 - ||S||^2\right) \tag{4.6}$$

In this study, Q is normalized by the maximum magnitude of Q in each instantaneous image. S and Ω in Equation (4.6) are defined as follows:

$$\begin{cases} S_{ij} = \dfrac{1}{2}\left(\dfrac{\partial u_i}{\partial x_j} + \dfrac{\partial u_j}{\partial x_i}\right) & (4.7) \\[2ex] \Omega_{ij} = \dfrac{1}{2}\left(\dfrac{\partial u_i}{\partial x_j} - \dfrac{\partial u_j}{\partial x_i}\right) & (4.8) \end{cases}$$

where S and Ω are the symmetric and antisymmetric components of ∇u, the rate-of-deformation tensor, respectively. S and Ω physically represent the rate of strain and the spin of fluid element, respectively. Therefore, the Q-criterion essentially represents the local balance between strain rate and the magnitude of vorticity. From this perspective, the

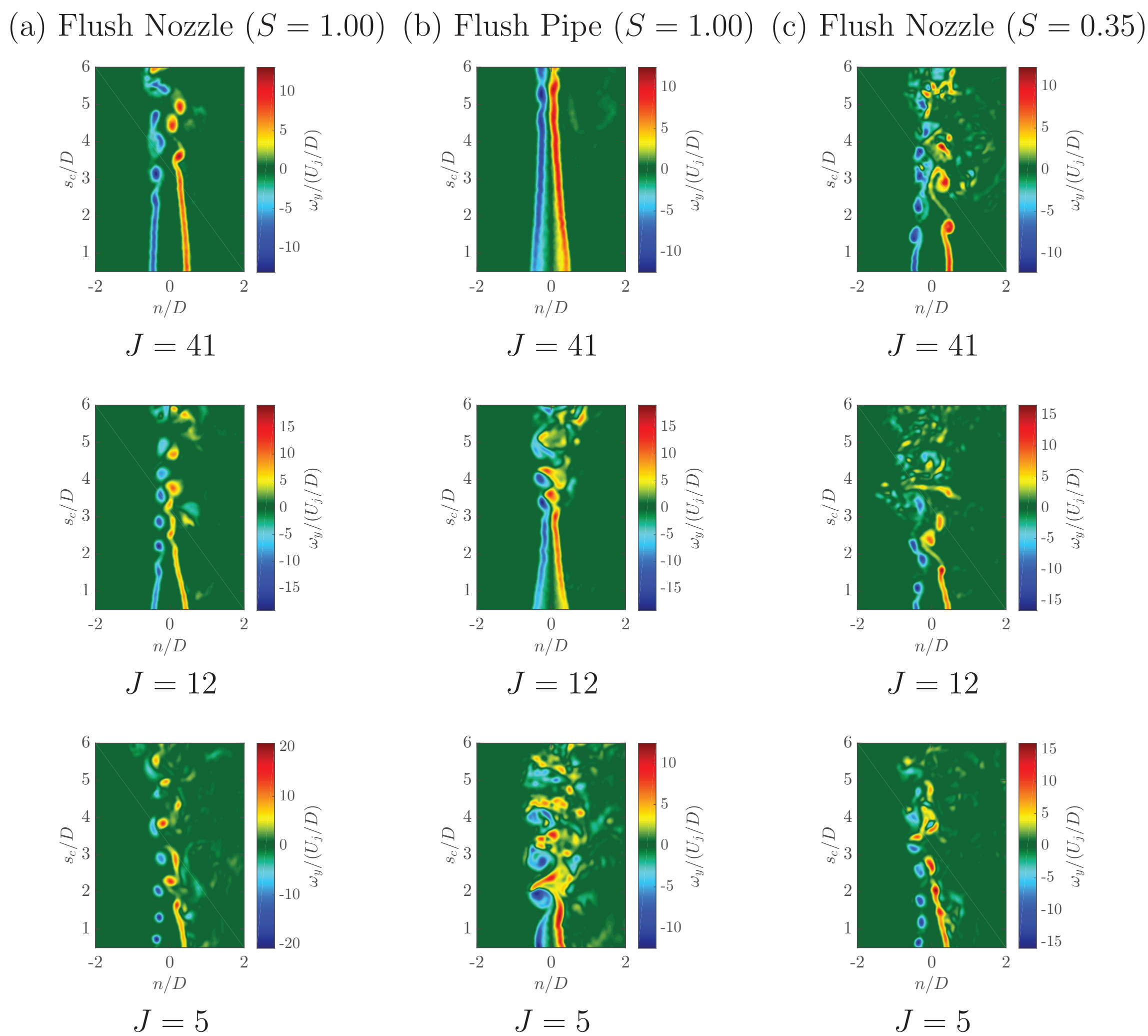

Figure 4.22: Instantaneous vorticity fields ω_y in the transformed plane ($s_c/D - n/D$) for the (a) equidensity flush nozzle-, (b) equidensity flush pipe- and (c) $S = 0.35$ flush nozzle-injected JICF at $J = 41$ (top row), 12 (middle row) and 5 (bottom row). Vorticity is non-dimensionalized by the mean jet velocity at the jet exit U_j and the jet diameter D.

Q-criterion in the range $0 \leq Q \leq 1$ (when $||\Omega||^2 \geq ||S||^2$) is used to define vortices in this study.

The Δ-criterion is also widely utilized to identify vortices defined by Dallmann (1983), Vollmers et al. (1983), and Chong et al. (1990) as regions where the eigenvalues of ∇u are complex. Physically, the flow regions defined by the Δ-criterion consist of the spiraling streamline and/or closed streamline in the Eulerian coordinate system. For incompressible flow, the definition of the Δ-criterion is provided as follows:

$$\Delta = \left(\frac{Q}{3}\right)^3 + \left(\frac{det\nabla v}{2}\right)^2 \tag{4.9}$$

As for the Q-criterion, the Δ-criterion is normalized by a maximum value in each instantaneous image to achieve a range of $0 \leq \Delta \leq 1$. Both the Q- and Δ-criteria can be quantified in the transformed plane $(n/D - s_c/D)$, similarly to the vorticity fields shown in Figure 4.22. The center locations of vortices are defined as local maxima based on the Q- and Δ-criterion fields. The local maxima are detected by a two-dimensional peak detection algorithm using a Matlab built-in function. In this exploration using PIV data, a main goal is to study the relationship between a local increase in the Unmixedness for various length scales and the initial rolled-up vortices on the upstream shear layer. Hence, only the initial rollups on the upstream shear layer are extracted from the results of the vortex identification. The initial vortex locations are detected in each transformed instantaneous image, and then averaged over 500 samples to define the mean center locations for all flow conditions.

In a computational study, vortical structures can be simply defined by $Q > 0$ as well as $\Delta > 0$. However, a certain threshold value larger than zero is required to experimentally define vortical structures by the Q- and Δ-criteria in order to extract vortices from the background in any experimental data. Moreover, some shear components are still captured in experimental data for these PIV measurements, although the Q-criterion and the Δ-criterion mostly distinguish the difference between shear strain rate and spin of fluid in a flowfield. Therefore, an appropriate threshold value has to be used to determine initial vortex locations. Appropriate threshold values for both criteria are determined using a threshold selection method developed by Otsu (1979). The threshold selection method basically determines an optimal threshold which produces the best separation of objects from the background by dichotomizing pixels into two classes. This method is applied to each instantaneous image to select appropriate threshold values for each image.

Figures 4.23 and 4.24 show instantaneous Q-criterion fields in the transformed plane ($s_c/D - n/D$) without and with employment of the above-noted optimized threshold values for the equidensity flush nozzle- and flush pipe-, as well as $S = 0.35$ flush nozzle-injected JICF. Note that these instantaneous fields are extracted using the same velocity fields as in the instantaneous vorticity fields shown in Figure 4.22. In Figure 4.23, background or shear components are captured in addition to actual vortical structures, especially in the upstream shear layer near the potential core region at $J = 41$, which prevents proper vortex identification. In Figure 4.24, with optimized threshold values, however,clear vortical structures are appropriately captured, with little spurious background noise or shear components. As compared with Figure 4.22, clear correspondence is observed between the Q-criterion fields with the optimal threshold in Figure 4.24 and regions of high magnitude in vorticity.

Figures 4.25 and 4.26 represent instantaneous Δ-criterion fields, without and with optimized threshold values, respectively. Note that the Δ-criterion fields without the threshold (Figure 4.25) reveal less in the way of background or shear components than Q-criterion fields (Figure 4.23) without a threshold, although the Δ-criterion fields still capture a small amount of background or shear in the quantification. The optimized threshold incorporation in Figure 4.26 successfully isolates vortex structures in the Δ-criterion fields from the background or shear components. The clear separation of vortex components from the other components was consistently observed in all instantaneous images for all injectors and flow conditions utilizing the method to define optimal threshold values, though it is noted that the Q-criterion captures more of the background (shear) structures than does the Δ-criterion.

The results of the detection of the initial vortex locations are shown in Figure 4.27. Figure 4.27 represents the mean initial rollup locations with respect to n/D and s_c/D locations based on the Q- and Δ-criterion fields. Recall that the equidensity flush pipe-injected JICF was the only configuration for which the local minima in $U_{c,sn}$ or an increase in $U_{c,sn}$ was observed (in Figures 4.6(c) and 4.7(c)). The locations of the rapid increase in the Unmixedness are

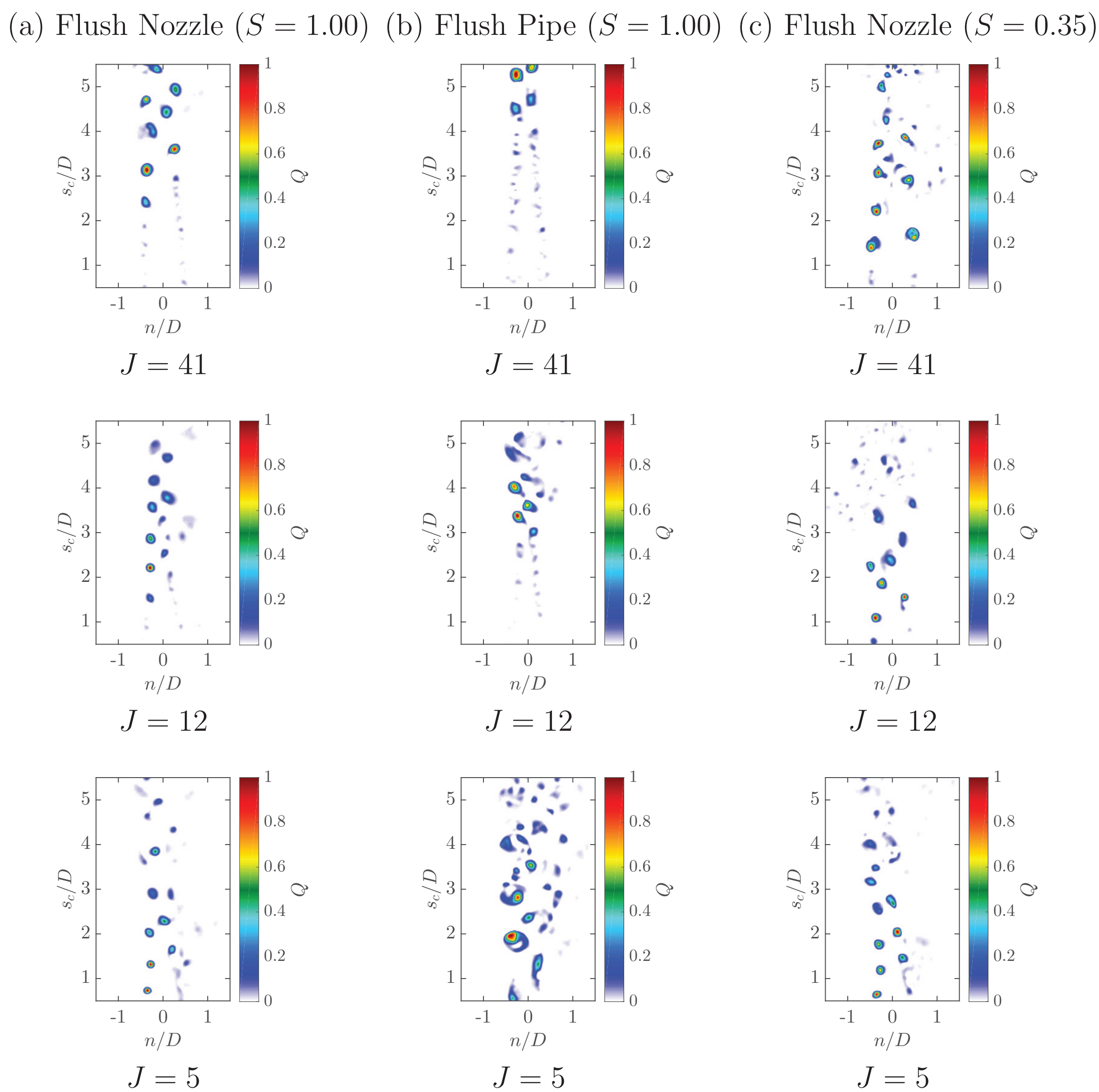

Figure 4.23: Instantaneous Q-criterion fields in the transformed plane ($s_c/D - n/D$) without optimized threshold values ($Q > 0$) for the (a) equidensity flush nozzle-, (b) equidensity flush pipe- and (c) $S = 0.35$ flush nozzle-injected JICF at $J = 41$ (top row), 12 (middle row) and 5 (bottom row).

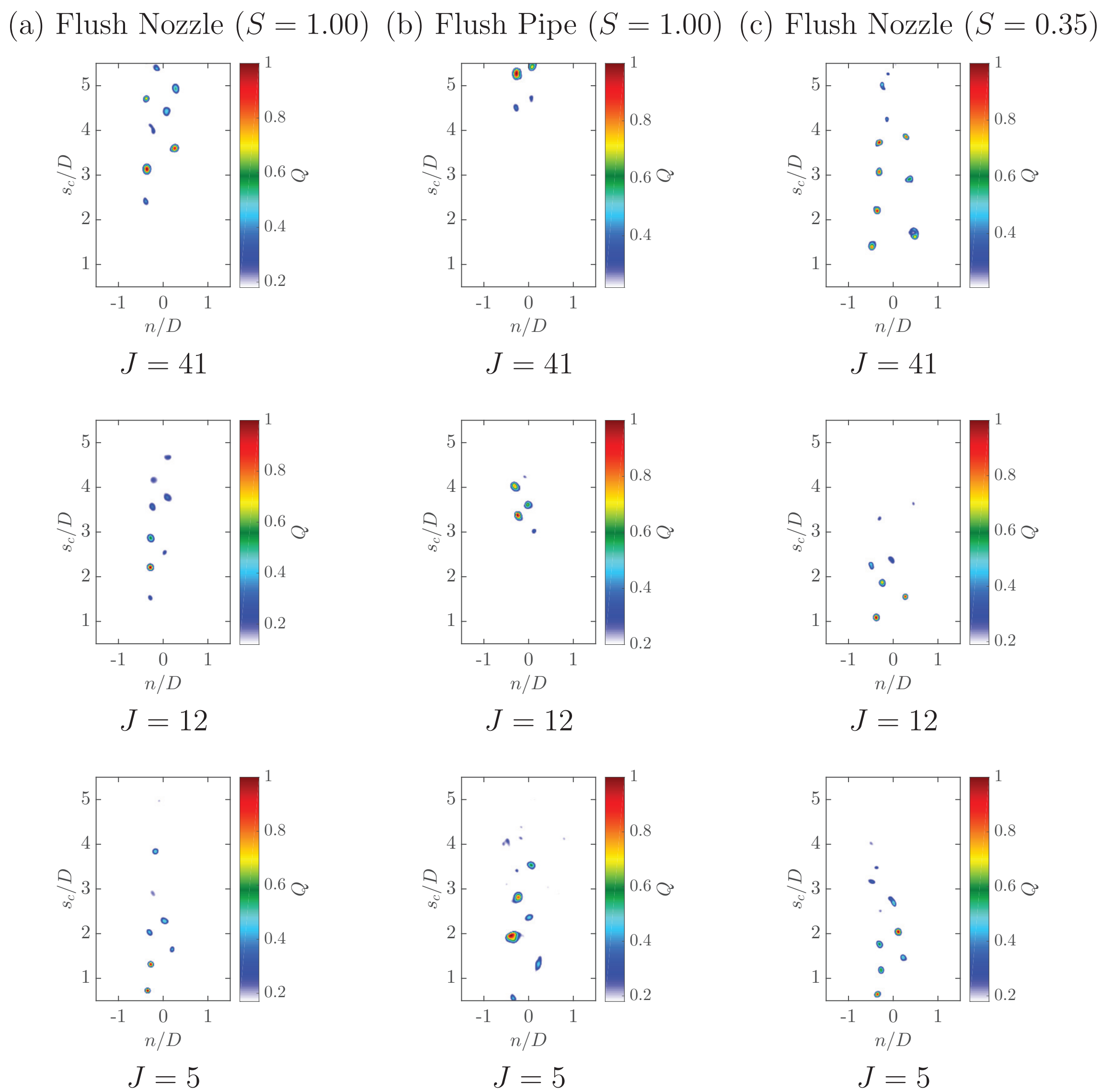

Figure 4.24: Instantaneous Q-criterion fields in the transformed plane ($s_c/D-n/D$) with optimized threshold values for the (a) equidensity flush nozzle-, (b) equidensity flush pipe- and (c) $S = 0.35$ flush nozzle-injected JICF at $J = 41$ (top row), 12 (middle row) and 5 (bottom row).

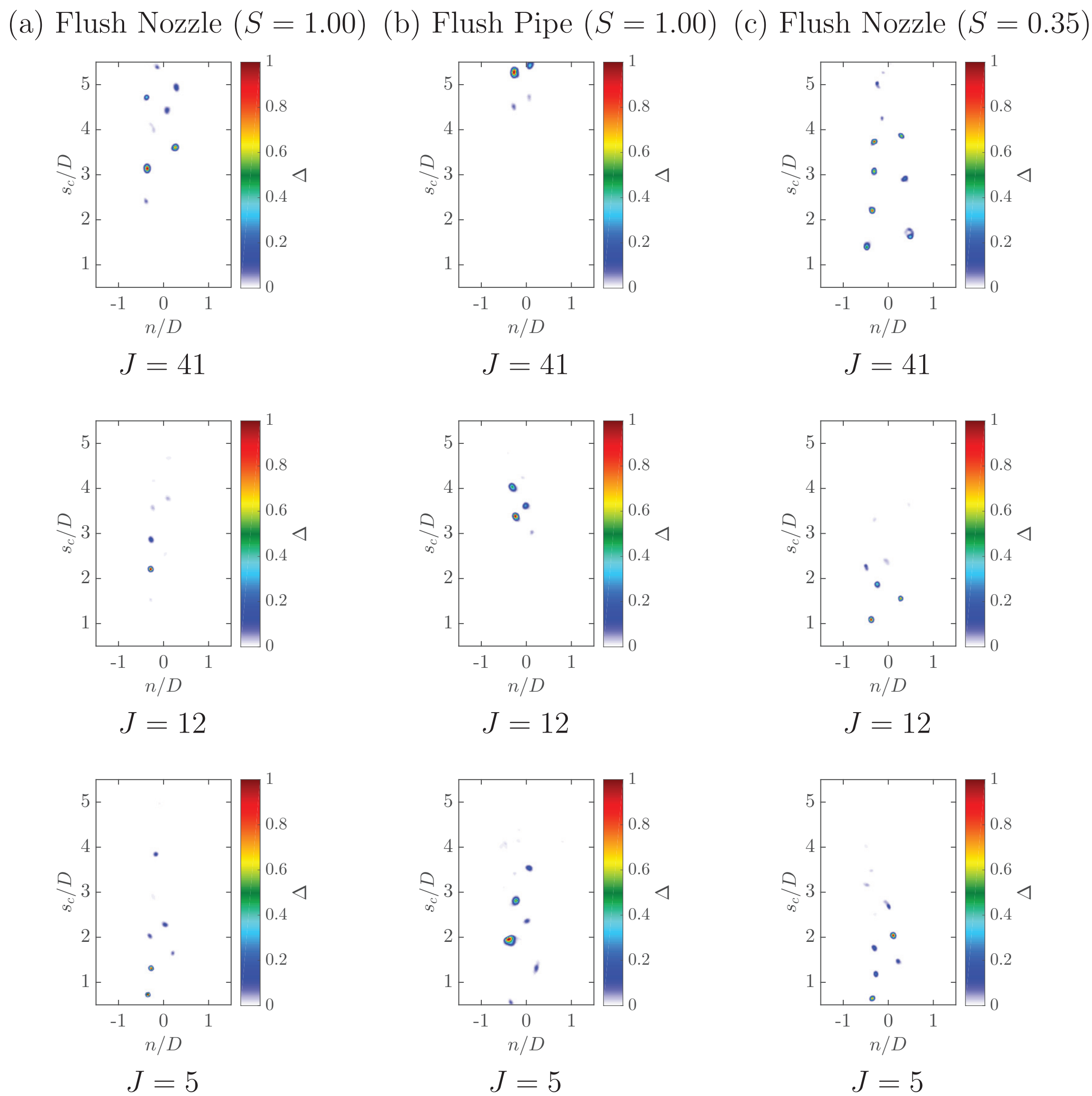

Figure 4.25: Instantaneous Δ-criterion fields in the transformed plane ($s_c/D - n/D$) without optimized threshold values ($\Delta > 0$) for the (a) equidensity flush nozzle-, (b) equidensity flush pipe- and (c) $S = 0.35$ flush nozzle-injected JICF at $J = 41$ (top row), 12 (middle row) and 5 (bottom row).

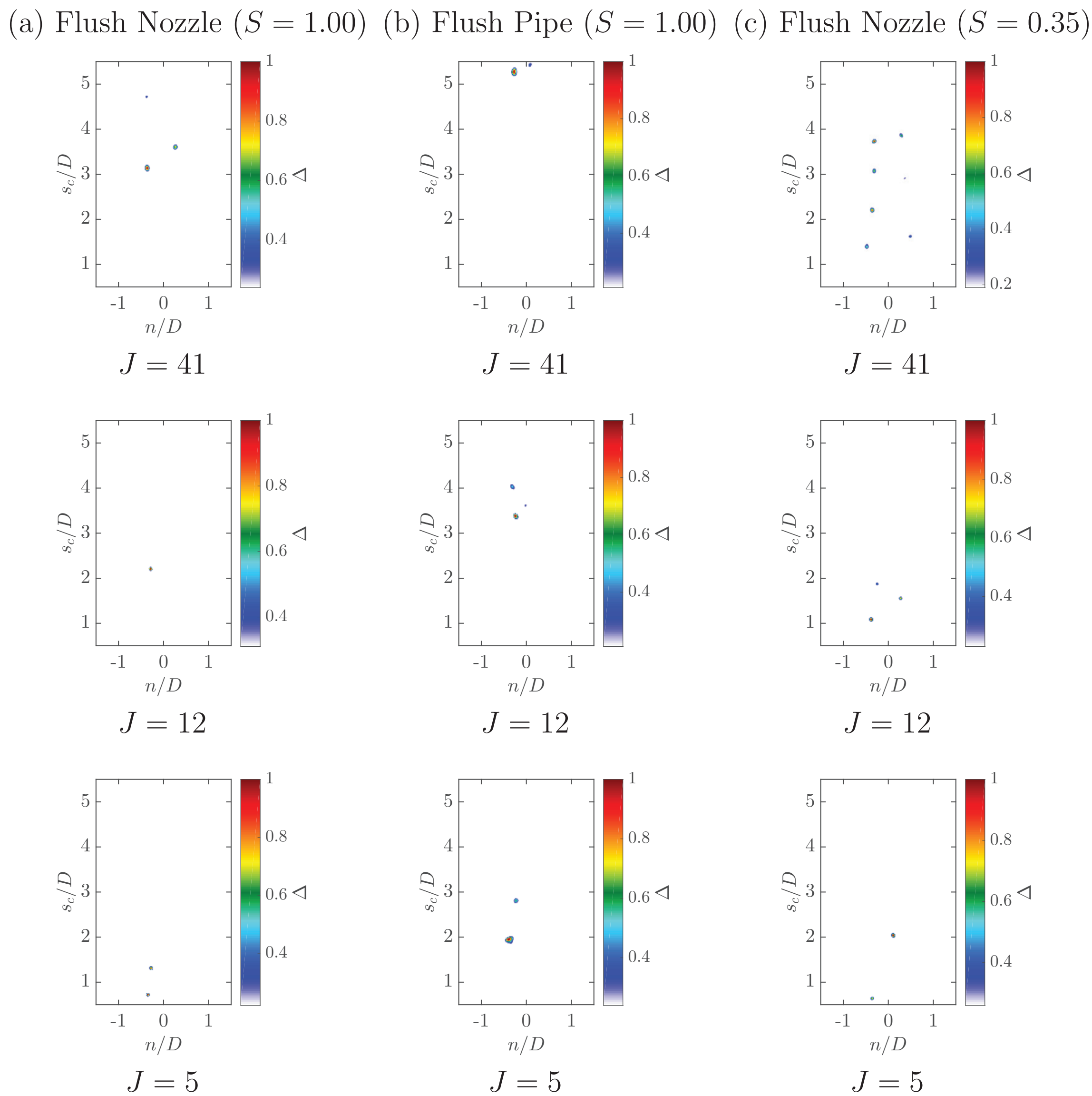

Figure 4.26: Instantaneous Δ-criterion fields in the transformed plane (s_c/D–n/D) with optimized threshold values for the (a) equidensity flush nozzle-, (b) equidensity flush pipe- and (c) $S = 0.35$ flush nozzle-injected JICF at $J = 41$ (top row), 12 (middle row) and 5 (bottom row).

Table 4.1: Initial peak locations in power spectra of the upstream shear layer instabilities at a fundamental natural frequency f_o, with respect to the upstream shear layer locations s/D. These locations are estimated from the data in Getsinger et al. (2012) and Getsinger et al. (2014).

	$J = 5$	$J = 12$	$J = 41$
Flush Nozzle ($S = 1.00$)	0.4	1.2	2.4
Flush Pipe ($S = 1.00$)	0.4	3.1	4.6
Flush Nozzle ($S = 0.35$)	0.5	1.0	1.5

also plotted in Figure 4.27 so that results can be compared. Again, since the Δ-criterion reveals less of the background or shear components than the Q-criterion, the Δ-criterion is interpreted as a "stricter" quantifier than the Q-criterion for the purpose of identifying vortices. The initial rollup locations with respect to s_c/D locations are observed to be consistently higher with the Δ-criterion than the Q-criterion.

Note also that in Figure 4.27 for plots associated with the s_c/D coordinate, the initial vortices on the upstream shear layer are created closer to the jet exit as J decreases, agreeing with the spectral and structural characteristics of the upstream shear layer acquired by Megerian et al. (2007) and Getsinger et al. (2012, 2014), some of which are shown in Figures 1.3 and 1.4. Interestingly, although the spectral data from the experimental studies (Megerian et al., 2007; Getsinger et al., 2012, 2014) are characterized along the upstream shear layer coordinate s/D, not the centerline s_c/D as in the present study, the locations of the initial vortices detected by this study and the initial peak locations in spectral data show good agreement. The initial peak locations are tabulated in Table 4.1. This good agreement also suggests that the comparison between the PIV data as a part of the simultaneous PLIF/PIV measurements and the PLIF data from PLIF-only imaging is reasonable, and the process of finding the vortex locations is correctly conducted.

Now, let us focus on the results for the equidensity flush pipe-injected JICF at three J values ($J = 41$, 12 and 5) in Figure 4.27(b) and the $S = 0.35$ flush nozzle-injected JICF at $J = 41$ in Figure 4.27(c), in which the increase in the Unmixedness for relatively larger length scales was observed. For the flush pipe case, the initial vortex locations on the upstream shear layer, especially as determined by the Δ-criterion, show excellent agreement with the locations at which the Unmixedness increases at relatively larger scales were determined (Figures 4.5(c)-4.7(c)). As suggested in Section 4.2, rollups on the upstream shear layer may indeed be related to the increase in the Unmixedness, and the initial rolled-up vortex locations appear to support the validity of this relationship. The initial locations of vorticity in the wake regions, however, are closer to the jet exit than the initial upstream rollup locations, confirming the relevance of the upstream shear layer to the alteration in Unmixedness seen for the flush pipe-injected JICF.

For the $S = 0.35$, flush nozzle-injected JICF at $J = 41$, the initial vortices identified by the Q- and Δ-criteria are located slightly closer to the jet exit ($s_c/D \approx 1.2 - 1.7$) than the locations where the abrupt increase in the Unmixedness was observed $s_c/D \approx 2.0$, as shown in Figure 4.27(c) for the s_c/D coordinate, while the initiation of the wake region $s_c/D \approx 2.0$ in Figure 4.15(c) shows much better correspondence. This exploration suggests a stronger correlation between the the increase in the Unmixedness for larger length scales and the initiation of wake regions on the downstream side (positive n/D side) for the $S = 0.35$ flush nozzle case at $J = 41$.

The location where the Unmixedness for the equidensity flush nozzle flow at $J = 12$ increases is also plotted in Figure 4.27(a) for the s_c/D coordinate, approximately at $s_c/D \approx 3.5$, which is extracted from Figure 4.6(a). The location for the increase in the Unmixedness does not agree with those from the Q- and Δ-criteria. As mentioned in Section 4.2, the increase in the Unmixedness from local minima to maxima for the equidensity flush nozzle-injected JICF at $J = 12$ is smaller than that for the flush pipe-injected JICF. In the instantaneous centerplane jet image, as shown in Figure 4.8(a), the data point location approximately at $s_c/D \approx 3.5$ corresponds to a location where vortical flow structures on the upstream shear layer begin to be more strongly disturbed and less distinguishable. Thus, the relatively small increase in the Unmixedness for the equidensity flush nozzle flow at $J = 12$ could be associated with different flow dynamics from the initiation of the vortical structures on the upstream shear layer, or with the averaging process over 200 instantaneous images, which

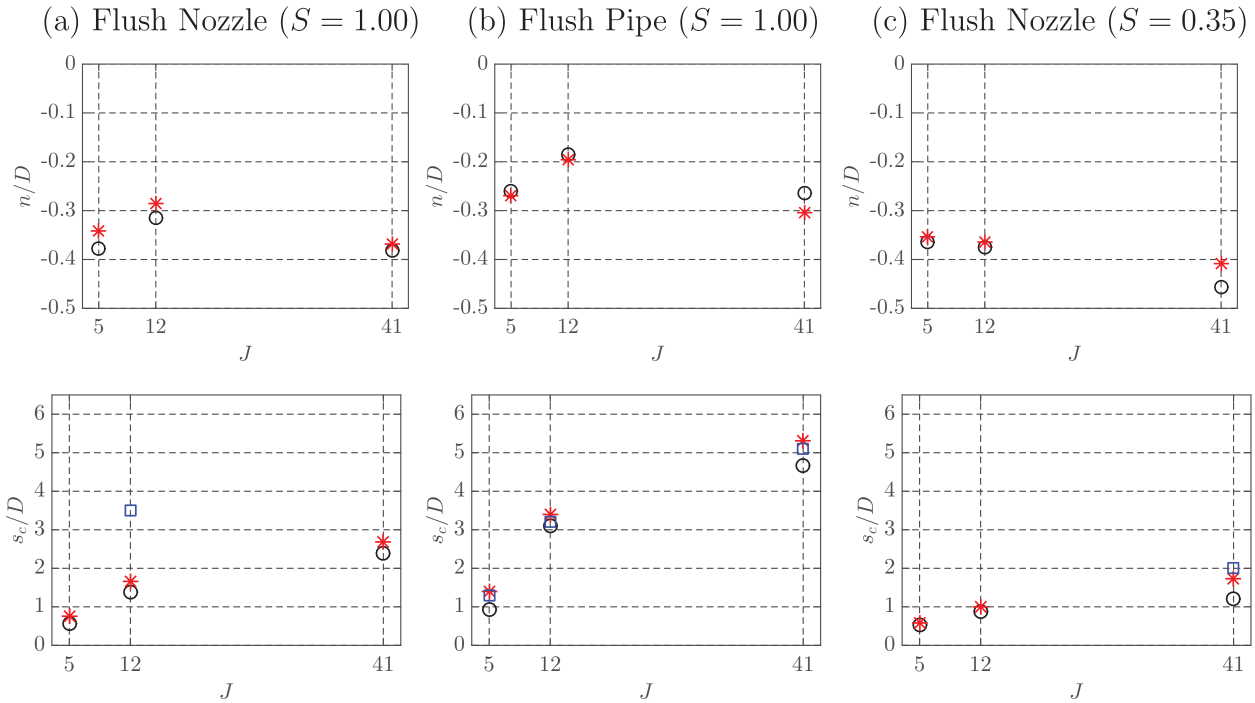

Figure 4.27: Mean initial vortex locations in n/D coordinate (top row) and s_c/D coordinate (bottom row) determined by Q-criterion (○) and Δ-criterion ($*$) with optimized threshold values over 500 instantaneous images. Data points (□), corresponding to the increase in the Unmixedness, are shown for the equidensity flush nozzle at $J = 12$ (from Figure 4.6(a)), for the equidensity flush pipe at $J = 5$, 12, and 41 (from Figure 4.6(c)), and for the $S = 0.35$ flush nozzle at $J = 41$ (from Figure 4.13(b)), in the s_c/D coordinate in the bottom row.

are typically very wavy, as shown in Figures 4.9-4.11.

In conclusion, the newly developed mixing metric based on the Unmixedness (Gevorkyan et al., 2016) and scale lengths related to the Mix-Norm (Mathew et al., 2005; Gubanov and Cortelezzi, 2010) can be successfully applied to the JICF for widely varied flow conditions. The ability of the mixing metric to capture the scale of segregation was validated by a test case inspired by the study of Kukukova et al. (2009), as well as in the application of the JICF. The application of the mean centerplane-based Unmixedness successfully captures mixing characteristics associated with various length scales and provides a different interpretation of the mixing characteristics as compared with those from those in Gevorkyan et al. (2016). For the equidensity flush nozzle- and elevated nozzle-injected JICF, flow structures, especially vortex rollup on the upstream shear layer and in the wake regions, generally contribute to better mixing at all length scales, while for the equidensity flush pipe-injected JICF, highly-concentrated rollups on the upstream shear layer are likely to cause a local increase in the Unmixedness (reduction in mixing) at relatively larger length scales associated with vortex structures.

For the lowered $S = 0.55$ and 0.35 flush nozzle-generated JICF, similar mixing characteristics were observed to those for the the equidensity flush nozzle- and elevated nozzle-injected JICF, that is, a monotonic decrease in the Unmixedness for various length scales, except for the case of the $S = 0.35$ JICF at $J = 41$. For this case, a relatively large wake region may be a main culprit of an abrupt increase in the Unmixedness. This interpretation is supported by between the increase in the Unmixedness at $s_c/D \approx 2.0$ and the initial vortex location of $s_c/D \approx 1.2 - 1.7$ extracted from the PIV data, while from the instantaneous image in Figure 4.15(c), the wake region was initially observed at $s_c/D \approx 2.0$, close to the increase in the Unmixedness.

All explorations conducted in this study, such as the mean and instantaneous Unmixedness, the Unmixedness with/without matching mean values, and initial vortex identification on the upstream shear layer using the PIV data acquired via simultaneous PLIF/PIV measurements, clearly suggest the relationships between various flow structures and mixing characteristics with different length scales. Most importantly, the newly developed mixing metric has an ability to capture different mixing characteristics for various length scales and provides a different interpretation from that obtained by classic mixing metrics.

CHAPTER 5

Effects of Axisymmetric Forcing on Transverse Jets - Sinusoidal Excitation

Axisymmetric forcing of the jet is a potentially effective method to control the degree of mixing for transverse jets (Johari et al., 1999; Eroglu and Breidenthal, 2001; M'Closkey et al., 2002; Narayanan et al., 2003; Shapiro et al., 2006; Megerian et al., 2007; Davitian et al., 2010b). To achieve an optimal mixing state in engineering applications, especially associated with aerospace engineering fields, "strategic" forcing is important based on the knowledge of the nature of naturally-occurring instabilities, and structural and mixing characteristics with and without external forcing. Hence, this chapter discusses the effect of axisymmetric forcing, specifically using sine wave forcing of the jet fluid created by an acoustic loud speaker, on instability, structural and mixing characteristics for the JICF via acetone PLIF. Note that only the equidensity ($S = 1.00$) flush nozzle-injected JICF for a range of momentum flux ratios ($5 \leq J \leq 41$) is explored in this experimental study.

5.1 Sinusoidal Forcing

Sinusoidal forcing created by an acoustic loud speaker is a relatively simple way to excite the JICF and potentially to enhance molecular mixing of the JICF. The effect of sine wave forcing on the JICF has been studied by many research groups (Vermeulen et al., 1992; M'Closkey et al., 2002; Narayanan et al., 2003; Muldoon and Acharya, 2010; Davitian et al., 2010b), although extensive study of jet structural characteristics and mixing quantification, utilizing various mixing metrics during such forcing, has not been conducted in depth to the best of our knowledge. Thus, the main goal of this part of our study is to explore instabilities, and structural as well as mixing characteristics for the JICF under sine wave excitation.

Sine wave excitation of the jets is generated by an acoustic loud speaker situated beneath the injection system, which includes an injector and a long pipe as a flow straightner as mentioned in Chapter 2. A sinusoidal signal with a prescribed forcing frequency f_f was initially created by a function generator. The function generator is followed by an amplifier with a constant gain of 30. Then, the amplified signal is transferred to the loud speaker to generate external, axisymmetric forcing to the JICF. The main interest in this experimental study is to investigate the effect of f_f on various characteristics of the JICF. For this purpose, applying effectively the same amplitude of sine wave forcing among various frequencies f_f is important for a direct comparison among all forcing and jet conditions. Hence, matching parameters associated with the energy input to the JICF via jet forcing is critical in this study. M'Closkey et al. (2002) and Davitian et al. (2010b) matched the root mean square (RMS) of the jet vertical velocity perturbation, $U'_{j,rms}$, acquired at the jet exit among all forcing conditions to achieve the effectively same degree of impulse imported to the jet. This approach enabled effective comparisons among different square wave excitation conditions as well. Shapiro et al. (2006) matched the peak-to-peak jet vertical velocity amplitude, ΔU_j, at the jet exit, primarily for single-pulse square wave forcing for JICF excitation. This experimental study determined to match $U'_{j,rms}$ in the vicinity of the jet exit, $0.2D$ above the jet exit plane, among all forcing conditions to achieve effectively the same-level forcing.

Hotwire anemometry was applied to measure the temporal vertical velocity, where temporal data are monitored on a PC to match $U'_{j,rms}$ among various forcing frequencies f_f by adjusting the amplitude of the initial sinusoidal signal on the function generator. The hotwire signal is first transmitted to an AC/DC signal splitter as a signal conditioner developed by Hendrickson (2012) and then to a data acquisition (DAQ) board with a sampling frequency of 20 kHz. The sampling frequency provides a maximum forcing frequency of $f_f = 10$ kHz based on the Nyquist sampling theorem to accurately match $U'_{j,rms}$ for all f_f. In this study, however, the maximum f_f is actually dependent on the amplitude of sine wave forcing because of the non-uniform frequency response of the actuation system. The maximum f_f, which is lower than 10 kHz, is attributed to a significant roll-off in response approximately

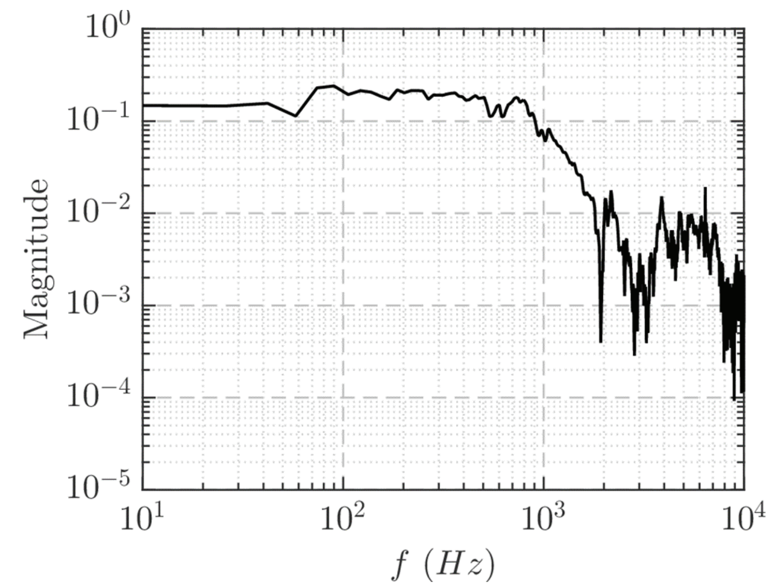

Figure 5.1: Magnitude of the frequency response of an actuation system, consisting of the amplifier, loudspeaker, hotwire, signal conditioner and DAQ board, calculated via a dynamic signal analyzer. The result is the product of a temporal average over 60 samples of a sweep of sinusoidal excitation over a range of frequencies at a fixed input amplitude.

above 1000 Hz for this actuation system, consisting of the amplifier, loud speaker, hotwire, signal conditioner and DAQ board; typical response is shown in Figure 5.1. Therefore, at higher forcing frequencies f_f, a much larger input amplitude is required to be able to match $U'_{j,rms}$, due to the significant roll-off. For example, for this system, the maximum f_f is 6000 Hz with $U'_{j,rms} = 0.07$ m/s, while the maximum frequency is 1210 Hz with $U'_{j,rms} = 0.55$ m/s, and 1100 Hz with $U'_{j,rms} = 1.00$ m/s.

Figure 5.2 represents the sample waveforms of the mean-subtracted temporal vertical velocity, $u_j - U_j$, for the equidensity flush nozzle-injected JICF at $J = 41$ ($U'_{j,rms} = 0.07$ m/s) and 5 ($U'_{j,rms} = 0.07$, 0.55 and 1.00 m/s), acquired 0.2D above the jet exit plane, with and without sine wave forcing. Note that in the absence of forcing, the $J = 41$ JICF has a convectively unstable upstream shear layer with a fundamental frequency of $f_o = 1600-1900$ Hz, while the $J = 5$ JICF is absolutely unstable with a (stronger) fundamental frequency $f_o = 2000$ Hz. Due to the relatively weak sine wave forcing and the sampling frequency of 20 kHz, temporal waveforms at $U'_{j,rms} = 0.07$ m/s and/or higher f_f are less smooth than the other waveforms, although even the less-smooth waveforms are clean enough to

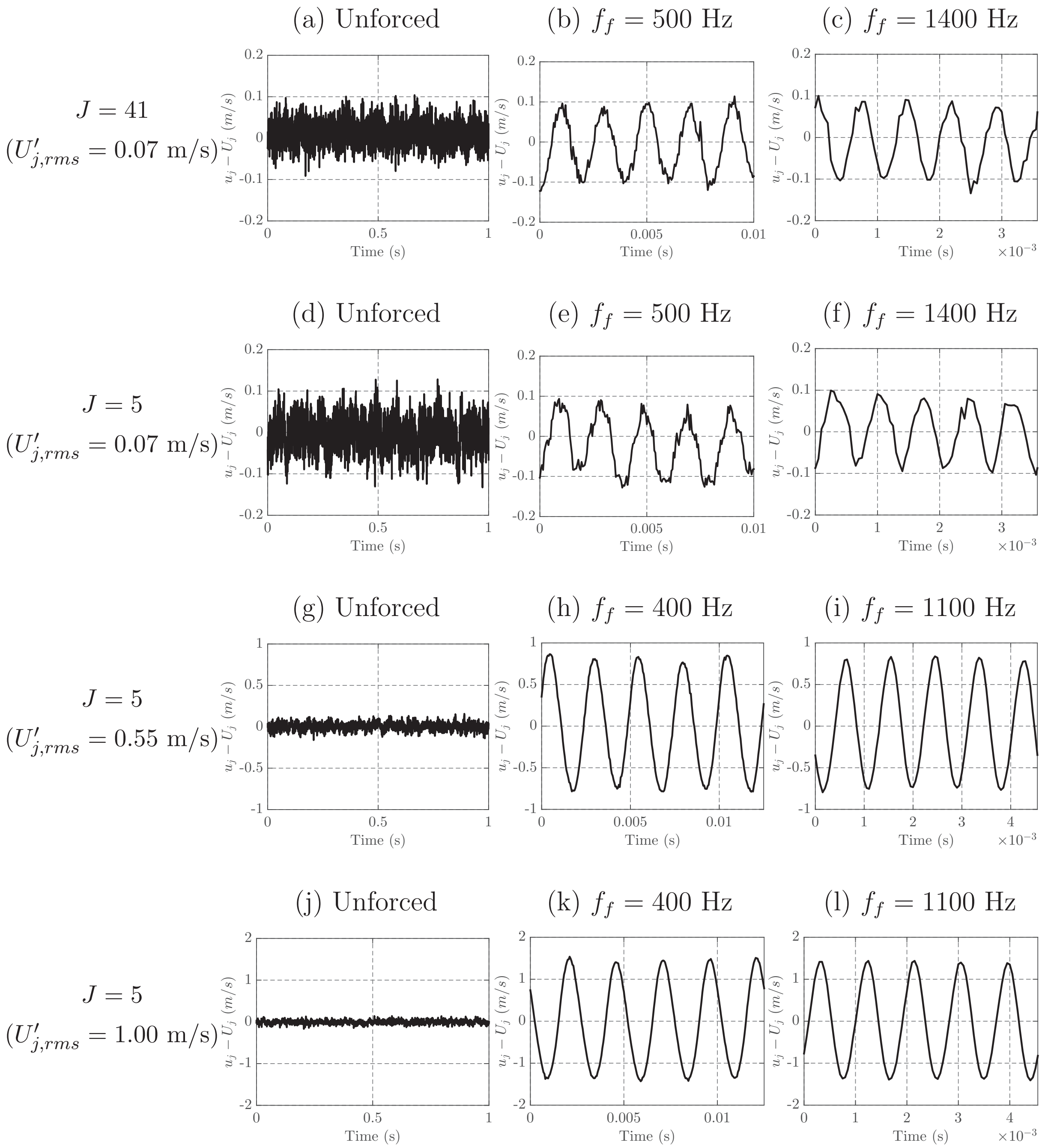

Figure 5.2: Temporal mean-subtracted jet vertical velocity profiles $u_j - U_j$ (m/s) without/with sine wave forcing measured via hotwire anemometry $0.2D$ above the jet exit plane at $J = 41$ ($U'_{j,rms} = 0.07$ m/s) and at $J = 5$ ($U'_{j,rms} = 0.07$, 0.55 and 1.00 m/s). Note that velocity RMS of the unforced cases is approximately $U'_{j,rms} \approx 0.02 - 0.03$ m/s at $J = 41$ and $U'_{j,rms} \approx 0.03 - 0.04$ m/s at $J = 5$.

show that the jets are actuated at the same frequency as the applied external forcing, and enable us to match $U'_{j,rms}$ among different f_f. At higher $U'_{j,rms}$ values in Figure 5.2, the temporal waveforms are clearer due to the larger amplitude, reflected in the stronger hotwire signals. Note that a feedback control system was not applied to modify the sinusoidal velocity variation here, in contrast to the control required for single- and double-pulse square wave forcing, which will be discussed in the next two chapters. Figure 5.2 demonstrates that a control system is unnecessary because of the fairly clear sinusoidal hotwire response even without control. Note that the naturally occurring velocity RMS for the unforced cases is approximately $U'_{j,rms} \approx 0.02 - 0.03$ m/s at $J = 41$, $U'_{j,rms} \approx 0.03$ m/s at $J = 12$, and $U'_{j,rms} \approx 0.03 - 0.04$ m/s at $J = 5$, so forcing at $U'_{j,rms} = 0.07$ m/s barely exceeds the natural instability amplitudes. Temporal velocity variation for other forcing conditions are shown in Appendix B.1.

The temporal data for matching $U'_{j,rms}$ for different flow conditions are not simultaneously taken with PLIF imaging because hotwire anemometry can not be employed in the presence of a laser sheet. Hence, the temporal data are taken right before the PLIF imaging, ensuring matching to the designated output $U'_{j,rms}$, and the same amplitude input is applied to the function generator in the actual measurements to achieve the desired $U'_{j,rms}$.

5.2 Instability Characteristics

For success for strategic control of structural and mixing characteristics of the JICF, understanding natural instability characteristics is very important. In this section, JICF instability characteristics are explored with and without sine wave forcing. The main focus of the study associated with instability characteristics lies in spectral measurements via hotwire anemometry along the upstream shear layer coordinate s/D, as well as in the “lock-in” behavior of the upstream shear layer to low level sinusoidal forcing at frequency f_f.

5.2.1 Spectral Measurements with/without Acetone

Our group has been extensively studying instability characteristics of transverse jets, especially for the upstream shear layer, for a range of J, S and injector configurations (Megerian et al., 2007; Davitian et al., 2010a; Getsinger et al., 2012, 2014). Yet, all spectral hotwire measurements in these earlier studies were conducted using a jet consisting only of nitrogen for equidensity cases ($S \approx 0.97$, strictly speaking for Megerian et al. (2007) and Davitian et al. (2010a)), and of nitrogen and helium for lowered-density ratio cases ($S = 0.14 - 0.90$ for Getsinger et al. (2012)). These prior studies, with the exception of preliminary structural data in Getsinger et al. (2014), did not involve acetone PLIF and hence did not include spectra with presence of acetone vapor for PLIF imaging. In this study, however, structural and mixing characteristics for the JICF are explored based on acetone concentration images taken via PLIF imaging, clearly with seeding of acetone vapor in the jets. Therefore, the effect of the presence of acetone vapor on shear layer instability characteristics should be first studied.

To investigate the instability characteristics with acetone vapor in the jets, spectral measurements in the upstream shear layer are performed. As in previous studies (Megerian et al., 2007; Davitian et al., 2010a; Getsinger et al., 2012, 2014), hotwire anemometry is utilized to obtain temporal vertical velocity fluctuations along the shear layer trajectory s/D. The hotwire in this spectral measurement is not calibrated because it is not possible to obtain calibrated velocity measurements in a flowfield where the local density is so highly variable, as is the case with mixtures of helium, nitrogen and acetone in a shear layer. The same applied to hotwire measurements in variable density flows in Getsinger et al. (2012). Yet the uncalibrated hotwire still yields a voltage signal containing the magnitude and frequency information of the velocity fluctuations, which are the only required data in spectral measurements. Hence, as done in the low density JICF experiments in Getsinger et al. (2012), hotwire anemometry is used here, where the hotwire signal is transmitted to a dynamic signal analyzer to apply a Fast Fourier Transformation (FFT) to the acquired signal. This procedure generates a magnitude in the power spectra pertaining to the vertical velocity fluctuation at the upstream shear layer. The hotwire was moved with a spatial resolution of $s/D = 0.1$ along the upstream shear layer for the range of $0.1 \leq s/D \leq 5.0$. The upstream shear layer trajectory itself was determined based on a best power-law fit to the center points of horizontal error function profiles associated with the vertical velocity on the upstream shear layer at variable vertical locations, z/D. The error function profiles are measured by traversing the hotwire at several z/D locations in the horizontal direction, x/D, with a spatial resolution of $x = 0.1$ mm ($x/D \approx 0.025$). Again, the spectral measurement was performed along the shear layer trajectory, s/D, not along z/D or s_c/D coordinates. The magnitude of the power spectra was obtained by averaging over 40 samples at each s/D location for statistical convergence. More details on the spectral measurement method may be found in Megerian et al. (2007); Davitian et al. (2010a); Getsinger et al. (2012).

Figure 5.3 shows contour maps of the magnitude of power spectra along the upstream shear layer as a function of the non-dimensional natural frequency or Strouhal number ($St \equiv fD/U_j$) for the equidensity flush nozzle-generated JICF at $J = 41$, 12, 10 and 5 without (in the left column) and with (in the right column) acetone vapor in the jets. The color bar corresponds to the magnitude of the local disturbance. Note that the Strouhal number is based on the jet diameter at the exit D, and the mean jet velocity at the jet exit U_j; in some studies, scaling based on the initial jet momentum thickness can be valuable (Alves et al., 2008; Davitian et al., 2010a). The results without acetone vapor are taken from Getsinger et al. (2014). As one can see, the basic qualitative instability trends are not altered with the presence of acetone vapor in the jets. At $J = 41$ and 12 (the convectively unstable regime), multiple natural modes of average frequency f_o (or St_o) in the upstream shear layer are observed, with some frequency-shifting and broadband peaks, depending on the s/D location. This "devil's staircase"(Jensen et al., 1983)-like frequency shifting in values of f_o suggests the presence of a tonal effect caused by the interaction of the hotwire itself with the upstream shear layer. This tonal interaction was first observed by Hussain and Zaman (1978) for free shear layers and is observed for the JICF with and without acetone. It should be noted that the average fundamental frequency f_o for these broadband (frequency-shifting) modes differs quantitatively between the cases with and without acetone. At $J = 10$ (a

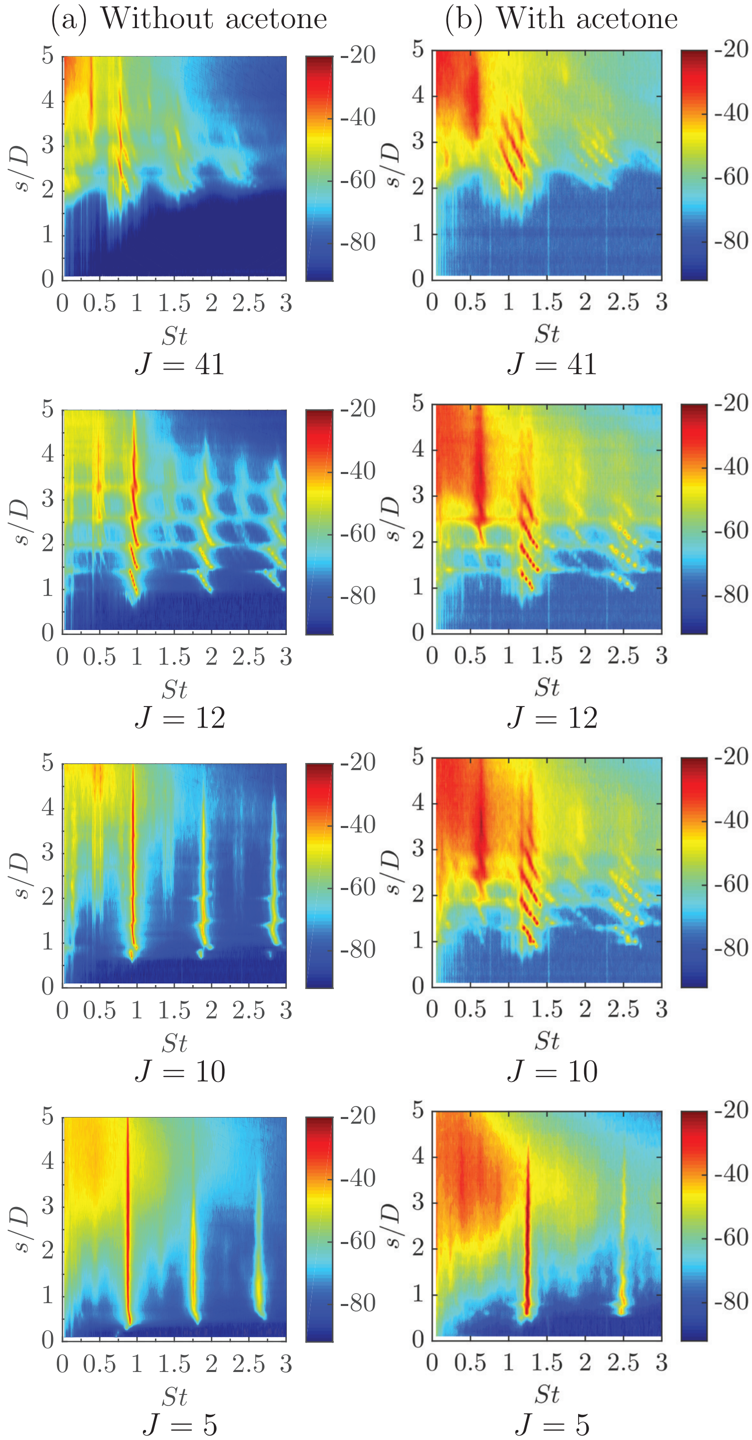

Figure 5.3: Contour maps for the magnitude of spectral density along the upstream shear layer trajectory coordinate s/D (a) without and (b) with seeding acetone in the equidensity flush nozzle-injected JICF at J = 41, 12, 10 and 5 in the absence of external forcing, acquired via hotwire anemometry. The data without acetone vapor in jets are taken from the study by Getsinger et al. (2014).

Table 5.1: Fundamental natural frequencies f_o on the JICF upstream shear layer with and without acetone vapor in the jet. Natural frequencies f_o in the absence of acetone vapor are obtained from Getsinger (2012).

	$J = 5$	$J = 10$	$J = 12$	$J = 41$
Without acetone (Hz)	1350	1460	$1380 - 1540$	$1130 - 1330$
With acetone (Hz)	2000	$1920 - 2250$	$1900 - 2230$	$1600 - 1900$

transition regime for convective to absolute instability), the spectral contour map shows clear, strong peaks with higher harmonics and no significant variation in f_o in the absence of acetone unlike the $J = 41$ and 12 cases. In contrast, the contour map for the JICF with acetone does not reveal clear peaks at $J = 10$, but still shows frequency shifting and jumping around an average f_o, as with a convectively unstable shear layer with tonal interactions (as with $J = 41$ and 12). Because the type of shear layer instability transitions around $J \approx 10$, that is, from convective to absolute instability, the behavior of the shear layer is sensitive to any perturbations that may arise due to changes in fluid properties, for example. Indeed, the fact that addition of acetone alone, while fixing average fluid density and other parameters, changes the spectral character, means that we are indeed very close to the transition point. Average fundamental frequencies also differ between the two cases. Finally, at $J = 5$, both spectra clearly show strong peaks at a fixed St_o with higher harmonics, initiated fairly close to the jet exit, consistent with absolutely unstable shear layers. From these observations, the existence of acetone vapor in the jets does not appear to alter qualitative behavior in the spectral characteristics, although there is a quantitative difference in f_o and there can be qualitative differences close to transition, as seen for $J = 10$.

In general, a natural frequency f_o on the upstream shear layer with acetone is observed to be higher than that without acetone. For instance, for cases with the inclusion of acetone vapor, the natural frequencies on the upstream shear layers are $f_o \approx 2000$ Hz at $J = 5$, $f_o \approx 1920 - 2250$ Hz at $J = 10$, $f_o \approx 1900 - 2230$ Hz at $J = 12$, and $f_o \approx 1600 - 1900$ Hz at $J = 41$, while those in the absence of acetone vapor are $f_o \approx 1350$ Hz at $J = 5$, $f_o \approx 1460$

Hz at $J = 10$, $f_o \approx 1380 - 1540$ Hz at $J = 12$, and $f_o \approx 1130 - 1330$ Hz at $J = 41$. These fundamental natural frequencies are tabulated in Table 5.1. This increase in f_o with acetone vapor suggests a change in flow time scale due to the addition of acetone, possibly due to the presence of different constituents and hence different speeds of sound. This quantitative difference in f_o is important to understand so that we may quantitatively relate f_f to f_o in the upstream shear layer under sine wave forcing in this study.

Another interesting point to be discussed in the spectral data is the non-dimensionalization of frequency. In Figure 5.3, St ($\equiv fD/U_j$) is utilized to non-dimensionalize frequency on the upstream shear layer. Yet there are significant differences in the values of f_o as well as St with and without acetone, suggesting the scaling for St may not be relevant to the JICF in fluids with different constituents yet the same bulk density. Interestingly, the increment in the fundamental natural frequency, Δf_o, induced by seeding the acetone in the jets is approximately linear with J values as shown in Figure 5.4(a). This linearity between Δf_o and J suggests that other scaling may possibly produce a better collapse of the spectral data with and without the acetone. Megerian et al. (2007) observed a fairly systematic increase in the momentum thickness of the nitrogen jets on the upstream and downstream shear layers for the equidensity JICF at $Re_j = 2000$ as R decreases. Therefore, $St_\theta = f\theta_j/U_j$ based on the jet momentum thickness, either in the upstream or downstream shear layer of the jet, may create a better collapse of the spectral data with and without acetone. Unfortunately, exploring alternative scaling via θ_j for better data collapse cannot be investigated in this study because of the difficulty in acquiring quantitative jet exit profiles with acetone via hotwire anemometry due to the limited range of hotwire calibration in the presence of acetone, as mentioned in Section 2.2.

Despite the fact that f_o is altered for given flow conditions with acetone in the jets, it is noted that qualitative trends associated with f_o are consistent with previous equidenisty (Megerian et al., 2007) and low density (Getsinger et al., 2012) JICF studies in the absence of acetone. That is, f_o on the upstream shear layer increases as J increases from 5 to 10 in the absolutely unstable regime, and then decreases as J increases from 10 to 41 in the convectively unstable regime, as shown in Figure 5.4(b). Therefore, the instability characteristics

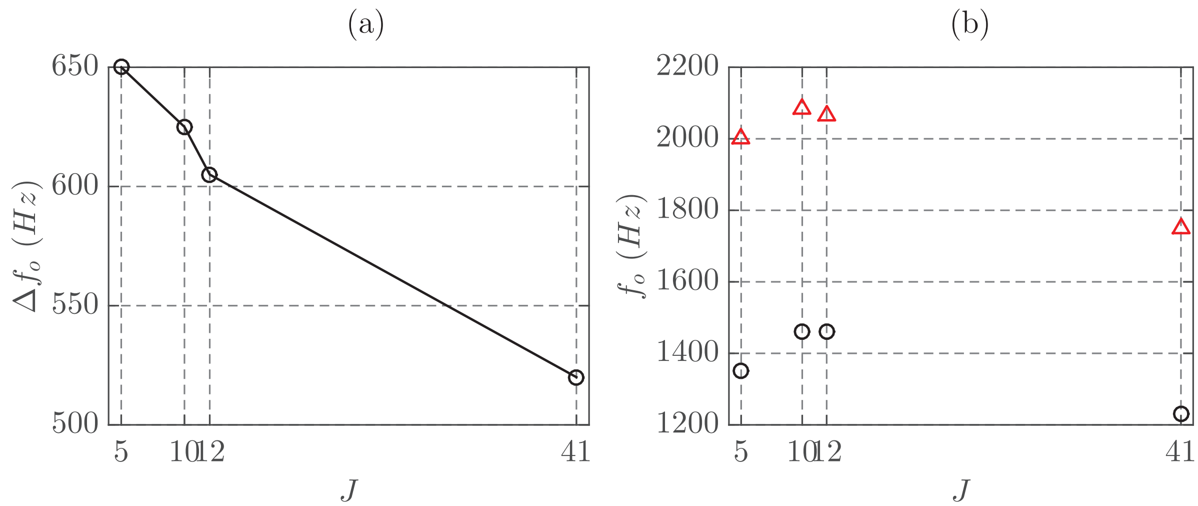

Figure 5.4: (a) Increment in the fundamental natural frequency, Δf_o, introduced by seeding the acetone vapor in the jet, and (b) fundamental natural frequencies f_o without (○) and with (△) acetone vapor in the jet. Both figures are plotted as a function of momentum flux ratio J.

with acetone vapor are qualitatively consistent with those without acetone, demonstrating the phenomenological similarity between the alteration in instabilities, although the actual f_o changes in the existence of acetone, possibly caused by the alteration of flow and acoustic time scales.

5.2.2 Lock-in Response

Several previous studies by Juniper et al. (2009) for the low density free jet and by Davitian et al. (2010a) and Getsinger et al. (2012) for the equidensity or low density JICF found that forcing frequency f_f is less dominant than f_o in the upstream shear layer under absolutely unstable condition at low amplitude sinusoidal forcing. But when the amplitude increases, the shear layer instability can become "locked-in" to f_f, depending on the range of f_f. This phenomenon is called "lock-in" for the upstream shear layer. Previous JICF instability studies (Davitian et al., 2010a; Getsinger et al., 2012) indicate that the absolutely unstable upstream shear layer displays in two different behaviors under sine wave forcing: (1) the upstream shear layer still contains a peek with an f_o component even with lower level sine wave forcing at f_f, and (2) at higher amplitudes, f_f overcomes f_o, and the frequency component at f_o visually disappears, corresponding to lock-in. This behavior is interesting because the lock-in not only demonstrates a transition to absolute instability, but it is related to structural and mixing characteristics of the absolutely unstable JICF, which will be discussed in this study.

For a study of the lock-in response, some criteria are required to judge if the upstream shear layer is locked-in to f_f. In previous studies (Juniper et al., 2009; Davitian et al., 2010a; Getsinger et al., 2012), lock-in was considered to occur when the peak at f_o in the upstream shear layer in the magnitude of spectra disappeared under external forcing, although any criterion or threshold for the assessment of the lock-in is not clearly defined. In the present study, a slightly different criterion was determined to define the lock-in more easily and consistently among all forcing conditions.

Spectral amplitudes around a critical forcing frequency for the lock-in, $f_{f,cr}$, acquired via hotwire anemometry are shown in Figure 5.5 for $J = 5$ and $Re_j = 1900$, with a mean jet velocity $U_j \approx 6.5$ m/s. The spectral magnitudes were measured at the shear layer location $s/D = 2.0$, the same s/D location as in Getsinger et al. (2012) to assess lock-in. In Figure 5.5(a), the black plot represents the hotwire voltage spectrum at $s/D = 2.0$ in the absence of sine wave forcing, with a single strong peak at $f_o = 2000$ Hz, while the red plot represents the spectrum under sine wave forcing at amplitude $U'_{j,rms} = 0.55$ m/s and at forcing frequency $f_f = 550$ Hz measured at the same location. The forced spectrum shows a strong peak at f_f and a weaker peak at $f_o = 2000$ Hz, in addition to multiple peaks which in some cases are harmonics of 550 Hz or differences between harmonics and adjacent peaks near 2000Hz. As f_f increases, it begins to become more dominant than the peak at f_o, where the amplitude at f_o lessens as compared with that for the unforced case. In Figure 5.5(c), the peak at f_o disappears with sine wave forcing at $f_f = 590$ Hz; this corresponds to the complete dominance of f_f over the natural mode in the upstream shear layer. In Figure 5.5(d), forcing at $f_f = 590$ Hz also produces no peak at f_o, and this is the case for higher f_f values. Such dominance of f_f over f_o, as well as the disappearance of f_o with external forcing are the essence of the lock-in response. In this study, the upstream shear layer is considered to be locked-in when forcing at f_f has caused the amplitude of the peak at f_o to

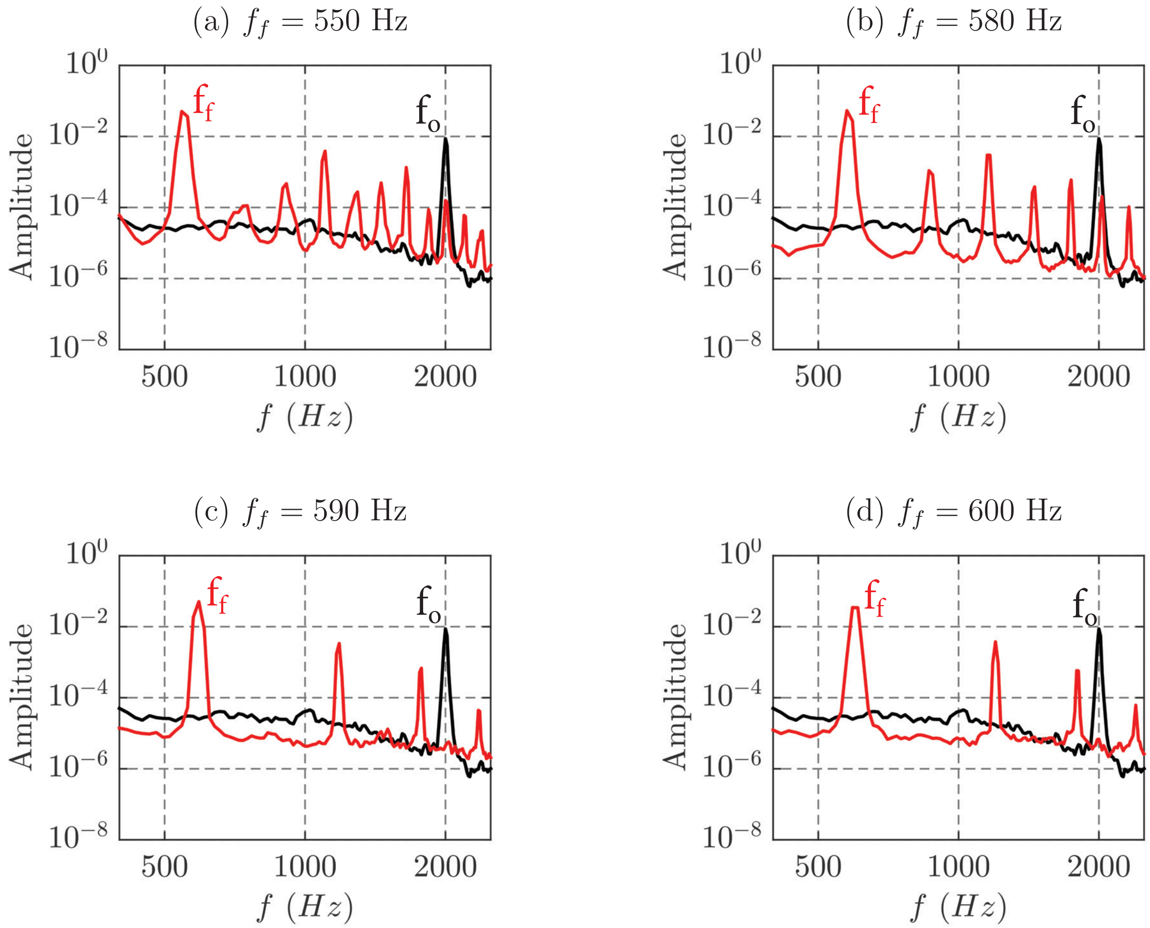

Figure 5.5: Amplitudes of spectra in the absence of forcing (—) and under sine wave forcing (—) acquired via hotwire anemometry at $s/D = 2.0$ along the upstream shear layer trajectory for $J = 5$ for the equidensity flush nozzle-injected JICF with acetone, at (a) $f_f = 550$ Hz, (b) 580 Hz, (c) 590 Hz and (d) 600 Hz. $U'_{j,rms}$ is matched among all forcing conditions at $U'_{j,rms} = 0.55$ m/s. Note that the critical forcing frequency for lock-in was determined as $f_{f,cr} = 590$ Hz at this $U'_{j,rms}$ amplitude.

be reduced by five orders of magnitude, or a factor of 10^5 lower than the peak at f_o without forcing. Using this threshold, the critical frequency for the lock-in in the case of $J = 5$ at $U'_{j,rms} = 0.55$ m/s shown in Figure 5.5 is determined to be $f_{f,cr} = 590$ Hz, at least, as f_f is increased toward $f_o = 2000$ Hz. This criterion is applied to all spectral data sets at $J = 5$ to create a lock-in diagram. To obtain the lock-in diagram, a frequency sweep was conducted at a fixed amplitude of forcing, $U'_{j,rms}$ in this study, at $s/D = 2.0$ and then the critical forcing frequency $f_{f,cr}$ for the lock-in was determined at each $U'_{j,rms}$. This method contrasts that used in Davitian et al. (2010a) and Getsinger et al. (2012), where the frequency f_f is fixed and the amplitude of excitation (pressure perturbation associated with applied excitation) is systematically increased until lock-in is observed.

The lock-in diagram was observed here to take the typical V shape, because $f_{f,cr}$ exists on the lower and higher frequency sides with respect to f_o at the same level of forcing (Juniper et al., 2009; Getsinger et al., 2012). Hence, the assessment of the lock-in is assumed to provide two critical frequencies for each $U'_{j,rms}$ in this study. However, as mentioned previously, sine wave forcing at relatively high f_f can not be achieved easily at higher amplitude $U'_{j,rms}$ because of the significant roll-off revealed in the frequency response of the actuation system after around 1000 Hz. The limitation in this range of f_f prevents the acquisition of $f_{f,cr}$ higher than f_o when $U'_{j,rms}$ is fairly large.

Based on the criterion described above, the lock-in diagram for the equidensity flush nozzle-injected JICF at $J = 5$ (an absolutely unstable condition) is generated, as shown in Figure 5.6. This includes plots of $U'_{j,rms}$ (Figure 5.6(a)) and $\sqrt{U'_{j,rms}}$ (Figure 5.6(b)), both of which are plotted against f_f. Previous experimental studies (Juniper et al., 2009; Davitian et al., 2010a; Getsinger et al., 2012) indicate that the lock-in diagram shows a linear relationship between $|f_f - f_o|$ and the critical acoustic pressure perturbation amplitude p'_{crit}, suggesting a Hopf bifurcation to a global mode (Huerre and Monkewitz, 1990; Juniper et al., 2009) and producing a "V" shape in the lock-in diagram involving p'. Figure 5.6(a) does not show a linear relation between $|f_f - f_o|$ and $U'_{j,rms}$, but it does produce a minimum at $f_o = 2000$ Hz, as expected. But clearly, $U'_{j,rms}$ and p'_{crit} do not have a linear relationship. To explore a different parameter used for the lock-in diagram, Figure 5.6(b) represents $\sqrt{U'_{j,rms}}$ as a function of f_f. is closer to a linear relationship, but in any case it again suggests a Hopf bifurcation to be associated with the transition to absolute instability, as seen in Juniper et al. (2009); Davitian et al. (2010a); Getsinger et al. (2012). As in other studies, the lock-in diagram demonstrates that, as forcing frequency approaches f_o, or as the amplitude of forcing frequency increases for a given f_f, the forcing can overtake the f_o even if it is absolutely unstable.

Interestingly, the V shape in the diagram displays an asymmetric slope between the lower-and higher-frequency regimes on either side of the natural frequency $f_o = 2000$ Hz. From Figure 5.6(b), the slope in the V shape is shallower for $(f_f - f_o) > 0$ than for $(f_f - f_o) < 0$, suggesting that the upstream shear layer is more sensitively affected by external forcing at higher f_f. This asymmetry as seen in Figure 5.6 is observed in previous studies as well (Juniper et al., 2009; Davitian et al., 2010a; Getsinger et al., 2012), although the direction of asymmetry is opposite to that in Juniper et al. (2009); Getsinger et al. (2012). The lock-in diagrams in Juniper et al. (2009); Getsinger et al. (2012) involve V shape which is inclined toward the lower-frequency side, in contrast to Davitian et al. (2010a) and the result in this study where the V shape inclines toward the higher-frequency side. The difference in the orientation of the asymmetry may be associated with different density ratios S. Juniper et al. (2009); Getsinger et al. (2012) utilized the lowered-density free jet and JICF, respectively, while Davitian et al. (2010a) and the current study examined the equidensity JICF. The spectral measurements in Getsinger et al. (2012) indicates that varying S significantly changes instability characteristics in the JICF even at the same Re_j and J. While it is possible that different density affects the orientation of the V shape in the lock-in diagram, this is only conjecture in that the lock-in diagram for the lowered-density flush nozzle-injected JICF with seeding acetone vapor was not examined in this study. But the important conclusion here is that the "lock-in" phenomenon can be achieved with sufficiently high amplitude forcing and/or forcing at a frequency close enough to f_o for an absolutely unstable shear layer, lock-in always occurs.

5.3 Structural Characteristics for the JICF

This section discusses jet structural characteristics under sine wave forcing based on instantaneous centerplane and mean cross-sectional PLIF images. This investigation is designed to show how jet structures are affected by sine wave forcing, depending on forcing frequency f_f as well as the nature of the instability on the upstream shear layer, convective or absolute.

In our group's previous structural and mixing studies on the JICF using smoke visualization (Davitian et al., 2010b), the convectively unstable jets at $R = 10$ ($J = 100$) are

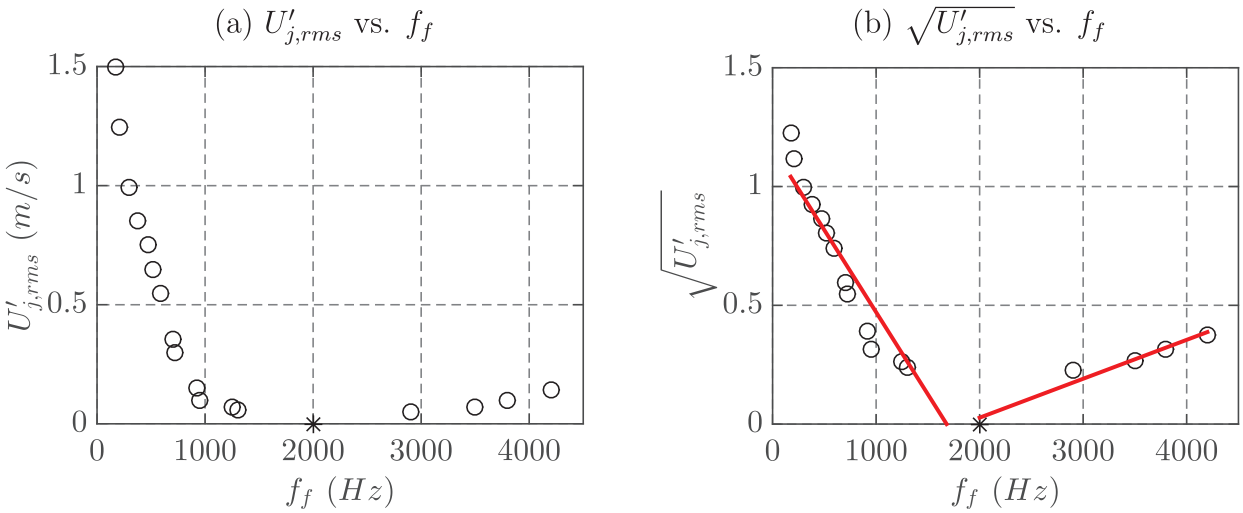

Figure 5.6: Lock-in diagrams for the equidensity flush nozzle-injected JICF at $J = 5$ under sine wave forcing at various forcing frequencies f_f, and velocity RMS $U'_{j,rms}$ as well as $\sqrt{U'_{j,rms}}$. The black open circles, black asterisk, and two red lines (only present in (b)) represent critical forcing frequencies $f_{f,cr}$ at the specific level of forcing, the natural frequency on the upstream shear layer f_o, and linearly fitted lines to $f_{f,cr}$ both on the lower and higher frequency side with respect to f_o, respectively.

significantly affected even by relatively weak sine wave forcing at $U'_{j,rms} = 0.55$ m/s, while absolutely unstable jets at $R = 3$ ($J = 9$) are hardly affected at all, even by relatively strong sine wave forcing at $U'_{j,rms} = 1.7$ m/s. For the studies the jet's mean velocity was fixed at $U_j = 8$ m/s, for $Re_j = 2000$. In the present studies, in-depth structural characteristics are examined using acetone PLIF imaging, providing more detailed structural characteristics as compared with the line-of-sight smoke visualization. All instantaneous PLIF images, both in the centerplane and cross-sectional views, were taken at a recording rate of 7.5 Hz without phase locking. Hence, f_f has to be carefully selected so as not to be divisible by the recording rate in order to avoid recording only at a single phase. 500 instantaneous images were taken for all conditions to ensure statistical convergence in the mixing evaluation, described in Section 5.4. Although this section only displays instantaneous centerplane images for purposes of discussion, mean centerplane images are also shown in Appendix C.

Figure 5.7 shows instantaneous centerplane acetone PLIF images for the equidensity flush nozzle-injected JICF at $J = 41$ with/without sine wave forcing at forcing frequency

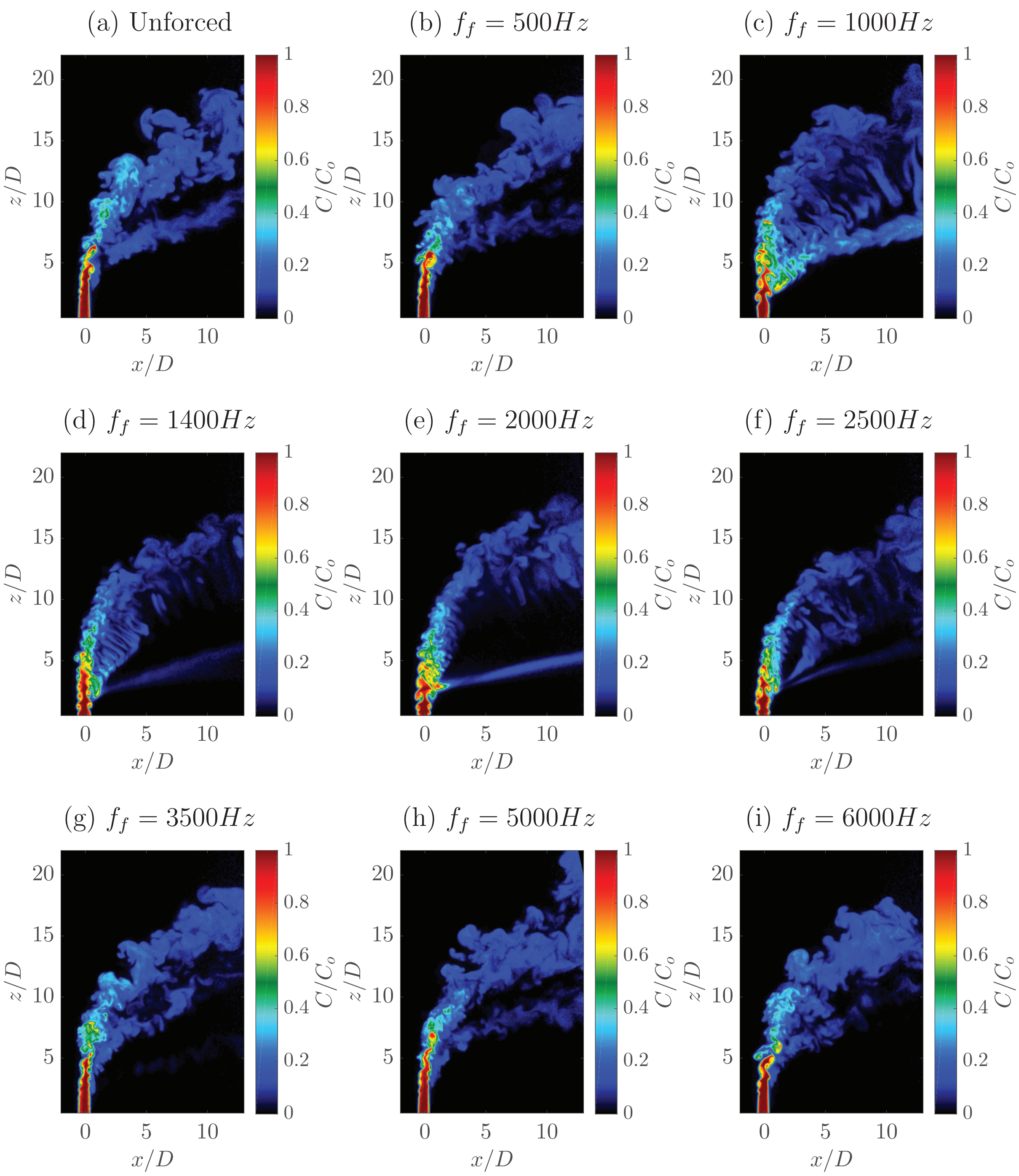

Figure 5.7: Instantaneous centerplane acetone concentration images in the regular plane ($x/D - z/D$) for the equidensity flush nozzle-injected JICF at $J = 41$ for (a) the unforced case (where $f_o = 1600 - 1900$ Hz) as well as (b)-(i) the forced cases under sine wave forcing at $f_f = 500 - 6000$ Hz and $U'_{j,rms} = 0.07$ m/s (approximately 1 % of U_j). Acetone concentration C is normalized by the mean concentration value inside the potential core C_o in each instantaneous image.

$f_f = 500 - 6000$ Hz. Again, the upstream shear layer is convectively unstable at $J = 41$. $U'_{j,rms}$ is matched among all forcing conditions at $U'_{j,rms} = 0.07$ m/s ($0.073 \lesssim U'_{j,rms} \lesssim 0.080$ m/s in actual measurements), approximately 1 % of the mean jet velocity U_j estimated at the jet exit ($U_j \approx 6.5$m/s). This is the weakest forcing amplitude considered in this study. Figure 5.7(a) shows the unforced case, where the jet structure mainly consists of the primary highly-concentrated potential core and mixed jet stream and a secondary, less-concentrated bifurcated jet structure creating a tertiary vortex, clearly shown in the cross-sectional view (Figure 5.8(a); to be discussed below). Upstream shear layer rollup is observed here to be initiated at approximately $z/D \approx 2$, roughly consistent with the instability shown in Figure 5.3(b). At $f_f = 500$ Hz in Figure 5.7(b), the centerplane structure does not seem to be affected significantly by sine wave forcing and behaves similarly to the unforced case (Figure 5.7(a)), although shear layer rollup appears to be somewhat stronger and to occur somewhat closer to injection than for the unforced case.

At $f_f = 1000$ Hz in Figure 5.7(c), however, the sine wave forcing significantly alters the centerplane structures. First, the rolled-up vortices on the upstream shear layer are initiated much closer to the jet exit than in the unforced case, indicating that sine wave forcing prompts the rapid initiation of rollup. Second, the spacing among the rollups is also different from that for the unforced case, suggesting clear lock-in of the upstream shear layer to f_f. Since the upstream shear layer is convectively unstable, the upstream shear layer is easily locked-in, in general, and the lock-in results in f_f dominating the shear layer rollup process. Moreover, the jet spreads more significantly at $f_f = 1000$ Hz than for the unforced case and the forced case at $f_f = 500$ Hz. The more vigorous jet spread and apparent bifurcation here may be created by the effect of the sine wave forcing on the secondary stream. The same structural characteristics as those at $f_f = 1000$ Hz can be also seen at $f_f = 1400 - 2500$ Hz in Figures 5.7(d)-(f), showing clear jet bifurcation as well as coherent rollup of the upstream shear layer initiated close to the jet exit. However, at a higher forcing frequency such as $f_f = 3500$ Hz in Figure 5.7(g), a lesser effect of external forcing is observed. In fact, for $f_f = 5000$ and 6000 Hz, the sine wave forcing has as little impact on structural characteristics in the centerplane as does the $f_f = 500$ Hz case, which is fairly close to the unforced jet structure. These jet structural characteristics at higher forcing frequencies f_f which are fairly far from the natural (unforced) frequency, f_o, around $1600 - 1900$ Hz, are seen possibly because the vortex generation on the upstream shear layer is not able to keep up with the high frequency of sine wave forcing. From the instantaneous centerplane PLIF images at $J = 41$ in Figure 5.7, it appears that jets react to sine wave forcing more vigorously at f_f fairly close to f_o, but less significantly at f_f further from f_o, somewhat similar to lock-in for absolutely unstable jets. Interestingly, even the convectively unstable JICF shows a preference in response for f_f near f_o in terms of structural behavior, although it is typically considered to be locked-in to any f_f. Further exploration of the instability characteristics at $J = 41$ will be required for a more complete assessment of the lock-in.

Figure 5.8 shows mean cross-sectional PLIF images for the equidensity flush nozzle-injected JICF at $J = 41$ at downstream locations of $x/D = 2.5$, 5.5 and 10.5, with and without sine wave forcing, corresponding to most of the instantaneous centerplane images in Figure 5.7. As with the instantaneous centerplane images, which suggest that the jets are affected by sine wave forcing more significantly at f_f closer to f_o, similar trends can be seen in the mean cross-sectional images. In the unforced case in Figure 5.8(a), one can see an asymmetric cross section with a tertiary vortex, especially at the downstream location $x/D = 10.5$. This asymmetry in the cross-sectional view is associated with the susceptibility of the relatively weak convectively unstable upstream shear layer to small imperfections in the wind tunnel, as documented in Getsinger et al. (2014). Such asymmetric cross sections for the unforced JICF have also been observed by other research groups (Kamotani and Greber, 1972; Kuzo, 1995; Smith and Mungal, 1998; Shan and Dimotakis, 2006; Muldoon and Acharya, 2010), generally at J values exceeding 20.

Remarkably, when f_f is relatively far from f_o, forcing has a little impact on the mean cross-sectional structures for the convectively unstable JICF, which is the same trend as the instantaneous centerplane jet structures. At $f_f = 500$, 3500 and 5000 Hz in Figures 5.8(b), (e) and (f), cross sections are still clearly asymmetric and, in the case of Figures 5.8(b) and (f), are virtually identical to the unforced case. However, when f_f becomes closer to f_o at which the jet responds and bifurcates, and where stronger coherent rollup of the

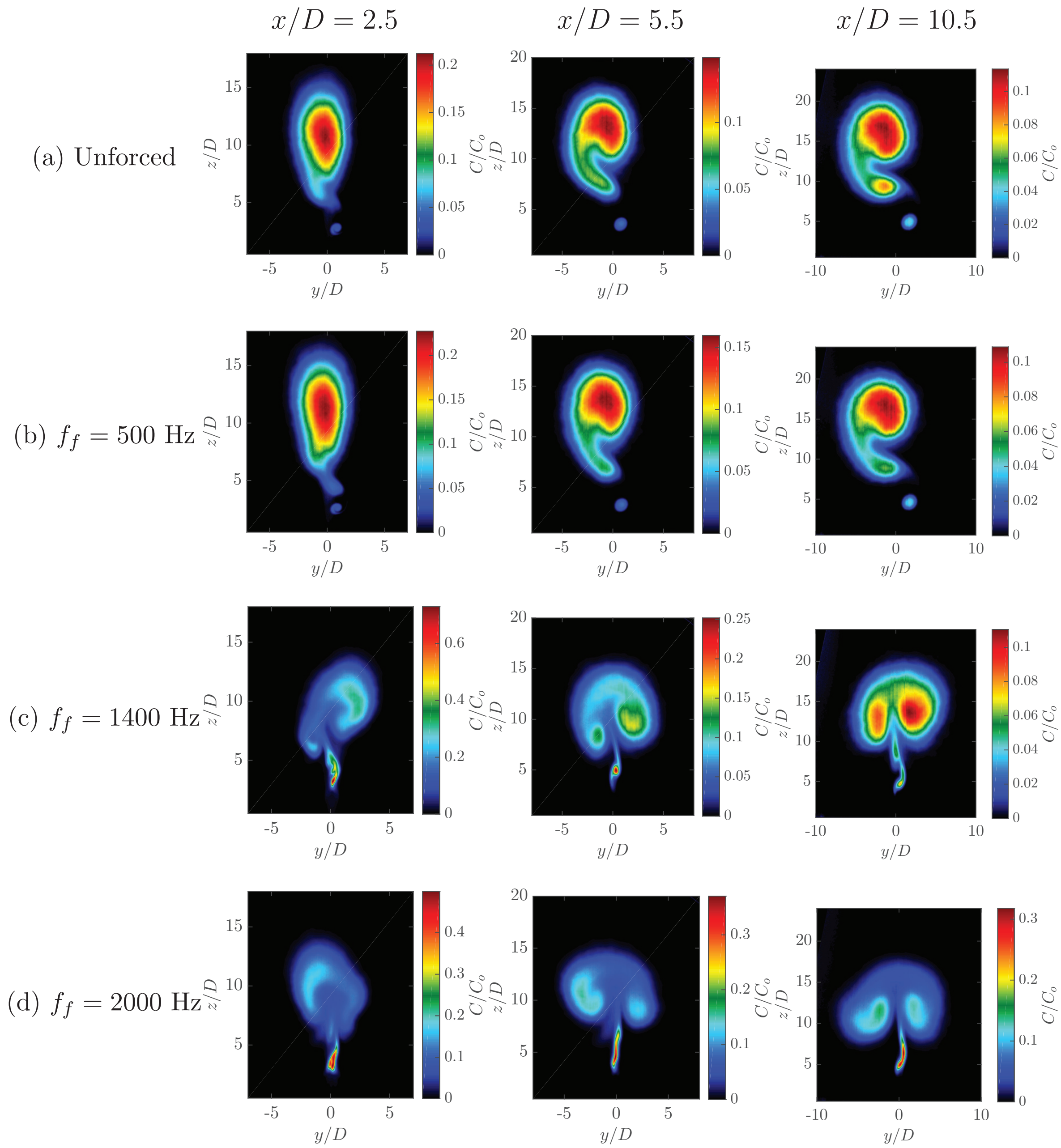

Figure 5.8: For more figures and caption see next page.

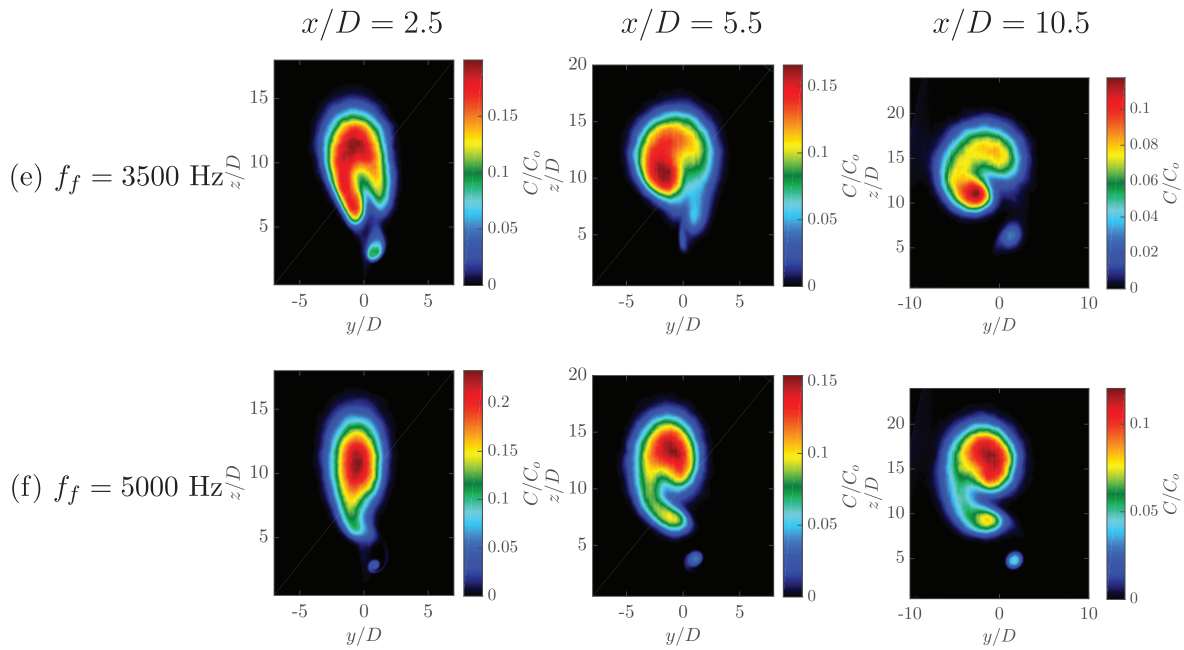

Figure 5.8: Mean cross-sectional acetone concentration images in the $y/D - z/D$ plane for the equidensity flush nozzle-injected JICF at $J = 41$, with natural frequency in the range $f_o = 1600-1900$ Hz, for (a) the unforced case as well as (b)-(f) the forced cases under sine wave forcing at $f_f = 500 - 5000$ Hz and $U'_{j,rms} = 0.07$ m/s (approximately 1 % of U_j). Acetone concentration C is normalized by the mean concentration value inside the potential core C_o calculated in centerplane images.

upstream shear layer is visible in the centerplane view, cross-sectional structures become more symmetric than for the unforced cases or the forced cases at $f_f = 500$, 3500 and 5000 Hz. At $f_f = 1400$ and 2000 Hz (Figures 5.8(c) and (d)), which are fairly close to the range of f_o, $1600-1900$ Hz, asymmetric cross sections become symmetric with different concentration profiles for each f_f. This effect is consistent with the observation in the instantaneous centerplane images, as shown in Figure 5.7(d) and (e). When f_f is a bit further from f_o, such as $f_f = 3500$ Hz in Figure 5.8(e), the degree of symmetry is slightly higher than the unforced case but is lower than the forced cases where f_f is closer to f_o. This observation clearly suggests that sine wave forcing has a greater effect on mean cross-sectional structures for f_f closer to f_o and a lesser effect as f_f is further from f_o. Interestingly, the relationship between f_f and structural behavior is observed both in the centerplane and cross-sectional views. Remarkably, these structural characteristics show that even the convectively unstable JICF requires a specific range of f_f to dramatically alter the structural characteristic for the jet's centerplane as well as cross section when the level of forcing is quite low, at about 1 % of the mean jet exit velocity, in this case.

Figure 5.9 represents instantaneous centerplane PLIF images for the equidensity flush nozzle-injected JICF at $J = 5$, with/without sine wave forcing at $f_f = 500 - 5000$ Hz and $U'_{j,rms} \cong 0.07$ m/s ($0.068 \lesssim U'_{j,rms} \lesssim 0.073$ m/s in actual measurements). Note that the upstream shear layer for this flow condition is absolutely unstable. As discussed in the previous section and shown in Figure 5.6, sine wave forcing in a narrow range of f_f induces lock-in to the forcing frequency on the upstream shear layer. It is desired to see if the lock-in may be also observed in the structural characteristics for the instantaneous centerplane images. Figure 5.9(a) displays the unforced jet centerplane structure, consisting of coherent rolled-up vortices on the upstream shear layer initiated close to the jet exit, which are typical characteristics of the absolutely unstable JICF. For the forced cases, however, this low amplitude sine wave forcing seems to have little effect on instantaneous centerplane structures, in general, although the spacing of the rolled-up vortices on the upstream shear layer is altered from the unforced case only when the upstream shear layer is locked-in to the forcing, in accordance with Figure 5.6, roughly for forcing frequencies in the range $1250 - 3500$ Hz for $U'_{j,rms} = 0.07$ m/s. At $f_f = 500$ Hz, for instance, the spacing of the rollups is essentially identical to the unforced case. However, at $f_f = 1400$ and 1700 Hz, at which the upstream shear layer is locked-in according to Figure 5.6, the spacing of each rollup becomes larger than that for the unforced case with $f_o = 2000$ Hz. As expected, the forcing at $f_f = 2000$ Hz produces visually the same spatial interval among the rollups because of the identical forcing frequency $f_f = f_o$. Remarkably, with sine wave forcing at $f_f = 2500$ Hz, which still generates a locked-in upstream shear layer, the spacing is still larger than the that for the unforced case, similar to $f_f = 1400$ Hz, despite the fact that f_f is higher than $f_o = 2000$ Hz. This unexpected structural behavior may be associated with a subharmonic of $f_f = 2500$ Hz, that is, 1250 Hz, hence triggering vortex coupling before rollup. For forcing outside of the lock-in region, $f_f = 3500$ and 5000 Hz, there is a again

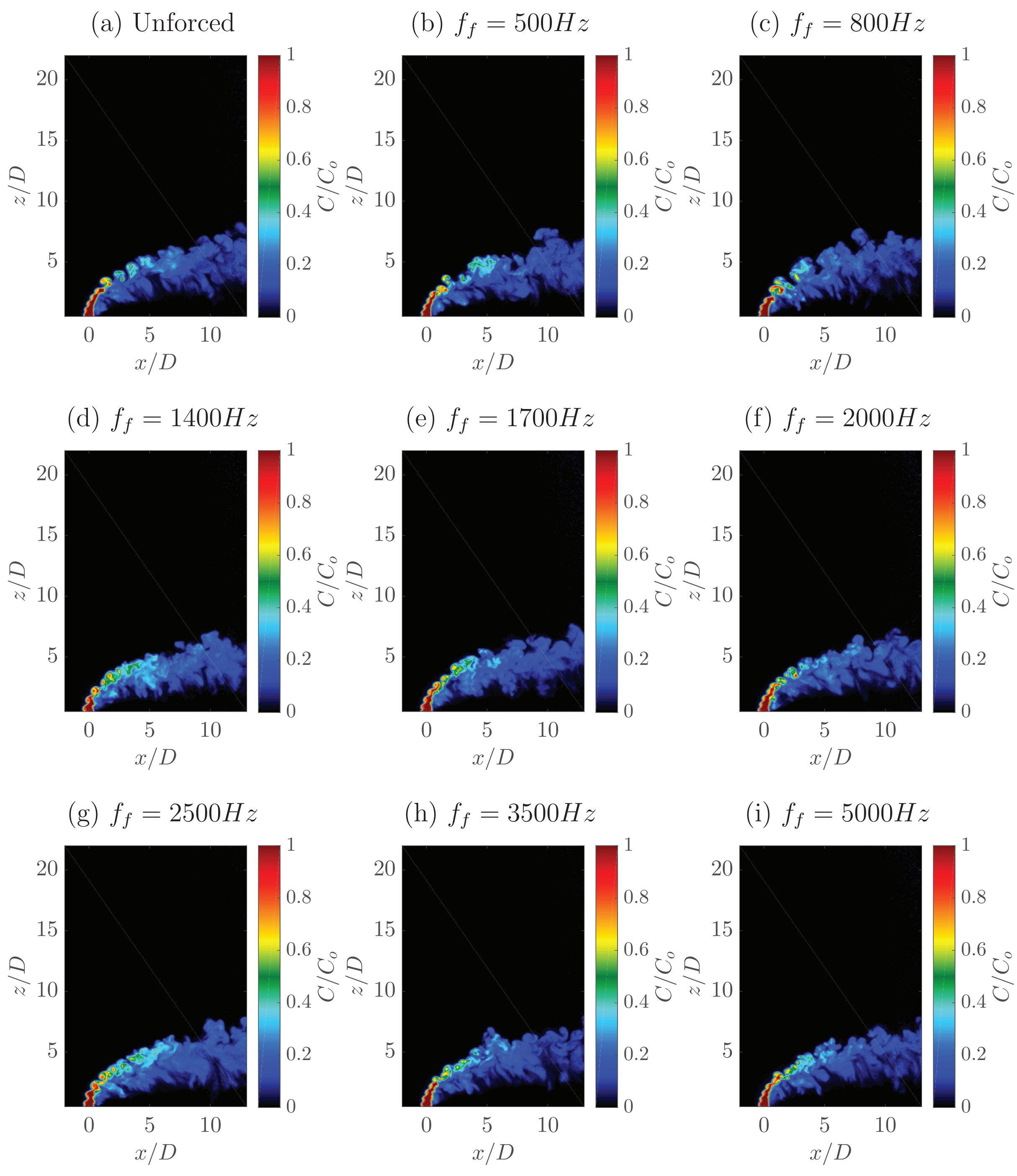

Figure 5.9: Instantaneous centerplane acetone concentration images in the regular plane ($x/D - z/D$) for the equidensity flush nozzle-injected JICF at $J = 5$ for (a) the unforced case (where $f_o = 2000$ Hz) as well as (b)-(i) the forced cases under sine wave forcing at $f_f = 500 - 5000$ Hz and $U'_{j,rms} = 0.07$ m/s (approximately 1 % of U_j). Acetone concentration C is normalized by the mean concentration value inside the potential core C_o in each instantaneous image. Note that the upstream shear layer without forcing is locked-in for $f_f \approx 1250 - 3500$ Hz.

little response by the jet, as with 500 Hz.

This visual inspection suggests that sine wave forcing can alter the structural characteristic of the upstream shear layer rollup, which are prominent jet structures in the jet's nearfield in the vicinity $-1 \lesssim x/D \lesssim 2$. Yet in the jet's mid-to-farfield region, $5 \leq x/D$, jet centerplane structures are very similar among all forcing conditions even compared with the unforced case, in general when the jet is naturally absolutely unstable. Hence for this lock-in behavior, sine wave forcing has a somewhat larger effect on the near-field jet centerplane structures, particularly the rolled-up vortices on the upstream shear layer, but only for a range of f_f fairly close to f_o. No evident alteration of the far-field jet structures is detected, suggesting minimal influence of sine wave forcing on overall jet behavior.

Figure 5.10 represents mean cross-sectional images at downstream locations of $x/D = 2.5$, 5.5 and 10.5, with/without sine wave forcing for most of the same flow conditions as Figure 5.9. As mentioned above, the rollups on the absolutely unstable upstream shear layer can be affected even by relatively weak sine wave forcing when the upstream shear layer is locked-in at f_f fairly close to f_o. In the cross-sectional view, similar structural characteristics can be recognized, although they are subtle. First, for the unforced cases shown in Figure 5.10(a), a clear, symmetric CVP structure is observed to develop and evolve, from $x/D = 2.5$ through 10.5. For the forced cases at f_f fairly far from f_o, that is, $f_f = 500$, 3500, and 5000 Hz, the mean cross-sectional structures appear to be nearly identical to those for the unforced case at all downstream locations, suggesting little influence of such forcing on structural characteristics. Yet slightly different cross-sectional structures are observed in the nearfield ($x/D = 2.5$) at $f_f = 1400$, 2000 and 2500 Hz, fairly close to f_o, generating the lock-in of the upstream shear layer. Such structural difference in the nearfield may be associated with the varied spacing among the vortical rollup on the upstream shear layer due to lock-in behavior, as seen in the instantaneous centerplane images. Experiments by Kelso et al. (1996) as well as computations by Cortelezzi and Karagozian (2001) indicate that upstream shear layer vorticity is largely distorted to lead to the evolution of CVP structures in the jet cross-sectional view. Interestingly, even relatively weak sinusoidal jet forcing close to f_o can alter the near-field structural characteristics for the absolutely unstable JICF, but at

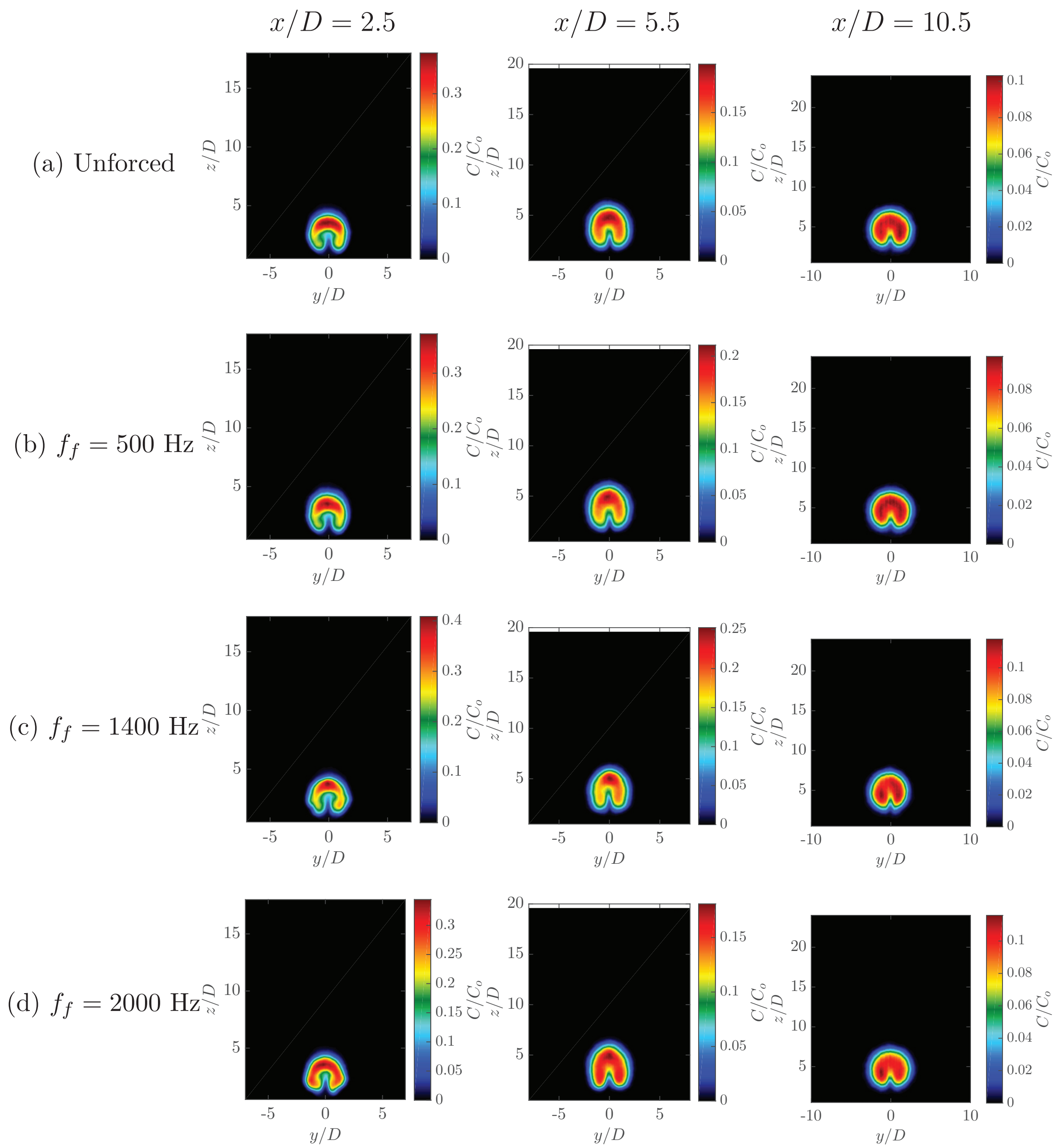

Figure 5.10: For more figures and caption see next page.

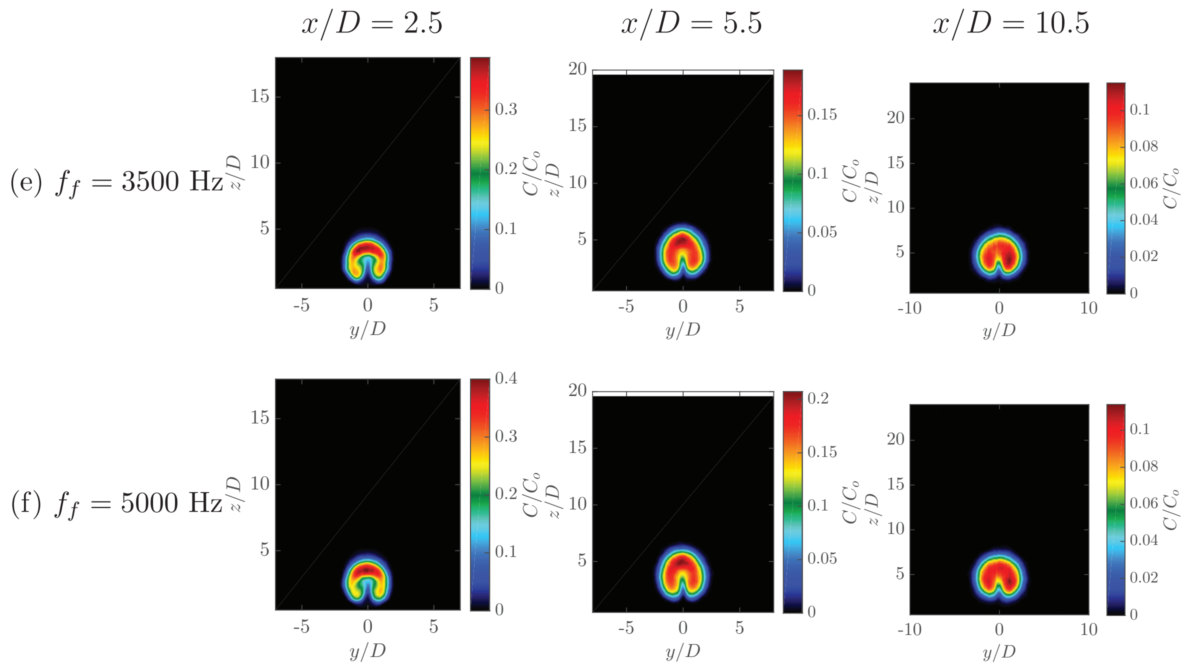

Figure 5.10: Mean cross-sectional acetone concentration images in the $y/D - z/D$ plane for the equidensity flush nozzle-injected JICF at $J = 5$, with natural frequency $f_o = 2000$ Hz, for (a) the unforced case as well as (b)-(f) the forced cases under sine wave forcing at $f_f = 500 - 5000$ Hz and $U'_{j,rms} = 0.07$ m/s (approximately 1 % of U_j). Acetone concentration C is normalized by the mean concentration value inside the potential core C_o calculated in centerplane images. Note that the upstream shear layer without forcing is locked-in for $f_f \approx 1250 - 3500$ Hz.

relatively far downstream locations of $x/D = 5.5$ and 10.5, since the sine wave forcing is relatively weak, cross-sectional as well as other jet structures are not significantly influenced by the forcing.

These observations for the absolutely unstable JICF at $J = 5$ suggests that even relatively low-level sine wave forcing can have a small effect on the nearfield upstream shear layer and hence the symmetry of the CVP structures for forcing frequencies close to f_o. Davitian et al. (2010b) utilized smoke visualization to study sinusoidal forcing's effect on structural characteristics for $J = 1.3$ to 100, but even relatively short exposure imaging was not able to clearly visualize vortex rollup on the upstream shear layer for absolutely unstable conditions. Additionally, Davitian et al. (2010b) applied sine wave forcing at $f_f = 1/10 f_o$, a frequency quite far from f_o because of requirements for comparable square wave forcing. The present experimental study shows an influence of forcing on structural characteristics for $0.7 \leq f_f/f_o \leq 1.25$, corresponding to $1400 \leq f_f \leq 2000$ Hz, as shown in Figures 5.9(d)-(g) and Figures 5.10(c) and (d). While Davitian et al. (2010b) noted that sine wave forcing for a jet with an absolutely unstable upstream shear layer has little effect on jet structures as well as jet spread and penetration, the very low forcing frequency could have influenced this finding. In contrast, Davitian et al. (2010b) found that single-pulse square wave forcing could alter jet structures as well as enhance penetration and spread for absolutely unstable jets. The fact that the present study using laser diagnostics shows that even relatively weak sine wave forcing near $f_f \cong f_o$ affects jet structures, both for the convectively and absolutely unstable JICF, is new and significant.

Figure 5.11 represents instantaneous centerplane PLIF images for the equidensity flush nozzle-injected JICF at $J = 12$ with/without sine wave forcing at $U'_{j,rms} = 0.07$ m/s ($0.077 \lesssim U'_{j,rms} \lesssim 0.080$ m/s in actual measurements). At $J = 12$, the upstream shear layer begins to transition from convective to absolute instability, but is not fully absolutely unstable, where $f_o \cong 1900 - 2230$ Hz for the upstream shear layer. These images demonstrate that similar structural trends to those for the $J = 5$ case are observed at $J = 12$. At f_f fairly far from f_o, such as $f_f = 500$, 3500, 5000 and 6000 Hz, centerplane structures consist of vortical rollup on the upstream shear layer with the same spacing as the unforced case in the nearfield, but identical far-field structures to the unforced case. At f_f fairly close to f_o, such as $f_f = 800 - 2500$ Hz, the rollup on the upstream shear layer is initiated closer to the jet exit than for the unforced case, with different spacing in comparison with the unforced case. Again, as with the $J = 5$ case, there are highly similar far-field structures to the unforced case. Hence, the structural characteristics at $J = 12$ suggests that centerplane structures with any types of instability explored in this study, convectively, absolutely or transitioning instability regimes, are all affected somewhat by relatively weak sine wave forcing at $U'_{j,rms} = 0.07$ m/s or an excitation amplitude of around 1 % of the mean jet velocity. But only clearly convecting unstable conditions (e.g., $J = 41$) for the unforced JICF seem to enable a full downstream influence of such low level forcing.

It is of interest to explore the effect of higher amplitude sine wave forcing on the abso-

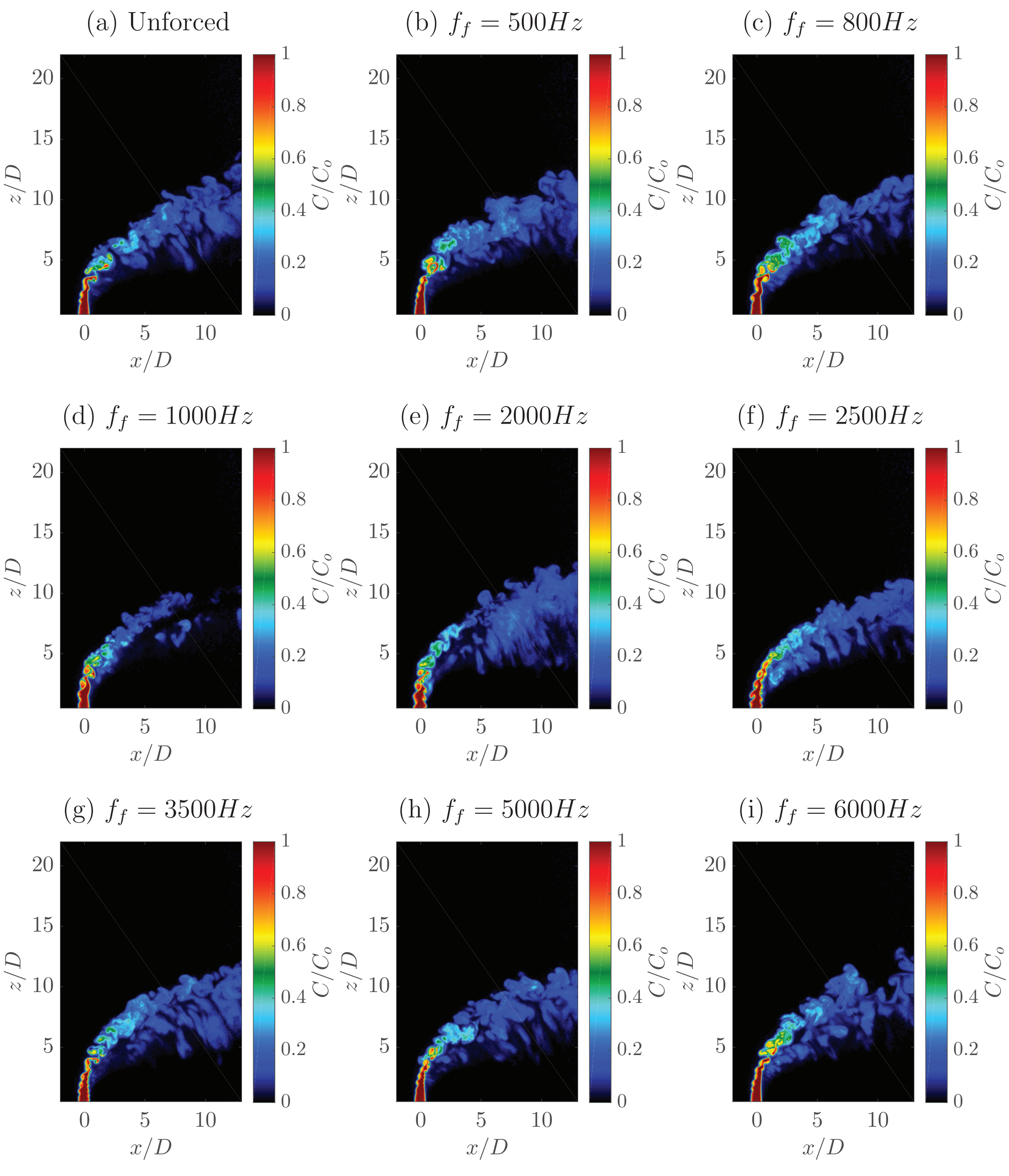

Figure 5.11: Instantaneous centerplane acetone concentration images in the regular plane ($x/D - z/D$) for the equidensity flush nozzle-injected JICF at $J = 12$ for (a) the unforced case (where $f_o = 1900 - 2230$ Hz) as well as (b)-(i) the forced cases under sine wave forcing at $f_f = 500 - 6000$ Hz and $U'_{j,rms} = 0.07$ m/s (approximately 1 % of U_j). Acetone concentration C is normalized by the mean concentration value inside the potential core C_o in each instantaneous image.

lutely unstable JICF, given the wider frequency range of responsiveness at high amplitudes per Figure 5.6. The structural investigation at $J = 5$ and $U'_{j,rms} \approx 0.07$ m/s demonstrated that lock-in might play a role on the alteration of structural characteristics for this absolutely unstable JICF in the nearfield. Now let us take a look at instantaneous centerplane images and mean cross-sectional images for the $J = 5$ JICF at a higher RMS of jet velocity perturbation $U'_{j,rms} = 0.55$ and 1.00 m/s, which are approximately 9 % and 15 % of the mean jet velocity at the jet exit ($U_j \approx 6.5$ m/s), respectively. These higher $U'_{j,rms}$ values enable a wider range of frequencies that can affect the shear layer, and may show a clearer relationship between lock-in and jet structure.

Figure 5.12 shows instantaneous centerplane images for the equidensity flush nozzle-injected JICF at $J = 5$ with/without sine wave forcing at $U'_{j,rms} = 0.55$ m/s ($0.548 \lesssim U'_{j,rms} \lesssim 0.568$ m/s in actual measurements). As mentioned previously, due to the significant roll-off at approximately 1000 Hz in the frequency response of the actuation system, as shown in Figure 5.1, the maximum achievable f_f lessens as $U'_{j,rms}$ becomes higher. At $U'_{j,rms} = 0.55$ m/s, the maximum achievable forcing frequency shown here is 1210 Hz, where again the natural frequency for the unforced JICF with $J = 5$ is $f_o = 2000$ Hz.

At $U'_{j,rms} = 0.55$ m/s, the lock-in occurs from $f_f = 590$ Hz to well over 4500 Hz, per the lock-in definition here and diagram shown in Figure 5.6. Figures 5.12(b)-(f), the forced cases at $200 \leq f_f \leq 500$ Hz without lock-in, show that the spacing of the rolled-up vortices in the nearfield upstream shear layer is fairly similar to that for the unforced case in Figure 5.12(a), close to $f_o = 2000$ Hz until around $f_f = 400$ Hz, although the general downstream jet structures are more disturbed than most of the forced cases at $U'_{j,rms} = 0.07$ m/s in Figure 5.9 due to the more moderate-level sine wave forcing. There begins to be some alteration of the nearfield rollup frequency for f_f at 400 Hz and above (Figures (d)-(f)). Once the upstream shear layer is closer to being locked-in to the forcing frequency $f_f = 590$ Hz and above, the rollup are likely to be generated primarily at f_f, resulting in different spacing between vortices on the upstream shear layer as compared with the unforced and forced cases in Figures 5.12(a)-(f). In Figure 5.12(g)-(m), coinciding with $550 \leq f_f \leq 1210$ Hz, the spacing of the nearfield rollup is different from that for the unforced case, becoming

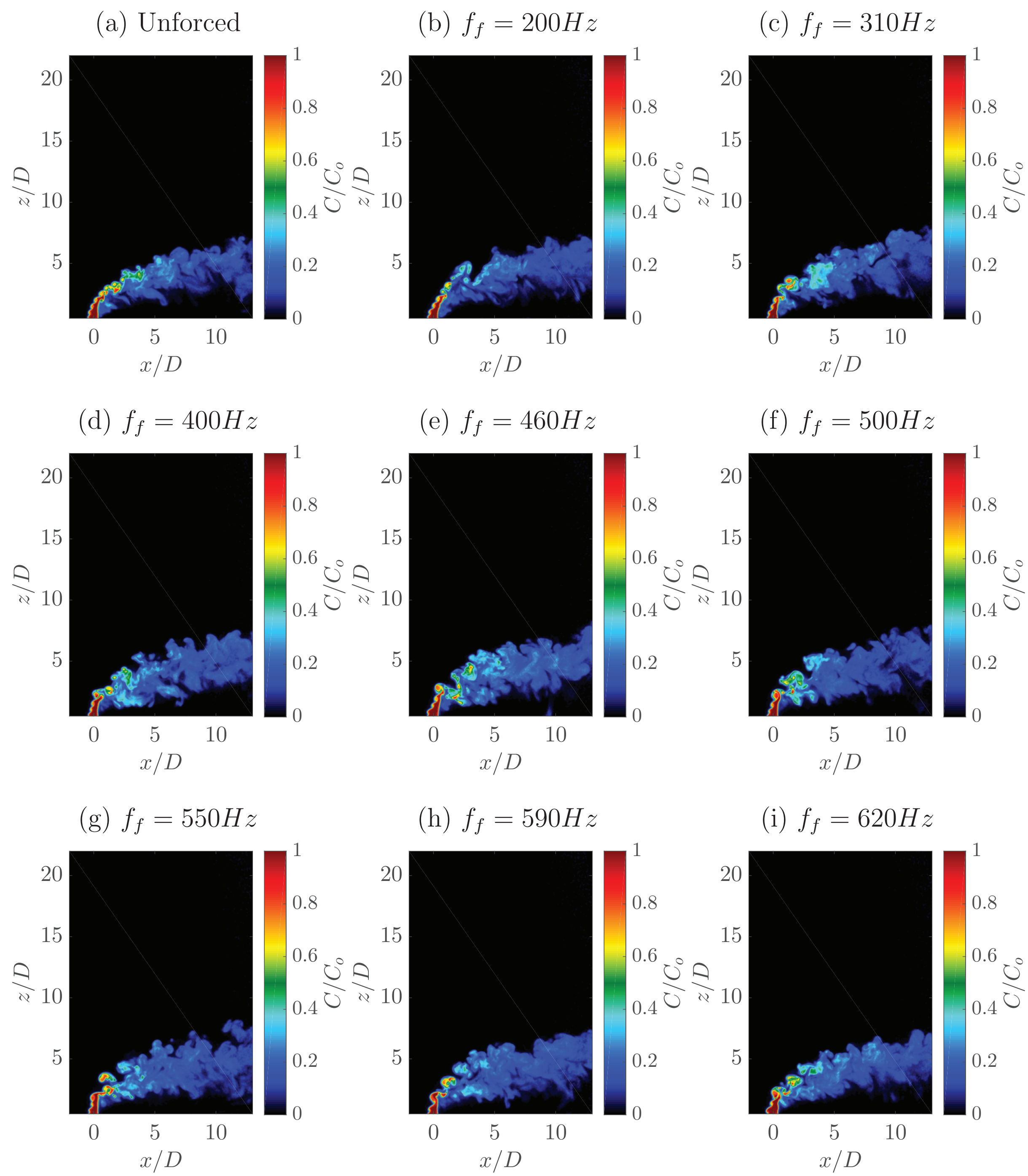

Figure 5.12: For more figures and caption see next page.

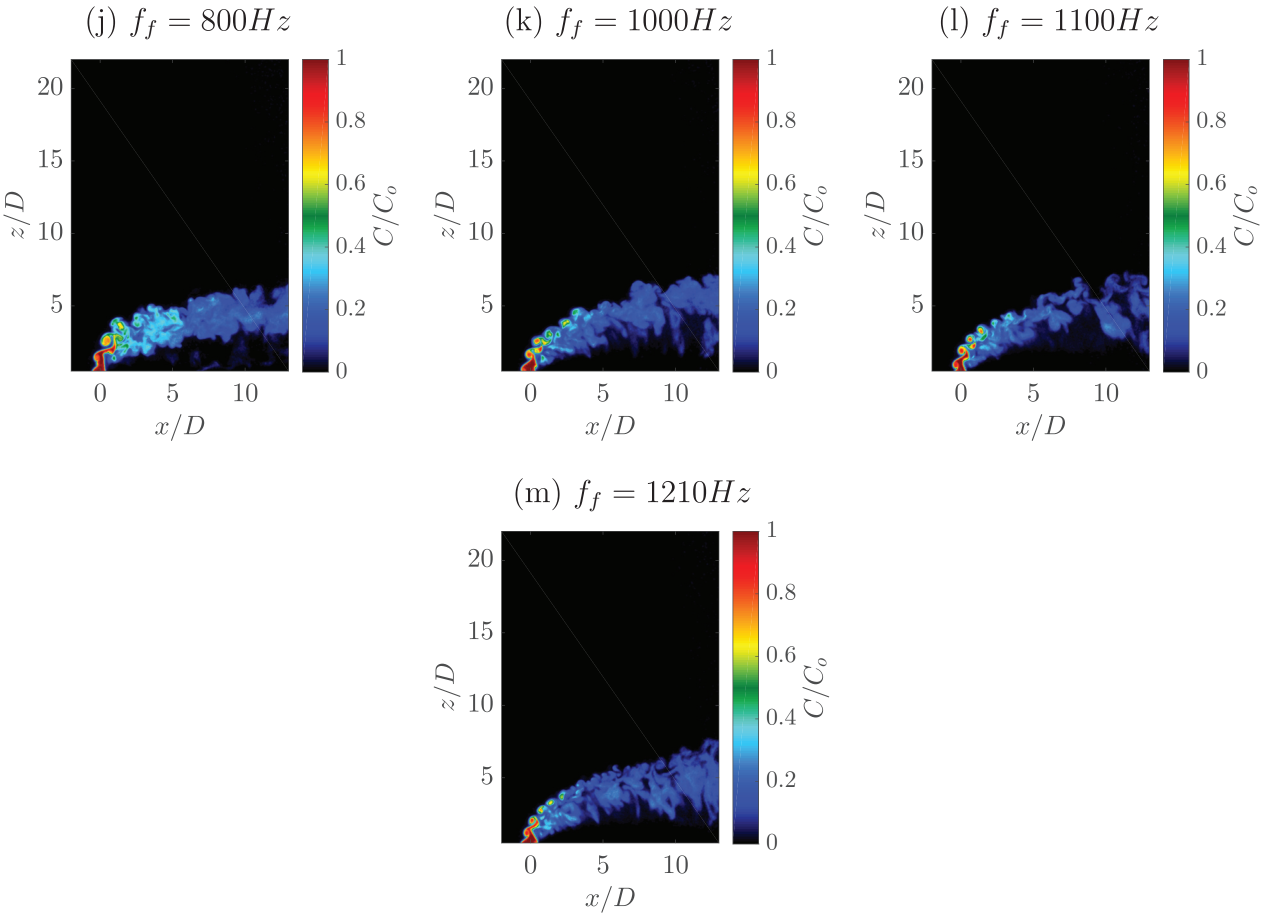

Figure 5.12: Instantaneous centerplane acetone concentration images in the regular plane ($x/D - z/D$) for the equidensity flush nozzle-injected JICF at $J = 5$ for (a) the unforced case (where $f_o = 2000$ Hz) as well as (b)-(l) the forced cases under sine wave forcing at $f_f = 200 - 1210$ Hz and $U'_{j,rms} = 0.55$ m/s (approximately 9 % of U_j). Acetone concentration C is normalized by the mean concentration value inside the potential core C_o in each instantaneous image. Note that the upstream shear layer without forcing is locked-in above around $f_f \approx 590$ Hz.

closer to separation associated with a lower frequency f_f. The separation becomes smaller as f_f becomes larger, closer to $f_o = 2000$ Hz. This trend was also seen in the forced cases at $U'_{j,rms} = 0.07$ m/s after lock-in in Figures 5.9(d)-(f), from $f_f = 1400$ to 2000 Hz. Interestingly, larger scale, continuously coherent, evenly spaced rollup on the upstream shear layer are not observed in Figure 5.12 until $f_f = 800$ Hz, and then such vortices start to be seen at $f_f = 1100$ as well as 1210 Hz. This difference may be attributed to the differences in f_f. At f_f fairly far from (well below) f_o on the upstream shear layer, the upstream shear layer is barely locked-in to the external forcing, and the natural dynamics of the shear layer at the fundamental frequency f_o, especially for the absolutely unstable JICF, may still be naturally selected by the flow to create clear, coherent vortex structures at or near f_o. On the other hand, at f_f fairly close to f_o on the upstream shear layer, much higher amplitude forcing then is necessary for lock-in, and at a frequency closer to the naturally selected condition, forcing overtakes the flow dynamics to produce coherent vortex structures on the upstream shear layer with a frequency closer to f_f. In the $U'_{j,rms} = 0.07$ m/s cases, this behavior is hardly seen, likely because the sine wave forcing was relatively weak and insufficient to overcome the natural dynamics of the flow.

Overall, while the near-field jet structures, specifically vortex rollup on the upstream shear layer, are clearly affected by sine wave forcing, the relatively far-field structures at $5 \leq x/D$ show little difference under the forcing. At lower frequency forcing, say $200 \leq f_f \leq 550$ Hz, one could argue that the jets are more disturbed between 2 and 5 diameters downstream, yet the far-field jet structures here and for other forcing conditions behave similarly to the unforced case. This result suggests that the even moderate-level sine wave forcing may have little impact on the far-field jet structures.

For sinusoidal forcing at $U'_{j,rms} = 0.55$ m/s, there seems to be mainly three regimes associated with jet's near-field structures, depending on f_f and its relationship to the frequency associated with the start of lock-in $f_{f,cr}$, which for $U'_{j,rms} = 0.55$ m/s is around $f_{f,cr} = 590$ Hz. These are: (1) when the upstream shear layer is not locked-in ($f_f < f_{f,cr}$), and f_o appears to dominate, but less so as f_f increases; (2) the upstream shear layer is locked-in and consists of disturbed, less coherent rollup ($f_f > f_{f,cr}$ but fairly far from f_o) where f_f begins to dominate the shear layer; and (3) the upstream shear layer is locked-in and consists of coherent, multiple evenly-spaced rollup at frequency f_f (where $f_f > f_{f,cr}$ and is fairly close to f_o). In contrast with the near-field structures, the far-field structures can only be slightly visibly altered by relatively moderate-level sine wave forcing.

Figure 5.13 represents mean cross-sectional images at the same flow conditions as in Figure 5.12 and at three different downstream locations. These mean cross-sectional images clearly reveal a remarkably similar trend in the relatively nearfield images at $x/D = 2.5$ as

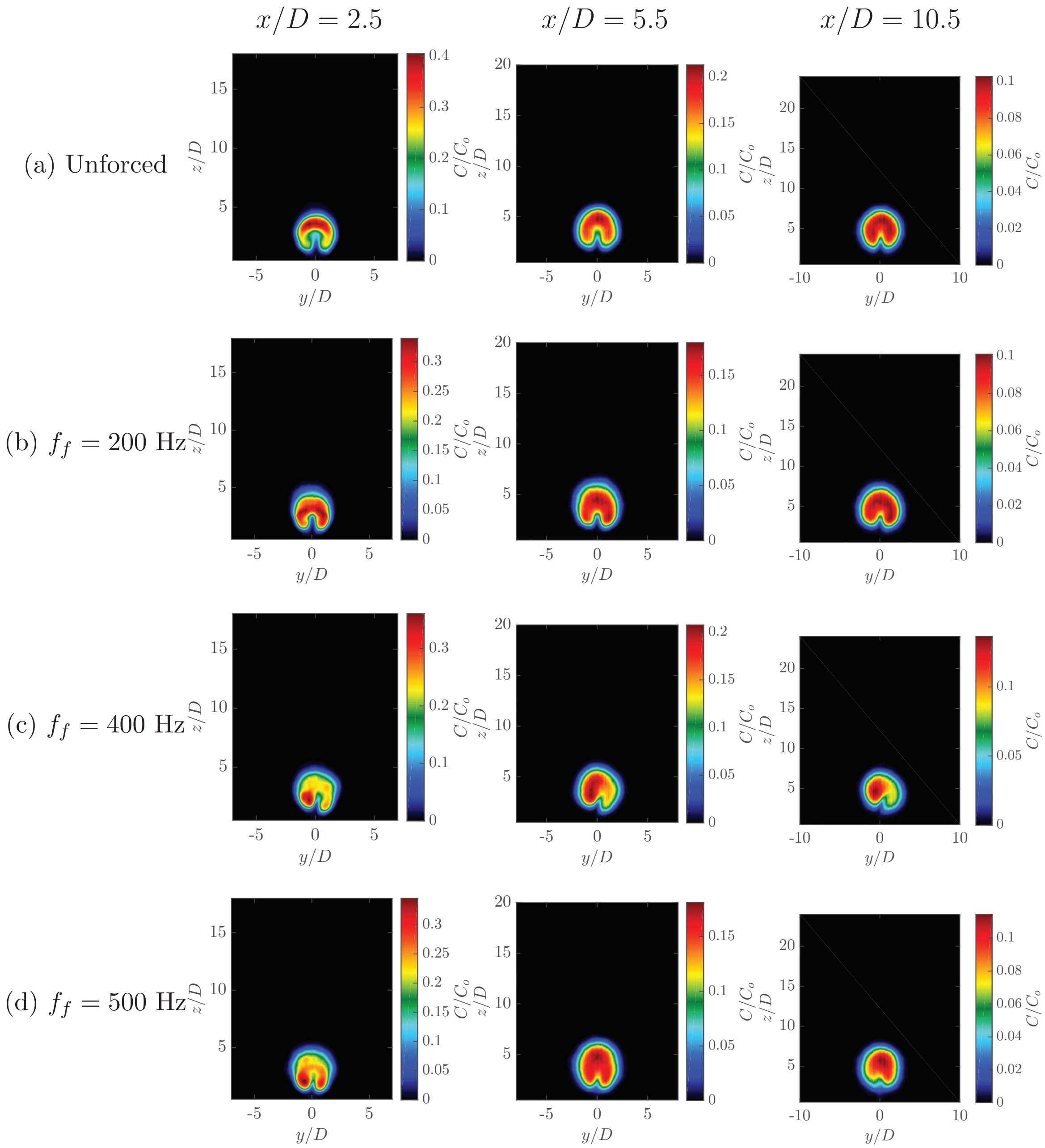

Figure 5.13: For more figures and caption see next page.

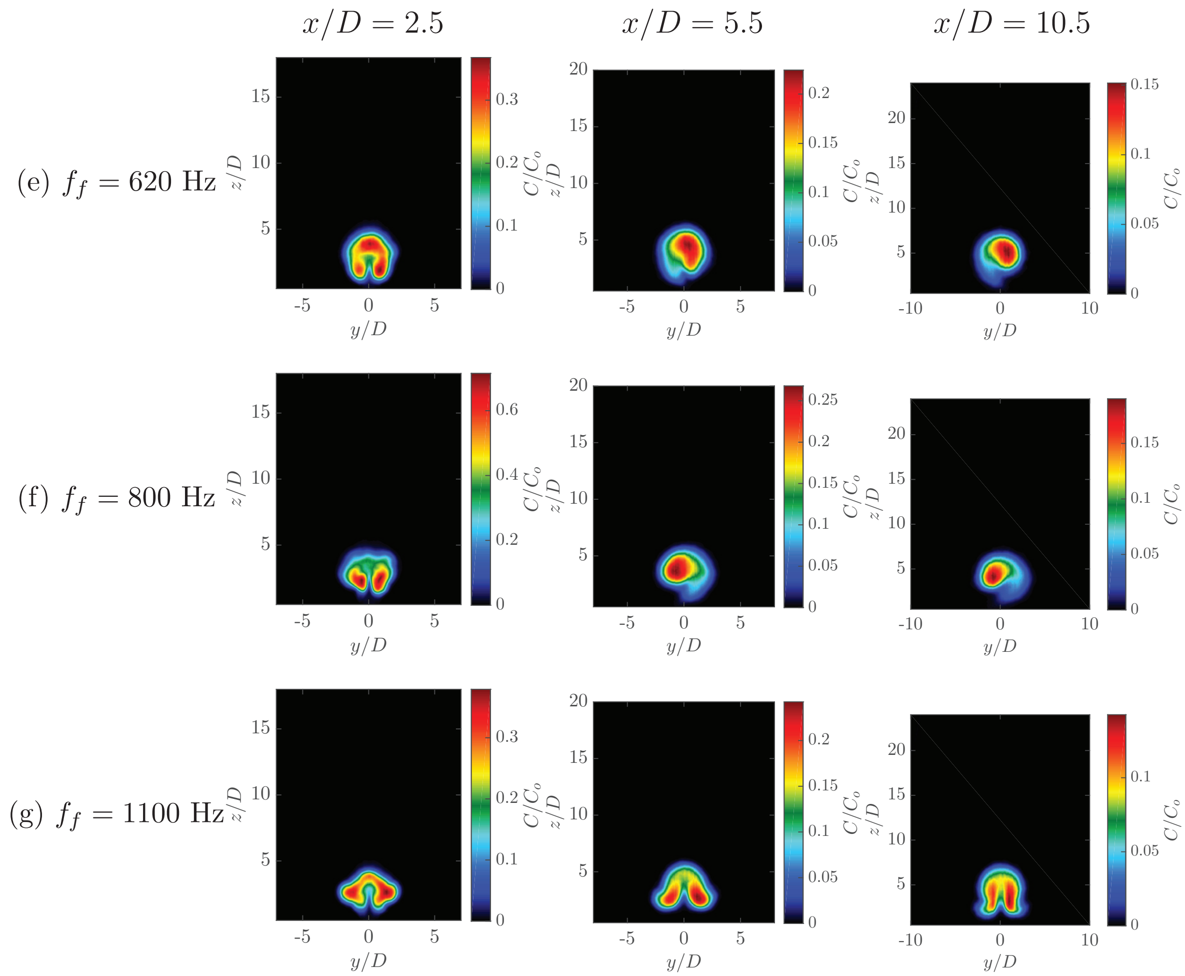

Figure 5.13: Mean cross-sectional acetone concentration images in the $y/D - z/D$ plane for the equidensity flush nozzle-injected JICF at $J = 5$, with natural frequency $f_o = 2000$ Hz, for (a) the unforced case as well as (b)-(g) the forced cases under sine wave forcing at $f_f = 200 - 1100$ Hz and $U'_{j,rms} = 0.55$ m/s (approximately 9 % of U_j). Acetone concentration C is normalized by the mean concentration value inside the potential core C_o in centerplane images. Note that the upstream shear layer without forcing is locked-in above around $f_f \approx 590$ Hz.

seen in the instantaneous centerplane images. When the jet is not forced, or forced but not clearly locked-in (Figures 5.13(a)-(b)), the near-field mean cross-sectional structures appear to be relatively symmetric and uniform in terms of concentration profiles. When the forcing frequency increases to 400 Hz (Figure 5.13(c)) or 500 Hz (Figure 5.13(d)), small structural difference is observed in the cross-section, where in fact asymmetries can be detected in both near and farfield. Once the jet is locked-in at f_f yet fairly far from f_o, $f_f = 620 - 800$ Hz

(Figures 5.13(d)-(f)), the mean cross-sectional structures become even more distorted and, further downstream, asymmetric and non-uniform with respect to concentration profiles in comparison to the unforced case. These alterations associated with the CVP structures and concentration profiles may be caused by the less coherent rollup on the upstream shear layer as seen in the centerplane view in Figures 5.12(d)-(j). Again, Cortelezzi and Karagozian (2001) indicate that the generation of CVP structures is related to vorticity on the upstream shear layer, and this is consistent with these observations. Hence, forcing at f_f fairly far from f_o, yet still generating lock-in, may disturb the naturally optimized, regularized creation of rollup on the upstream shear layer, and hence non-uniform CVP structures in the cross-sectional view can arise. At higher f_f, a bit closer to f_o on the upstream shear layer, as in $f_f = 1100$ Hz in Figure 5.13(g), the mean cross-sectional structure at $x/D = 2.5$ becomes more clearly symmetric and with uniform concentration profiles, although the shapes are not the typical CVP structure. Again, this return to symmetry could be possibly due to the coherent rollup observed in Figure 5.12(l). These cross-sectional structures are also consistent with the three different near-field structural regimes under sine wave forcing for various forcing frequencies f_f, as mentioned for the centerplane discussion for $U'_{j,rms} = 0.55$ m/s in Figure 5.12.

Interestingly, one can recognize a more significant effect of moderate sine wave forcing on mid- and far-field cross-sectional structures than in the centerplane images. From the centerplane structures, there is little structural alteration that is obvious under sine wave forcing seen in Figure 5.12, at least in the farfield. The far-field mean cross-sectional structures at $x/D = 10.5$, however, are significantly varied, depending on f_f, and there are differences at $x/D = 5.5$ as well. When the upstream shear layer is not locked-in at $f_f = 200$ Hz, the mean cross-sectional structures are fairly symmetric (Figure 5.13(b)). But as f_f becomes larger, even well before lock-in, minor distortions in the nearfield appear to lead to asymmetric cross-sectional structures (Figures 5.13(c) and (d)). These continue after lock-in (Figures 5.13(e) and (f)), despite no significant farfield changes in the centerplane view in Figures 5.12(g)-(j). Such asymmetric cross-sectional structures may be related to the nature of the incoherent, disturbed vorticity rollup on the upstream shear layer in the nearfield in this regime, where clear vortical structures are not observed downstream of $1-2$ diameters. As f_f increases toward f_o, the jet cross section finally becomes more symmetric, as shown in Figure 5.13(g), but without the clear CVP shape. The relevance of periodic vortex rollup in the nearfield, shown in Figure 5.12(l), suggests a deeper relationship between the nearfield rollup generation and the far-field CVP structures than discussed by Cortelezzi and Karagozian (2001), one where the actual CVP shape and structure are affected by lock-in related forcing.

From an examination of jet's centerplane and cross-sectional structures at $U'_{j,rms} = 0.55$ m/s, there are likely to be three different regimes with respect to the jet's structures, depending on f_f relative to f_o on the upstream shear layer. Further structural exploration can explore this possible structural trend, using data at a higher value of $U'_{j,rms} = 1.00$ m/s. Figures 5.14 and 5.15 show the instantaneous centerplane and the mean cross-sectional PLIF images, respectively, for the equidensity flush nozzle-injected JICF at $J = 5$ with/without sine wave forcing at $U'_{j,rms} = 1.00$ m/s ($1.04 \lesssim U'_{j,rms} \lesssim 1.08$ m/s in actual measurements),or approximately 15 % of the mean jet velocity. At this $U'_{j,rms}$, the maximum achievable forcing frequency is 1100 Hz.

At this relatively high $U'_{j,rms}$, the upstream shear layer is locked-in at a fairly low forcing frequency, $f_{f,cr} \approx 390$ Hz as estimated by the lock-in diagram shown in Figure 5.6. When the jet is unforced, or forced at $200 \leq f_f \leq 350$ where the upstream shear layer is not locked-in, the spacing amongst the rollup on the upstream shear layer is relatively the same in Figures 5.14(a)-(d), although the jet core and structures within $1-2$ diameters are significantly perturbed by the relatively strong forcing. Under such forcing conditions, the mean cross-sectional structures become fairly symmetric at most downstream locations shown in Figures 5.15(b)-(c), although distorted CVPs are observed at $x/D = 10.5$. A highly disturbed cross-sectional structure for $f_f = 350Hz$ at $x/D = 2.5$, and to a lesser extent for $f_f = 200$ Hz, likely corresponds to the strong nearfield distortion around 2 diameters downstream seen in Figures 5.14(b) and (d). Once the upstream shear layer is locked-in at $400 \leq f_f \leq 700$ Hz where f_f is fairly far from f_o, the rollup seems to have frequencies closer to f_f but are less coherent and persistent than the unforced case (see Figures 5.14(e)-(i)). In the cross-

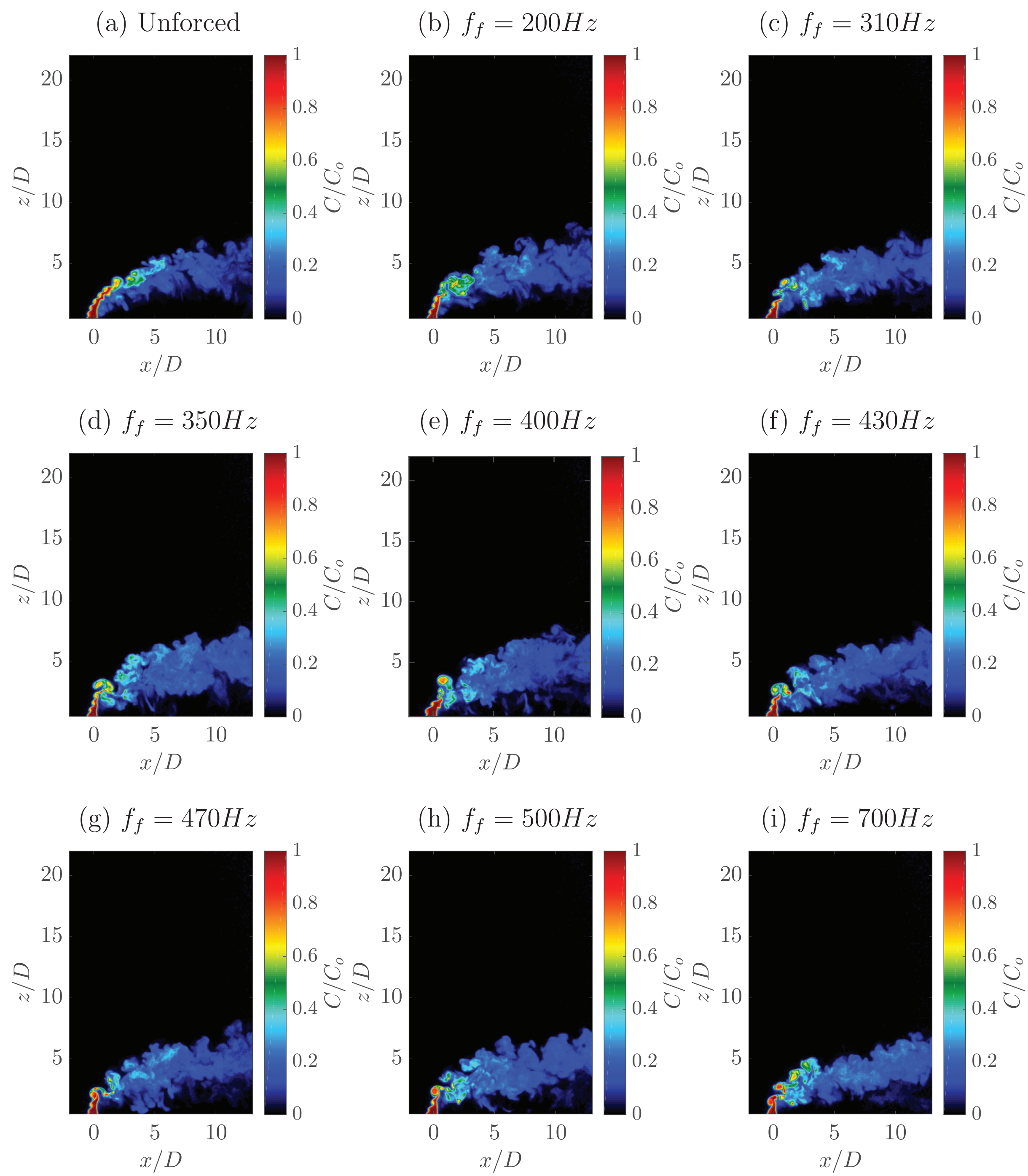

Figure 5.14: For more figures and caption see next page.

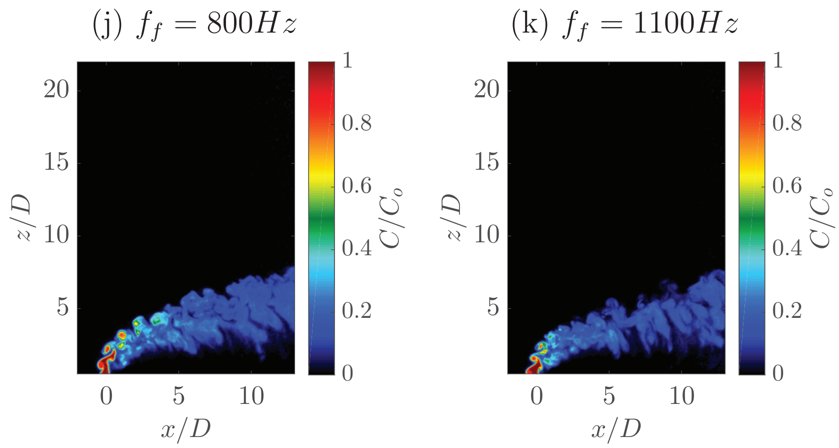

Figure 5.14: Instantaneous centerplane acetone concentration images in the regular plane ($x/D - z/D$) for the equidensity flush nozzle-injected JICF at $J = 5$ for (a) the unforced case (where $f_o = 2000$ Hz) as well as (b)-(k) the forced cases under sine wave forcing at $f_f = 200 - 1100$ Hz and $U'_{j,rms} = 1.00$ m/s (approximately 15 % of U_j). Acetone concentration C is normalized by the mean concentration value inside the potential core C_o in each instantaneous image. Note that the upstream shear layer without forcing is locked-in above around $f_f \approx 300$ Hz.

sectional view for this kind of forcing condition shown in Figure 5.15(d), highly distorted asymmetric structures, as well as non-uniform concentration profiles, are observed in the nearfield at $x/D = 2.5$. While subsequent periodic rollup before $x/D = 5$ in Figure 5.14(g) seems to produce greater symmetry in the CVP in Figure 5.15(d) at $x/D = 5.5$, in the farfield at $x/D = 10.5$, cross-sectional structures are still observed to be fairly asymmetric. At f_f in the range $800 \le f_f \le 1100$ Hz with clear lock-in per Figure 5.6, more coherent and periodic rollup on the upstream shear layer in the centerplane view (Figures 5.14(j)-(k)) as well as more symmetric mean cross-sectional structures both in the nearfield and farfield are observed, although, as for moderate forcing, standard CVP structures are not formed. Interestingly, as mentioned previously, the three different structural regimes for varied f_f are still observed, and again these differences may be associated with lock-in and the magnitude of f_f relative to f_o. Furthermore, at $U'_{j,rms} = 1.00$ m/s, the coherent rollups on the upstream shear layer start to be seen at $f_f = 800$ Hz, lower than $f_f = 1100$ Hz in the $U'_{j,rms} = 0.55$ m/s cases, suggesting that coherent vortex rollup on the upstream shear layer and fairly symmetric cross-sectional structures is more easily generated with stronger

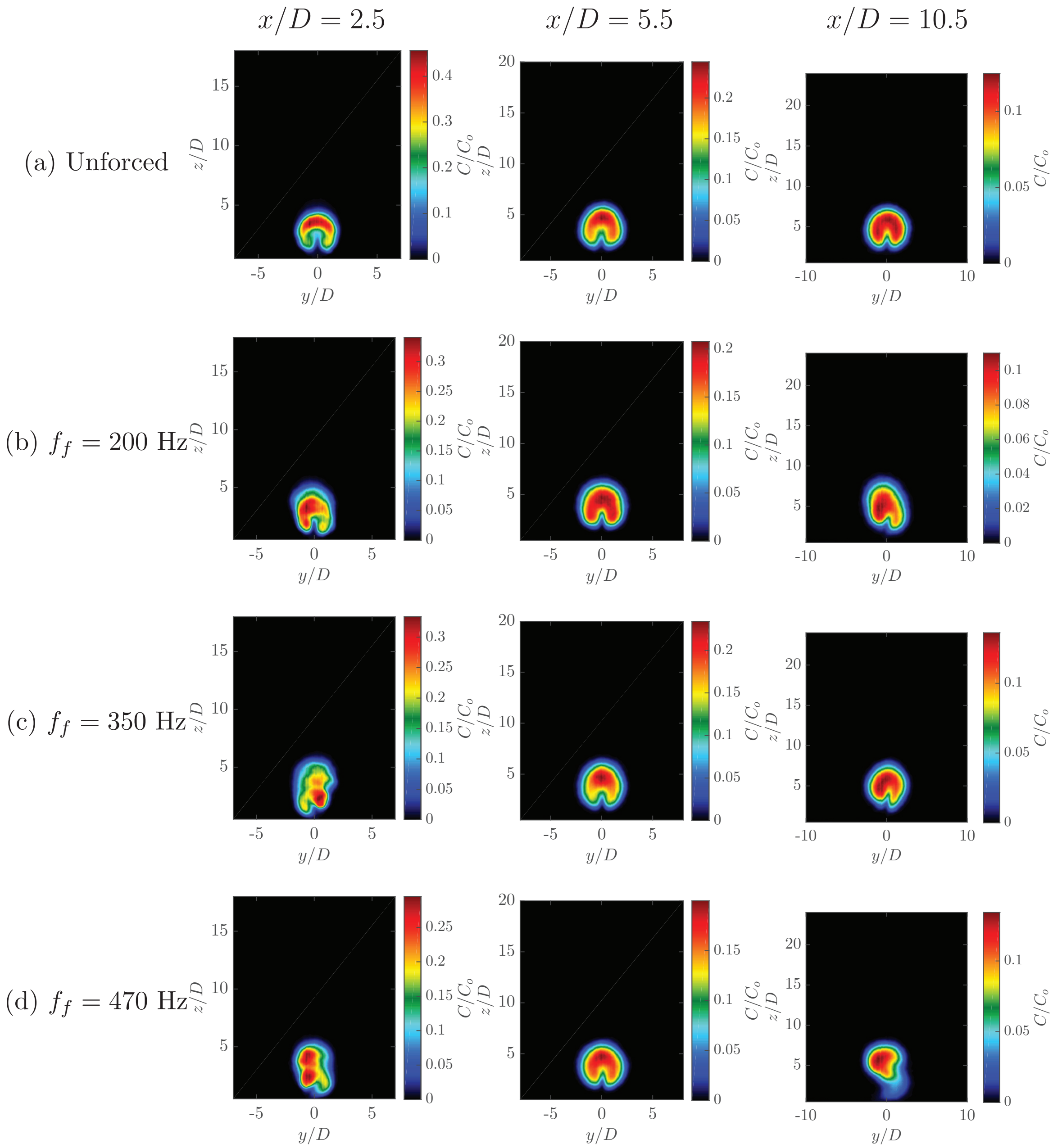

Figure 5.15: For more figures and caption see next page.

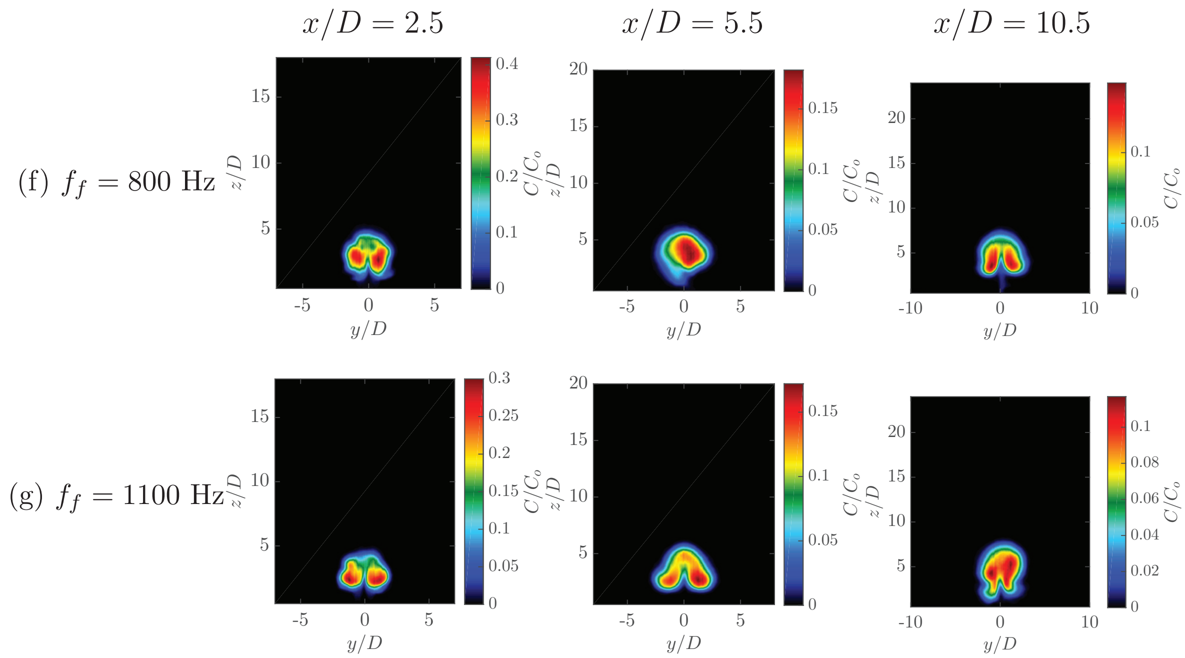

Figure 5.15: Mean cross-sectional acetone concentration images in the $y/D - z/D$ for the equidensity flush nozzle-injected JICF at $J = 5$, with natural frequency $f_o = 2000$ Hz, for (a) the unforced case as well as (b)-(g) the forced cases under sine wave forcing at $f_f = 200 - 1100$ Hz and $U'_{j,rms} = 1.00$ m/s (approximately 15 % of U_j). Acetone concentration C is normalized by the mean concentration value inside the potential core C_o in centerplane images. Note that the upstream shear layer without forcing is locked-in above around $f_f \approx 300$ Hz.

sine wave forcing.

This structural study of the impact of sinusoidal forcing on the JICF reveals new insights, some of which expand on earlier observations in M'Closkey et al. (2002), Shapiro et al. (2006), and Davitian et al. (2010b). As observed earlier, the convectively unstable JICF (e.g., $J = 41$) is affected by sine wave forcing for a wide range of forcing frequencies, but if f_f is significantly far from the natural frequency f_o of the upstream shear layer, there can be a much lesser degree of influence. This would be expected for an absolutely unstable shear layer under lock-in conditions, but the convectively unstable jet always is "locked-in" with external forcing. For the absolutely unstable JICF, sine wave moderate forcing had been thought to have little effect on the jet structures via observations using smoke visualization (M'Closkey et al., 2002; Davitian et al., 2010b) and via excitation at frequencies far from f_o.

But the present studies show that, especially at high amplitudes and at lock-in frequencies, sine wave forcing can have a fairly significant impact both on the centerplane and cross-sectional structures. The jet response to the sine wave forcing in terms of centerplane and cross-sectional structures seems to be mainly classified according to three regimes for the range of amplitudes $U'_{j,rms}$ investigated in this study. First, when the jet is not locked-in per the definition and conditions shown in Figure 5.6, both instantaneous centerplane as well as mean cross-sectional structures, in the nearfield and farfield, behave very similarly to the unforced case. Second, when the jet is locked-in at f_f or nearly so, but with f_f fairly far from f_o, the vortex rollup on the upstream shear layer becomes less coherent and periodic with vortex spacing corresponding to f_f, but with limited near-field interactions of the rollups to create a clear CVP, and hence resulting in less-symmetric cross-sectional structures. Third, when the jet is locked-in at f_f, with f_f fairly close to f_o, coherent and more extensive periodic vortex rollup, as well as fairly symmetric cross sections, are observed, although the traditional CVP structure may not necessarily form. Hence the notion of "lock-in" for the shear layer dynamics in response to sinusoidal forcing can have a significant influence on JICF structure.

5.4 Mixing Quantification

In the previous section, the structural characteristics under sine wave forcing were investigated among various forcing frequencies f_f and amplitude $U'_{j,rms}$. In this section, the effect of sine wave forcing on JICF mixing characteristics is explored. The main purpose of external forcing is, of course, to enhance or even control the degree of mixing in the JICF. Hence, appropriate mixing evaluation methods are quite important. Gevorkyan et al. (2016) utilized several alternative mixing metrics relevant to open-boundary flow systems in-depth and evaluated mixing characteristics of the JICF for a range of flow conditions as well as injector configurations. Hence, mixing metrics applied in this study are mostly based on the study by Gevorkyan et al. (2016), although further discussion on mixing quantification will be also documented. To quantify the degree of mixing for the JICF, there are two types of mixing metrics described in this study: mean and instantaneous mixing metrics, based on mean and instantaneous PLIF images, respectively.

As mean mixing metrics, this study utilizes jet spread and penetration in the centerplane view. These classic mean mixing metrics have been widely used to evaluate JICF mixing (Kamotani and Greber, 1972; Fearn and Weston, 1974; Su and Mungal, 2004; Davitian et al., 2010b). Although instantaneous mixing metrics are more appropriate to quantify detailed molecular mixing, in order to account for molecular transport spatial and time scales, mean metrics are still useful for the global quantification of mixing in a relatively simplified manner, as well as for comparison to instantaneous mixing metrics. Beyond this, the degree of jet spread and penetration are often practically important in engineering applications such as dilution jet injection (Kamotani and Greber, 1972; Holdeman, 1993).

For jet spread, this study uses three different types of evaluation: vertical spread, δ_z, evaluated at different locations along the horizontal coordinate x/D; spread normal to the unforced jet centerline trajectory, $\delta_{n,unforced}$; and spread normal to each jet centerline trajectory in question δ_n. Jet penetration z_p, on the other hand, is calculated as the z-location of the top of the jet, as a function of x/D. Note that all mean mixing metrics are scaled by the jet diameter at the exit, D, when analyzed. Physically, it is more appropriate to evaluate the jet spread normal to each jet centerline trajectory in question, forced or unforced, not scaled with respect to the unforced jet centerline trajectory. The jet centerline trajectory in this study is defined as corresponding to the maximum concentration loci in mean images, representing to the most probable jet fluid trajectory. However, external forcing at some forcing conditions yields jet bifurcations, e.g., as seen in Figures 5.7(c)-(e). Such bifurcations make jet trajectory determinations very difficult. Therefore, jet spread is evaluated along two alternative jet trajectory coordinates and then are compared to investigate the effect of different coordinates on mixing characteristics.

Quantifying any of these mean mixing metrics requires a threshold for the pixel intensity to define "jet fluid" or jet boundary in mean images. Su and Mungal (2004) and Getsinger (2012) both applied a threshold of 20 % of maximum concentration for jet spread and 5 % for penetration, respectively, for these mean images. The maximum typically corresponds to the concentration value inside the potential core region of the JICF. Gevorkyan (2015) explored how the jet spread and penetration are affected by the choice of threshold values, suggesting that mixing trends of even the unforced JICF are dependent on choice of the threshold value. Hence, a threshold value based on $\overline{C/C_o}$ in mean PLIF images has to be carefully determined in this study to appropriately capture representative jet structures of interest in the centerplane view, especially under sine wave forcing, and to include them in the mixing quantification.

Figure 5.16 shows sample mean centerplane images with color maps showing thresholds of $\overline{C/C_o} \geq 0.01$, $\overline{C/C_o} \geq 0.05$, $\overline{C/C_o} \geq 0.10$ and $\overline{C/C_o} \geq 0.20$, which can be used to define jet's boundary. Images are shown for the unforced case (Figure 5.16(a)) as well as forced cases at $f_f = 1400$ Hz (Figure 5.16(b)) and 2000 Hz (Figure 5.16(c)), the latter two of which show clear bifurcation. For the unforced case, the jet boundary gradually becomes narrower as the threshold value of $\overline{C/C_o}$ increases, as expected. More importantly, the jet's natural bifurcation is captured with a threshold of $\overline{C/C_o} \geq 0.01$ and $\overline{C/C_o} \geq 0.05$ but not with $\overline{C/C_o} \geq 0.10$ and $\overline{C/C_o} \geq 0.20$, showing that the actual jet structure as well as mean mixing evaluation are highly dependent on the threshold value. Furthermore, for the forced case at $f_f = 1400$ and 2000 Hz as shown in Figure 5.16(b) and (c), respectively, even the threshold of $\overline{C/C_o} \geq 0.05$ is not able to fully capture the jet bifurcation. In this study with sine wave forcing, the jet bifurcation is important and these remarkable flow structures have to be considered in mixing. Hence, this study evaluated mean mixing metrics with a threshold based on mean concentration $\overline{C/C_o} \geq 0.01$ or 1 % concentration of the maximum concentration in mean images to properly capture the jet bifurcation in the centerplane. This applied to both jet penetration and spread measures.

As for instantaneous mixing metrics, centerplane- and cross-section-based mean Unmixedness, as well as the cross-section-based mean Probability Density Function (PDF) of concentration values C/C_o were applied. Quantitative scaling of cross-sectional concentrations relies on calibration with centerplane data, as described in Section 2.3.1. The method to evaluate the Unmixedness is the same as in Gevorkyan et al. (2016), and is discussed in some detail in the context of scale lengths in Chapter 4. Unmixedness is defined as the

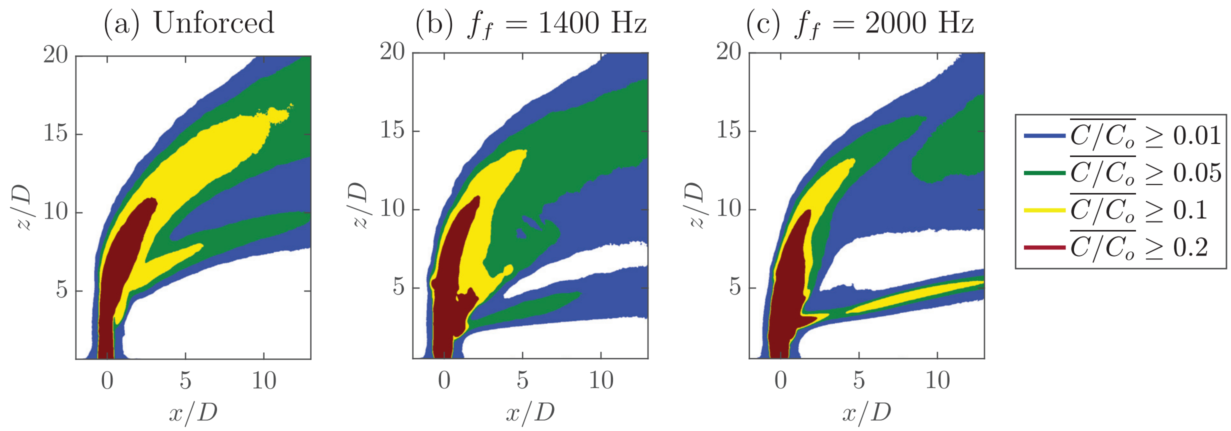

Figure 5.16: Mean centerplane PLIF images for the equidensity JICF with $J = 41$ with a threshold of $\overline{C/C_o} \geq 0.01$ (1 % concentration), $\overline{C/C_o} \geq 0.05$ (5 % concentration), $\overline{C/C_o} \geq 0.10$ (10 % concentration) and $\overline{C/C_o} \geq 0.20$ (20 % concentration) to define the boundary of the jet. These figures are for (a) the unforced case, (b) the forced cases at $f_f = 1400$ Hz, and (c) 2000 Hz. Note that maximum normalized concentration is approximately $\overline{C/C_o} \approx 1.0$ inside the potential core region.

second moment of the scalar field as noted in Equation (1.6).

The centerplane-based Unmixedness can be evaluated along three different coordinates, as with mean mixing metrics: the horizontal coordinate x/D, the unforced jet trajectory coordinate $s_{c,unforced}/D$, and each jet trajectory coordinate used for given forcing conditions, s_c/D. The centerplane-based Unmixedness with three types of coordinates will be compared to explore the difference in mixing behavior along various coordinates. The centerplane-based Unmixedness is first quantified inside an interrogation area with a seven-pixel width at a given location in each instantaneous image. The quantification is performed at all locations and in all instantaneous images, and then mean Unmixedness is quantified by averaging over 500 instantaneous images at each location.

In the cross-sectional view, instantaneous cross-section-based Unmixedness and PDF are quantified at downstream locations $x/D = 2.5$, 5.5 and 10.5. Unlike the centerplane-based Unmixedness, an interrogation area covers the entire cross-sectional structure at each x/D location. Again, averaging 500 instantaneous data yields the mean Unmixedness and PDF. For both centerplane- and cross-section-based instantaneous mixing metrics, the mean concentration value inside each interrogation area is matched to a reference value for effective consistency with mass conservation along the jet (Gevorkyan et al., 2016). In the present study the reference mean corresponds to the mean concentration at $s_c/D \approx 15$ for the $J = 5$ case for the centerplane-based Unmixedness and at $x/D = 10.5$ for the $J = 2$ case for the cross-section-based Unmixedness and PDF, which are the same as that in Gevorkyan et al. (2016). It should be noted that Gevorkyan et al. (2016) demonstrated very little sensitivity of the Unmixedness quantification to choice of the mean reference value. More details on these mixing metrics, the algorithm for mixing quantification, and mixing characteristics in the absence of external forcing for a range of S, J and injector configurations may be found in Gevorkyan (2015) and Gevorkyan et al. (2016). Note that the cross-section-based Unmixedness and PDF cannot be calculated for a few cases or certain downstream locations because cross-sectional images cannot be appropriately scaled in comparison with the corresponding mean centerplane image, as mentioned in Chapter 2. Hence, the data points for the cases without correct scaling will not be shown in figures in this section.

Figure 5.17 shows the results for a range of mean mixing metrics, in addition to mean jet trajectories, for the equidensity flush nozzle-injected JICF at $J = 41$ and with sinusoidal excitation amplitude corresponding to $U'_{j,rms} = 0.07$ m/s. Figure 5.17(a) represents jet centerline trajectories for the unforced and all forced cases. Interestingly, jet trajectories at $f_f = 1000$ and 2000 Hz are much lower than the other trajectories because the lower branch of the bifurcating jet for these cases contains higher concentrations of the jet fluid than the upper branch, which the power-law fitting was applied to. If the trajectory is determined based focusing on higher branch of the bifurcating jet, the trajectory becomes closer to the other trajectories in Figure 5.17(a). These different trajectories among a few forcing conditions suggest the necessity of analyzing spread based on the unforced jet trajectory as a reference and then each trajectory in question for comparison.

Figures 5.17(b) and (c) represent jet penetration z_p/D and jet vertical spread δ_z/D as a function of horizontal coordinate x/D. The jet penetration shows that the forced jets at $f_f = 2000$ and 2500 Hz clearly penetrate less than the unforced case, classically interpreted to suggest “less mixed” conditions (Kamotani and Greber, 1972; Yuan and Street, 1998; Eroglu

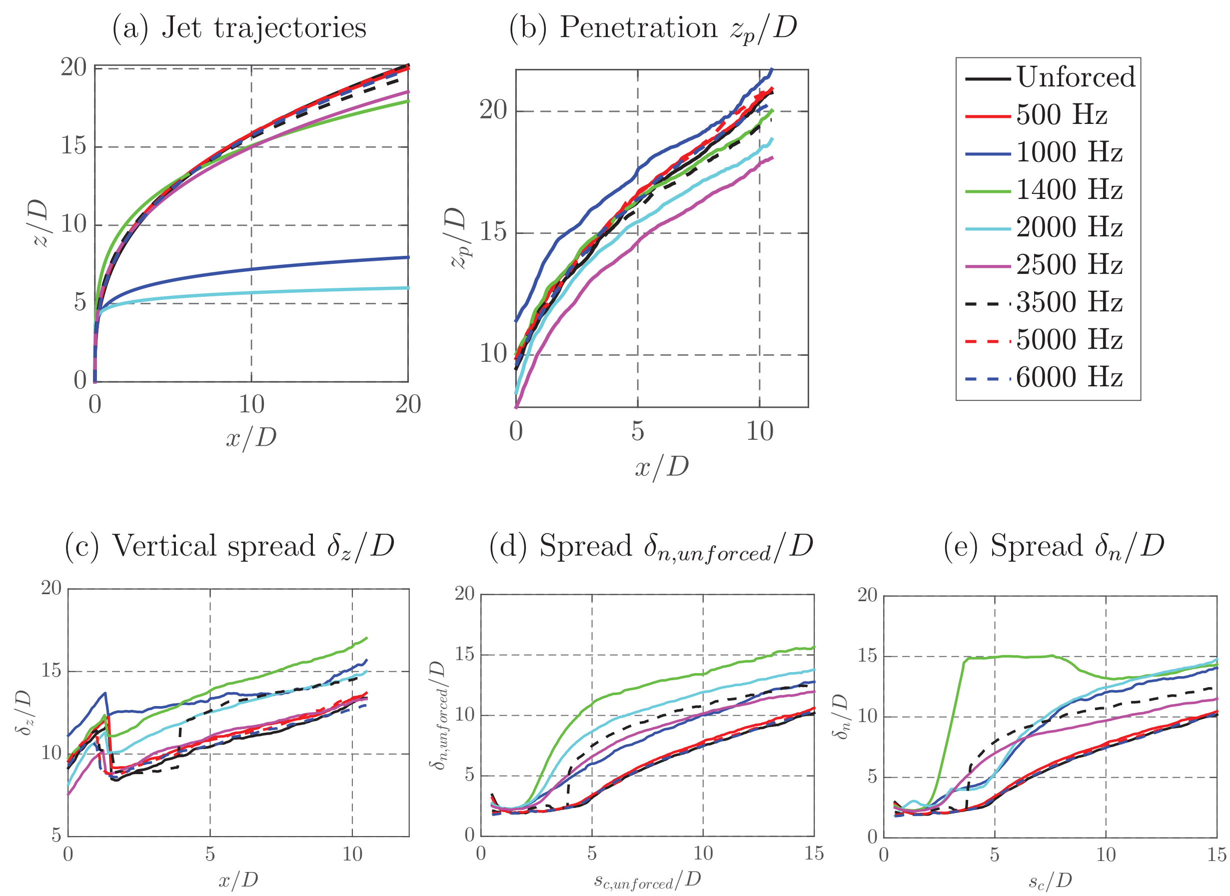

Figure 5.17: Mean mixing metrics for the equidensity flush nozzle-injected JICF at $J = 41$ for the unforced case as well as the forced cases under sine wave forcing at $f_f = 500 - 6000$ Hz and $U'_{j,rms} = 0.07$ m/s (approximately 1 % of U_j): (a) Jet trajectories, (b) jet penetration z_p/D, (c) jet vertical spread δ_z/D, (d) jet spread normal to the unforced jet trajectory $\delta_{n,unforced}/D$ and (e) jet spread normal to each jet trajectory in question δ_n/D.

and Breidenthal, 2001; Reynolds et al., 2003; Su and Mungal, 2004). While the convectively unstable JICF here is forced at f_f (2000 and 2500 Hz) fairly close to f_o (1600−1900 Hz) which significantly alters jet centerplane structures, as shown in Figure 5.7, overall the penetration worsens. In terms of jet spread (Figures 5.17(c)-(e)), in contrast to the jet penetration, the unforced case shows one of the worst jet vertical spreads, while the forced case at $f_f = 2000$ Hz vertically spreads more than the unforced case. This difference is related to how sine wave forcing affects jet structures. Since even relatively weak sine wave forcing can have an impact on jet structures, the forced jets at $f_f = 2000$ and 2500 Hz are strongly distorted, in the mean and instantaneously, by the sine wave forcing. This forcing effect produces a lower overall jet penetration for the forced cases than the unforced case because the jet penetration metric only accounts for the highest location at which the jet fluid (defined in terms of $\overline{C/C_o}$) is found. On the other hand, forced jets at f_f fairly close to f_o bifurcate into lower and higher jet branches, toward the wind tunnel floor and ceiling, respectively. Due to the presence of the lower jet branch, per momentum and mass conservations, the trajectory of the upper branch and the vertical spread can become higher for the forced cases, which is clearly observed in Figure 5.7(e). Therefore, the mixing results based on typical mean mixing metrics are not entirely consistent for forced jets, so the degree of mixing has to be comprehensively investigated using several alternative mean and instantaneous mixing metrics.

Figures 5.17(d) and (e) show jet spread normal to the unforced jet trajectory and normal to each jet trajectory in question, respectively. As one can see, the general qualitative mixing trends are similar in both metrics, yet there are some quantitative differences. Forced cases at $f_f = 1400$ and 2000 Hz show better spread compared with the other cases in each of Figures 5.17(d) and (e), mainly due to the jet bifurcation, while the forced cases at $f_f = 1000$ and 1400 Hz vertically spread more than the other cases in Figure 5.17(c). The difference for $f_f = 1000$ Hz is purely derived from the differences in coordinate systems. This comparison indicates that the mixing evaluation based on mean mixing metrics can be affected by the choice of coordinate systems. Therefore, appropriate coordinate systems should be utilized in such studies, depending on the interest in the study or the practical purpose in its engineering applications. In the present study, several possible coordinate systems are utilized for all mean and instantaneous mixing metrics, because one of the purposes in this study is to compare these mixing metrics and comprehensively determine the effect of sine wave forcing on such characteristics when viewed from different perspectives.

The results in Figure 5.17 suggest that the jet spread and penetration for the equidensity flush nozzle-injected JICF at $J = 41$ are clearly altered even with relatively low-level sine wave forcing at 1 % of the mean velocity ($U'_{j,rms} = 0.07$ m/s), although some differences are present between jet penetration and spread, especially at f_f close to f_o on the upstream shear layer. For the jet penetration, the forcing at f_f fairly far from f_o enhances the jet penetration more than does forcing at f_f fairly close to f_o. For the jet spread, however, forcing at f_f fairly close to f_o ($f_f \sim 1400$ and 2000 Hz) enhances this metric more than the other forcing cases, which is different from the trend in the jet penetration, which is lowered compared with the unforced case at these forcing frequencies. This difference may be associated with the nature of the response of the jet to the sine wave forcing. Although the jet responds more significantly at f_f closer to f_o, creating the jet bifurcation and more symmetric cross sections, more effective external forcing at f_f near f_o slightly bends the jet in the crossflow direction and hence lessens the jet penetration. Hence, in general, from the observation of the mean mixing metrics at $J = 41$ (in the convectively unstable regime) and $U'_{j,rms} = 0.07$ m/s, jets spread more widely at forcing where f_f is fairly close to f_o, yet this improved jet spread does not necessarily coincide with better jet penetration.

Figure 5.18 represents instantaneous mixing metrics, namely, the centerplane- and cross-section-based mean Unmixedness as well as the cross-section-based mean PDF for the equidensity flush nozzle-injected JICF at $J = 41$ under sine wave forcing at $U'_{j,rms} = 0.07$ m/s. Interestingly, all Unmixedness evaluations in Figures 5.18(a)-(d) consistently show a lower Unmixedness, corresponding to better molecular mixing, under sine wave forcing at forcing frequencies f_f fairly close to f_o, that is, $f_f = 1400$, 2000 and 2500 Hz, regardless of whether the Unmixedness was evaluated in different views (centerplane as in Figures 5.18(a)-(c) or cross section as in Figure 5.18(d)) or plotted using various coordinates. From the cross-section-based PDFs in Figures 5.18(e)-(g) at $x/D = 2.5$, 5.5 and 10.5, respectively, these conditions with f_f fairly close to f_o generally provide a narrower distribution range of concentrations and hence they generate more uniform concentration profiles than for the other cases. This corresponds to enhanced molecular mixing, which is consistent with the centerplane- and cross-section-based Unmixedness evaluations in this figure. As opposed to different trends among mean mixing metrics, such as spread and penetration, all instantaneous mixing metrics provide remarkably consistent results with one another. As mentioned previously, instantaneous mixing metrics are considered to be a more appropriate way to evaluate molecular mixing than mean mixing metrics, as the former account directly molec-

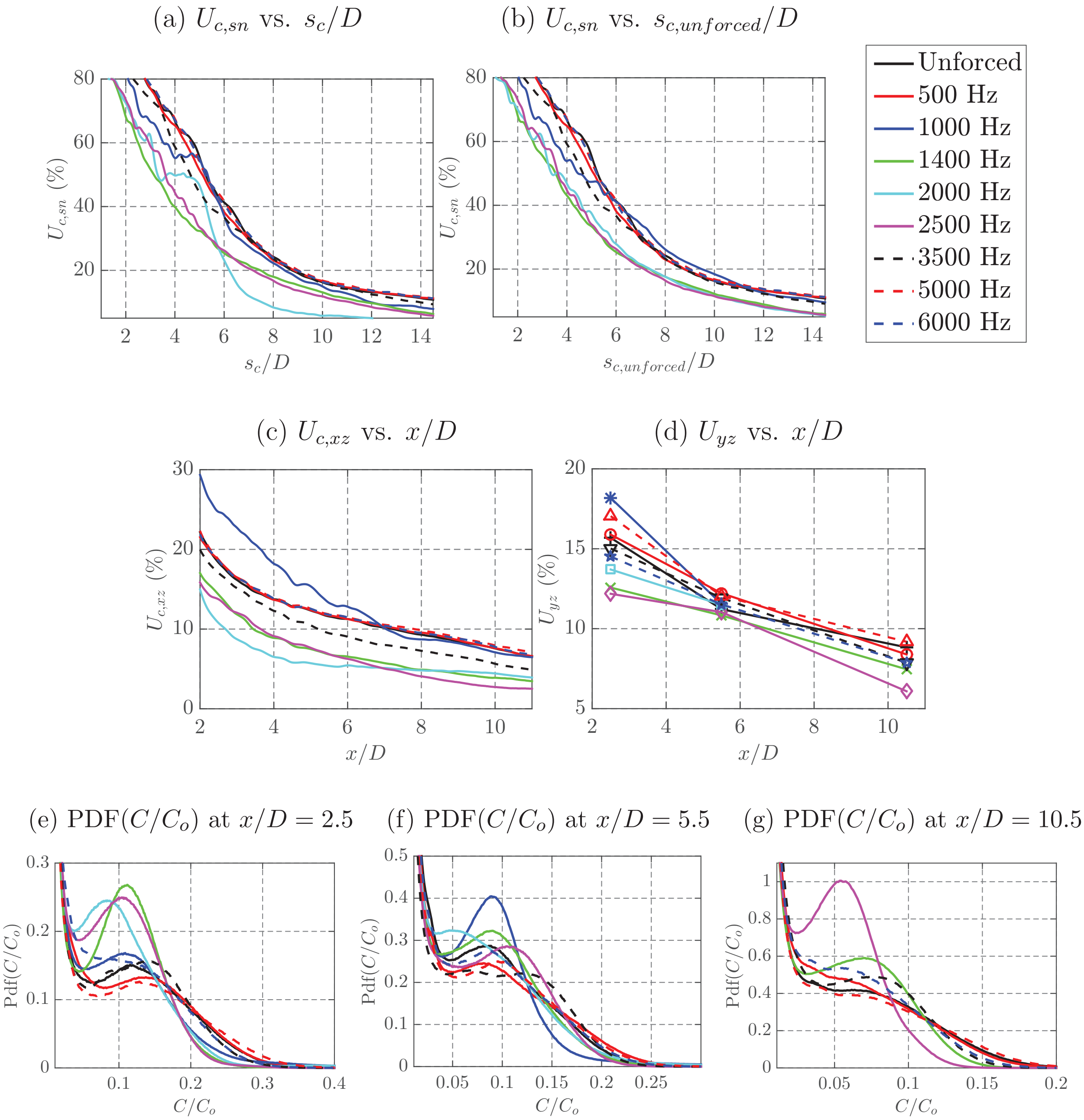

Figure 5.18: Instantaneous mixing metrics for the equidensity flush nozzle-injected JICF at $J = 41$ for the unforced and forced cases under sine wave forcing at $f_f = 500 - 6000$ Hz and $U'_{j,rms} = 0.07$ m/s. Each figure represents (a) the centerplane-based mean Unmixedness $U_{c,sn}$ along s_c/D, (b) $U_{c,sn}$ along $s_{c,unforced}/D$, (c) centerplane-based mean Unmixedness $U_{c,xz}$ along x/D, (d) cross-section-based mean Unmixedness U_{yz} along x/D, and (e)-(g) cross-section-based mean probability density function (PDF) of normalized concentration PDF(C/C_o) at $x/D = 2.5$, 5.5 and 10.5, respectively.

ular transport phenomena. Hence, the molecular mixing for the convectively unstable JICF at $J = 41$ under relatively weak sine wave forcing analyzed in this study may be considered to be enhanced at f_f fairly close to f_o on the upstream shear layer, in some cases significantly enhanced.

In the comparison of the instantaneous mixing metrics with mean mixing metrics as noted earlier, better jet spread is generally observed at f_f close to f_o, consistent with lower Unmixedness, although the jet does not spread relatively widely at $f_f = 2500$ Hz. The jet penetration shows largely opposite trends to those for the Unmixedness, despite the fact that penetration has been used for decades as a mixing metric (Margason, 1993). Nevertheless, an investigation of the mean mixing metrics is still important to estimate the applicability of the JICF to engineering systems for a given flow condition. Hence, mean mixing metrics will be documented through this experimental study.

Interestingly, the forcing at f_f fairly close to f_o, suggesting better molecular mixing, also generated more symmetric cross-sectional structures, as shown in Figure 5.8. Historically, the more symmetric CVP cross-sectional structures have been thought to be responsible for improved mixing by the JICF as compared with the free jet (Karagozian, 2010), and these findings may be related to this traditional view. Furthermore, although centerplane structures do not capture the symmetry in the cross-sectional view, the centerplane-based Unmixedness also suggests better molecular mixing at the same f_f, at which the forcing generates more symmetric cross-sectional structures. Hence these JICF data at $J = 41$ suggest that more symmetric cross-sectional structures at f_f adjacent to f_o could correspond to better molecular mixing than for the other forcing frequencies with effectively the same-level forcing. Such consistency between the centerplane- and cross-sectional-based Unmixedness is quite interesting because the symmetry or asymmetry in the cross-sectional view cannot be observed in the centerplane view, and thus is not represented in that evaluation.

Another interesting trend to note here is that sine wave forcing enhances mixing not only in the nearfield, but also in the farfield for the convectively unstable JICF when f_f is fairly close to f_o. Even at the farthest downstream location in Figure 5.18, one can clearly recognize the enhanced molecular mixing. In the structural exploration at $J = 41$, the jet bifurcation in the centerplane as well as in the symmetric cross-sectional structures were observed, even in the farfield.

As with the previous studies by M'Closkey et al. (2002), Shapiro et al. (2006), and Davitian et al. (2010b), this study has found that the mixing characteristics of the convectively unstable JICF are easily affected by relatively weak sine wave forcing. Now we focus on the investigation of mixing characteristics on the absolutely unstable JICF. For these explorations, the equidensity flush nozzle-injected JICF at $J = 5$ is utilized with sine wave forcing at various velocity RMS values of $U'_{j,rms}$: 0.07, 0.55 and 1.00 m/s. Mean mixing metrics and the centerplane-based Unmixedness for the equidensity flush nozzle-injected JICF at $J = 5$ at $U'_{j,rms} = 0.22$ and 0.30 m/s are also determined, which are shown in Appendix B.

Figure 5.19 shows jet trajectories, penetration, vertical spread, and spread normal to the unforced jet trajectory as well as normal to each trajectory in question for the equidensity flush nozzle-injected JICF at $J = 5$ with sine wave forcing at $U'_{j,rms} = 0.07$ m/s. As one can clearly see, these mean mixing metrics suggest that the unforced as well as forced jets have similar trajectories, penetration, and spread at all forcing frequencies, although there are slight enhancements in jet penetration and spread at $f_f = 800$ and 2500 Hz. Because the differences in jet penetration and spread among all f_f conditions do not differ significantly from the unforced case, are not clearly distinguishable, one can say that the sine wave forcing has little effect on the mean mixing metrics for the absolutely unstable JICF investigated in this study, as observed in smoke visualization in M'Closkey et al. (2002) and Davitian et al. (2010b). From our structural investigation in the previous section, even low-level sine wave forcing is observed to affect the spacing of vortex rollups on the upstream shear layer, related to the lock-in process. However, based on the mean mixing metrics, it is likely that the lock-in does not necessarily improve the jet penetration and spread, especially when the forcing is relatively weak.

Now we investigate instantaneous mixing metrics for the absolutely unstable JICF at $J = 5$ and $U'_{j,rms} = 0.07$ m/s. Figure 5.20 represents the centerplane- and cross-section-based mean Unmixedness, as well as cross-section-based mean PDF for the equidensity flush nozzle-injected JICF at $J = 5$ under sine wave forcing at $U'_{j,rms} = 0.07$ m/s. Even using

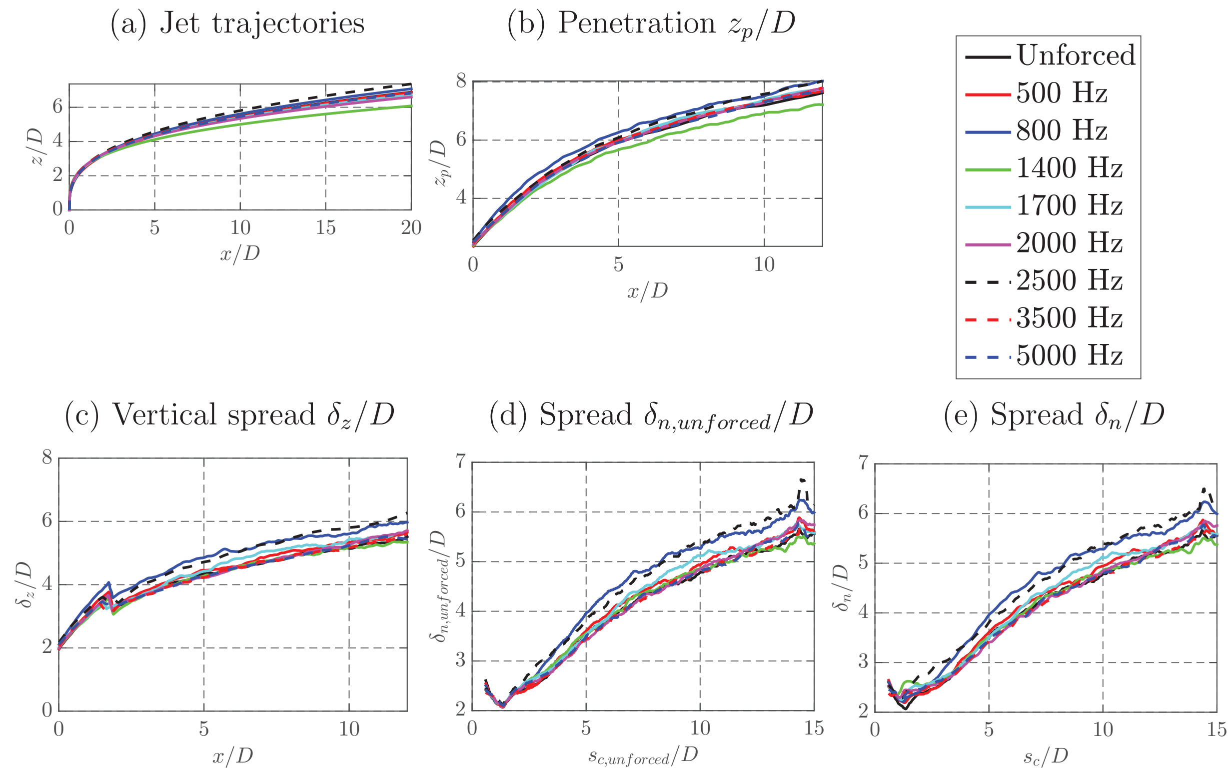

Figure 5.19: Mean mixing metrics for the equidensity flush nozzle-injected JICF at $J = 5$ for the unforced case as well as forced cases under sine wave forcing at $f_f = 500 - 5000$ Hz and $U'_{j,rms} = 0.07$ m/s (approximately 1 % of U_j): (a) Jet trajectories, (b) jet penetration z_p/D, (c) jet vertical spread δ_z/D, (d) jet spread normal to the unforced jet trajectory $\delta_{n,unforced}/D$ and (e) jet spread normal to each jet trajectory in question δ_n/D. Note that the upstream shear layer is locked-in for $f_f \approx 1250 - 3500$ Hz.

the instantaneous mixing metrics, little significant enhancement in molecular mixing in the relatively nearfield is obtained, although there seems to be a slight enhancement in the Unmixedness, U_{yz} at $f_f = 800$ Hz and $U_{c,sn}$ at $f_f = 1400$ Hz in the nearfield. $f_f = 800$ Hz also appears to provide better nearfield mixing as determined by PDFs in Figures 5.20(e) and (f). Yet trends are not clear enough to significantly differentiate the degree of mixing among all conditions from these results. Hence, both mean and instantaneous mixing metrics suggest that relatively weak sine wave forcing at $U'_{j,rms} = 0.07$ m/s may only slightly enhance the molecular mixing in the nearfield at specific frequencies f_f, but generally this has little impact on mixing characteristics.

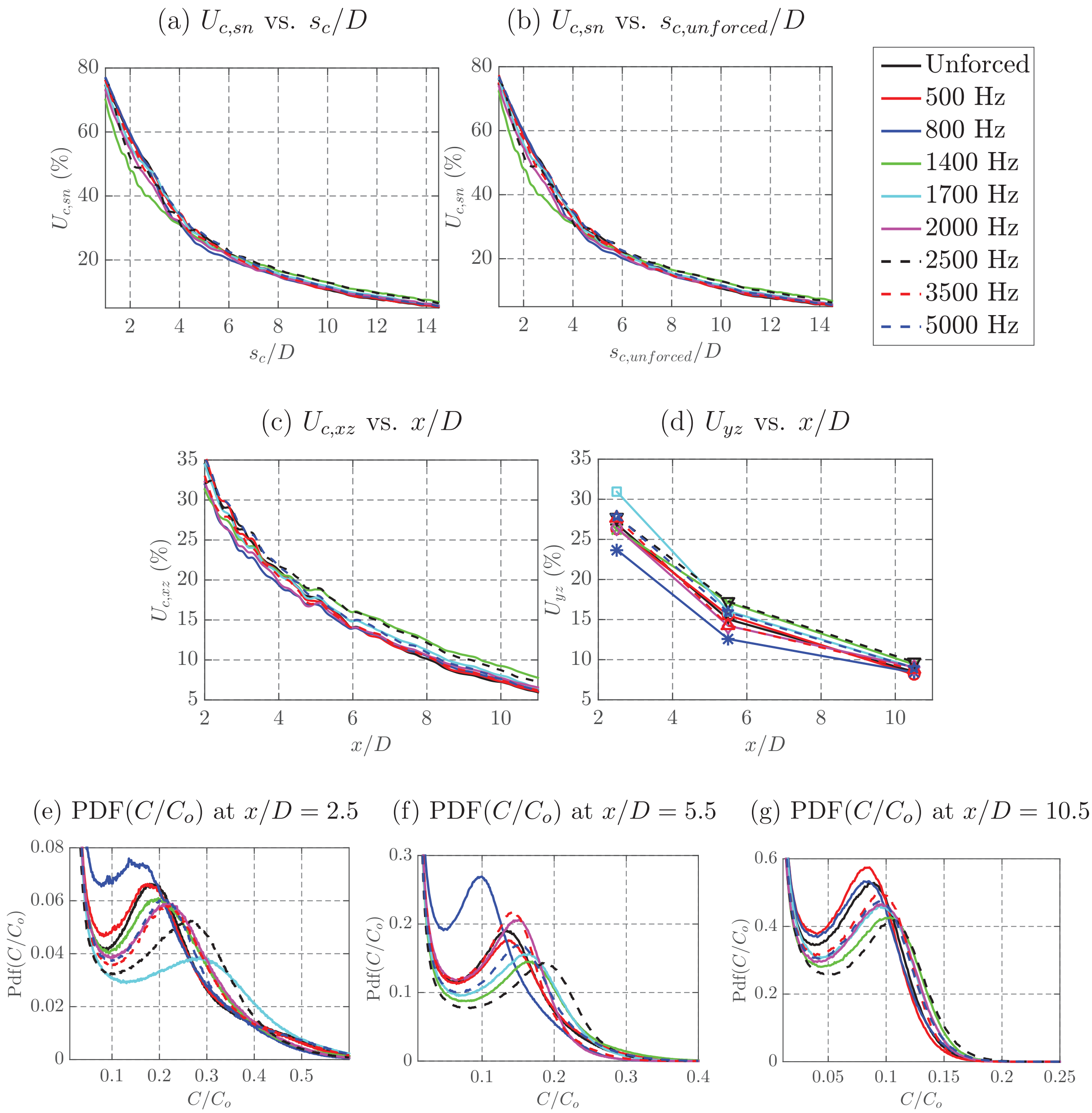

Figure 5.20: Instantaneous mixing metrics evaluated for the equidensity flush nozzle-injected JICF at $J = 5$ for the unforced and forced cases under sine wave forcing at $f_f = 500 - 5000$ Hz and $U'_{j,rms} = 0.07$ m/s. Each figure represents (a) centerplane-based mean Unmixedness $U_{c,sn}$ along s_c/D, (b) $U_{c,sn}$ along $s_{c,unforced}/D$, (c) centerplane-based mean Unmixedness $U_{c,xz}$ along x/D, (d) cross-section-based mean Unmixedness U_{yz} along x/D, and (e)-(g) cross-section-based mean probability density function (PDF) of normalized concentration PDF(C/C_o) at $x/D = 2.5$, 5.5 and 10.5, respectively. Note that the upstream shear layer is locked-in for $f_f \approx 1250 - 3500$ Hz.

Figures 5.21 and 5.22 represent results of mean mixing metrics for the JICF at $J = 5$, now with moderate-to-high sine wave forcing at $U'_{j,rms} = 0.55$ and 1.00 m/s, respectively. At $U'_{j,rms} = 0.55$ m/s in Figure 5.21, the mean mixing metrics still show similar mixing characteristics among all forcing frequencies, including the unforced case, although one may be able to differentiate jet penetration and spread for each forcing condition and extract some qualitative trends. First of all, interestingly, sine wave forcing at f_f approaching f_o (2000 Hz), specifically in the range $f_f = 1000-1210$ Hz which produces a locked-in upstream shear layer, with strong shear layer rollup, generally provides less jet penetration as well as lowered spread than the unforced cases against any coordinate systems used in this study. As with the mean mixing metrics at $J = 41$ in Figure 5.17, the $J = 5$ jet is more strongly affected by the forcing at lock-in, and at f_f fairly close to f_o on the upstream shear layer can be deflected more by the effective forcing, resulting in less jet penetration. Unlike the convectively unstable JICF, the jet does not bifurcate or significantly spread toward the wind tunnel floor, as observed in Figure 5.12.

Secondly, forcing at 500 or 550 Hz seems to produce slightly better penetration and spread; these conditions are close to the start of lock-in. This trend may be associated with the structural characteristics discussed in the previous section. At the forcing frequency $f_f \sim 500 - 590$ Hz, the upstream shear layer is locked-in but consists of less coherent rollup as compared with the forced cases at f_f fairly close to f_o, shown in Figure 5.12. Here the jet is more disturbed, especially in the nearfield, and thus spreads and penetrates more than the other cases, although the enhancement in jet penetration and spread is still small. Overall, however, these mean metrics for the absolutely unstable JICF are affected relatively little by even relatively moderate-level sine wave forcing, with only modest improvements at lower frequency forcing.

Interestingly, these trends are more clearly seen in the $U'_{j,rms} = 1.00$ m/s cases, as shown in Figure 5.22. At f_f fairly far from f_o, specifically $f_f \lesssim 700$ Hz at $U'_{j,rms} = 1.00$ m/s, jet penetration and spread are highly enhanced with sine wave forcing as compared with the unforced case. In particular, when the upstream shear layer is locked-in, at $300 \leq f_f \leq 700$ Hz fairly far from f_o, jets penetrate and spread the most significantly, consistent with images

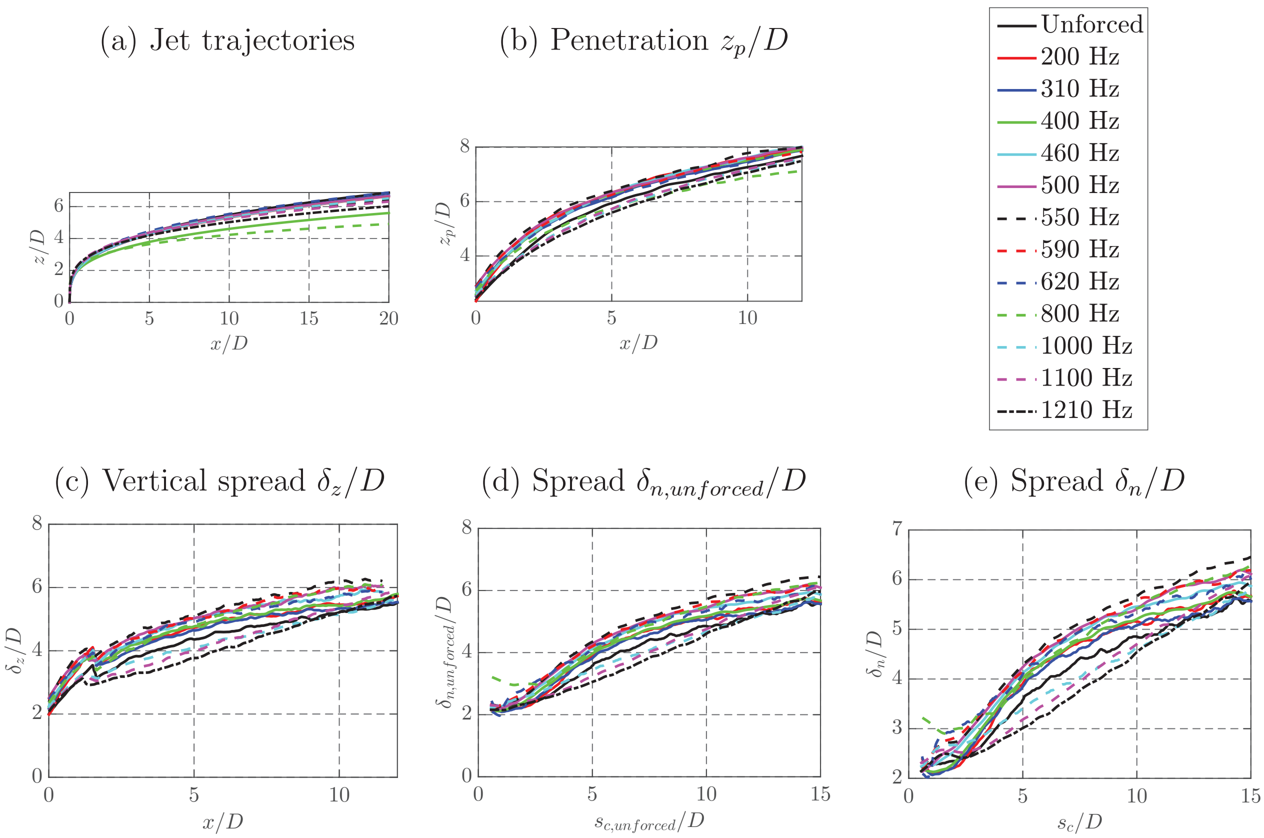

Figure 5.21: Mean mixing metrics for the equidensity flush nozzle-injected JICF at $J = 5$ for the unforced case as well as forced cases under sine wave forcing at $f_f = 200 - 1210$ Hz and $U'_{j,rms} = 0.55$ m/s (approximately 9 % of U_j): (a) Jet trajectories, (b) jet penetration z_p/D, (c) jet vertical spread δ_z/D, (d) jet spread normal to the unforced jet trajectory $\delta_{n,unforced}/D$ and (e) jet spread normal to each jet trajectory in question δ_n/D. Note that the upstream shear layer is locked-in starting around $f_f \approx 590$ Hz.

in Figure 5.14. As with the $U'_{j,rms} = 0.55$ m/s cases, sine wave forcing at these lower forcing frequencies can generate deeply penetrated structures and more widely spreading jets. At $800 \lesssim f_f \lesssim 1100$ Hz, however, the jet spread and penetration are generally smaller than the unforced case or at least become similar to the unforced case. When the upstream shear layer is locked-in and creates more coherent, evenly spaced rollup, sine wave forcing creates a similar structure to the unforced jet, which may bend jets and provide the same or lower jet penetration and spread. From the exploration of the mean mixing metrics at higher velocity RMS of $U'_{j,rms} = 0.55$ and 1.00 m/s, two qualitative trends were mainly observed

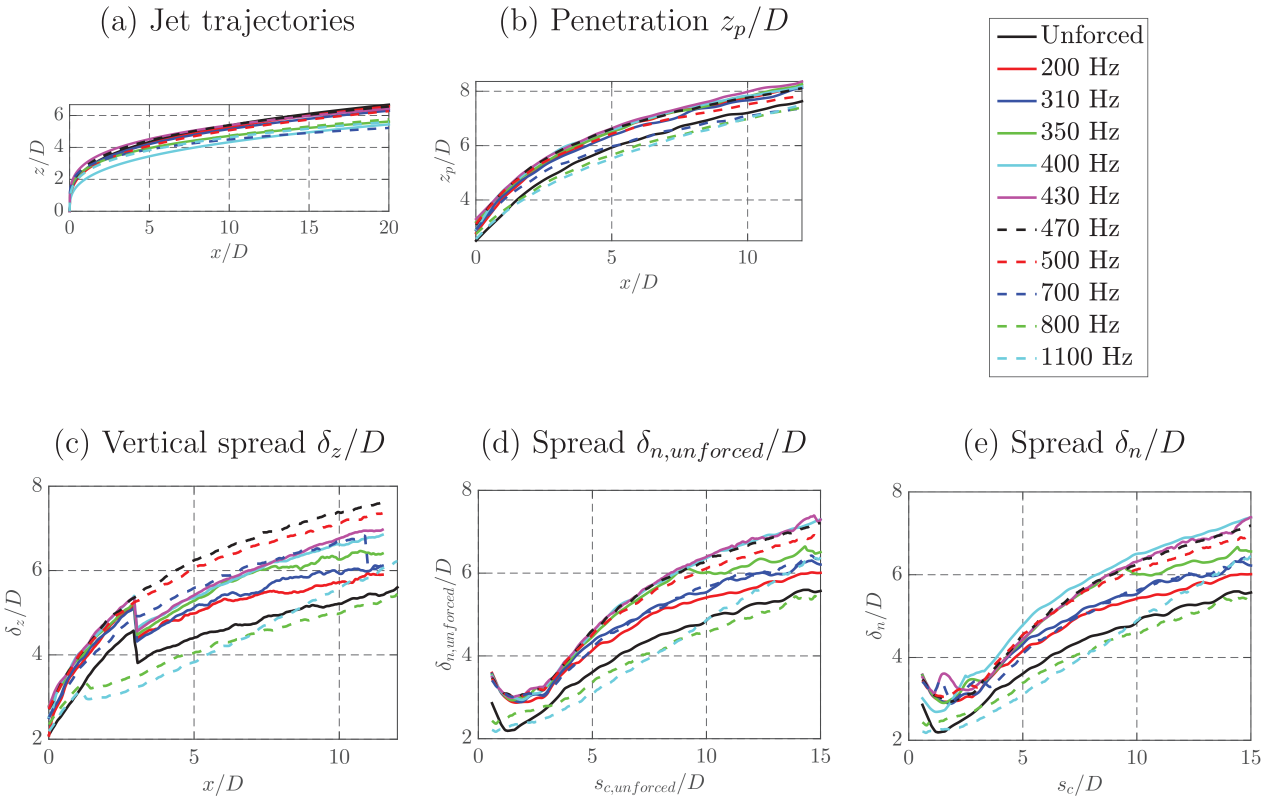

Figure 5.22: Mean mixing metrics for the equidensity flush nozzle-injected JICF at $J = 5$ for the unforced case as well as forced cases under sine wave forcing at $f_f = 200 - 1100$ Hz and $U'_{j,rms} = 1.00$ m/s (approximately 15 % of U_j): (a) Jet trajectories, (b) jet penetration z_p/D, (c) jet vertical spread δ_z/D, (d) jet spread normal to the unforced jet trajectory $\delta_{n,unforced}/D$ and (e) jet spread normal to each jet trajectory in question δ_n/D. Note that the upstream shear layer is locked-in above around $f_f \approx 300$ Hz.

with respect to the unforced case, which are remarkably consistent in both $U'_{j,rms}$ cases: (1) the jet penetrates and spreads more than the unforced case when the upstream shear layer is not locked-in or locked-in at f_f fairly far from f_o, and (2) jet penetration and spread lessens when the upstream shear layer is locked-in at f_f approaching f_o, where more coherent, evenly spaced rollup in the centerplane are present.

From this investigation of the mean mixing metrics, it appears that the jet spread and penetration can worsen with sine wave forcing, even at relatively high amplitude $U'_{j,rms}$. Yet better jet spread and penetration are not necessarily equivalent to lower Unmixedness, and hence better molecular mixing, per our earlier discussion. Figures 5.23 and 5.24 show results for instantaneous mixing metrics, representing the centerplane- and cross-section-based mean Unmixedness, as well as cross-section-based mean PDF for the equidensity flush nozzle-injected JICF at $J = 5$ at $U'_{j,rms} = 0.55$ and 1.00 m/s, respectively.

In Figures 5.23(a)-(c) at $U'_{j,rms} = 0.55$ m/s, all centerplane-based Unmixedness in different coordinates show consistent results, where the molecular mixing becomes enhanced at $f_f = 1100$ and 1210 Hz in the near-to-midfield. In contrast, at these forcing frequencies, jet spread and penetration lessen, as shown in Figure 5.21. This comparison suggests an opposite trend, and clearly improved mean mixing metrics do not necessarily coincide with improved instantaneous mixing metrics. In terms of the estimation of molecular mixing, the Unmixedness is believed to be a more appropriate indicator than the mean mixing metrics utilized in this study (Smith et al., 1997; Dimotakis, 2005; Gevorkyan et al., 2016). Hence, we may conclude that sine wave forcing at f_f fairly close to f_o generates an upstream shear layer with the coherent rollup and fairly symmetric cross-sectional structures both in the nearfield and farfield, as well as less jet penetration and spread but better molecular mixing from the perspective of centerplane-based Unmixedness. As mentioned in the previous section, sine wave forcing has a stronger effect on structural characteristics for the absolutely JICF in the nearfield than the farfield. This trend is also observed in the centerplane-based Unmixedness. After $s_c/D \approx 10$, $s_{c,unforced}/D \approx 10$, or $x/D \approx 8$, all Unmixedness basically show similar values among all conditions, even including the unforced case.

On the other hand, at $f_f \leq 800$ Hz, the centerplane-based Unmixedness is not significantly enhanced as compared with the unforced case, although jet spread and penetration are observed to improve at these forcing conditions. Again, this seeming contradiction can also be explained based on the structural characteristics acquired from the instantaneous centerplane PLIF images. At the lower forcing frequencies, the upstream shear layer is not locked-in or locked-in at f_f fairly far from f_o, creating relatively incoherent, disturbed rollup. Because the jet is more disturbed, the jet may penetrate and spread more significantly, but less coherent rollup may prevent the enhancement of molecular mixing. In the previous section, it was noted that the centerplane structures for the absolutely unstable JICF behaved in three different ways. When the upstream shear layer is not locked-in or locked-in at f_f

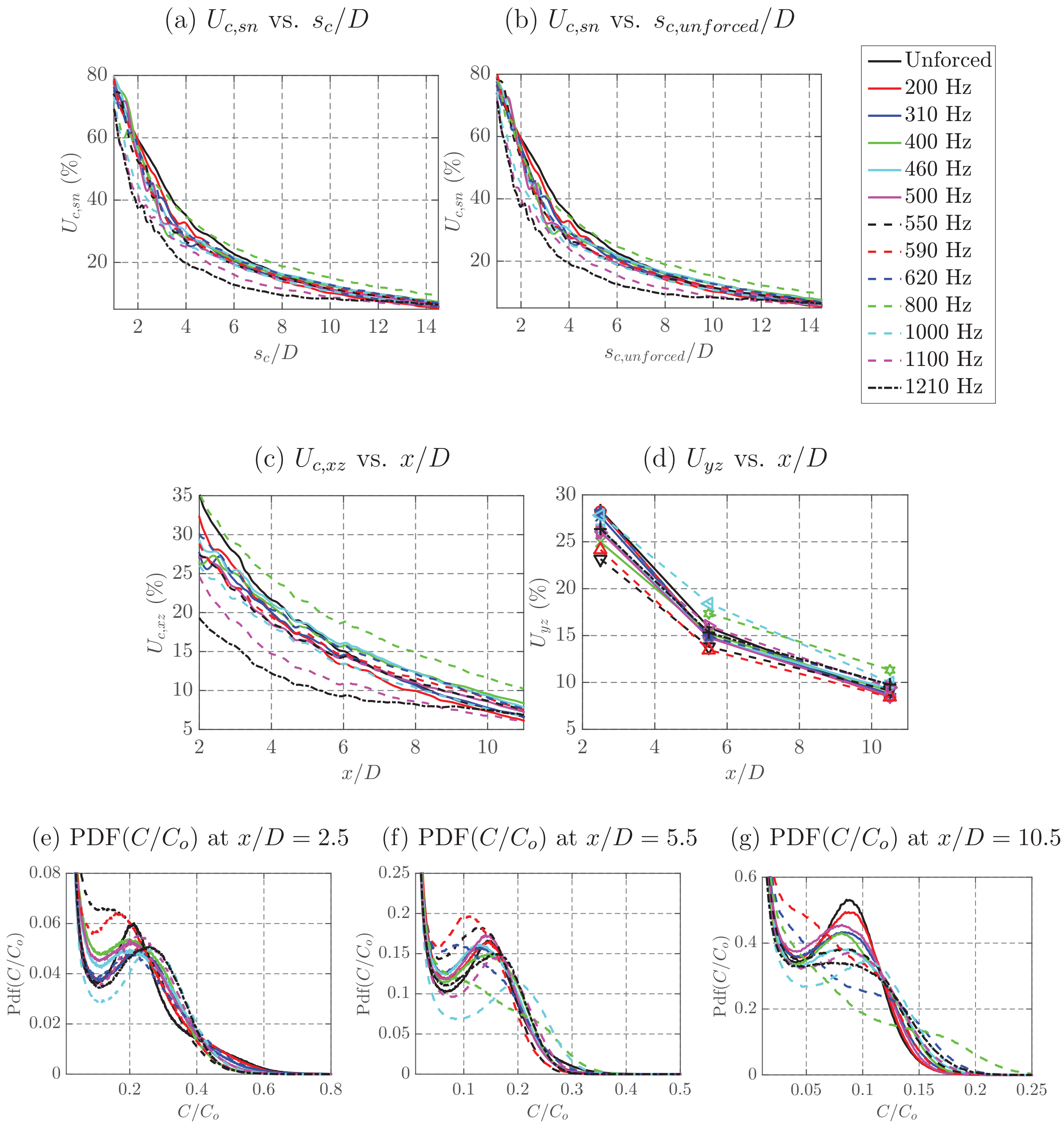

Figure 5.23: Instantaneous mixing metrics evaluated for the equidensity flush nozzle-injected JICF at $J = 5$ for the unforced and forced cases under sine wave forcing at $f_f = 200 - 1210$ Hz and $U'_{j,rms} = 0.55$ m/s. Each figure represents (a) centerplane-based mean Unmixedness $U_{c,sn}$ along s_c/D, (b) $U_{c,sn}$ along $s_{c,unforced}/D$, (c) centerplane-based mean Unmixedness $U_{c,xz}$ along x/D, (d) cross-section-based mean Unmixedness U_{yz} along x/D, and (e)-(g) cross-section-based mean probability density function (PDF) of normalized concentration PDF(C/C_o) at $x/D = 2.5$, 5.5 and 10.5, respectively. Note that the upstream shear layer is locked-in starting around $f_f \approx 590$ Hz.

fairly far from f_o, the jet behaves similar to the unforced case or generates disturbed, incoherent rollup on the upstream shear layer. For the forcing condition, the centerplane-based Unmixedness provides fairly close values to that for the unforced case, which is consistent with the observation in the instantaneous centerplane structures. When the upstream shear layer is locked-in at f_f fairly close to f_o, clear, coherent vortical structures are seen on the upstream shear layer, which seems to improve the centerplane-based Unmixedness. Interestingly, the centerplane-based mixing characteristics seem to be related to the structural characteristics. Additionally, as mentioned in the previous section, sine wave forcing has stronger effect on structural characteristics for the absolutely JICF in the nearfield than the farfield. This trend is also observed in the centerplane-based Unmixedness. After $s_c/D \approx 10$, $s_{c,unforced}/D \approx 10$, or $x/D \approx 8$, all Unmixedness metrics basically show show highly similar values among all conditions, even including the unforced case.

While the centerplane-based Unmixedness shows clear differences among all forcing conditions, the cross-section-based Unmixedness shows somewhat different trends. In the centerplane, clear structural differences in the vortical structures on the upstream shear layer were found, leading to an improvement of the centerplane-based Unmixedness. On the other hand, there is not as significant a structural or concentration profile difference in the cross-sectional view of the jet, shown in Figure 5.13, although the cross section becomes more symmetric or asymmetric depending on f_f. Interestingly, the lowest cross-sectional Unmixedness in Figure 5.23(d) appear to be for $f_f = 550$ and 590 Hz, for fairly symmetric structures as in Figures 5.13(c)-(e).The PDF of concentration also shows few differences among all conditions, but with some improvement at $550 - 590$ Hz, suggesting that the forcing can enhance or alter the concentration profiles in cross section if in the appropriate forcing frequency range. This discussion associated with the mixing characteristics indicates that the locked-in upstream shear layer to f_f fairly close to f_o with coherent rollup enhanced molecular mixing in the centerplane view, but the cross-section-based instantaneous mixing metrics provide a little difference (with improvement for f_f further from f_o). This discrepancy between centerplane- and cross-section-based metrics might be associated with the moderate-level sine wave forcing, which is probably not large enough to provide a clear effect on the jet and hence the cross-section-based Unmixedness, or with the asymmetry in the cross-sectional view, which cannot be captured in the centerplane. In contrast to differences in the nearfield, even the cross-section-based Unmixedness exhibits similar values in the farfield at $x/D = 10.5$, which is consistent with the centerplane-based Unmixedness.

Although the cross-section-based Unmixedness does not show clear trends and differences among all forcing frequencies under sine wave forcing at $U'_{j,rms} = 0.07$ and 0.55 m/s, clear enhancement in molecular mixing can be seen with stronger sine wave forcing at $U'_{j,rms} = 1.00$ m/s, as shown in Figure 5.24. First, the centerplane-based Unmixedness clearly shows consistent trends. At f_f as close as possible to f_o, $f_f = 1100$ Hz here at which coherent rollup on the locked-in upstream shear layer as well as symmetric cross sections are observed, the centerplane-based Unmixedness shows significantly enhanced molecular mixing as compared with other cases along any coordinate systems utilized in this study.

Second, in the cross-section-based Unmixedness, there is also clearer distinction among all forcing conditions, which was not seen at lower $U'_{j,rms}$. The sine wave forcing at any f_f clearly enhances molecular mixing as compared with the unforced case. More interestingly, now consistent with the centerplane-based Unmixedness, the cross-section-based Unmixedness also suggests that the forcing at $f_f = 1100$ Hz significantly enhances molecular mixing, especially in the relative nearfield at $x/D = 2.5$ and 5.5, where the sine wave forcing has a stronger effect than in the farfield. In the cross-section-based PDF, the sine wave forcing at $f_f = 1100$ Hz generates a more uniform concentration profile, directly related to lower Unmixedness and hence better molecular mixing. As observed in the $U'_{j,rms} = 0.55$ m/s cases, molecular mixing basically becomes similar among all conditions even including the unforced case in the farfield, specifically after $s_c/D \approx 12$, $s_{c,unforced}/D \approx 12$, or $x/D \approx 10$, which are farer than those at $U'_{j,rms} = 0.55$ m/s due to the stronger forcing.

Overall, a significant connection among instability, structural and mixing characteristics was confirmed in this section. It is noted that better mean mixing metrics do not necessarily correspond to better molecular mixing evaluated based on instantaneous mixing metrics, the latter of which is considered to provide a more accurate evaluation of molecular mixing. Hence, classically and widely used mean mixing metrics such as jet spread and penetration do

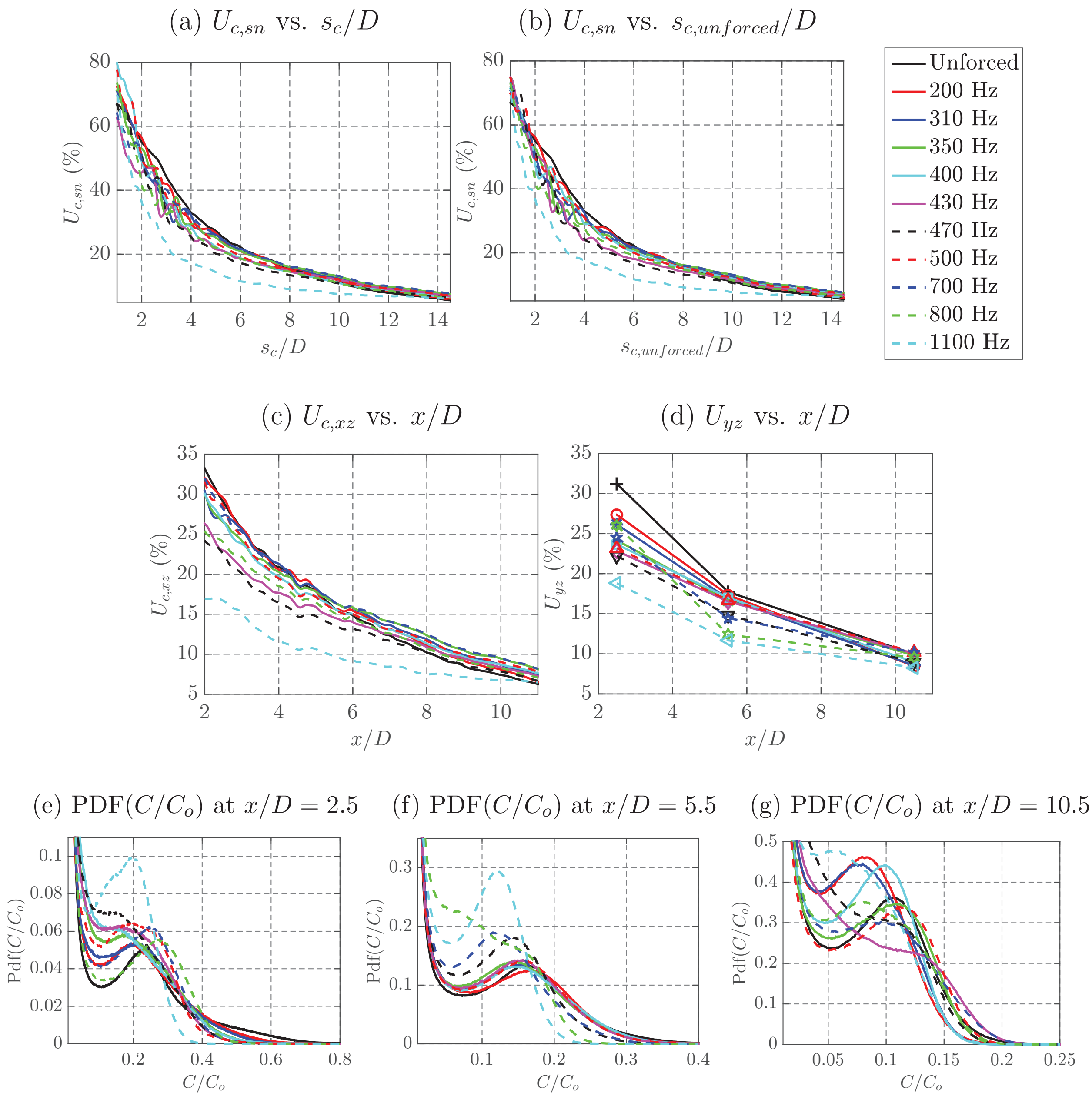

Figure 5.24: Instantaneous mixing metrics evaluated for the equidensity flush nozzle-injected JICF at $J = 5$ for the unforced and forced cases under sine wave forcing at $f_f = 200 - 1100$ Hz and $U'_{j,rms} = 1.00$ m/s. Each figure represents (a) centerplane-based mean Unmixedness $U_{c,sn}$ along s_c/D, (b) $U_{c,sn}$ along $s_{c,unforced}/D$, (c) centerplane-based mean Unmixedness $U_{c,xz}$ along x/D, (d) cross-section-based mean Unmixedness U_{yz} along x/D, and (e)-(g) cross-section-based mean probability density function (PDF) of normalized concentration PDF(C/C_o) at $x/D = 2.5$, 5.5 and 10.5, respectively. Note that the upstream shear layer is locked-in above around $f_f \approx 300$ Hz.

not always provide appropriate information on actual mixing, and in-depth, comprehensive investigation is required for the study in the mixing characteristics for the JICF. As expected, the discussion of the mixing characteristics indicates that the convectively unstable JICF is more easily affected by the sine wave forcing than the absolutely unstable JICF. Molecular mixing for the convectively unstable JICF is significantly enhanced even with relatively weak sine wave forcing at $U'_{j,rms} = 0.07$ m/s, approximately 1 % of U_j, especially when f_f is fairly close to f_o on the upstream shear layer. This latter observation was unexpected.

On the other hand, the absolutely unstable JICF is hardly affected by sine wave forcing at relatively low level, $U'_{j,rms} = 0.07$ m/s in this study. However, the near-to-midfield molecular mixing of the absolutely unstable JICF can actually be enhanced with stronger sine wave forcing at a specific range of f_f with respect to f_o. When one applies the relatively strong sine wave forcing, at $U'_{j,rms} = 0.55$ and 1.00 m/s in this study, 9 % and 15 % of U_j, respectively, with f_f fairly close to f_o, the upstream shear layer is locked-in, resulting in clear, coherent rollup on the upstream shear layer, more symmetric cross-sectional structures and hence enhanced molecular mixing in the near-to-midfield. Although it is difficult to enhance molecular mixing for the absolutely unstable JICF in the farfield, the far-field molecular mixing is more enhanced as sine wave forcing becomes stronger.

CHAPTER 6

Effects of Axisymmetric Forcing on Transverse Jets - Single-Pulse Square Wave Excitation

The previous chapter demonstrated that structural and mixing characteristics for the equidensity ($S = 1.00$) flush nozzle-injected absolutely unstable JICF (at the jet-to-crossflow momentum flux ratio of $J = 5$) were altered only when relatively strong sine wave forcing at a forcing frequency f_f fairly close to the natural frequency of the upstream shear layer f_o was applied. This forcing created a "lock-in response" of the upstream shear layer to the external forcing. This restriction on forcing conditions to have an effect on JICF characteristics suggested the inefficiency in the use of sine wave forcing for the absolutely unstable JICF. A different type of axisymmetric forcing is thus required to more efficiently or significantly enhance jet response and, potentially, molecular mixing, for the absolutely unstable JICF.

Previous studies (Eroglu and Breidenthal, 2001; M'Closkey et al., 2002; Shapiro et al., 2006; Sau and Mahesh, 2010; Davitian et al., 2010b) have shown that single-pulse square wave excitation, especially with control of the waveform shape, can dramatically enhance jet penetration and spread, even for absolutely unstable transverse jets. The "strategic forcing" explored in Davitian et al. (2010b) demonstrates the benefits of square wave forcing for the JICF in the absolutely unstable regime, but that low frequency sinusoidal forcing has little effect. These previous investigations suggest that single-pulse square wave forcing of jet fluid is a potential method to enhance jet spread and penetration, and potentially molecular mixing, for the absolutely unstable JICF.

It is currently of interest to utilize planar laser-induced fluorescence (PLIF) imaging as with sine wave forcing experiments and examine the effect of single-pulse square wave forcing on the jet's characteristics, in particular, on the JICF structures and molecular mixing. To achieve a clean square wave in terms of the temporal jet velocity at the jet exit, a simple feedback control system was established, described in detail in the next section. As with sine wave forcing, the equidensity flush nozzle-injected JICF was explored here with varying momentum flux rations, in the range $5 \leq J \leq 41$. As mentioned in Section 2.4, the PVC pipe situated in between the injector and plexiglass plenum housing enclosing the acoustic loudspeaker was removed from the actuation system in these experiments for better controllability of jet excitation. Hence, the "actuation system" in this chapter includes the data acquisition (DAQ) board through the hotwire anemometry configuration (see Sections 2.2 and 2.4 for more information).

6.1 Feedback Control of Single-Pulse Square Wave Excitation

The current actuation system inherently contains a non-flat frequency response in terms of magnitude, with a significant roll-off approximately after 1000 Hz, as shown in Figure 5.1, as well as non-linear interactions among all subharmonic and harmonic series. Because of this, square wave temporal jet velocity variation cannot be achieved at the jet exit by simply applying an ideal square wave signal as input to the loudspeaker, as demonstrated in M'Closkey et al. (2002) and Davitian et al. (2010b). In contrast, sine wave forcing can result in the appropriate output signal with sufficient amplitude, as shown in the previous chapter. Hence, a control system is required to determine the appropriate input signal into the loudspeaker to produce a cleaner square wave response of the jet at its exit.

Our group at UCLA previously utilized several different controllers for such purposes, including a feedforward dynamic compensator using a linear mathematical model with an eight-pole transfer function (M'Closkey et al., 2002; Shapiro et al., 2006), a controller utilizing the first 10 components of a Fourier series with a fundamental frequency and its harmonics simply based on the frequency response of the actuation system (Davitian et al., 2010b), and a feedback controller with modulation and demodulation (Hendrickson, 2012; Hendrickson and M'Closkey, 2012). The present experimental study, however, developed a new feedback controller partially originating from the ideas on the feedback controller established by Hendrickson (2012).

The present feedback controller superposes the first 10 sinusoidal components of a Fourier series with a given fundamental frequency, or equivalently, a prescribed forcing frequency f_f, and higher harmonics up to $10f_f$, as input signal into the loudspeaker. Amplitudes and phases of the 10 components are determined by this feedback controller so that an improved square-wave response can be created at the exit plane of the jet. The 10 sinusoidal signals as input are created by the DAQ board, and delivered to the amplifier with a constant gain of 30 after their superposition, then to the loudspeaker to excite the jet. This system is schematically shown as a block diagram in Figure 6.1. As with the sine wave forcing experiments, hotwire anemometry was implemented to measure the temporal jet vertical velocity variation at a location 0.2 jet diameters above the center of the jet exit plane. The forcing frequency for single-pulse square wave excitation is fixed at $f_f = 100$ Hz amongst all forcing conditions explored in this study, yielding harmonics up to 1000 Hz. 100 Hz is chosen mainly because a higher forcing frequency than 100 Hz requires harmonics at higher frequency than 1000 Hz to create the square-wave jet response, yet 1000 Hz is where the roll-off is seen in the frequency response of the actuation system (see Figure 5.1). Additionally, due to the lesser impact of sine wave forcing at f_f fairly far from f_o, as suggested by the experiments in Chapter 5, greater differences in the JICF between sine and single-pulse square wave forcing may be more evident at such low forcing frequencies $f_f = 100$ Hz. To determine amplitudes and phases of the 10 sinusoidal input signals in the DAQ board, the frequency response of the actuation system with respect to magnitude and phase has to be characterized. Because only 10 frequency components from 100 Hz to 1000 Hz are utilized in the feedback controller, the frequency response was taken at discrete frequencies within the frequency range of interest at $100 \leq f \leq 1000$ Hz, as shown in Figure 6.2. Here, the 10 sinusoidal input signals at 100 Hz to 1000 Hz at the same amplitudes and phases are superposed in the DAQ board and then utilized for the frequency response measurement to focus on only the 10 frequencies. Although the frequency response of the present actuation system can be characterized without the JICF on, the frequency response is characterized here for the jet with seeded

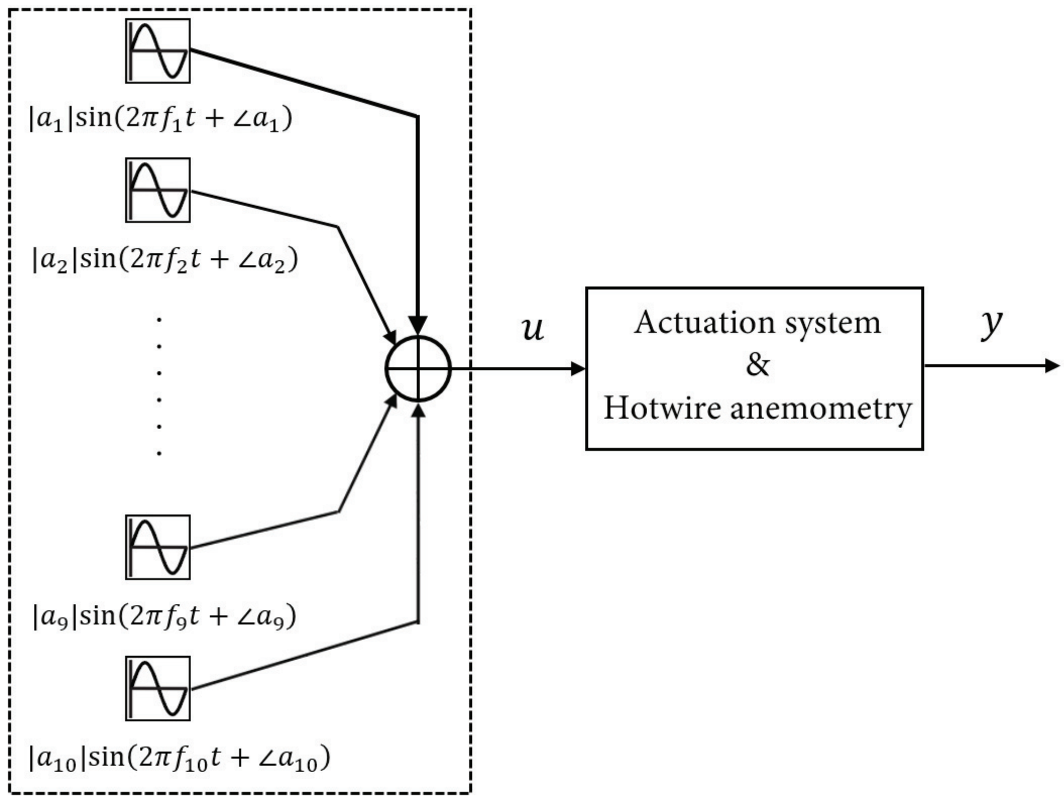

Figure 6.1: Block diagram associated with 10 sinusoidal input waves as a function of time t with a frequency f_i and Fourier coefficient a_i ($1 \leq i \leq 10$). The part surrounded by the dashed line is dealt in the data acquisition (DAQ) board. The superposed input wave into the actuation system as well as the output signal from the hotwire are represented as u and y, respectively. The hotwire output signal y is captured by the DAQ board after the signal splitter (see Section 2.2), which is utilized in the feedback process.

acetone (and air crossflow) because the existence of JICF slightly alters the behavior of the actuation system. The frequency response assessment is administrated independently for each of the J values to account for the influence of variable crossflow velocity U_∞.

For this controller, a target waveform at the jet exit, or more specifically target complex Fourier coefficients a_i ($a_i \in \mathbb{C}$) for the 10 frequency components ($i = 1, 2, ..., 10$), is required for the feedback control process. The target waveform here is an ideal square wave at a desired forcing frequency f_f, duty cycle α and root-mean-squared (RMS) velocity perturbation of the jet, $U'_{j,rms}$. The Fast Fourier Transformation (FFT) was applied to the desired

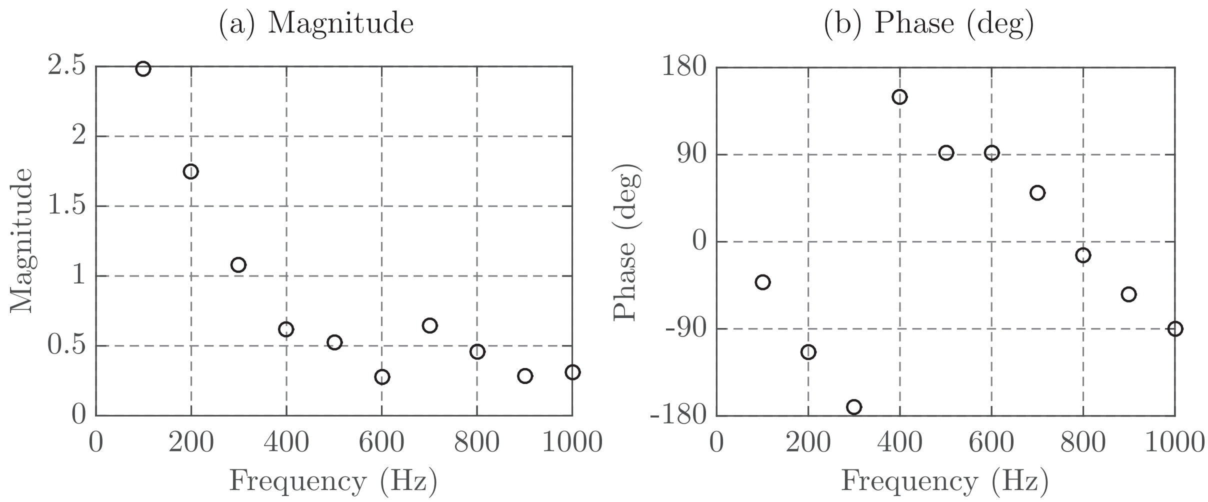

Figure 6.2: Frequency response of the actuation system from 100 Hz to 1000 Hz associated with (a) magnitude and (b) phase in degree. The frequency response is characterized in the existence of the JICF at $J = 5$ with seeding acetone in the jet.

square waveform in order to obtain target Fourier coefficients a_i at each frequency (100 Hz to 1000 Hz) contributing to the square wave at the jet exit. Based on the frequency response of the actuation system (Figure 6.2) as well as the target Fourier coefficients at the jet exit a_i, initial amplitudes and phases for the 10 sinusoidal waves created in the DAQ board are inversely determined. However, as mentioned, square-wave jet response identical to an ideal waveform can be achieved only in a perfectly linear system with the initial inputs; non-linear interactions among all subharmonic and harmonic series prevent the creation of the ideal or even a fairly clean square wave excitation of the jet at its exit. Therefore, a feedback control system is administered to tune the amplitudes and phases of the 10 sinusoidal input waves, and hence to improve the jet's square wave response at the exit plane.

The feedback controller first requires the characterization of non-linearity of the actuation system. That is, the degree of non-linear interactions among all frequency components from 100 Hz to 1000 Hz has to be quantified, which is administered as follows. First, only the 1st sinusoidal signal at 100 Hz is slightly perturbed by δ' ($\delta' \in \mathbb{R}$, $\delta' > 0$) in the DAQ board and the other sinusoidal signals are kept identical to the initial ones. These signals are superposed and then transmitted to the loudspeaker. The jet response to the slightly altered forcing of the jet from the initial conditions is measured via hotwire anemometry. This procedure yields a slightly perturbed output signal as well caused by the small perturbation δ' to the 1st input sinusoidal signal at 100 Hz. This method using small perturbations to a frequency component of the input signal is administered one by one over the all frequency components $100 - 1000$ Hz. By comparing Fourier coefficients from 100 Hz to 1000 Hz associated with the jet response at the exit, with and without the perturbation δ' to the input signal into the loudspeaker, the effect of the perturbation on the output signal can be characterized. Because of the non-linearity of the actuation system, Fourier coefficients a_i associated with the output signal differ from ones without the perturbation not only at the 1st frequency of 100 Hz but also at the other frequencies at 200 Hz through 1000 Hz. Applying such a process independently at all frequencies from 100 Hz to 1000 Hz, using the same perturbation δ', characterizes the effect of each input frequency component of the 10 output frequency components. This characterization of the actuation system is applied to determine Fourier coefficients for the next 10 sinusoidal input waves in a feedback manner to create improved square wave response by accounting for the non-linear effect.

To implement the procedure above in this control system, however, there are two issues that need to be resolved. First, because the Fourier coefficients a_i are typically complex, there is difficulty in comparing the output Fourier coefficients with and without perturbation. Second, if the perturbation to each frequency component is only applied to the magnitude of the input signal and not to the phase, the non-linear effects of the phase differences will not be accounted for, although applying perturbations to phases is more challenging than applying them to magnitudes. To solve these issues, a special treatment is implemented. The i-th sinusoidal component, $|a_i|sin(2\pi f_i t + \angle a_i)$, is treated as the sum of a sine and cosine wave in the controller as follows:

$$|a_i|sin(2\pi f_i t + \angle a_i) = Re(a_i)cos(2\pi f_i t) + Im(a_i)sin(2\pi f_i t) \tag{6.1}$$

where a_i, f_i and t are the Fourier coefficient, frequency of the i-th sinusoidal component ($i = 1, 2, ..., 10$), and time, respectively. Such decomposition of a single sine wave enables a perturbation δ' ($\delta' \in \mathbb{R}$) to be applied only to the magnitude of the sine or cosine wave,

$Im(a_i) + \delta'$ or $Re(a_i) + \delta'$, which takes into account the effect of both amplitudes and phase differences for each frequency component. Based on Equation (6.1), any signal in this controller can be expressed mainly in two different manners as the amplitudes of 10 frequency components: (1) a 10-dimensional column vector containing 10 complex Fourier coefficients a_i ($a_i \in \mathbb{C}$) or (2) a 20-dimensional column vector associated with the real-number amplitudes of the decomposed sine and cosine waves, $Im(a_i)$ or $Re(a_i)$, where odd and even entries in the column vector correspond to sine and cosine waves, respectively. For simplicity, instead of the 10-dimensional column vector with complex a_i, the 20-dimensional column vector related to the decomposed sine and cosine waves is utilized to express all signals in the present controller.

Now, the comparison between the output hotwire signals with and without perturbation to the input signal is made in order to assess the non-linearity of the actuation system using the 20-dimensional column vector. Here, the 20-dimensional column vector associated with the hotwire output signal with the perturbations is subtracted from that without perturbations, which quantitatively characterizes the effect of the small perturbation to the input signal or, equivalently, the degree of non-linear interactions among all frequency components. This process of subtraction is performed overall 20 times in a single iteration, for 10 sine and 10 cosine components from 100 Hz to 1000 Hz. The resultant twenty column vectors are combined together to generate a 20×20 matrix, where all entries are real. This 20×20 matrix is the so-called perturbation matrix K. The perturbation matrix K satisfies the following equation:

$$\boldsymbol{d} = \boldsymbol{h} + K\boldsymbol{\delta} \tag{6.2}$$

where $\boldsymbol{d}$, $\boldsymbol{h}$ and $\boldsymbol{\delta}$ ($\boldsymbol{d}, \boldsymbol{h}, \boldsymbol{\delta} \in \mathbb{R}$) represent a 20-dimensional column vector pertaining to the desired waveform (i.e., the ideal waveform), the output signal acquired via hotwire anemometry without any perturbation, and the perturbation to the input signals for the next iteration, respectively. That is, the column vector $\boldsymbol{\delta}$ is added to the initial input signals in the absence of perturbation to generate the modified input signal for the next iteration. Thus, Equation (6.2) has to be solved for $\boldsymbol{\delta}$ using the inversion of the perturbation matrix, K^{-1}, as follows:

$$\boldsymbol{\delta} = K^{-1}(\boldsymbol{d} - \boldsymbol{h}) \tag{6.3}$$

Equation (6.3) provides the vector $\boldsymbol{\delta}$ which is added to the amplitudes of the input signal for the next iteration. This feedback control is iterated until convergence, determined by visual inspection based on the hotwire output signal as compared with the desired waveform. In addition, the 2-norm condition number of the perturbation matrix K, the ratio of the largest singular value of K to the smallest one, is monitored for each iteration to assess the sensitivity of the solution $\boldsymbol{\delta}$ to any experimental errors. The perturbation matrix is considered to be well-conditioned if the 2-norm condition number is close to a unity. A typical value of the 2-norm condition number in the current actuation system is approximately 40, but it can be up to 100, depending on forcing conditions, due to strong non-linearity. The 2-norm condition number is calculated utilized Equation (6.4) as follows, where λ represents eigenvalues of a matrix.

$$cond(K) = \sqrt{\frac{\lambda(K^T K)_{max}}{\lambda(K^T K)_{min}}} \tag{6.4}$$

This control system was first applied to a linear system for validation. The signal splitter (see Section 2.2) was utilized as the representation of a linear system by directly connecting to the DAQ board without the current actuation system as well as the hotwire anemometry configuration. First, a random noise signal composed of 10 frequency components from 100 Hz to 1000 Hz was transmitted to the signal splitter directly from the DAQ board. Then, the feedback controller was implemented to create a square wave signal from the random initial signal. Since the signal splitter is a linear component, just one iteration results in the convergence almost exactly to the desired waveform, as demonstrated by the example in Figure 6.3(a). Figure 6.3(b) represents a 20×20 perturbation matrix K that represents interactions among all frequency components. The matrix K clearly shows strong coupling between sine and cosine components at the same frequency (e.g., in the 2×2 matrices on a diagonal line) but does not show non-linear interactions among different frequency components. Such strong coupling is more clearly observed in Figure 6.3(c) as a 10×10

norm perturbation matrix K_n, which is created by calculating a norm of 2×2 submatrices over the entire 20×20 matrix without overlaps with each other. The matrix K_n only contains diagonal components and no off-diagonal components, which is a typical characteristic of a linear system. The 2-norm condition number of the perturbation matrix K in Figure 6.3(b) is 1.04, suggesting a well-conditioned matrix typically seen in a linear system. Therefore, such a well-conditioned perturbation matrix coincides with the absence of non-linear interactions, that is, a perturbation to a given frequency component only affects the output signal in the same frequency component but not the other frequency components. This expected result using a linear component indicates the validity of the feedback controller.

Note that the actual actuation system involves non-linearity, however, so that a perturbation matrix contains larger off-diagonal components, unlike that with a linear system. An example is shown in Figure 6.4. The perturbation matrix K as well as norm perturbation matrix K_n in Figure 6.4 are obtained at $J = 5$ with forcing at a frequency $f_f = 100$ Hz, input duty cycle $\alpha_{input} = 20$ % and RMS jet velocity perturbation $U'_{j,rms} = 1.7$ m/s. This stronger non-linearity can be also numerically observed as a larger 2-norm condition number of 41. However, as one can see, components in the vicinity to the diagonal line are still stronger than the other components due to the coupling at the same frequency. In addition, non-linear interactions are more frequently observed at lower frequencies in the proximity of 100 Hz to 300 Hz because lower frequency components are more dominant in the output signal for forcing conditions in the present study due to the forcing frequency of 100 Hz.

Using the above feedback controller process, a cleaner square wave excitation of the jet at the jet exit is achieved, as shown by the comparison in hotwire signals shown in Figure 6.5. Figure 6.5 represents the temporal mean-subtracted vertical jet velocity $u_j - U_j$ at the jet exit, with and without control, for the equidensity flush nozzle-injected JICF at $J = 5$ for prescribed duty cycles of $\alpha_{input} = 20$ (Figure 6.5(a)) and 50 % (Figure 6.5(b)). In both figures, the temporal jet velocity distributions without control are distorted as compared with the reference ideal waveform, while with the feedback control of the jet velocity, there is a cleaner square wave-like response of the jet at the exit for both forcing cases shown. Temporal jet response at all input duty cycles α_{input}, RMS velocity perturbations $U'_{j,rms}$ as

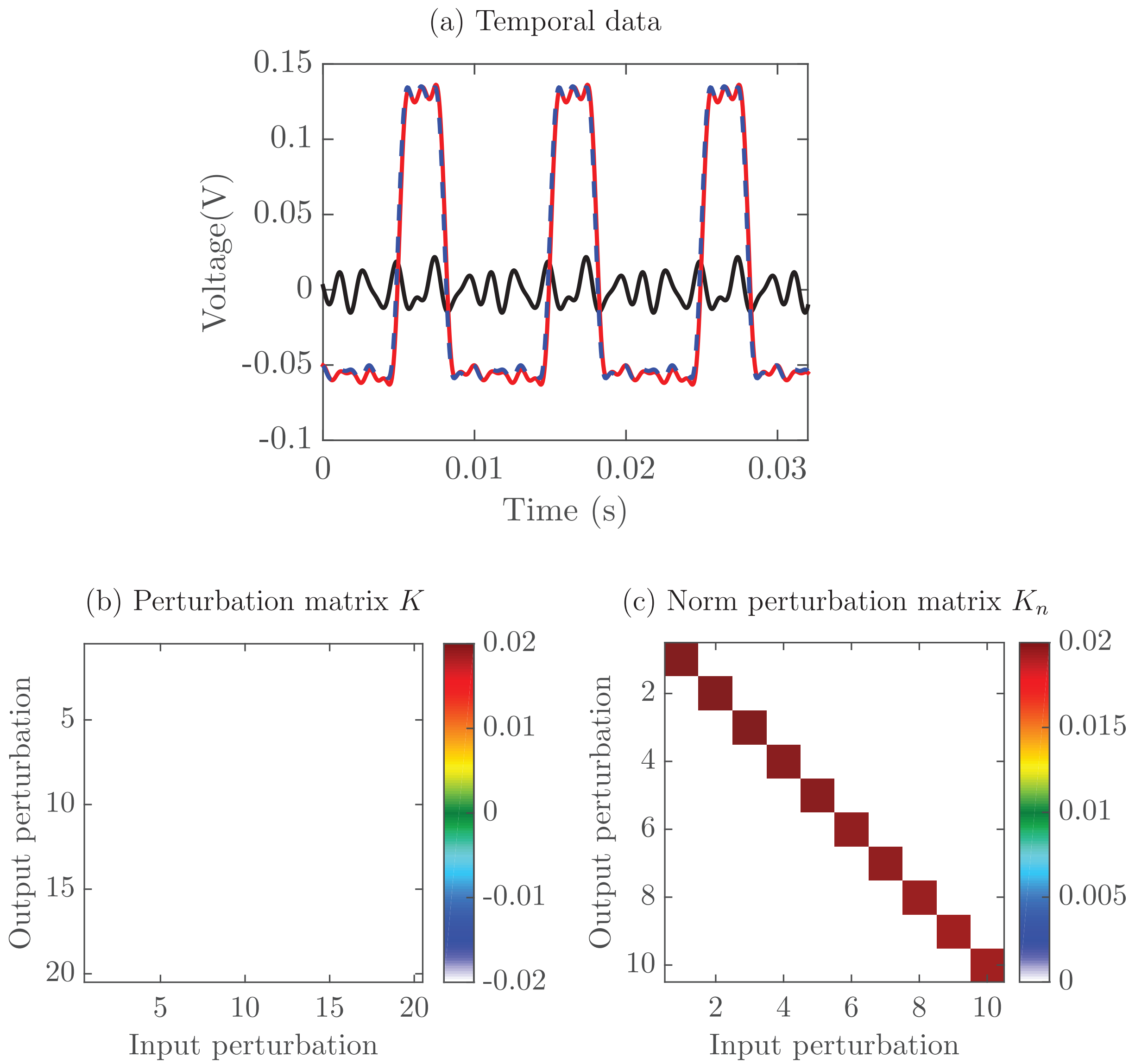

Figure 6.3: (a) Temporal voltage data associated with random initial signal (—), output signal after one iteration (—), and target waveform (- -). The temporal data are constructed using the first 10 Fourier series at 100 Hz to 1000 Hz. (b) 20×20 perturbation matrix where odd and even entries are associated with sine and cosine input components from 100 Hz to 1000 Hz (the 2-norm condition number of 1.04). (c) 10×10 perturbation matrix created by calculating norm of 2×2 submatrices of 20×20 perturbation matrix. These matrices are created in the feedback process to create single-pulse square wave response through the linear signal splitter.

well as jet-to-crossflow momentum flux ratios J is shown in Appendix C. Typically, $1 - 3$ iterations are required until convergence of the waveform, depending on forcing conditions,

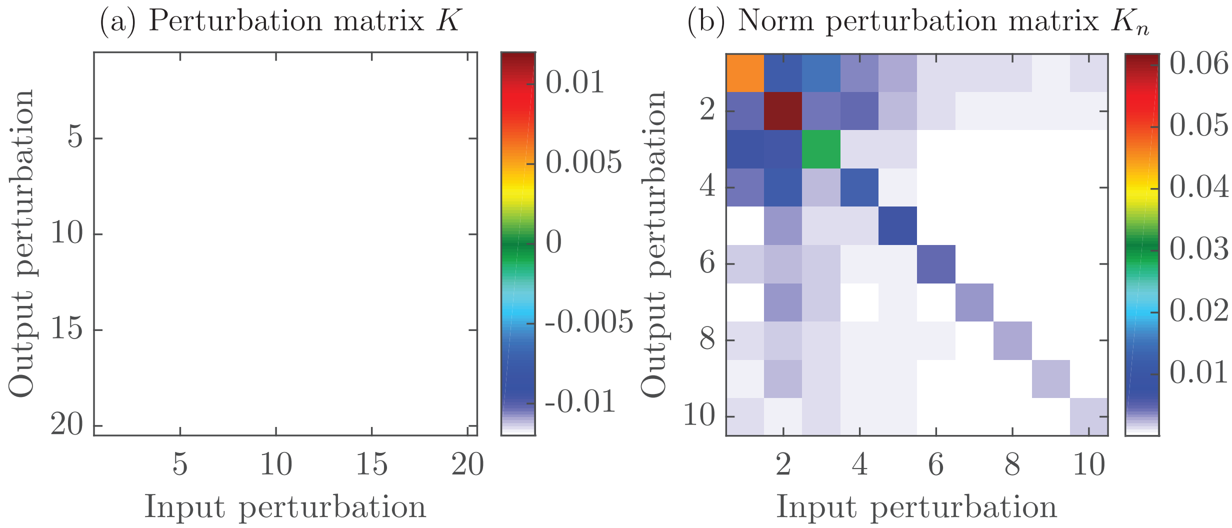

Figure 6.4: (a) 20×20 perturbation matrix where odd and even entries are associated with sine and cosine input components from 100 Hz to 1000 Hz (the 2-norm condition number of 41). (b) 10×10 perturbation matrix created by calculating norm of 2×2 submatrices of 20×20 perturbation matrix. These matrix are for the equidensity flush nozzle-injected flush nozzle at $J = 5$ under single-pulse square wave forcing at a forcing frequency $f_f = 100$ Hz, input duty cycle $\alpha_{input} = 20$ % and RMS velocity perturbation $U'_{j,rms} = 1.7$ m/s.

as assessed by visual inspection.

The feedback controller is required to determine 20-dimensional column vectors or, equivalently, amplitudes of sine and cosine input components at 100 Hz to 1000 Hz for all forcing conditions to be explored. However, because the determined temporal jet velocity distribution does not perfectly become an ideal waveform, the actual RMS velocity perturbation $U'_{j,rms}$ is often slightly off from the target value. Hence, to correct this, as with the sine wave forcing experiments, RMS velocity perturbation $U'_{j,rms}$ is precisely set to be a desired condition right before the PLIF imaging by adjusting a gain imposed on all input components; this gain approximately ranges from 0.9 to 1.1. This narrow range of gain, being fairly close to unity, does not considerably alter the waveforms created by the feedback control. Matching $U'_{j,rms}$ is important among different excitation and flow conditions in order to understand which produce truly optimized conditions.

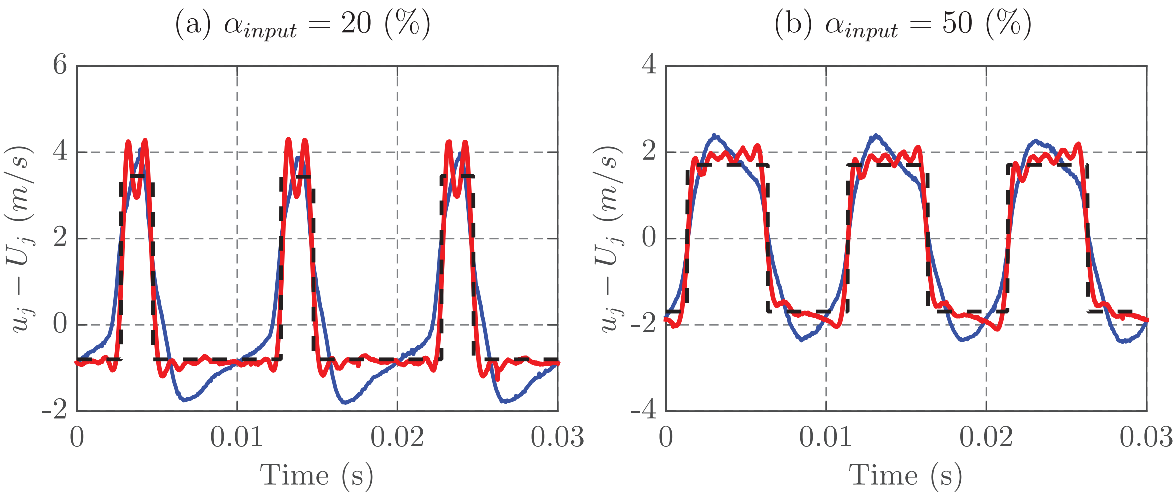

Figure 6.5: Single-pulse square wave temporal vertical jet velocity distributions at a forcing frequency $f_f = 100$ Hz as well as input duty cycles (a) $\alpha_{input} = 20$ % and (b) $\alpha_{input} = 50$ % without (—) and with (—) control for the equidensity flush nozzle-injected flush nozzle at $J = 5$. The ideal square wave (**--**) is also shown as a reference. The RMS velocity perturbation is matched for both conditions at $U'_{j,rms} = 1.7$ m/s.

6.2 Evaluation of Stroke Ratio

The stroke ratio L/D is associated with a universal time scale for optimum vortex ring formation in quiescent surroundings. The work of Gharib et al. (1998) has shown that with single pulsation generated by a piston, optimum vortex formation occurs at a critical stroke ratio $L/D \approx 4$. As summarized in Section 1.4, several previous experimental and computational studies for the transverse jet (Johari et al., 1999; M'Closkey et al., 2002; Shapiro et al., 2006; Johari, 2006; Sau and Mahesh, 2008, 2010; Davitian et al., 2010b; Hendrickson, 2012) suggest that the stroke ratio can also be used to characterize square wave pulsation of the jet into crossflow. Due to the relationship between JICF characteristics and stroke ratio, an accurate determination of the stroke ratio is critical in this study in order to explore structural and mixing characteristics of JICF under single-pulse square wave forcing.

The definition of stroke ratio for fully modulated flows (Johari et al., 1999; Johari, 2006; Sau and Mahesh, 2008), or equivalently flows in the absence of a mean bulk velocity, is simply the integration of temporal jet velocity at the jet exit u_j within a temporal pulse width τ divided by the jet's exit diameter D as follows:

$$\frac{L}{D} = \frac{1}{D}\int_0^{\tau} u_j dt \tag{6.5}$$

However, when flow is partially modulated, with an underlying bulk mean velocity, on top of which there is pulsation, a different method could and should be utilized to estimate the effective stroke ratio comparable. One of our previous experimental studies (Shapiro et al., 2006) as well as a computational study (Sau and Mahesh, 2010) pertaining to the partially modulated JICF utilized the peak-to-peak velocity amplitude ΔU_j and approximate temporal pulse width τ associated with the variable jet velocity at the exit plane. Using these parameters and the jet's diameter D, an initial stroke ratio L/D was estimated as follows:

$$\frac{L}{D} = \frac{\Delta U_j \tau}{D} \tag{6.6}$$

Equation (6.6) technically treats a temporal waveform as an ideal waveform simply by multiplying the height and width of a square pulse. This definition basically focuses on the pulsation effect on the jet effectively by using a reference frame traveling with the jet in the mean, without pulsation.

Some previous studies related to the partially modulated JICF with a mean bulk velocity (Davitian et al., 2010b; Hendrickson, 2012) calculated stroke ratio L/D by fully integrating the temporal jet velocity at the jet exit, u_j, within a temporal pulse width τ extracted from temporal data and using Equation (6.5). Since the JICF is partially modulated, the integration of u_j obviously includes the effect of the non-zero mean bulk jet velocity, providing a higher effective stroke ratio than that for the fully modulated flows even with the same peak-to-peak velocity amplitudes ΔU_j and temporal pulse width τ. Such evaluation of stroke ratio accounts for the total impulse of fluid introduced by the jet into stationary fluid in the laboratory reference frame, not just the net impulse introduced by excitation. While a more proper evaluation of stroke ratio would subtract the mean, in order to consider the net effect, it could be instructive on the basis of impulsively generated vortex rings, to include the mean velocity.

In experimental studies, because the shape of a square pulse is not perfect, an actual temporal pulse width τ_{actual} in temporal data is different from a prescribed pulse width τ_{input}. To define τ_{actual}, the "5 % criterion" suggested by Johari et al. (1999) was applied in several earlier previous experimental studies (Johari et al., 1999; Shapiro et al., 2006; Davitian et al., 2010b; Hendrickson, 2012) as follows. First, the peak-to-peak velocity amplitude of a square pulse ΔU_j was evaluated for each pulse in the temporal data. These experimental studies defined ΔU_j between a local minimum point before the upsweep of the square pulse, $U_{min,1}$, and the first local maximum point within the same square pulse $U_{max,1}$ after the local minimum point, that is, $\Delta U_j = U_{max,1} - U_{min,1}$. Then, 5 % of ΔU_j was added to the local minimum point $U_{min,1}$ to define a so-called 5 % point $U_{5\%}$ (where $U_{5\%} = U_{min,1} + 0.05\Delta U_j$). An actual temporal pulse width τ_{actual} is defined between the 5 % points on each side of a square pulse. The actual temporal pulse width τ_{actual} was also applied to evaluate the stroke ratio using Equations (6.5) and (6.6).

In this study, however, a local minimum point before the upsweep of a square pulse $U_{min,1}$ cannot be used for some forcing conditions where a local minimum point after the downsweep of a square pulse $U_{min,2}$ is considerably smaller than that before the upsweep $U_{min,1}$. Figure 6.6 represents the temporal mean-subtracted jet velocity at the exit for the equidensity flush nozzle-injected JICF at $J = 5$ in two different forcing conditions, with prescribed input duty cycles of $\alpha_{input} = 20$ and 50 %. The markers in Figure 6.6 stand for the 5 % points to define an actual temporal pulse width τ_{actual} ($\circ$), as well as points to define the peak-to-peak velocity amplitude before the upsweep of square pulses $\Delta U_j = U_{max,1} - U_{min,1}$ ($\triangle$) and after the downsweep of square pulses $\Delta U_j = U_{max,2} - U_{min,2}$ ($\square$). In Figure 6.6(a) at $\alpha_{input} = 20$ %, the local minimum points before the upsweep $U_{min,1}$ can be used to define the 5 % points because the 5 % point before the upsweep is larger than the local minimum point after the downsweep ($U_{min,1} + 0.05\Delta U_j > U_{min,2}$). On the other hand, in Figure 6.6(b) at $\alpha_{input} = 50$ %, because the 5 % point before the upsweep is smaller than the local minimum point after the downsweep ($U_{min,1} + 0.05\Delta U_j < U_{min,2}$), the quantification of τ_{actual} fails using the same definition as in previous studies. Hence, the peak-to-peak velocity amplitude as well as the actual temporal pulse width may be defined in two different ways

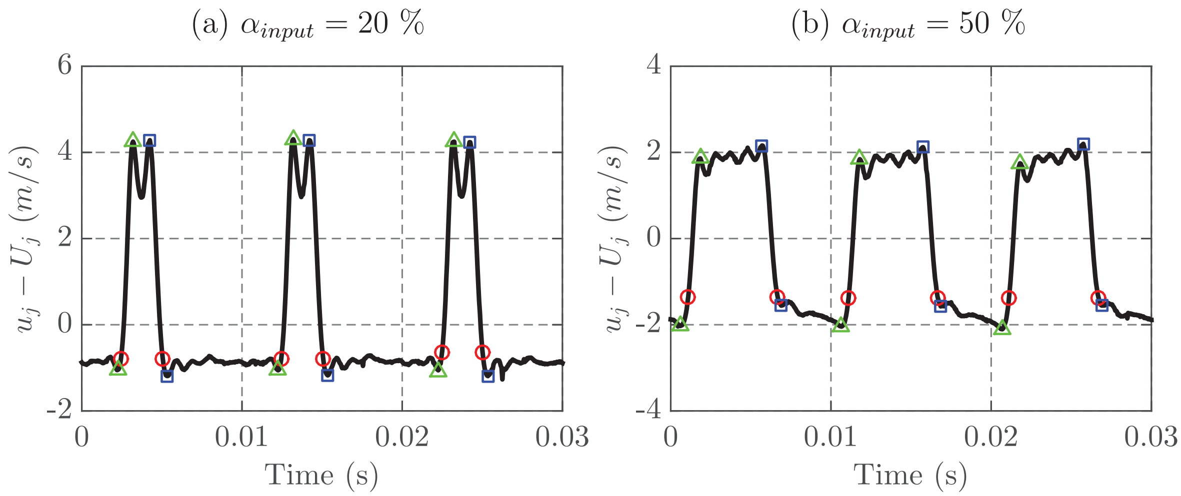

Figure 6.6: Temporal square-wave mean-subtracted jet velocity distribution at a forcing frequency $f_f = 100$ Hz as well as input duty cycles (a) $\alpha_{input} = 20$ % and (b) $\alpha_{input} = 50$ % for the equidensity flush nozzle-injected JICF at $J = 5$. Markers on figures represent 5 % points to define actual temporal pulse width τ_{actual} (○), as well as points to define peak-to-peak velocity amplitude before the upsweep of pulses (△) and after the downsweep of pulses (□).

in this study: (1) $\Delta U_j = U_{max,1} - U_{min,1}$ based on the 5 % points at $U_{min,1} + 0.05\Delta U_j$ when $U_{min,1} \geq U_{min,2}$ as shown in Figure 6.6(a), and (2) $\Delta U_j = U_{max,2} - U_{min,2}$ based on the 5 % points at $U_{min,2} + 0.05\Delta U_j$ when $U_{min,1} < U_{min,2}$ as shown in Figure 6.6(b).

When stroke ratio is calculated in the current study, because the jet is not fully modulated and has a mean bulk jet velocity, the 5 % points $U_{5\%}$ must be subtracted from the temporal jet velocity distribution u_j to only account for the net pulsation effect, i.e., by considering a jet reference frame without pulsation. For the present study the stroke ratio is estimated as follows:

$$\frac{L}{D} = \frac{1}{D} \int_0^{\tau_{actual}} (u_j - U_{5\%}) dt \tag{6.7}$$

Equation (6.7) effectively yields a stroke ratio for a partially modulated jet which is comparable to one for fully modulated flow as well as one based on Equation (6.6). Note that the current definition is different from Equation (6.5), so that it does not represent a stroke based on the total impulse of the jet.

The integration in Equation (6.7) was operated within the actual temporal pulse width τ_{actual}, determined from the red circles in Figure 6.6. In this computation, the time-dependent stroke ratio was calculated for each square pulse over the entire set of temporal data, and then a mean stroke ratio was obtained by averaging at least 10 temporal cycles of square wave forcing. This process of acquiring the actual temporal pulse width τ_{actual}, equivalent to an actual duty cycle $\alpha_{actual} = \tau_{actual}/T$, and then the mean stroke ratio L/D was implemented for all forcing conditions. Some of these forcing outcomes for L/D using Equation (6.7) are shown in Tables 6.1, 6.2, 6.3, and 6.4 for $J = 41$, 20, 10, and 5, respectively, at $U'_{j,rms} = 1.7$ m/s. As a reference, stroke ratio L/D using Equation (6.5) including the mean jet flow and Equation (6.6) with the simplified relation, are also tabulated. These values are an average of temporal data applied for centerplane as well as cross-sectional view at downstream locations of $x/D = 2.5$, 5.5 and 10.5. The fairly low 95 % confidence interval shown in Tables 6.1 to 6.4 indicates that temporal excitation of the jet is highly periodic and consistent amongst experiments involving centerplane and cross-sectional slices of the jet. Quantification of these parameters for the other forcing conditions at $1.0 \leq U'_{j,rms} \leq 3.0$ m/s is given in Appendix C, although the range of actual duty cycles α_{actual} or stroke ratio L/D becomes narrower as $U'_{j,rms}$ increases because a very high peak velocity can exceed the calibration range of our hotwire anemometry (see Section 2.2). The forcing conditions described in the Appendix C are only measured for PLIF experiments involving the centerplane view; cross-sectional data are acquired only at $U'_{j,rms} = 1.7$ m/s.

In general, an actual duty cycle α_{actual} is always larger than the prescribed one α_{input}, by approximately $5-10$ %, because the actual temporal pulse uses only 10 frequency components and the steep upsweep and downsweep is not exactly replicated in the actual waveform. Such quantitative trends pertaining to the increase in the actual duty cycle over the input was also observed in Davitian et al. (2010b). In addition, stroke ratios without integration, as defined by the simplified expression in Equation (6.6), are consistently larger than L/D with integration as evaluated by Equation (6.7) for two reasons. First, the stroke ratio without integration is based on the full value of ΔU_j, while the one with integration accounts only for 95 % of ΔU_j in the integration. More importantly, the stroke ratio without integration approximates the square pulse as an ideal waveform just by multiplying ΔU_j by τ_{actual}, which could include additional area not represented in the integration. The stroke ratio obtained from Equation (6.5), including the mean jet velocity, clearly shows significantly higher values than that based on Equation (6.7) because of the different definition and inclusion of mean velocity described above. In most cases for low level forcing, L/D from Equation (6.5) is about twice the magnitude of L/D from Equation (6.7).

In this study, since L/D with integrating $U - U_{5\%}$ is likely to represent pulsation effect more reasonably than those based on the other two definitions, Equation (6.7) is the primary means of determining L/D and its relation to JICF characteristics.

Table 6.1: Forcing conditions at $J = 41$ with matching root-mean-squared velocity perturbation at $U'_{j,rms} = 1.7$ m/s ($1.70 \leq U'_{j,rms} \leq 1.71$ m/s) among all forcing conditions. Actual duty cycles α_{actual}, as well as three stroke ratios L/D evaluated by the present method in Equation (6.7) (third column), Equation (6.6) with the simplified relation (fourth column) and Equation (6.5) with inclusion of the mean jet velocity (fifth column). There is a 95 % confidence interval for input duty cycles α_{input}.

α_{input} (%)	α_{actual} (%)	L/D (Eq. 6.7)	L/D (Eq. 6.6)	L/D (Eq. 6.5)
10	14.5 ± 0.09	1.29 ± 0.01	2.62 ± 0.08	3.57 ± 0.03
15	20.6 ± 0.05	1.79 ± 0.01	2.79 ± 0.04	4.80 ± 0.01
20	25.3 ± 0.04	1.96 ± 0.01	3.15 ± 0.05	5.70 ± 0.01
25	30.3 ± 0.05	2.32 ± 0.01	3.34 ± 0.04	6.64 ± 0.01
30	35.7 ± 0.08	2.63 ± 0.01	3.81 ± 0.03	7.58 ± 0.01
35	40.7 ± 0.07	2.96 ± 0.02	4.02 ± 0.04	8.43 ± 0.01
40	46.5 ± 0.05	3.28 ± 0.01	4.39 ± 0.03	9.37 ± 0.01
45	50.8 ± 0.09	3.60 ± 0.02	4.58 ± 0.02	10.1 ± 0.01
50	56.9 ± 0.07	4.12 ± 0.01	5.25 ± 0.02	11.0 ± 0.01
60	67.0 ± 0.08	5.04 ± 0.02	6.11 ± 0.07	12.5 ± 0.01
70	77.3 ± 0.12	6.35 ± 0.02	7.49 ± 0.05	13.9 ± 0.02

Table 6.2: Forcing conditions at $J = 20$ with matching root-mean-squared velocity perturbation at $U'_{j,rms} = 1.7$ m/s ($1.70 \leq U'_{j,rms} \leq 1.71$ m/s) among all forcing conditions. Actual duty cycles α_{actual}, as well as three stroke ratios L/D evaluated by the present method in Equation (6.7) (third column), Equation (6.6) with the simplified relation (fourth column) and Equation (6.5) with inclusion of the mean jet velocity (fifth column). There is a 95 % confidence interval for input duty cycles α_{input}.

α_{input} (%)	α_{actual} (%)	L/D (Eq. 6.7)	L/D (Eq. 6.6)	L/D (Eq. 6.5)
10	14.9 ± 0.05	1.39 ± 0.01	2.74 ± 0.04	3.63 ± 0.01
15	20.9 ± 0.04	1.91 ± 0.01	2.96 ± 0.02	4.84 ± 0.01
20	26.0 ± 0.06	2.15 ± 0.01	3.34 ± 0.02	5.79 ± 0.01
25	30.9 ± 0.08	2.52 ± 0.01	3.50 ± 0.02	6.71 ± 0.01
30	36.3 ± 0.05	2.81 ± 0.01	4.00 ± 0.03	7.63 ± 0.01
35	41.2 ± 0.14	3.15 ± 0.02	4.27 ± 0.02	8.48 ± 0.02
40	46.8 ± 0.15	3.51 ± 0.03	4.76 ± 0.04	9.40 ± 0.02
45	51.1 ± 0.17	3.82 ± 0.03	4.91 ± 0.05	10.1 ± 0.02
50	56.8 ± 0.21	4.20 ± 0.04	5.46 ± 0.04	11.0 ± 0.03
70	76.7 ± 0.14	6.24 ± 0.05	7.82 ± 0.03	13.9 ± 0.02

Table 6.3: Forcing conditions at $J = 10$ with matching root-mean-squared velocity perturbation at $U'_{j,rms} = 1.7$ m/s ($1.70 \leq U'_{j,rms} \leq 1.71$ m/s) among all forcing conditions. Actual duty cycles α_{actual}, as well as three stroke ratios L/D evaluated by the present method in Equation (6.7) (third column), Equation (6.6) with the simplified relation (fourth column) and Equation (6.5) with inclusion of the mean jet velocity (fifth column). There is a 95 % confidence interval for input duty cycles α_{input}.

α_{input} (%)	α_{actual} (%)	L/D (Eq. 6.7)	L/D (Eq. 6.6)	L/D (Eq. 6.5)
10	14.7 ± 0.10	1.33 ± 0.01	2.80 ± 0.07	3.61 ± 0.03
15	–	–	–	–
20	25.9 ± 0.08	2.09 ± 0.02	3.33 ± 0.04	5.79 ± 0.01
25	–	–	–	–
30	36.2 ± 0.08	2.75 ± 0.01	3.92 ± 0.04	7.63 ± 0.01
35	41.2 ± 0.12	3.08 ± 0.02	4.18 ± 0.03	8.48 ± 0.02
40	46.8 ± 0.16	3.41 ± 0.03	4.65 ± 0.06	9.41 ± 0.02
45	51.2 ± 0.19	3.71 ± 0.03	4.98 ± 0.04	10.1 ± 0.03
50	56.9 ± 0.24	4.16 ± 0.04	5.40 ± 0.05	11.0 ± 0.03
70	76.7 ± 0.20	6.16 ± 0.04	7.61 ± 0.04	13.9 ± 0.02

Table 6.4: Forcing conditions at $J = 5$ with matching root-mean-squared velocity perturbation at $U'_{j,rms} = 1.7$ m/s ($1.70 \leq U'_{j,rms} \leq 1.71$ m/s) among all forcing conditions. Actual duty cycles α_{actual}, as well as three stroke ratios L/D evaluated by the present method in Equation (6.7) (third column), Equation (6.6) with the simplified relation (fourth column) and Equation (6.5) with inclusion of the mean jet velocity (fifth column). There is a 95 % confidence interval for input duty cycles α_{input}.

α_{input} (%)	α_{actual} (%)	L/D (Eq. 6.7)	L/D (Eq. 6.6)	L/D (Eq. 6.5)
10	15.0 ± 0.07	1.38 ± 0.01	2.72 ± 0.04	3.65 ± 0.02
15	21.2 ± 0.07	1.87 ± 0.02	2.98 ± 0.03	4.87 ± 0.02
20	26.0 ± 0.09	2.10 ± 0.01	3.35 ± 0.03	5.79 ± 0.02
25	31.0 ± 0.12	2.45 ± 0.01	3.44 ± 0.02	6.71 ± 0.02
30	36.2 ± 0.09	2.72 ± 0.02	3.89 ± 0.04	7.63 ± 0.02
35	41.1 ± 0.14	3.04 ± 0.02	4.12 ± 0.03	8.47 ± 0.03
40	46.7 ± 0.17	3.37 ± 0.03	4.57 ± 0.04	9.37 ± 0.03
45	51.2 ± 0.18	3.69 ± 0.04	4.87 ± 0.03	10.1 ± 0.03
50	56.8 ± 0.25	4.07 ± 0.06	5.26 ± 0.05	11.0 ± 0.04
70	78.3 ± 0.77	6.22 ± 0.07	7.82 ± 0.14	14.0 ± 0.08

6.3 Structural Characteristics for the JICF

Structural characteristics of the JICF exposed to single-pulse square wave jet forcing is explored at four different J values: J = 41, 20, 10 and 5. The upstream shear layer has been determined for the flush nozzle to be convectively unstable at J = 41 and 20, and absolutely unstable at $J = 10$ and 5, although $J = 10$ is near the critical transition between the convective and absolute instability (Megerian et al., 2007; Davitian et al., 2010a). This section only shows results under single-pulse square wave forcing at $U'_{j,rms} = 1.7$ m/s (the same velocity perturbation explored in Davitian et al. (2010b) and in sinusoidal excitation in Chapter 5) approximately 26 % of the mean jet velocity at the exit plane U_j. PLIF data have been taken for a range of values, however, $1.0 \leq U'_{j,rms} \leq 3.0$ m/s, and these results are given in Appendix C. RMS velocity perturbation $U'_{j,rms}$ is matched among different forcing conditions to achieve effectively the same level of forcing (net impulse), but with variable duty cycles, the range of stroke ratios can vary by a factor of 3 or more (see Tables 6.1-6.4).

As in the study of sine wave forcing, instantaneous centerplane ($y = 0$ plane) and mean cross-sectional (an ensemble of 500 instantaneous images) PLIF images at x/D = 2.5, 5.5 and 10.5 are explored primarily. As mentioned in Section 6.1, forcing frequency f_f is fixed at f_f = 100 Hz, while a duty cycle α and hence stroke ratio L/D is systematically varied, as tabulated in Tables 6.1 to 6.4. For comparison, results under sine wave forcing as well as single-pulse square wave forcing without control are shown here as well with matching $U'_{j,rms}$ at 1.7 m/s.

Figure 6.7 shows instantaneous centerplane images for the equidensity flush nozzle-injected JICF at J = 41 with matching RMS velocity perturbation at $U'_{j,rms}$ = 1.7 m/s among all forcing conditions. Note that instantaneous centerplane images in this chapter are logarithmically scaled in concentration to easily focus on deeply-penetrating vortical flow structures, which are observed at $J = 5 - 20$. As one can observe in Figure 6.7, the jet generally bifurcates at low L/D, but as L/D increases, the jet itself widely spreads and deeply penetrates due to the strong pulsation (Figure 6.7(a)). Overall, though, there are few structural differences among all forcing conditions under square wave forcing with con-

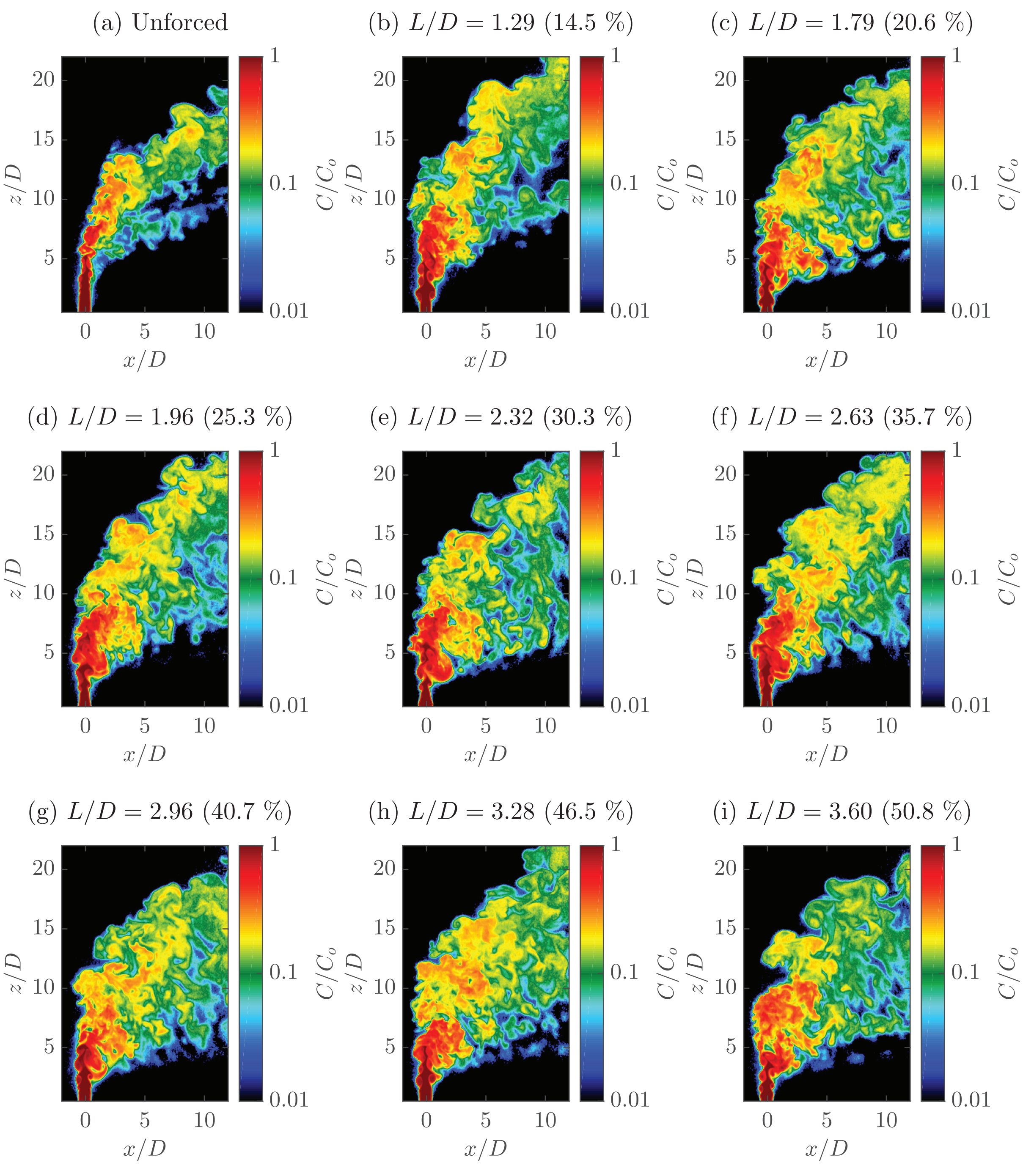

Figure 6.7: For more figures and caption see next page.

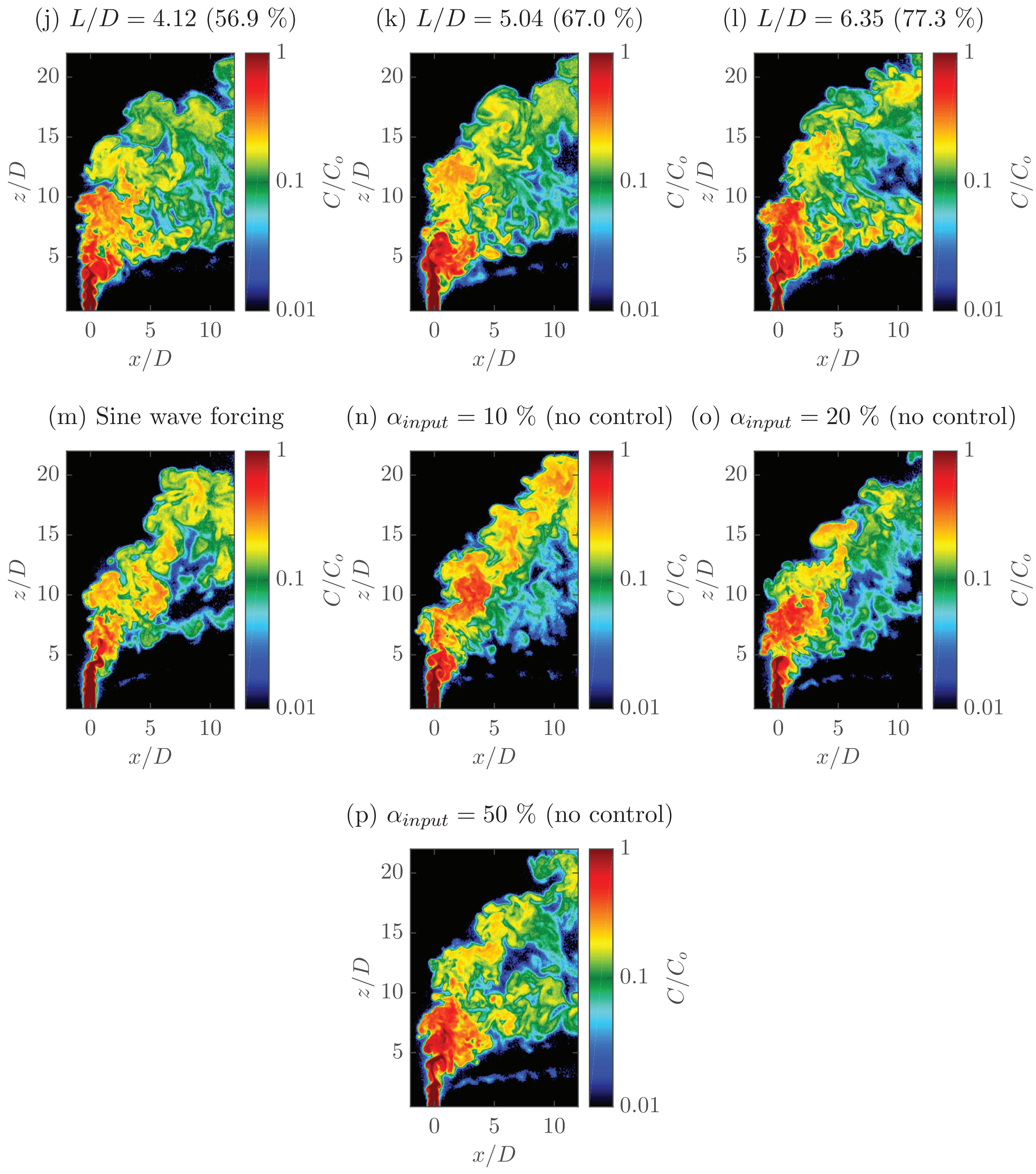

Figure 6.7: Instantaneous centerplane PLIF images in the $x/D - z/D$ plane for the equidensity flush nozzle-injected JICF at $J = 41$ for (a) the unforced case, (b)-(l) the forced cases under single-pulse square wave forcing with control at stroke ratios ranging $L/D = 1.29 - 6.35$ (actual duty cycle α_{actual} (%) in parentheses), (m) under sine wave forcing, as well as (n)-(p) under single-pulse square wave forcing without control at $\alpha_{input} = 10 - 50$ %. All forcing conditions are at $f_f = 100$ Hz and $U'_{j,rms} = 1.7$ m/s (approximately 26 % of U_j).

trol (Figures 6.7(b)-(l)), and there are few instances where there are distinct vortex “puffs” produced by such forcing. These similarities among forcing conditions may be related to the fact that the convectively unstable JICF is easily affected by external forcing as described in the previous section. The sensitivity to external perturbations contributes to the significant structural alteration under any forcing conditions shown here for $J = 41$, seen previously in Davitian et al. (2010a) as well as earlier studies. Additionally, recall Figure 5.6 associated with instantaneous centerplane images at $J = 41$ under sine wave forcing; this figure indicates the significant effect of varying forcing frequency f_f on the jet structures, even for convectively unstable conditions at higher J values. From this perspective, the relatively low forcing frequency of $f_f = 100$ Hz might not generate distinct differences among the range of forcing conditions in Figure 6.7. Despite the small structural differences, some difference is still observed in Figure 6.7, especially between $L/D = 1.29$ and 6.35, the minimum and maximum L/D values explored in this study at $J = 41$. At $L/D = 1.29$, possibly because of the relatively small duty cycle, corresponding to a short temporal pulse width τ, the jet spread is not as great as for other cases but its penetration is quite high. At $L/D = 6.35$, on the other hand, due to the longer temporal pulse width, the longer relative pulsation of fluid causes the jet to more clearly bifurcate and spread as compared with the unforced case. Fairly strong jet bifurcation also appears at $L/D = 5.04$.

Figures 6.7(m)-(p) show instantaneous centerplane images under sine wave forcing and square wave forcing without control at $U'_{j,rms} = 1.7$ m/s as well. Note that sine wave forcing does not distinctively alter the jet structure in comparison with the unforced case with $f_f = 100$ Hz fairly far from f_o. This trend is consistent with the observation in Figure 5.6 at $U'_{j,rms} = 0.07$ m/s, although the RMS of velocity perturbation here is much higher. Also, square wave forcing without control has a lesser effect on the jet's structures, as well as jet spread and penetration, compared with those with control at the same input duty cycle ($\alpha_{input} = 10$ % for Figures 6.7(b) and (n), $\alpha_{input} = 20$ % for Figures 6.7(d) and (o), and $\alpha_{input} = 50$ % for Figures 6.7(j) and (p)). This centerplane observation suggests an improved effectiveness of the controlled square wave forcing and creation of more distinct pulses, although the convectively unstable JICF can be easily affected by any external forcing, in general, as seen in this figure.

Figure 6.8 shows mean cross-sectional PLIF images at the same flow and forcing conditions as in Figure 6.7 at three different downstream locations. First of all, note that all forced cases including sine and square wave forcing with/without control create more symmetric cross sections than in the unforced case, as shown in Figure 6.8(a). Such symmetrization can be achieved by this fairly strong external forcing ($U'_{j,rms} = 1.7$ m/s), even at a relatively low forcing frequency of $f_f = 100$ Hz. Also, as observed in the instantaneous centerplane images, cross sections under sine wave forcing as well as square wave forcing without control contain more uniform concentration profiles, particularly in the vertical direction z/D, as compared with the other forced cases due to less jet bifurcation. This is consistent with the fact that temporal square wave forms without control are more similar to sine waves than to square waves, e.g., as in Figure 6.5. In contrast, a less uniform concentration distribution in z/D direction is present in the mean cross-sectional structures under square wave forcing with control for all forcing conditions. This trend is more significant at a higher $L/D = 6.35$, likely due to the stronger jet bifurcation seen in the centerplane structural characteristics. Interestingly, all fairly strong forcing at $U'_{j,rms} = 1.7$ m/s shown here creates an elongated near-field ($x/D = 2.5$) cross-sectional structure in the z/D direction, without the typical round fluid distribution associated with counter-rotating vortex pair (CVP) evolution, as observed in the unforced case. This near-field forcing effect on jet structures contributes to the far-field structures, which do evolve into rounded highly-concentrated structures and a long tail, without the asymmetric CVP structures as in the unforced case. Hence overall, a structural exploration of the JICF at $J = 41$, both in centerplane and cross-sectional views, suggests that jet structures behave very similarly among all forcing conditions under single-pulse square wave forcing with control. There are only slight differences relevant to jet bifurcation at relatively higher L/D values, ranging from $L/D = 5.04 - 6.35$.

Next, the structural characteristics for JICF at a lowered J value are explored. Figure 6.9 represents the instantaneous centerplane images for the equidensity flush nozzle-injected JICF at $J = 20$ under square wave forcing with/without control as well as sine wave forcing. Again, the upstream shear layer is convectively unstable in this flow condition. Unlike

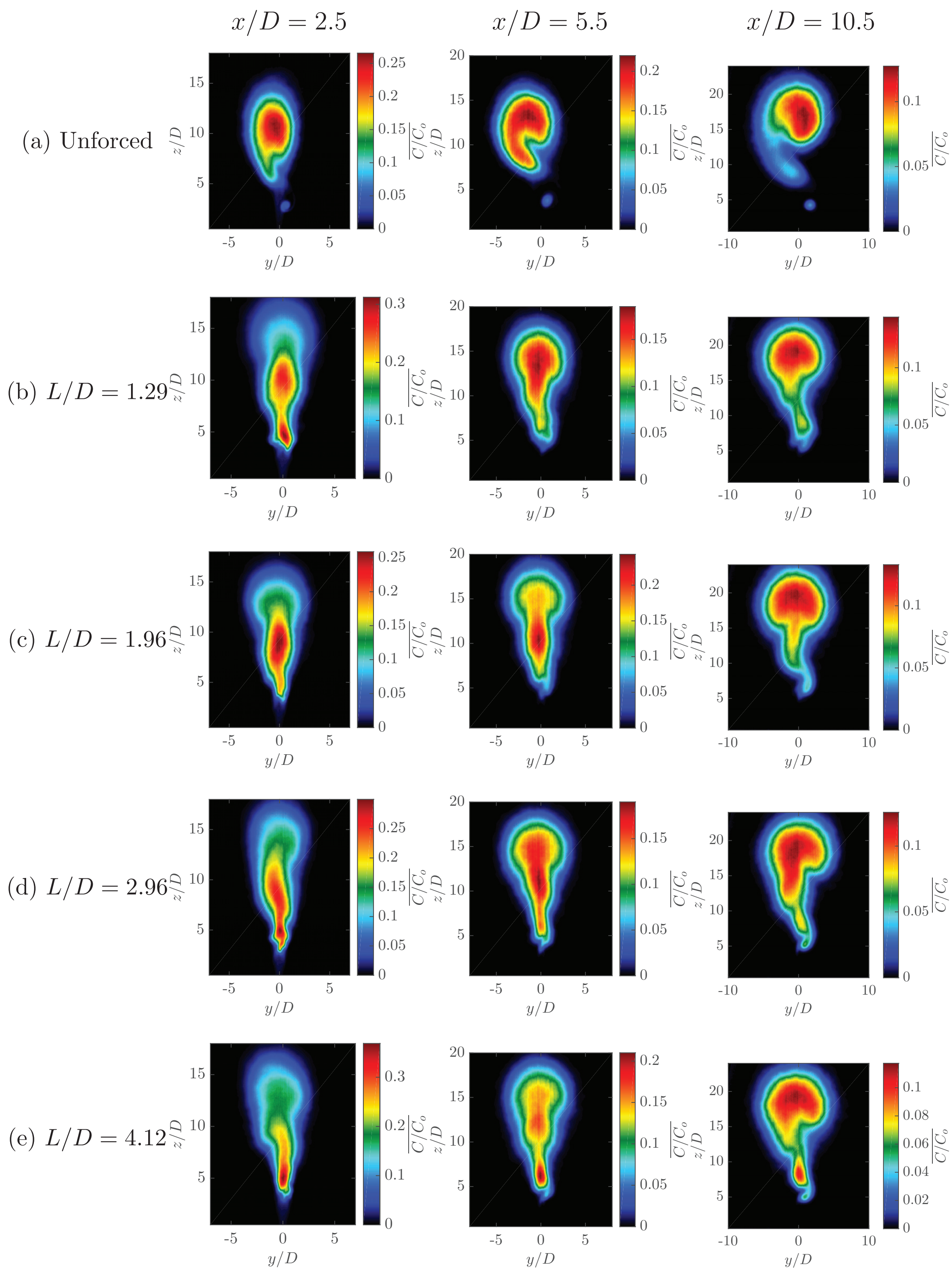

Figure 6.8: For more figures and caption see next page.

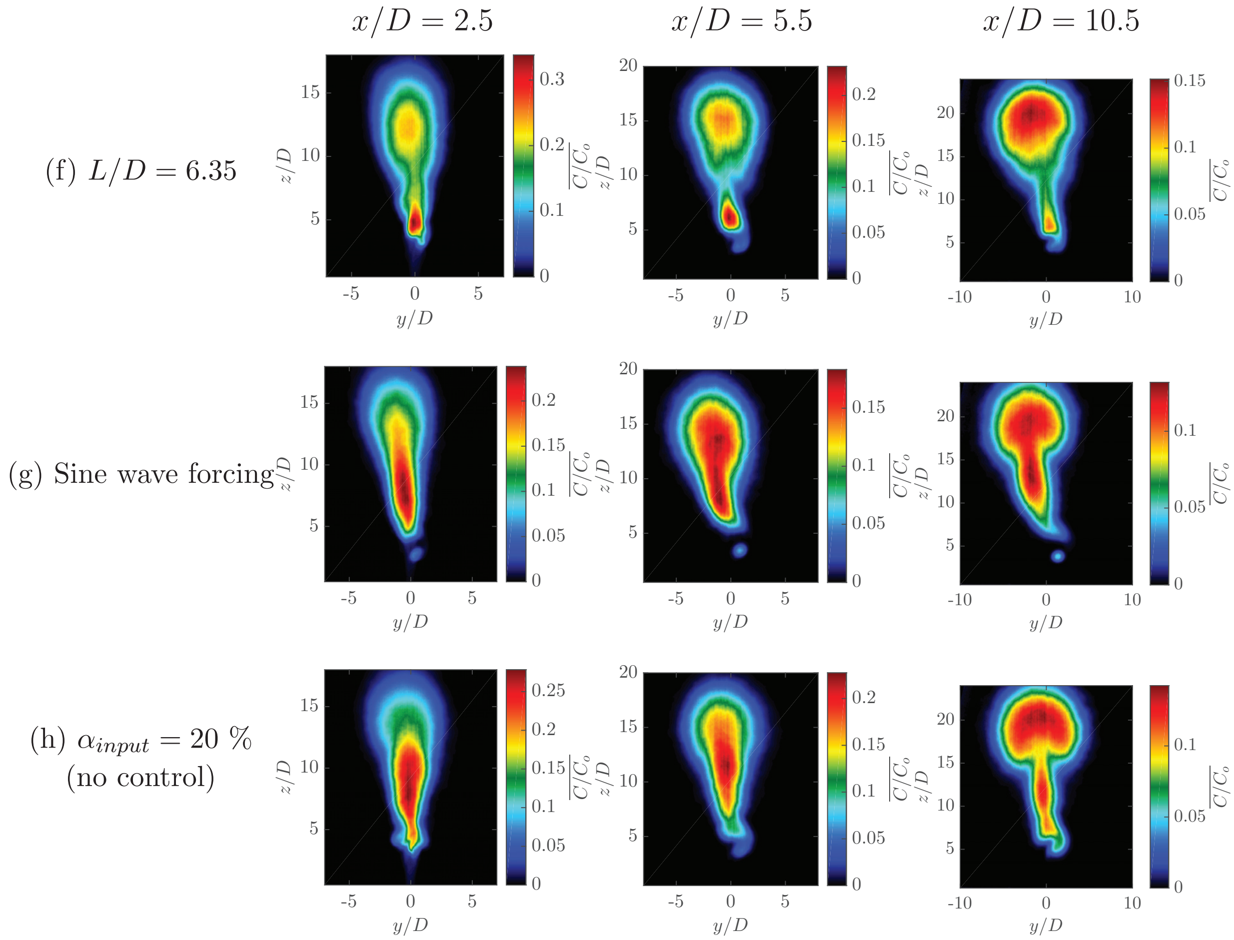

Figure 6.8: Mean cross-sectional PLIF images in the $y/D - z/D$ plane for the equidensity flush nozzle-injected JICF at $J = 41$ for (a) the unforced case, (b)-(f) the forced cases under single-pulse square wave forcing at stroke ratios ranging $L/D = 1.29 - 6.35$, (g) under sine wave forcing, as well as (h) under single-pulse square wave forcing without control at $\alpha_{input} = 20$ %. All forcing cases are at $f_f = 100$ Hz and $U'_{j,rms} = 1.7$ m/s (approximately 26 % of U_j).

the $J = 41$ case, deeply-penetrating puff-like vortical flow structures start to be observed, depending on stroke ratios L/D. The existence of vortical flow structures is assessed by visual inspection, that is, the vortical structures are judged to exist if the flow structures can be fairly frequently and consistently distinguished in multiple instantaneous images. An asterisk is indicated for stroke ratios L/D in Figure 6.9 when puffing vortical structures are determined to exist (e.g., $L/D = 1.39^*$ in Figure 6.9(b)). Note that in many cases, the vortical structures penetrate upstream, rather than vertically, in the lab reference frame.

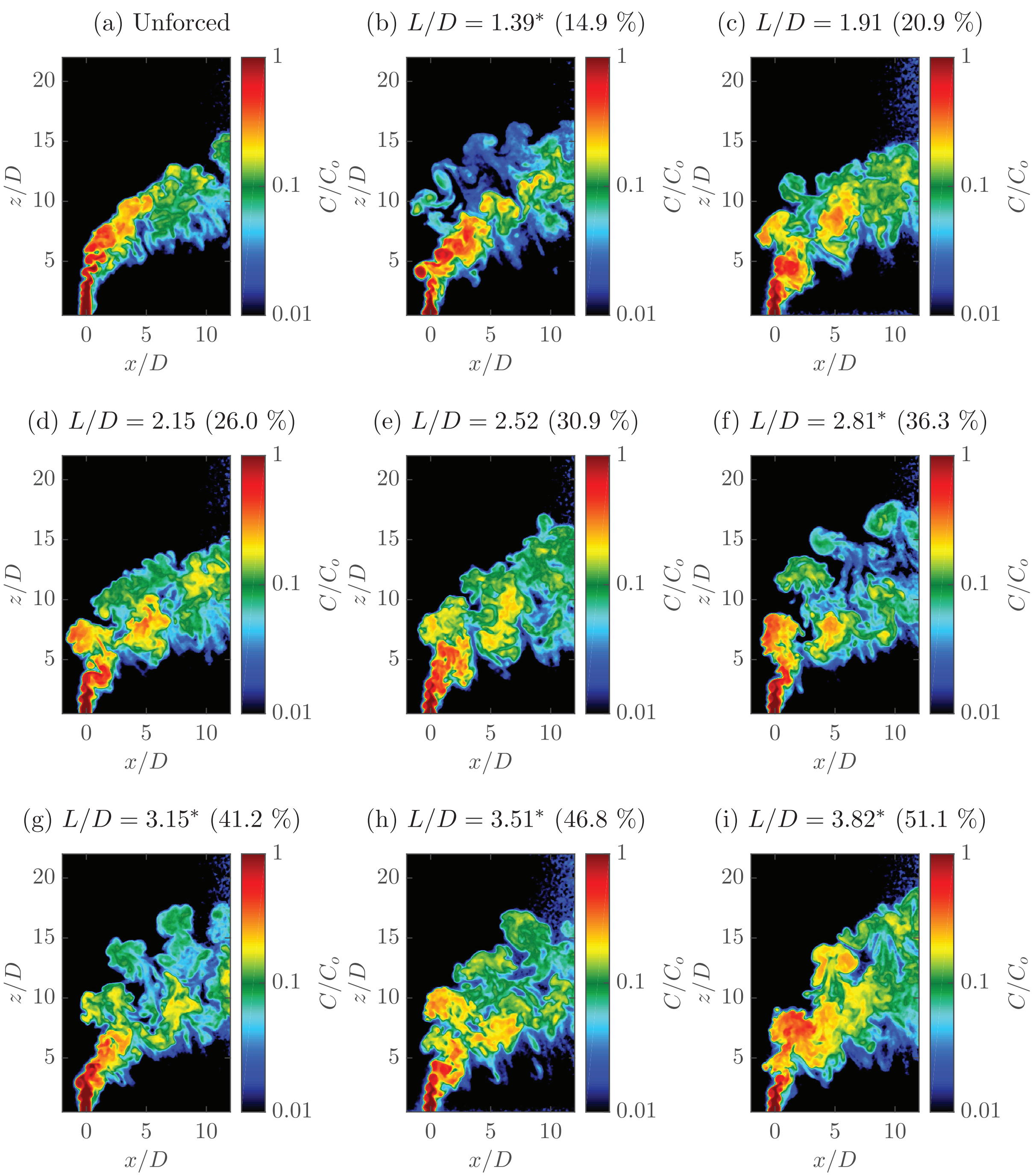

Figure 6.9: For more figures and caption see next page.

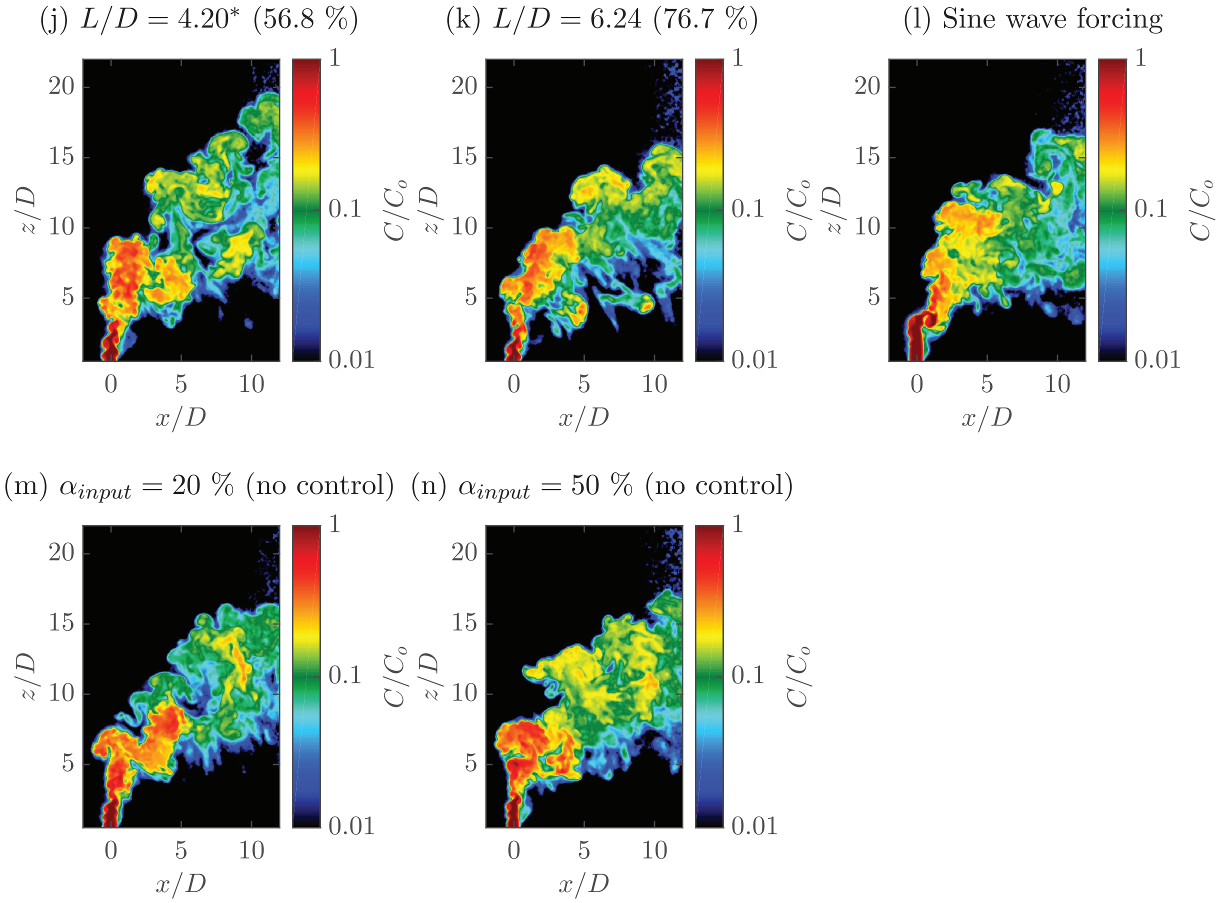

Figure 6.9: Instantaneous centerplane PLIF images in the $x/D - z/D$ plane for the equidensity flush nozzle-injected JICF at $J = 20$ for (a) the unforced case, (b)-(k) the forced cases under single-pulse square wave forcing with control at stroke ratios ranging $L/D = 1.39 - 6.24$ (actual duty cycle α_{actual} (%) in parentheses), (l) under sine wave forcing, as well as (m)-(n) under single-pulse square wave forcing without control at $\alpha_{input} = 20 - 50$ %. All forcing conditions are at $f_f = 100$ Hz and $U'_{j,rms} = 1.7$ m/s (approximately 26 % of U_j). Stroke ratio L/D with asterisk corresponds to the existence of deeply-penetrating puff-like vortical flow structures.

For the forced condition at $L/D = 1.39$, deeply-penetrating, puff-like vortical structures are clearly observed. Interestingly, such flow structures disappear as L/D increases in the range $1.91 \leq L/D \leq 2.52$, and then begin to be observed again as L/D increases around $2.81 \leq L/D \leq 4.20$. At even larger stroke ratios, $L/D = 6.24$, the vortical flow structures are not observed again and jet penetration is quite low. For the range of $1.91 \leq L/D \leq 2.52$, the jet is strongly disturbed by pulsations, resulting in wider jet penetration than the unforced case, even though no deeply-penetrating vortical structures are observed. For $2.81 \leq L/D \leq 4.20$, larger-scale vortical structures with higher concentration fluid inside the flow structures are created, as compared with the $L/D = 1.39$ case. This difference could possibly be caused by the longer temporal pulse width for larger L/D. The range of stroke ratio of $L/D = 2.81 - 4.20$ is closer to the universal time scale for vortex ring formation $L/D \approx 4$ as suggested by Gharib et al. (1998) or the optimal stroke ratio for the best jet spread and penetration as reported in several previous studies (Shapiro et al., 2006; Davitian et al., 2010b), although the definition of stroke ratio is slightly different among these earlier studies. Once L/D becomes higher than this range, the vortical structures disappear again. However, for $L/D = 6.24$, vortical flow structures are created which convect downward toward the test section floor in the wake region. Such oppositely convecting vortical structures are possibly induced by the short temporal interval between relatively long temporal pulses, which may act similarly to short temporal pulses with a long temporal interval at smaller L/D values. These vortical flow structures are not present under sine wave forcing and square wave forcing without control, even with the same input duty cycle as the square wave forcing with control. This structural difference clearly suggests the importance of the feedback control to be able to create clearly defined waveforms and significantly alter jet structural characteristics.

Mean cross-sectional images at the same forcing conditions are also investigated for $J = 20$, shown in Figure 6.10. Interestingly, mean cross-sectional structures at the far downstream location of $x/D = 10.5$ remain asymmetric for square wave forcing with control at relatively low stroke ratios $L/D = 1.39$ and 2.15, as well as sine and square wave forcing without control, although they are more symmetric than the unforced case, as shown in Figure 6.10(a). Interestingly, the asymmetric orientation of the unforced JICF for $J = 20$ in Figure 6.10(a) is opposite to that for $J = 41$ in Figure 6.8(a). Asymmetric cross-sectional structures, even under square wave forcing with control, were not seen in the $J = 41$ cases in Figure 6.8, suggesting a lesser sensitivity of the $J = 20$ JICF to external forcing than for the $J = 41$ cases. Additionally, this structural characteristic also suggests that forcing at a fairly small L/D seems to have an effect on the near-field jet's structures but that this does not persist to the far-field structures. Forcing at relatively higher L/D stroke ratios affects both near-

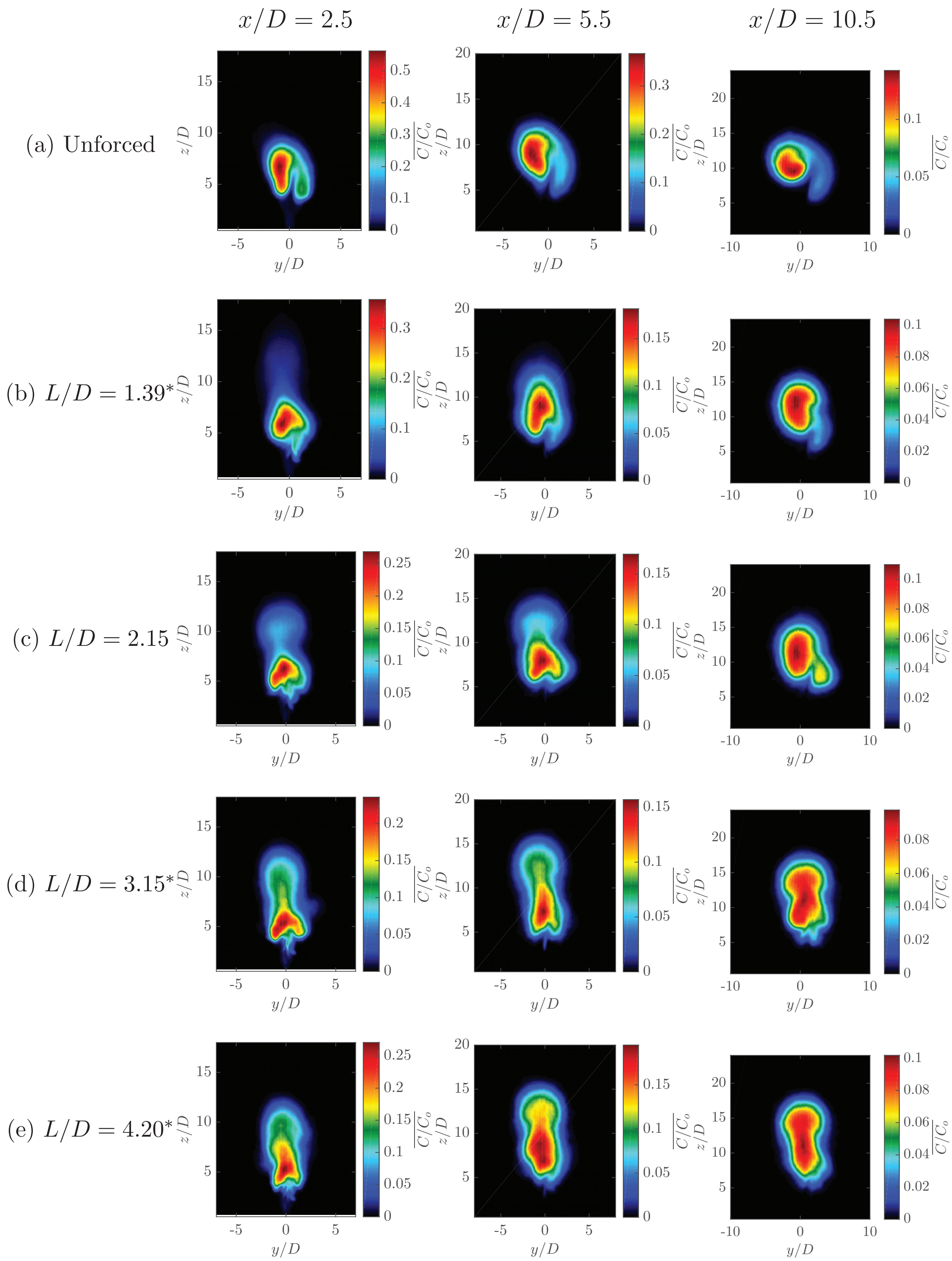

Figure 6.10: For more figures and caption see next page.

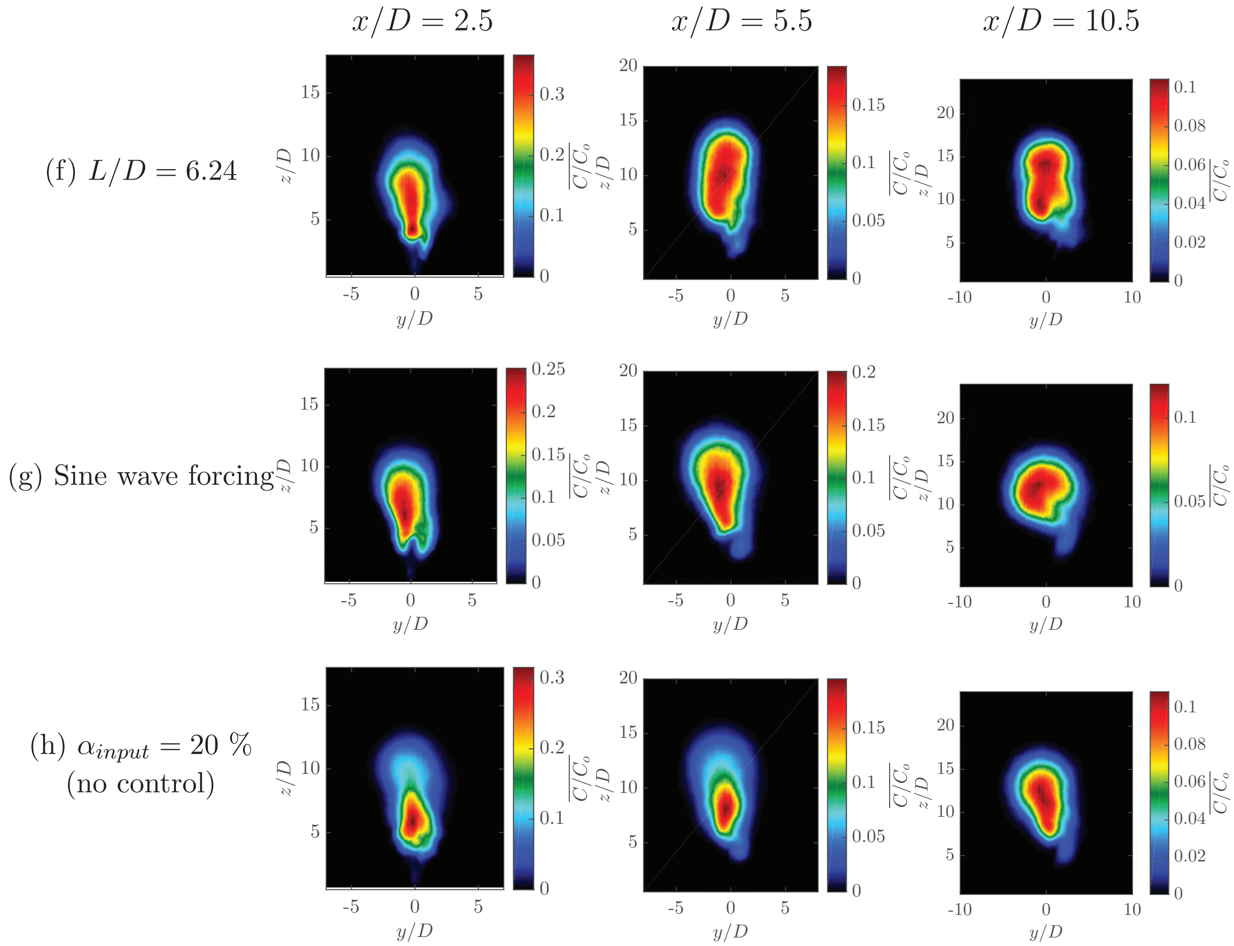

Figure 6.10: Mean cross-sectional PLIF images in the $y/D - z/D$ plane for the equidensity flush nozzle-injected JICF at $J = 20$ for (a) the unforced case, (b)-(f) the forced cases under single-pulse square wave forcing at stroke ratios ranging $L/D = 1.39 - 6.24$, (g) under sine wave forcing, as well as (h) under single-pulse square wave forcing without control at $\alpha_{input} = 20$ %. All forcing cases are at $f_f = 100$ Hz and $U'_{j,rms} = 1.7$ m/s (approximately 26 % of U_j). Stroke ratio L/D with asterisk corresponds to the existence of deeply-penetrating puff-like vortical flow structures observed in instantaneous centerplane images.

and far-field jet's structures, in contrast.

Regarding the deeply-penetrating vortical structures, there are interesting structural characteristics in the cross-sectional view. At $L/D = 1.39$, deeply-penetrating vortical flow structures containing relatively low jet fluid concentrations are observed, particularly in the nearfield at $x/D = 2.5$, in both Figures 6.9(b) and 6.10(b). Similarly, for $3.15 \leq L/D \leq 4.20$

in Figures 6.10(d)-(e), the vortical structures are observed only in the nearfield, although these flow structures contain higher concentrations than for the $L/D = 1.39$ case, consistent with the instantaneous centerplane structures in Figures 6.9(g) and 6.9(j). These concentration differences inside the vortical structures with varying L/D are possibly caused by the variable temporal pulse width of square wave forcing inserting jet fluid at specific times within the square wave cycle. For example, a relatively short duty cycle of 10 % generates mostly lower jet velocity pulsation for 90 % of the period T, with a short (10 % of period T) but higher jet velocity during the rest of the cycle, creating less-concentrated penetrating vortex rings.

Therefore, from structural exploration for the $J = 20$ cases in both centerplane and cross-sectional views, deeply-penetrating vortical structures are seen to contain higher fluid concentrations as L/D increases, and cross sections become more symmetric as compared with the unforced case and with forced cases at relatively low L/D. In addition, vortical flow structures from the JICF propagating upward and upstream are observed to be created at L/D values generally consistent with the range for maximum penetration observed by Shapiro et al. (2006) ($L/D \approx 1.7 - 2.0 and 3.2 - 4.2$) and Davitian et al. (2010b) ($L/D \approx 3.1 - 3.7$). Note that these prior experimental studies utilized different flow conditions, e.g, jet Reynolds number, jet-to-crossflow velocity ratio, and/or RMS velocity perturbation, as well as different definitions of stroke ratio. In the present study, the strongest vortical structures are observed at two different stroke ratio regimes: (1) a relatively low $L/D = 1.39$, which is fairly far from the universal time scale for the vortex ring formation of $L/D \approx 4$ (Gharib et al., 1998) but somewhat close to the L/D range suggested by Shapiro et al. (2006), and (2) $L/D \approx 2.81 - 4.20$, relatively close to the L/D range observed in previous studies.

The convectively unstable jets in crossflow at $J = 41$ and 20 are easily affected by square wave forcing with and even without control, as well as sine wave forcing, although deeply-penetrating vortical structures are observed only at $J = 20$ and not at $J = 41$, even with the same RMS of the velocity perturbation. Now, structural exploration based on instantaneous centerplane and mean cross-sectional images is performed for the equidensity flush nozzle-injected absolutely unstable JICF at $J = 10$, close to the critical J value for

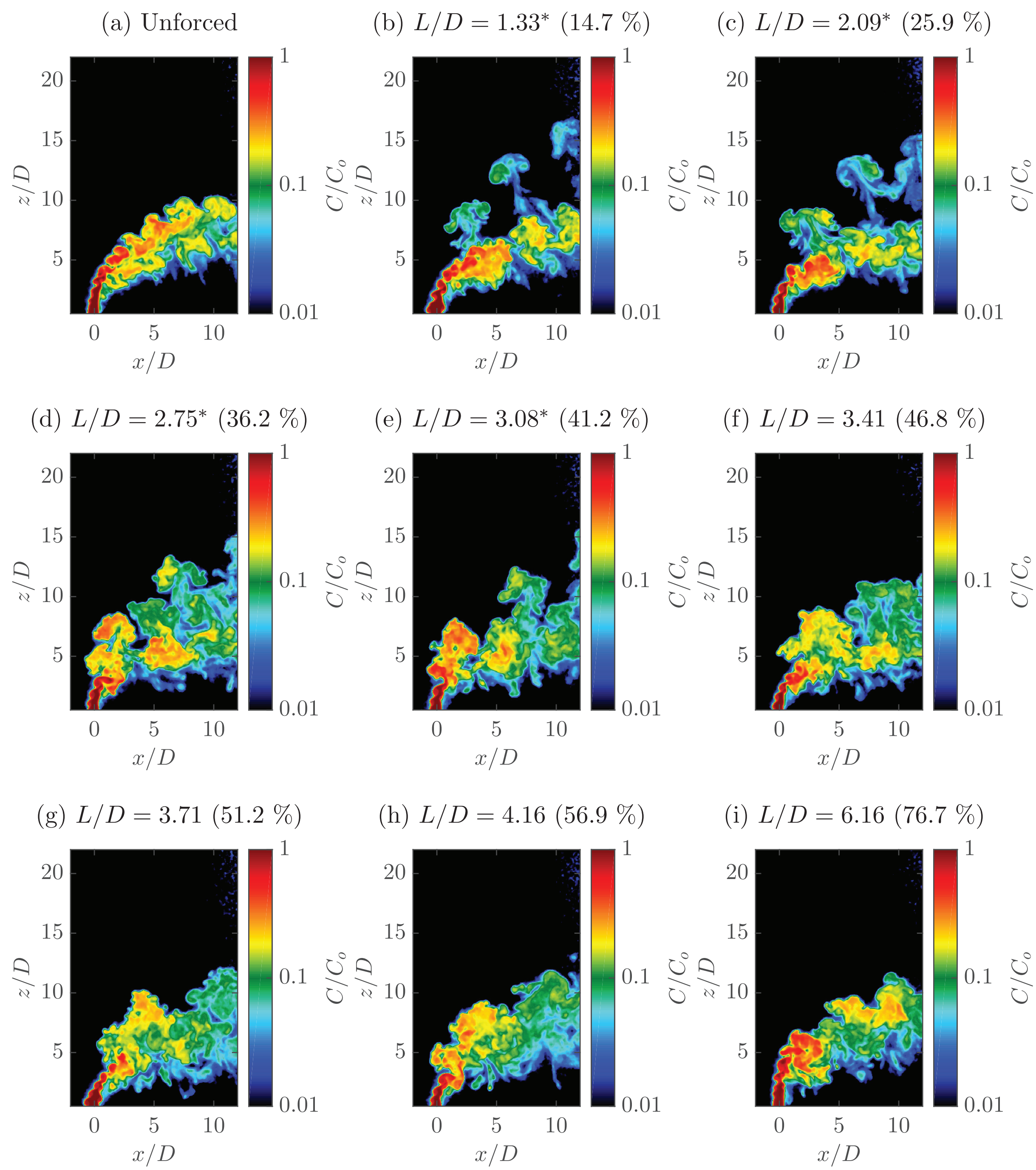

Figure 6.11: For more figures and caption see next page.

(j) Sine wave forcing (k) $\alpha_{input} = 20$ % (no control) (l) $\alpha_{input} = 50$ % (no control)

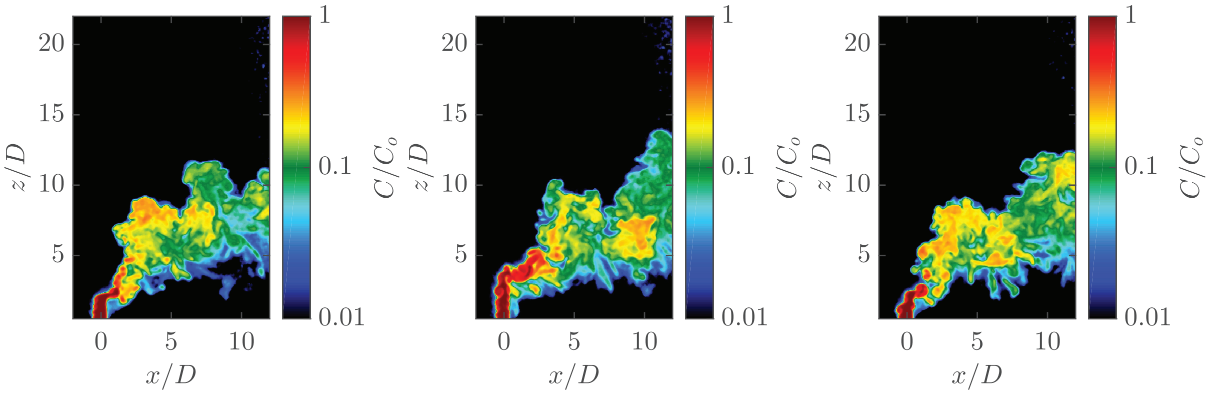

Figure 6.11: Instantaneous centerplane PLIF images in the $x/D - z/D$ plane for the equidensity flush nozzle-injected JICF at $J = 10$ for (a) the unforced case, (b)-(i) the forced cases under single-pulse square wave forcing with control at stroke ratios ranging $L/D = 1.33 - 6.16$ (actual duty cycle α_{actual} (%) in parentheses), (j) under sine wave forcing, as well as (k)-(l) under single-pulse square wave forcing without control at $\alpha_{input} = 20 - 50$ %. All forcing conditions are at $f_f = 100$ Hz and $U'_{j,rms} = 1.7$ m/s (approximately 26 % of U_j). Stroke ratio L/D with asterisk corresponds to the existence of deeply-penetrating puff-like vortical flow structures.

transition from convective to absolute instability (Megerian et al., 2007). Results for these centerplane and cross-sectional images are shown in Figures 6.11 and 6.12, respectively. In the centerplane view, deeply-penetrating puff-like vortical structures are observed at L/D in the range $1.33 \leq L/D \leq 3.08$, lower than the universal stroke ratio $L/D \approx 4$. Within this stroke ratio range, similar structural characteristics can be recognized to those at $J = 20$, depending on L/D. The vortical flow structures are first relatively small and contain lower jet concentrations at fairly low L/D, although very distinct vortex structures are produced at low L/D, e.g., $L/D = 1.33$ in Figure 6.11(b). As L/D increases, the vortical structures begin to become larger or more strongly interact with the jet, as well as to contain more jet fluid. Once L/D exceeds a certain critical value around 3.41 in Figure 6.11(f), vortical structures disappear or are completely merged into the jet due to the temporally long pulsations, rendering pulsed fluid to be less distinguished from the non-pulsed "off" portion of the cycle. At $J = 10$, distinct vortical flow structures are observed at a maximum stroke ratio of $L/D = 3.08$, which is lower than $L/D = 4.20$ at $J = 20$. Because the minimum stroke ratio to create the vortical flow structures is approximately the same for both J cases (1.33 for $J = 10$ and 1.39 for $J = 20$), the lowered maximum stroke ratio for the vortical flow structures for $J = 10$ suggests that the range of impactful L/D values is narrower for $J = 10$ than for $J = 20$. Hence, the $J = 10$ JICF is less affected by or responsive to external forcing than the $J = 20$ case, most likely associated with the nature of the instability of the upstream shear layer or the stronger effects of crossflow. As expected from the results at $J = 20$, sine and square wave forcing without control do not create strong vortical structures for $J = 10$, either, yet even forcing without control does disturb the jet structure in general.

These structural trends are clearly seen in cross-sectional views for the $J = 10$ case as well, shown in Figure 6.12. The cross-sectional structure for the unforced case is more symmetric and more similar to the classic CVP shape than that for the unforced cases at $J = 41$ and 20, although the asymmetry is still detectable at all downstream locations $x/D = 2.5$, 5.5 and 10.5. Again, as with the previous case at $J = 20$, an asymmetric cross-section under single-pulse square wave forcing with control only occurs at relatively low stroke ratios of $L/D = 1.33$ and 2.09. As stroke ratio increases, cross-sectional structures become more symmetric in the mid-to-farfields ($x/D = 5.5$ and 10.5), but are slightly asymmetric in the near-field cross-sectional structures at $x/D = 2.5$. Such trends may demonstrate that square wave forcing can yield symmetrically evolved cross-sectional structures in the mid-to-farfield region but may create asymmetric cross sections in the relative nearfield. Interestingly, sine and square wave forcing without control create fairly symmetric cross sections at mid-to-farfield locations ($x/D = 5.5$ and 10.5) and even at $x/D = 2.5$ have some degree of cross-sectional symmetry.

Finally, Figures 6.13 and 6.14 represent the instantaneous centerplane and mean cross-sectional PLIF images, respectively, for the equidensity flush nozzle-injected JICF at $J = 5$, corresponding to the absolutely unstable upstream shear layer. For the absolutely unstable JICF at $J = 5$, deeply penetrating vortical flow structures are observed in instantaneous centerplane images with an even narrower range of stroke ratios, ranging from $1.38 \leq L/D \leq 2.10$ (see Figure 6.13) as compared with that at $J = 20$ and 10. As mentioned for the $J = 10$ case, this narrower range of stroke ratios creating strong vortical flow structures may pertain

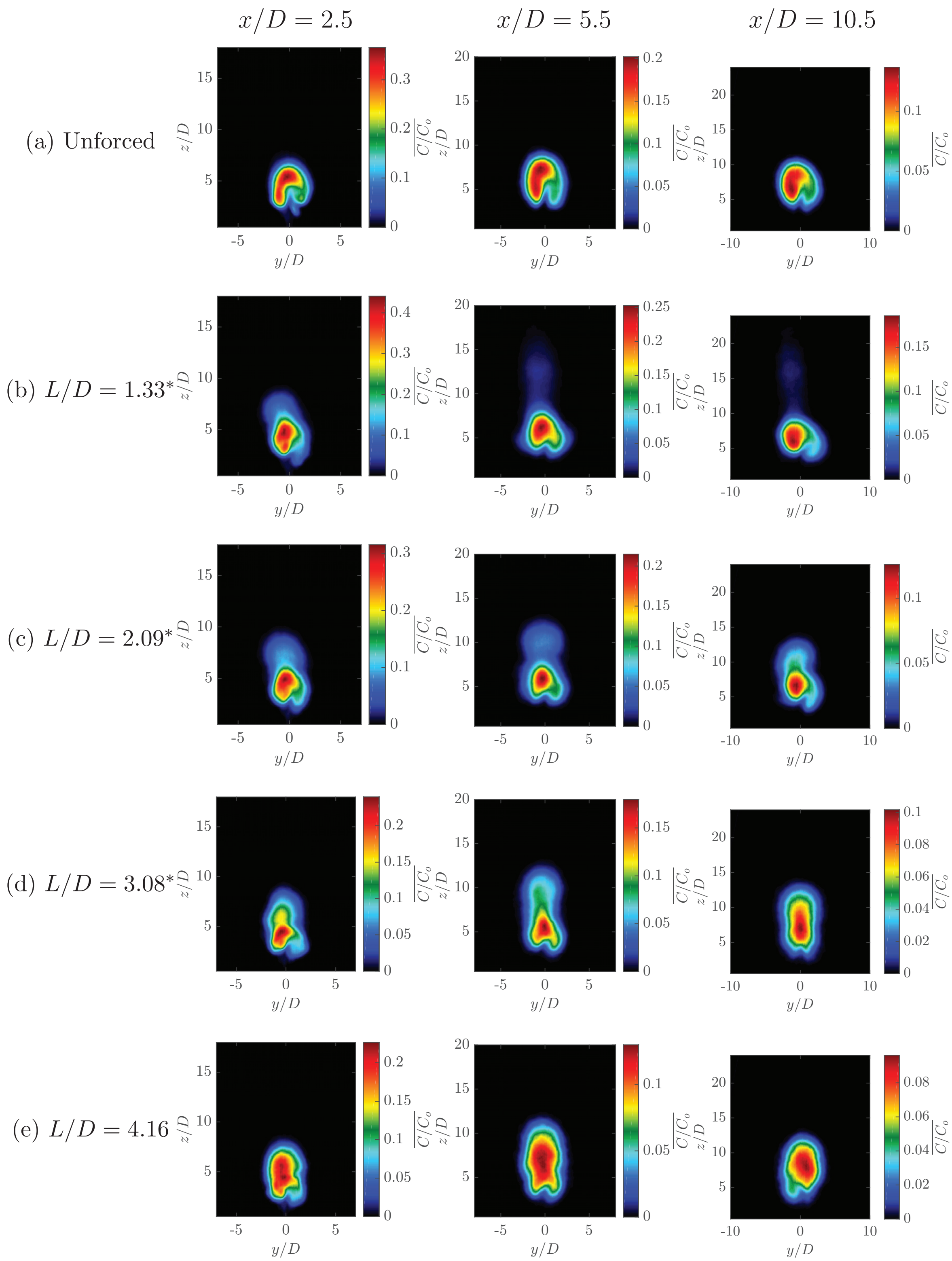

Figure 6.12: For more figures and caption see next page.

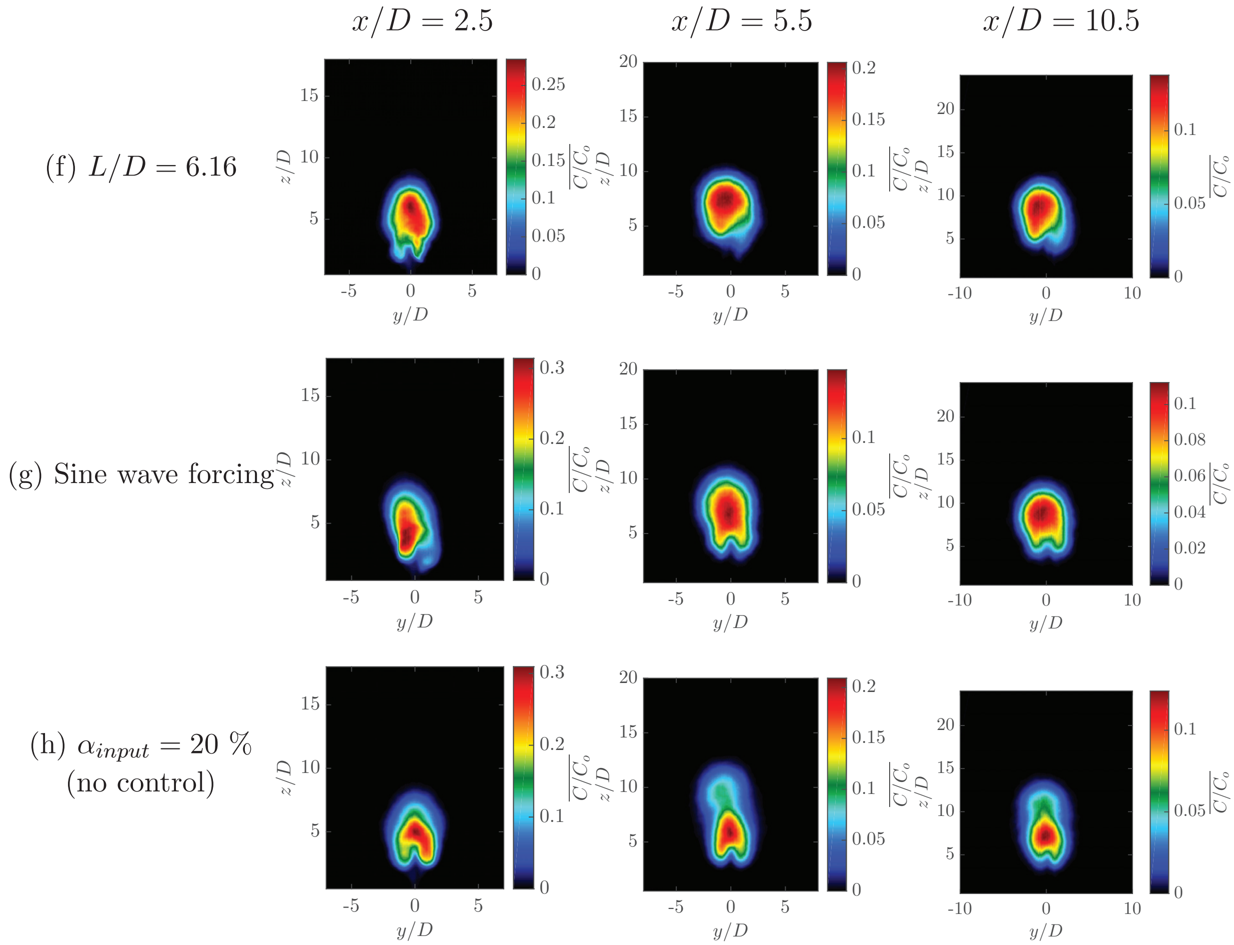

Figure 6.12: Mean cross-sectional PLIF images in the $y/D - z/D$ plane for the equidensity flush nozzle-injected JICF at $J = 10$ for (a) the unforced case, (b)-(f) the forced cases under single-pulse square wave forcing at stroke ratios ranging $L/D = 1.33 - 6.16$, (g) under sine wave forcing, as well as (h) under single-pulse square wave forcing without control at $\alpha_{input} = 20$ %. All forcing cases are at $f_f = 100$ Hz and $U'_{j,rms} = 1.7$ m/s (approximately 26 % of U_j). Stroke ratio L/D with asterisk corresponds to the existence of deeply-penetrating puff-like vortical flow structures observed in instantaneous centerplane images.

to the insensitivity of the absolutely unstable JICF to external forcing, as also suggested by Megerian et al. (2007) and Davitian et al. (2010a,b). Once the stroke ratio becomes larger than or equal to 2.45 for $J = 5$, there seem to be little centerplane structural differences among all forcing conditions, including sine wave forcing and square wave forcing without control. While these other forcing conditions do perturb the jet and produce large scale

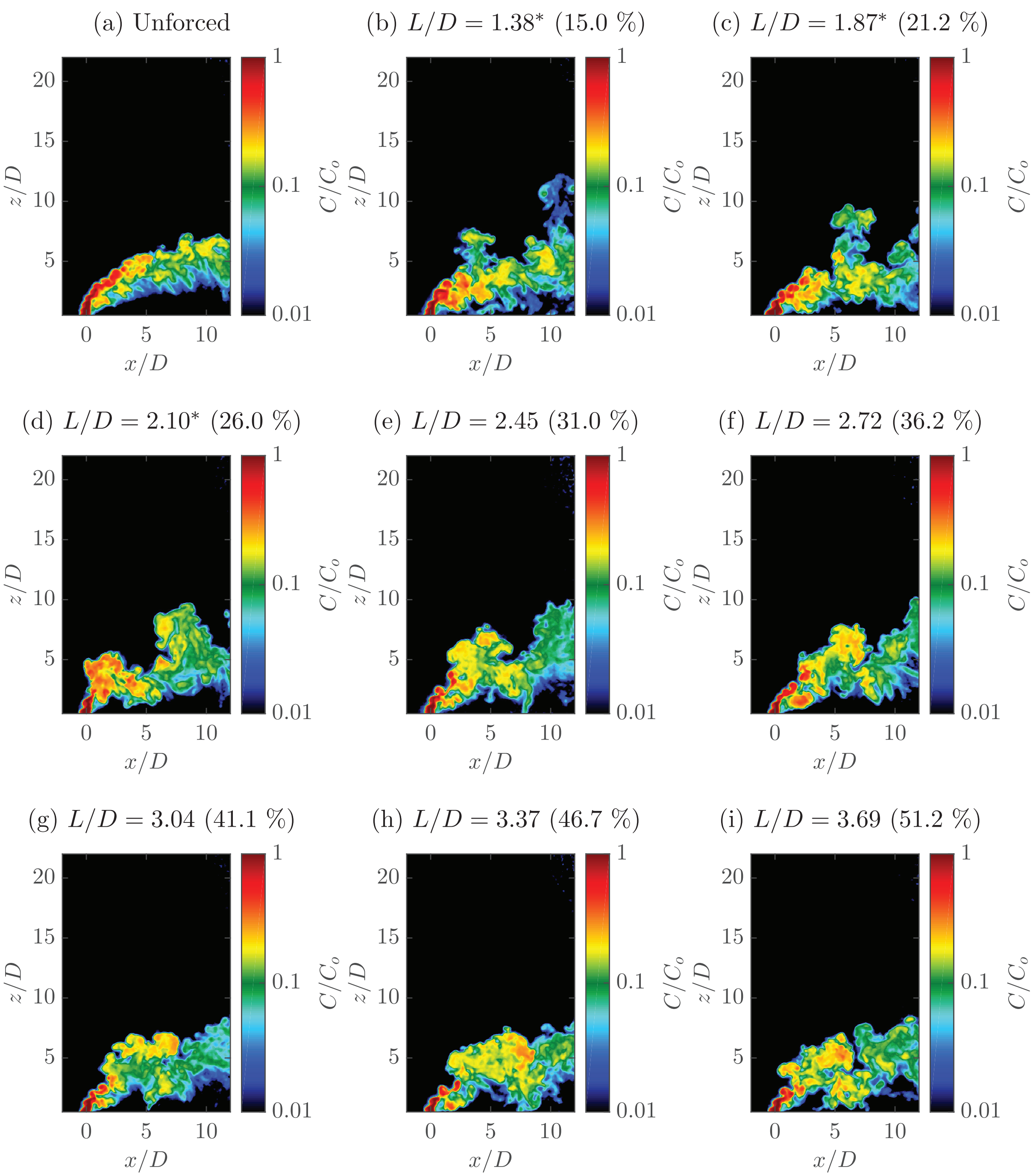

Figure 6.13: For more figures and caption see next page.

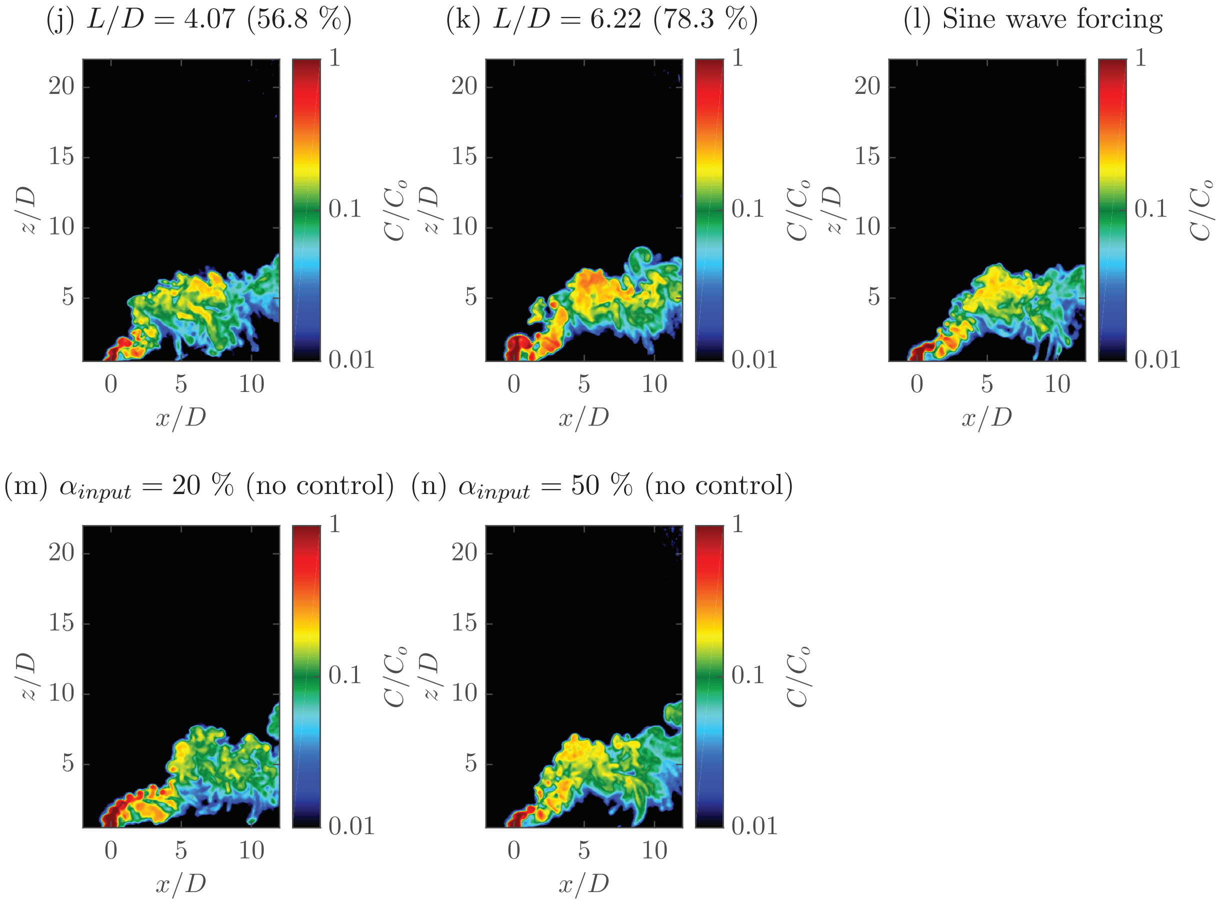

Figure 6.13: Instantaneous centerplane PLIF images in the $x/D - z/D$ plane for the equidensity flush nozzle-injected JICF at $J = 5$ for (a) the unforced case, (b)-(k) the forced cases under single-pulse square wave forcing with control at stroke ratios ranging $L/D = 1.38 - 6.22$ (actual duty cycle α_{actual} (%) in parentheses), (l) under sine wave forcing, as well as (m)-(n) under single-pulse square wave forcing without control at $\alpha_{input} = 20 - 50$ %. All forcing conditions are at $f_f = 100$ Hz and $U'_{j,rms} = 1.7$ m/s (approximately 26 % of U_j). Stroke ratio L/D with asterisk corresponds to the existence of deeply-penetrating puff-like vortical flow structures.

waviness in the jet, the results also indicate that the absolutely unstable JICF cannot be significantly affected even by square wave forcing with control. As seen previously, the vortical structures become larger and contain higher concentration as L/D increases from 1.38 to 2.10. It appears that the jet's centerplane structures qualitatively behave similarly at all J values explored in this study but with varied ranges of stroke ratio for the deeply-penetrating vortical structures.

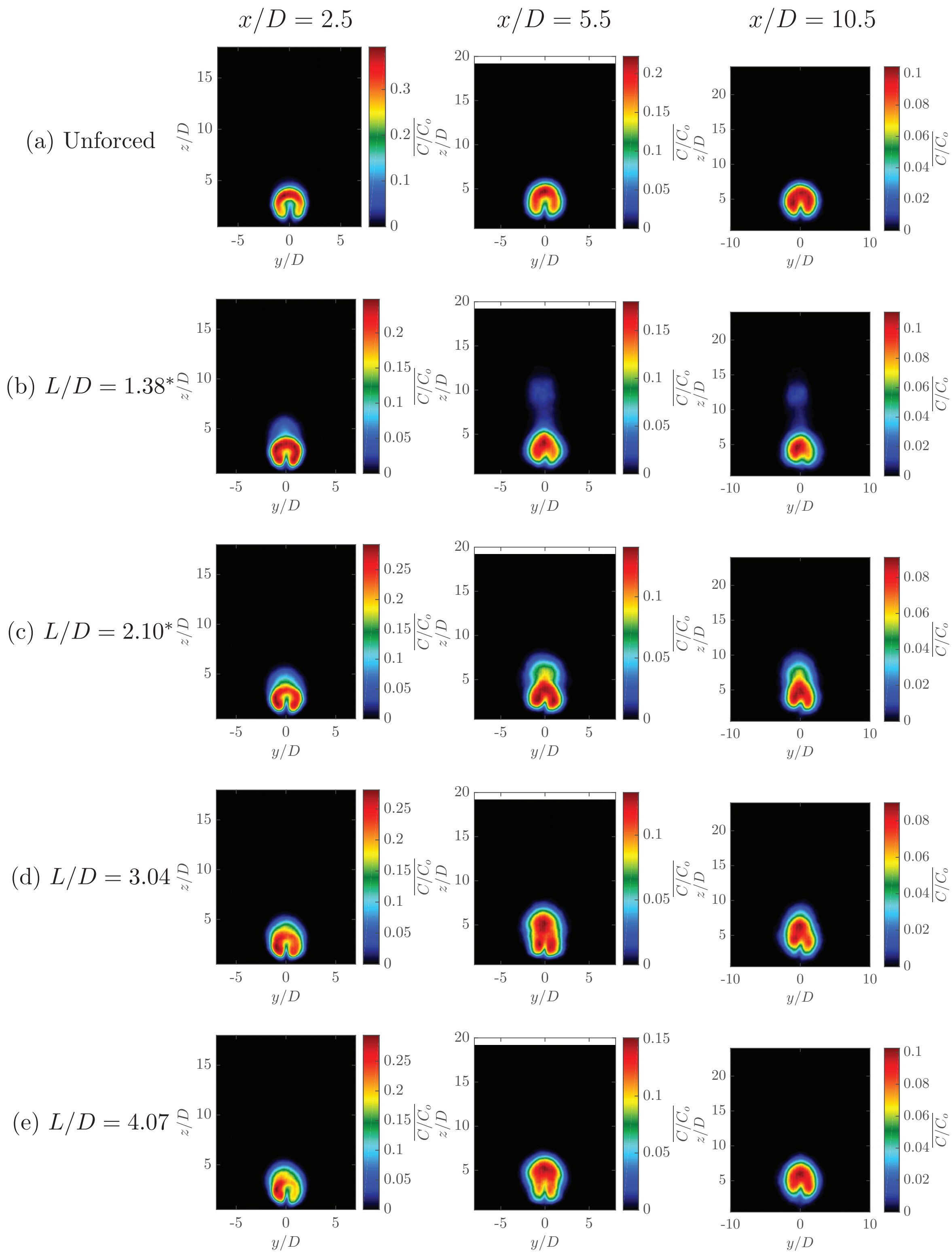

Figure 6.14: For more figures and caption see next page.

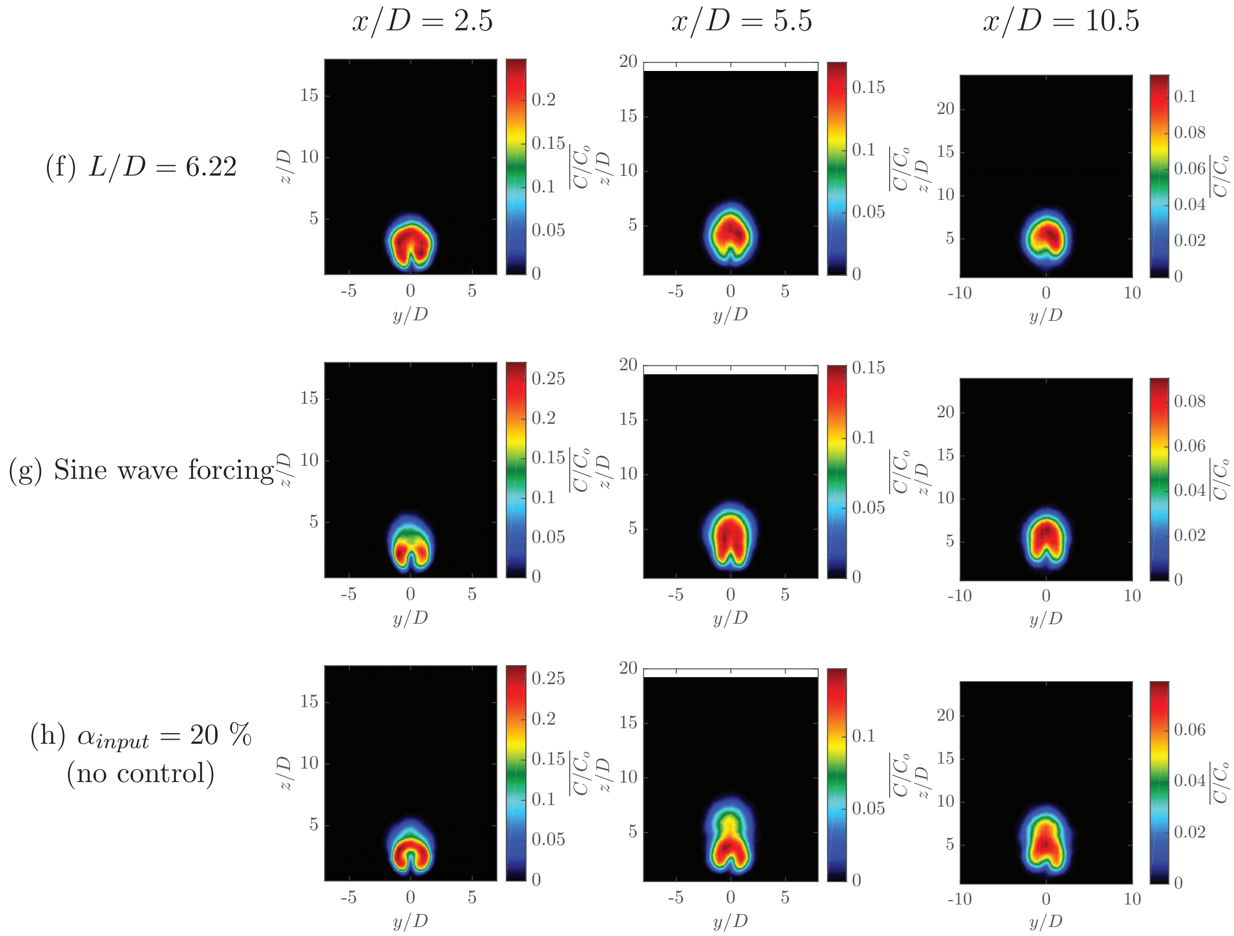

Figure 6.14: Mean cross-sectional PLIF images in the $y/D - z/D$ plane for the equidensity flush nozzle-injected JICF at $J = 5$ for (a) the unforced case, (b)-(f) the forced cases under single-pulse square wave forcing at stroke ratios ranging $L/D = 1.38 - 6.22$, (g) under sine wave forcing, as well as (h) under single-pulse square wave forcing without control at $\alpha_{input} = 20$ %. All forcing cases are at $f_f = 100$ Hz and $U'_{j,rms} = 1.7$ m/s (approximately 26 % of U_j). Stroke ratio L/D with asterisk corresponds to the existence of deeply-penetrating puff-like vortical flow structures observed in instantaneous centerplane images.

In the cross-sectional view for $J = 5$ in Figure 6.14, we first note that mean jet structures at all downstream locations are fairly symmetric because the unforced jet structure is already symmetric with a clear CVP, a typical characteristic of the absolutely unstable JICF (Getsinger et al., 2014). Although the jet's cross-sectional structures are disturbed by forcing at all of these conditions with $U'_{j,rms} = 1.7$ m/s, the cross-sectional structures are not significantly altered at most square wave forcing conditions with control, as well as sine and square wave forcing without control, except when the forcing generates the deeply penetrating vortical flow structures at fairly low L/D. This is seen particular in Figures 6.14(c) and (h).

For the above range of structural observations at $5 \leq J \leq 41$, the deeply-penetrating puff-like vortical structures are observed at $J = 20$, 10 and 5 but not at $J = 41$. At $J = 41$, square wave forcing with control generates enhanced jet spread and penetration and more symmetric cross-sectional structures, but without distinct periodic vortex rings. Interestingly, for $J = 41$ jet bifurcation is more vigorously created at fairly high stroke ratios in the range $L/D \approx 5.04 - 6.35$, but there is no evidence of distinct vortical puffs. For $J \leq 20$, the deeply-penetrating puff-like vortical structures are created at a specific range of stroke ratio: $L/D \approx 1.4$ and $2.8 - 4.2$ for $J = 20$, $L/D \approx 1.3 - 3.1$ for $J = 10$ and $L/D \approx 1.4 - 2.1$ for $J = 5$, which generally becomes narrower as J decreases but with approximately the same minimum stroke ratio to create such structures. These vortical flow structures are not present under sine and square wave forcing without control for $J \leq 20$ due to the lack of strong pulsations. These waveforms tend to be more sine-like without control. Hence, structural characteristics of the absolutely unstable JICF can be significantly altered only by single-pulse square wave forcing only within a relatively narrow L/D range.

Structural characteristics of the vortical flow structures with respect to size and concentration as well as cross-sectional symmetry also depend on stroke ratios. At relatively low L/D, smaller vortical ring-like structures are observed, containing fairly low jet fluid concentrations, while higher concentrations are captured inside the relatively larger vortical structures that form at relatively higher L/D. Since the effect of square wave forcing with control seems to be less significant at lower L/D, thus may be the reason that more asymmetric cross sections are observed at $J = 20$ and 10. This does not occur for $J = 41$ and 5, possibly because of relatively weak convective instability of the upstream shear layer for $J = 41$, and because of the relatively strong absolute instability creating the naturally symmetric cross-sectional structures in the absence of forcing for $J = 5$. Interestingly, for $J = 10$ and 20, deeply-penetrating vortical structures are more likely to be observed at the fairly low stroke ratios with more asymmetric cross sections.

6.4 Mixing Quantification

Now mixing characteristics for the JICF under single-pulse square wave forcing with and without control, as well as for sine wave forcing, are quantified. As done for sine wave forcing in the previous chapter, we use mean and instantaneous mixing metrics. Again, the mean mixing metrics utilized in this study are jet penetration z_p/D, vertical spread δ_z/D, jet spread normal to the unforced jet centerline trajectory $\delta_{n,unforced}/D$, and spread normal to each jet trajectory in question δ_n/D. Instantaneous mixing metrics representing molecular mixing include the centerplane-based Unmixedness with three different coordinates, and the cross-section-based Unmixedness as well as Probability Density Function (PDF) at $x/D = 2.5$, 5.5 and 10.5. These mixing metrics are evaluated using the same methods as described in Section 5.4. It should be noted that mean mixing metrics are quantified based on normalized jet fluid concentrations larger than 1 %, that is, with the criterion $C/C_o \geq 0.01$.

Figures 6.15 and 6.16 show the results of mixing evaluations for the equidensity flush nozzle-injected convectively unstable JICF at $J = 41$ using mean and instantaneous mixing metrics, respectively. Here, square wave forcing with control with various stroke ratios L/D (calculated by Equation (6.7)) as well as sine wave forcing are both explored. Results under square wave forcing without control are also shown later in Figure 6.23. Again, the RMS velocity perturbation is matched among all forcing conditions at $U'_{j,rms} = 1.7$ m/s so that all results have effectively comparable pulsation magnitudes or fluid impulse.

Figure 6.15 clearly shows that jet penetration, vertical spread, and spread with respect to two different coordinates are all improved over the unforced case by external forcing, especially by single-pulse square wave forcing. The improved penetration and spread with square wave forcing as compared with sine wave forcing suggests a greater efficiency of square wave forcing, even at low frequencies ($f_f = 100$ Hz) and without distinct vortex ring formation, as seen in Figure 6.7. The structural observations in Section 6.3 suggest that jet bifurcation is more vigorously triggered at relatively higher L/D for the $J = 41$ case, at

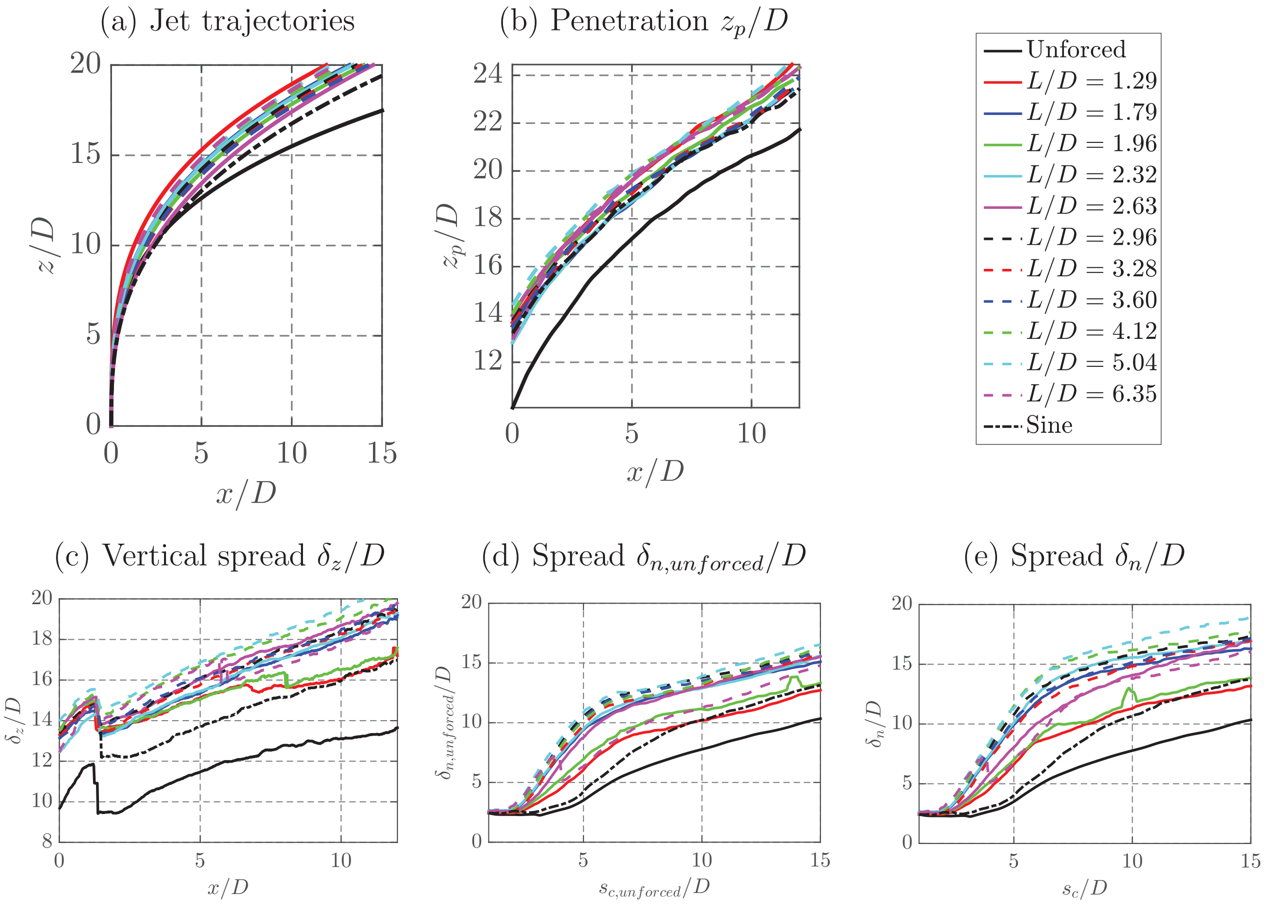

Figure 6.15: Mean mixing metrics for the equidensity flush nozzle-injected JICF at $J = 41$ for the unforced case and forced cases under sine wave forcing as well as single-pulse square wave forcing with control ($1.29 \leq L/D \leq 6.35$) at $f_f = 100$ Hz and $U'_{j,rms} = 1.7$ m/s (approximately 26 % of U_j): (a) Jet trajectories, (b) jet penetration z_p/D, (c) jet vertical spread δ_z/D, (d) jet spread normal to the unforced jet trajectory $\delta_{n,unforced}/D$ and (e) jet spread normal to each jet trajectory in question δ_n/D.

which the jet vertical spread, as well as spread with two different coordinates are generally more greatly enhanced ($L/D \approx 3.60 - 5.04$). Jet penetration, represented the top of the jet, does not vary significantly among all forcing conditions, although the centerline trajectory is higher with square wave forcing. Enhanced jet spread but not penetration indicates that the square wave forcing with control contributes mainly to jet spread downward or toward the test section floor but not upward, yielding a bifurcating jet at relatively higher L/D. Hence, mixing characteristics based on the mean mixing metrics are consistent with visible structural characteristics, and the best jet spread is observed approximately at $L/D \approx 3.60 - 5.04$.

In the instantaneous mixing metrics in Figure 6.16, however, one generally does not see significant differences among all forcing conditions. First, the centerplane-based Unmixedness along s_c/D and $s_{c,unforced}/D$ displays slightly enhanced molecular mixing under both sine wave forcing and square wave forcing with control, as compared with the unforced case, although sine wave forcing does not significantly alter mixing characteristics from the unforced case. Additionally, all stroke ratios shown here generate a similar degree of molecular mixing, and even higher L/D in the range that improves spread ($L/D \approx 3.6 - 5.0$) does not show consistent trends. The centerplane-based Unmixedness along x/D also does not show significant differences among all conditions, even including the unforced case. Note that the unforced jet centerline trajectory distance of $s_c/D \approx 10.0$ corresponds to a horizontal location of $x/D \approx 2.0$ for $J = 41$. As compared with the instantaneous mixing metric evaluation under sine wave forcing with variable forcing frequency f_f in Figures 5.17(a)-(c), the centerplane-based Unmixedness was more enhanced even at weaker level of forcing at $U'_{j,rms} = 0.07$ m/s only when f_f is fairly close to f_o, per lock-in behavior. This result may indicate that sine wave forcing with a specific f_f closer to f_o is a more efficient method to enhance molecular mixing for the JICF at $J = 41$, although more exploration with square wave forcing at various forcing frequencies may be required to confirm the possible efficiency of sine wave forcing for this convectively unstable condition.

Interestingly, the cross-section-based Unmixedness U_{yz} in Figure 6.16(d) shows highly improved near-field molecular mixing at $x/D = 2.5$ under both sine wave forcing as well as square wave forcing with control in comparison to the unforced case. This discrepancy between the trends in centerplane- and cross-section-based Unmixedness is likely attributed to the asymmetry in the unforced jet's cross section, which is not captured in the centerplane view. In contrast, a similarity between the centerplane- and cross-section-based Unmixedness that can be recognized here is that centerplane Unmixedness U_{yz} is similar in magnitude among all forcing conditions, including sine wave forcing. In addition, the difference in molecular mixing between forced and unforced cases becomes smaller in the mid-to-farfield locations $x/D = 5.5 - 10.5$. Therefore, one may surmise for $J = 41$ that single-pulse square

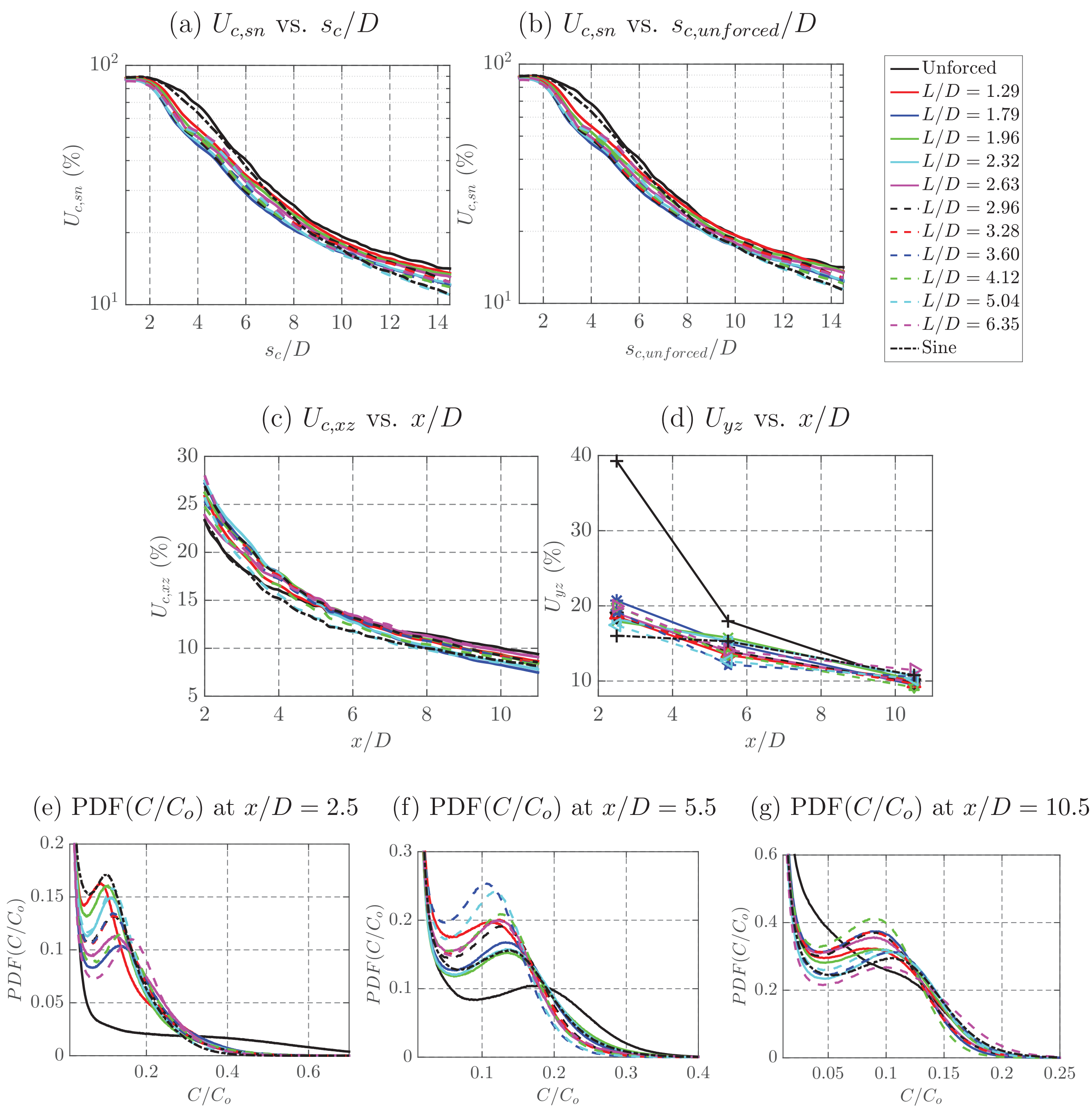

Figure 6.16: Instantaneous mixing metrics for the equidensity flush nozzle-injected JICF at $J = 41$ for the unforced and forced cases under sine wave forcing as well as single-pulse square wave forcing with control ($1.29 \leq L/D \leq 6.35$) at $f_f = 100$ Hz and $U'_{j,rms} = 1.7$ m/s. Each figure represents (a) centerplane-based mean Unmixedness $U_{c,sn}$ along s_c/D, (b) $U_{c,sn}$ along $s_{c,unforced}/D$, (c) centerplane-based mean Unmixedness $U_{c,xz}$ along x/D, (d) cross-section-based mean Unmixedness U_{yz} along x/D, and (e)-(g) cross-section-based mean probability density function (PDF) of normalized concentration PDF(C/C_o) at $x/D = 2.5$, 5.5 and 10.5, respectively.

wave forcing with control may slightly improve the near-field molecular mixing as compared with the unforced case but it does not significantly alter the overall mixing characteristics when the jet is weakly convectively unstable. Also, it may be a possibility that sine wave forcing at a carefully chosen forcing frequency, close to f_o, has more of an impact on mixing characteristics than single-pulse square wave forcing, yet more exploration will be required to make this conclusive. Again, as previously mentioned, selection of appropriate mixing metrics and hence forcing methods does depend on the application for the flowfield.

Figures 6.17 and 6.18 represent the results of the mixing evaluation for $J = 20$ under sine wave forcing and square wave forcing with control at $f_f = 100$ Hz and $U'_{j,rms} = 1.7$ m/s. Note that the upstream shear layer in this flow condition is still convectively unstable. In the previous section, the $J = 20$ cases showed remarkable structural differences among varied forcing conditions, with deeply-penetrating puff-like vortical structures in a specific L/D range. Because of such distinctive structural characteristics, mixing results also provide clearer differences, depending on forcing conditions, especially on stroke ratios L/D. First, jet penetration, vertical spread, and spread with respect to two different trajectory coordinates (Figure 6.17(b)-(e)) are seem to be enhanced at any forcing conditions in comparison with the unforced case. The best jet penetration is generally achieved by single-pulse square wave forcing at stroke ratios of $L/D = 3.15 - 4.20$, fairly close to the universal time scale of $L/D \approx 4$ suggested by Gharib et al. (1998). Yet the $L/D = 1.39$ case yields the best jet penetration only in the nearfield at $x/D \lesssim 2$, which is related to the near-field forcing effect creating the deeply-penetrating vortical flow structures seen in Figure 6.9(b). The best jet spread is also observed around the same range of stroke ratios ($L/D = 3.15 - 4.20$), although the $L/D = 6.24$ case also shows large jet spread, as seen in 6.17(d) and (e). The optimal stroke ratio for the best jet spread and penetration here is comprehensively determined to be around $L/D = 3.15 - 4.20$, and clearly corresponds to the existence of penetrating vortical structures.

In the instantaneous mixing metrics shown in Figure 6.18 for $J = 20$, again, more distinct differences are observed among various forcing conditions. Consistent mixing trends in the centerplane-based Unmixedness are recognized among all coordinate systems, s_c/D,

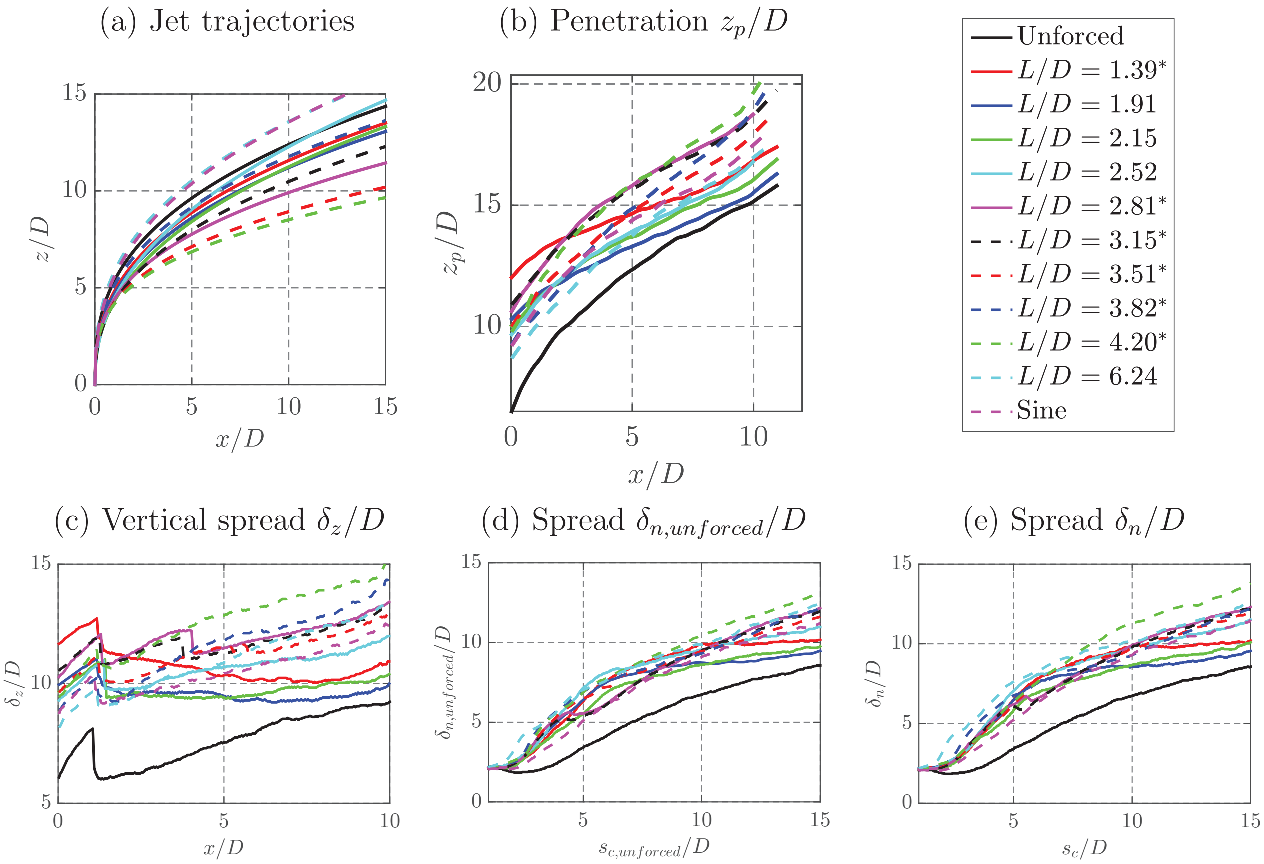

Figure 6.17: Mean mixing metrics for the equidensity flush nozzle-injected JICF at $J = 20$ for the unforced case and forced cases under sine wave forcing as well as single-pulse square wave forcing with control ($1.39 \leq L/D \leq 6.24$) at $f_f = 100$ Hz and $U'_{j,rms} = 1.7$ m/s (approximately 26 % of U_j): (a) Jet trajectories, (b) jet penetration z_p/D, (c) jet vertical spread δ_z/D, (d) jet spread normal to the unforced jet trajectory $\delta_{n,unforced}/D$ and (e) jet spread normal to each jet trajectory in question δ_n/D. Stroke ratio L/D with asterisk corresponds to the existence of deeply-penetrating puff-like vortical flow structures observed in instantaneous centerplane images.

$s_{c,unforced}/D$ and x/D. It should be noted that the unforced jet centerline trajectory distance of $s_c/D \approx 7.3$ coincides with the horizontal location of $x/D \approx 2.0$, so direct qualitative comparison of mixing characteristics can be administered to corresponding locations. Along the jet centerline trajectory as shown in Figures 6.18(a) and (b), the centerplane-based Unmixedness values among all square wave forcing conditions are similar to one another, although lower L/D values producing deep vortex penetration (2.81 and 3.15) tend to have the lowest Unmixedness in the farfield. Sine wave forcing is not as favorable in the nearfield, although all forcing conditions enhance molecular mixing (lower Unmixedness) as compared with the unforced case. Beyond $s_c/D, s_{c,unforced}D \geq 8$, approximately equivalent to $x/D \geq 2$ in Figure 6.18(c), sine wave forcing enhances molecular mixing more than square wave forcing with control at several of the stroke ratios. This difference suggests that mixing characteristics can be altered by forcing, depending on mainly two spatial regions of the flow: $x/D \leq 2$ and $x/D \geq 2$, or equivalently $s_c/D, s_{c,unforced}/D \leq 8$ and $s_c/D, s_{c,unforced}/D \geq 8$ for $J = 20$.

Upstream of $x/D \approx 2.0$, the centerplane-based Unmixedness (Figures 6.18(a) and (b)) becomes the lowest, corresponding to the best molecular mixing, at $L/D \approx 1.91 - 2.52$ or $L/D = 6.24$, none of which create deep vortex penetration. But beyond $x/D \approx 2.0$ Figures 6.18(a)-(c) suggest the best molecular mixing to be achieved at $L/D \approx 2.81 - 3.15$, where there has been deep vortex penetration in the jet. In the relative nearfield, square wave forcing that does not create deeply-penetrating vortical structures may trigger more vigorous near-field interactions of jet and crossflow fluids, and hence molecular mixing could be increased. On the other hand, in the relative farfield, molecular mixing could be enhanced if the deeply penetrating vortical structures convect downstream and interact with other structures, engulfing crossflow and contributing to better uniformity of mixed fluid in the entire field of view.

The cross-section-based Unmixedness U_{yz} in Figure 6.18(d) shows improved molecular mixing at $x/D = 2.5$ for both sine wave and square wave forcing as compared with the unforced case, with $L/D = 2.81$ and 2.15 producing the best mixing throughout. This difference between the centerplane- and cross-section-based Unmixedness in the nearfield is probably associated with the asymmetry in the unforced cross-sectional structure, which is not captured in the centerplane view. This inconsistency was also observed in the $J = 41$ case, which also involved considerably asymmetric cross-sectional structures. Nevertheless, the cross-section-based Unmixedness is generally consistent with the centerplane-based Unmixedness in the farfield. In addition, the cross-section-based Unmixedness, as shown in Figure 6.18(d), suggests that external forcing at all forcing conditions enhances molecular mixing as compared with the unforced case at $x/D = 2.5$ and 5.5 but not at $x/D = 10.5$, consistent with the centerplane-based Unmixedness, suggesting that farfield effects of forc-

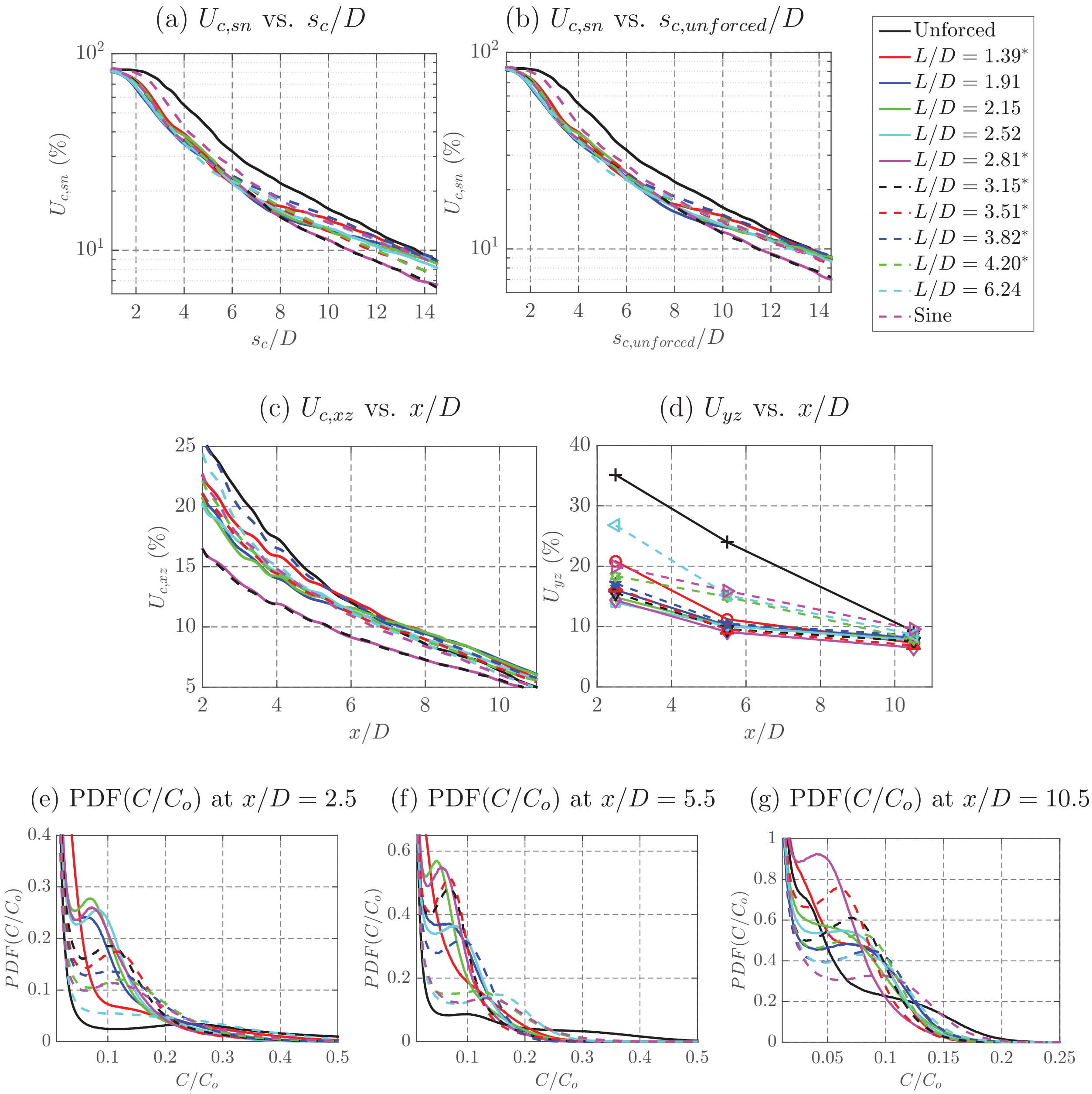

Figure 6.18: Instantaneous mixing metrics for the equidensity flush nozzle-injected JICF at $J = 20$ for the unforced and forced cases under sine wave forcing as well as single-pulse square wave forcing with control ($1.39 \leq L/D \leq 6.24$) at $f_f = 100$ Hz and $U'_{j,rms} = 1.7$ m/s. Each figure represents (a) centerplane-based mean Unmixedness $U_{c,sn}$ along s_c/D, (b) $U_{c,sn}$ along $s_{c,unforced}/D$, (c) centerplane-based mean Unmixedness $U_{c,xz}$ along x/D, (d) cross-section-based mean Unmixedness U_{yz} along x/D, and (e)-(g) cross-section-based mean probability density function (PDF) of normalized concentration PDF(C/C_o) at $x/D = 2.5$, 5.5 and 10.5, respectively.

ing tend to be diminished. Moreover, the best molecular mixing in the cross-sectional view is observed approximately in the range $L/D \approx 2.52 - 3.51$, which lies within the range of L/D values associated with the optimal stroke ratio for the centerplane-based Unmixedness, $L/D \approx 2.81 - 3.15$. Overall, although there are a few differences, the instantaneous mixing metrics are generally consistent with one another. From this mixing evaluation, the best molecular mixing for $J = 20$ is observed for square wave forcing with control at $L/D \approx 1.91 - 2.52$ or $L/D = 6.24$ when $x/D \leq 2$, and $L/D \approx 2.52 - 3.51$ when $x/D \geq 2$. In the present study, to characterize molecular mixing over the majority of the spatial range ($x/D \geq 2$), one would say the "optimal" stroke ratios for enhanced molecular mixing at $J = 20$ are $L/D \approx 2.5 - 3.5$.

Mixing characteristics are observed to become more distinctive among different forcing conditions as J decreases in the convectively unstable regime. Now, mixing characteristics for the absolutely unstable JICF at $J = 10$ are explored, shown in Figures 6.19 and 6.20. $J = 10$ is close to a critical jet-to-crossflow momentum flux ratio between transitioning the shear layer convective and absolute instability. As expected from the PLIF images, mean jet spread and penetration are improved with square wave forcing at $1.33 \leq L/D \leq 3.08$, corresponding to creation of deeply-penetrating vortical structures. Yet all external forcing shown here enhances jet spread and penetration as compared with the unforced case. The improvement is consistently observed among all mean mixing metrics shown in Figures 6.19(b)-(e).

Interestingly, for the instantaneous mixing metrics such as Unmixedness in Figures 6.20(a)-(d), at $L/D = 1.33$ and 2.09, which create the best jet penetration and spread, molecular mixing is not as enhanced as for the other forcing conditions, despite the fact that clear penetrating vortical structures are formed. This suggests that vortical structures do not necessarily enhance molecular mixing, or that good jet penetration and spread do not necessarily coincide with good molecular mixing for the transverse jet. It should be noted that the unforced jet centerline trajectory distance of $s_c/D \approx 5.6$ coincides with the horizontal location of $x/D \approx 2.0$ for $J = 10$. As with the $J = 20$ cases, mixing trends are altered depending on spatial locations. In the relative nearfield ($s_c/D, s_{c,unforced}/D \leq 6.0$ or $x/D \leq 2.0$), the JICF is more mixed at $L/D \approx 3.71 - 6.16$, while further downstream,

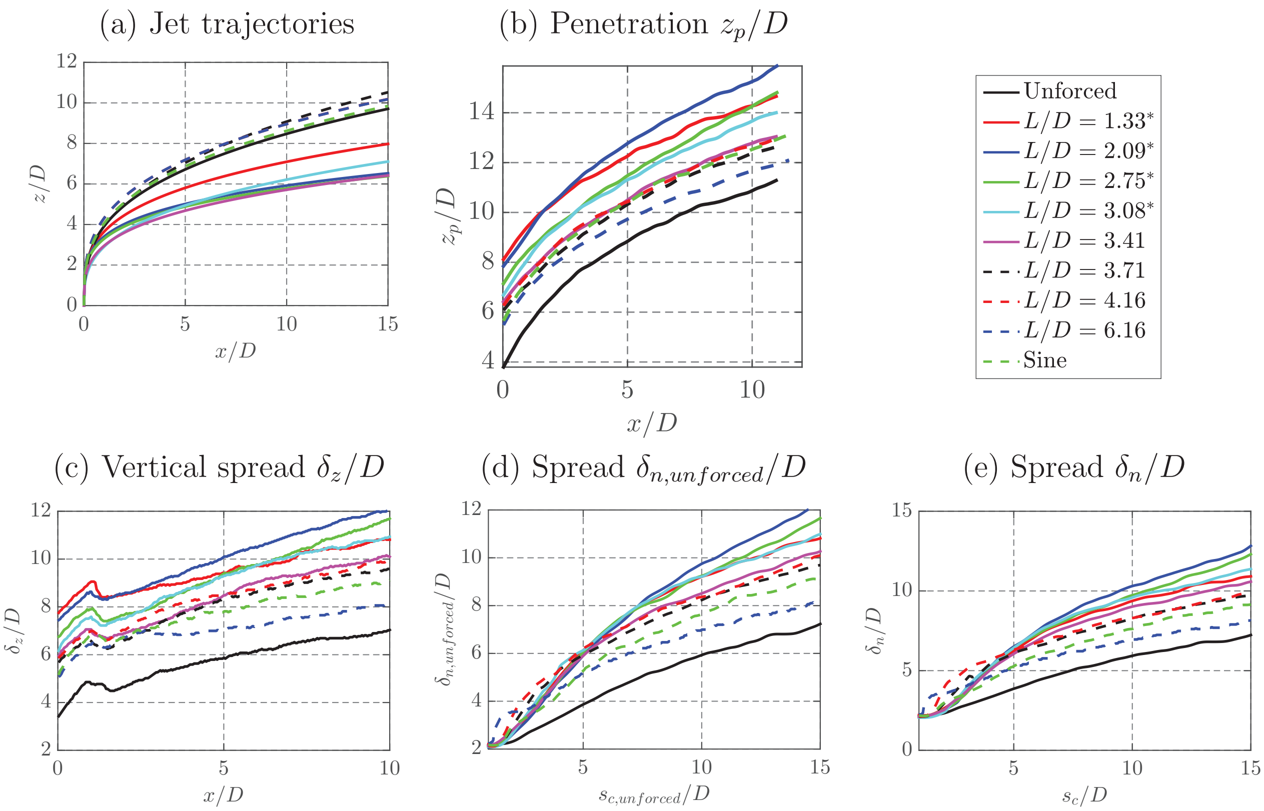

Figure 6.19: Mean mixing metrics for the equidensity flush nozzle-injected JICF at $J = 10$ for the unforced case and forced cases under sine wave forcing as well as single-pulse square wave forcing with control ($1.33 \leq L/D \leq 6.16$) at $f_f = 100$ Hz and $U'_{j,rms} = 1.7$ m/s (approximately 26 % of U_j): (a) Jet trajectories, (b) jet penetration z_p/D, (c) jet vertical spread δ_z/D, (d) jet spread normal to the unforced jet trajectory $\delta_{n,unforced}/D$ and (e) jet spread normal to each jet trajectory in question δ_n/D. Stroke ratio L/D with asterisk corresponds to the existence of deeply-penetrating puff-like vortical flow structures observed in instantaneous centerplane images.

molecular mixing is more greatly enhanced for stroke ratios $L/D \approx 3.08 - 4.16$ (that is, for $s_c/D, s_{c,unforced}/D \geq 6.0$ and $x/D \geq 2.0$). At relatively high L/D values, near-field jet interactions occur vigorously due to the temporally long pulsation and its potential contribution to good molecular mixing close to the jet exit. In contrast, a relatively smaller stroke ratio, one which is fairly close to the universal time scale around 4, may lead to more efficient vorticity generation and spatial evolution of the JICF, resulting in better molecular mixing over a wide range of flowfield conditions. Hence, the best molecular mixing for $J = 10$ in this study is achieved at a relatively high stroke ratio for mixing close to the jet exit and at

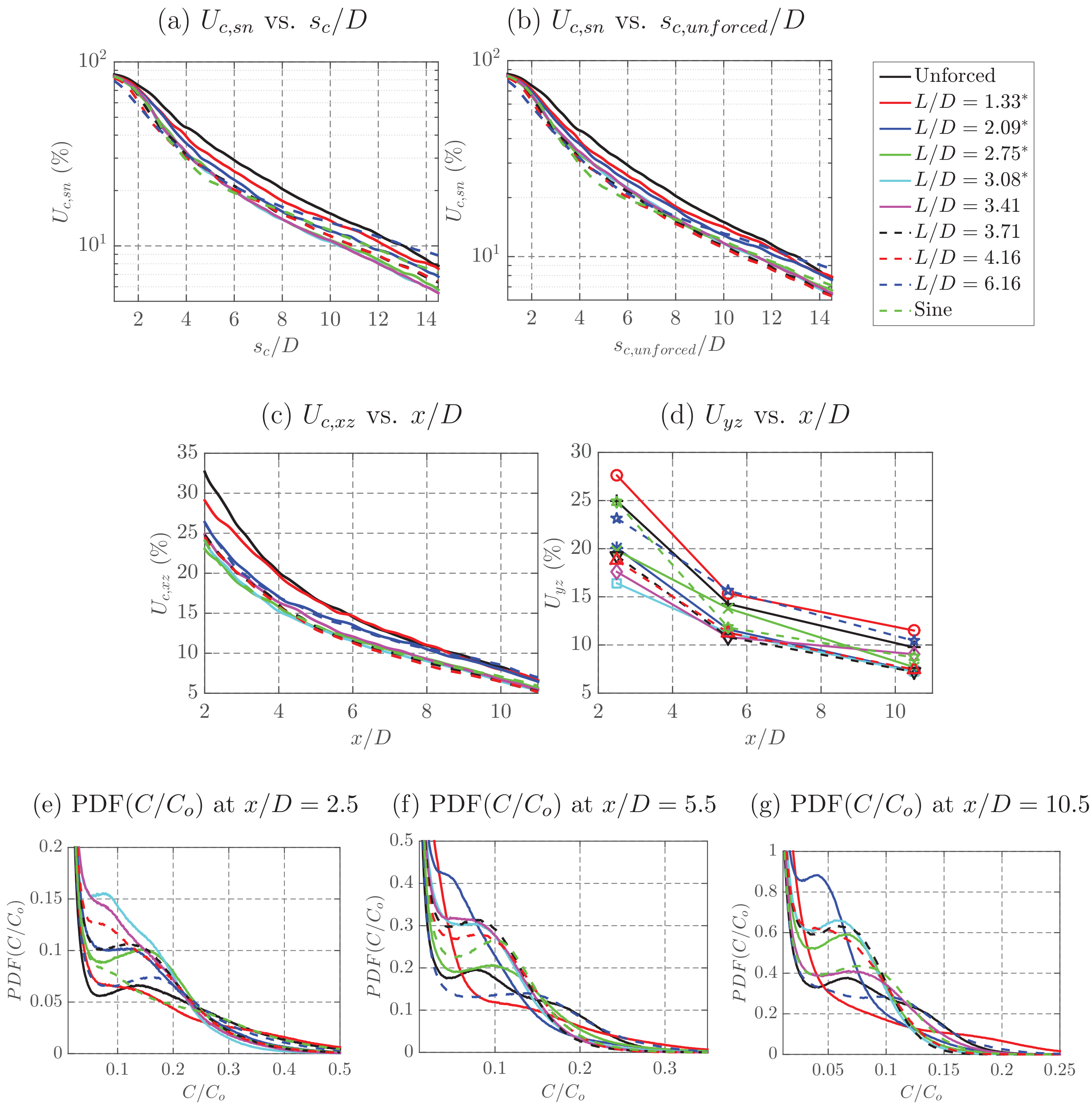

Figure 6.20: Instantaneous mixing metrics for the equidensity flush nozzle-injected JICF at $J = 10$ for the unforced and forced cases under sine wave forcing as well as single-pulse square wave forcing with control ($1.33 \leq L/D \leq 6.16$) at $f_f = 100$ Hz and $U'_{j,rms} = 1.7$ m/s. Each figure represents (a) centerplane-based mean Unmixedness $U_{c,sn}$ along s_c/D, (b) $U_{c,sn}$ along $s_{c,unforced}/D$, (c) centerplane-based mean Unmixedness $U_{c,xz}$ along x/D, (d) cross-section-based mean Unmixedness U_{yz} along x/D, and (e)-(g) cross-section-based mean probability density function (PDF) of normalized concentration PDF(C/C_o) at $x/D = 2.5$, 5.5 and 10.5, respectively.

relatively low stroke ratios for optimized mixing fairly far from the jet exit, although square wave forcing in the range $L/D \approx 3.08 - 4.16$ can be considered to be the overall optimal forcing conditions for enhanced molecular mixing over a wide spatial range, as mentioned for the $J = 20$ case as well.

Finally, mixing characteristics are evaluated for the absolutely unstable flush nozzle-injected JICF at $J = 5$, as represented in Figures 6.21 and 6.22. As observed in the $J = 20$ and 10 cases, jet spread and penetration are maximized at $L/D \approx 1.38 - 2.10$, corresponding to cases when deeply-penetrating vortical structures are created. In general, jet spread and penetration decrease as L/D increases within the range of L/D values explored in this study.

For the instantaneous mixing metrics in Figure 6.22, as observed for the $J = 41$, 20 and 10 cases, the forced cases for $J = 5$ are all better mixed than the unforced case, especially in the spatial range $2 \leq x/D \leq 8$. In the relative farfield, all molecular mixing is similar among the unforced case and forced cases under sine wave and square wave excitation with control, which is consistent among all flow conditions in this study. This indicates that even square wave forcing with deeply penetrating vortices has little effect on the far-field mixing characteristics both for the convectively and absolutely unstable JICF. Nevertheless, single-pulse square wave forcing does enhance molecular mixing in the near-to-midfield region for $J = 5$ more efficiently than does sine wave forcing at the same locations. Again, the best molecular mixing is obtained for different forcing conditions at different spatial regions: (1) for stroke ratios $L/D \approx 2.10 - 3.04$ when $s_c/D, s_{c,unforced}/D \leq 4.0$ or equivalently $x/D \leq 2.0$, and (2) for $L/D \approx 2.45 - 3.69$ when $s_c/D, s_{c,unforced}/D \geq 4.0$ or equivalently $x/D \geq 2.0$. Even at the relatively low $J = 5$ with an absolutely unstable shear layer, the same mixing characteristics are observed as for other cases. First, the optimal stroke ratio in terms of molecular mixing is different depending on spatial region. Secondly, deeply-penetrating vortical structures do not necessarily contribute to better molecular mixing as compared with cases without such vortical flow structures. Overall, square wave forcing with control at $L/D \approx 2.45 - 3.69$ optimally enhances molecular mixing at $J = 5$ for the widest spatial region.

The mixing quantification for the forced JICF in this section has shown better enhance-

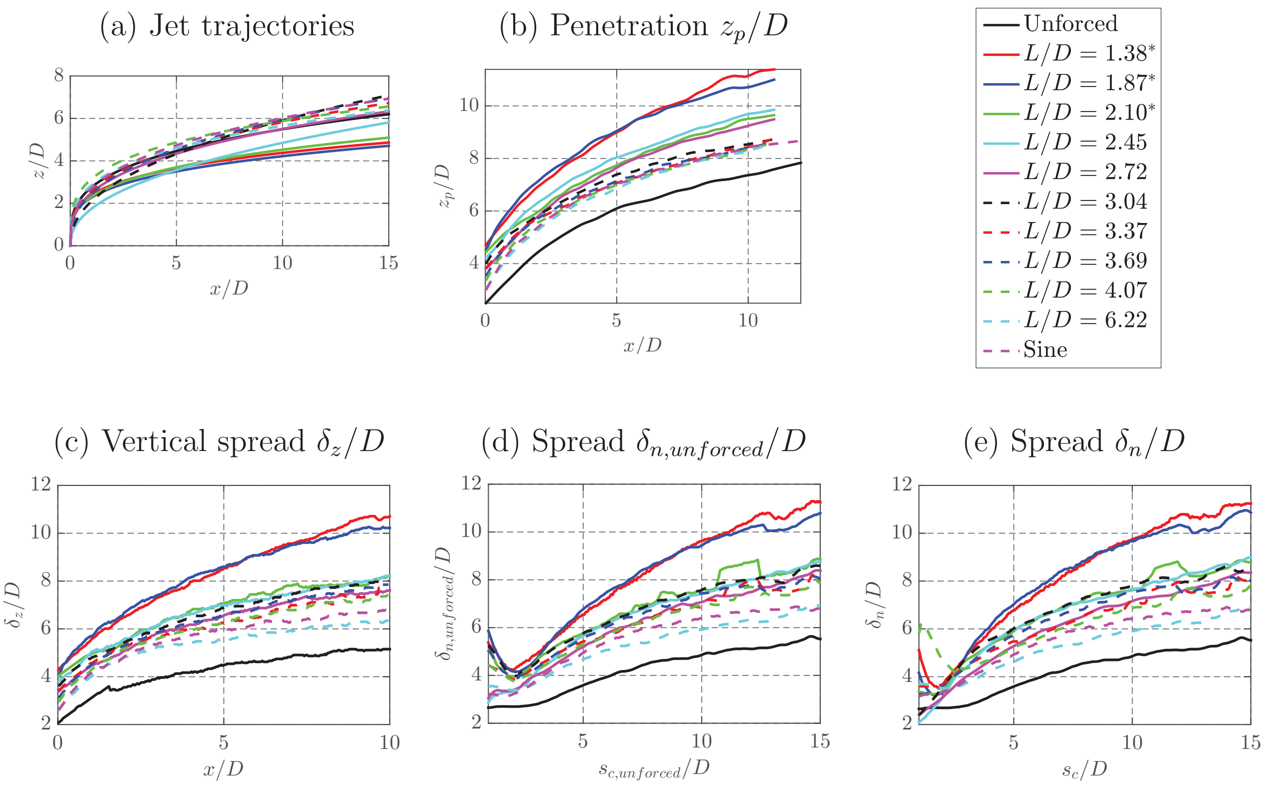

Figure 6.21: Mean mixing metrics for the equidensity flush nozzle-injected JICF at $J = 5$ for the unforced case and forced cases under sine wave forcing as well as single-pulse square wave forcing with control ($1.38 \leq L/D \leq 6.22$) at $f_f = 100$ Hz and $U'_{j,rms} = 1.7$ m/s (approximately 26 % of U_j): (a) Jet trajectories, (b) jet penetration z_p/D, (c) jet vertical spread δ_z/D, (d) jet spread normal to the unforced jet trajectory $\delta_{n,unforced}/D$ and (e) jet spread normal to each jet trajectory in question δ_n/D. Stroke ratio L/D with asterisk corresponds to the existence of deeply-penetrating puff-like vortical flow structures observed in instantaneous centerplane images.

ment in molecular mixing under square wave forcing with control than with sine wave forcing. As documented in Section 6.1, however, creating a clean square-waveform in temporal jet response is challenging because of non-linearity in the actuation systems, requiring a feedback controller. To explore this requirement, mixing characteristics under square wave forcing without control are also compared with those with control to investigate the effect of cleaner waveform. The computational study of the partially modulated JICF by Sau and Mahesh (2010) found little structural difference for the forced JICF between an ideal square wave and a distorted square-waveform representing jet velocity at the jet exit, but which have the

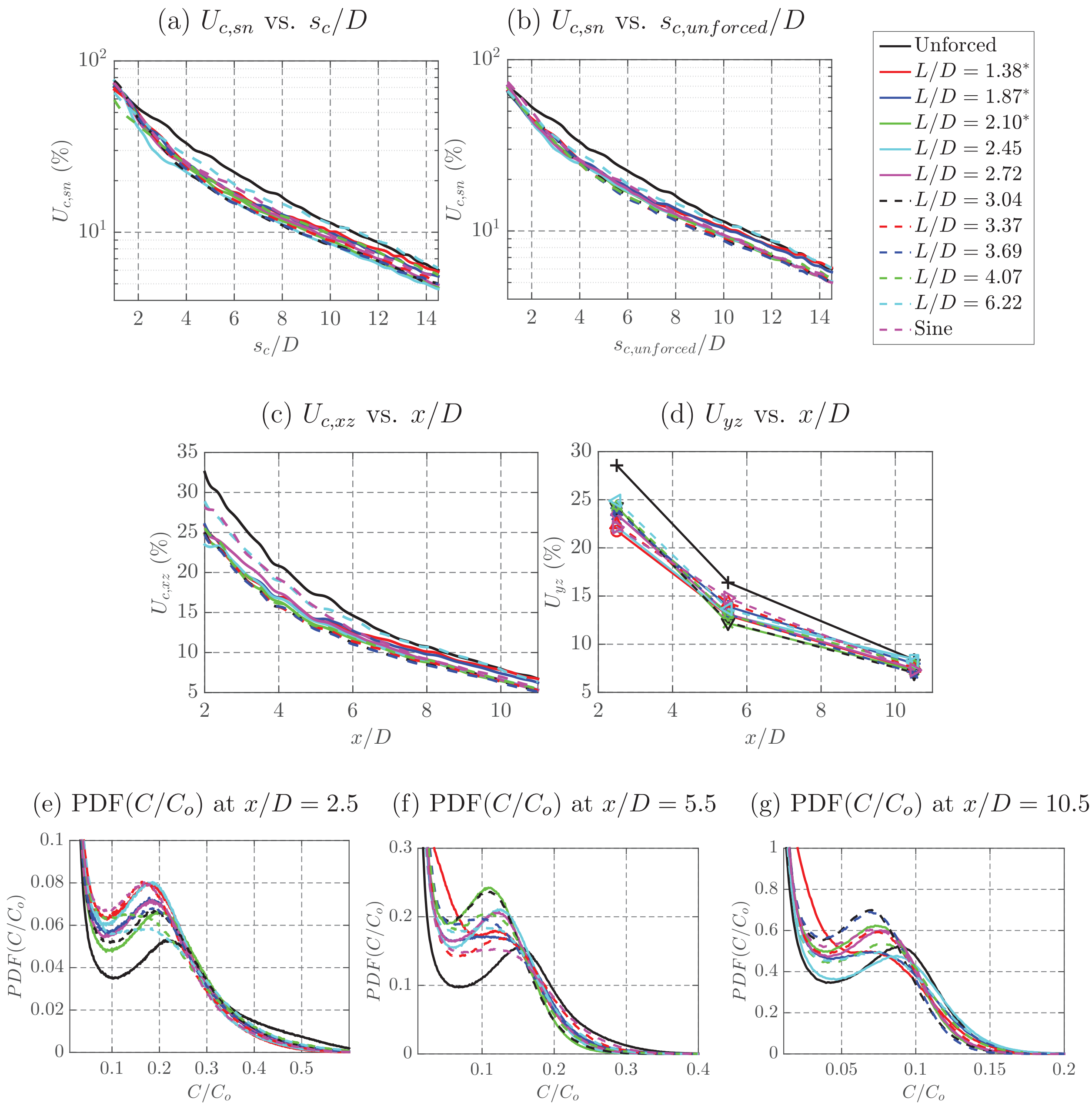

Figure 6.22: Instantaneous mixing metrics for the equidensity flush nozzle-injected JICF at $J = 5$ for the unforced and forced cases under sine wave forcing as well as single-pulse square wave forcing with control ($1.38 \leq L/D \leq 6.22$) at $f_f = 100$ Hz and $U'_{j,rms} = 1.7$ m/s. Each figure represents (a) centerplane-based mean Unmixedness $U_{c,sn}$ along s_c/D, (b) $U_{c,sn}$ along $s_{c,unforced}/D$, (c) centerplane-based mean Unmixedness $U_{c,xz}$ along x/D, (d) cross-section-based mean Unmixedness U_{yz} along x/D, and (e)-(g) cross-section-based mean probability density function (PDF) of normalized concentration PDF(C/C_o) at $x/D = 2.5$, 5.5 and 10.5, respectively.

same effective stroke ratio and duty cycle. The distorted square waveforms here were the ones used in the controlled square wave experiments in Shapiro et al. (2006), which involved an open-loop controller. Note that in Sau and Mahesh (2010), molecular mixing was not quantified. Note further that it is impossible in the present experiments to replicate what Sau and Mahesh did in their computations, i.e., to compare the effect of a prefect square wave with our imperfect yet controlled square wave forcing. Nevertheless, it is possible to compare controlled and non-controlled square wave forcing and associated Unmixedness for different input or prescribed duty cycles α_{input} for a range of flow conditions. The RMS velocity perturbation is matched among all forcing conditions at $U'_{j,rms} = 1.7$ m/s for this comparison.

Figure 6.23 represents the centerplane- and cross-section-based Unmixedness as a function of horizontal coordinate x/D for the equidensity flush nozzle-injected JICF at $J = 41$, 20, 10 and 5 under square wave forcing with/without control. At $J = 41$ in Figure 6.23(a), all forcing conditions show similar quantitative and qualitative trends in mixing with and without control. Since the convectively unstable JICF is easily affected by external forcing, even sinusoidal forcing, especially at relatively higher J values, it makes sense that there is little difference in the effect of controlled vs. uncontrolled square wave forcing on mixing characteristics for the JICF as long as effectively the same level of forcing is applied (e.g., matched $U'_{j,rms}$). At $J = 20$ in Figure 6.23(b), the centerplane-based Unmixedness suggests that molecular mixing is more enhanced with control than that without control, both at $\alpha_{input} = 20$ % and 50 %. However, the cross-section-based Unmixedness shows enhanced molecular mixing only at $\alpha_{input} = 20$ % with control. At $\alpha_{input} = 50$ %, forcing with and without control basically produces a similar cross-section-based Unmixedness. This difference may be associated with experimental uncertainty or bias errors associated with PLIF imaging, which are difficult to quantify. On the other hand, the output duty cycles between controlled and non-controlled jets could be quite different, so this too could explain some differences in mixing.

For the absolutely unstable JICF at $J = 10$ in Figure 6.23(c), although all forcing conditions with and without control generate a similar degree of molecular mixing, square

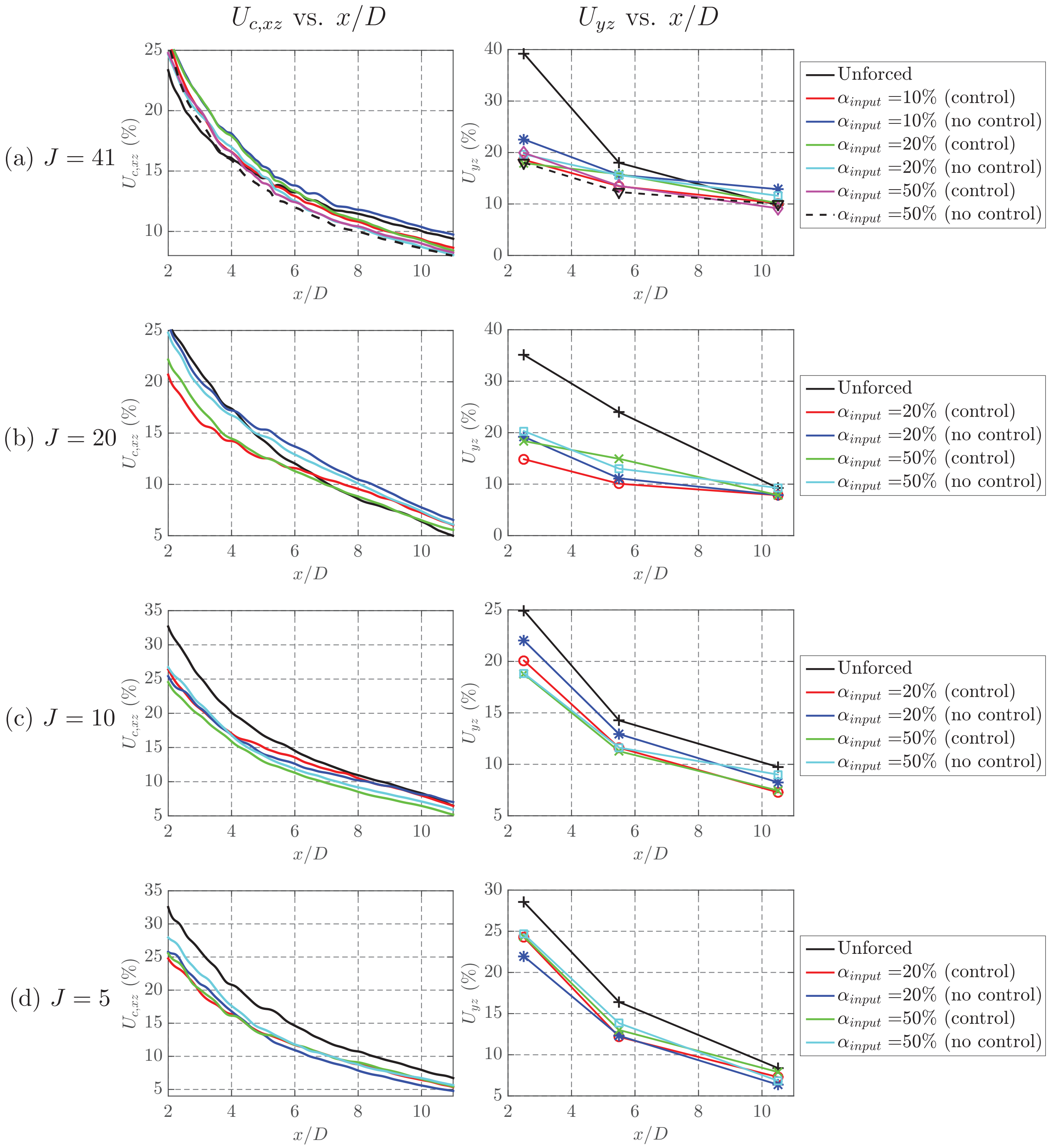

Figure 6.23: Instantaneous mixing metrics for the equidensity flush nozzle-injected JICF at (a) $J = 41$, (b) 20, (c) 10 and (d) 5 for the unforced case and the forced cases under single-pulse square wave forcing with and without control at $f_f = 100$ Hz and $U'_{j,rms} = 1.7$ m/s. The centerplane-based mean Unmixedness $U_{c,xz}$ and cross-section-based mean Unmixedness U_{yz} along x/D at $x/D = 2.5$, 5.5 and 10.5 are displayed.

wave forcing with control slightly enhances molecular mixing compared to the absence of control, based on the cross-section-based Unmixedness in general, especially at $\alpha_{input} = 20\,\%$. At $J = 5$, however, there is no distinctive enhancement with control or difference in mixing characteristics with/without control, although molecular mixing is higher with all forcing conditions than the unforced case. While these comparisons suggest that an improved square waveform with control may only slightly enhance molecular mixing as compared with that without control, we again note that the output duty cycles, temporal pulse widths, and hence stroke ratio L/D could be quite different between controlled and non-controlled cases.

Based on the present extensive exploration of mixing characteristics under sine wave forcing as well as single-pulse square wave forcing with/without control with a range of stroke ratios, some key conclusions may be reached. The optimal stroke ratio to enhance transverse jet penetration and spread (mean characteristics) is generally observed to be approximately $L/D \approx 3.6 - 5.0$ for $J = 41$ (a convectively unstable JICF), and $L/D \approx 3.2 - 4.2$ for $J = 20$ (also a convectively unstable JICF), and these are close to the "universal" time scale of $L/D \approx 4$ for vortex ring formation (Gharib et al., 1998). At lower J values, the optimal stroke ratios are $L/D \approx 1.3 - 3.1$ for $J = 10$ (an absolutely unstable JICF) and $L/D = 1.4 - 2.1$ for $J = 5$ (also an absolutely unstable JICF), which are further from the universal time scale value. Interestingly, the optimal stroke ratio for the "best" jet spread and penetration gradually decreases as J decreases. Previous computational studies by Sau and Mahesh (2008) and Sau and Mahesh (2010) also note that the optimal L/D for creation of deeply-penetrating vortical structures, generally equivalent to optimal jet penetration and spread in this study, becomes lower as J decreases. Their calculations were consistent with experimental results for the square wave-forced transverse jet by Eroglu and Breidenthal (2001) and Shapiro et al. (2006). Furthermore, Davitian et al. (2010b) generally observes a higher optimal stroke ratio for the greatest jet spread and penetration at a velocity ratio $R = 10$ or a momentum flux ratio $J \approx 100$ (a convectively unstable JICF) but a lower stroke ratio for $R = 3$ and 1.15 or equivalently $J \approx 9$ and 1.3 (for the absolutely unstable JICF). Recall that these studies utilized smoke visualization to determine "optimal" spread and penetration.

Sau and Mahesh (2008) and Sau and Mahesh (2010) indicate that a decrease in the optimal stroke ratio to produce the best jet spread and penetration arises from different vortical structures created by square wave forcing of the jet primarily with variable stroke ratios L/D and ring velocity ratios $r_{ring} = \Delta U_j / U_\infty$, as defined in Equation (1.4) (see Figure 1.9). These computational studies suggest that the optimal stroke ratio for the best jet spread and penetration decreases as a ring velocity ratio r_{ring} decreases, with lower ΔU_j for weaker forcing and/or higher U_∞ for a stronger crossflow, because a structural transition from successive vortex rings to a vortex ring with a trailing column occurs at a lower r_{ring}, resulting in a less jet penetration. In the present study, because the jet Reynolds number Re_j is kept constant at $Re_j = 1900$ and the crossflow velocity is varied to achieve the desired J, the crossflow velocity U_∞ for the convectively unstable JICF ($J > 10$) is smaller than that for the absolutely unstable JICF ($J \leq 10$). Hence, the reduced crossflow velocity for the convectively unstable JICF, and stronger crossflow for the absolutely unstable JICF could be the cause for the optimal stroke ratio's reduction with lower J. Also, it should be noted that the formation number of $L/D \approx 4$ (Gharib et al., 1998) was determined using a piston-driven vortex ring in a quiescent atmosphere, which is equivalently a free jet or vortex ring in the absence of crossflow (at $J = \infty$) in this study. Hence, the optimal stroke ratio for the best jet spread and penetration determined in this study is actually close to the universal time scale at large J because of the reduced crossflow effect. This notion is also investigated in Sau and Mahesh (2008) and Sau and Mahesh (2010), who concluded that the optimal stroke ratio for the JICF converges to $L/D \approx 4$ as the crossflow velocity approaches zero.

More interestingly, the optimal stroke ratio for the best molecular mixing (per the instantaneous metrics) does not necessarily coincide with that for the best jet spread and penetration, which generally correspond to jets with deeply-penetrating vortical structures. For the J values explored in this study, the best molecular mixing was achieved at an optimal stroke ratio of $L/D \approx 2.5 - 3.5$ for $J = 20$, $L/D \approx 3.1 - 4.2$ for $J = 10$ and $L/D \approx 2.5 - 3.7$ for $J = 5$. Interestingly, the optimal stroke ratio for the best molecular mixing in this study is approximately in the same range for different J values, unlike the jet spread and penetration. That is, the optimal stroke ratio for the best molecular mixing seems to be less independent of J. This observation is important because a "target" stroke ratio could be used in a practical system to achieve the best molecular mixing, independently of the flow conditions for the jet. Furthermore, these results suggest the possibility that jet spread and penetration can be independently optimized, as compared with molecular mixing, depending on the application.

As mentioned in Section 6.2, additional RMS velocity perturbations were explored, in addition to $U'_{j,rms} = 1.7$ m/s; these are in the range $1.0 \leq U'_{j,rms} \leq 3.0$ m/s, as shown in Appendix C. The optimal stroke ratio for the best jet spread and penetration as well as the optimal molecular mixing can be determined for all forcing conditions, and the results are summarized in Figure 6.24. The maximum RMS velocity perturbation in the figure is $U'_{j,rms} = 2.0$ m/s; a higher $U'_{j,rms}$ can only allow study of a narrow range of stroke ratios caused by the limited hotwire velocity calibration range (see Section 2.2). Points and bars in the figure refer to the middle value of the optimal stroke ratio range and the optimal range, respectively. As one can clearly see, the optimal stroke ratio for the best jet spread and penetration decreases as J decreases at all RMS velocity perturbation magnitudes, consistent with the ideas of Sau and Mahesh (2010). But the optimal L/D for the best molecular mixing does not considerably change with J as long as $U'_{j,rms}$ is the same. In addition, the optimal stroke ratio for best jet spread and penetration as well as molecular mixing increases as $U'_{j,rms}$ increases for a given J.These characteristics indicate that the optimal stroke ratio is dependent on the strength of forcing. The strength of forcing here is quantified by $U'_{j,rms}$ which is related to the square root of the jet's impulse. As impulse is associated with the generation of vorticity (Lamb, 1895; Broadwell and Breidenthal, 1984), one could argue that the nature of the vorticity generation through distinct pulses of fluid has tremendous control over transverse jet mixing and spread.

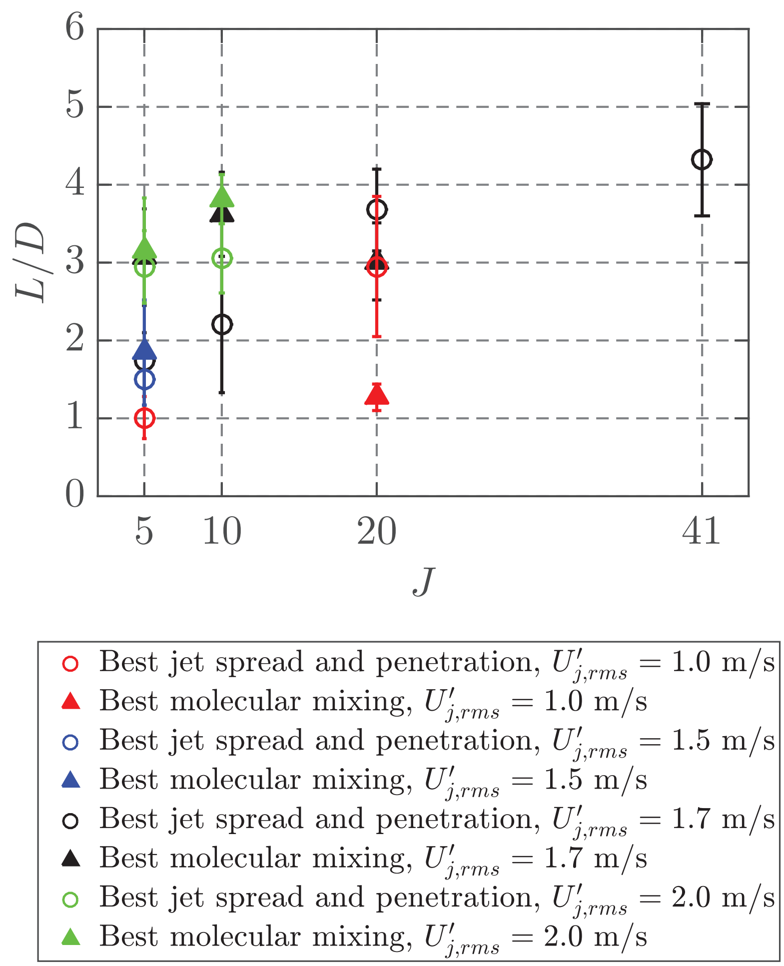

Figure 6.24: Optimal range of stroke ratios L/D estimated using Equation (6.7) for the best jet spread and penetration (hollow circles) as well as molecular mixing (solid triangles) with varied J ($5 \leq J \leq 41$) and $U'_{j,rms}$ ($1.0 \leq U'_{j,rms} \leq 2.0$ m/s). All mixing evaluations are shown in Section 6.4 and Appendix C.

CHAPTER 7

Effects of Axisymmetric Forcing on Transverse Jets - Double-Pulse Square Wave Excitation

The previous chapter has discussed the effect of single-pulse square wave forcing with control on the structural and mixing characteristics of transverse jets, suggesting that deeply-penetrating puff-like vortical structures are created within an appropriate range of stroke ratios L/D, depending on flow conditions and types of shear layer instabilities in the JICF. Jet spread and penetration are significantly enhanced as compared with the unforced case and other forced cases for which penetrating flow structures are absent. Such penetrating vortical structures, however, do not necessarily contribute to better molecular mixing, possibly because the flow structures capture highly concentrated jet fluid inside themselves and reduce the uniformity of concentration scalar values over the entire flowfield. On the other hand, molecular mixing may be able to be significantly enhanced if the puff-like vortex flow structures are carefully controlled so as to trigger vortex interaction or collision. This chapter describes a newly developed method for temporal forcing, the so-called "double-pulse" square wave forcing (as described in Section 2.4).

Double-pulse square wave forcing of the jet in time consists of two temporal square pulses within one single temporal period $T = 1/f_f$. The amplitudes and temporal pulse widths of the two pulses are independently controlled, each of which forms a vortex ring or deeply penetrating vortical structure with the desired forcing conditions. These independently-generated vortex rings can induce near-field vortex interaction or collision in the jet, which may contribute to a more uniform jet fluid spatial distribution as compared with that generated by single-pulse square wave forcing. This double-pulse forcing could potentially enhance molecular mixing of the JICF.

To focus on the near-field vortex interactions and collisions in detail, the flush nozzle with the larger exit diameter of $D = 7.59$ mm (see Section 2.1) is utilized, which is larger than the flush nozzle employed in Chapters 3-6 of this study. The larger flush nozzle typically generates larger-scale vortical structures than those for the flush nozzle with $D = 4.04$ mm. This larger flush nozzle was utilized in previous experimental studies by M'Closkey et al. (2002) and Shapiro et al. (2006), focusing on single-pulse square wave forcing with control. Only the equidensity ($S = 1.00$) larger flush nozzle-injected JICF at the jet Reynolds number $Re_j = 1500$ and jet-to-crossflow momentum flux ratio $J \approx 6.7$ ($R = 2.58$) is explored in the present study, with variable forcing conditions associated with the temporal waveform (see Section 7.3). Here a forcing frequency f_f and root-mean-square (RMS) of the jet velocity perturbation $U'_{j,rms}$ were fixed in most cases at $f_f = 55$ Hz and $U'_{j,rms} = 1.7$ m/s (approximately 63 % of the mean jet velocity at the jet exit plane, $U_j = 2.7$ m/s) among all forcing conditions in order to impose external forcing effectively at the same level, although in a few cases the peak-to-peak jet velocity amplitude of the temporal square pulses, ΔU_j, is matched rather than $U'_{j,rms}$, in order to explore the effect of temporal upsweep in the pulsations. Because of the lower mean jet velocity than that for the smaller flush nozzle, the level of external forcing is relatively stronger with double-pulse square wave forcing for the same RMS of the jet velocity perturbation. The flow conditions, $Re_j = 1500$, $S = 1.00$ and $J = 6.7$, as well as an RMS of jet velocity perturbation of $U'_{j,rms} = 1.7$ m/s were chosen to be approximately the same as those in M'Closkey et al. (2002). The forcing frequency of double-pulse square wave forcing at $f_f = 55$ Hz is effectively the same as a forcing frequency of 110 Hz with single-pulse square wave forcing, studied by M'Closkey et al. (2002) (see Figure 1.10(e)). Hence, double-pulse square wave forcing at $f_f = 55$ Hz with evenly-spaced dual temporal pulses at the same amplitudes and temporal pulse widths is identical to single-pulse square wave forcing at $f_f = 110$ Hz, as long as $U'_{j,rms}$ is identical. For comparison, PLIF data were taken at one of the forcing conditions studied in M'Closkey et al. (2002) (see Figure 1.10(e)). To create cleaner double-pulse square wave response of the jet at the injector exit, specifically at a location 0.1D downstream of the center of the exit plane, the same feedback control system developed in Section 6.1 was implemented with/without some improvements, as documented in Section 7.2.

This chapter first investigates the instability characteristics for the larger flush nozzle-injected JICF with seeded acetone for a range of J values ($2 \leq J \leq 10$). The improvements or differences in the feedback controller from that in Section 6.1 are also explained. Then, structural and mixing characteristics for the larger flush nozzle-injected JICF under double-pulse square wave forcing are explored and compared via acetone PLIF imaging in the centerplane and cross-sectional views as done in Chapters 5 and 6, but at various recording rates from 1 to 7.5 Hz.

7.1 Spectral Measurements for JICF with Acetone

As noted earlier, our group has been extensively studying stability characteristics of transverse jets, especially upstream shear layer instabilities, for a range of S, J, Re_j, and for different injectors (Megerian et al., 2007; Davitian et al., 2010a; Getsinger et al., 2012, 2014). In Chapter 5, the effect of the existence of acetone seeders in the jet on spectral characteristics were also explored for the equidensity flush nozzle-injected JICF at $Re_j = 1900$ and $5 \leq J \leq 41$. However, JICF stability characteristics using the larger flush nozzle have not been explored in the past. Instability characteristics, more specifically the type of instability and its natural frequency on the upstream shear layer of the jet, are required to be evaluated in order to examine the effect of external forcing of the jet, both on structural and mixing characteristics. Therefore, spectral measurements were administered to obtain the fundamental shear layer stability characteristics of the larger flush nozzle-injected JICF. As with the spectral measurements conducted in several previous experimental studies (Megerian et al., 2007; Davitian et al., 2010a; Getsinger et al., 2012, 2014) as well as in Section 5.2.1, hotwire anemometry was employed to acquire jet vertical velocity spectra along upstream shear layer trajectory coordinate s ($0.1 \leq s/D \leq 3.0$). Again, the spatial and frequency resolutions of the spectral measurement were $s/D = 0.1$ and 8 Hz, respectively.

Figure 7.1 represents contour maps associated with power spectra for natural jet velocity perturbations in the vertical direction along the upstream shear layer trajectory coordinate

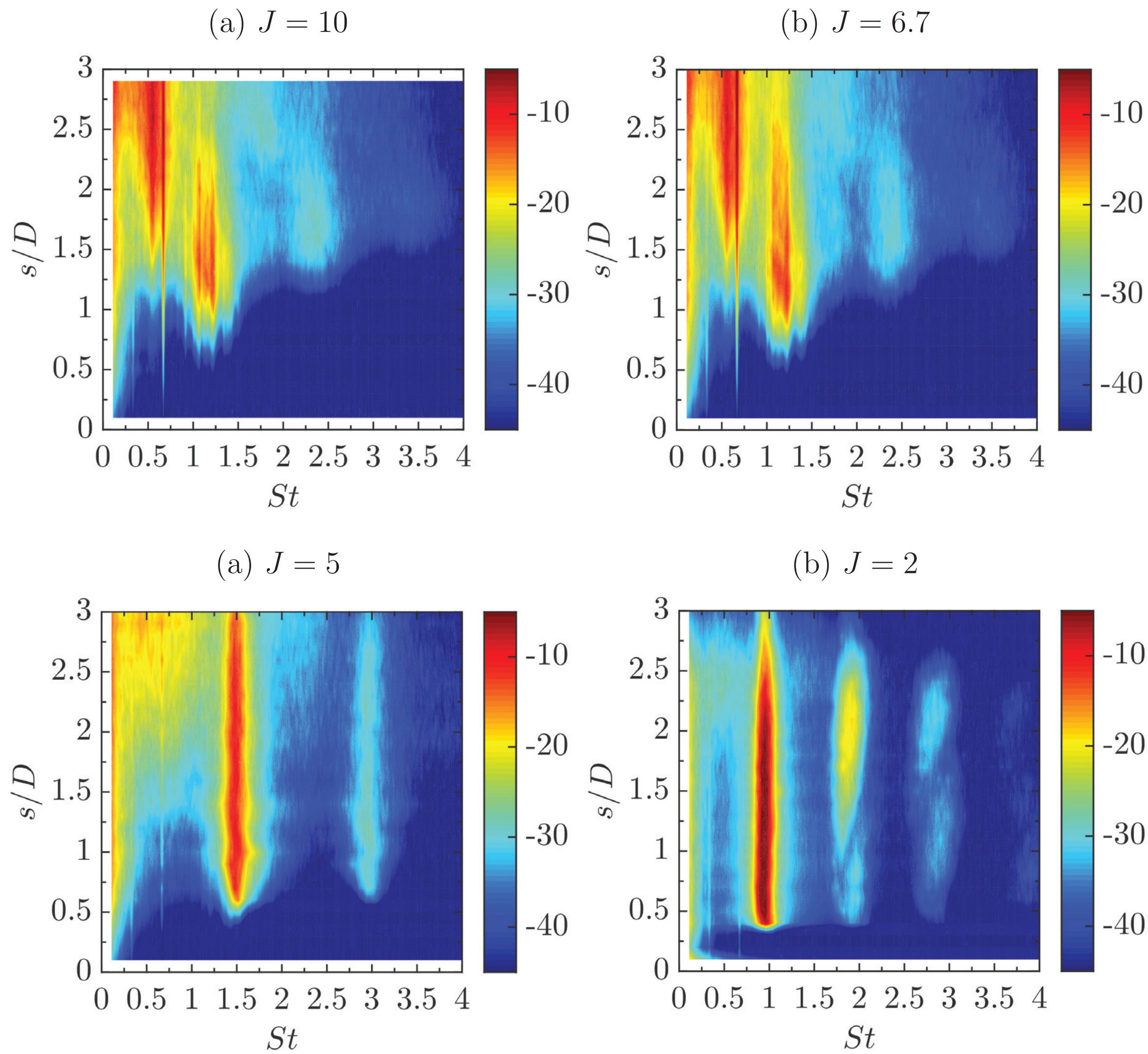

Figure 7.1: Power spectra of the upstream shear layer instabilities for the equidensity larger flush nozzle-injected JICF at (a) $J = 10$ with a fundamental frequency of $f_o \approx 410$ Hz ($St \approx 1.14$), (b) $J = 6.7$ with $f_o \approx 420$ Hz ($St \approx 1.16$), (c) $J = 5$ with $f_o \approx 540$ Hz ($St \approx 1.47$) and (d) $J = 2$ with $f_o \approx 340$ Hz ($St \approx 0.94$).

s/D, with acetone seeded in the jet. Four different J values in the vicinity of J of interest (around $J = 6.7$), $J = 10$, 6.7, 5 and 2, were explored here. At $J = 10$ in Figure 7.1(a), a fairly broadband spectral peak is initiated at $s/D \approx 1.0$ at a fundamental frequency of $St \approx 1.14$ ($f_o \approx 410$ Hz). While a relatively stronger subharmonic spectral peak, typically corresponding to the pairing and merger of vortex structures on the upstream shear layer, begins to be observed at $s/D \approx 1.5$ at $St \approx 0.6$, there are no evident higher harmonic peaks. In comparison with the previous studies (Megerian et al., 2007; Davitian et al., 2010a; Getsinger et al., 2012, 2014), such spectral characteristics correspond to a convectively unstable upstream shear layer, although there is no significant frequency-shifting or mode hopping, as seen with acetone for the same J value for the smaller nozzle (see Figure 5.3(b)). This suggests a weaker degree of tonal interference between the hotwire and the shear layer for the larger jet diameter case. At $J = 6.7$, which is explored in detail in this chapter, a slightly stronger but still broadband peak at a natural frequency of $St \approx 1.16$ ($f_o \approx 420$ Hz) is initiated closer to the jet exit at $s/D \approx 0.7$ as compared with the $J = 10$ case. As with the $J = 10$ case, a subharmonic spectral peak is still present, but with an absence of higher harmonic peaks. Such qualitative trends suggest that both $J = 10$ and 6.7 experience convective or transitional instability in the upstream shear layer, as contrasted with the smaller nozzle's characteristics. The spectral characteristics in Figure 7.1(b) for $J = 6.7$ ($R = 2.58$) with acetone also appear to be different from that for the same nozzle at $R = 2.58$ in the absence of acetone as documented for one location in Shapiro et al. (2006), which suggests the likelihood of absolute instability.

For the larger nozzle's $J = 5$ case, a fairly strong spectral peak is initiated at $s/D \approx 0.5$ at a natural frequency of $St \approx 1.47$ ($f_o \approx 540$ Hz), which is closer to the jet exit plane than in the previous two cases. In contrast to $J = 10$ and 6.7, a higher harmonic peak is recognized for $J = 5$ at $St \approx 3.0$, although a subharmonic spectral peak becomes considerably weaker and broadband, reflecting the absence of vortex merger. This behavior is qualitatively consistent with the spectral characteristics of an absolutely upstream shear layer (Megerian et al., 2007; Davitian et al., 2010a; Getsinger et al., 2012, 2014), hence, the upstream shear layer in this case is considered to be absolutely unstable. At $J = 2$, even stronger peaks at a natural frequency of $St \approx 0.94$ ($f_o \approx 340$ Hz), initiated close to the jet exit at $s/D \approx 0.3$, as well as higher harmonic frequencies, are present, with almost non-existent subharmonic components as compared with the $J = 5$ case, suggesting a stronger absolutely unstable upstream shear layer.

From the observation of the spectral characteristics, the slight difference in J from $J = 6.7$ to 5 dramatically altered the spectral characteristics. Additionally, a natural frequency of the upstream shear layer f_o first increases as J is decreased from 10 to 5, and then f_o decreases as J is decreased further from 5 to 2. Such a transition from an increase in f_o to a decrease in f_o as J is reduced typically corresponds to the transition from convectively to absolutely unstable upstream shear layers (Megerian et al., 2007). This evidence suggests that a critical J for the transition from convectively to absolutely unstable upstream shear layers may lie in the range of $5 \leq J \leq 6.7$, which is smaller than $J_{cr} \approx 10$ suggested by Megerian et al. (2007). This discrepancy may be associated with (1) the existence of acetone in the jet, as noted above, (2) a lower jet Reynolds number of $Re_j = 1500$ than in previous studies and (3) possibly the larger jet diameter of $D = 7.59$ mm, although differences with respect to spectra in Shapiro et al. (2006) suggest this is unlikely. An in-depth stability analysis was not conducted in this study. Hence, from the spectral measurements, the flow conditions of $J = 6.7$ explored in this study is considered to generate a convectively unstable or transitional upstream shear layer between convective and absolute instability, at a natural frequency of the upstream shear layer at $f_o \approx 420Hz$. Further exploration may be required to explore the natural instabilities in the upstream shear layer with the larger flush nozzle, and to determine the effect of double-pulse forcing.

7.2 Improvement in Feedback Controller

The same feedback controller to create single-pulse square wave forcing of the jet in the previous chapter was also implemented for double-pulse square wave forcing. While the first ten components of a Fourier series at a fundamental forcing frequency of $f_f = 100$ Hz are superposed for single-pulse square wave forcing, the first 15 components of the Fourier series at $f_f = 55$ Hz are utilized for double-pulse square wave forcing, because a double-pulse square waveform is generally more complex than one that is single-pulsed, and hence a larger number of harmonics are required to create a sufficiently clean waveform at the jet exit. As with single-pulse square wave forcing, the frequency response of the actuation system was characterized only using 15 harmonics, from 55 Hz to 825 Hz, associated with the first 15 components of the Fourier series. As before, the PVC pipe situated between the loudspeaker and the injector was removed from the actuation system to achieve better controllability (see Section 2.4).

Due to a more complex waveform for the double-pulse square wave than for the single-pulse square wave, cleaner excitation of the jet at the exit plane is more difficult to achieve. Hence, the feedback controller was improved to obtain cleaner double-pulse square wave excitation. First and most importantly, a low-pass filter (1st-order Butterworth filter) at a corner frequency of $f_c = 600$ Hz, approximately $11f_f$, was applied to a desired or target waveform to lessen the effect of higher harmonics. As shown in Figure 5.1, the frequency response of the preset actuation system inherently consists of a significant roll-off after 1000 Hz. Moreover, Figure 6.2 suggests that frequency response becomes fairly low after 400 Hz. Hence, a higher input voltage is required for higher harmonics due to the roll-off toward higher frequencies, which sometimes induces an input voltage that is higher than the tolerance voltage of the loudspeaker, suggesting a sensitivity of the actuation system to higher frequencies. Because 15 harmonics are utilized for double-pulse square wave forcing, cleaner waveforms are more likely to be created, yet high-frequency noise can be more frequently present in temporal waveforms. Weaker higher harmonic effects in the target waveform contribute to less noise in the jet response as well as better convergence of the feedback controller.

The corner frequency was carefully chosen to be small enough to effectively remove the effect of higher harmonics but large enough not to miss higher harmonic components for a better temporal waveform. Figure 7.2 represents the effect of varying the corner frequency in the low-pass filter on the target waveform. Without the low-pass filter in Figure 7.2(a), the desired waveform consists of dual peaks in each square pulse at $u_j - U_j \approx 2.6$ m/s as well as high-frequency oscillations in the waveform outside of pulses at $u_j - U_j \approx -1.1$ m/s. This temporal noise is created by the effect of the higher harmonics. As a corner frequency is decreased from 1000 Hz to 300 Hz, the target waveform becomes less noisy or smoother, although the waveform at $f_c = 1000$ Hz still contains higher harmonic-associated temporal noise, and at $f_c = 300$ Hz the waveform is so smooth that it shows a sine-wave-like behavior. Therefore, a corner frequency in the low-pass filter was determined to be optimal at $f_c = 600$ Hz in this study. The effect of the low-pass filter at $f_c = 600$ Hz on the magnitude reduction

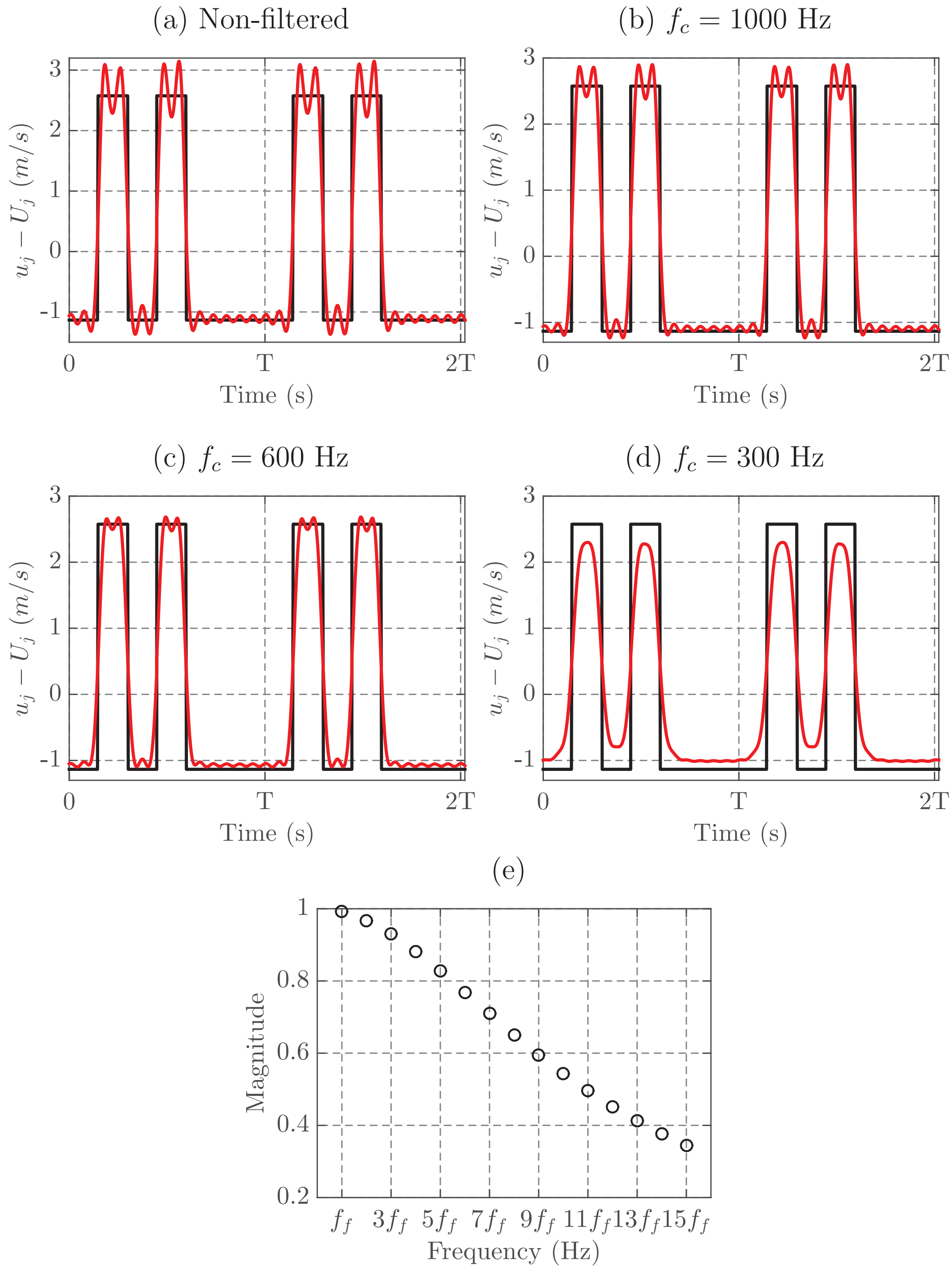

Figure 7.2: Ideal (—) and target temporal double-pulse square waveforms constructed using the first 15 Fourier series (—) at a fundamental or equivalently forcing frequency of $f_f = 55$ Hz and RMS jet velocity perturbation of $U'_{j,rms} = 1.7$ m/s (a) without a low-pass filter (1st-order butterworth filter), as well as with the low-pass filter at (b) a corner frequency of $f_c = 1000$ Hz, (c) $f_c = 600$, and (d) $f_c = 300$. The effect of the low-pass filter at $f_c = 600$ Hz on each frequency component in the target waveform is shown in (e) as a ratio of the magnitude with to without the low-pass filer.

of each frequency components is shown in Figure 7.2(e). Because of the low-pass filter, the RMS of the jet velocity perturbation $U'_{j,rms}$ for double-pulse square wave excitation of the jet becomes lower than the prescribed value of $U'_{j,rms} = 1.7$ m/s. Therefore, a gain larger than unity is applied to all input sinusoidal waves at $f = 55 - 825$ Hz to achieve the desired $U'_{j,rms}$ after the feedback iteration. Since the applied gain is confirmed to be fairly close to the unity for all forcing conditions in the current study, the waveform is not altered and sustained as a fairy clean square waveform.

Second, a perturbation to the input sine and cosine amplitudes to characterize the actuation system (e.g., a perturbation matrix K in Figure 6.4) is determined independently for each frequency component. Previously, the perturbation was a manually-determined constant value for all frequency components in each iteration. Now, a base constant value was multiplied by the magnitude of input sine and cosine voltages to assign the scaled magnitude of perturbation in the feedback iteration. This treatment prevents very high perturbations to each frequency component from occurring, especially for higher harmonics, which are more sensitive to the perturbations than are lower harmonics.

Third, the convergence of the iterative process is assessed by quantifying differences in the sine and cosine amplitudes for the first 15 components of the Fourier series at 55 to 825 Hz, between the target and actual waveforms, instead of via visual inspection. The maximum difference between the target and actual waveforms is set to be 1×10^{-3}, i.e., all differences in the amplitudes of sine and cosine components at each frequency are on the order of 10^{-4}. This criterion was chosen after trial and error to be sufficiently small enough to achieve a clean waveform but large enough to avoid the difficulty in convergence and excessive numbers of iterations that do not dramatically alter the resultant temporal waveforms.

While the first improvement, the low-pass filter, directly contributes to a much cleaner waveform, the last two improvements are associated with better convergence and convenience of the control system, which dramatically shorten the time to achieve the convergence. Because these improvements were applied after many PLIF experiments were already conducted, most results shown in this dissertation were taken under double-pulse square wave excitation created by the feedback controller without these second and third improvements. It will be mentioned in the results whether or not the forcing was created with or without the improvements in the following sections.

7.3 Structural Characteristics for the JICF

Using acetone PLIF imaging in the centerplane and cross-sectional views, structural characteristics under double-pulse square wave forcing of the jet is explored. In addition to a PLIF recording rate of 7.5 Hz for sine and single-pulse square wave forcing, alternative recording rates are explored, mainly to capture a wider range of phases, but also to investigate the effect of the recording rate artifact on mixing quantification. Recording rates of 1, 5 and 7.5 Hz are applied in this study. If PLIF imaging were conducted exactly at a recording rate of 1 or 5 Hz, the resultant images would be only taken at one single phase for external forcing at $f_f = 55$ Hz. However, because the PLIF data acquisition system, including the laser, camera and the external programmable timing unit (see Section 2.3) inherently holds a slight temporal shift from shot to shot during the experiments, the recordings at 1 and 5 Hz can capture instantaneous images with gradually shifting phases, effectively producing "phase-locked" like data, although the PLIF imaging is technically not phase-locked here. A series of phase-locked-like instantaneous centerplane as well as cross-sectional images are shown in this section to clearly reveal the near-field flow dynamics (e.g., vortex interactions or collisions).

7.3.1 Baseline Reference Cases

Before an exploration of the forced JICF, the unforced JICF is explored for the $J = 6.7$ case, as shown in Figure 7.3. From the instantaneous centerplane image in Figure 7.3(a), coherent rollups on the upstream shear layer are initiated at $z/D \approx 1.5$, roughly consistent with initiation of the shear layer instability in Figure 7.1(b). As compared with the smaller flush nozzle-injected JICF, larger rollups are observed with the larger flush nozzle, which enables easier visual inspection of flow structures. Figures 7.3(c)-(f) are mean cross-sectional images

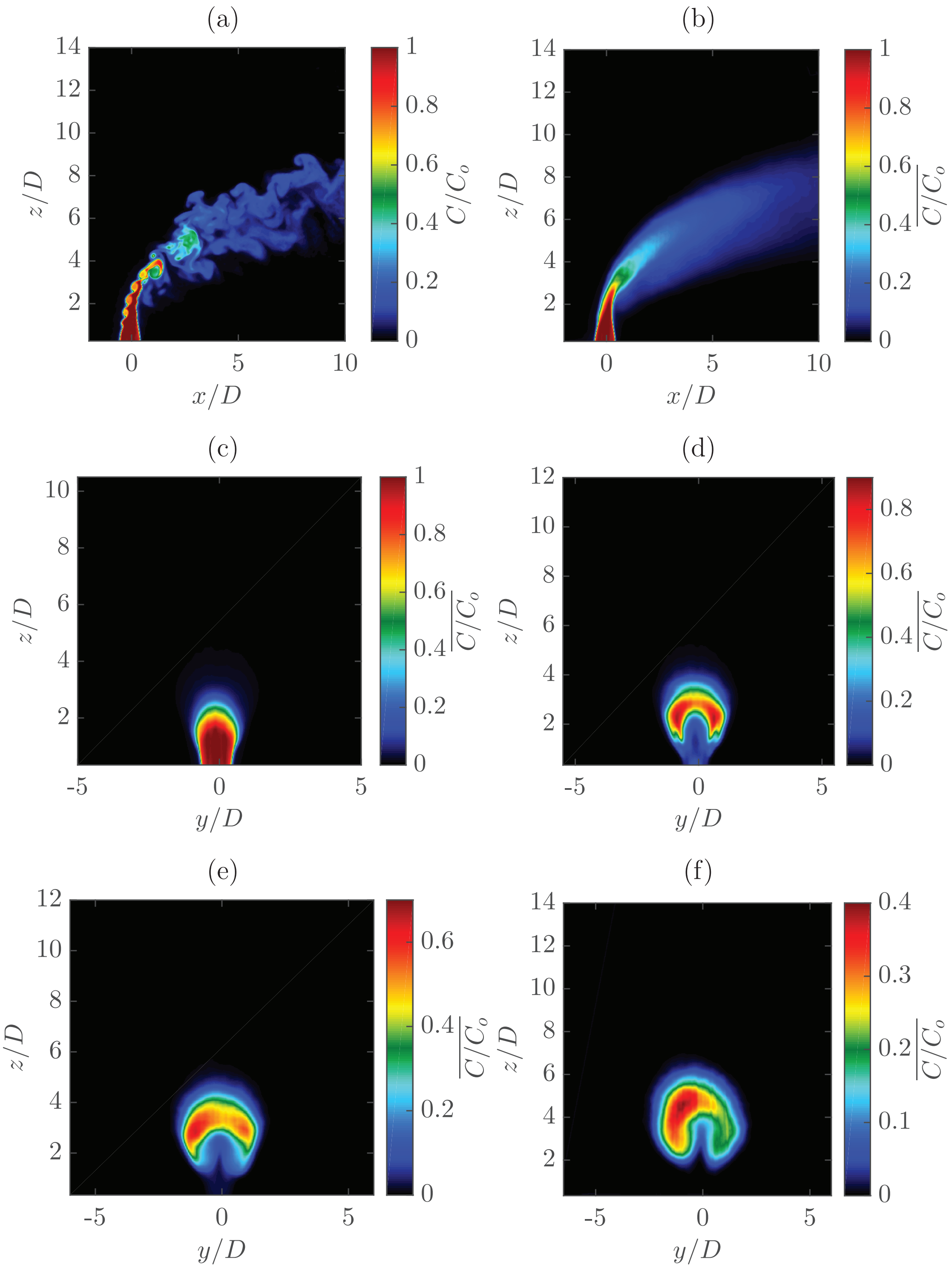

Figure 7.3: PLIF images for the unforced equidensity larger flush nozzle-injected JICF at $J = 6.7$: (a) instantaneous centerplane, (b) mean centerplane, (c)-(f) mean cross sections at downstream locations of $x/D = 0$, 0.5, 1.0 and 2.5, respectively. These images were acquired at a recording rate of 1 Hz.

of the jet at downstream locations $x/D = 0$, 0.5, 1.0 and 2.5, showing the development and evolution of a fairly symmetric CVP structure, although the concentration distribution in the jet's cross-sectional structure is slightly asymmetric at $x/D = 2.5$. It should be noted that the maximum height of the field of view at $z/D \approx 14$ in Figures 7.3(a) and (b) is fairly close to the test section ceiling.

Now the forced JICF under double-pulse square wave forcing with control is explored, but with conditions creating the equivalent of single pulse forcing at a frequency of 110 Hz. Because the RMS of jet velocity perturbation is fixed at $U'_{j,rms} = 1.7$ m/s, double-pulse square wave forcing at $f_f = 55$ Hz, consisting of two equally-spaced pulses with the same temporal pulse widths and amplitudes, is identical to single-pulse square wave forcing at $f_f = 110$ Hz. This 110 Hz case is the same as one of the forcing conditions in M'Closkey et al. (2002) utilizing smoke visualization (see Figure 1.10(e)). Therefore, the same forcing condition as this "reference case" in M'Closkey et al. (2002) was first applied, to examine the similarities or differences from the reference case when one utilizes acetone PLIF rather than smoke visualization. For this reference case, three types of double-pulse square wave forcing were first implemented: (1) a case without the improvements in the feedback controller (labeled as "No filter" or Case 1a in this study) as described in Section 7.2, (2) a case with the improvements noted (labeled as "Filtered" or Case 1b) and (3) a waveform designed to replicate the reference case's waveform in M'Closkey et al. (2002) (labeled as "Replicated" or Case 1c). The temporal jet responses at the jet exit for these three forcing cases acquired via hotwire anemometry are shown in Figure 7.4. The temporal waveforms taken from M'Closkey et al. (2002) are also displayed as a reference in Figure 7.4(d). Note that the forcing with the low-pass filter (Figure 7.4(b)) is cleaner than that without the filter (Figure 7.4(a)). In particular, as mentioned in Section 7.2, the amplitudes of dual peaks during the pulsation at $u_j - U_j \approx 2.8$ m/s as well as the flat parts at the trough of the square pulse at $u_j - U_j \approx -1.1$ m/s are cleaner with the low-pass filter. Figure 7.4(c) is the replicated waveform from M'Closkey et al. (2002) created by the present feedback controller based on the waveform Figure 7.4(d) as a target waveform. By comparing Figure 7.4(c) with Figure 7.4(d), we see that the temporal excitation of the jet is well replicated. Hence, similar

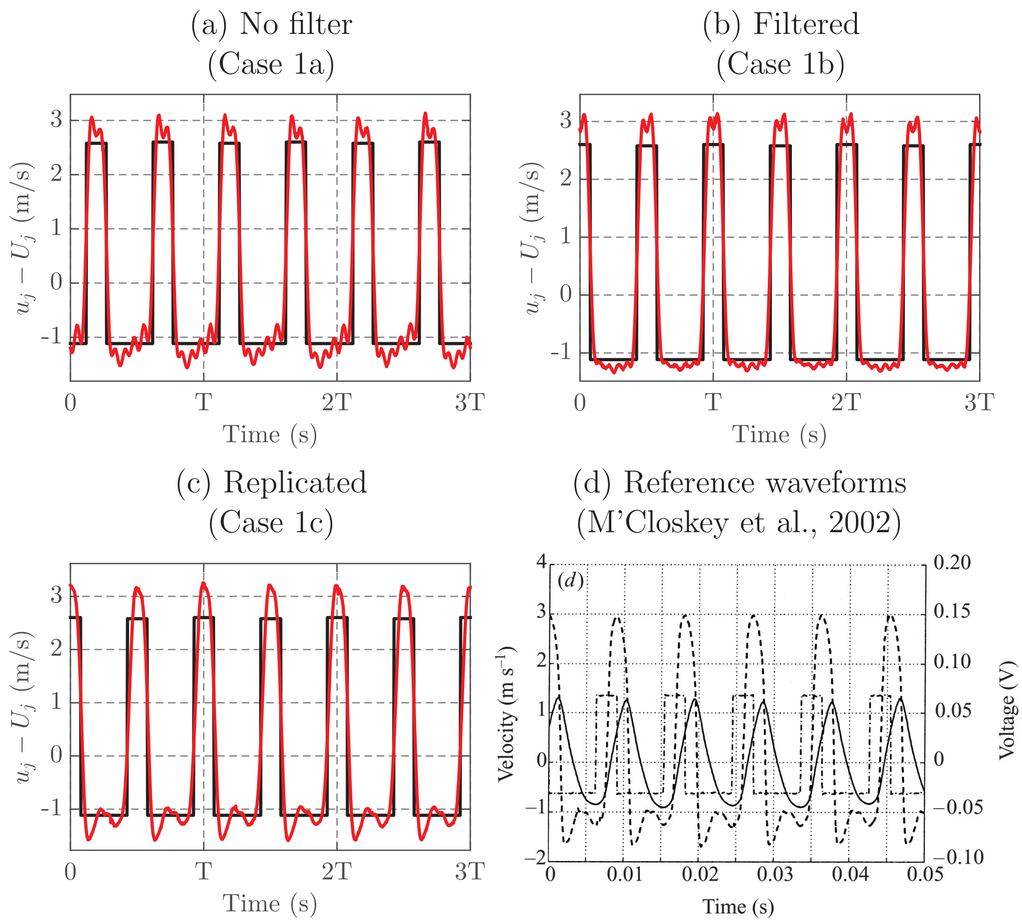

Figure 7.4: Ideal (—) and actual (—) temporal jet response to double-pulse square wave forcing (f_f = 55 Hz) at the jet exit acquired via hotwire anemometry: (a) double-pulse square wave forcing without the improvements in the feedback controller (Case 1a), (b) double-pulse square wave forcing with the improvements (Case 1b), (c) double-pulse square wave forcing with the improvements replicated using a waveform from the previous study (M'Closkey et al., 2002) (Case 1c), and (d) reference single-pulse square wave forcing at $f_f = 110$ Hz taken from M'Closkey et al. (2002) plotted as a dashed line (--). RMS of jet velocity perturbation is matched among all forcing conditions at $U'_{j,rms} = 1.7$ m/s.

structural characteristics are expected under forcing conditions shown in Figures 7.4(c) and (d).

Figure 7.5 represents centerplane instantaneous images via acetone PLIF imaging as well as smoke visualization taken by M'Closkey et al. (2002), which utilized the same injector as well as wind tunnel facility as in the current study (see Section 2.1). As one can see, all instantaneous centerplane structures clearly consist of deeply-penetrating coherent vortex rings with trailing tails, as well as a bifurcating jet structure with a lower part flowing relatively close to the test section floor around $z/D \approx 2.0$ in Figures 7.5(a)-(c). Hence, regarding the vortex ring formation itself, instantaneous centerplane structural characteristics shown here are fairly similar. However, all jets in the present study (Figures 7.5(a)-(c)), including the replicated case in Figure 7.5(c), penetrate much more deeply than the reference case (Figure 7.5(d)). As mentioned previously, the height of the field of view in these instantaneous images is fairly close to the test section ceiling, so the jets in Figures 7.5(a)-(c) are likely to hit the test section ceiling, although the reference case in Figure 7.5(d) did not appear to hit the ceiling. Even with the replicated waveform in Figure 7.5(c), the instantaneous centerplane structure in terms of the jet penetration is considerably different.

Such a discrepancy is possibly associated with two culprits, as follows. First, while the jet density in the present study ρ_j is matched to the air crossflow density ρ_∞ by carefully adjusting the amounts of nitrogen, helium and acetone vapor in the jet (see Section 2.1), the jet density in M'Closkey et al. (2002) was not matched with the crossflow density, suggesting that S may well be larger than unity in this earlier study due to the addition of liquid paraffin solution to the nitrogen jet for smoke visualization. For example, if liquid paraffin solution with a typical molecular weight of 350 g/mol (Pearson et al., 1986) is added to a gaseous nitrogen jet, with a paraffin mole fraction of 10 % of the jet, S becomes approximately 2, which is considerably larger than unity. Getsinger et al. (2012) suggested that the effect of different density ratios S on the instability characteristics are significant, at least, when $S < 1$ and there is a greater propensity for transition to absolute instability. Moreover, if one compares the unforced JICF images in Figure 7.3(a) with acetone, with Figure 1.10(a) from M'Closkey et al. (2002) with smoke, there appears to be lesser penetration for the latter case, consistent with a higher density jet with $S > 2$. Hence, the density ratio discrepancy may cause the different jet responses to external excitation, and hence the varied forced jet penetration seen in Figure 7.5.

Additionally, the hotwire used to characterize the single-pulse square wave excitation in M'Closkey et al. (2002) was not calibrated utilizing the actual jet fluid consisting of nitrogen

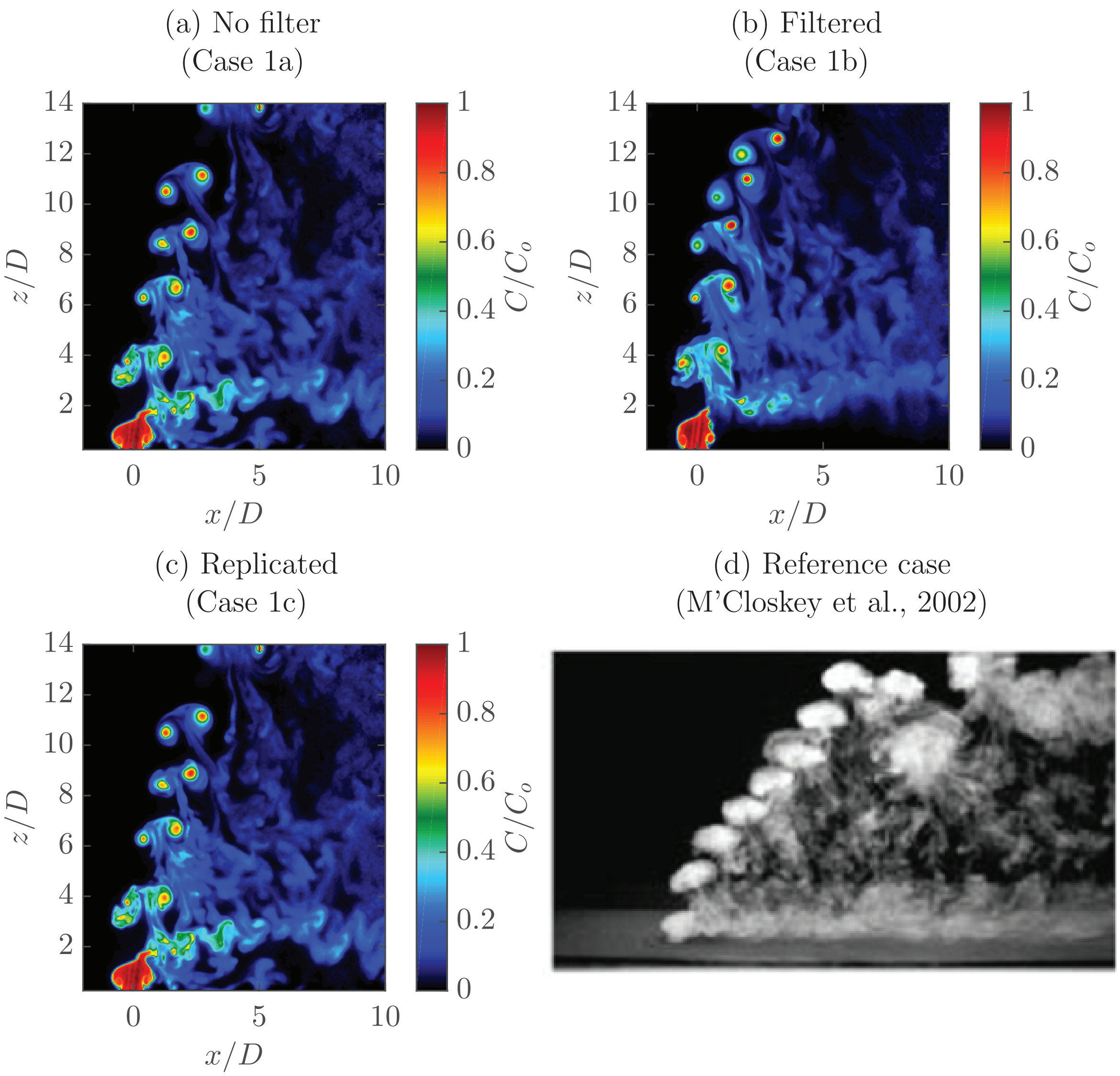

Figure 7.5: Instantaneous centerplane PLIF images under double-pulse square wave forcing at f_f = 55 Hz: (a) without the improvements in the feedback controller (Case 1a), (b) with the improvements (Case 1b), (c) with the improvements replicated using a waveform from the previous study (M'Closkey et al., 2002) (Case 1c) and (d) reference single-pulse square wave forcing at f_f = 110 Hz taken from M'Closkey et al. (2002). RMS of jet velocity perturbation is matched among all forcing conditions at $U'_{j,rms}$ = 1.7 m/s. These images were acquired at a recording rate of 5 Hz.

and liquid paraffin solution, but just using air in order to avoid corruption of the wire. The difference in the gas constituents significantly alters the hotwire response, as documented in this dissertation in Section 2.2. The hotwire in the present study is always calibrated with air or the actual jet fluid used in PLIF imaging so that the jet response to external forcing can be accurately captured. The difference in the hotwire calibration process may cause a different quantification of the jet's response to single-pulse square wave excitation in M'Closkey et al. (2002), perhaps suggesting that the present study possibly applied stronger excitation of the jet, equivalent to a higher $U'_{j,rms}$, and thus resulting in higher jet penetration.

Because of these possible two culprits mentioned above, the same degree of jet penetration as the reference case from M'Closkey et al. (2002) could not be achieved, even after many experiments. Nevertheless, the same coherent, deeply-penetrating vortex rings are formed for all forcing conditions. Hence, one may be able to control the spacing or timing of the vortex ring formation by varying forcing conditions relative to this reference case and hence to induce vortex interactions and collisions, which is the main interest in this part of the study.

Interestingly, the jet penetration for Case 1a without a filter is slightly lower than that for the case 1b, which will be discussed more in detail in Section 7.4.1. The main difference in temporal waveforms between these two cases (Figures 7.4(a) and (b)) are whether or not the trough part of the square pulse at $u_j - U_j \approx -1.1$ m/s is flat. Hence, before changing forcing conditions to trigger near-field vortex interactions and collisions, the effect of alteration in the temporal waveform must be explored.

Figure 7.6 represents temporal jet responses to external forcing at the jet exit with altered waveforms altered from those in Cases 1a-1c. These temporal jet responses were created using the feedback controller with the improvements to enable the creation of more complicated waveforms. The first forcing condition shown in Figure 7.6(a) includes a gradual, fairly linear increase in the jet velocity between two pulses. This forcing condition is labeled as "Flat slope" or Case 1d, which is applied in order to investigate the effect of a gradual increase in the jet velocity between the square pulses. The second forcing condition in Figure 7.6(b) additionally includes temporal oscillations between the pulses, on top of the gradual slope in Case 1d, which is labeled as "Slope plus ringing" or Case 1e. This case is fairly similar to Case 1a generated without the low-pass filter in the feedback controller. Starting with Case 1e, if the amplitude of the temporal oscillation and the slope of the lower-velocity part

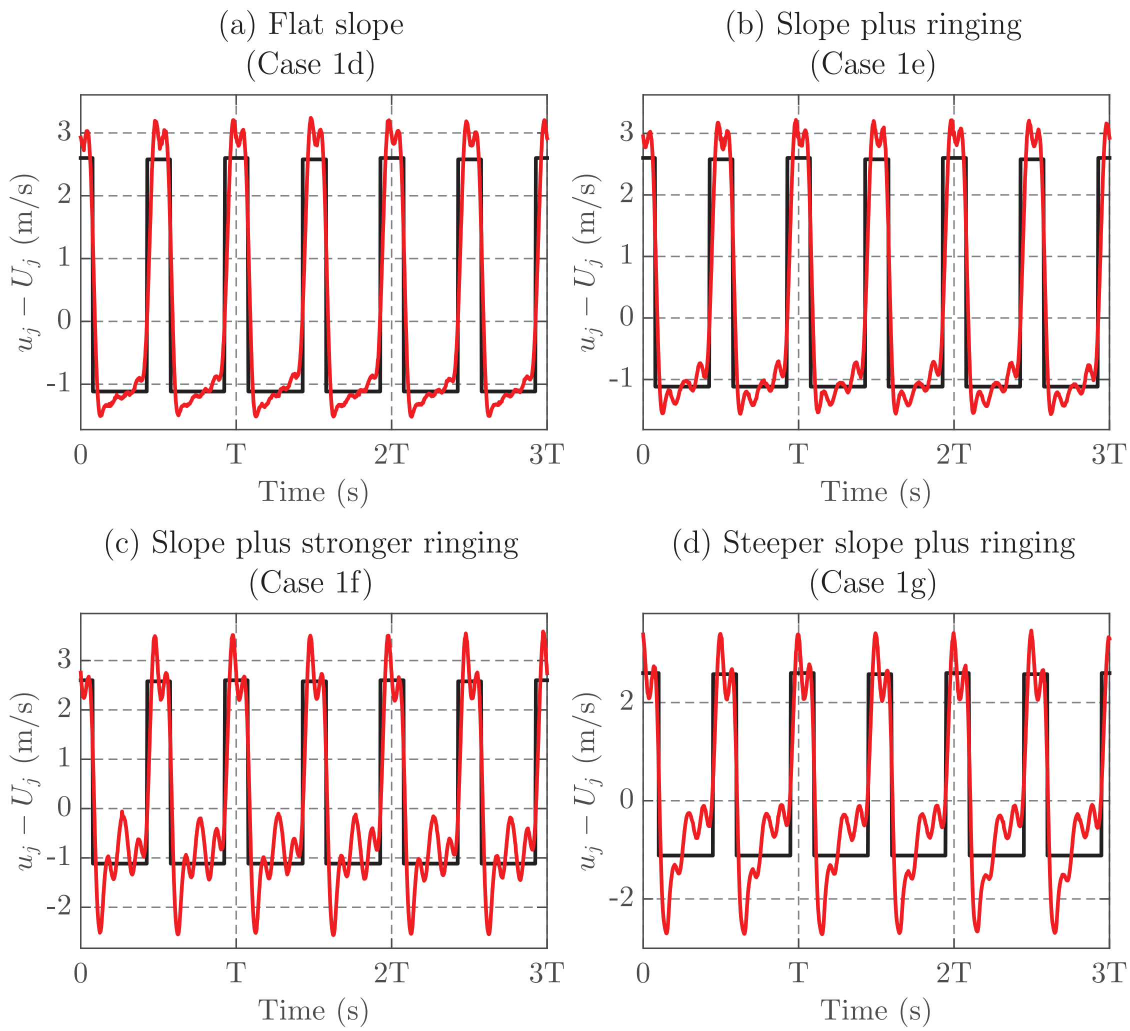

Figure 7.6: Ideal (—) and actual (—) temporal jet response to double-pulse square wave forcing (f_f = 55 Hz) at the jet exit acquired via hotwire anemometry with the improvements in the feedback controller: (a) with fairly linear increase in jet velocity between two pulses (Case 1d), (b) with an increase in jet velocity between two pulses with temporal oscillation (Case 1e), (c) with an increase in jet velocity between two pulses with relatively strong temporal oscillation (Case 1f), and (d) with an greater increase in jet velocity between two pulses with temporal oscillation (Case 1g). RMS of jet velocity perturbation is matched among all forcing conditions at $U'_{j,rms} = 1.7$ m/s.

where the jet velocity gradually increases are independently increased, this creates a "Slope plus stronger ringing" or Case 1f. If the slope is further increased, we obtain the "Steeper slope plus ringing" or Case 1g. For Cases 1f and 1g, because the temporal waveforms are required to become relatively oscillatory as compared with Cases 1a-1e, the shape of the square pulses at the peaks is also slightly distorted in order to achieve a greater temporal oscillation and steeper jet velocity slope only using the first 15 components of the Fourier series.

Instantaneous centerplane images under double-pulse square wave forcing conditions in Cases 1d-1g are shown in Figure 7.7. Again, the RMS of jet velocity perturbation is still matched among all forcing conditions at $U'_{j,rms} = 1.7$ m/s. As one can clearly observe, jet penetration becomes significantly lower for all forcing conditions in comparison to Cases 1a-1c. Even for Cases 1d and 1e, which are fairly similar to Case 1a, the jet penetration is lowered, and deeply-penetrating vortex rings became less coherent than in Cases 1a-1c. For Cases 1f and 1g, since temporal jet responses to external forcing are relatively oscillatory, the jet is quite disturbed and hence there is no clear, coherent vortex ring formation. These results suggest that slight differences in the temporal jet waveform during external forcing may significantly alter instantaneous jet centerplane structures. Such characteristics suggest that it could be difficult to accurately apply double-pulse square wave forcing to strategically enhance molecular mixing.

The experimental study in Chapter 6 indicated that structural and mixing characteristics for the forced JICF under single-pulse square wave forcing are significantly affected by the stroke ratio L/D extracted from temporal data. Hence, such parameters are extracted from the temporal data shown in Figures 7.4 and 7.6 in this section as well. In addition to actual temporal pulse width τ_{actual} and stroke ratio L/D as in Section 6.2, the peak-to-peak velocity amplitude of square pulses ΔU_j is also quantified. The same method (e.g., a 5 % criterion and the integration of $u_j - U_{5\%}$ during the temporal pulse width based on Equation (6.7)) was applied to evaluate these parameters (described in Section 6.2). Since double-pulse square wave forcing consists of two pulses with varied amplitudes and temporal pulse widths, the temporal parameters are independently evaluated for each pulse. For Cases 1a-1g in this section, although the external forcing is identical to single-pulse square wave forcing at a forcing frequency $f_f = 110$ Hz, there temporal parameters are extracted independently from the "first" and "second" pulses within a period. Obviously, it is technically double-pulse square wave forcing at $f_f = 55$ Hz, so all temporal parameters from the first and second

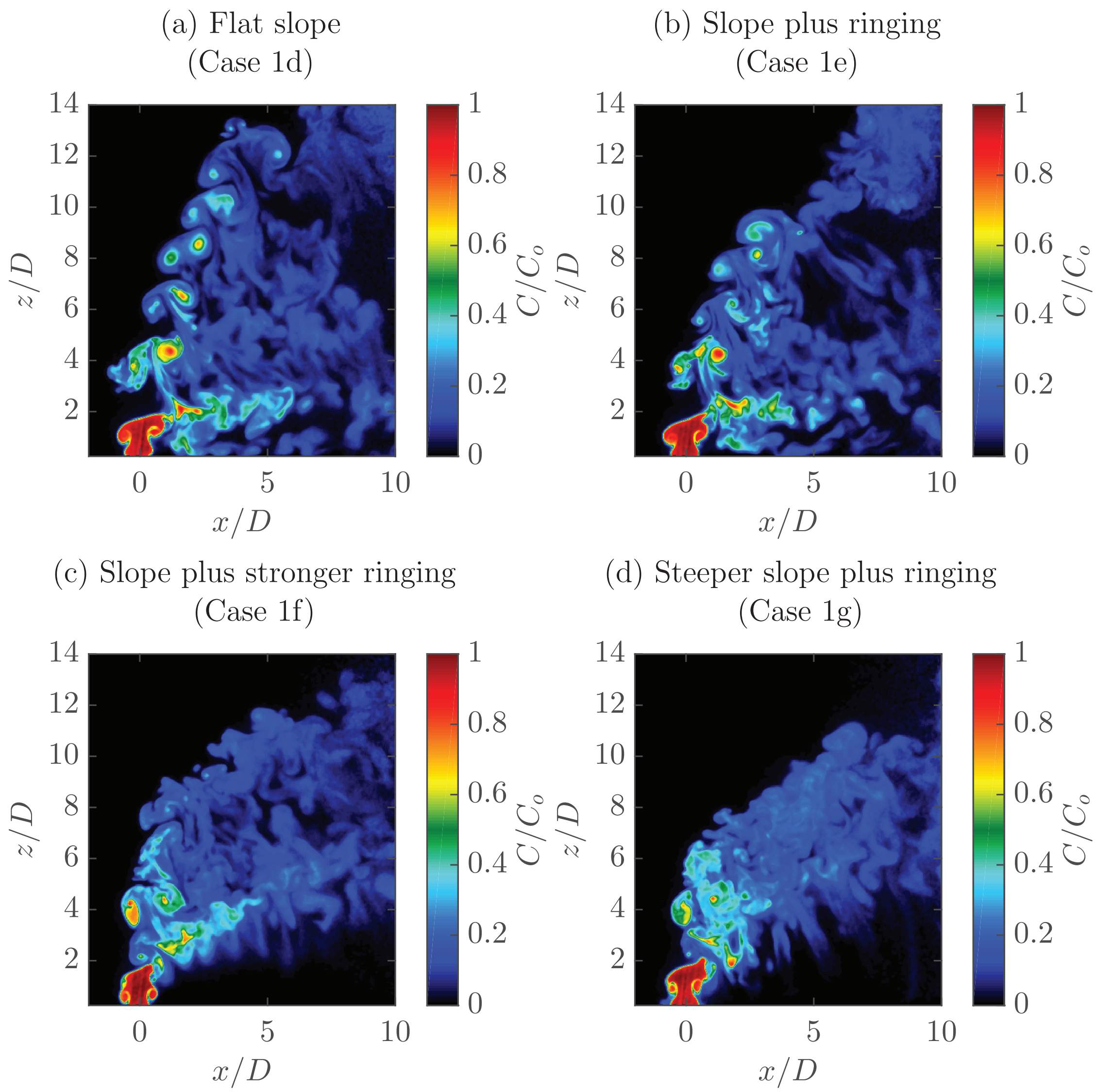

Figure 7.7: Instantaneous centerplane PLIF images under double-pulse square wave forcing ($f_f =$ 55 Hz) with the improvements in the feedback controller: (a) with fairly linear increase in jet velocity between two pulses (Case 1d), (b) with an increase in jet velocity between two pulses with temporal oscillation (Case 1e), (c) with an increase in jet velocity between two pulses with relatively strong temporal oscillation (Case 1f), and (d) with an greater increase in jet velocity between two pulses with temporal oscillation (Case 1g). RMS of jet velocity perturbation is matched among all forcing conditions at $U'_{j,rms} = 1.7$ m/s. These images were acquired at a recording rate of 5 Hz.

pulses here should be fairly close. As explained in Section 6.2, at least 10 temporal cycles are averaged to calculate the mean temporal parameters in jet forcing.

The extracted temporal parameters for Cases 1a-1g with matching $U'_{j,rms} = 1.7$ m/s

Table 7.1: Temporal data-extracted parameters for the first (subscript 1) and second (subscript 2) temporal square pulses within a period T with matching the RMS of jet velocity perturbation at $U'_{j,rms} = 1.7$ m/s, for $f_f = 55$ Hz and equal input pulses. The parameters here are actual temporal pulse width normalized by a period τ_{actual}/T, peak-to-peak jet velocity amplitude of pulsation ΔU_j and stroke ratio L/D. 95 % confidence intervals are also shown with an effective digit of the second decimal point. All parameters are averaged over at least 10 temporal cycles.

	$\tau_{actual,1}/T$	$\tau_{actual,2}/T$	$\Delta U_{j,1}$ (m/s)	$\Delta U_{j,2}$ (m/s)	L_1/D	L_2/D
Case 1a	0.20 ± 0.00	0.20 ± 0.00	4.15 ± 0.02	4.18 ± 0.02	1.27 ± 0.00	1.32 ± 0.00
Case 1b	0.21 ± 0.00	0.20 ± 0.00	4.28 ± 0.01	4.28 ± 0.02	1.35 ± 0.00	1.32 ± 0.01
Case 1c	0.21 ± 0.00	0.22 ± 0.00	4.47 ± 0.02	4.51 ± 0.01	1.35 ± 0.01	1.38 ± 0.01
Case 1d	0.19 ± 0.00	0.19 ± 0.00	4.12 ± 0.01	4.13 ± 0.02	1.22 ± 0.01	1.22 ± 0.01
Case 1e	0.19 ± 0.00	0.19 ± 0.00	4.17 ± 0.02	4.17 ± 0.03	1.22 ± 0.01	1.22 ± 0.00
Case 1f	0.17 ± 0.00	0.18 ± 0.00	4.38 ± 0.02	4.48 ± 0.01	1.11 ± 0.00	1.16 ± 0.00
Case 1g	0.17 ± 0.00	0.17 ± 0.00	3.89 ± 0.01	3.93 ± 0.03	0.97 ± 0.01	0.98 ± 0.01

amongst all forcing conditions are tabulated in Table 7.1. Here, the parameters with subscripts 1 and 2 are relevant to the first and second temporal square pulses, respectively. Note that the mean actual temporal pulse widths for the first and second square pulses, $\tau_{actual,1}/T$ and $\tau_{actual,2}/T$, are slightly larger than the prescribed $\tau_{input}/T = 0.15$, which is consistent with the evaluation for single-pulse square wave forcing in Section 6.2. Second, note that the stroke ratios L/D are fairly similar among Cases 1a-1e, but are not similar to Cases 1f and 1g, suggesting that stroke ratio may not be a culprit of the different jet penetration seen in Cases 1d and 1e. More importantly, the peak-to-peak jet velocity amplitude ΔU_j is considerably different among all forcing conditions. Physically, ΔU_j is associated with the effective velocity or upsweep in pulsation for a square pulse. Therefore, the difference in ΔU_j among all forcing conditions possibly causes the discrepancy in jet penetration observed in Figures 7.5 and 7.7, although similarities in ΔU_j between Cases 1a and 1e do not produce similar penetration.

Shapiro et al. (2006) matched the peak-to-peak velocity amplitude of the pulsation ΔU_j

instead of RMS jet velocity perturbation $U'_{j,rms}$ in their experimental study to effectively achieve the same level of pulsation among all forcing conditions. The computational study by Sau and Mahesh (2010) did the same, using single-pulse square wave forcing.The computations indicated that the alteration of the shape of temporal waveforms associated with the jet response at the jet exit (e.g., a perfect square waveform vs. an imperfect square waveform) does not affect the jet trajectory and vorticity field as long as the stroke ratio, velocity ratio and duty cycle are matched between the forcing conditions. Since these studies evaluated stroke ratios using Equation (6.6) ($L/D = \Delta U_j \tau / D$), the peak-to-peak jet velocity amplitude ΔU_j is also required to be matched to achieve the same jet trajectory and vorticity field. These previous studies suggest that matching ΔU_j may produce more similar jet penetration. Hence, the present study also matched ΔU_j among all forcing conditions, in addition to $U'_{j,rms}$, to investigate the effect of matching different temporal data-associated parameters.

Figure 7.8 represents temporal waveform data with a matched peak-to-peak jet velocity amplitude ΔU_j among all forcing conditions, approximately with $\Delta U_j \approx 4.3$ m/s. Note that $U'_{j,rms}$ is obviously not matched among all forcing conditions when ΔU_j is matched instead. The value of $\Delta U_j \approx 4.3$ m/s is chosen to be approximately the same as that for Case 1b in Table 7.1 as a reference because the forcing condition creates the closest waveform to the ideal one, although there is a slight difference in ΔU_j because matching this parameter is more difficult using the current feedback controller than matching $U'_{j,rms}$, which is tabulated in Table 7.1.

Table 7.2 shows temporal parameters extracted from Figure 7.8 with matching ΔU_j instead of $U'_{j,rms}$. Again, the actual temporal pulse widths τ_{actual} for the first and second pulses are fairly close among all forcing conditions and are slightly higher than the prescribed value of $0.15T$, which is consistent with values for τ_{actual} in Table 7.1, and under single-pulse square wave forcing in Section 6.2. Additionally, the stroke ratio L/D is also similar for Cases 1a-1e in Table 7.2 but is lower for Cases 1f and 1g, although the stroke ratio for Cases 1d and 1e are also slightly lower than that for Cases 1a-1c. Because ΔU_j is matched among all forcing conditions in Table 7.2, ΔU_j values are fairly close for all different cases, with only

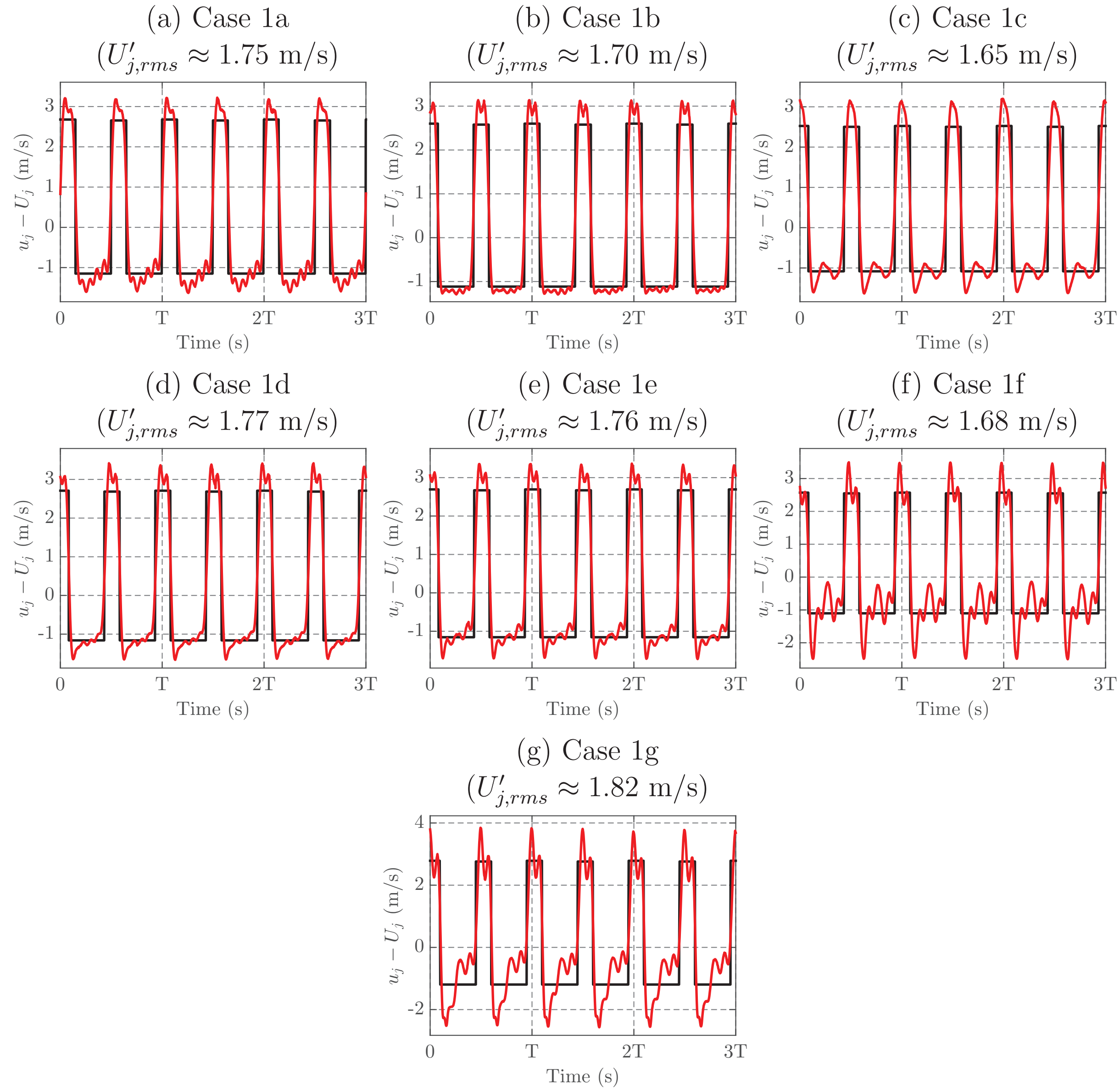

Figure 7.8: Ideal (—) and actual (—) temporal jet response to double-pulse square wave forcing ($f_f = 55$ Hz) at the jet exit acquired via hotwire anemometry for Cases 1a-1g with matching peak-to-peak jet velocity amplitude at $\Delta U_j \approx 4.3$ m/s. RMS of jet velocity perturbation $U'_{j,rms}$ for each forcing condition is also shown in parentheses.

slight differences arising from the difficulty in matching the parameter ΔU_j as mentioned previously. Using this temporal jet excitation equivalent to single-pulse square wave forcing at $f_f = 110$ Hz, centerplane PLIF imaging was performed for the forced JICF as follows.

Figure 7.9 represents instantaneous centerplane PLIF images of the jet under double-pulse

Table 7.2: Temporal data-extracted parameters for the first (subscript 1) and second (subscript 2) temporal square pulses within a period T with matching peak-to-peak jet velocity amplitude at $\Delta U_j \approx 4.3$ m/s, for $f_f = 55$ Hz and equal input pulses. The parameters here are actual temporal pulse width normalized by a period τ_{actual}/T, peak-to-peak jet velocity amplitude of pulsation ΔU_j and stroke ratio L/D. 95 % confidence intervals are also shown with an effective digit of the second decimal point. All parameters are averaged over at least 10 temporal cycles.

	$\tau_{actual,1}/T$	$\tau_{actual,2}/T$	$\Delta U_{j,1}$ (m/s)	$\Delta U_{j,2}$ (m/s)	L_1/D	L_2/D
Case 1a	0.20 ± 0.00	0.20 ± 0.00	4.29 ± 0.01	4.31 ± 0.02	1.30 ± 0.01	1.35 ± 0.00
Case 1b	0.20 ± 0.00	0.20 ± 0.00	4.32 ± 0.01	4.32 ± 0.01	1.31 ± 0.00	1.34 ± 0.00
Case 1c	0.21 ± 0.00	0.22 ± 0.00	4.38 ± 0.02	4.40 ± 0.02	1.31 ± 0.00	1.34 ± 0.00
Case 1d	0.19 ± 0.00	0.19 ± 0.00	4.34 ± 0.01	4.34 ± 0.02	1.26 ± 0.00	1.26 ± 0.01
Case 1e	0.19 ± 0.00	0.19 ± 0.00	4.34 ± 0.01	4.35 ± 0.02	1.25 ± 0.01	1.25 ± 0.01
Case 1f	0.17 ± 0.00	0.18 ± 0.00	4.28 ± 0.01	4.36 ± 0.01	1.08 ± 0.00	1.13 ± 0.00
Case 1g	0.17 ± 0.00	0.17 ± 0.00	4.27 ± 0.01	4.35 ± 0.02	1.04 ± 0.01	1.05 ± 0.00

square wave forcing, corresponding to temporal parameters for ΔU_j matched as in Table 7.2. While the jet penetration was considerably different among difference forcing conditions with matching $U'_{j,rms}$ as shown in Figures 7.5 and 7.7, jet penetration with matched ΔU_j is similar amongst most forcing conditions (Cases 1a-1e). The exceptions are Cases 1f and 1g as shown in Figures 7.9(f) and (g), where temporal waveforms include relatively strong and sharp temporal oscillations. As discussed later in Section 7.4.1, the jet penetrates similarly for Cases 1a-1c but it is very slightly lower for Cases 1d-1e and then much more so for Cases 1f-1g, despite the fact that temporal waveforms are fairly similar. This difference may indicate that slight differences in the stroke ratio between Cases 1a-1c and Cases 1f-1g significantly alter jet penetration and response to external forcing, in general, although further exploration of the effect of this difference is needed.

Nevertheless, these structural characteristics suggest that jet penetration via deeply penetrating vortex structures is more dependent on the value of ΔU_j than of $U'_{j,rms}$. Because controlling jet penetration enables better controllability of the near-field vortex interaction

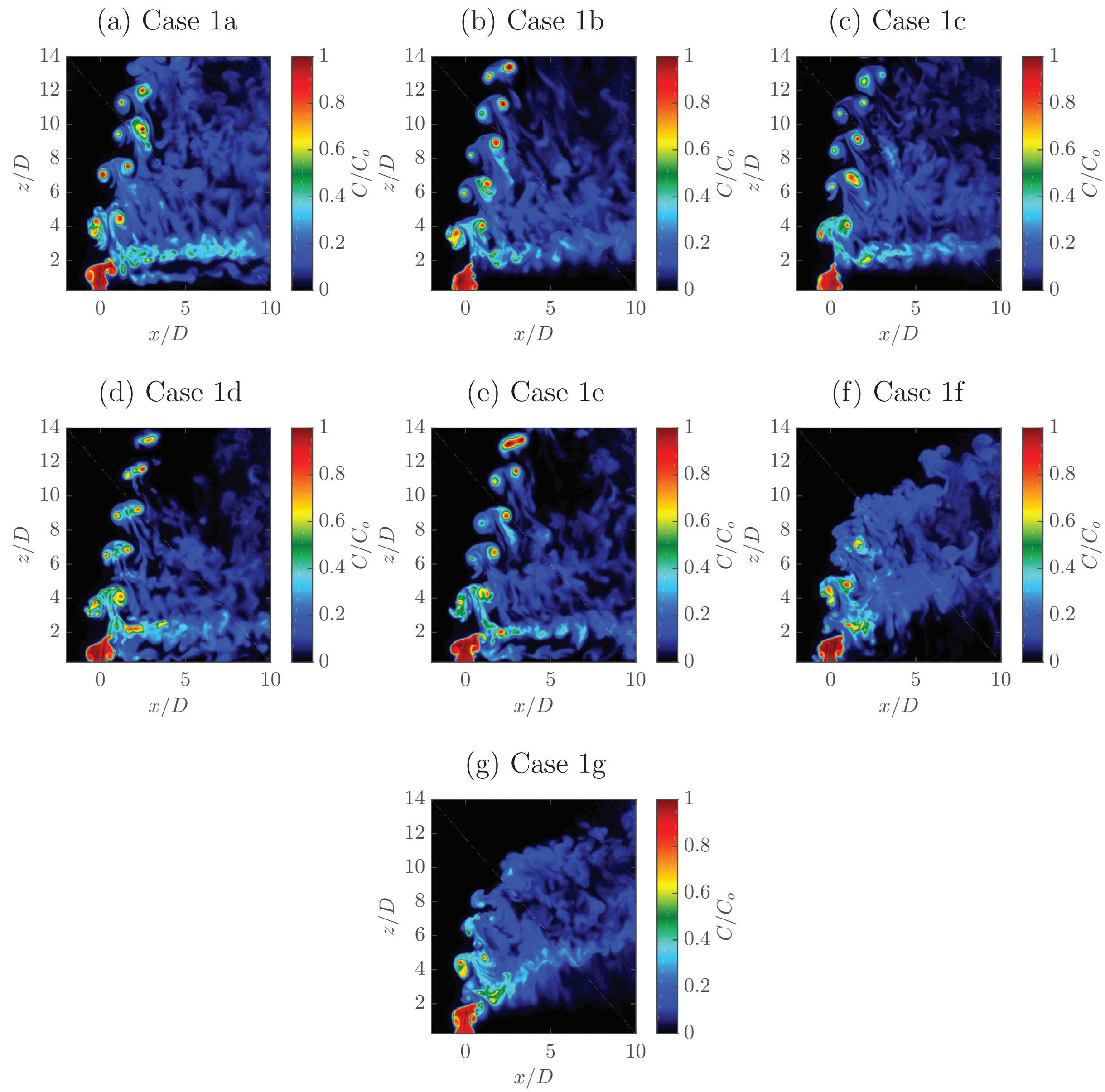

Figure 7.9: Instantaneous centerplane PLIF images under double-pulse square wave forcing (f_f = 55 Hz) for Cases 1a-1g with matching peak-to-peak jet velocity amplitude at $\Delta U_j \approx 4.3$ m/s. These images were acquired at a recording rate of 5 Hz.

and collision, the effect of ΔU_j is important, although this study matches $U'_{j,rms}$ instead of ΔU_j in the following sections, mainly for comparison to earlier chapters' results. Nevertheless, feedback control with or without the improvements as described in Section 7.2 successfully creates coherent deeply-penetrating puff-like vortex rings as with the reference case in M'Closkey et al. (2002), but with higher jet penetration. This discrepancy in jet penetration can be fairly well compensated by matching ΔU_j instead of $U'_{j,rms}$ among all forcing conditions, suggesting that ΔU_j is an appropriate parameter to be matched in order to control jet structures as well as molecular mixing.

7.3.2 Near-Field Vortex Interaction and Collision

In the previous section, deeply-penetrating puff-like vortex rings are clearly created with the larger flush nozzle during effectively single pulse square wave excitation. If the spacing of these vortex rings is carefully manipulated, vortex interactions or even collisions may be achieved in jet's nearfield, and these interactions could potentially enhance molecular mixing of the JICF. Hence, this section deals with two data sets, labeled as Cases 2a-2d and 3a-3d, to explore the flow dynamics and structural characteristics associated with near-field vortex ring interactions and collisions. As mentioned in Section 7.2, all data shown in this section are taken without the improvements (e.g., the low-pass filter) in the feedback controller. The RMS of jet velocity perturbation is matched among all forcing conditions at $U'_{j,rms} = 1.7$ m/s, not the peak-to-peak jet velocity amplitude of pulsation ΔU_j.

A test matrix associated with input conditions for the two data sets is shown in Table 7.3. The two data sets represent (1) Cases 2a-2d, where a prescribed temporal pulse width of the first pulse $\tau_{input,1}$ and the temporal interval between the first and second pulses, $\Delta\tau_{1\to2}$ or $\Delta\tau_{2\to1}$, which were systematically increased and reduced, respectively, with a constant temporal pulse width of the second pulse $\tau_{input,2}$ and (2) Cases 3a-3d, where a prescribed temporal pulse width of the first pulse $\tau_{input,1}$ was systematically increased with a constant prescribed temporal pulse width of the second pulse $\tau_{input,2}$ as well as a constant temporal interval from the first to second pulse $\Delta\tau_{1\to2}$. For the first data set, although the temporal interval between the pulses is varied, the temporal distance between the center of the two pulses is kept constant at $0.5T$. It should be noted that Case 2a is the same as the reference case from M'Closkey et al. (2002) shown in Section 7.3.1, producing effectively a single square wave pulsation at $f_f = 110$ Hz. When the temporal pulse width is altered among different forcing conditions, the amplitude of the pulse is also adjusted so that the RMS of jet velocity

Table 7.3: Test matrix for two data sets Cases 2a-2d and 3a-3d at $f_f = 55$ Hz with matching RMS of jet velocity perturbation at $U'_{j,rms} = 1.7$ m/s. Temporal data-associated parameters for the first (subscript 1) and second (subscript 2) temporal square pulses within a period T here are input or prescribed temporal pulse width normalized by a period τ_{input}/T and temporal separation between the first and second pulses normalized by a period $\Delta\tau/T$.

	$\tau_{input,1}/T$	$\tau_{input,2}/T$	$\Delta\tau_{1\to2}/T$	$\Delta\tau_{2\to1}/T$
Case 2a	0.15	0.15	0.35	0.35
Case 2b	0.25	0.15	0.30	0.30
Case 2c	0.35	0.15	0.25	0.25
Case 2d	0.45	0.15	0.20	0.20
Case 3a	0.15	0.15	0.15	0.55
Case 3b	0.25	0.15	0.15	0.45
Case 3c	0.35	0.15	0.15	0.35
Case 3d	0.45	0.15	0.15	0.25

perturbation is still matched at $U'_{j,rms} = 1.7$ m/s among all forcing conditions. For example, going from Cases 3a to 3b, since $\tau_{input,1}$ becomes longer, changing from $0.15T$ to $0.25T$, the amplitude of the first pulse accordingly becomes lower, equivalent to a slower jet velocity during the pulsation, to still match $U'_{j,rms}$. Therefore, from Table 7.3, the amplitude or velocity of the first pulse is always smaller than or equal to that for the second pulse in this study.

The purpose of the first data set (Cases 2a-2d) is to explore the effect of temporal pulse width of the first pulse as well as the temporal interval between the pulses. The temporal jet response at the jet exit acquired via hotwire anemometry for the first data set is shown in Figure 7.10. For Case 2a, which is the forcing condition shown in the previous section, because the two square pulses are evenly situated within a period with the same amplitudes and temporal pulse widths, vortex collisions will not occur, and coherent deeply-penetrating vortex rings are formed, as shown in Figure 7.5(a). As the temporal pulse width of the first pulse is increased and the temporal interval between two pulses is decreased, the amplitude of the first pulse is accordingly reduced to match $U'_{j,rms}$. As a result, the first pulse becomes slower and also closer to the second (faster) pulse, which may induce near-field vortex interactions. Also, as temporal waveforms become more complicated, moving from Case 2a to Cases 2b-2d, the temporal waveforms become noisier as well as deviating from the ideal waveforms. Note that the improvements in the feedback controller can achieve cleaner temporal jet response, although these data are not presented in this study. Hence, from Cases 2a to 2d, the distance between two vortex rings becomes closer, the implications of which shown as follows for the transverse jet.

Instantaneous centerplane structures for Case 2b from PLIF imaging are shown in Figure 7.11. The sequential instantaneous centerplane images shown in this section are all taken at a recording rate of 1 Hz so that one can observe flow dynamics as in a successive series of phase-locked images. For Case 2b, less coherent vortex rings than those for the Case 1a or equivalently, Case 2a (reference case), are formed. This is possibly due to stronger near-field vortex interactions induced by the closer imposed spacing between two vortex rings. The first slower vortex ring is observed to be formed at around the jet exit in Figures 7.11(a)-(d). After the first vortex ring formation, the second pulse is also observed to be generated, as recognized in Figures 7.11(d)-(g). However, these vortex rings do not collide because the second vortex ring can not "catch up" with the first one as one, can observe in Figures 7.11(g)-(i). In addition, some vortex rings are observed to "flee" from the jet toward the test section ceiling. These convecting vortex rings from the jet seem to enhance jet spread and penetration, which will be discussed in Section 7.4.2. If the temporal pulse width of the first pulse $\tau_{input,1}$ is broadened and hence the first vortex ring becomes slower, or the temporal distance between the first and second pulses is shortened and hence the spatial distance between two vortex rings becomes shorter than in Case 2b, stronger near-field vortex interaction or collision is expected to occur.

For Cases 2c and 2d, which are shown in Figures 7.12 and 7.13, respectively, $\tau_{input,1}$ is systematically increased and the amplitude of the first temporal square pulse accordingly becomes slower. Hence, the spatial distance between the two vortex rings is also shortened.

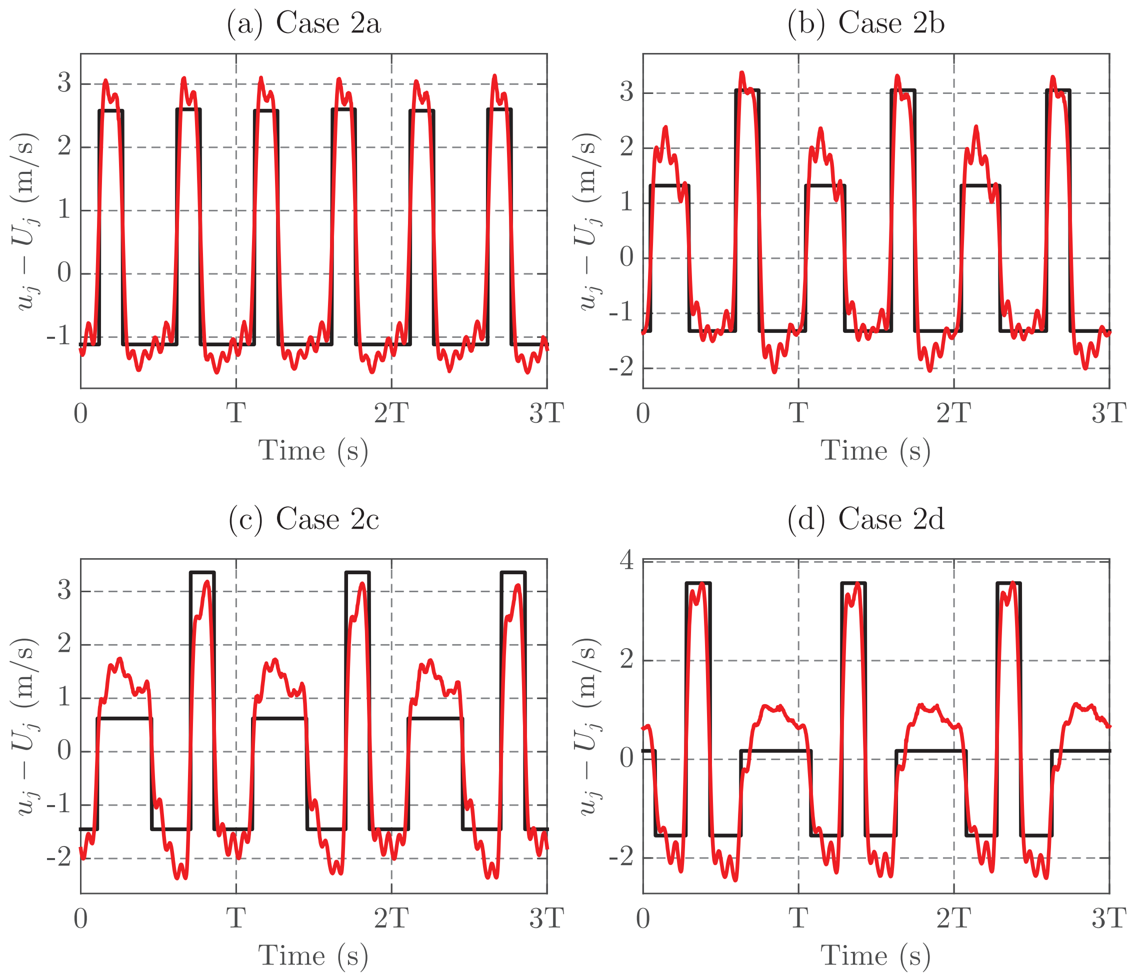

Figure 7.10: Ideal (—) and actual (—) temporal jet response to double-pulse square wave forcing (f_f = 55 Hz) at the jet exit acquired via hotwire anemometry without the improvements in the feedback controller for Cases 2a-2d with matching RMS of jet velocity perturbation at $U'_{j,rms} = 1.7$ m/s.

For Case 2c, the first vortex ring created around the jet exit (Figures 7.12(a)-(d)) is followed by the second vortex ring as observed (Figures 7.12(d)-(g)). However, there is still no clear vortex ring collision in Figure 7.12(g)-(i), although the two vortex rings may more strongly interact in the nearfield than in Case 2b.

In contrast, Case 2d begins to trigger the near-field vortex collisions. As with the previous cases, the first and second vortex rings are formed successively, as shown in Figures 7.13(a)-(d) and 7.13(d)-(g), respectively. These vortices appear to collide around $(x/D, z/D) \approx (0.5, 4.5)$, which can be recognized in Figures 7.13(g)-(i). Interestingly, while convecting

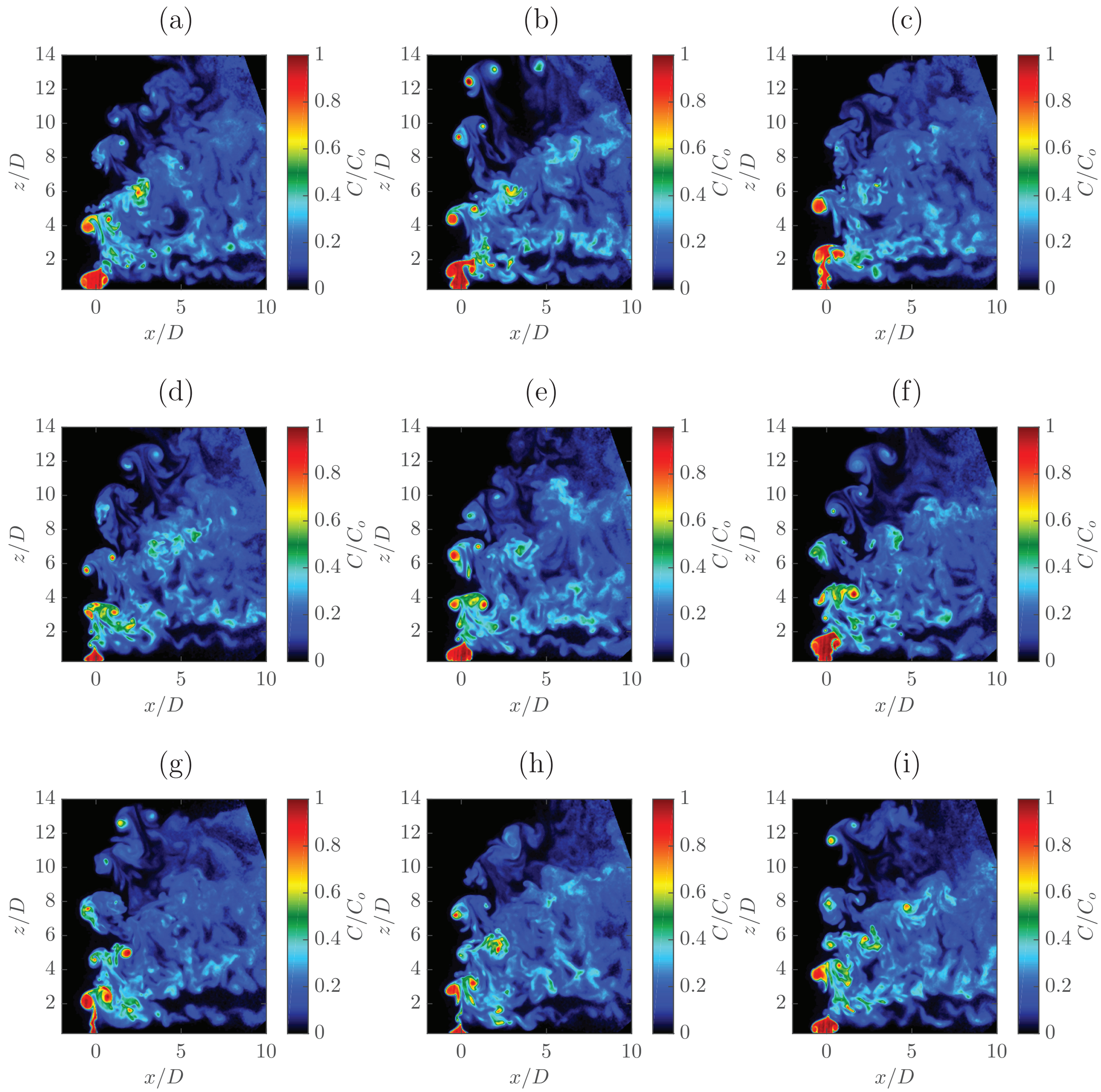

Figure 7.11: Sequential instantaneous centerplane PLIF images for the equidensity flush nozzle-injected JICF at $J = 6.7$ under double-pulse square wave forcing at $f_f = 55$ Hz and $U'_{j,rms} = 1.7$ m/s (Case 2b). These images were acquired at a recording rate of 1 Hz.

vortex rings toward the test section ceiling are consistently observed for Case 2d as well as Case 2b, where near-field vortex collision occurs, these vortex rings are not clearly seen to move toward the ceiling for Case 2c, possibly because strong near-field vortex interaction prevents vortex rings from fleeing from the jet. The occurrence of the near-field vortex collisions with a shorter $\tau_{input,1}$ or equivalently a slower first vortex ring suggests that such phenomena could be controlled by adjusting the velocity of the first vortex ring as well as the temporal interval from the first to the second vortex ring's formation.

From the observation of this first data set in Cases 2a-2d, it is possible that a shorter temporal interval from the first to second vortex ring $\Delta\tau_{1\to2}$ may induce a stronger near-field vortex collision. Hence, for the second data set in this section, Cases 3a-3d, $\Delta\tau_{1\to2}$ is kept constant at $0.15T$, which is shorter than the shortest temporal separation in the first data set ($0.20T$). As with the first data set, $\tau_{input,1}$ is systematically increased, or the velocity of the first vortex ring is gradually reduced.

Temporal waveforms for the second data set, Cases 3a-3d, are shown in Figure 7.14. Because these jet responses are created without the improvements in the feedback controller as discussed in Section 7.2, there are some temporal oscillations in the waveforms. Also, although the jet response is fairly close to the ideal waveforms in terms of pulse widths, there are some discrepancies between them. Most clearly, for instance, the amplitudes of two pulses within a period are ideally identical in Case 3a, but these are different due to the temporal oscillations in the waveform. Nevertheless, interesting flow dynamics (e.g., clear near-field vortex collision) are observed in sequential instantaneous centerplane jet images as follows.

Figure 7.15 represents a series of instantaneous centerplane images for Case 3a, with the shortest temporal pulse width for the first pulse in the second data set. As one can see, there is clear vortex ring collision. The first temporal pulse creates the first vortex ring as shown in Figures 7.15(a)-(d) in the vicinity of the jet exit. The second vortex ring was successively generated after the first vortex ring, as recognized in Figures 7.15(e)-(g). These vortex rings collide right above the jet exit, approximately at $(x/D, z/D) \approx (0.1, 3.6)$ (seen in Figures 7.15 (h) and (i)). As compared with the data set in the previous section (Cases 1a-1g) as

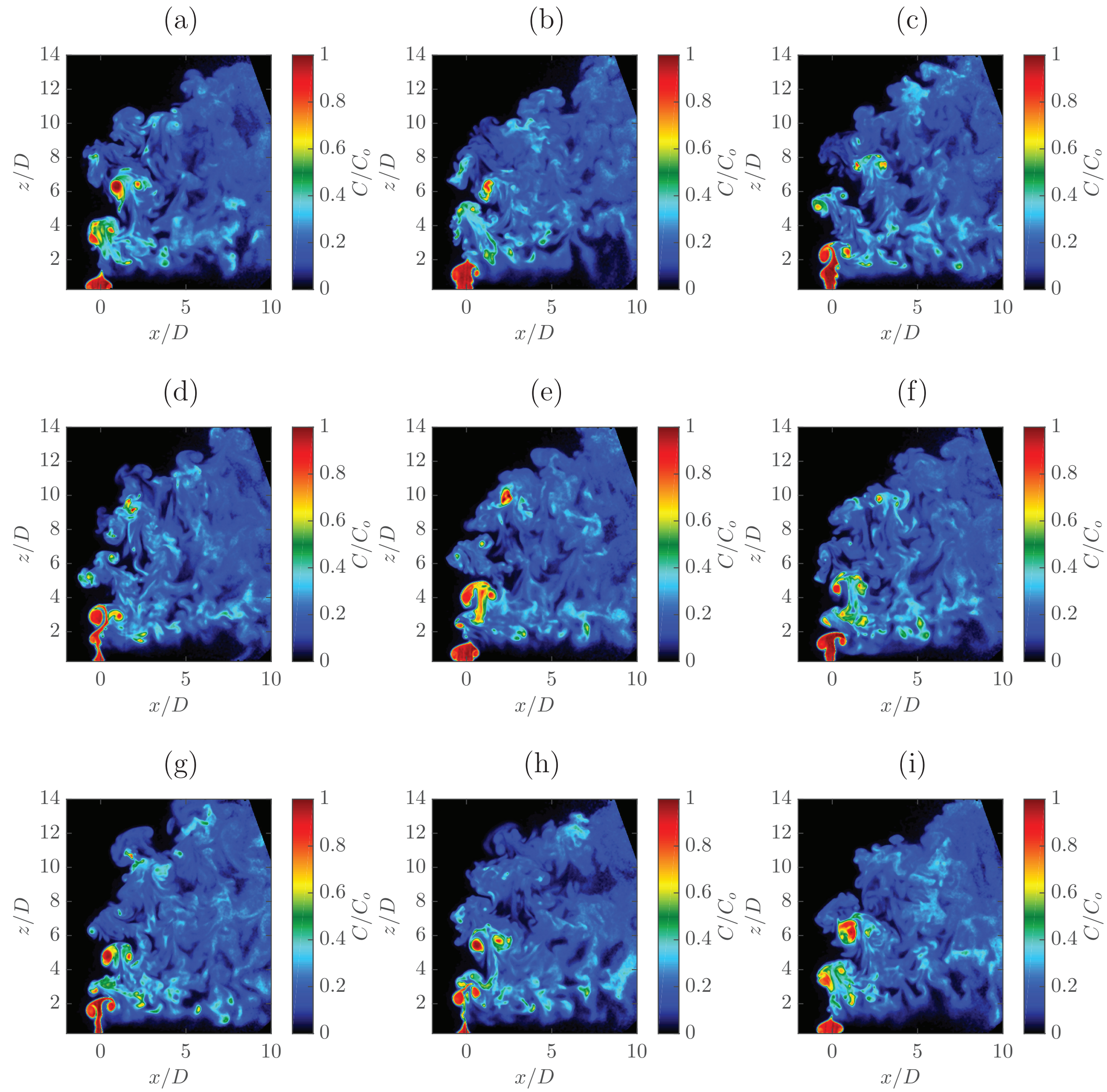

Figure 7.12: Sequential instantaneous centerplane PLIF images for the equidensity flush nozzle-injected JICF at $J = 6.7$ under double-pulse square wave forcing at $f_f = 55$ Hz and $U'_{j,rms} = 1.7$ m/s (Case 2c). These images were acquired at a recording rate of 1 Hz.

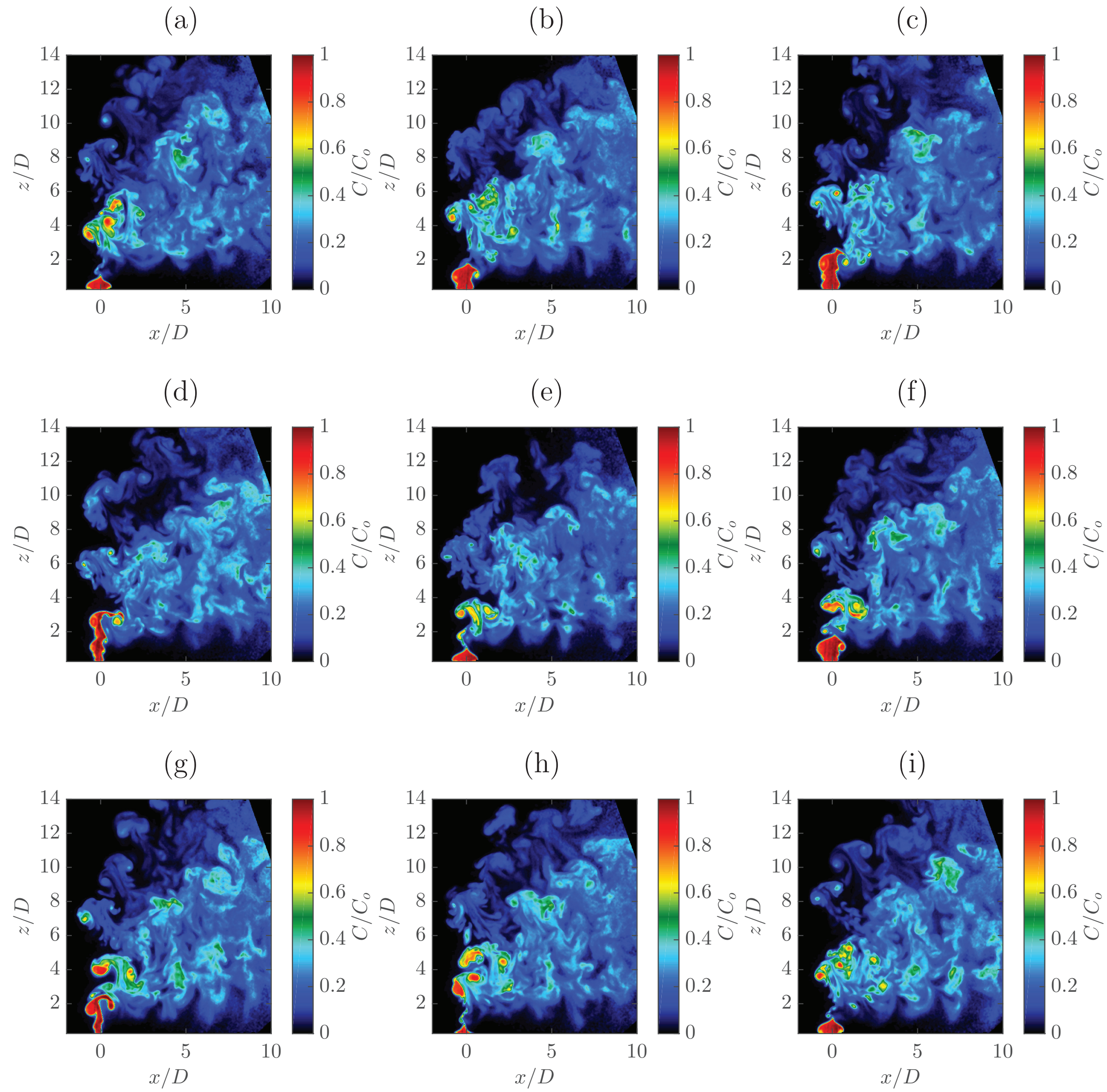

Figure 7.13: Sequential instantaneous centerplane PLIF images for the equidensity flush nozzle-injected JICF at $J = 6.7$ under double-pulse square wave forcing at $f_f = 55$ Hz and $U'_{j,rms} = 1.7$ m/s (Case 2d). These images were acquired at a recording rate of 1 Hz.

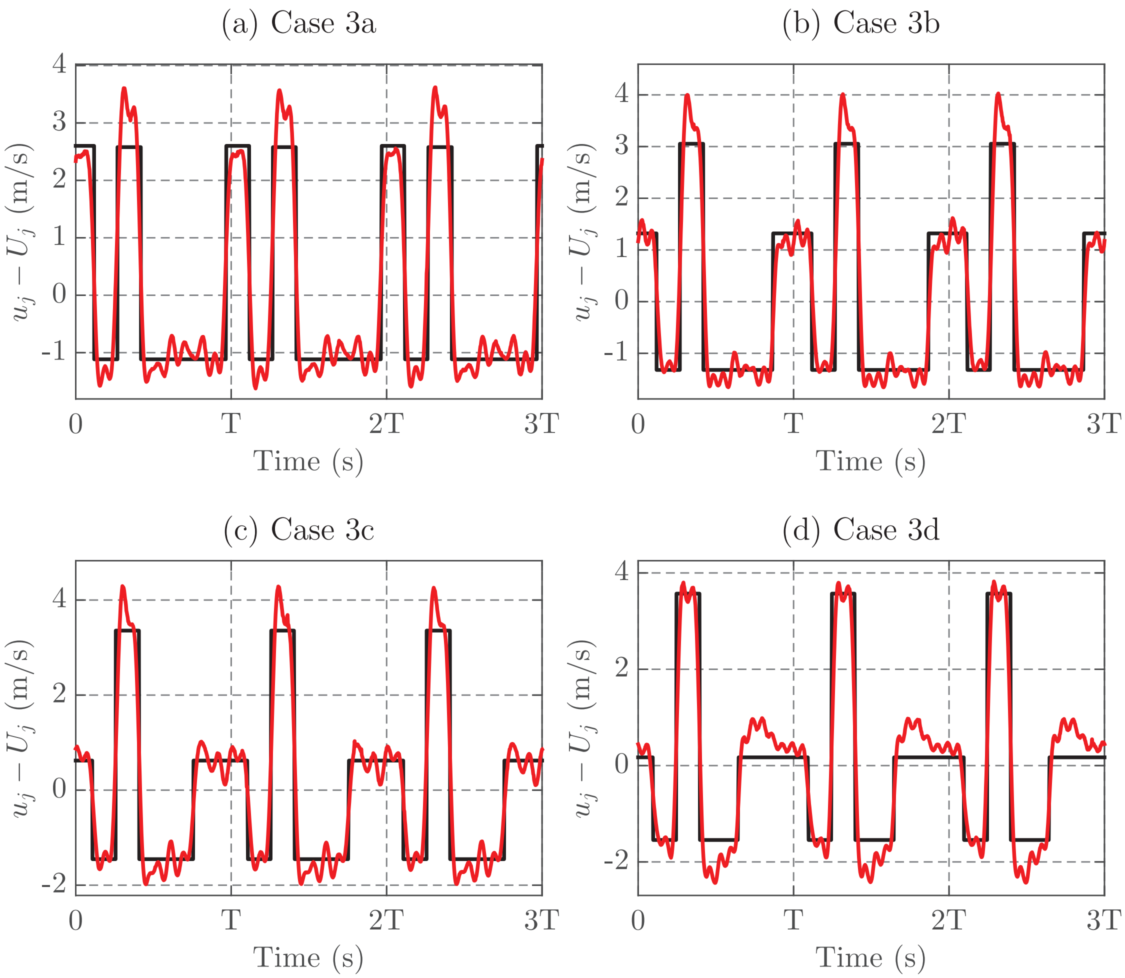

Figure 7.14: Ideal (—) and actual (—) temporal jet response to double-pulse square wave forcing (f_f = 55 Hz) at the jet exit acquired via hotwire anemometry without the improvements in the feedback controller for Cases 3a-3d with matching RMS of jet velocity perturbation at $U'_{j,rms} = 1.7$ m/s.

well as the first data set in this section (Cases 2a-2d), the jet penetrates less because of the near-field vortex collision.

For Case 3b (for images shown in Figure 7.16), with a longer temporal pulse width of the first pulse, or equivalently a slower first pulse, clear vortex collision is still observed but at a slightly further downstream location in the x direction. The vortex collision seen in Figures 7.16(h)-(i) is likely to be induced by the first vortex ring created in Figures 7.16(a)-(d), and the second vortex ring in Figures 7.16(e)-(g), occurring approximately at $(x/D, z/D) \approx (0.4, 3.5)$, further from the jet exit in terms of x/D locations than in Case 3a.

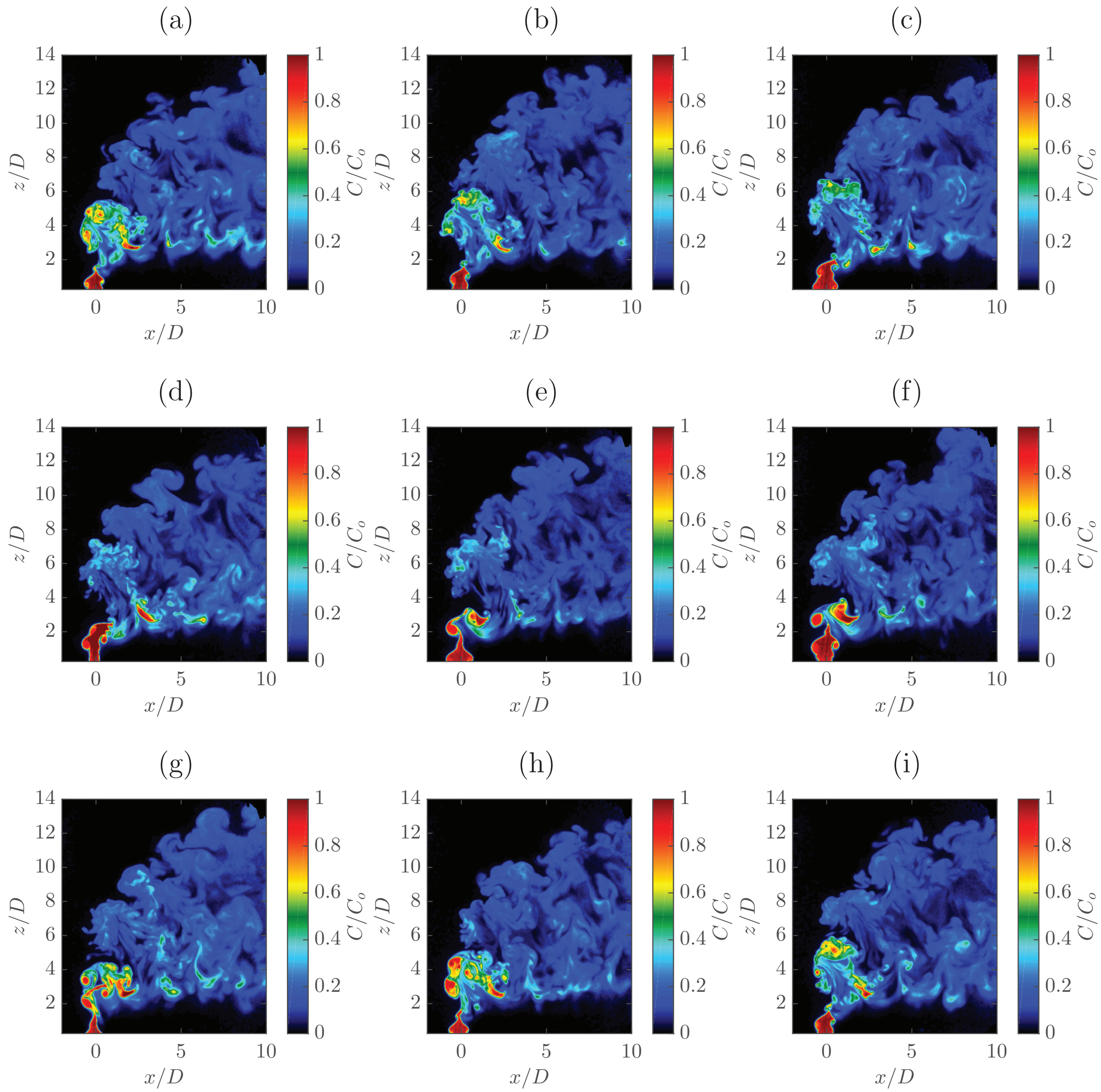

Figure 7.15: Sequential instantaneous centerplane PLIF images for the equidensity flush nozzle-injected JICF at $J = 6.7$ under double-pulse square wave forcing at $f_f = 55$ Hz and $U'_{j,rms} = 1.7$ m/s (Case 3a). These images were acquired at a recording rate of 1 Hz.

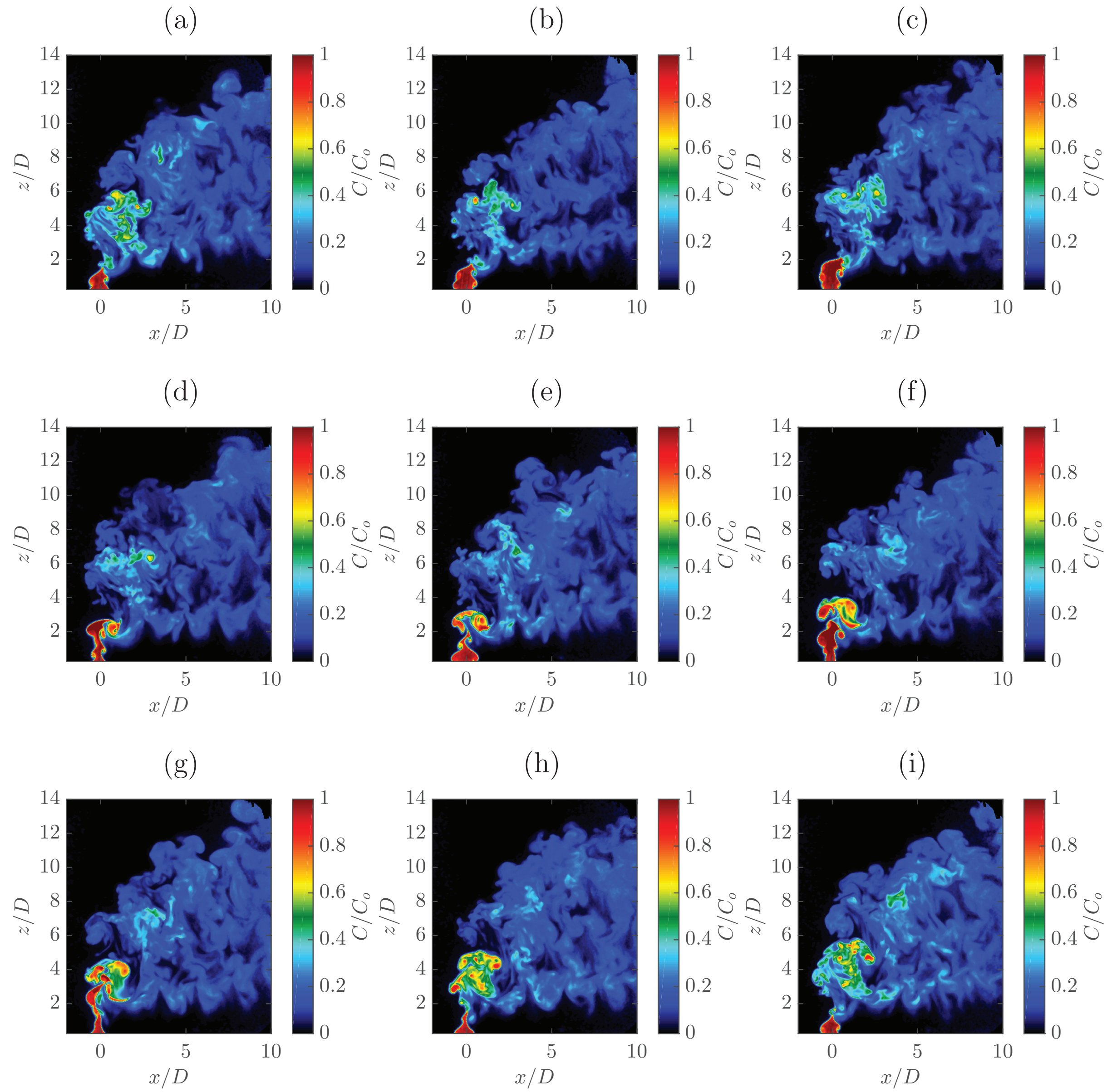

Figure 7.16: Sequential instantaneous centerplane PLIF images for the equidensity flush nozzle-injected JICF at $J = 6.7$ under double-pulse square wave forcing at $f_f = 55$ Hz and $U'_{j,rms} = 1.7$ m/s (Case 3b). These images were acquired at a recording rate of 1 Hz.

However, the vortex collision for Case 3b occurs at approximately the same z/D location as Case 3a.

For Case 3c, the temporal pulse width of the first pulse systematically increases. As one can expect from the structural trends in Cases 3a and 3b, the vortex collision for Case 3c, shown in the instantaneous images in Figure 7.17, occurs even further from the jet exit with respect to the x/D location, approximately at $(x/D, z/D) \approx (0.7, 3.6)$, observed in Figures 7.17(g)-(i). Here again, the overall jet penetration is clearly lowered as compared with the previous two cases. Such a characteristic suggests the possibility of controlling jet penetration by adjusting the location of the near-field vortex collision. The jet penetration will be quantified and discussed in Section 7.4.2.

Finally, PLIF imaging for Case 3d is shown in Figure 7.18. Interestingly, there is no clear vortex collision here, but interactions between the trailing tail of the first pulse, as observed in Figures 7.18(a)-(d), and the second vortex ring, as observed in Figures 7.18(e)-(g), do occur. Also, there is a vortex ring with a trailing tail that "flees" from the jet at $(x/D, z/D) \approx (0.6, 12)$, as observed in Figure 7.18(h). Such a convecting vortex ring was also observed for Case 2b and 2d in Figures 7.11 and 7.13, respectively, possibly suggesting a relatively weaker near-field vortex interaction may have taken place. Moreover, between the formation of the first and second vortex rings for Case 3d, a jet with rolled-up vortical structures on the upstream and downstream shear layers is observed in Figure 7.18(d), where the jet with vortex rollups follows the first vortex ring formation. Because the jet is not fully modulated, the jet fluid issues into crossflow even without pulsation, so that this type of shear layer jet structure is created; this also may play a role in the near-field flow dynamics.

From the observation of the sequential instantaneous centerplane structures, the nearfield vortex collision occurs at $x/D \approx 0.1$, 0.4 and 0.7 in Cases 3a, 3b and 3c, respectively. Hence, to explore the near-field flow dynamics in detail, cross-sectional PLIF images were taken as well at $x/D = 0$, 0.5 and 1.0, where the near-field vortex collision is likely to occur from the instantaneous centerplane images. Additionally, the cross-sectional measurement was also administered at $x/D = 2.5$ to explore the relatively mid-to-far field flow dynamics as well as mixing characteristics, described later in Section 7.4. The cross-sectional PLIF images

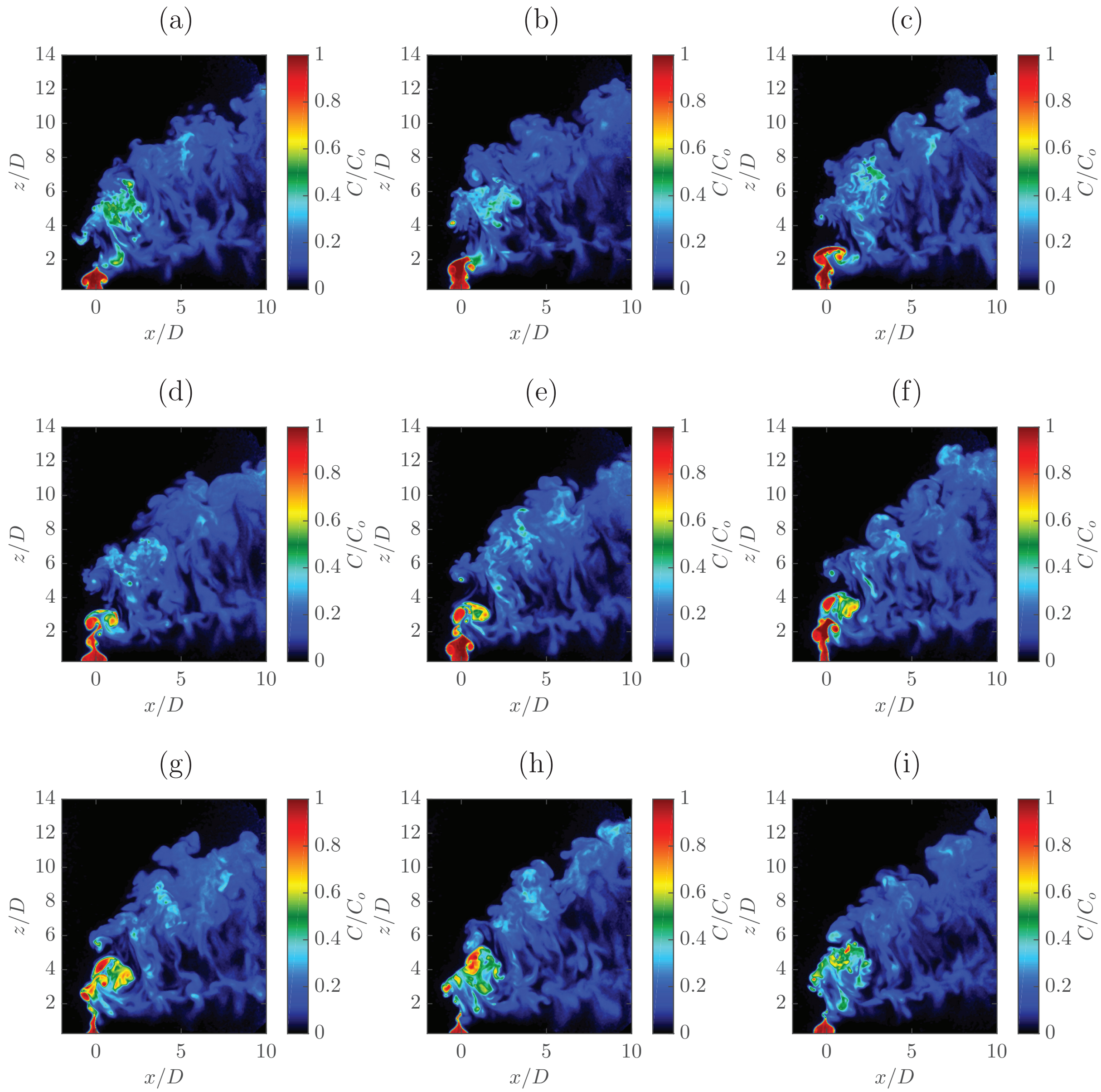

Figure 7.17: Sequential instantaneous centerplane PLIF images for the equidensity flush nozzle-injected JICF at $J = 6.7$ under double-pulse square wave forcing at $f_f = 55$ Hz and $U'_{j,rms} = 1.7$ m/s (Case 3c). These images were acquired at a recording rate of 1 Hz.

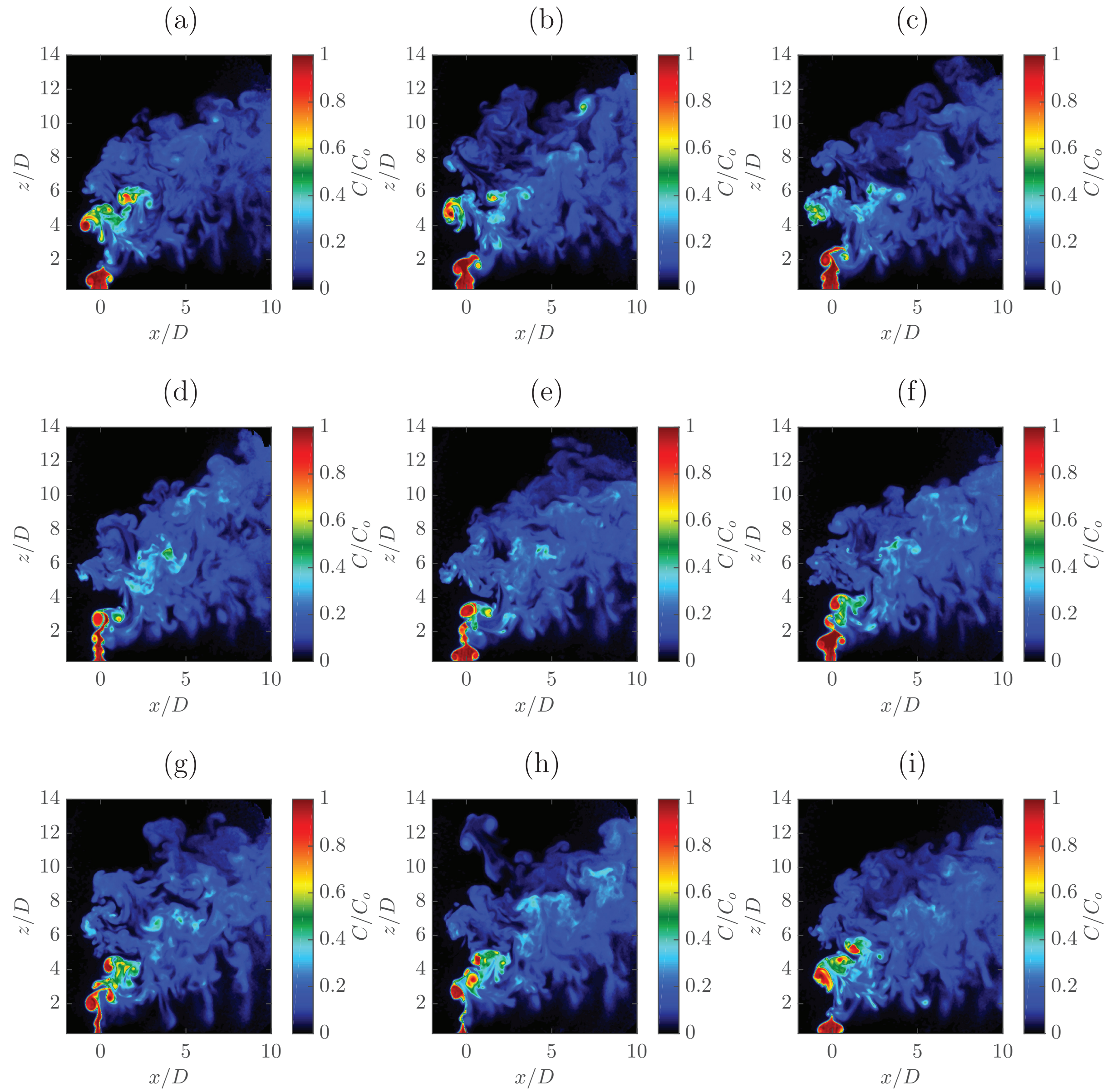

Figure 7.18: Sequential instantaneous centerplane PLIF images for the equidensity flush nozzle-injected JICF at $J = 6.7$ under double-pulse square wave forcing at $f_f = 55$ Hz and $U'_{j,rms} = 1.7$ m/s (Case 3d). These images were acquired at a recording rate of 1 Hz.

shown here were also recorded at 1 Hz, providing a phase-locked-like series of snapshots. Some results are shown in this section as follows, and the rest of the results are documented in Appendix D.

Figures 7.19(a)-(h) represent sequential instantaneous cross-sectional images for Case 3a at the jet exit, $x/D = 0$. A mean cross-sectional image created by an ensemble of 500 instantaneous images is also shown in Figure 7.19(i). As observed in the instantaneous centerplane structures shown in Figure 7.15, clear vortex collision is also seen in the cross-sectional view. The first vortex ring is generated by a relatively slower and temporally longer square pulse, as shown in Figures 7.19(a)-(d). The second vortex ring follows the first one, as shown in Figures 7.19(d)-(f). These vortex rings evidently collide in Figures 7.19(f)-(h), approximately at $z/D \approx 3.5$, which is consistent with the location extracted in the centerplane view. Hence, the series of cross-sectional instantaneous images also clearly illustrates the near-field vortex collision for this condition.

Figure 7.20 shows sequential instantaneous ((a)-(h)) and mean ((i)) cross-sectional images for Case 3b at $x/D = 0.5$, the location at which near-field vortex collision occurs as suggested by the instantaneous centerplane images shown in Figure 7.16. Again, the first vortex ring (Figures 7.20(a)-(d)) is followed by the second one (Figures 7.20(d)-(f)), which triggers a near-field vortex collision seen in Figures 7.20(f)-(h), approximately at the vertical location $z/D \approx 3.6$, which agrees well with the z/D location estimated for the centerplane view in Figure 7.16. Vortex collision can be also recognized for Case 3c, shown in sequential images of the jet cross-section at $x/D = 1.0$ in Figures 7.21(a)-(h), with a mean image shown in Figure 7.21(i). The collision here occurs approximately at $z/D \approx 3.6$., consistent with that extracted from the centerplane data in Figure 7.17. Hence for Cases 3a-3c, the instantaneous cross-sectional images are also able to clearly capture the near-field vortex collisions at the relevant downstream locations of $x/D = 0$, 0.5 and 1.0, at around the same heights (z/D locations) as those observed in the centerplane images.

However, as one might expect for the results in Figure 7.18, there is no clear near-field vortex collision for Case 3d, as seen in cross-sectional images in Figure 7.22, acquired at $x/D = 0.5$. The first vortex ring appears in $x/D = 0.5$ plane in Figures 7.22(a)-(d), followed

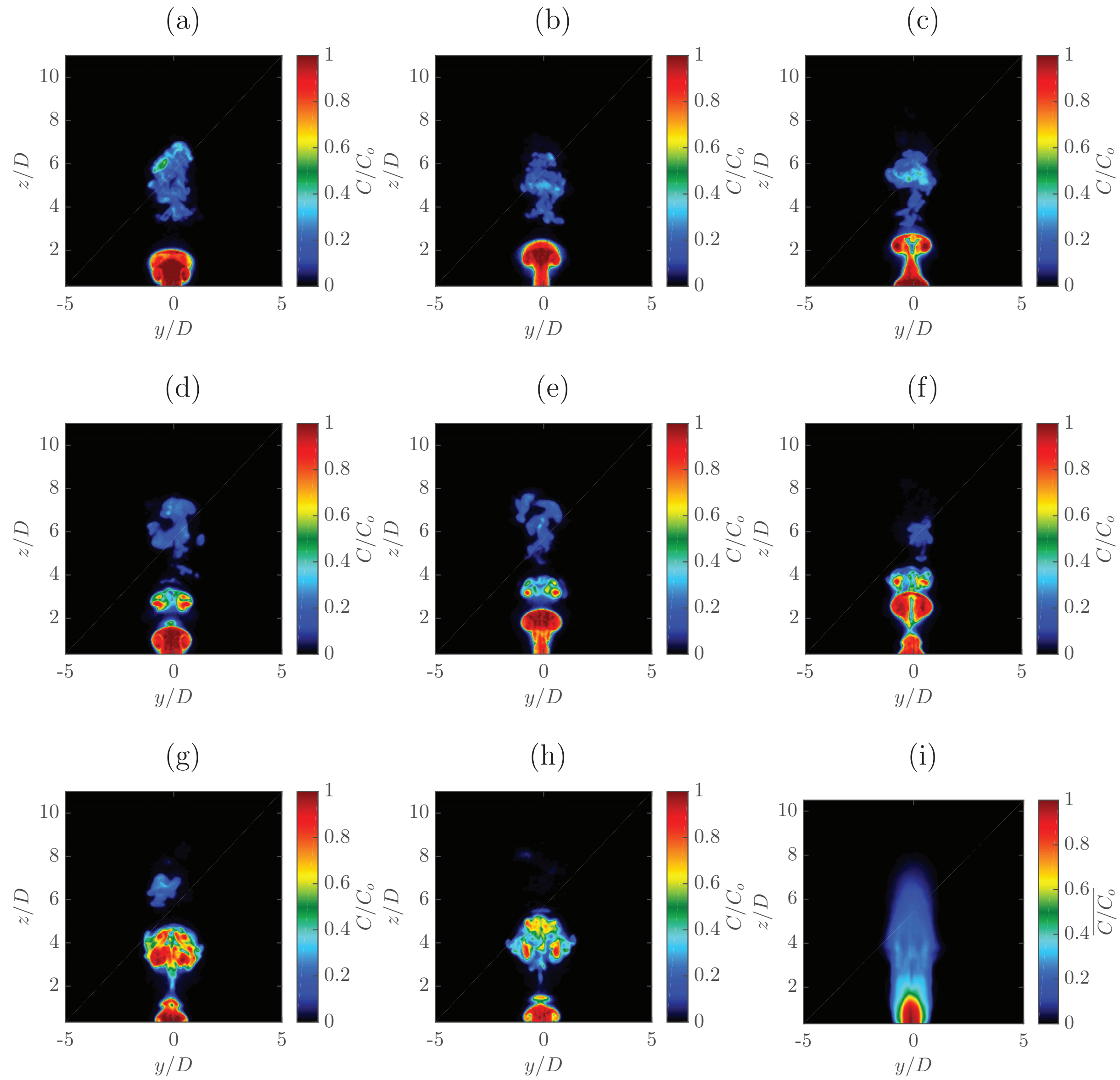

Figure 7.19: (a)-(h) Sequential instantaneous and (i) mean cross-sectional PLIF images (ensemble of 500 instantaneous images) under double-pulse square wave forcing at $f_f = 55$ Hz and $U'_{j,rms} = 1.7$ m/s acquired at the downstream location of $x/D = 0$ (Case 3a). These images were acquired at a recording rate of 1 Hz.

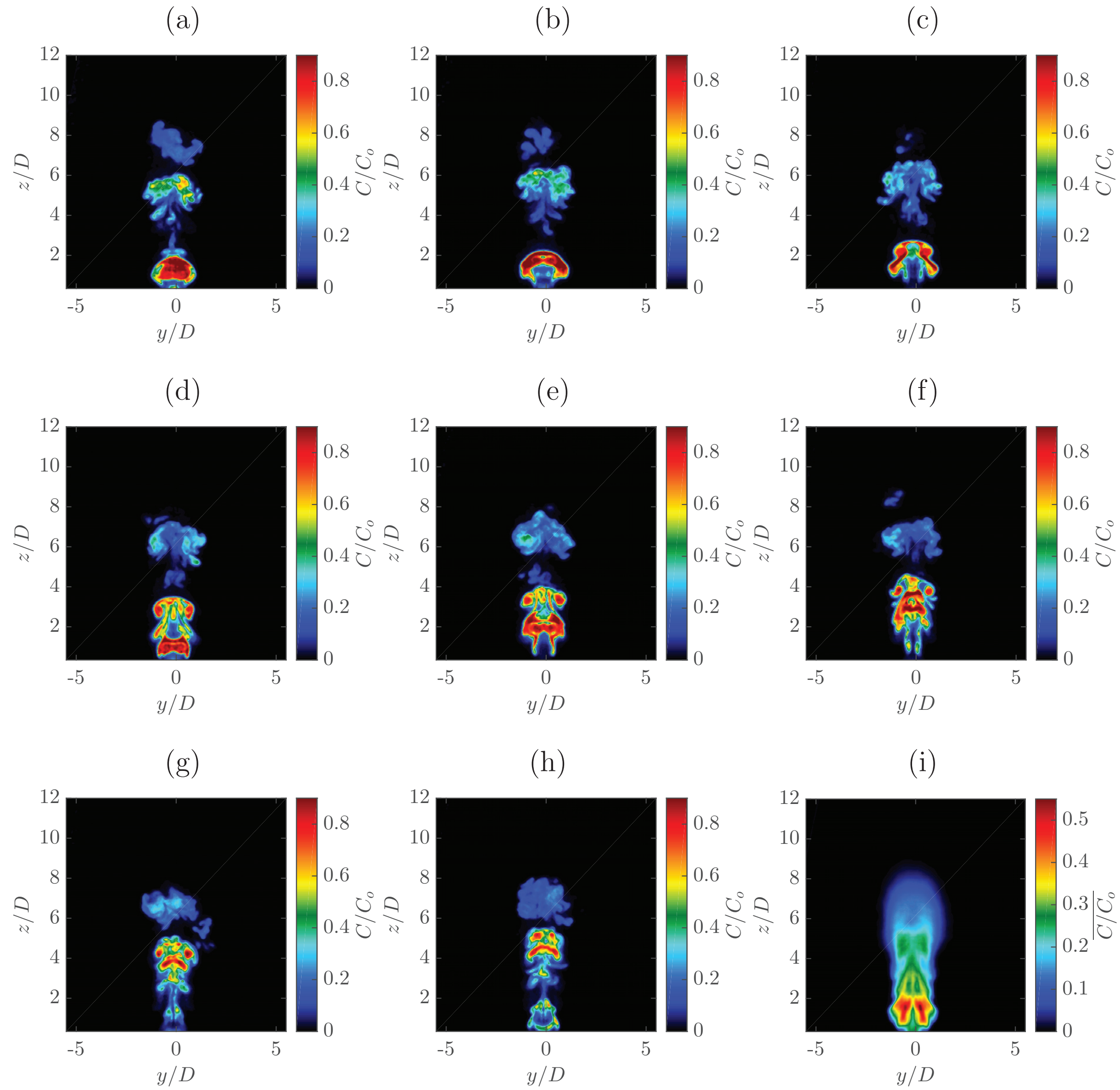

Figure 7.20: (a)-(h) Sequential instantaneous and (i) mean cross-sectional PLIF images (ensemble of 500 instantaneous images) under double-pulse square wave forcing at $f_f = 55$ Hz and $U'_{j,rms} = 1.7$ m/s acquired at the downstream location of $x/D = 0.5$ (Case 3b). These images were acquired at a recording rate of 1 Hz.

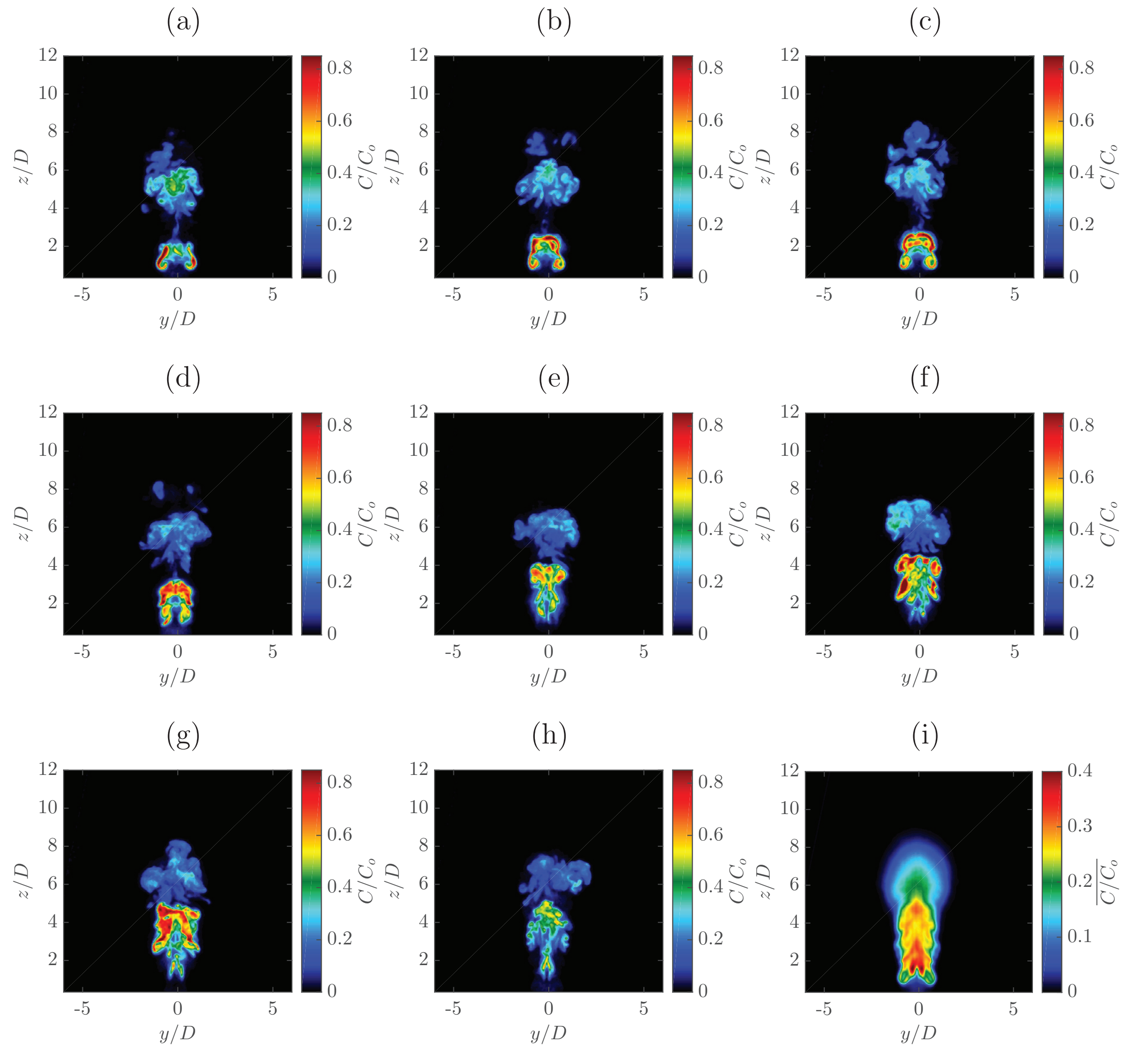

Figure 7.21: (a)-(h) Sequential instantaneous and (i) mean cross-sectional PLIF images (ensemble of 500 instantaneous images) under double-pulse square wave forcing at $f_f = 55$ Hz and $U'_{j,rms} = 1.7$ m/s acquired at the downstream location of $x/D = 1.0$ (Case 3c). These images were acquired at a recording rate of 1 Hz.

by the second vortex ring in Figures 7.22(d)-(f). However, before the second vortex ring collides with the first one, the first vortex ring disappears from the $x/D = 0.5$ plane because it has convected downstream, to the $x/D > 0.5$ plane. There is some degree of near-field interaction and merger of the vortex structures, seen in the instantaneous centerplane images and resulting in disturbed vortex rings (Figures 7.22(g) and (h)). In the instantaneous centerplane image in Figure 7.18(h), a vortex ring convecting upward from the jet toward the test section ceiling was observed. The same vortex ring with a trailing tail is also seen in the cross-sectional view, as shown in Figure 7.22(g) approximately at $z/D \approx 11.2$, fairly close to the z/D location estimated in the centerplane image. The vortex collision was not clearly observed in these instantaneous cross-sectional images in Figure 7.22, not only at $x/D = 0.5$ shown here, but also at $x/D = 0$, 1.0 and 2.5, which are shown in Figures D.14, D.15, and D.16 respectively. It also should be noted that jet centerplane and cross-sectional structures, as well as the occurrence of near-field vortex collisions, are highly repetitive, day by day, for the same forcing conditions, suggesting that vortex collisions can be consistently achieved once an appropriate forcing condition is determined.

One may conclude, from the structural observations in the sequential centerplane and cross-sectional images above, that in general, near-field vortex collisions occur further from the jet exit as the first temporal pulse width becomes temporally longer and hence the first vortex ring accordingly becomes slower, from Cases 3a to 3d, to match $U'_{j,rms}$. Although this trend is consistent both in the centerplane and cross-sectional views, the trend may be counter-intuitive. One might expect that the slower first pulse could trigger a vortex interaction closer to the jet exit than a faster one. If the vortex ring is faster, it seems to convect further downstream of the exit, and hence prevent the near-field vortex interaction from taking place. This trend may be explained by possible two culprits. First, as mentioned previously, the temporal waveforms are not perfect square waves. For Case 3a, the amplitude of two pulses should be ideally the same, but they deviate from the ideal waveform due to temporal oscillations created by the controller. If the pulses were the same, the vortex collision might not happen at all, but this is not knowable. Secondly, since the jet is not fully modulated, the jet fluid continues to issue from the nozzle even without pulsation, resulting

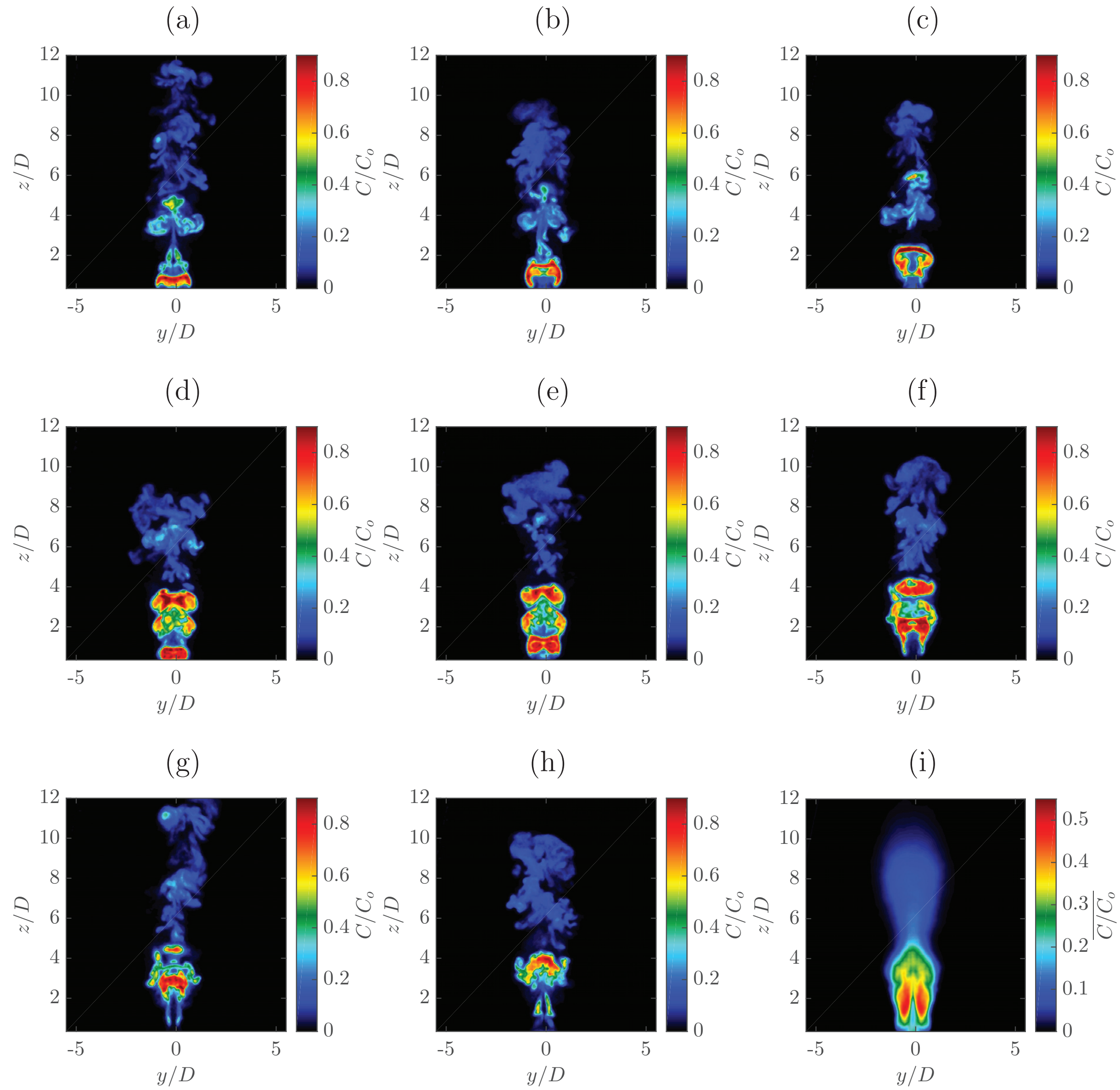

Figure 7.22: (a)-(h) Sequential instantaneous and (i) mean cross-sectional PLIF images (ensemble of 500 instantaneous images) under double-pulse square wave forcing at $f_f = 55$ Hz and $U'_{j,rms} = 1.7$ m/s acquired at the downstream location of $x/D = 0.5$ (Case 3d). These images were acquired at a recording rate of 1 Hz.

in a jet with vortex rollup on the upstream and downstream shear layers as described for Case 3d in Figure 7.18(d). This jet structure could interact with the first and/or second vortex ring and hence alters the velocity of the first and/or second vortex ring.

Furthermore, to explore the trends in greater detail, the actual temporal pulse width parameters extracted from temporal data are quantified, as done with waveforms studied in Section 7.3.1 (see Tables 7.1 and 7.2). The actual temporal pulse width τ_{actual}, the peak-to-peak jet velocity amplitude ΔU_j, and the stroke ratio L/D are again estimated independently for two square pulses, and these are tabulated in Table 7.4. For Cases 3a-3d, since cross-sectional data are taken, at least 50 cycles are utilized to extract the mean values (that is, for at least 10 cycles, from centerplane data and then from cross-sectional data at four different downstream locations). Again, the parameters with subscripts 1 and 2 are relevant to the first and second temporal square pulses, respectively. In addition, the first square pulse is always slower than (equivalently temporally longer) or at the same velocity (equivalently the same temporal pulse width) as the second pulse.

For Cases 3a-3c, where the near-field vortex collision occur, the peak-to-peak jet velocity amplitude and stroke ratio for the first pulse, $\Delta U_{j,1}$ and L_1/D, are smaller than those for the second pulse, $\Delta U_{j,2}$ and L_2/D, as shown in Table 7.4. Similarly, $\Delta U_{j,1}$ is still smaller than $\Delta U_{j,2}$ for Case 3d, where there is no clear vortex collision. However, interestingly, the stroke ratio for the first pulse L_1/D for Case 3d becomes larger than that for the second pulse L_2/D, which is opposite to that in Cases 3a-3c. As previously mentioned, the stroke ratio represents the strength of pulsation of square wave forcing. Hence, if the first vortex ring is more strongly pulsed than the second vortex ring, Cases 3a-3d suggest that the near-field vortex ring collision may not occur. Thus, the occurrence of vortex ring collisions in the JICF are likely to be related to the magnitudes of relative stroke ratios between the first and second temporal square pulses.

Yet in the first data set in this section (Cases 2a-2d), the near-field vortex ring collision was clearly recognized only for Case 2d, in which $L_1/D > L_2/D$ in Table 7.4. Additionally, Table 7.4 shows $L_1/D < L_2/D$ in Case 2a, where vortex ring collision was not observed. This difference between the first and second data sets in this section suggests that stroke ratio is

Table 7.4: Temporal data-extracted parameters for the first (subscript 1) and second (subscript 2) temporal square pulses within a period T at $f_f = 55$ Hz with matching RMS of jet velocity perturbation at $U'_{j,rms} = 1.7$ m/s. The parameters here are actual temporal pulse width normalized by a period τ_{actual}/T, peak-to-peak jet velocity amplitude of pulsation ΔU_j and stroke ratio L/D. 95 % confidence intervals are also shown with an effective digit of the second decimal point. All parameters are averaged over at least 10 temporal cycles.

	$\tau_{actual,1}/T$	$\tau_{actual,2}/T$	$\Delta U_{j,1}$ (m/s)	$\Delta U_{j,2}$ (m/s)	L_1/D	L_2/D
Case 2a	0.20 ± 0.00	0.20 ± 0.00	4.15 ± 0.02	4.18 ± 0.02	1.27 ± 0.00	1.32 ± 0.00
Case 2b	0.28 ± 0.00	0.19 ± 0.00	2.40 ± 0.01	4.62 ± 0.04	1.51 ± 0.01	1.40 ± 0.02
Case 2c	0.45 ± 0.00	0.19 ± 0.01	3.34 ± 0.02	4.81 ± 0.07	2.47 ± 0.01	1.43 ± 0.04
Case 2d	0.56 ± 0.00	0.19 ± 0.00	2.83 ± 0.02	5.70 ± 0.03	2.98 ± 0.01	1.77 ± 0.01
Case 3a	0.20 ± 0.00	0.22 ± 0.00	3.73 ± 0.04	4.83 ± 0.04	1.18 ± 0.01	1.53 ± 0.02
Case 3b	0.29 ± 0.00	0.20 ± 0.00	2.46 ± 0.05	5.13 ± 0.06	1.22 ± 0.04	1.53 ± 0.02
Case 3c	0.40 ± 0.00	0.20 ± 0.00	2.15 ± 0.05	5.63 ± 0.03	1.54 ± 0.03	1.65 ± 0.01
Case 3d	0.49 ± 0.00	0.20 ± 0.00	1.88 ± 0.01	5.69 ± 0.02	1.97 ± 0.02	1.77 ± 0.00

not the only factor that is involved with characterizing vortex collisions. As mentioned, the temporal interval between the first and second square pulses, $\Delta\tau_{1\to2}$, is larger for the first data set than the second one. Clearly, a shorter $\Delta\tau_{1\to2}$ makes the spatial distance of two vortex rings closer, which in turn is more likely to induce near-field vortex ring collisions. This observation suggests that $\Delta\tau_{1\to2}$ may also be a factor in characterizing near-field flow dynamics with double-pulse square wave forcing.

These trends suggest that vortex collisions may be dependent on the temporal interval between two square pulses as well as the magnitude relation of the stroke ratios between the two pulses, effectively corresponding to the spacing and strength of the pulsation for the two vortex rings, respectively. Hence, vortex collisions may be able to be triggered at a desired location in the flowfield by a clearer understanding of the relationship between flow dynamics and the temporal parameters as well as the ability to more precisely control these temporal parameters.

7.4 Mixing Quantification for Double Pulsed JICF

Structural exploration of the double-pulsed JICF has shown that deeply-penetrating vortex rings as well as their interactions or collisions were created in the nearfield for some forcing conditions, but only at various downstream locations. Here, it is of interest to investigate the possible molecular mixing enhancement under double-pulse square wave forcing, especially in relation to near-field vortex ring collisions. As with sine and single-pulse square wave forcing, mean and instantaneous mixing metrics with the same algorithm are utilized here to quantify mixing of the JICF. For mean mixing metrics, jet penetration and vertical spread along horizontal spatial coordinate x/D are only shown in this section. Similarly, centerplane- and cross-section-based Unmixedness as well as the Probability Density Function (PDF) along the axis x/D are discussed here. Because jet trajectories are significantly altered under double-pulse square wave forcing as compared with the unforced case, this makes the determination of various jet trajectories difficult, and hence the validity of mixing quantification along the unforced trajectory vs. that for each trajectory in question is complicated. Nevertheless, mixing evaluations using all mixing metrics as a function of all possible coordinates are shown for completeness in Appendix D. Additionally, the mixing quantification was administrated utilizing PLIF data acquired at different recording rates to explore the effect of capturing different phases with respect to external forcing on mixing characteristics.

7.4.1 Baseline Reference Cases

First, mixing metrics for the JICF are characterized for the reference case under the same forcing condition in M'Closkey et al. (2002), discussed in Section 7.3.1. For this reference case, cross-sectional PLIF data were not taken, so only mixing quantification based on centerplane PLIF images are administered. Mean (jet penetration and vertical spread) and instantaneous (centerplane-based Unmixedness) mixing metrics are quantified in Figure 7.23. Here, PLIF data with matched RMS values of jet velocity perturbations at $U'_{j,rms} = 1.7$ m/s are utilized.

First of all, jet penetration z_p/D (Figure 7.23(a)), vertical spread δ_z/D (Figure 7.23(b))

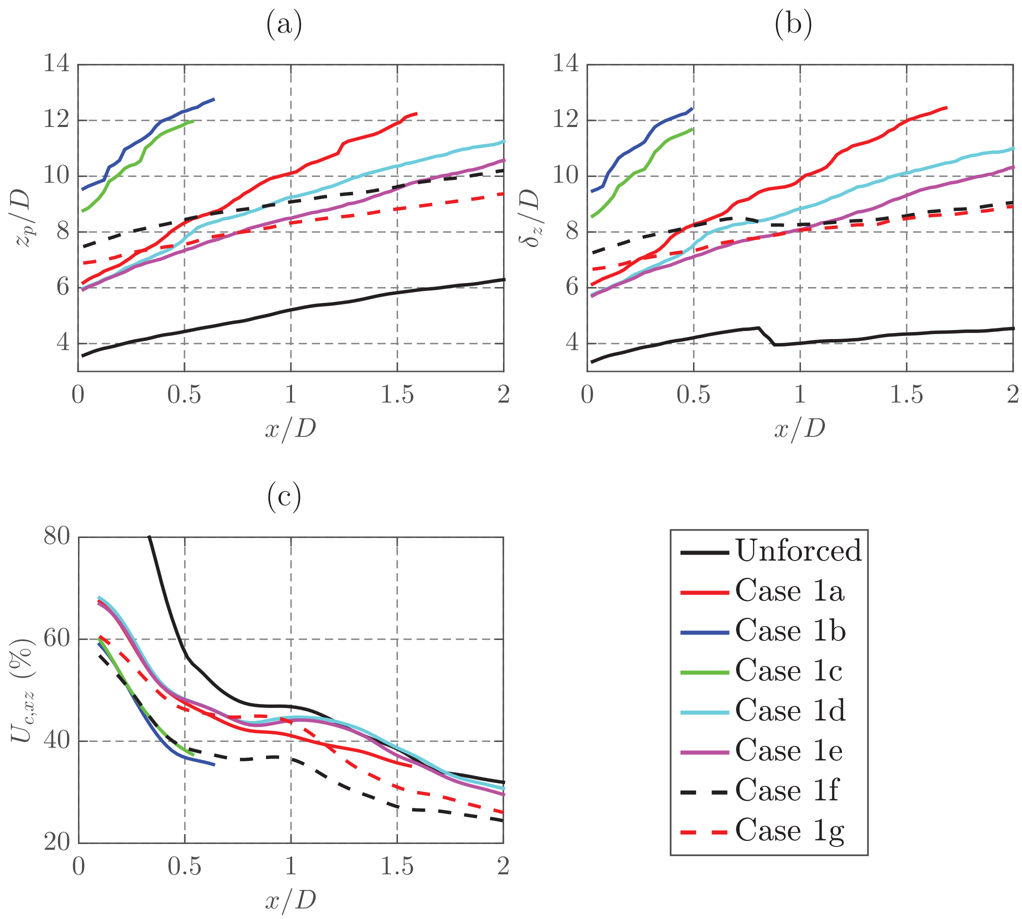

Figure 7.23: Quantification of centerplane-based mean and instantaneous mixing metrics along x/D for Cases 1a-1g with matching RMS of jet velocity perturbation at $U'_{j,rms} = 1.7$ m/s: (a) jet penetration z_p/D, (b) jet vertical spread δ_z/D, and (c) Unmixedness $U_{c,xz}$. The quantification is based on PLIF data acquired at a recording rate of 5 Hz.

and centerplane-based Unmixedness $U_{c,xz}$ (Figure 7.23(c)) are all significantly enhanced under double-pulse forcing under any forcing conditions here, as compared with the unforced case. As previously discussed, since the peak-to-peak jet velocity amplitude of pulses, ΔU_j, is not matched here, jet penetration and vertical spread are quite different between Case 1a and Case 1b or 1c, even with fairly similar temporal jet responses at the injector exit as shown in Figure 7.4. Additionally, the slope of the jet penetration and vertical spread for Cases 1b and 1c in Figures 7.23(a) and (b) are higher than the other cases, which may be also caused by different ΔU_j.

For the centerplane-based Unmixedness, mixing trends are fairly consistent with jet penetration and vertical spread except for Case 1f, which provides a relatively small jet penetration and vertical spread, suggesting worse mixing, but a lower Unmixedness, equivalently to better molecular mixing, as compared with Cases 1a, 1d, 1e and 1g. The enhanced molecular mixing for Case 1f is likely to be associated with the relatively strong temporal oscillation in jet response as shown in Figure 7.6(c), creating highly disturbed jet centerplane structures.

Next, mixing characteristics for the reference case (M'Closkey et al., 2002) with matched peak-to-peak jet velocity amplitude ΔU_j instead of a matched RMS of the jet velocity perturbation $U'_{j,rms}$ are shown in Figure 7.24. Again, jet penetration, vertical spread and centerplane-based Unmixedness for the forced cases are all enhanced as compared with the unforced case. Since ΔU_j is currently matched, the jet penetration and vertical spread for Cases 1a-1c collapse well onto one another, although the other forced cases provide lower jet penetration and vertical spread. For Cases 1f and 1g, since the temporal jet responses at the jet exit (Figures 7.8(f) and (g)) consist of fairly strong oscillations, the jet is vigorously disturbed and hence does not penetrate as deeply or spread as widely in the vertical direction z/D. For Cases 1d and 1e in Figures 7.8(d) and (e), however, the temporal jet responses are fairly similar to those for Cases 1a-1c. Such different jet penetration and vertical spread even with similar temporal jet responses may be caused by a slightly lower stroke ratio for Cases 1d and 1e, as discusses in Section 7.3.1 (see Table 7.2). As also discussed in Section 7.3.2, the stroke ratio L/D, which corresponds to the relative strength of pulsation, seems to play an important role in the characterization of the near-field vortex interactions and collisions. Hence, it may be possible that even a slight difference in stroke ratio L/D (e.g., approximately a 5 % difference in L/D between Cases 1a-1c and 1d-1e estimated from Table 7.2) alters jet penetration and vertical spread, although an in-depth exploration will be required to clarify such differences.

The centerplane-based Unmixedness in Figure 7.24 exhibits similar characteristics to those in Figure 7.23(c) with a matched $U'_{j,rms}$ except that there is enhanced molecular mixing for Case 1a with a matched ΔU_j instead of $U'_{j,rms}$. For this reference case, better jet penetration and vertical spread basically coincide with better molecular mixing where there is matching of both $U'_{j,rms}$ and ΔU_j. This possibly occurs because the optimal stroke ratio

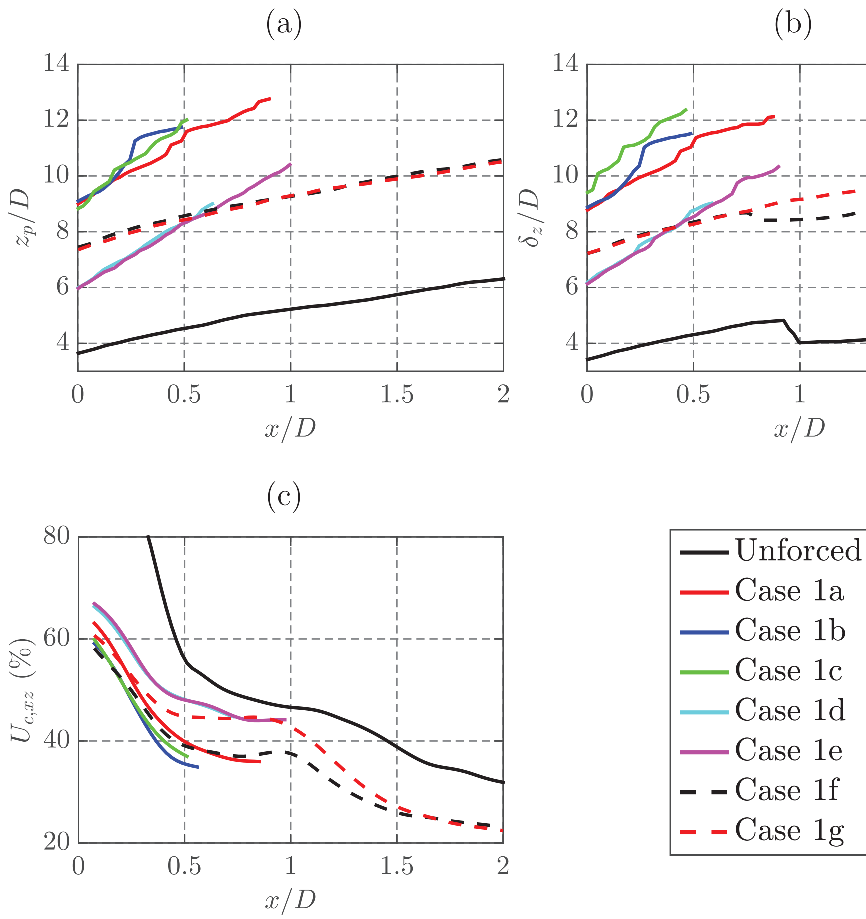

Figure 7.24: Quantification of centerplane-based mean and instantaneous mixing metrics along x/D for Cases 1a-1g with matching peak-to-peak jet velocity amplitude at $\Delta U_j \approx 4.3$ m/s: (a) jet penetration z_p/D, (b) jet vertical spread δ_z/D, and (c) Unmixedness $U_{c,xz}$. The quantification is based on PLIF data acquired at a recording rate of 5 Hz.

L/D for the best jet penetration and vertical spread as well as the best molecular mixing lies within approximately the same range as for the $J = 20$ cases in the previous section for single-pulse square wave forcing of the jet.

This mixing evaluation for the reference case with various temporal jet responses at the jet exit, as well as with matching $U'_{j,rms}$ and ΔU_j values, demonstrates that coherent deeply-penetrating vortex rings does enhance jet penetration and vertical spread, as well as molecular mixing, suggesting that the near-field vortex interactions and collisions induced by the vortex rings can potentially yield further enhancement of molecular mixing. The effect of controlling the spacing of the vortex rings is discussed in the next section.

7.4.2 Effect of Vortex Interactions and Collisions

Mean and instantaneous mixing metrics utilized in Section 7.4.1 are also quantified for the forcing conditions tabulated in Tables 7.3 (Cases 2a-2d and 3a-3d). For Cases 3a-3d, since cross-sectional PLIF data are acquired at four different downstream locations at $x/D = 0$, 0.5, 1.0 and 2.5, the cross-section-based mixing metrics are also quantified. In addition, mixing metrics are quantified based on separate sets of PLIF data taken at a recording rate of 1 and 7.5 Hz, to investigate the effect of recording rate on quantified mixing characteristics. Note that the RMS of jet velocity perturbation is matched at $U'_{j,rms} = 1.7$ m/s amongst all forcing conditions in this section, but not the peak-to-peak jet velocity amplitude ΔU_j.

Mean and instantaneous mixing quantification for Cases 2a-2d using centerplane PLIF data acquired at 1 and 7.5 Hz are shown in Figure 7.25. First, we see that in comparing among mixing characteristics with a recording rate of 1 and 7.5 Hz, mixing characteristics are qualitatively and even quantitatively similar, suggesting that the different recording rates do not affect the mixing quantification when averaged over 500 instantaneous images. As previously mentioned, the current data acquisition system for PLIF imaging inherently includes a slight time shift at each snap shot. Hence, as long as a large number of instantaneous images is utilized for mixing quantification, instantaneous PLIF images can be obtained at various phases of external forcing regardless of recording rates, even without a phase-locked measurement, and hence mixing characteristics are highly consistent at varied recording rates.

Within Cases 2a-2d, the best jet penetration and vertical spread are achieved for Cases 2b and 2d, although the jet penetration and vertical spread for even Cases 2a and 2c are enhanced as compared with the unforced case. The jet penetration and vertical spread may be associated with the near-field flow dynamics such as vortex ring interactions and collisions. As observed in the reference case in Section 7.4.1, forcing conditions in which the best jet penetration and vertical spread are achieved also yield the best molecular mixing for this data set. Remarkably, in Case 2d where the near-field vortex collision occurs, there is great enhancement in molecular mixing, although even Case 2b reveals similar mixing

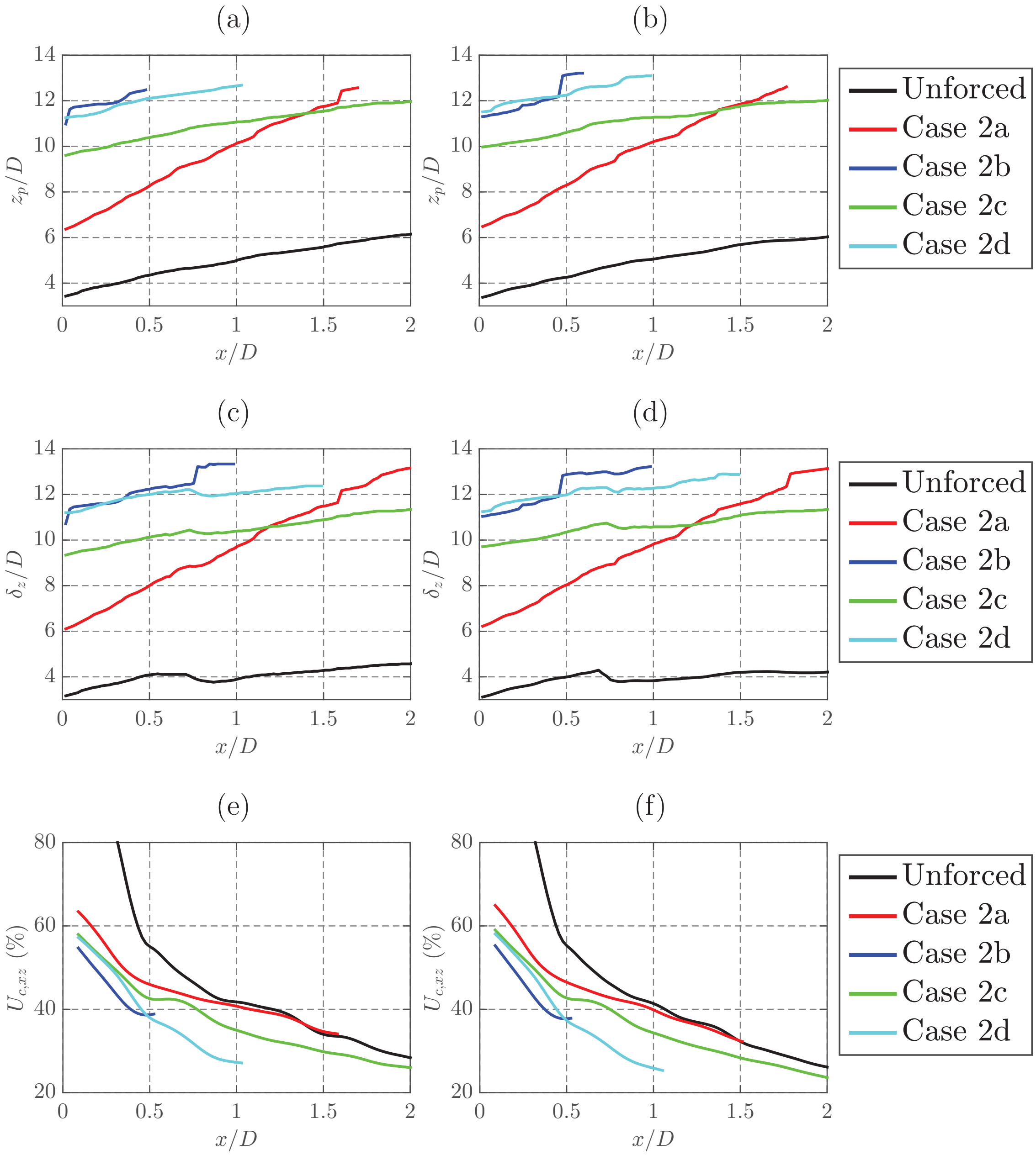

Figure 7.25: Quantification of centerplane-based mean and instantaneous mixing metrics along x/D for Cases 2a-2d with matching RMS of jet velocity perturbation at $U'_{j,rms} = 1.7$ m/s: (a,b) jet penetration z_p/D, (c,d) jet vertical spread δ_z/D, and (e,f) Unmixedness $U_{c,xz}$. The quantification is based on PLIF data acquired at a recording rate of (a,c,e) 1 Hz and (b,d,f) 7.5 Hz.

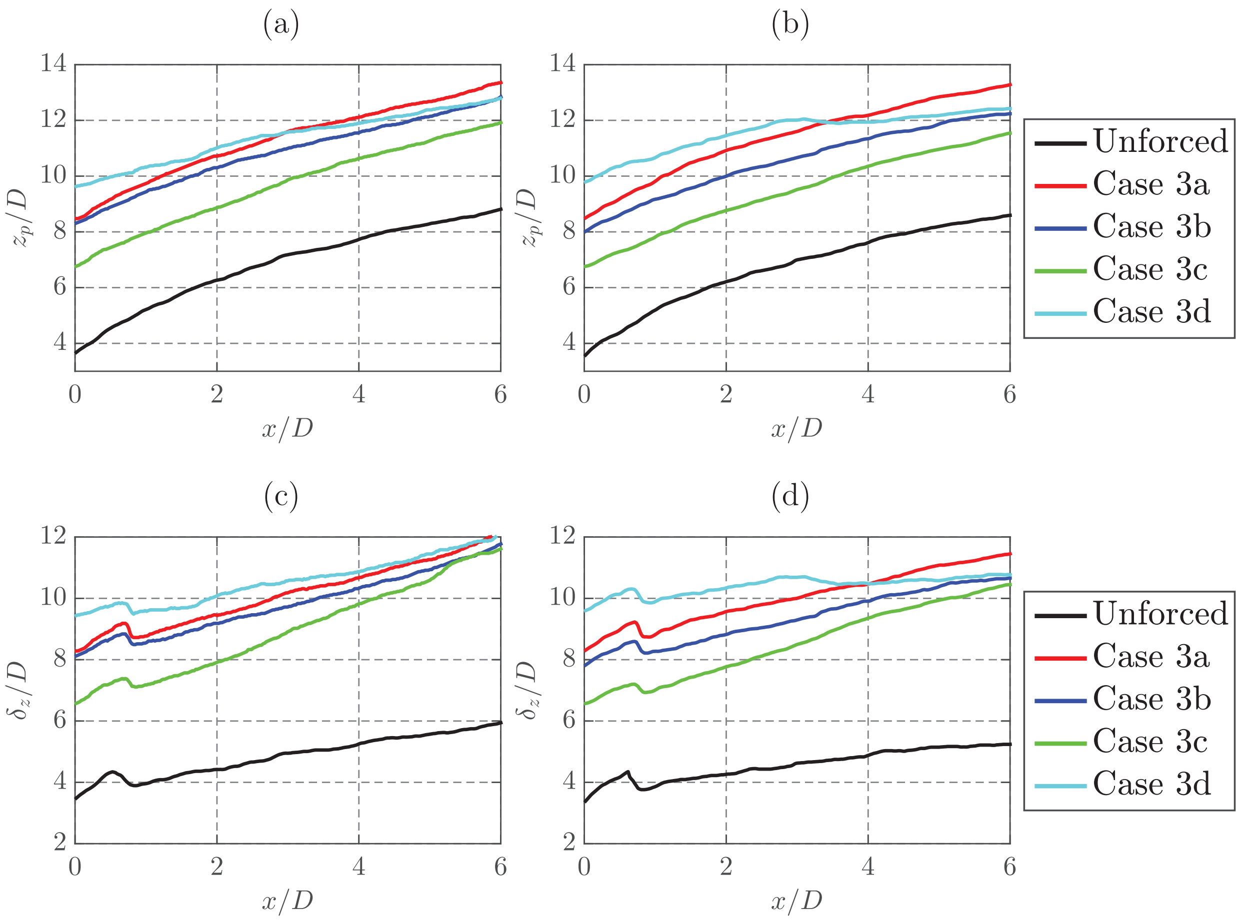

Figure 7.26: Quantification of centerplane-based mean mixing metrics along x/D for Cases 3a-3d with matching RMS of jet velocity perturbation at $U'_{j,rms} = 1.7$ m/s: (a,b) jet penetration z_p/D and (c,d) jet vertical spread δ_z/D. The quantification is based on PLIF data acquired at a recording rate of (a,c) 1 Hz and (b,d) 7.5 Hz.

characteristics, without clear vortex ring collisions. The Unmixedness at $x/D \gtrsim 1.0$ for Case 2a, where coherent deeply-penetrating vortex rings are observed, becomes very close to the unforced case. In contrast, molecular mixing for the other forced cases is still better than that for the unforced case at $x/D \gtrsim 1.0$. Therefore, the occurrence of the near-field vortex ring interactions or collisions enhances molecular mixing, not only fairly close to the jet exit but also further from the exit.

Mixing characteristics are also explored for Cases 3a-3d, and these are shown in Figures 7.26 and 7.27. Here, Figures 7.27(c) and (d) represent the cross-section-based Unmixedness quantified from PLIF data at a recording rate of 1 and 7.5 Hz respectively. First, all mixing

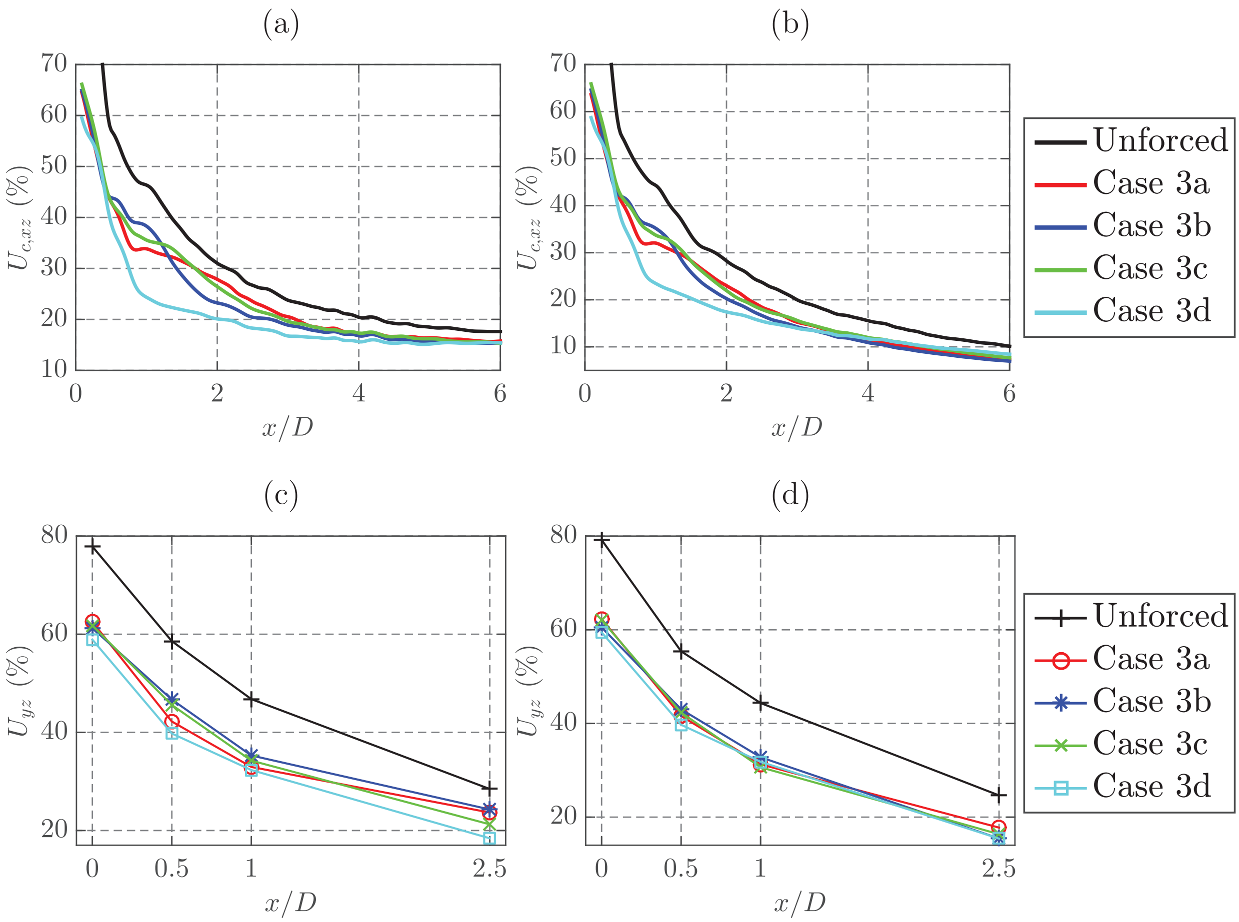

Figure 7.27: Quantification of (a,b) centerplane- and (c,d) cross-section-based Unmixedness along x/D for Cases 3a-3d with matching RMS of jet velocity perturbation at $U'_{j,rms} = 1.7$ m/s. The quantification is based on PLIF data acquired at a recording rate of (a,c) 1 Hz and (b,d) 7.5 Hz.

characteristics are highly consistent regardless of the recording rates of PLIF imaging, as observed for Cases 2a-2d. Such consistency again suggests that 500 instantaneous images are sufficient enough to capture a wide range of phases with respect to external forcing, and hence to achieve convergence even at different recording rates.

In Figure 7.26, jet penetration and vertical spread are gradually reduced as the first temporal pulse width $\tau_{actual,1}$ increases from Case 3a to 3c. While the near-field vortex ring collision occurs fairly close to the jet exit in terms of the x/D location in Case 3a, the vortex collision is observed at a further x/D downstream location in Case 3c because two vortex rings convect in the x/D direction before they collide. The convection of the vortex rings may contribute to the lower jet penetration and vertical spread. Because there is no clear vortex collision in Case 3d, jet penetration and vertical spread becomes relatively high again. This trend indicates that vortex interactions and collisions are deeply associated with jet penetration and spread.

From the Unmixedness evaluation in Figure 7.27, molecular mixing for all forced cases shown here is significantly enhanced as compared with the unforced case. Also, there is no significant qualitative discrepancy between mixing evaluations with data taken at 1 and 7.5 Hz, both in centerplane and cross-sectional views. Although there is a slight quantitative difference in the Unmixedness at 1 and 7.5 Hz, it is considered to be within the experimental uncertainty in PLIF imaging and mixing evaluation, and mixing characteristics are quantitatively fairly similar as well. In Figures D.17-D.20 in Appendix D, the centerplane- and cross-section-based Unmixedness are quantified as an ensemble of various number of samples from 10 to 400 acquired at a recording rate of 1 and 7.5 Hz, suggesting that the Unmixedness is qualitatively and quantitatively converged with only 200-300 instantaneous data. Hence, all explorations associated with various recording rates as well as number of samples indicate that a recording rate of PLIF imaging does not affect the mixing quantifications as long as more than 300 instantaneous images are utilized. This is why this experimental study in Chapters 5-7 characterizes mixing of JICF based on 500 instantaneous images (more than 300 images) to remove the effect of recording rate, even without performing phase-locked measurement. More interestingly, molecular mixing extracted both from the centerplane- and cross-section-based Unmixedness is the most enhanced for Case 3d without clear vortex collisions, which may be counter-intuitive. A further explanation is required using the cross-section-based PDF, which is shown in Figure 7.28 acquired at 1 Hz.

As one can observe, Case 3d at all downstream locations, $x/D = 0$, 0.5, 1.0 and 2.5, clearly yields a higher peak at lower normalized concentration scalar values C/C_o, corresponding to more uniform concentration distributions in cross-sectional structures. These figures suggest that the near-field vortex collisions may not necessarily make more uniform the concentration distributions and hence improved molecular mixing.

As previously mentioned, mixing quantification along jet centerline trajectories is ques-

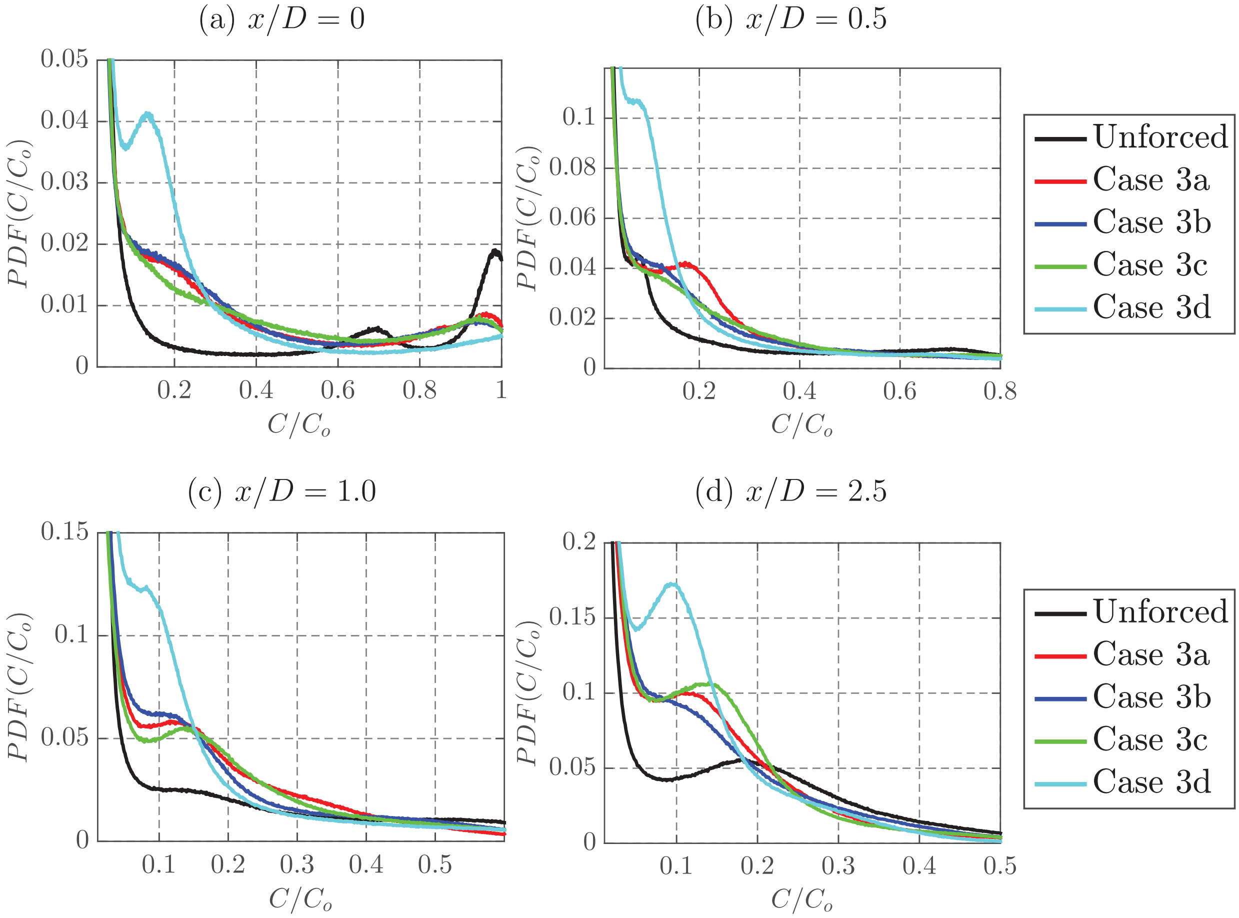

Figure 7.28: Quantification of cross-section-based probability density function (PDF) of normalized concentration scalar values C/C_o based on PLIF data acquired at a recording rate of 1 Hz at downstream locations of (a) $x/D = 0$, (b) 0.5, (c) 1.0, and (d) 2.5. The quantifications is based on PLIF data acquired at a recording rate of 1 Hz.

tionable due to many alternative trajectories that describe such forced jets. However, the centerplane-based Unmixedness along the unforced jet trajectory as well as along each jet trajectory in question (see Figures D.24 and D.26) suggests that Case 3c enhances molecular mixing more than the other forcing conditions. Hence, mixing characteristics of the JICF with near-field vortex ring collisions are likely to be affected by the variation in the choice of the spatial coordinate system for mixing quantification, unlike that for sine and single-pulse square wave forcing in Chapters 5 and 6.

Future studies associated with the flow dynamics of vortex ring interactions and collisions for the JICF clearly will be required to clarify why vortex collisions for Case 3a-3c do not necessarily enhance molecular mixing more than the vortex interactions for Case 3d, as mentioned above. Nevertheless, the excitation studies described here indicate that double-pulse square wave forcing does enable the control of the near-field flow dynamics, and potentially could significant enhance molecular mixing. With a better understanding of the near-field flow interaction mechanisms, better controllability of vortex ring collisions and molecular mixing may be successfully achieved.

CHAPTER 8

Conclusions and Future Work

The experimental studies in this dissertation have explored the relationship between velocity and scalar fields (Chapter 3), mixing characterization for variable scale lengths (Chapter 4), and the effect of axisymmetric forcing of jet fluid on JICF stability, structural, and mixing characteristics (Chapters 5-7). In Chapter 3, exploration of the interplay between scalar and velocity fields, using simultaneous PLIF/PIV measurements in the jet's centerplane, provided important insights into diffusion/mixing and transport processes in the JICF. POD analyses using PLIF and PIV images generally showed a good correspondence between the dynamics of the velocity and scalar fields. The equidensity ($S = 1.00$) flush nozzle- and flush pipe-injected JICF were dominated by shear layer structures, and the periodicity of the upstream shear layer was augmented as J values were reduced from $J = 41$ to $J = 5$, with a clear transition from convective to absolute instability of the upstream shear layer. Differences in the periodicity between the first and second modes extracted from PIV and PLIF data for the equidensity flush injection at a transitional condition, $J = 12$, suggested different responses of velocity and scalar fields to growing flow perturbations. Moreover, for the absolutely unstable conditions for the $S = 0.35$, flush nozzle-injected JICF, although lee-side stabilities were revealed in PLIF POD mode structures at $J = 41$, both PIV and PLIF mode structures clearly showed strong upstream shear layer-behavior dominance at lower J values, associated with the absolutely unstable upstream shear layer below the critical density ratio $S \cong 0.40 - 0.45$ (Getsinger et al., 2012). PLIF-based POD analyses with higher resolution PLIF images showed slight differences as compared with those for lower resolution PLIF images, however, with strong periodicity at lower J values. In general, scalar mode structures were consistent between lower- and higher-resolution PLIF images.

Strain rates on the upstream and downstream mixing layers were extracted from PLIF and PIV data. The Strained Dissipation and Reaction Layer (SDRL) model was directly applied to PLIF images to extract the one-dimensional, quasi-steady strain rates. The results for the equidensity flush nozzle- and pipe-injected JICF showed remarkable qualitative correspondence between PLIF- and PIV-based strain rates, although there were considerable quantitative differences, mainly associated with the effect of spatial resolution in PLIF images, as described in Gevorkyan (2015) and Gevorkyan et al. (2017). Lower strain rates were more often observed on the downstream mixing layer, suggesting the propensity for more robust ignition for the equivalent reactive flowfield. Strain rates were also evaluated for the $S = 0.35$ flush nozzle-injected JICF by applying the Howarth transformation in order to deal with the variation in density through out the flowfield. The results showed good qualitative agreement, but again significant quantitative discrepancies between PLIF- and PIV-based strain rates, consistent with the equidensity flush injection cases. As observed in the equidensity jets, strain rates in the upstream mixing layer were larger in the nearfield than those for the downstream mixing layer, suggesting that ignition tends to occur more easily on the lee side of the jet. These findings are consistent with the experimental studies of the reactive JICF (Wagner et al., 2015).

A new algorithm, based on the concepts of the Mix-Norm (Mathew et al., 2005; Gubanov and Cortelezzi, 2010) and the Unmixedness (Danckwerts, 1952; Dimotakis and Miller, 1990; Smith et al., 1997; Gevorkyan et al., 2016), but taking into account variable mixing scale lengths, was developed here. This approach enabled us to obtain an additional interpretation of mixing characteristics for the JICF associated with variable flow dynamics, e.g., fluid mechanical stirring and molecular diffusion. The new algorithm, equivalently the Unmixedness with variable scale lengths, successfully captured different mixing characteristics related to varying scale lengths from PLIF images, for a range of S values ($0.35 \leq S \leq 1.00$), J values ($5 \leq J \leq 41$), and alternative injectors. The results showed there could be a local increase in the Unmixedness at a s_c/D location, then a later decrease, instead of a monotonic decrease in the Unmixedness, i.e., an increase in mixing. This occurred for relatively large scale lengths for the equidensity flush pipe-injected JICF at all J values explored. The s_c/D

locations where the increase in the Unmixedness was observed remarkably corresponded to initial locations of vortical flow structures on the upstream shear layer, which were extracted from the PIV data portion of the simultaneous PLIF/PIV measurements. This suggested that rolled-up vortical structures on the upstream shear layer may indeed cause an increase in the Unmixedness, or a worsening mixing, possibly due to relatively high concentrations of jet fluid captured by vortices, as discussed in Mathew et al. (2005) and Gubanov and Cortelezzi (2010). A relatively small increase in the Unmixedness was observed for some other flow conditions, e.g., for the $S = 1.00$ flush nozzle at $J = 12$, the $S = 1.00$ elevated nozzle at $J = 12$ and 5, the $S = 0.55$ flush nozzle at $J = 12$, and the $S = 0.35$ flush nozzle at $J = 41$, although there was a lesser correspondence to locations of initial rolled-up vortical structures for these cases. These results imply that the vortical flow structures could but do not necessarily always enhance fluid mechanical stirring, which may be important for a specific engineering application. Hence, mixing characterization with variable scale lengths is potentially a useful tool to investigate flow mixing mechanisms in depth, and thus to optimize mixing in engineering systems.

The effect of axisymmetric, external forcing of jet fluid on JICF instability, structural, and mixing characteristics was extensively studied ultimately for the optimization or strategic control of molecular mixing of the JICF, using PLIF-only imaging. Sinusoidal forcing at a forcing frequency f_f fairly close to a fundamental natural frequency f_o on the upstream shear layer for the $S = 1.00$ flush nozzle-injected JICF at $J = 41$ (the convectively unstable condition) created a jet bifurcation in the centerplane view, a symmetrized mean cross-section, and enhanced molecular mixing, even at a relatively low forcing amplitude, $U'_{j,rms} = 0.07$ m/s (approximately 1 % of the mean jet velocity $U_j \approx 6.5$ m/s). This observation suggests that even the convectively unstable JICF required a specific range of forcing frequencies f_f to enhance molecular mixing. For the $S = 1.00$ flush nozzle-injected JICF at $J = 5$ (the absolutely unstable condition), however, a relatively high sinusoidal forcing amplitude was required to alter jet structures and enhance molecular mixing, but only at a narrow range of forcing frequencies f_f close to f_o. At these forcing frequencies, the upstream shear layer became visually locked-in to external forcing from instantaneous centerplane PLIF images.

Based on these results, JICF characteristics with sinusoidal excitation are likely related to lock-in of the upstream shear layer to external forcing.

Single-pulse square wave excitation of the jet with a feedback control system significantly altered jet structures, even in the absolutely unstable condition at $J = 5$, creating deeply-penetrating puff-like vortical structures at a specific range of stroke ratios L/D. Based on mean mixing metrics, the penetrating vortical structures greatly enhanced jet spread and penetration, even for the absolutely unstable JICF at $J = 10$ and 5 in this dissertation. The optimal stroke ratio L/D for the best jet penetration and spread decreased as J values were reduced from 41 to 5. The qualitative trend in the varying stroke ratio L/D with respect to different J values was consistent with the computational observations of Sau and Mahesh (2010), although the stroke ratio was not necessarily close to a universal time scale for optimum vortex ring formation in quiescent surroundings, $L/D \approx 4$ (Gharib et al., 1998). Interestingly, instantaneous mixing metrics showed that deep jet penetration and wide jet spread did not necessarily coincide with enhanced molecular mixing. In addition, the optimal stroke ratio for the best molecular mixing was approximately the same, or in the same range for different J values at a given forcing frequency f_f and amplitude $U'_{j,rms}$, suggesting that a fixed stroke ratio could be utilized in a practical system to optimize molecular mixing. The observation also suggested that the optimal stroke ratio L/D for the best jet spread and penetration was also not necessarily the same as that for the best molecular mixing. The optimal stroke ratio L/D for the best jet penetration and spread, as well as molecular mixing increased at a given J value as the forcing amplitude $U'_{j,rms}$ was systematically increased.

Double-pulse square wave excitation successfully created successive vortex rings at the jet exit, which interacted and even collided, depending on temporal parameters associated with two pulses, e.g., temporal intervals, temporal pulse widths, and amplitudes. Sequential instantaneous PLIF images in the centerplane and cross-sectional views clearly illustrated nearfield vortex interaction and collision occurring at different downstream locations x/D. Locations of nearfield vortex ring collision were altered with different temporal parameters such as temporal pulse widths and amplitudes of two pulses, suggesting that vortex collision could be potentially controlled with a deeper understanding of the mechanism of nearfield vortex collisions, and with an improved control system. The results of mean and instantaneous mixing metrics suggested that all forcing conditions with double-pulse square wave forcing enhanced jet penetration and spread, as well as molecular mixing for the JICF, as compared with the unforced case. Both the centerplane- and cross-section-based Unmixedness demonstrated that vortex collisions did not necessarily enhance molecular mixing more than the vortex interactions. Although further exploration will be required to understand this counter-intuitive trend, this new forcing method enabled the control of the near-field flow dynamics, and potentially could significant enhance and strategically control molecular mixing, particularly in the jet's nearfield.

The mixing characterization of the JICF with these excitation methods has significant implications, mainly for the different responsibility of mean and instantaneous mixing metrics, and the effectiveness of varying excitation methods for optimized molecular mixing. As described above, mixing metrics for the forced JICF clearly revealed that the best jet spread and penetration do not necessarily correspond to the best molecular mixing. This finding is extremely important because it casts doubt on a classical concept that jet penetration and spread represented the degree of mixing. Although mean metrics are still quite useful in that jet spread and penetration are often practically important in engineering applications such as dilution jet injection and turbine film cooling, mixing quantification should be comprehensively administered using several different methods, mean and instantaneous mixing metrics, to understand the implications for molecular mixing characteristics in detail.

For strategic control of molecular mixing of the JICF, making a connection between the fundamental characteristics of the JICF and practical requirements in engineering systems is crucial. This study demonstrated that effective forcing methods can be different depending on natural instability and structural characteristics for the JICF in the absence of external forcing. Hence, from a practical perspective, a deeper understanding of flowfields in actual engineering systems contributes to the selection of an optimized forcing method, again based on the metric that best represents the desired goal.

While the present studies have uncovered several new features of structural and mixing characteristics for the unforced and forced JICF, they also suggest the need for further studies as follows:

- Further exploration on double-pulse square wave forcing of the JICF. As described above, vortex collisions do not necessarily enhance molecular mixing more than simpler vortex interactions. A understanding of this counter-intuitive phenomenon is important to more significantly enhance molecular mixing for the JICF using double-pulse square wave forcing and thus to strategically maximize or optimize molecular mixing with improved controllability in the feedback control system.

- An application of asymmetric forcing of jet fluid, particularly for convectively unstable conditions, which might structurally alter jet structures and hence potentially enhance mixing characteristics. As noted in Section 1.3, asymmetries for transverse jets in cross-sectional views were observed in the experimental study by Getsinger et al. (2014) in the absence of forcing, depending on flow conditions (high J) and types of injection. If this asymmetric structure is an inherent feature of the jets when they are convectively unstable, the jet excitation of positive or negative helical modes could potentially augment or cancel the mechanism of initiation of the asymmetry, possibly resulting in an alteration of mixing characteristics. As noted in the transverse jet shear layer's linear stability analysis by Alves et al. (2007), positive and negative helical growth rates can be unequal, especially at very high R or J values. Therefore, strategic asymmetric forcing might be capable of weakening or strengthening the level of inherent asymmetry in the jet and thus improving mixing.

- Passive control of the JICF using variable shapes of injectors, e.g., non-circular injectors, or an injector with a tab on its exit. Because a passive control system can be implemented in engineering propulsion system in a relatively simplified manner as compared with an active control system, the effect of a passive control system on structural and mixing JICF characteristics could be practically useful. Although there are previous studies associated with non-circular injectors (Humber et al., 1993; Liscinsky et al., 1996; New et al., 2004; Plesniak and Cusano, 2005), and a tab on a nozzle exit (Zaman, 1998; Zaman and Milanovic, 2012) for the JICF, mixing characterization, e.g., molecular mixing of the JICF, has not been comprehensively administered using mean and instantaneous mixing metrics, as done in this dissertation. Hence, an exploration of the influence of a passive control system could be interesting for further future work.

- Cross-sectional PIV in order to understand vorticity distribution in cross-sections, especially with external forcing. This thesis has shown that external forcing has a significant impact on cross-sectional structural and mixing characteristics. With a specific forcing condition, an asymmetric cross-section, typically observed for the convectively unstable JICF, became more symmetric, which generally provided enhanced molecular mixing as compared with that for more asymmetric cross-sections (Gevorkyan et al., 2016). Hence, a structural exploration using cross-sectional PIV measurements may clarify mechanisms of the evolution of CVP structures with external forcing, and thus contribute to a better strategic control of molecular mixing in the cross-sectional view. Cross-sectional PIV measurements will be very useful, especially with asymmetric (or helical mode) forcing of the jet to clarify the mechanism of symmetrization of a cross-section.

- Phase-locked PLIF imaging (and potentially PIV measurements) for both centerplane and cross-sectional slices of jets. An understanding of forced JICF structural and mixing characteristics at a specific phase in temporal forcing of jet fluid may be important for precise control of molecular mixing. Phase-locked measurements could be used to investigate the temporal formation or growth of vortical and flow structures, and associating molecular mixing of forced transverse jets. This phase-locked measurements will clarify the behavior of typical flow structures widely observed by many studies (Johari et al., 1999; Eroglu and Breidenthal, 2001; M'Closkey et al., 2002; Shapiro et al., 2006; Sau and Mahesh, 2010; Davitian et al., 2010b), as well as in this study, and will correlate forced-jet structures with mixing characteristics more in depth.

APPENDIX A

Mixing Scale Length Data

The following results correspond to data associated with the study of mixing characterization with variable scale lengths in Chapter 4.

A.1 Unmixedness with Various Scale Lengths without Matching Mean Values

This section shows the results of mixing evaluation which was not shown in Chapter 4.

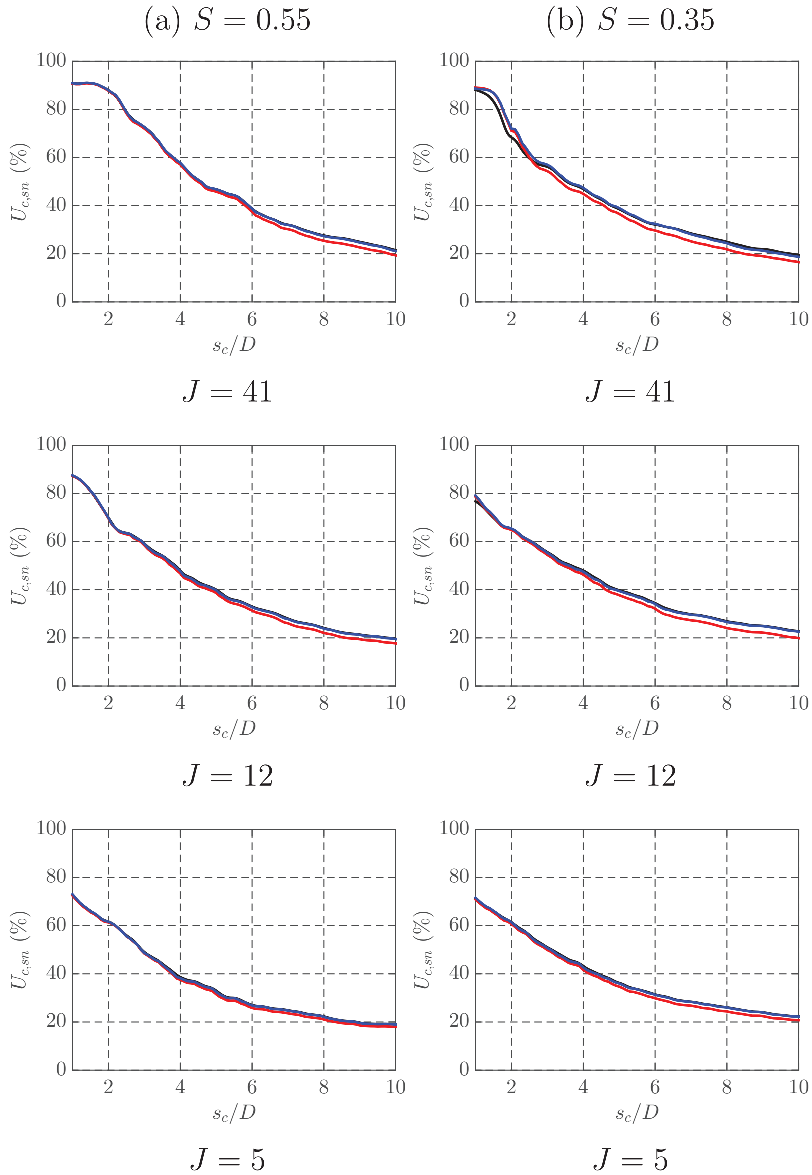

Figure A.1: Comparison of Unmixedness $U_{c,sn}$ evaluated in the transformed plane $(s_c/D - n/D)$ along the jet centerline trajectory s_c/D with the smallest length scale ($\delta_s = \delta p$) in PLIF images for the (a) $S = 0.55$, and (b) $S = 0.35$ flush nozzle-injected JICF at $J = 41$ (top row), 12 (middle row) and 5 (bottom row). Each plot corresponds to the Unmixedness with: seven-pixel-width interrogation area with mean values matched by Gevorkyan et al. (2016) (—), one-pixel-width interrogation area without mean values matched (—), as well as with mean values matched (—).

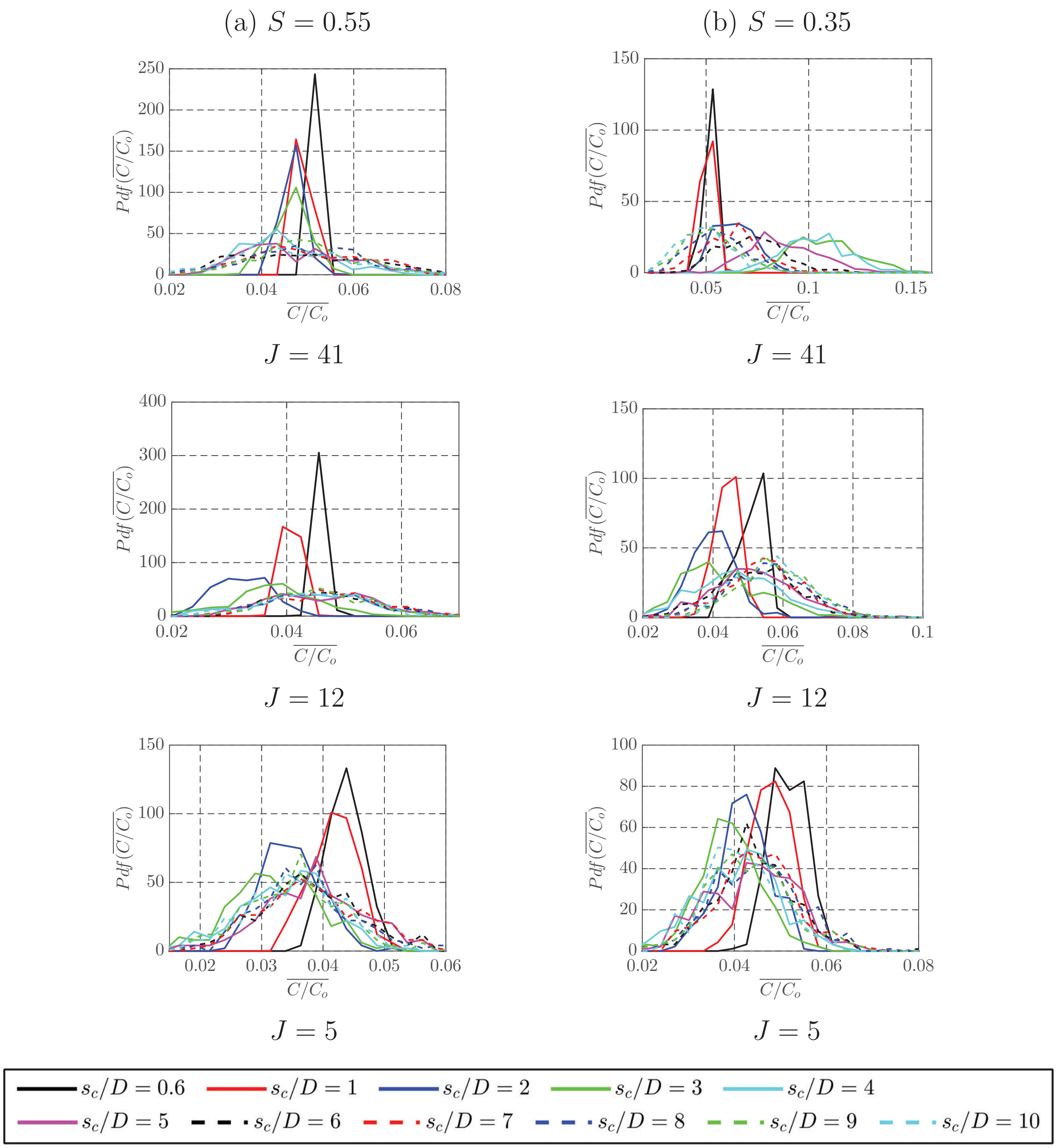

Figure A.2: Probability Density Function (PDF) evaluated in the transformed plane ($s_c/D-n/D$) for the range of mean concentration values $C\bar{/}C_o$ over 200 instantaneous images at a given jet centerline trajectory location s_c/D for the (a) $S = 0.55$, and (b) $S = 0.35$ flush nozzle-injected JICF at $J = 41$ (top row), 12 (middle row) and 5 (bottom row).

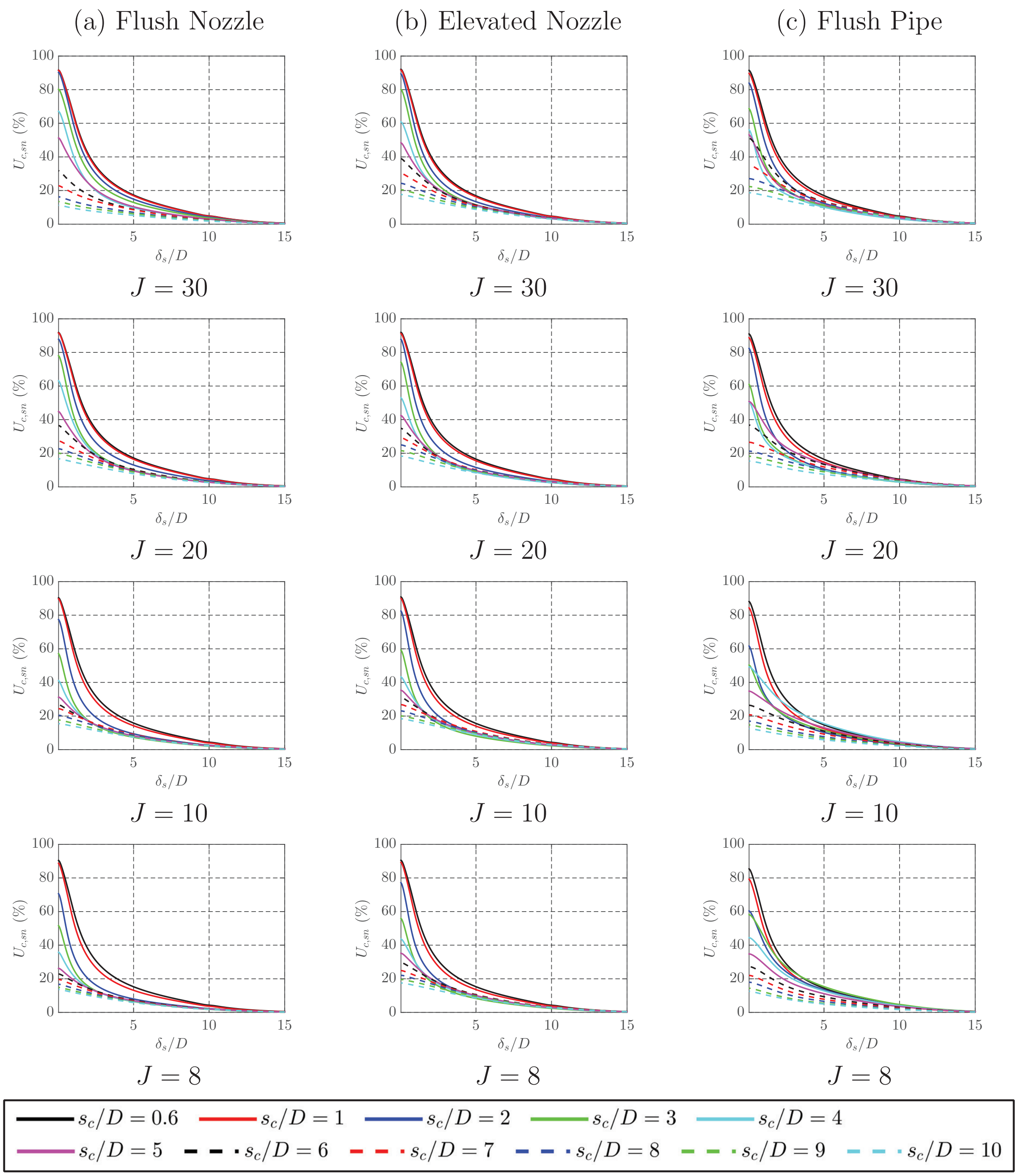

Figure A.3: Mean centerplane-based Unmixedness $U_{c,sn}$ evaluated in the transformed plane as a function of various length scales normalized by the jet diameter δ_s/D at a given jet centerline trajectory coordinate s_c/D for the equidensity (a) flush nozzle-, (b) elevated nozzle- and (c) flush pipe-injected JICF at $J = 30$ (top row), 20 (second row), 10 (third row), and 8 (bottom row). Mean concentration values in each interrogation area are not matched.

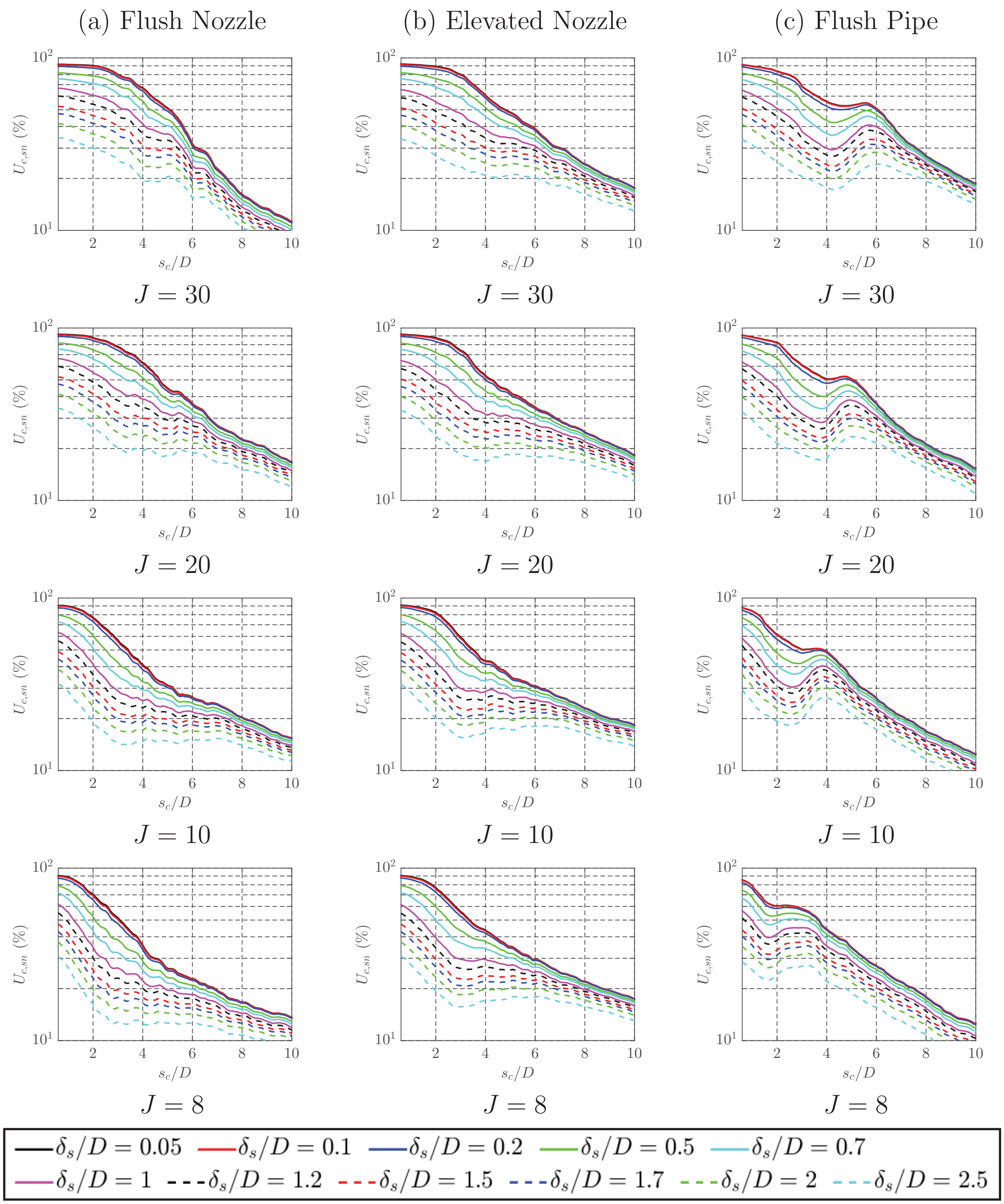

Figure A.4: Mean centerplane-based Unmixedness $U_{c,sn}$ evaluated in transformed plane as a function of jet centerline trajectory coordinate s_c/D with a given length scale δ_s/D for the equidensity (a) flush nozzle-, (b) elevated nozzle- and (c) flush pipe-injected JICF at $J = 30$ (top row), 20 (second row), 10 (third row), and 8 (bottom row). Mean concentration values in each interrogation area are not matched.

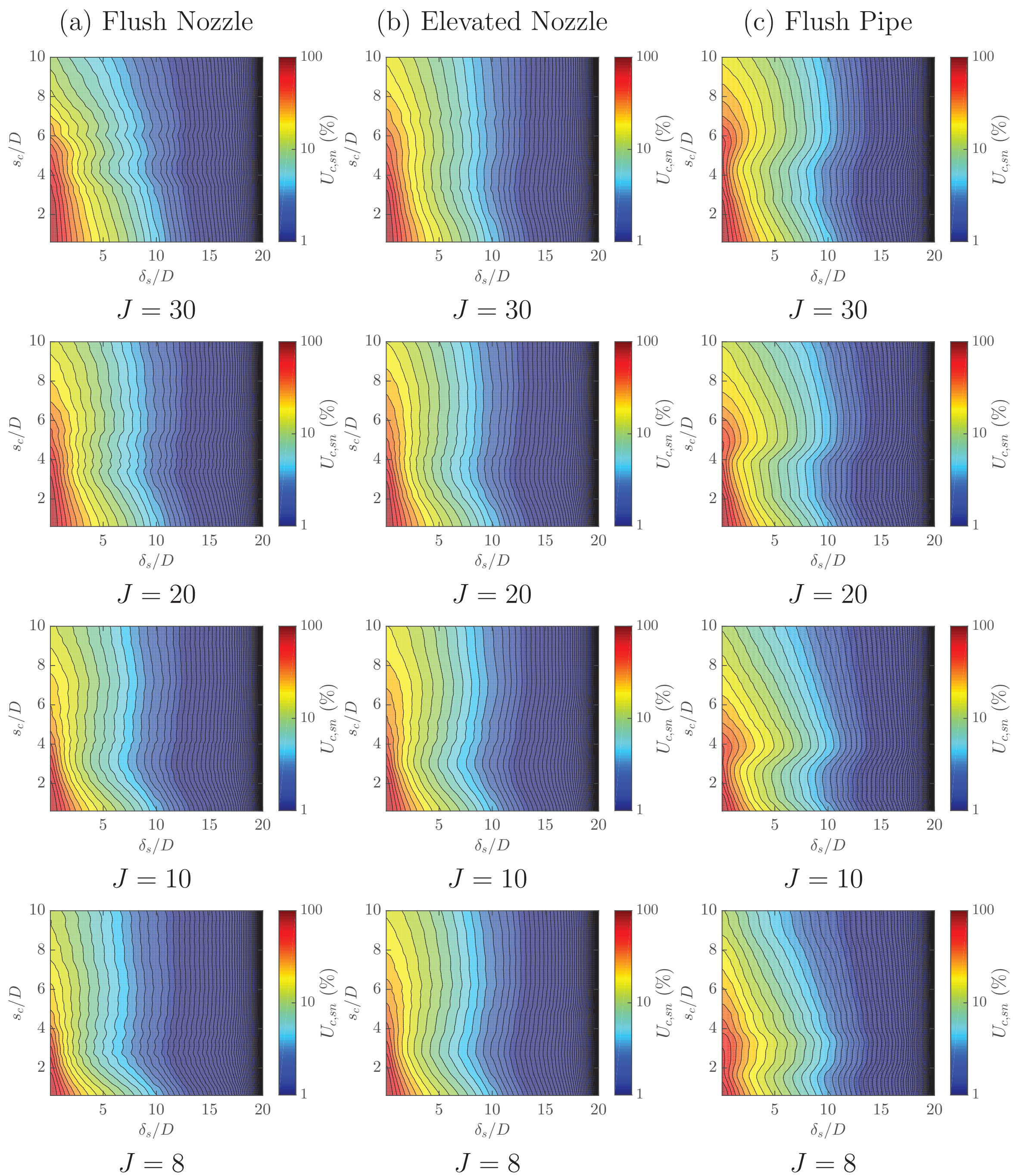

Figure A.5: Contour maps of the mean centerplane-based Unmixedness $U_{c,sn}$ evaluated in transformed plane ($s_c/D - n/D$) as a function of various length scales normalized by the jet diameter δ_s/D (x axis) and jet centerline trajectory coordinate s_c/D (y axis) for the equidensity (a) flush nozzle-, (b) elevated nozzle- and (c) flush pipe-injected JICF at $J = 30$ (top row), 20 (second row), 10 (third row), and 8 (bottom row). Mean concentration values in each interrogation area are not matched to the reference value here.

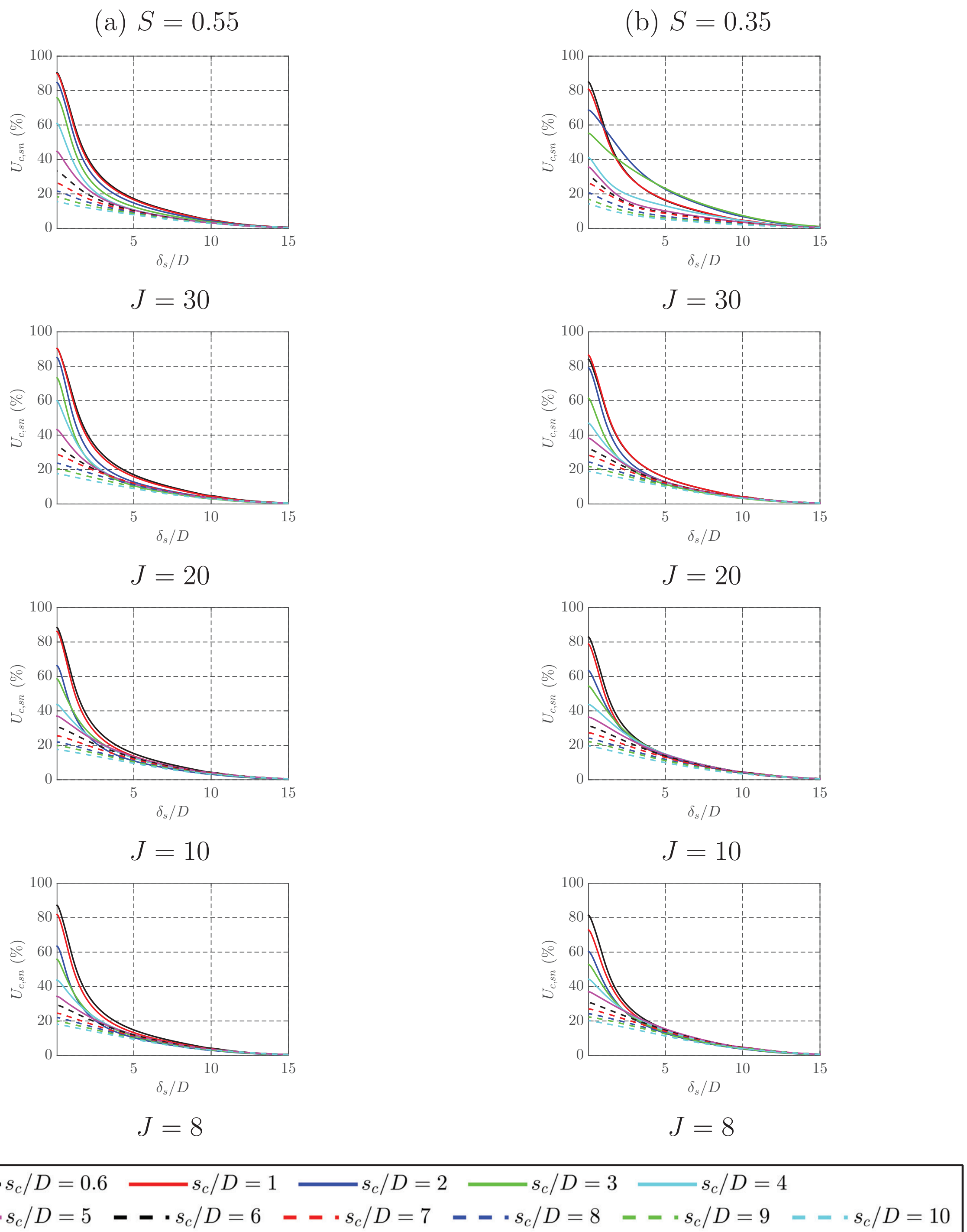

Figure A.6: Mean centerplane-based Unmixedness $U_{c,sn}$ evaluated in the transformed plane as a function of various length scales normalized by the jet diameter δ_s/D at a given jet centerline trajectory location s_c/D for the (a) $S = 0.55$ and (b) $S = 0.35$, flush nozzle-injected JICF at $J = 30$ (top row), 20 (second row), 10 (third row), and 8 (bottom row). Mean concentration values in each interrogation area are not matched.

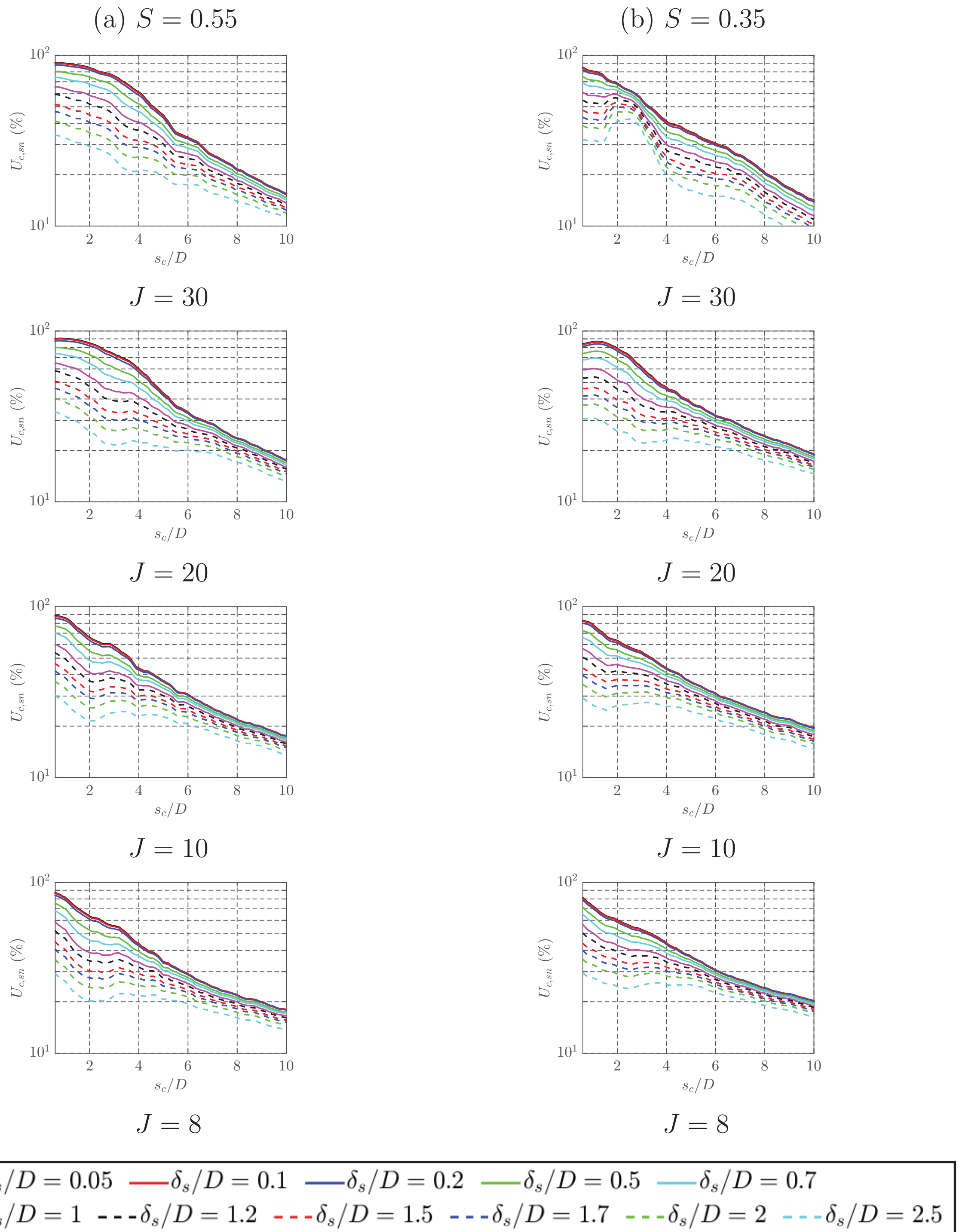

Figure A.7: Mean centerplane-based Unmixedness $U_{c,sn}$ evaluated in the transformed plane as a function of jet centerline trajectory coordinate s_c/D with a given length scale δ_s/D for the (a) $S = 0.55$ and (b) $S = 0.35$, flush nozzle-injected JICF at $J = 30$ (top row), 20 (second row), 10 (third row), and 8 (bottom row). Mean concentration values in each interrogation area are not matched.

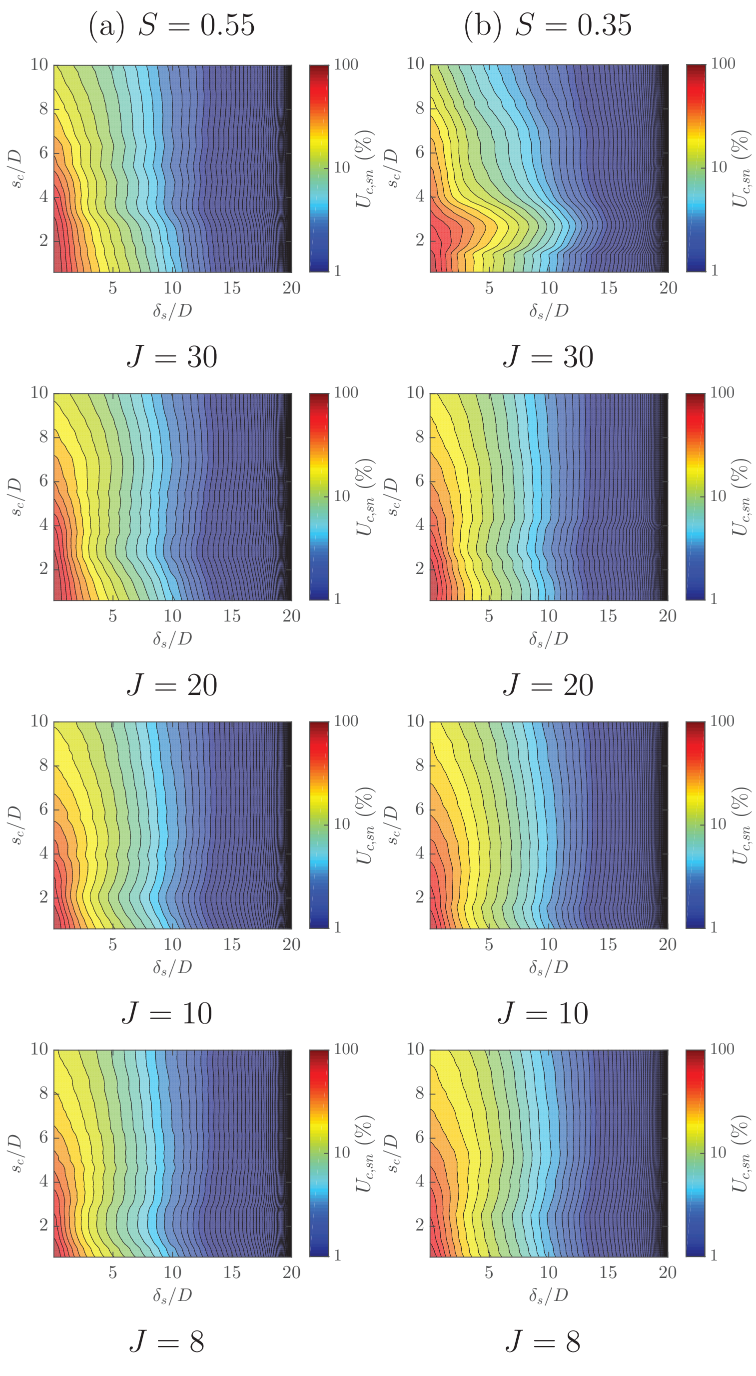

Figure A.8: Contour maps of the mean centerplane-based Unmixedness $U_{c,sn}$ evaluated in the transformed plane (s_c/D–n/D) as a function of various length scales normalized by the jet diameter δ_s/D (x axis) and jet centerline trajectory coordinate s_c/D (y axis) for the (a) $S = 0.55$ and (b) $S = 0.35$, flush nozzle-injected JICF at $J = 30$ (top row), 20 (second row), 10 (third row), and 8 (bottom row). Mean concentration values in each interrogation area are not matched to the reference value here.

APPENDIX B

Sine Wave Forcing Data

The following results correspond to data associated with the study of sine wave forcing of the JICF in Chapter 5.

B.1 Temporal Velocity Variation for Sine Wave Forcing

This section shows temporal jet velocity variations at the jet exit with all sinusoidal forcing conditions explored in this study, which were not shown in Chapter 5.

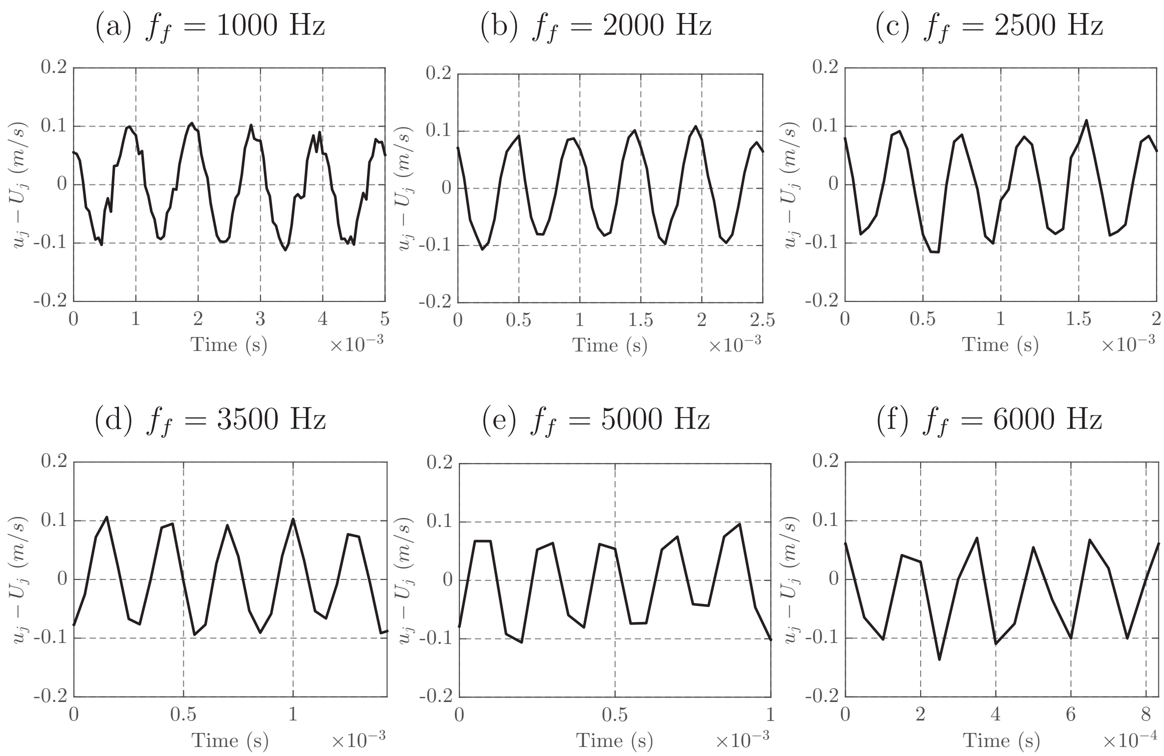

Figure B.1: Temporal mean-subtracted jet vertical velocity profiles $u_j - U_j$ (m/s) without/with sine wave forcing measured via hotwire anemometry $0.2D$ above the jet exit plane at $J = 41$ ($U'_{j,rms} = 0.07$ m/s). Note that velocity RMS of the unforced cases is approximately $U'_{j,rms} \approx 0.02 - 0.03$ m/s at $J = 41$.

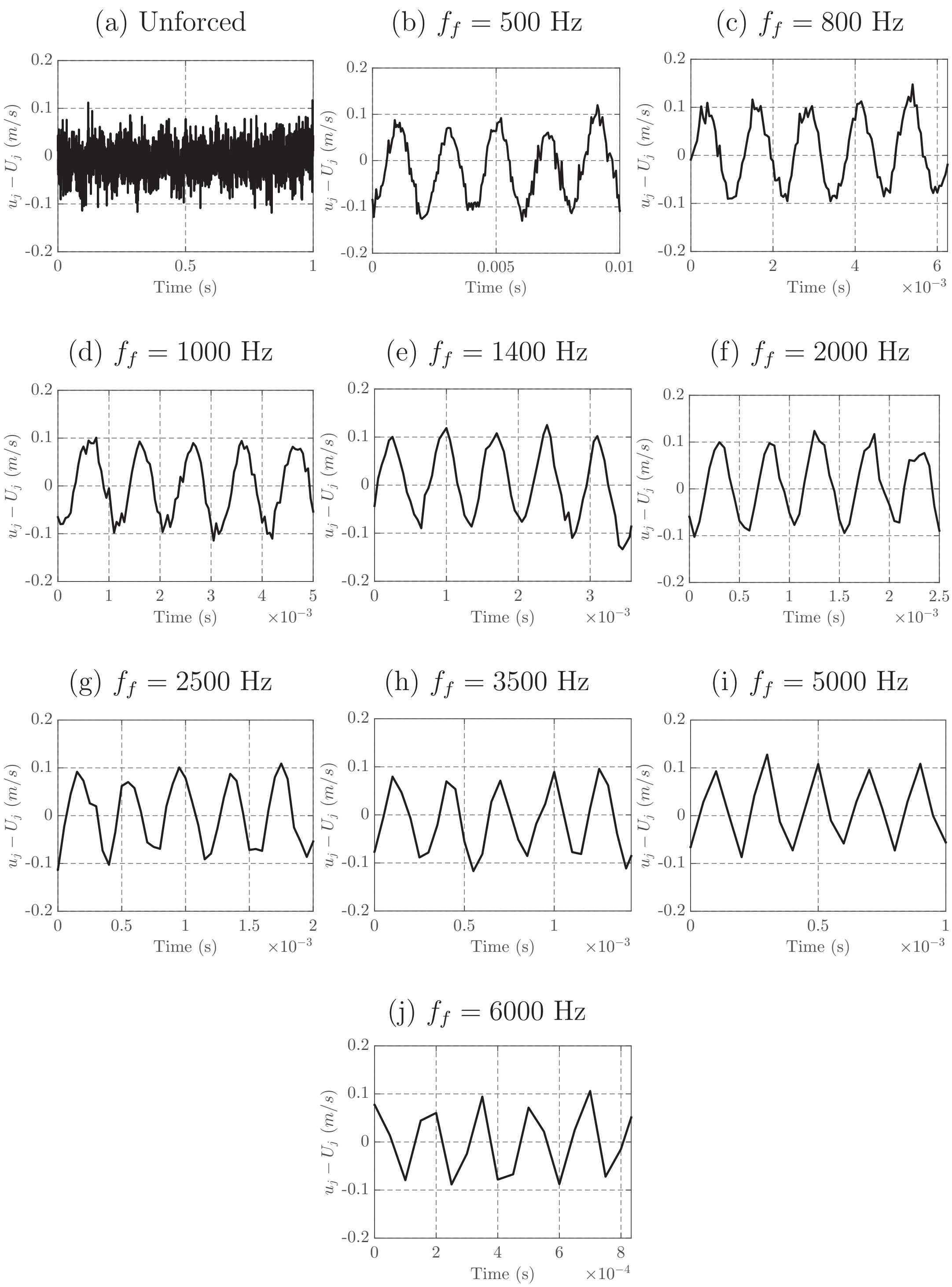

Figure B.2: Temporal mean-subtracted jet vertical velocity profiles $u_j - U_j$ (m/s) without/with sine wave forcing measured via hotwire anemometry $0.2D$ above the jet exit plane at $J = 12$ ($U'_{j,rms} = 0.07$ m/s). Note that velocity RMS of the unforced cases is approximately $U'_{j,rms} \approx 0.03$ m/s at $J = 12$.

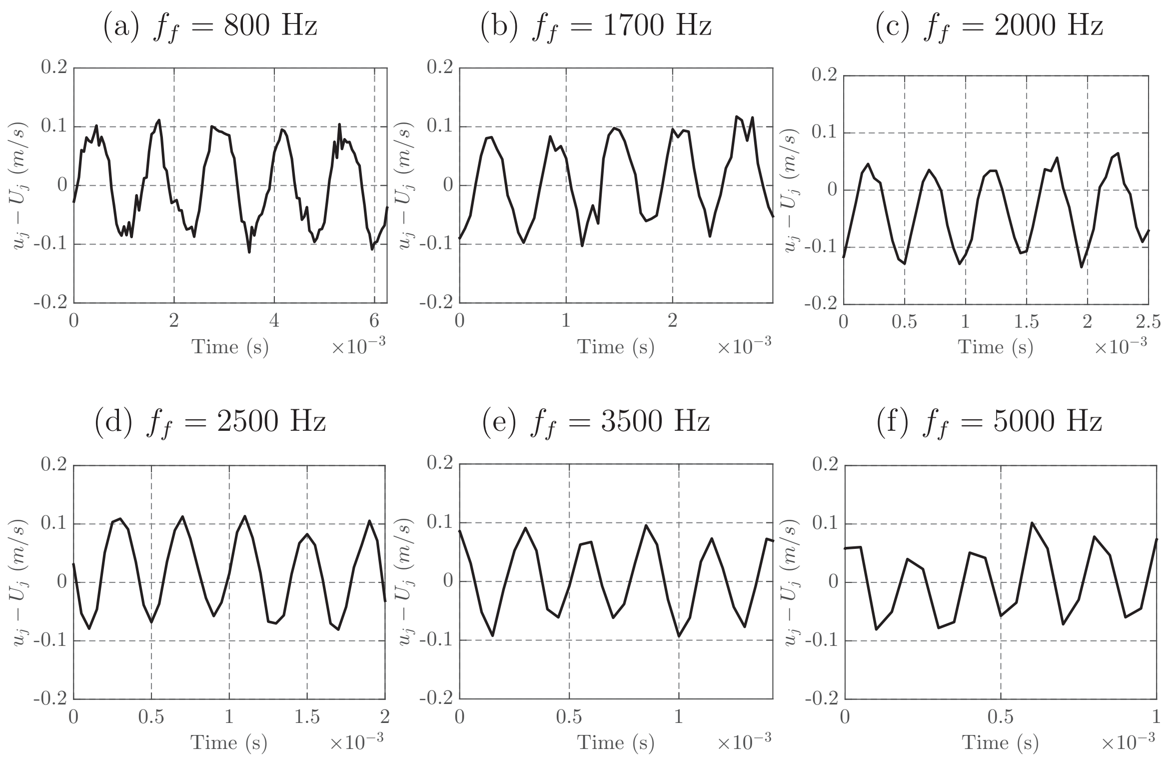

Figure B.3: Temporal mean-subtracted jet vertical velocity profiles $u_j - U_j$ (m/s) without/with sine wave forcing measured via hotwire anemometry $0.2D$ above the jet exit plane at $J = 5$ ($U'_{j,rms} = 0.07$ m/s). Note that velocity RMS of the unforced cases is approximately $U'_{j,rms} \approx 0.03 - 0.04$ m/s at $J = 5$.

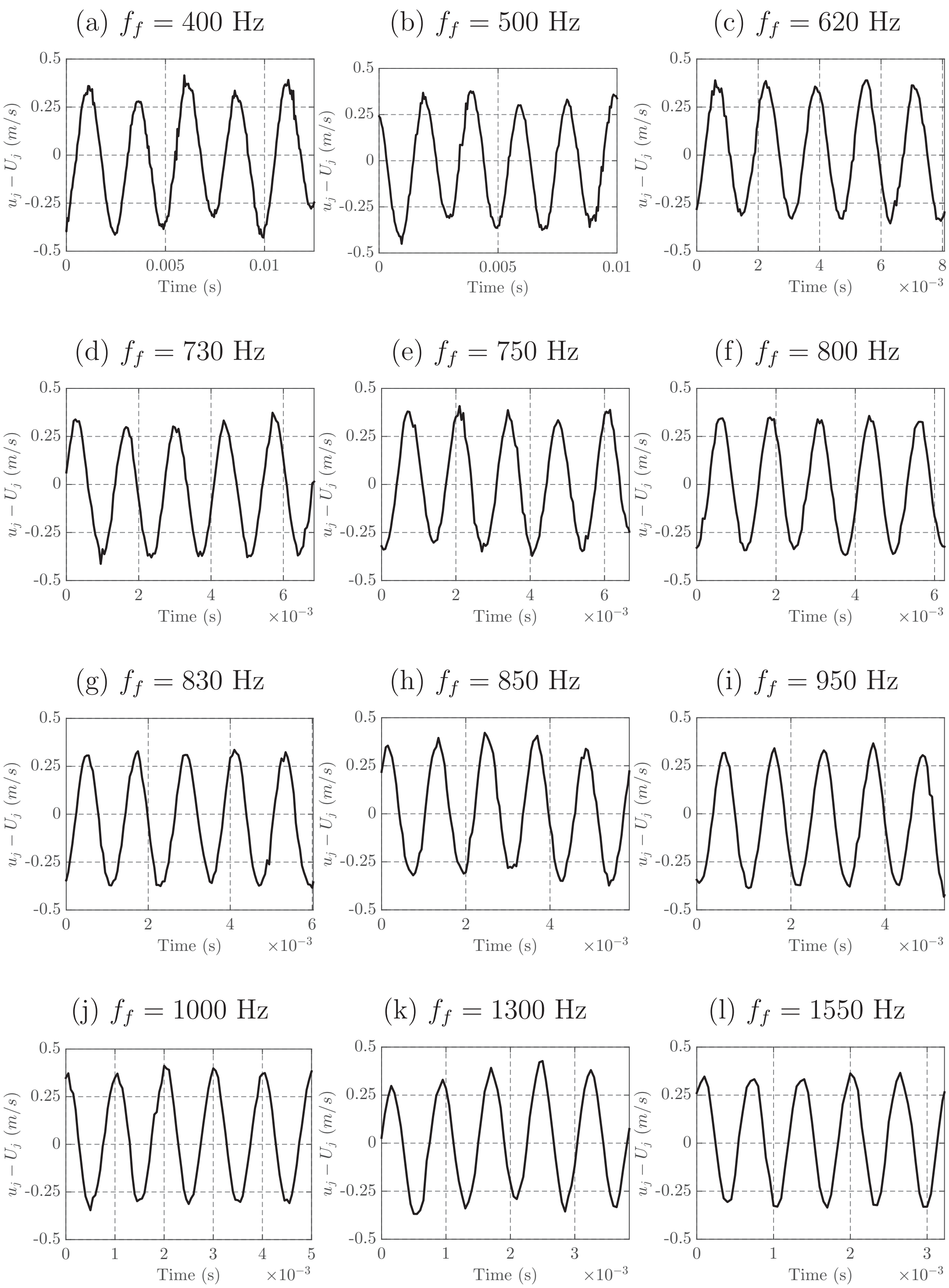

Figure B.4: Temporal mean-subtracted jet vertical velocity profiles $u_j - U_j$ (m/s) without/with sine wave forcing measured via hotwire anemometry $0.2D$ above the jet exit plane at $J = 5$ ($U'_{j,rms} = 0.22$ m/s). Note that velocity RMS of the unforced cases is approximately $U'_{j,rms} \approx 0.03 - 0.04$ m/s at $J = 5$.

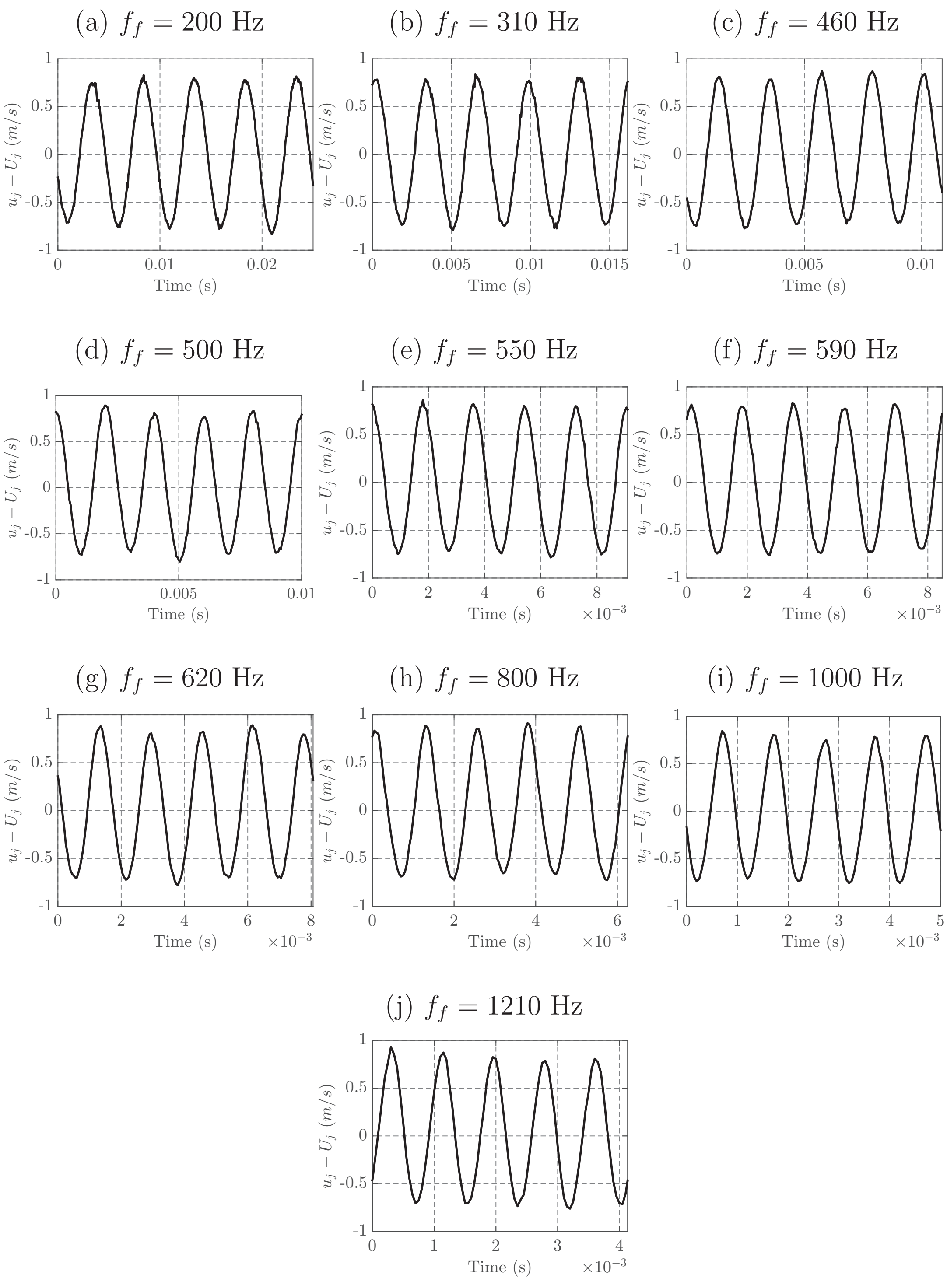

Figure B.5: Temporal mean-subtracted jet vertical velocity profiles $u_j - U_j$ (m/s) without/with sine wave forcing measured via hotwire anemometry $0.2D$ above the jet exit plane at $J = 5$ ($U'_{j,rms} = 0.55$ m/s). Note that velocity RMS of the unforced cases is approximately $U'_{j,rms} \approx 0.03 - 0.04$ m/s at $J = 5$.

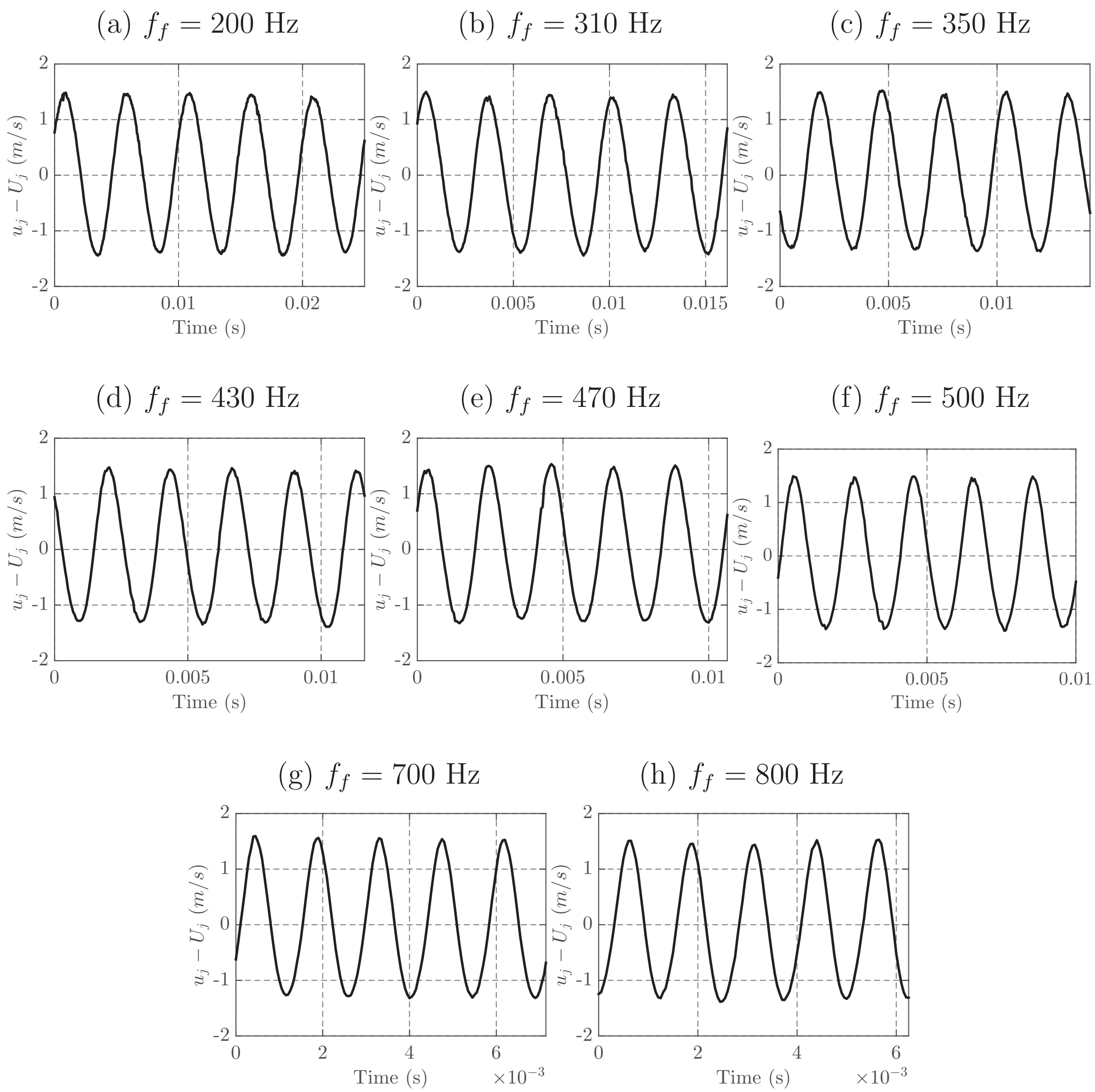

Figure B.6: Temporal mean-subtracted jet vertical velocity profiles $u_j - U_j$ (m/s) without/with sine wave forcing measured via hotwire anemometry $0.2D$ above the jet exit plane at $J = 5$ ($U'_{j,rms} = 1.00$ m/s). Note that velocity RMS of the unforced cases is approximately $U'_{j,rms} \approx 0.03 - 0.04$ m/s at $J = 5$.

B.2 Instantaneous and Mean Centerplane PLIF Images

This section represents instantaneous and mean centerplane PLIF images with sinusoidal forcing of the jet, which were not shown in Chapter 5. All mean images shown here are created by averaging 500 instantaneous images.

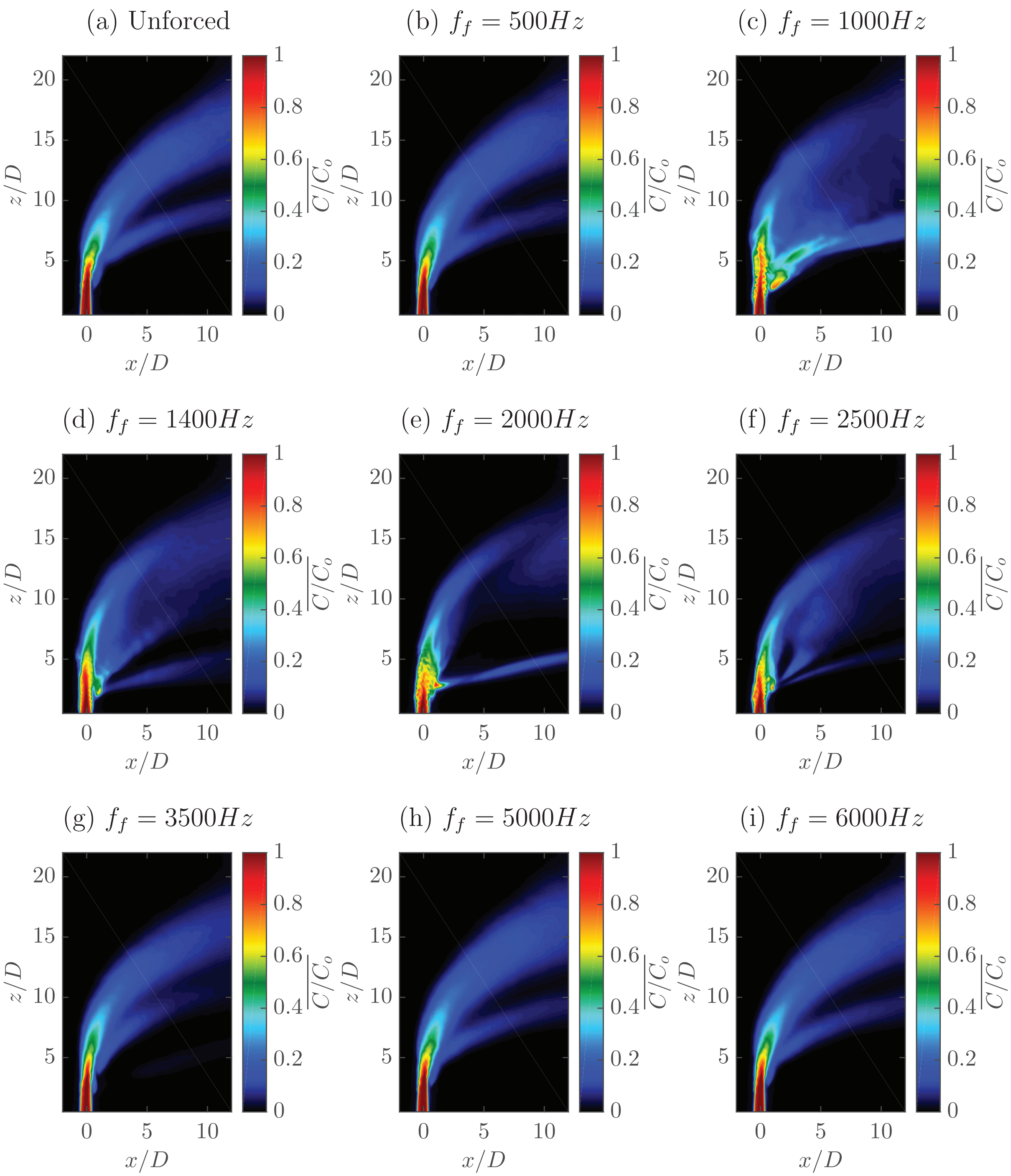

Figure B.7: Mean centerplane acetone concentration images in the regular plane ($x/D - z/D$) for the equidensity flush nozzle-injected JICF at $J = 41$ for (a) the unforced case (where $f_o = 1600 - 1900$ Hz) as well as (b)-(i) the forced cases under sine wave forcing at $f_f = 500 - 6000$ Hz and $U'_{j,rms} = 0.07$ m/s (approximately 1 % of U_j).

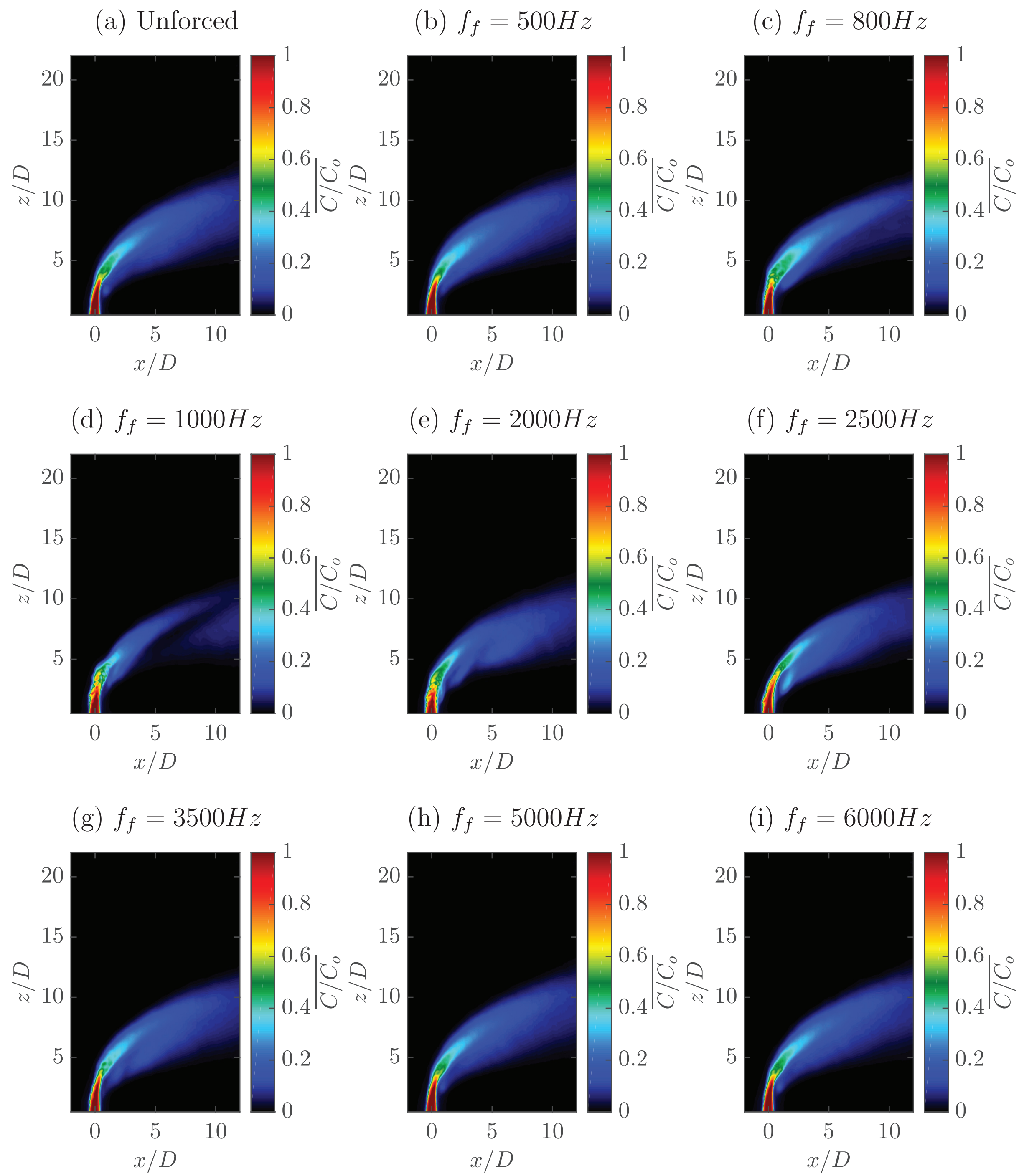

Figure B.8: Mean centerplane acetone concentration images in the regular plane ($x/D - z/D$) for the equidensity flush nozzle-injected JICF at $J = 12$ for (a) the unforced case (where $f_o = 1900 - 2230$ Hz) as well as (b)-(i) the forced cases under sine wave forcing at $f_f = 500 - 6000$ Hz and $U'_{j,rms} = 0.07$ m/s (approximately 1 % of U_j).

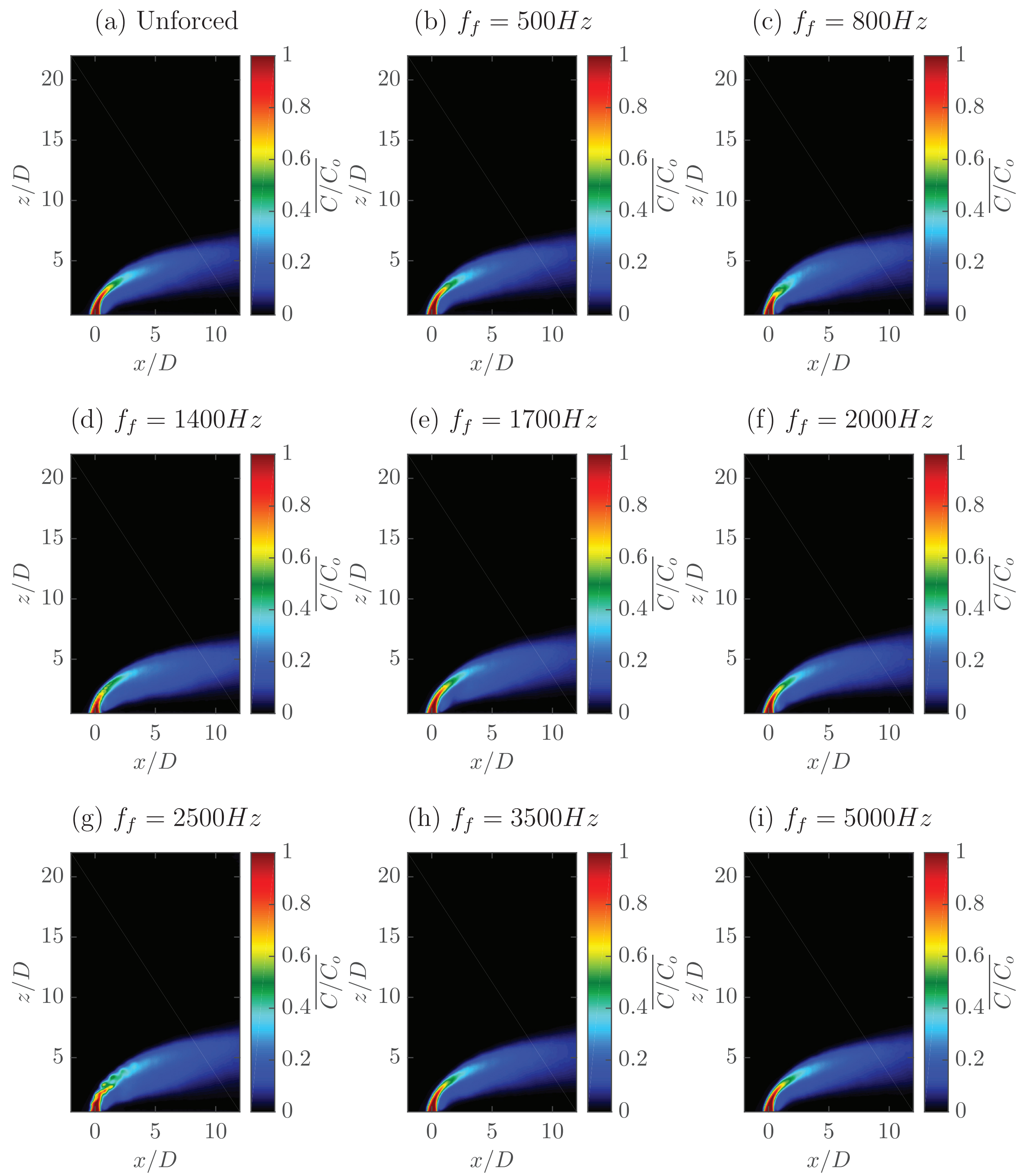

Figure B.9: Mean centerplane acetone concentration images in the regular plane ($x/D - z/D$) for the equidensity flush nozzle-injected JICF at $J = 5$ for (a) the unforced case (where $f_o = 2000$ Hz) as well as (b)-(i) the forced cases under sine wave forcing at $f_f = 500 - 5000$ Hz and $U'_{j,rms} = 0.07$ m/s (approximately 1 % of U_j). Note that the upstream shear layer without forcing is locked-in for $f_f \approx 1250 - 3500$ Hz.

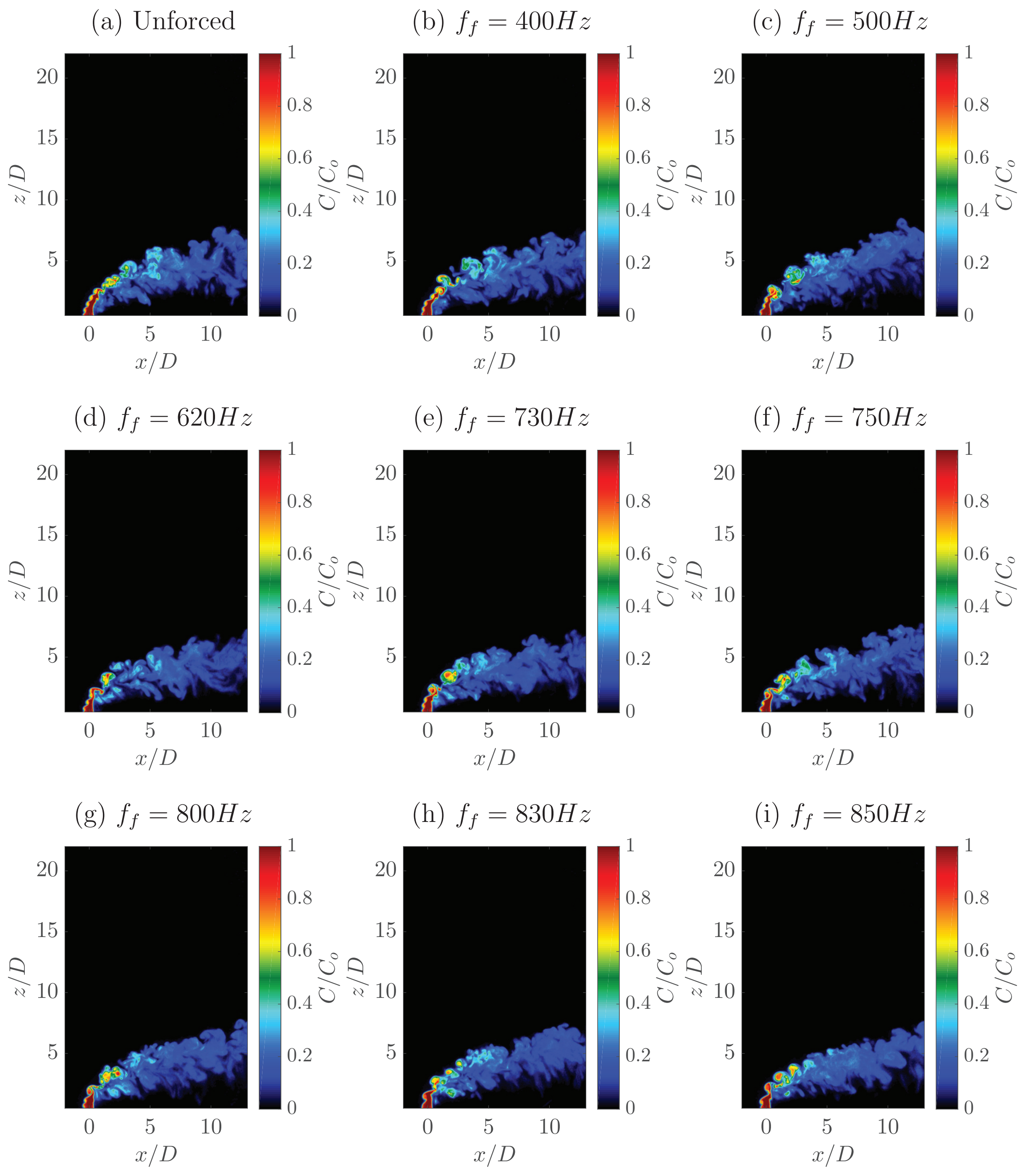

Figure B.10: For more figures and caption see next page.

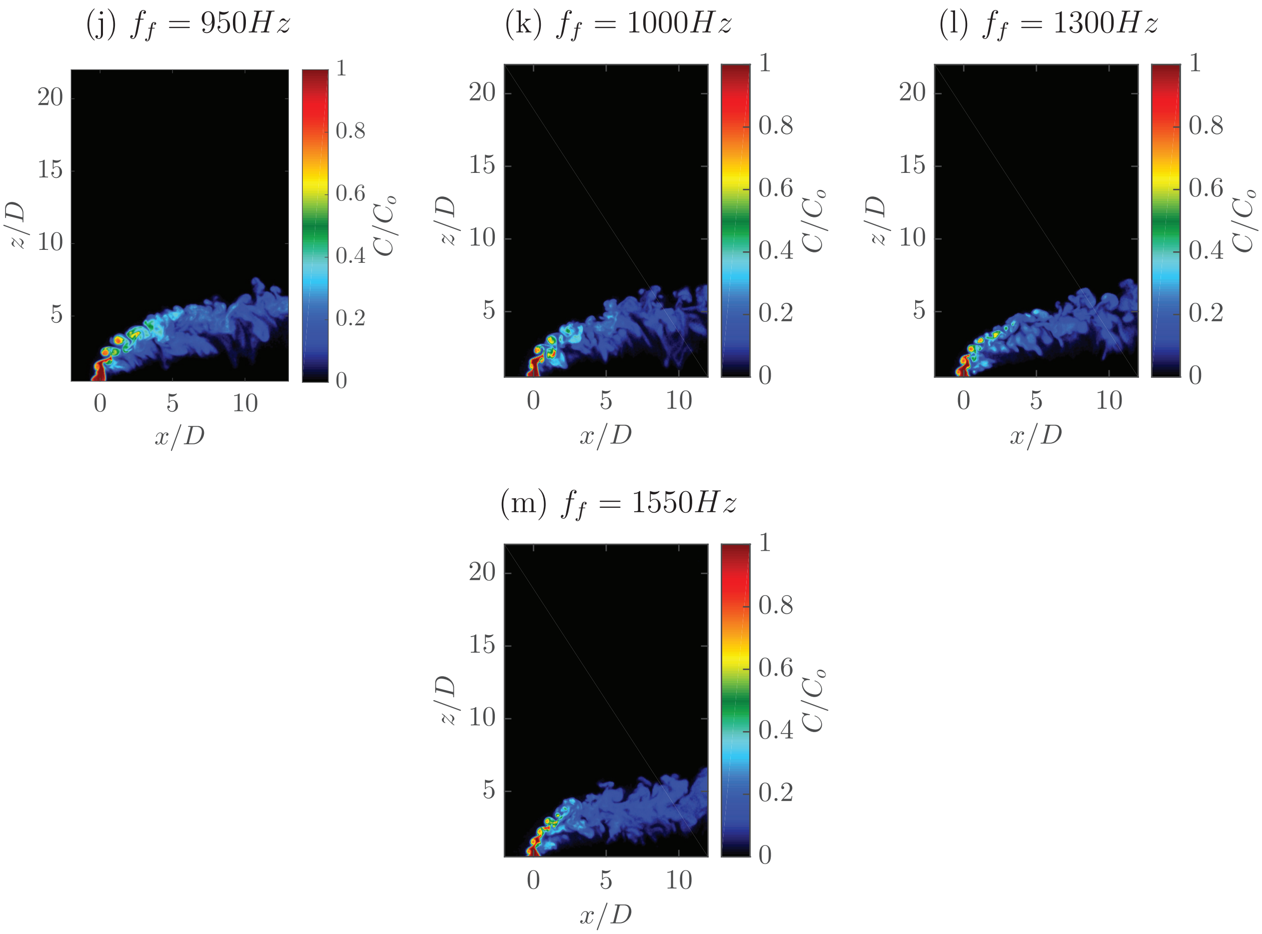

Figure B.10: Instantaneous centerplane acetone concentration images in the regular plane ($x/D - z/D$) for the equidensity flush nozzle-injected JICF at $J = 5$ for (a) the unforced case (where $f_o = 2000$ Hz) as well as (b)-(m) the forced cases under sine wave forcing at $f_f = 400 - 1550$ Hz and $U'_{j,rms} = 0.22$ m/s (approximately 3 % of U_j). Note that the upstream shear layer without forcing is locked-in above around $f_f \approx 820$ Hz.

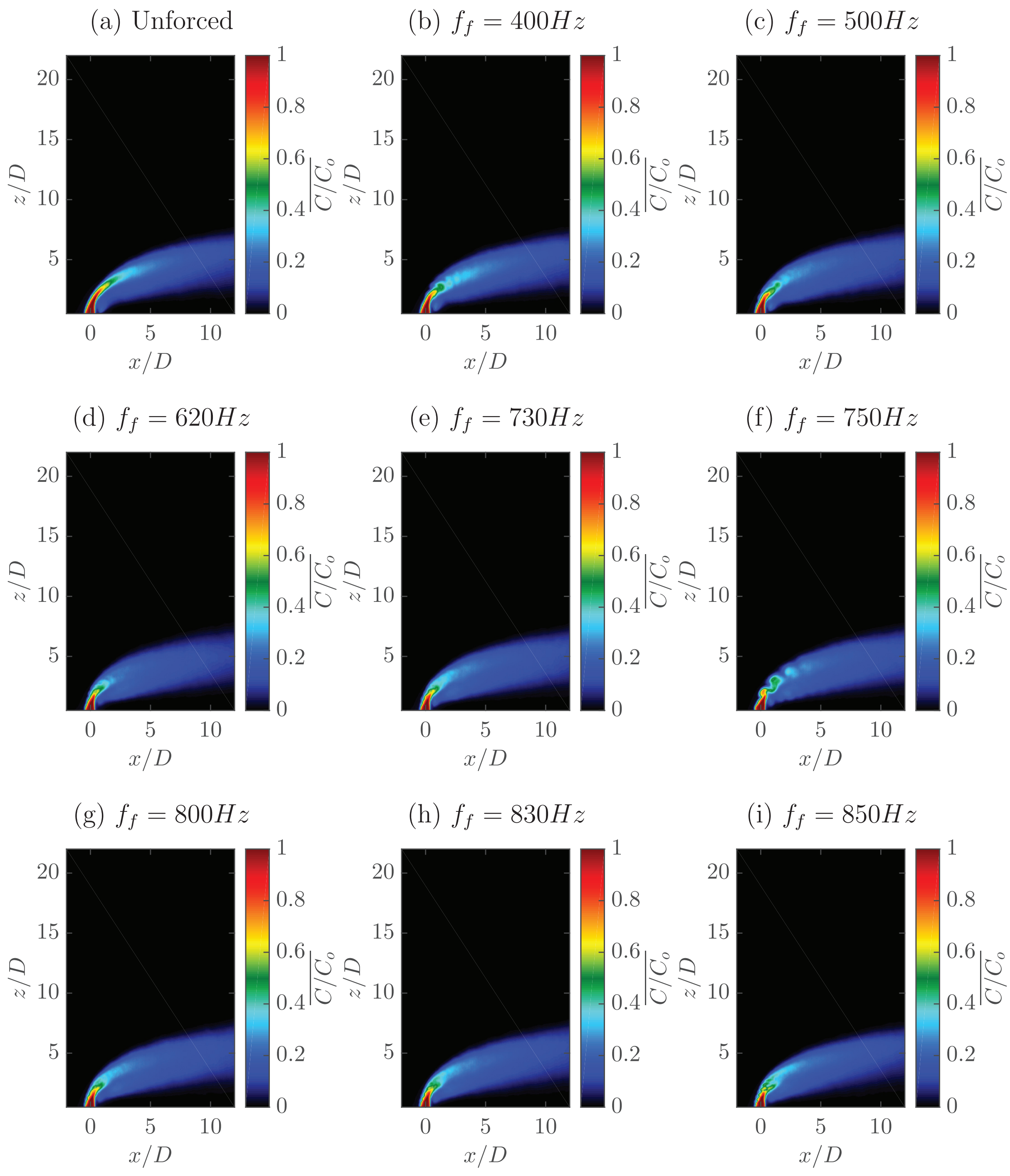

Figure B.11: For more figures and caption see next page.

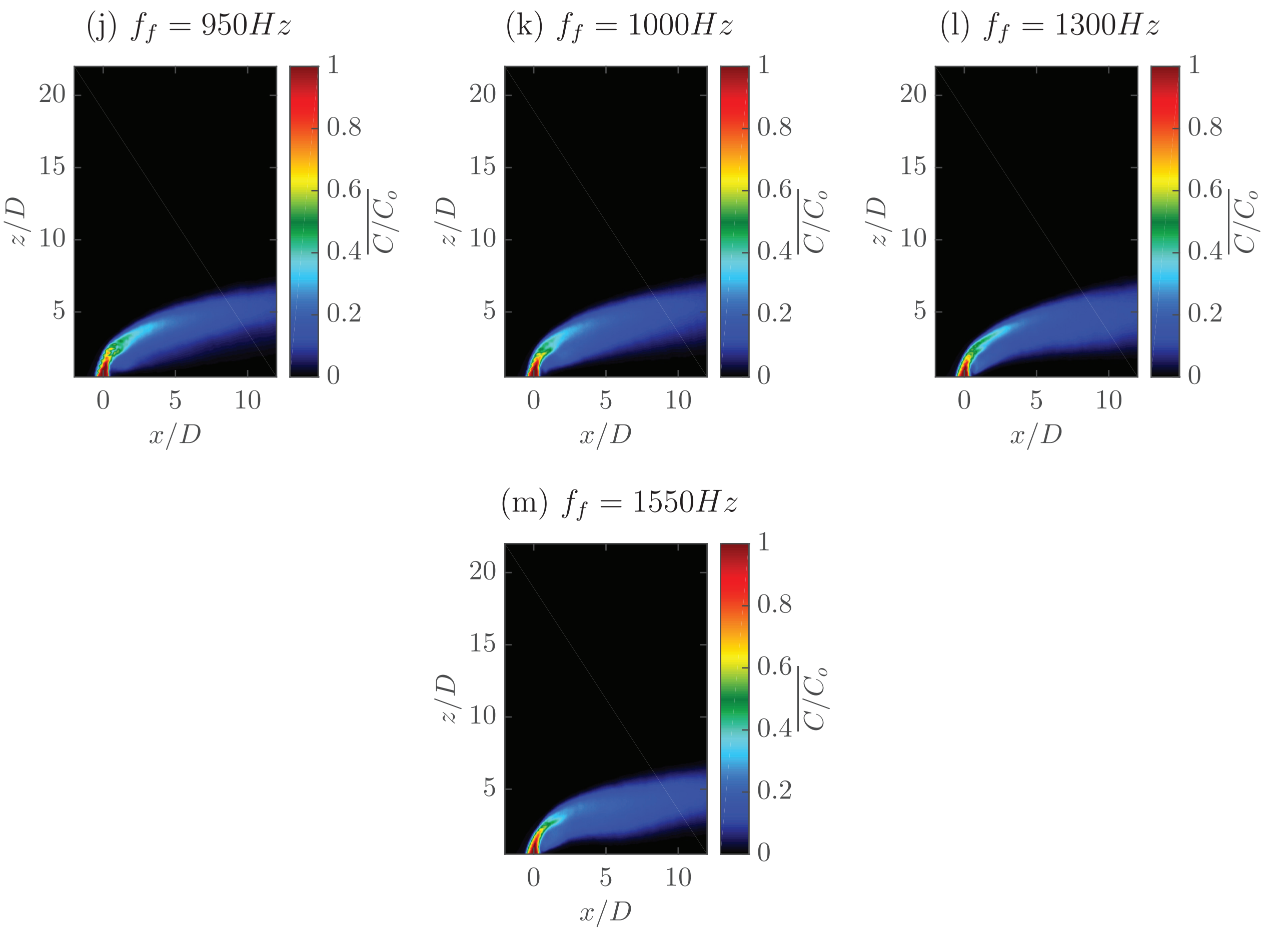

Figure B.11: Mean centerplane acetone concentration images in the regular plane ($x/D - z/D$) for the equidensity flush nozzle-injected JICF at $J = 5$ for (a) the unforced case (where $f_o = 2000$ Hz) as well as (b)-(m) the forced cases under sine wave forcing at $f_f = 400 - 1550$ Hz and $U'_{j,rms} = 0.22$ m/s (approximately 3 % of U_j). Note that the upstream shear layer without forcing is locked-in above around $f_f \approx 820$ Hz.

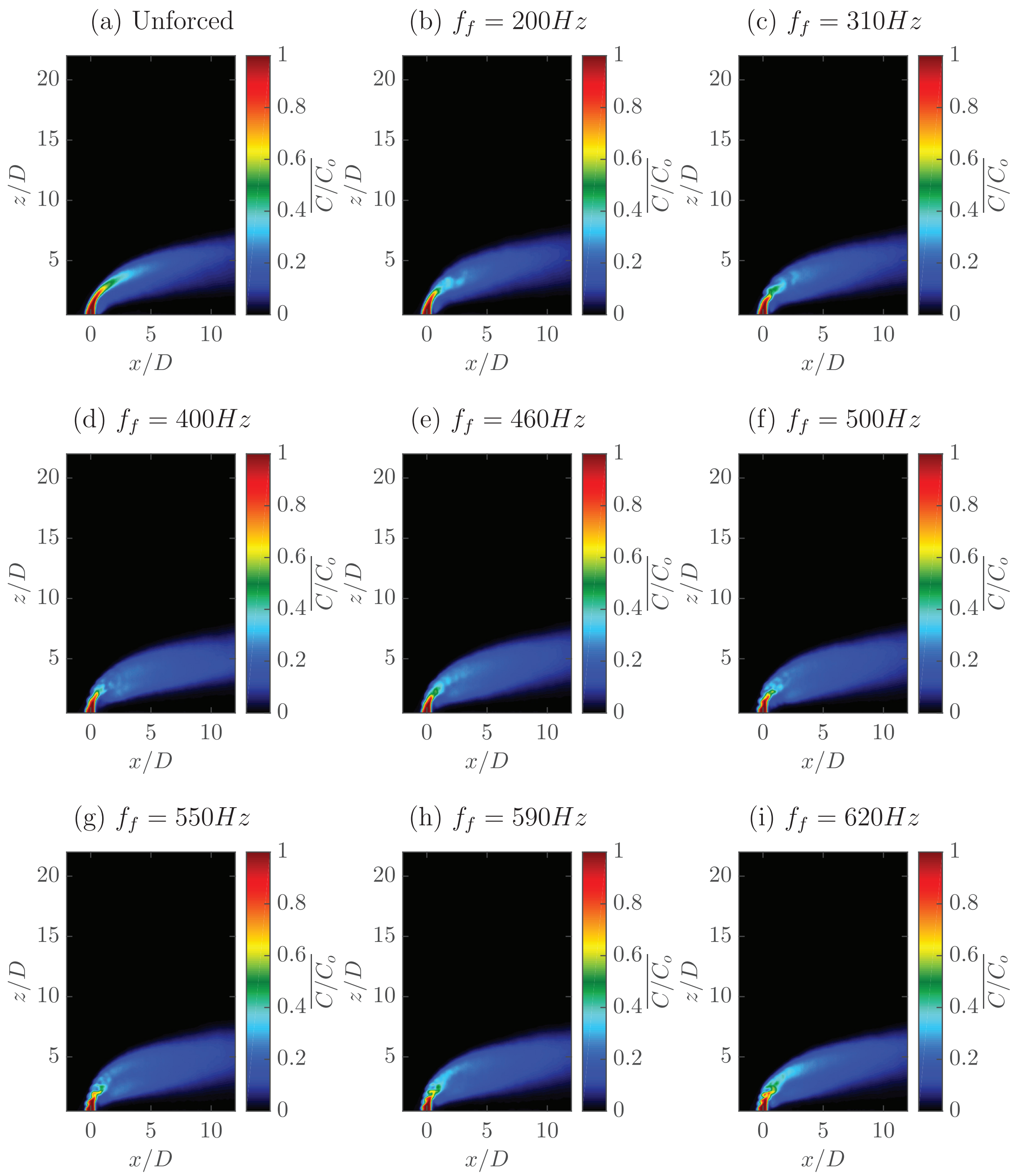

Figure B.12: For more figures and caption see next page.

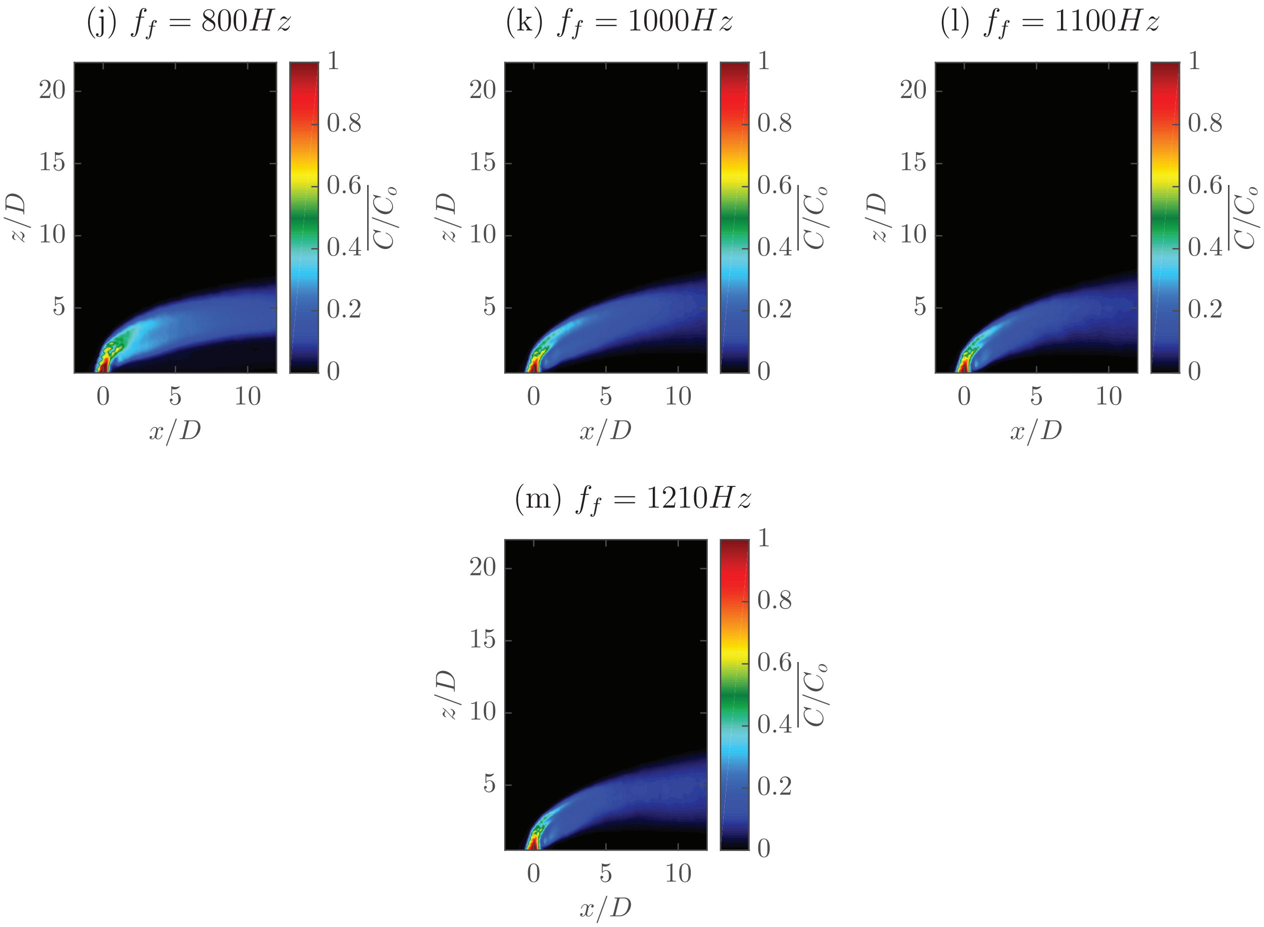

Figure B.12: Mean centerplane acetone concentration images in the regular plane ($x/D - z/D$) for the equidensity flush nozzle-injected JICF at $J = 5$ for (a) the unforced case (where $f_o = 2000$ Hz) as well as (b)-(m) the forced cases under sine wave forcing at $f_f = 200 - 1210$ Hz and $U'_{j,rms} = 0.55$ m/s (approximately 9 % of U_j). Note that the upstream shear layer without forcing is locked-in above around $f_f \approx 590$ Hz.

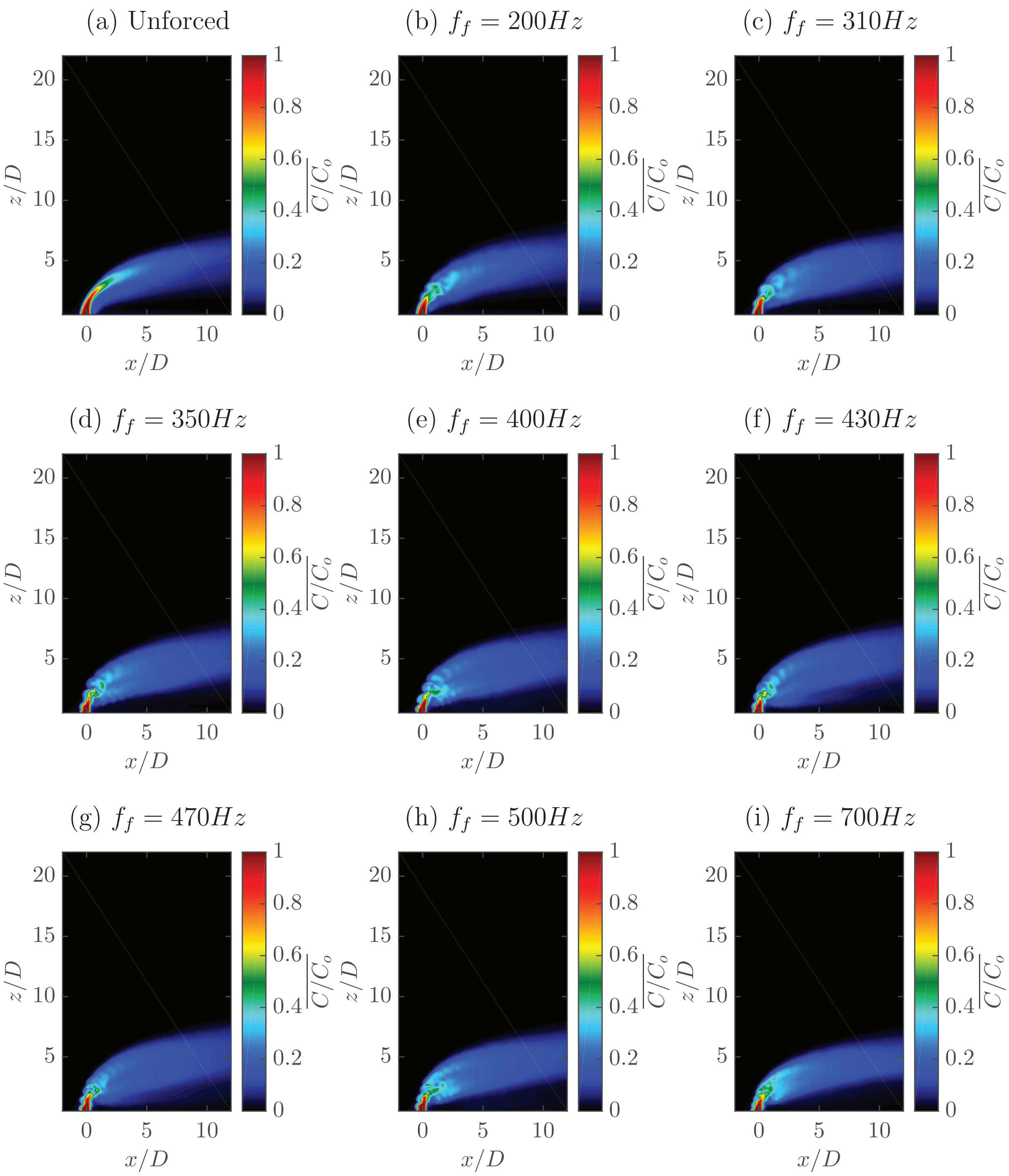

Figure B.13: For more figures and caption see next page.

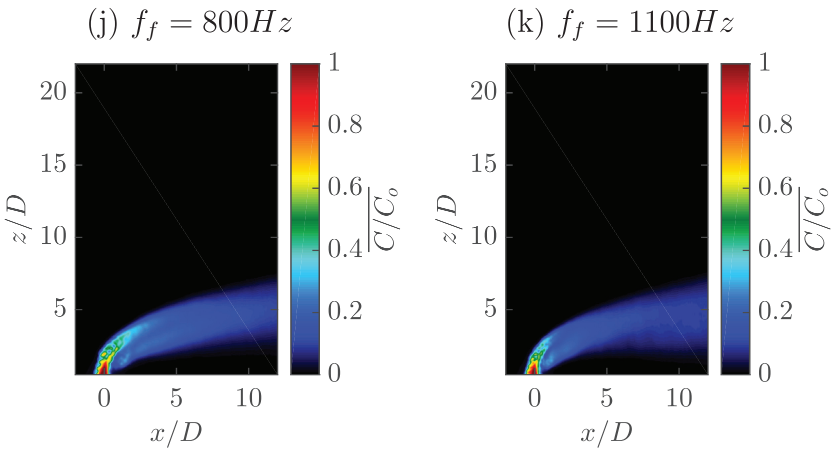

Figure B.13: Mean centerplane acetone concentration images in the regular plane ($x/D - z/D$) for the equidensity flush nozzle-injected JICF at $J = 5$ for (a) the unforced case (where $f_o = 2000$ Hz) as well as (b)-(k) the forced cases under sine wave forcing at $f_f = 200 - 1100$ Hz and $U'_{j,rms} = 1.00$ m/s (approximately 15 % of U_j). Note that the upstream shear layer without forcing is locked-in above around $f_f \approx 300$ Hz.

B.3 Mean Cross-Sectional PLIF Images

This section represents mean cross-sectional PLIF images with sinusoidal forcing of the jet, which were not shown in Chapter 5. All mean images shown here are created by averaging 500 instantaneous images.

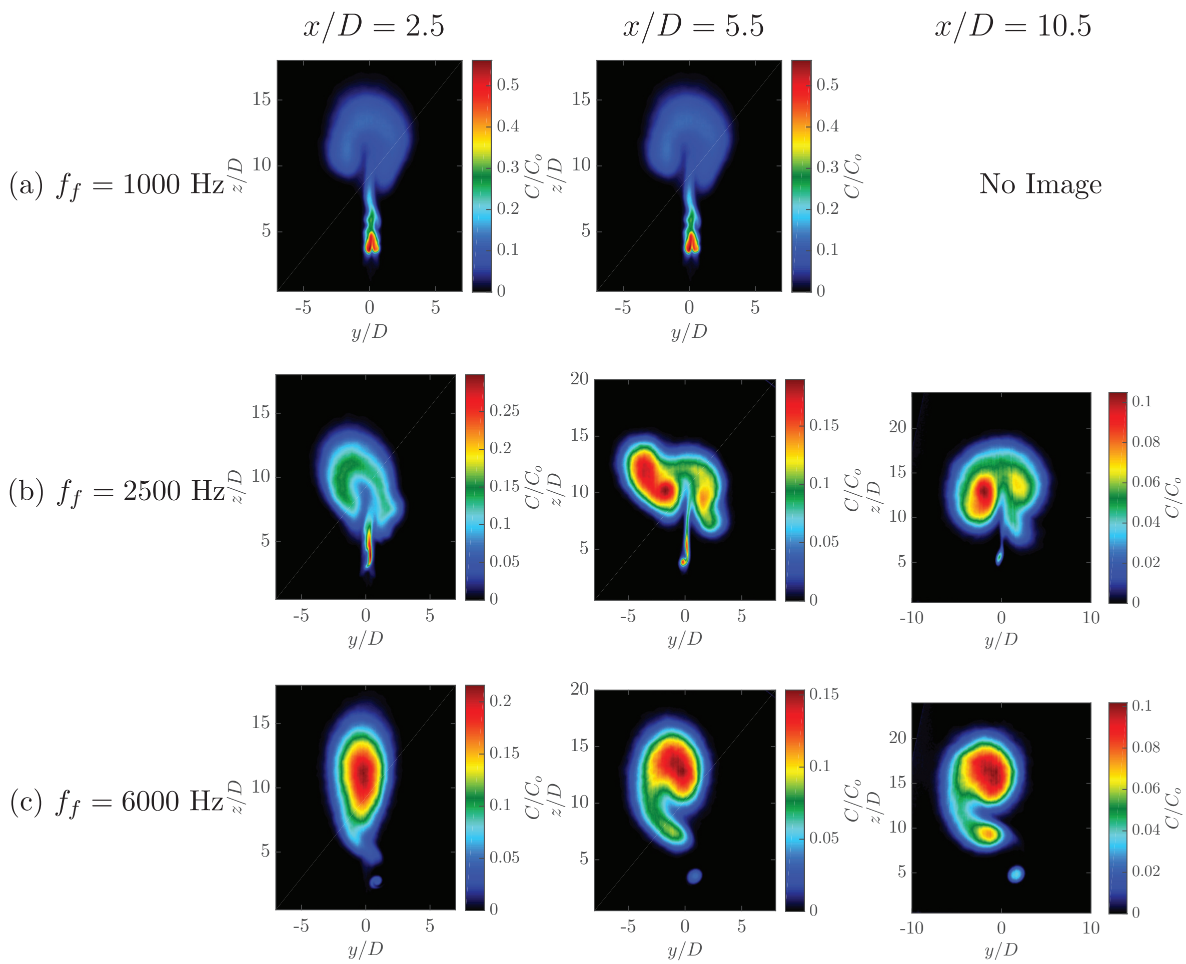

Figure B.14: Mean cross-sectional acetone concentration images in the $y/D - z/D$ plane for the equidensity flush nozzle-injected JICF at $J = 41$, with natural frequency $f_o = 2000$ Hz, for (a)-(c) the forced cases under sine wave forcing at $f_f = 1000 - 6000$ Hz and $U'_{j,rms} = 0.07$ m/s (approximately 1 % of U_j).

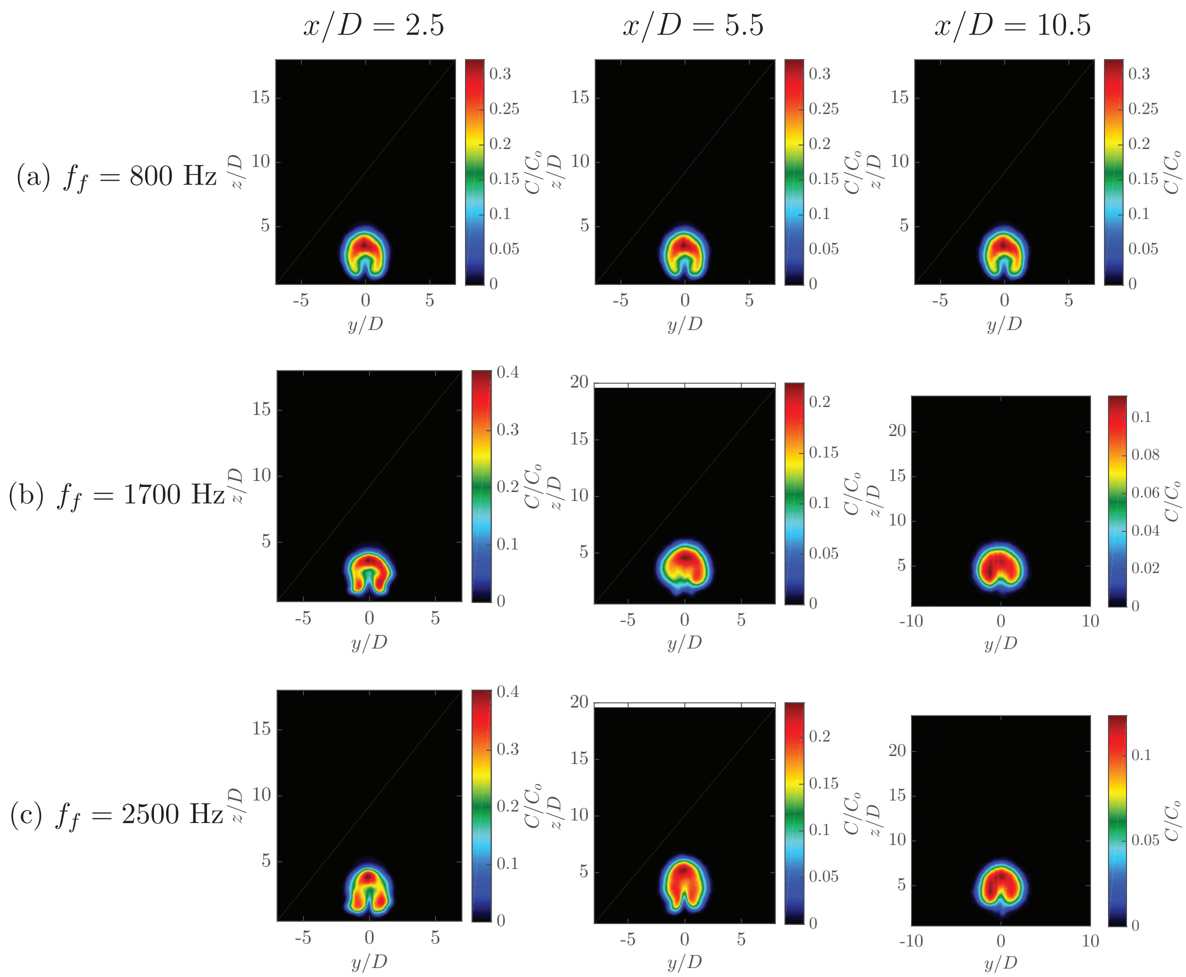

Figure B.15: Mean cross-sectional acetone concentration images in the $y/D - z/D$ plane for the equidensity flush nozzle-injected JICF at $J = 5$, with natural frequency $f_o = 2000$ Hz, for (a)-(c) the forced cases under sine wave forcing at $f_f = 800 - 2500$ Hz and $U'_{j,rms} = 0.07$ m/s (approximately 1 % of U_j). Note that the upstream shear layer without forcing is locked-in for $f_f \approx 1250 - 3500$ Hz.

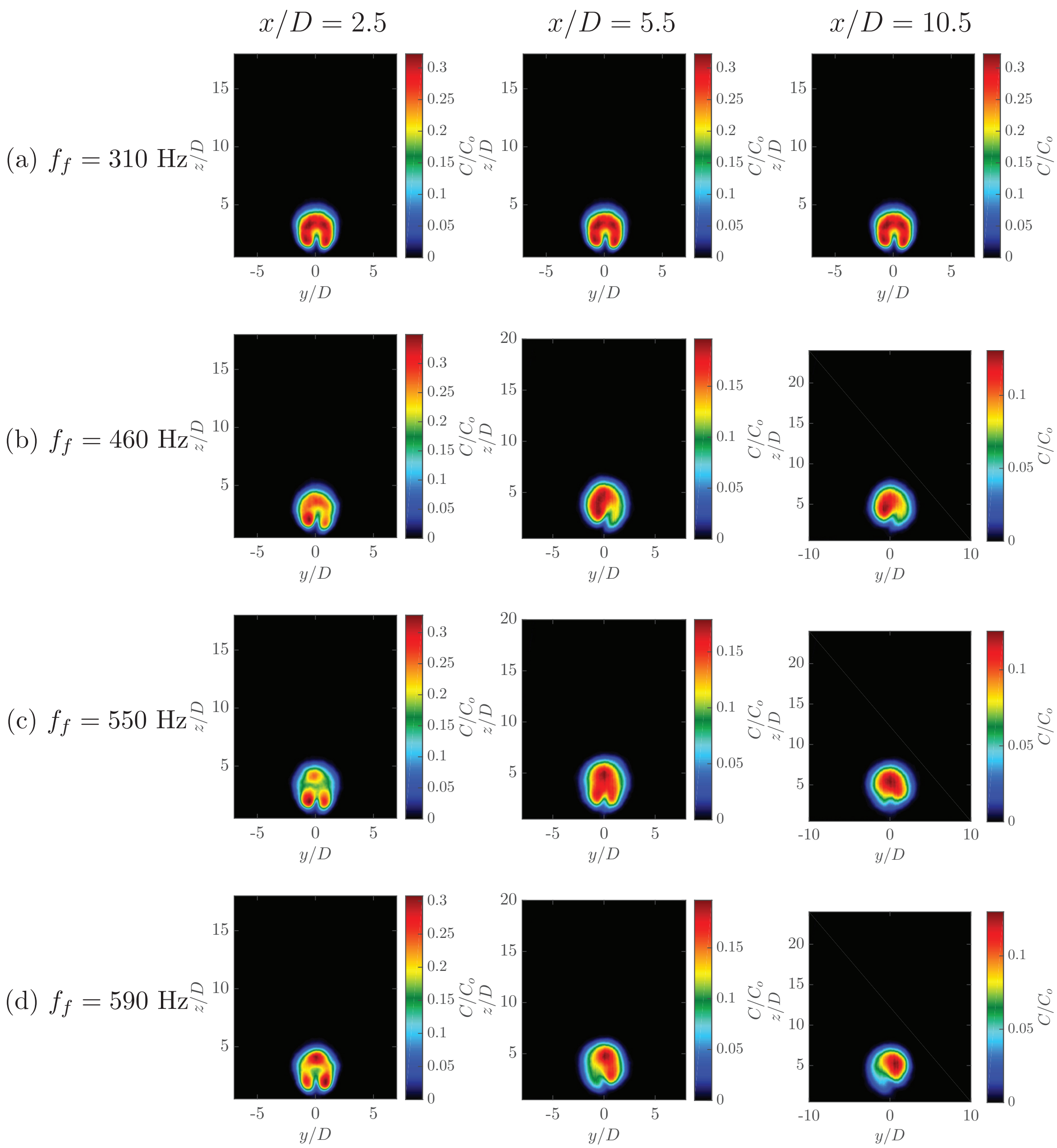

Figure B.16: For more figures and caption see next page.

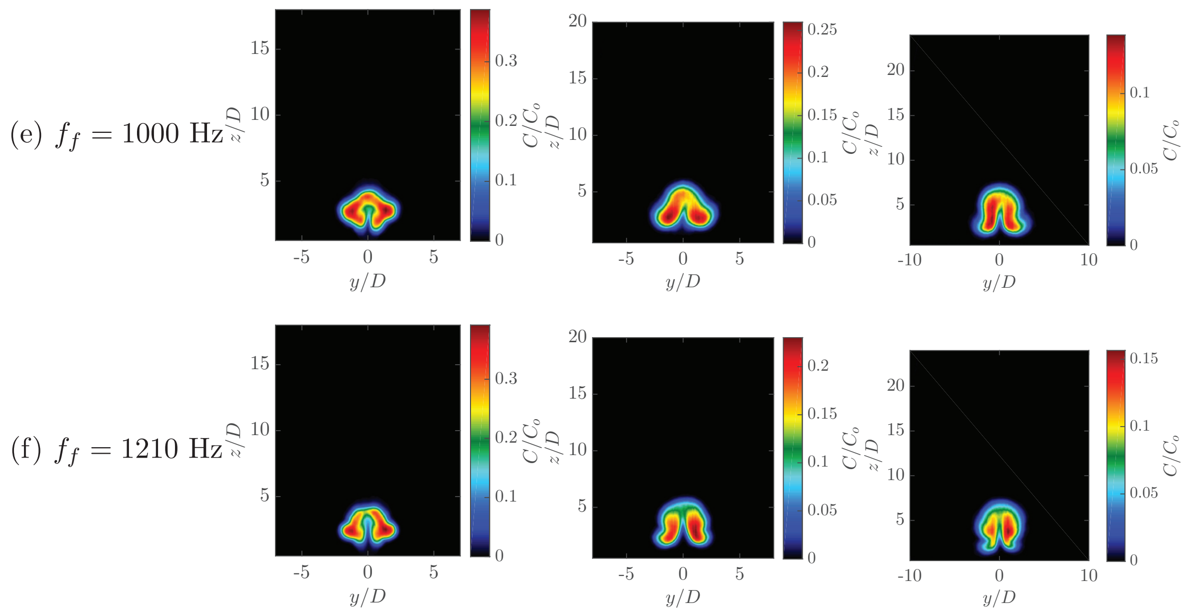

Figure B.16: Mean cross-sectional acetone concentration images in the $y/D - z/D$ plane for the equidensity flush nozzle-injected JICF at $J = 5$, with natural frequency $f_o = 2000$ Hz, for (a)-(f) the forced cases under sine wave forcing at $f_f = 310 - 1210$ Hz and $U'_{j,rms} = 0.55$ m/s (approximately 9 % of U_j). Note that the upstream shear layer without forcing is locked-in above around $f_f \approx 590$ Hz.

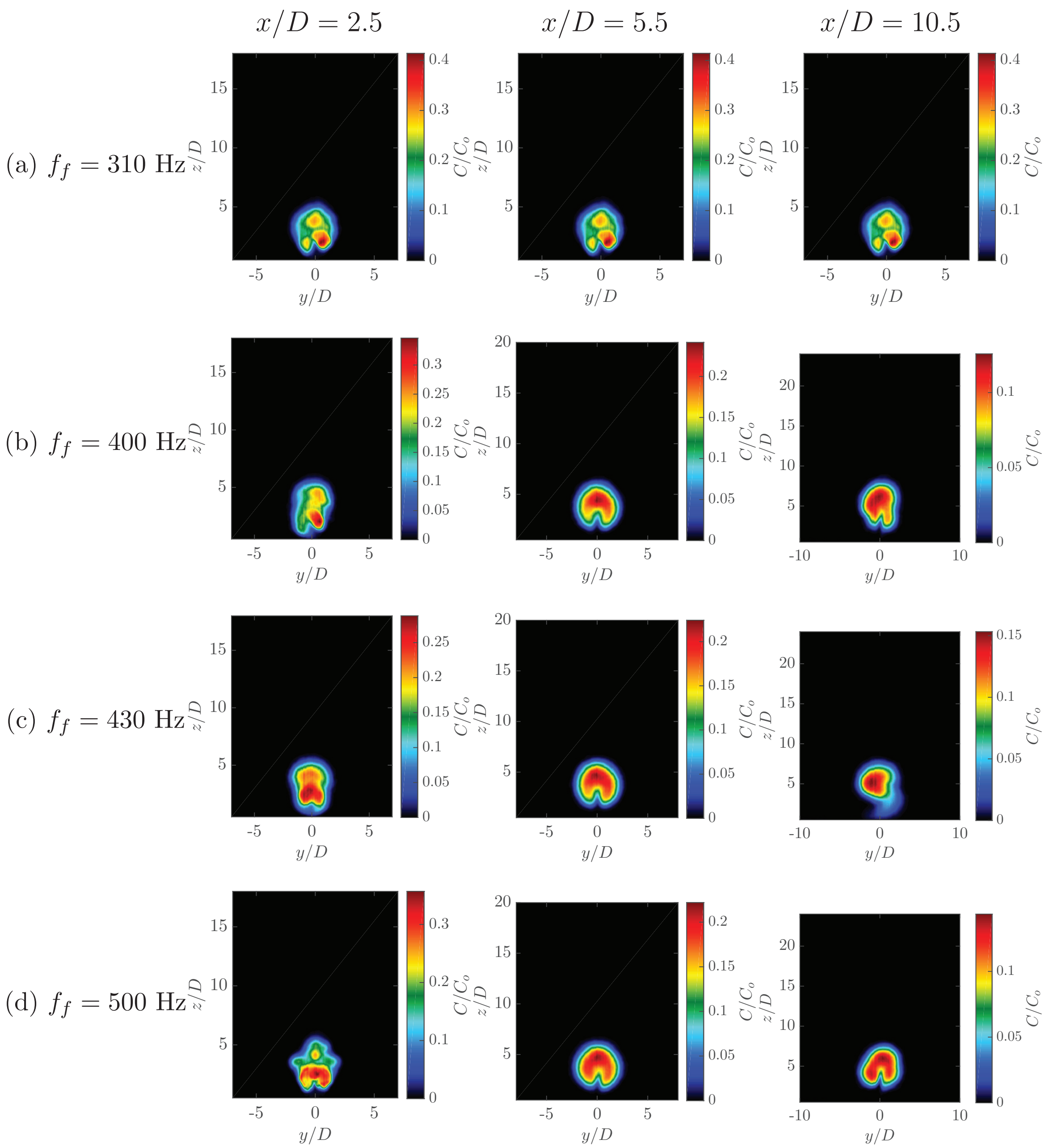

Figure B.17: For more figures and caption see next page.

(e) $f_f = 700$ Hz

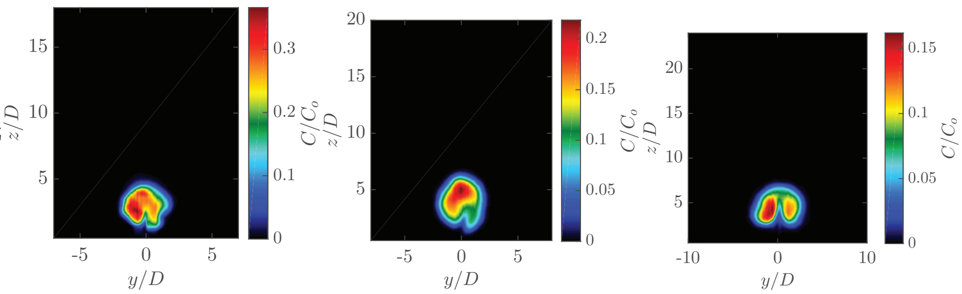

Figure B.17: Mean cross-sectional acetone concentration images in the $y/D - z/D$ plane for the equidensity flush nozzle-injected JICF at $J = 5$, with natural frequency $f_o = 2000$ Hz, for (a)-(e) the forced cases under sine wave forcing at $f_f = 310 - 700$ Hz and $U'_{j,rms} = 1.00$ m/s (approximately 15 % of U_j). Note that the upstream shear layer without forcing is locked-in above around $f_f \approx 300$ Hz.

B.4 Mixing Quantification for Forced JICF

This section represents the results of mixing quantification, which were not shown in Chapter 5.

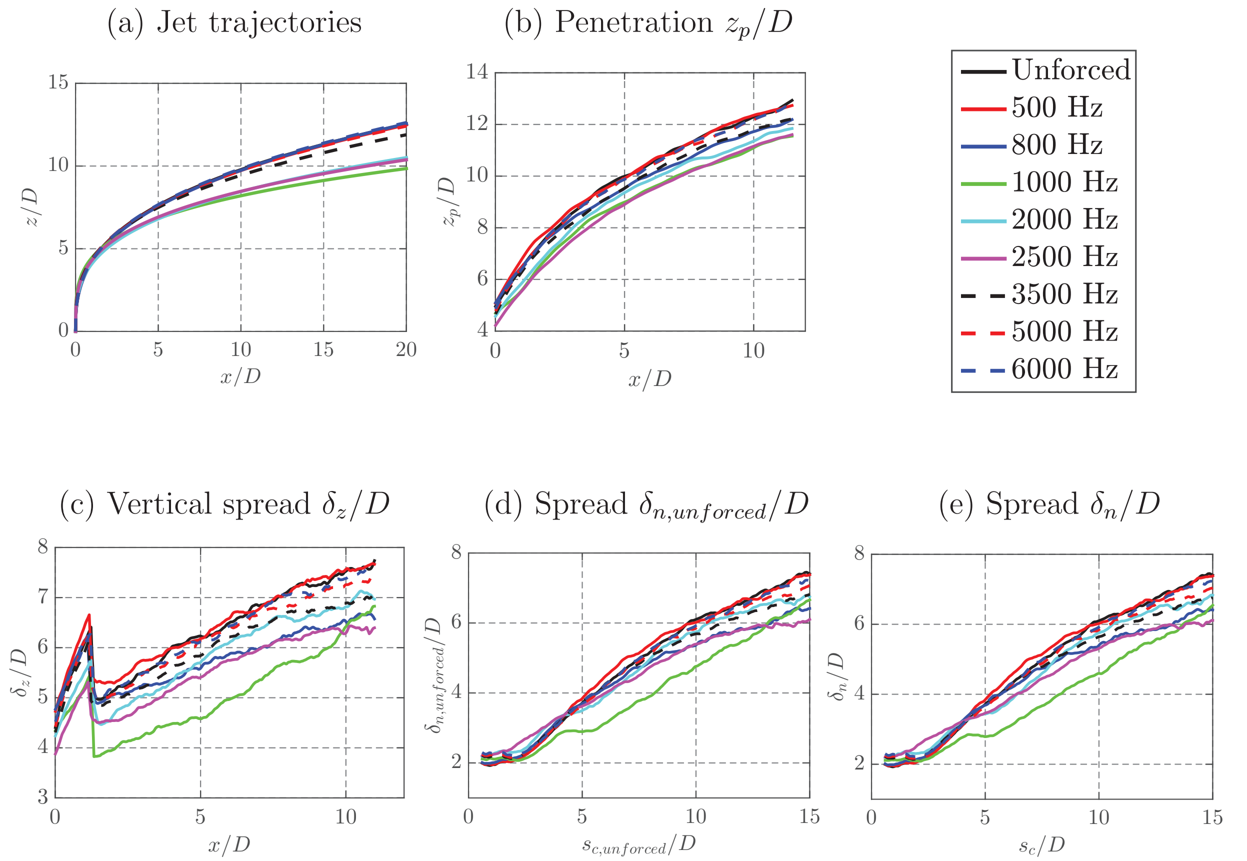

Figure B.18: Mean mixing metrics for the equidensity flush nozzle-injected JICF at $J = 12$ for the unforced case as well as the forced cases under sine wave forcing at $f_f = 500 - 5000$ Hz and $U'_{j,rms} = 0.07$ m/s (approximately 1 % of U_j): (a) Jet trajectories, (b) jet penetration z_p/D, (c) jet vertical spread δ_z/D, (d) jet spread normal to the unforced jet trajectory $\delta_{n,unforced}/D$ and (e) jet spread normal to each jet trajectory in question δ_n/D.

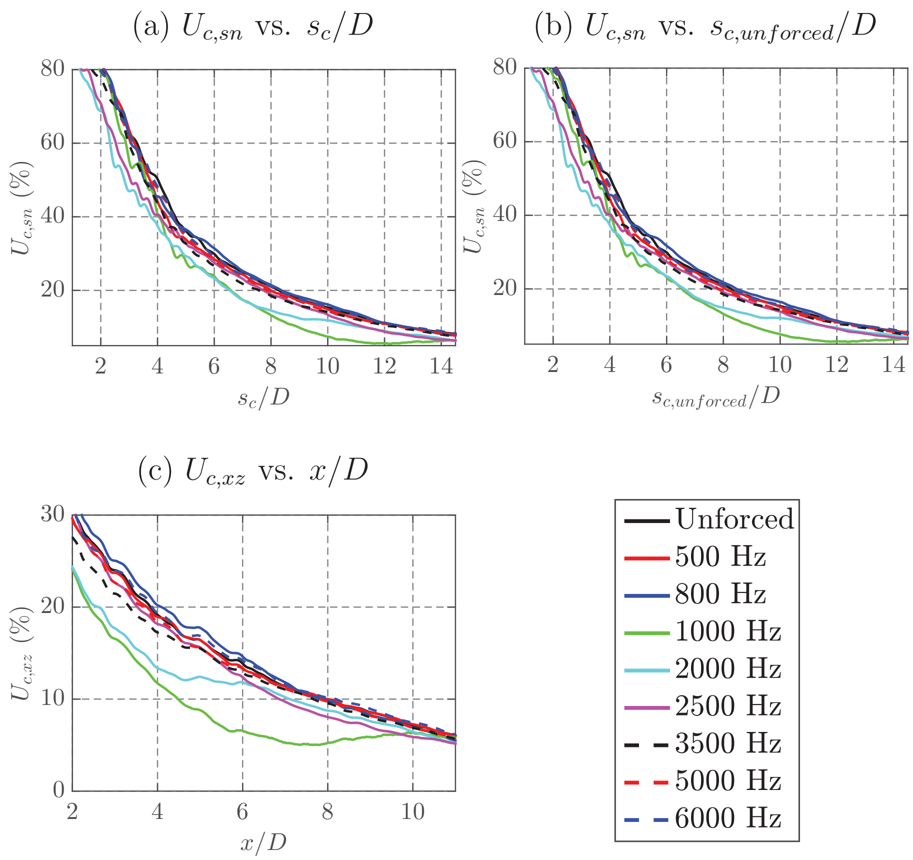

Figure B.19: Instantaneous mixing metrics evaluated for the equidensity flush nozzle-injected JICF at $J = 12$ for the unforced and forced cases under sine wave forcing at $f_f = 500 - 5000$ Hz and $U'_{j,rms} = 0.07$ m/s. Each figure represents (a) centerplane-based mean Unmixedness $U_{c,sn}$ along s_c/D, (b) $U_{c,sn}$ along $s_{c,unforced}/D$, (c) centerplane-based mean Unmixedness $U_{c,xz}$ along x/D, (d) cross-section-based mean Unmixedness U_{yz} along x/D, and (e)-(g) cross-section-based mean probability density function (PDF) of normalized concentration PDF(C/C_o) at $x/D = 2.5$, 5.5 and 10.5, respectively.

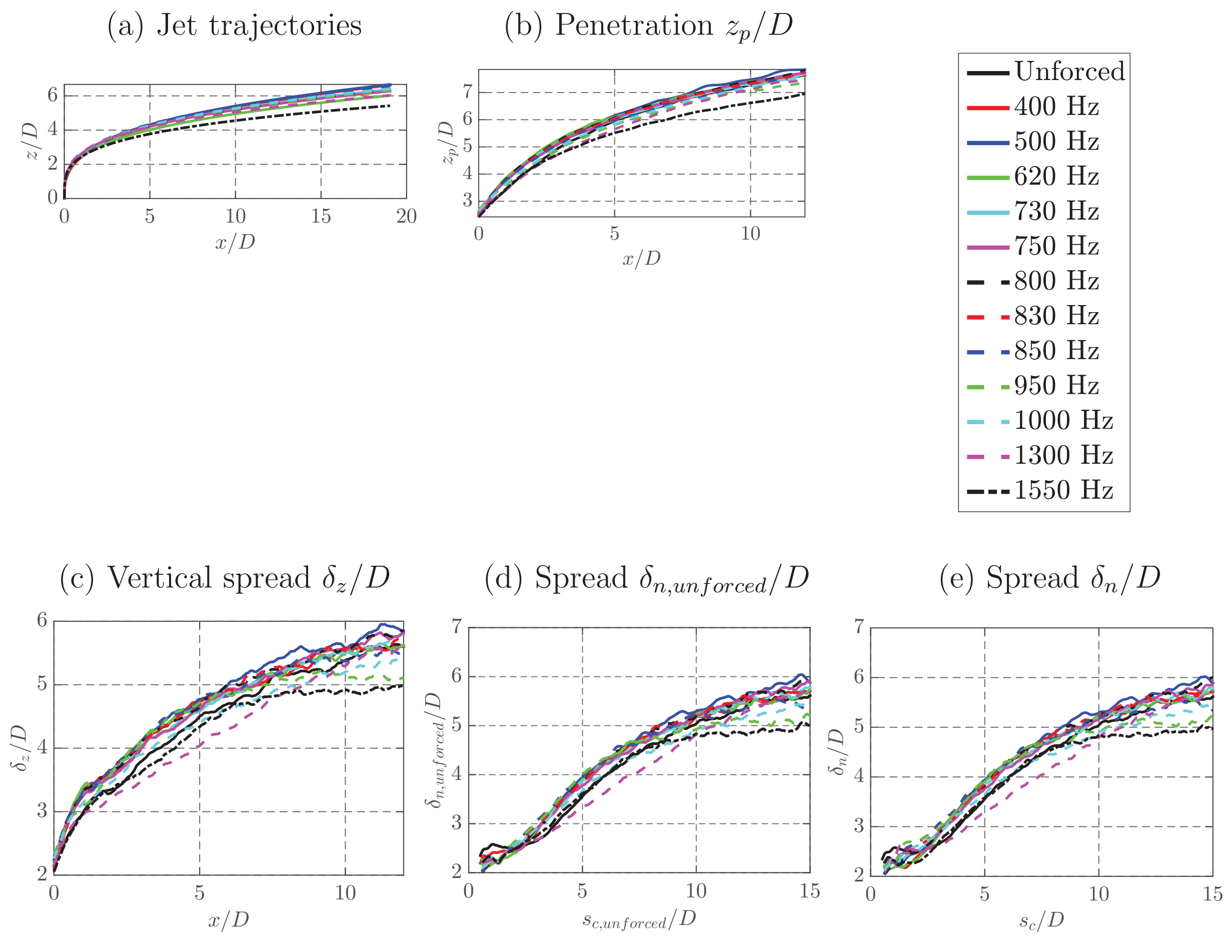

Figure B.20: Mean mixing metrics for the equidensity flush nozzle-injected JICF at $J = 5$ for the unforced case as well as the forced cases under sine wave forcing at $f_f = 400 - 1550$ Hz and $U'_{j,rms} = 0.22$ m/s (approximately 3 % of U_j): (a) Jet trajectories, (b) jet penetration z_p/D, (c) jet vertical spread δ_z/D, (d) jet spread normal to the unforced jet trajectory $\delta_{n,unforced}/D$ and (e) jet spread normal to each jet trajectory in question δ_n/D. Note that the upstream shear layer without forcing is locked-in above around $f_f \approx 820$ Hz.

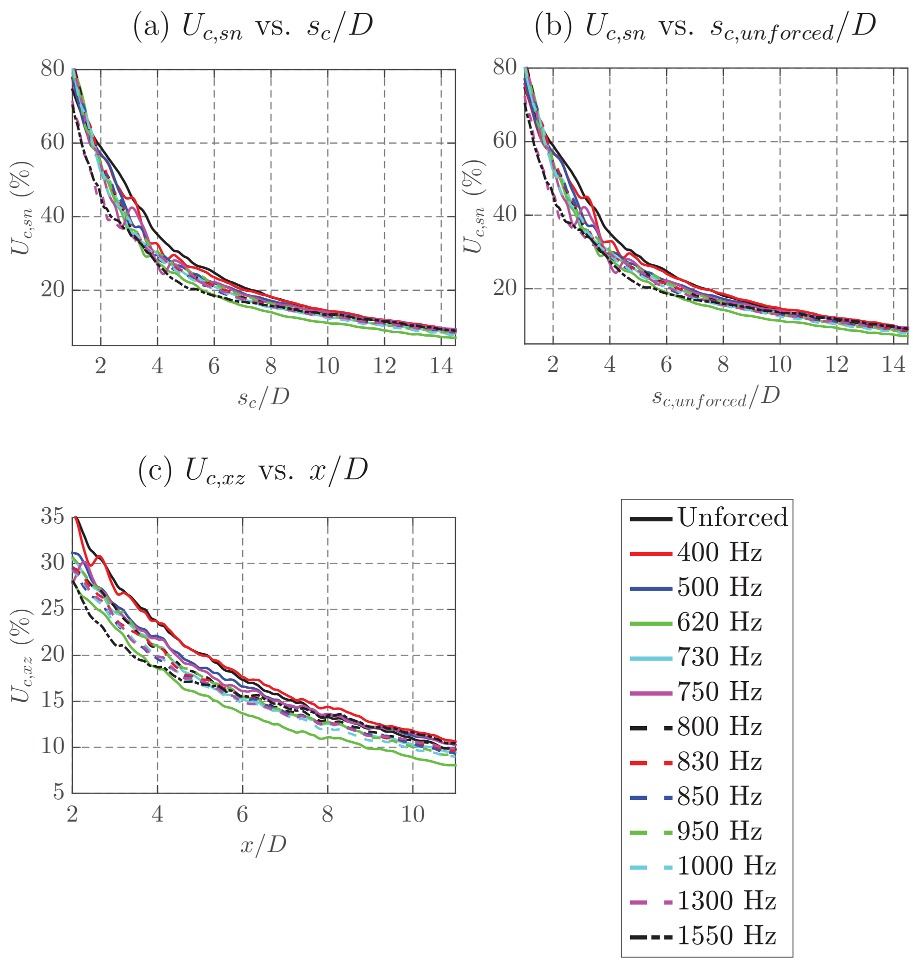

Figure B.21: Instantaneous mixing metrics evaluated for the equidensity flush nozzle-injected JICF at $J = 5$ for the unforced and forced cases under sine wave forcing at $f_f = 400 - 1550$ Hz and $U'_{j,rms} = 0.07$ m/s. Each figure represents (a) centerplane-based mean Unmixedness $U_{c,sn}$ along s_c/D, (b) $U_{c,sn}$ along $s_{c,unforced}/D$, (c) centerplane-based mean Unmixedness $U_{c,xz}$ along x/D, (d) cross-section-based mean Unmixedness U_{yz} along x/D, and (e)-(g) cross-section-based mean probability density function (PDF) of normalized concentration PDF(C/C_o) at $x/D = 2.5$, 5.5 and 10.5, respectively. Note that the upstream shear layer without forcing is locked-in above around $f_f \approx 820$ Hz.

APPENDIX C

Single-Pulse Square Wave Forcing Data

The following results correspond to data associated with the study of single-pulse square wave forcing of the JICF in Chapter 6.

C.1 Forcing Conditions for Square Wave Forcing

This section represents forcing conditions for all data sets explored in this study.

Table C.1: Forcing conditions at $J = 41$ with matching root-mean-squared velocity perturbation at $U'_{j,rms} = 1.0$ m/s ($0.99 \leq U'_{j,rms} \leq 1.01$ m/s) among all forcing conditions. Actual duty cycles α_{actual}, as well as three stroke ratios L/D evaluated by the present method in Equation (6.7) (third column), Equation (6.6) with the simplified relation (fourth column) and Equation (6.5) with inclusion of the mean jet velocity (fifth column). There is a 95 % confidence interval for input duty cycles α_{input}.

α_{input} (%)	α_{actual} (%)	L/D (Eq. 6.7)	L/D (Eq. 6.6)	L/D (Eq. 6.5)
5	11.0 ± 0.12	0.71 ± 0.01	1.50 ± 0.02	2.36 ± 0.02
10	14.6 ± 0.10	0.78 ± 0.01	1.60 ± 0.02	3.07 ± 0.02
15	20.5 ± 0.15	1.07 ± 0.01	1.68 ± 0.04	4.17 ± 0.03
20	25.7 ± 0.19	1.19 ± 0.01	1.94 ± 0.02	5.09 ± 0.03
25	30.5 ± 0.12	1.39 ± 0.02	2.06 ± 0.03	5.93 ± 0.03
30	35.9 ± 0.21	1.56 ± 0.02	2.31 ± 0.04	6.84 ± 0.04
35	40.7 ± 0.34	1.75 ± 0.03	2.41 ± 0.03	7.64 ± 0.05
40	46.4 ± 0.27	1.98 ± 0.02	2.68 ± 0.06	8.56 ± 0.05
45	50.5 ± 0.41	2.16 ± 0.04	2.74 ± 0.06	9.25 ± 0.06
50	56.4 ± 0.13	2.46 ± 0.02	3.09 ± 0.02	10.2 ± 0.03
60	66.9 ± 0.41	3.05 ± 0.03	3.66 ± 0.09	11.8 ± 0.06
70	76.7 ± 0.26	3.82 ± 0.04	4.42 ± 0.05	13.2 ± 0.04

Table C.2: Forcing conditions at $J = 20$ with matching root-mean-squared velocity perturbation at $U'_{j,rms} = 1.0$ m/s ($0.99 \leq U'_{j,rms} \leq 1.00$ m/s) among all forcing conditions. Actual duty cycles α_{actual}, as well as three stroke ratios L/D evaluated by the present method in Equation (6.7) (third column), Equation (6.6) with the simplified relation (fourth column) and Equation (6.5) with inclusion of the mean jet velocity (fifth column). There is a 95 % confidence interval for input duty cycles α_{input}.

α_{input} (%)	α_{actual} (%)	L/D (Eq. 6.7)	L/D (Eq. 6.6)	L/D (Eq. 6.5)
5	11.2 ± 0.06	0.71 ± 0.01	1.50 ± 0.02	2.41 ± 0.01
10	15.0 ± 0.09	0.80 ± 0.01	1.65 ± 0.01	3.15 ± 0.01
15	21.1 ± 0.18	1.10 ± 0.01	1.74 ± 0.02	4.24 ± 0.03
25	31.0 ± 0.20	1.44 ± 0.01	2.06 ± 0.03	5.99 ± 0.04
30	36.7 ± 0.21	1.65 ± 0.02	2.34 ± 0.03	6.94 ± 0.03
35	41.2 ± 0.14	1.85 ± 0.01	2.46 ± 0.02	7.71 ± 0.03
40	46.8 ± 0.19	2.05 ± 0.02	2.72 ± 0.04	8.61 ± 0.04
45	51.4 ± 0.23	2.27 ± 0.01	2.79 ± 0.04	9.35 ± 0.02
50	57.2 ± 0.37	2.51 ± 0.04	3.12 ± 0.08	10.3 ± 0.06
60	67.2 ± 0.16	3.08 ± 0.02	3.70 ± 0.06	11.8 ± 0.03
70	77.2 ± 0.18	3.85 ± 0.04	4.44 ± 0.05	13.3 ± 0.05

Table C.3: Forcing conditions at $J = 10$ with matching root-mean-squared velocity perturbation at $U'_{j,rms} = 2.0$ m/s ($1.99 \leq U'_{j,rms} \leq 2.05$ m/s) among all forcing conditions. Actual duty cycles α_{actual}, as well as three stroke ratios L/D evaluated by the present method in Equation (6.7) (third column), Equation (6.6) with the simplified relation (fourth column) and Equation (6.5) with inclusion of the mean jet velocity (fifth column). There is a 95 % confidence interval for input duty cycles α_{input}.

α_{input} (%)	α_{actual} (%)	L/D (Eq. 6.7)	L/D (Eq. 6.6)	L/D (Eq. 6.5)
20	26.1 ± 0.06	2.61 ± 0.01	4.19 ± 0.02	6.12 ± 0.02
30	36.1 ± 0.07	3.29 ± 0.01	4.85 ± 0.02	7.92 ± 0.01
35	40.6 ± 0.08	3.50 ± 0.01	4.89 ± 0.03	8.73 ± 0.02
40	46.0 ± 0.17	3.89 ± 0.03	5.41 ± 0.04	9.63 ± 0.03
45	50.3 ± 0.14	4.13 ± 0.03	5.82 ± 0.03	10.3 ± 0.02
50	55.7 ± 0.10	4.58 ± 0.03	6.16 ± 0.11	11.2 ± 0.02
70	76.4 ± 1.27	6.98 ± 0.35	9.07 ± 0.34	14.1 ± 0.11

Table C.4: Forcing conditions at $J = 5$ with matching root-mean-squared velocity perturbation at $U'_{j,rms} = 1.0$ m/s ($1.00 \leq U'_{j,rms} \leq 1.02$ m/s) among all forcing conditions. Actual duty cycles α_{actual}, as well as three stroke ratios L/D evaluated by the present method in Equation (6.7) (third column), Equation (6.6) with the simplified relation (fourth column) and Equation (6.5) with inclusion of the mean jet velocity (fifth column). There is a 95 % confidence interval for input duty cycles α_{input}.

α_{input} (%)	α_{actual} (%)	L/D (Eq. 6.7)	L/D (Eq. 6.6)	L/D (Eq. 6.5)
5	11.3 ± 0.16	0.74 ± 0.01	1.70 ± 0.08	2.38 ± 0.03
10	15.5 ± 0.18	0.83 ± 0.01	1.79 ± 0.03	3.21 ± 0.03
15	21.4 ± 0.22	1.14 ± 0.02	1.85 ± 0.04	4.30 ± 0.04
20	26.1 ± 0.18	1.28 ± 0.03	1.99 ± 0.03	5.15 ± 0.05
25	31.1 ± 0.69	1.50 ± 0.06	2.17 ± 0.09	6.01 ± 0.13
30	36.4 ± 0.59	1.67 ± 0.04	2.37 ± 0.05	6.90 ± 0.10
35	40.4 ± 0.25	1.80 ± 0.03	2.42 ± 0.07	7.60 ± 0.04
40	46.7 ± 0.54	2.04 ± 0.05	2.77 ± 0.07	8.60 ± 0.09
45	51.0 ± 0.78	2.24 ± 0.08	3.15 ± 0.08	9.29 ± 0.12
50	56.0 ± 0.48	2.43 ± 0.07	3.24 ± 0.08	10.1 ± 0.09
60	66.0 ± 0.60	2.96 ± 0.06	3.78 ± 0.09	11.6 ± 0.09
70	76.3 ± 0.39	3.72 ± 0.07	4.66 ± 0.12	13.2 ± 0.06

Table C.5: Forcing conditions at $J = 5$ with matching root-mean-squared velocity perturbation at $U'_{j,rms} = 1.5$ m/s ($1.48 \leq U'_{j,rms} \leq 1.52$ m/s) among all forcing conditions. Actual duty cycles α_{actual}, as well as three stroke ratios L/D evaluated by the present method in Equation (6.7) (third column), Equation (6.6) with the simplified relation (fourth column) and Equation (6.5) with inclusion of the mean jet velocity (fifth column). There is a 95 % confidence interval for input duty cycles α_{input}.

α_{input} (%)	α_{actual} (%)	L/D (Eq. 6.7)	L/D (Eq. 6.6)	L/D (Eq. 6.5)
10	14.9 ± 0.07	1.17 ± 0.01	2.69 ± 0.04	3.40 ± 0.02
15	21.0 ± 0.35	1.68 ± 0.05	2.73 ± 0.06	4.65 ± 0.09
20	25.7 ± 0.11	1.84 ± 0.02	2.91 ± 0.02	5.50 ± 0.02
25	30.8 ± 0.18	2.24 ± 0.02	3.18 ± 0.04	6.44 ± 0.03
30	36.0 ± 0.29	2.52 ± 0.03	3.60 ± 0.04	7.37 ± 0.03
35	40.4 ± 0.25	2.69 ± 0.03	3.68 ± 0.05	8.14 ± 0.04
40	46.3 ± 0.37	3.08 ± 0.06	4.36 ± 0.08	9.09 ± 0.07
45	50.5 ± 0.35	3.32 ± 0.07	4.90 ± 0.03	9.77 ± 0.08
50	55.8 ± 0.45	3.60 ± 0.08	5.00 ± 0.09	10.6 ± 0.07
60	65.6 ± 0.39	4.30 ± 0.11	5.96 ± 0.12	12.1 ± 0.11
70	76.2 ± 0.35	5.36 ± 0.08	6.97 ± 0.12	13.6 ± 0.08

Table C.6: Forcing conditions at $J = 5$ with matching root-mean-squared velocity perturbation at $U'_{j,rms} = 2.0$ m/s ($1.99 \leq U'_{j,rms} \leq 2.02$ m/s) among all forcing conditions. Actual duty cycles α_{actual}, as well as three stroke ratios L/D evaluated by the present method in Equation (6.7) (third column), Equation (6.6) with the simplified relation (fourth column) and Equation (6.5) with inclusion of the mean jet velocity (fifth column). There is a 95 % confidence interval for input duty cycles α_{input}.

α_{input} (%)	α_{actual} (%)	L/D (Eq. 6.7)	L/D (Eq. 6.6)	L/D (Eq. 6.5)
20	25.9 ± 0.14	2.48 ± 0.01	4.06 ± 0.03	6.03 ± 0.02
25	31.3 ± 0.13	2.93 ± 0.02	4.23 ± 0.03	7.03 ± 0.03
30	36.0 ± 0.26	3.19 ± 0.05	4.71 ± 0.04	7.90 ± 0.06
35	40.4 ± 0.09	3.41 ± 0.01	4.80 ± 0.03	8.70 ± 0.01
40	46.0 ± 0.29	3.83 ± 0.05	5.36 ± 0.06	9.62 ± 0.05
45	50.1 ± 0.29	4.03 ± 0.06	5.68 ± 0.06	10.3 ± 0.06
50	55.5 ± 0.15	4.43 ± 0.04	6.04 ± 0.06	11.2 ± 0.04
70	82.8 ± 0.91	7.60 ± 0.05	10.3 ± 0.38	14.7 ± 0.07

Table C.7: Forcing conditions at $J = 5$ with matching root-mean-squared velocity perturbation at $U'_{j,rms} = 2.5$ m/s ($2.48 \leq U'_{j,rms} \leq 2.51$ m/s) among all forcing conditions. Actual duty cycles α_{actual}, as well as three stroke ratios L/D evaluated by the present method in Equation (6.7) (third column), Equation (6.6) with the simplified relation (fourth column) and Equation (6.5) with inclusion of the mean jet velocity (fifth column). There is a 95 % confidence interval for input duty cycles α_{input}.

α_{input} (%)	α_{actual} (%)	L/D (Eq. 6.7)	L/D (Eq. 6.6)	L/D (Eq. 6.5)
30	36.2 ± 0.13	4.02 ± 0.02	5.77 ± 0.04	8.46 ± 0.04
40	46.4 ± 0.36	4.83 ± 0.04	6.47 ± 0.09	10.2 ± 0.05
50	55.6 ± 0.41	5.84 ± 0.11	7.72 ± 0.13	11.7 ± 0.08
70	75.7 ± 0.72	8.79 ± 0.25	10.7 ± 0.24	14.5 ± 0.07

Table C.8: Forcing conditions at $J = 5$ with matching root-mean-squared velocity perturbation at $U'_{j,rms} = 3.0$ m/s ($2.98 \leq U'_{j,rms} \leq 3.03$ m/s) among all forcing conditions. Actual duty cycles α_{actual}, as well as three stroke ratios L/D evaluated by the present method in Equation (6.7) (third column), Equation (6.6) with the simplified relation (fourth column) and Equation (6.5) with inclusion of the mean jet velocity (fifth column). There is a 95 % confidence interval for input duty cycles α_{input}.

α_{input} (%)	α_{actual} (%)	L/D (Eq. 6.7)	L/D (Eq. 6.6)	L/D (Eq. 6.5)
40	45.8 ± 0.30	5.66 ± 0.07	7.72 ± 0.10	10.7 ± 0.05
45	50.3 ± 0.36	6.26 ± 0.10	8.74 ± 0.11	11.5 ± 0.06
50	55.3 ± 0.28	6.79 ± 0.10	9.19 ± 0.09	12.3 ± 0.05
70	75.2 ± 0.33	10.3 ± 0.16	12.6 ± 0.17	14.9 ± 0.04

C.2 Temporal Velocity Variation for Single-Pulse Square Wave Forcing

This section shows temporal jet velocity variations at the jet exit with all single-pulse square wave forcing conditions explored in this study, which were not shown in Chapter 6.

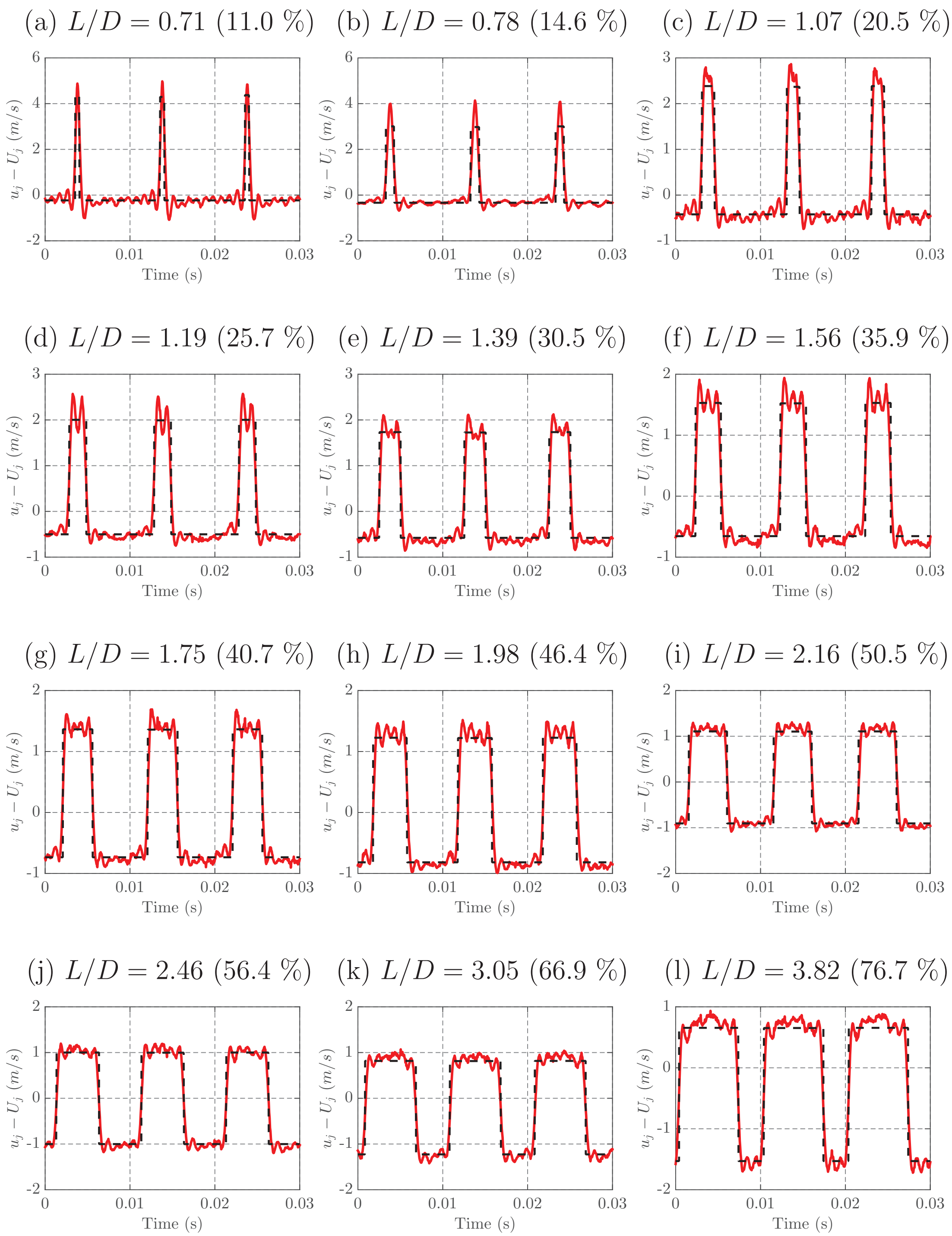

Figure C.1: For more figures and caption see next page.

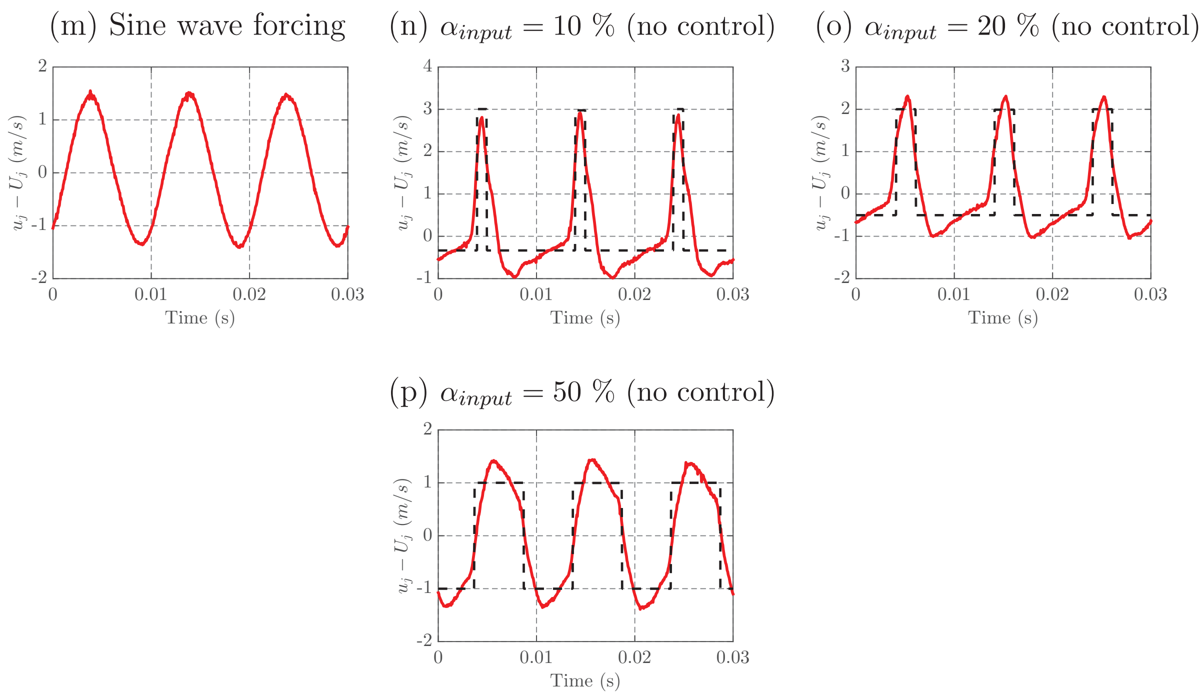

Figure C.1: Temporal mean-subtracted jet vertical velocity profiles $u_j - U_j$ (m/s) (—) with single-pulse square wave forcing measured via hotwire anemometry $0.2D$ above the jet exit plane at $S = 1.00$, and $J = 41$ ($f_f = 100$ Hz and $U'_{j,rms} = 1.0$ m/s) with seeded acetone. Ideal waveforms (--) are also plotted for square wave forcing with and without control.

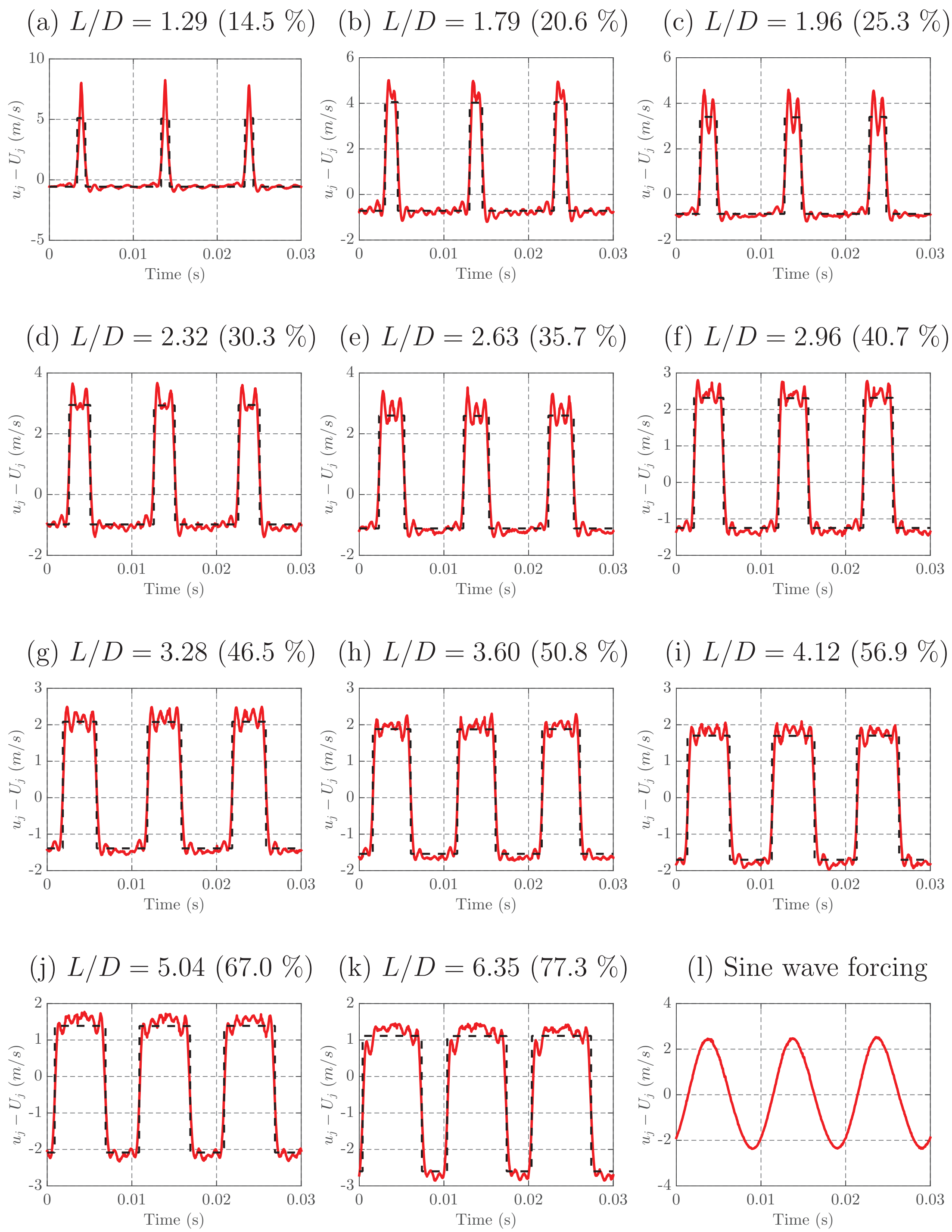

Figure C.2: For more figures and caption see next page.

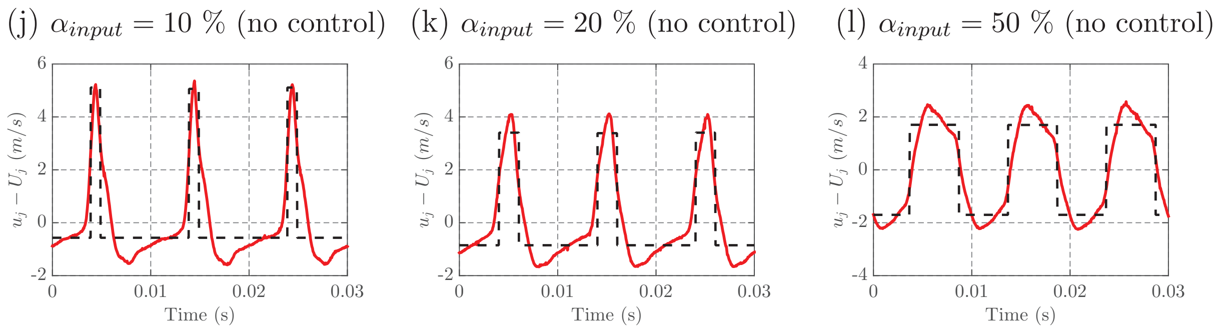

Figure C.2: Temporal mean-subtracted jet vertical velocity profiles $u_j - U_j$ (m/s) (—) with single-pulse square wave forcing measured via hotwire anemometry $0.2D$ above the jet exit plane at $S = 1.00$, and $J = 41$ ($f_f = 100$ Hz and $U'_{j,rms} = 1.7$ m/s) with seeded acetone. Ideal waveforms (--) are also plotted for square wave forcing with and without control.

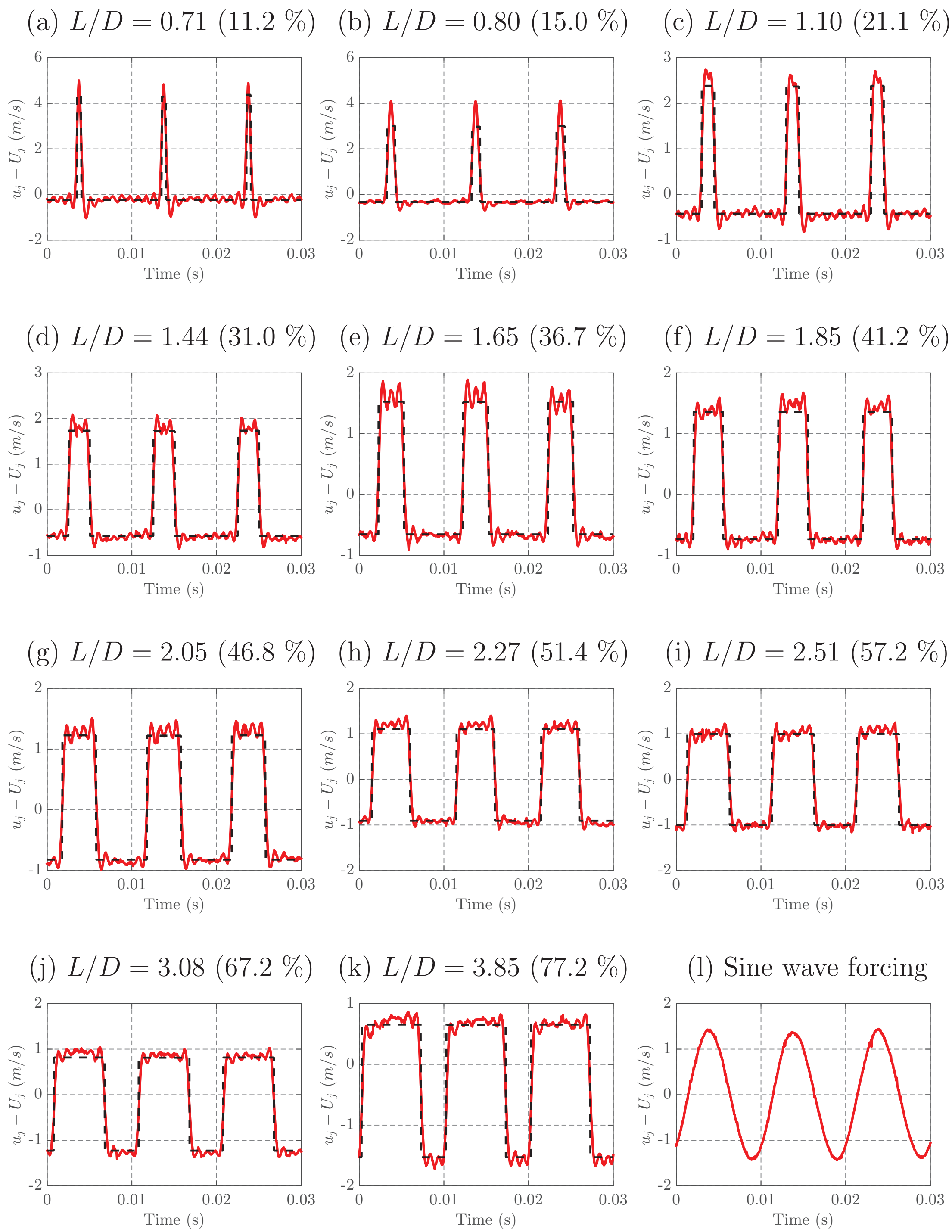

Figure C.3: For more figures and caption see next page.

(m) $\alpha_{input} = 10$ % (no control) (n) $\alpha_{input} = 20$ % (no control) (o) $\alpha_{input} = 50$ % (no control)

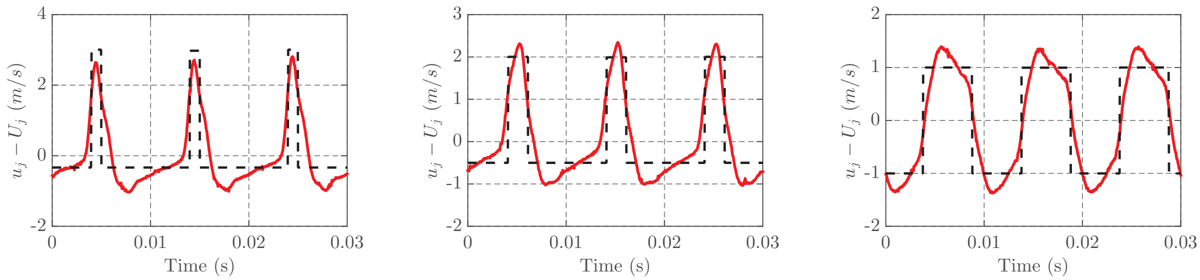

Figure C.3: Temporal mean-subtracted jet vertical velocity profiles $u_j - U_j$ (m/s) (—) with single-pulse square wave forcing measured via hotwire anemometry $0.2D$ above the jet exit plane at $S = 1.00$, and $J = 20$ ($f_f = 100$ Hz and $U'_{j,rms} = 1.0$ m/s) with seeded acetone. Ideal waveforms (--) are also plotted for square wave forcing with and without control.

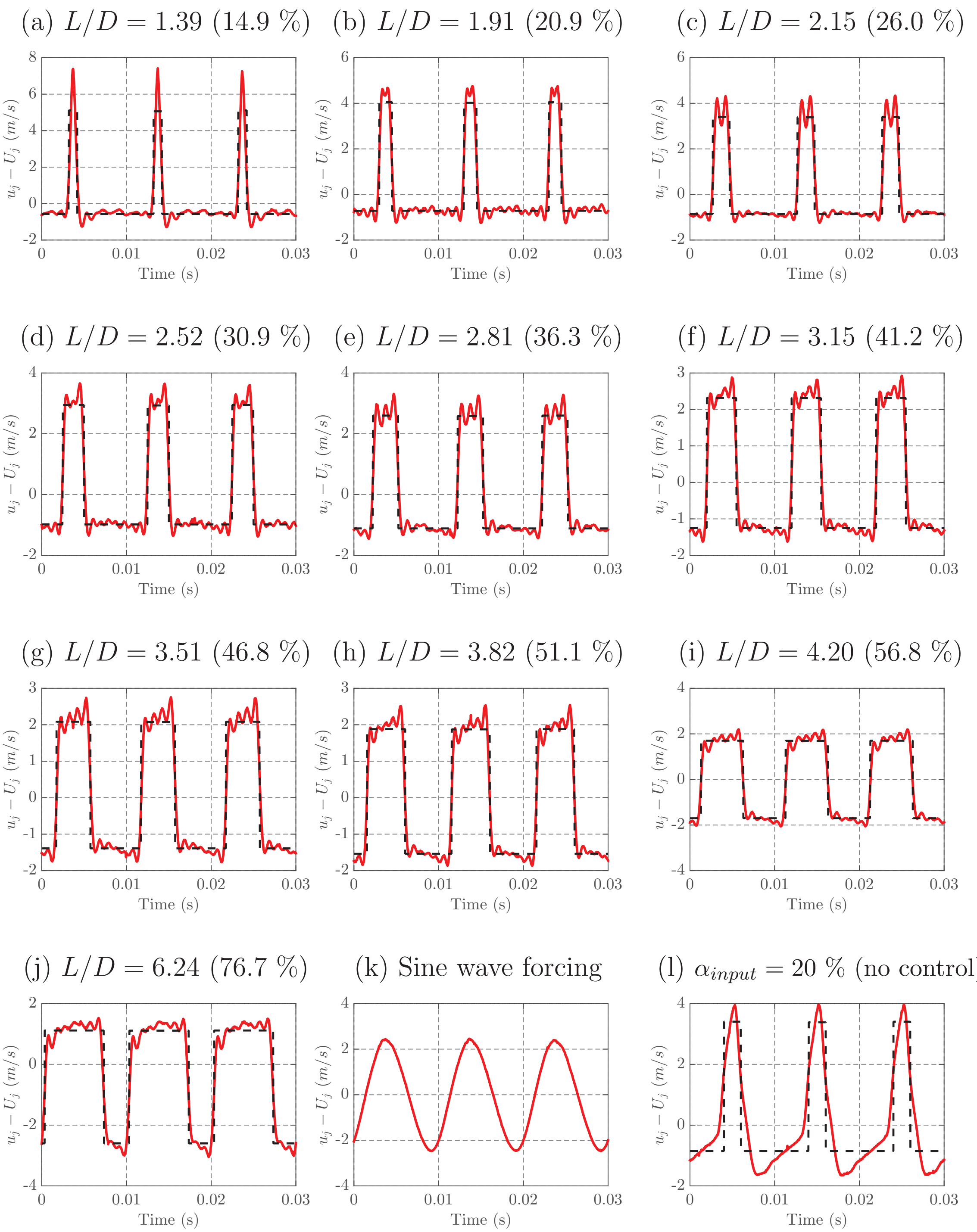

Figure C.4: For more figures and caption see next page.

(m) $\alpha_{input} = 50$ % (no control)

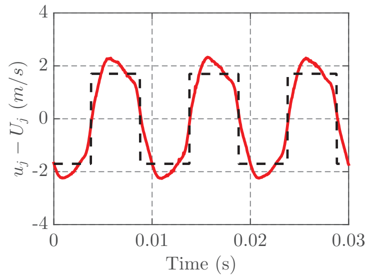

Figure C.4: Temporal mean-subtracted jet vertical velocity profiles $u_j - U_j$ (m/s) (—) with single-pulse square wave forcing measured via hotwire anemometry $0.2D$ above the jet exit plane at $S = 1.00$, and $J = 20$ ($f_f = 100$ Hz and $U'_{j,rms} = 1.7$ m/s) with seeded acetone. Ideal waveforms (--) are also plotted for square wave forcing with and without control.

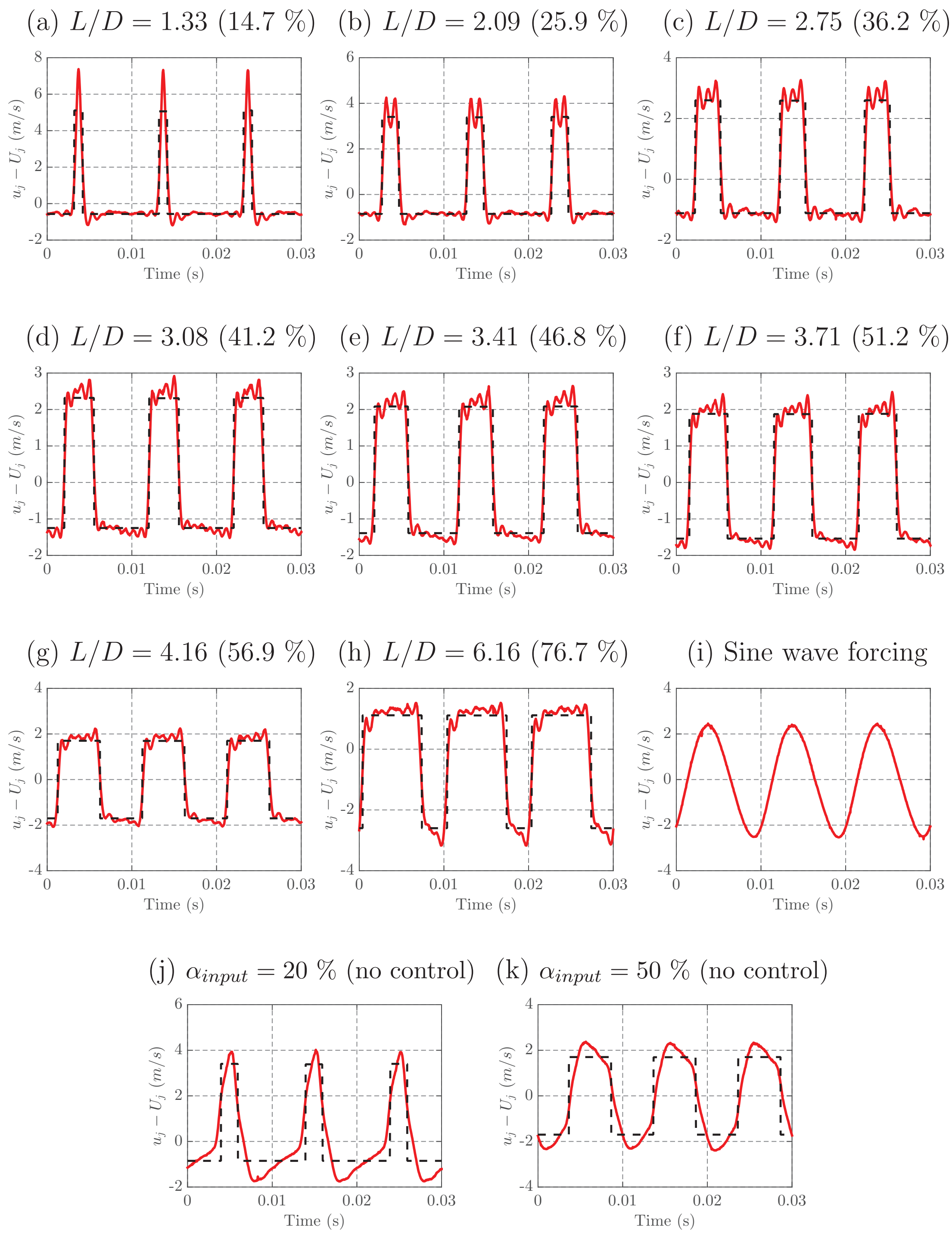

Figure C.5: Temporal mean-subtracted jet vertical velocity profiles $u_j - U_j$ (m/s) (—) with single-pulse square wave forcing measured via hotwire anemometry $0.2D$ above the jet exit plane at $S = 1.00$, and $J = 10$ ($f_f = 100$ Hz and $U'_{j,rms} = 1.7$ m/s) with seeded acetone. Ideal waveforms (**--**) are also plotted for square wave forcing with and without control.

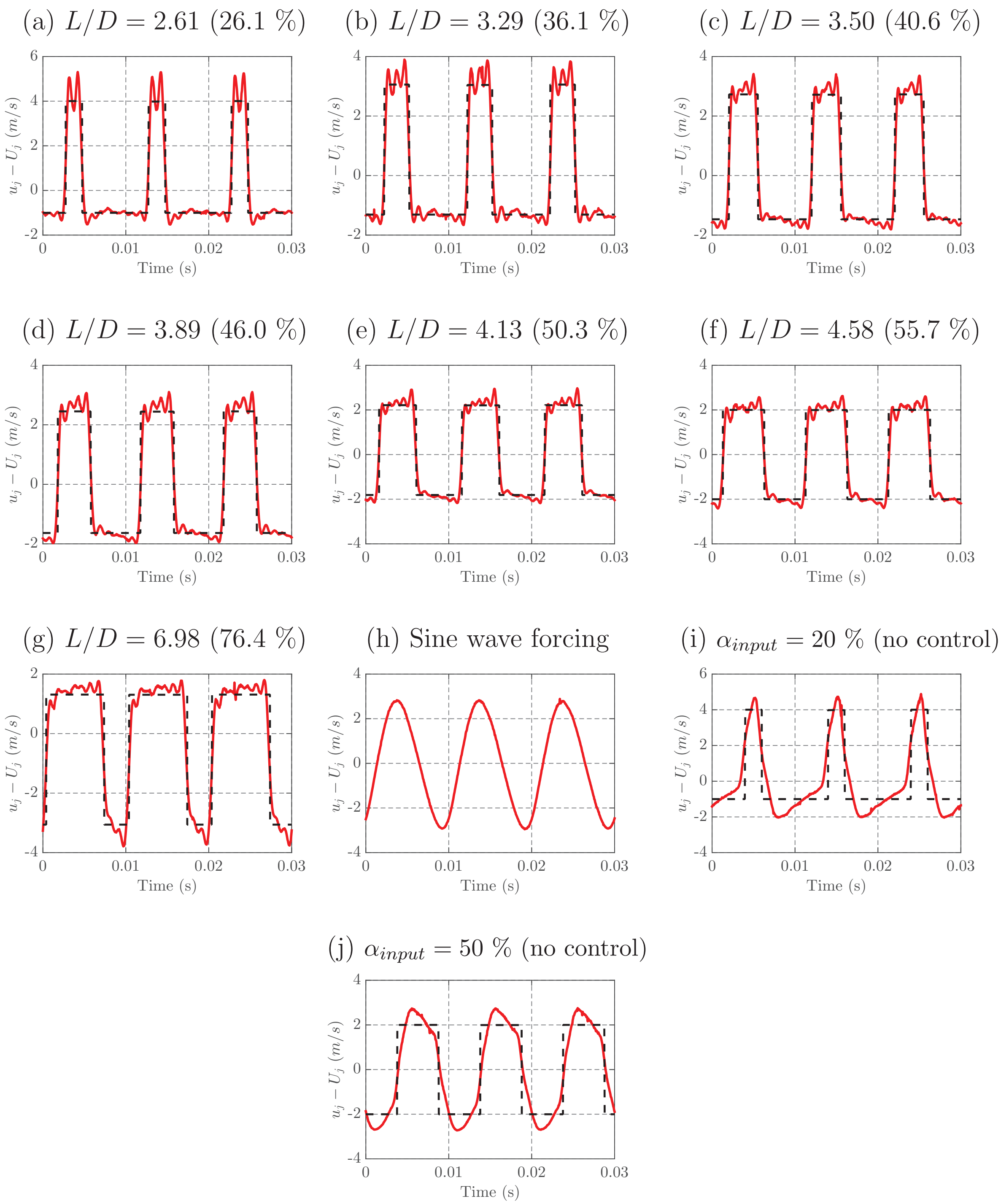

Figure C.6: Temporal mean-subtracted jet vertical velocity profiles $u_j - U_j$ (m/s) (—) with single-pulse square wave forcing measured via hotwire anemometry $0.2D$ above the jet exit plane at $S = 1.00$, and $J = 10$ ($f_f = 100$ Hz and $U'_{j,rms} = 2.0$ m/s) with seeded acetone. Ideal waveforms (--) are also plotted for square wave forcing with and without control.

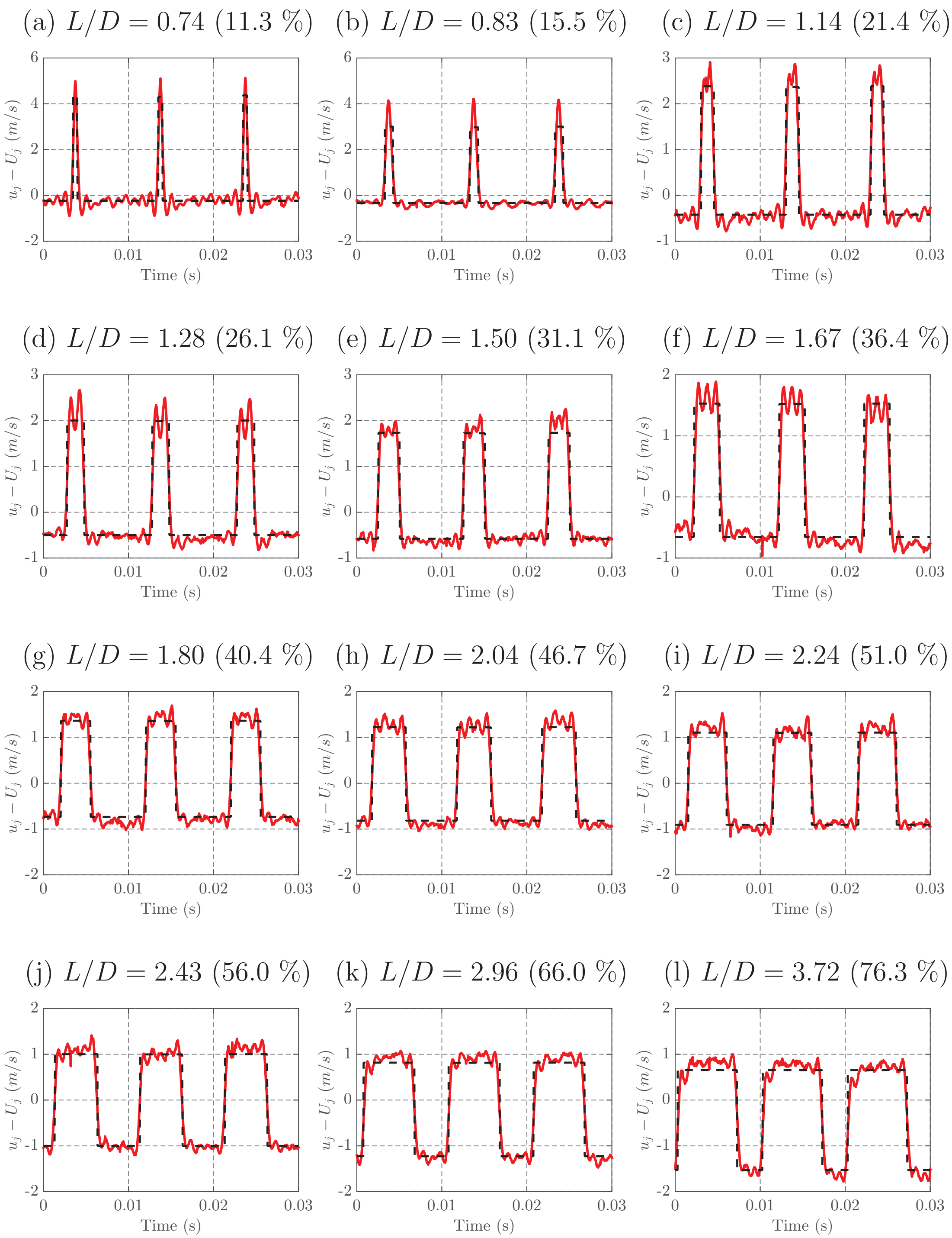

Figure C.7: For more figures and caption see next page.

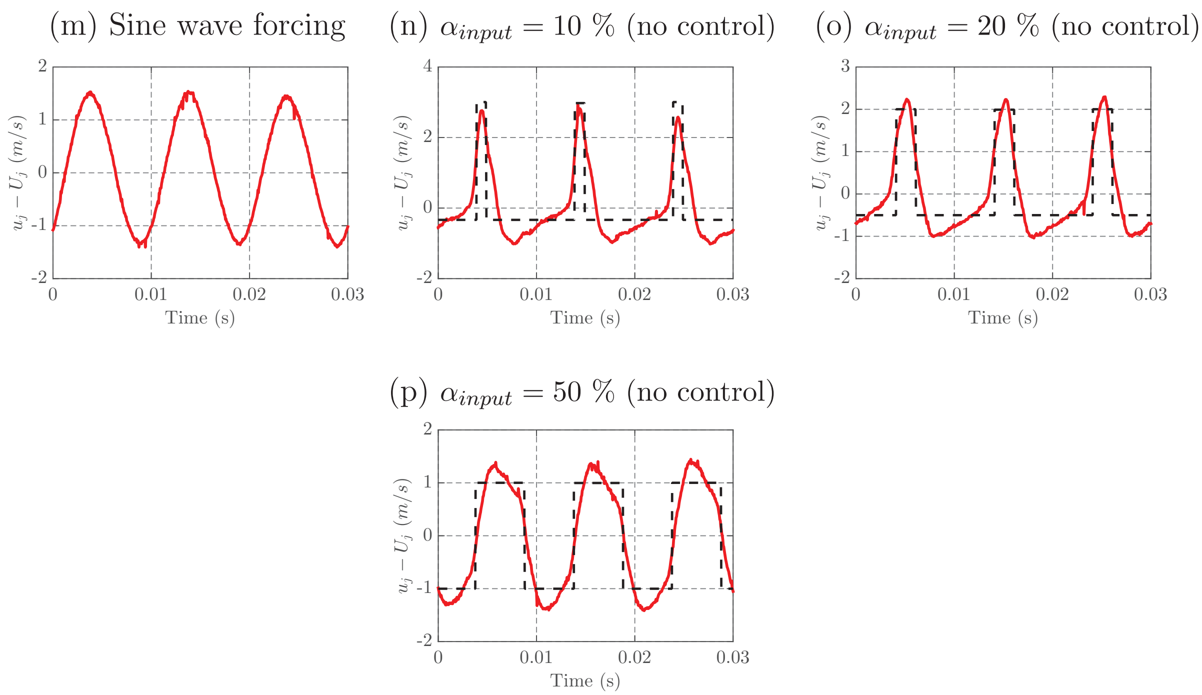

Figure C.7: Temporal mean-subtracted jet vertical velocity profiles $u_j - U_j$ (m/s) (—) with single-pulse square wave forcing measured via hotwire anemometry $0.2D$ above the jet exit plane at $S = 1.00$, and $J = 5$ ($f_f = 100$ Hz and $U'_{j,rms} = 1.0$ m/s) with seeded acetone. Ideal waveforms (- -) are also plotted for square wave forcing with and without control.

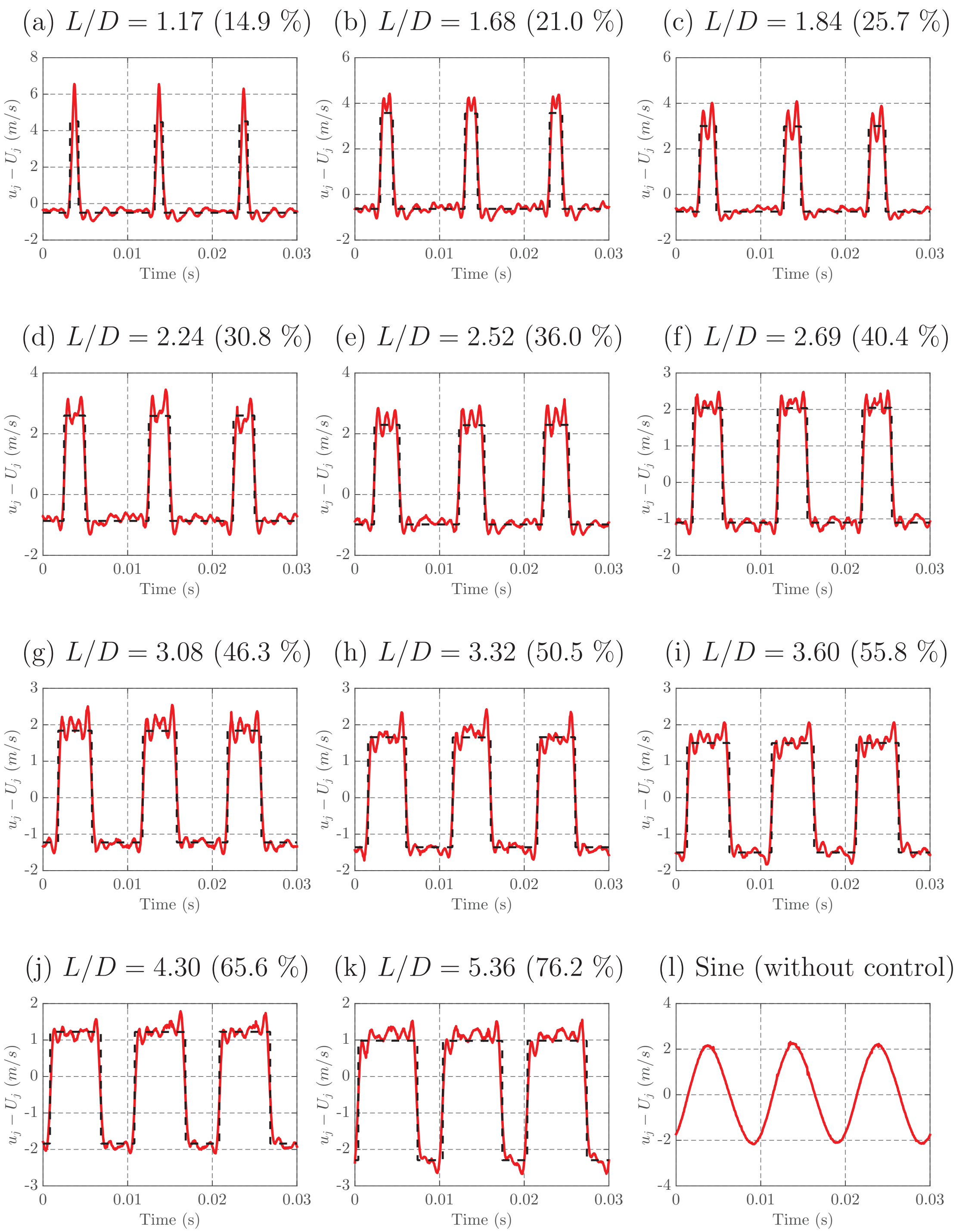

Figure C.8: For more figures and caption see next page.

(k) $\alpha_{input} = 10$ % (no control) (k) $\alpha_{input} = 20$ % (no control) (k) $\alpha_{input} = 50$ % (no control)

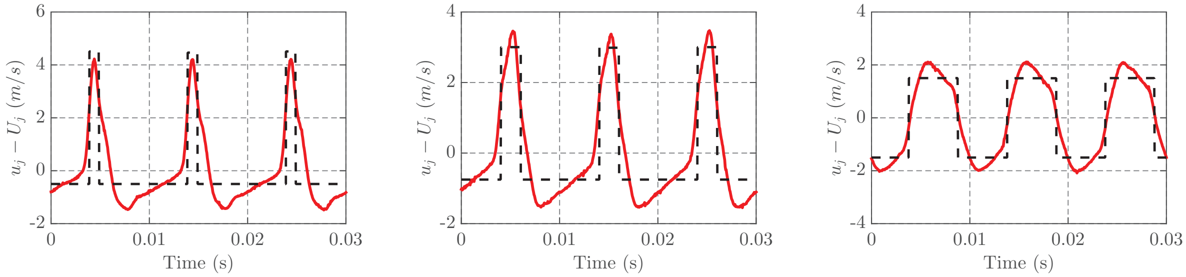

Figure C.8: Temporal mean-subtracted jet vertical velocity profiles $u_j - U_j$ (m/s) (—) with single-pulse square wave forcing measured via hotwire anemometry $0.2D$ above the jet exit plane at $S = 1.00$, and $J = 5$ ($f_f = 100$ Hz and $U'_{j,rms} = 1.5$ m/s) with seeded acetone. Ideal waveforms (- -) are also plotted for square wave forcing with and without control.

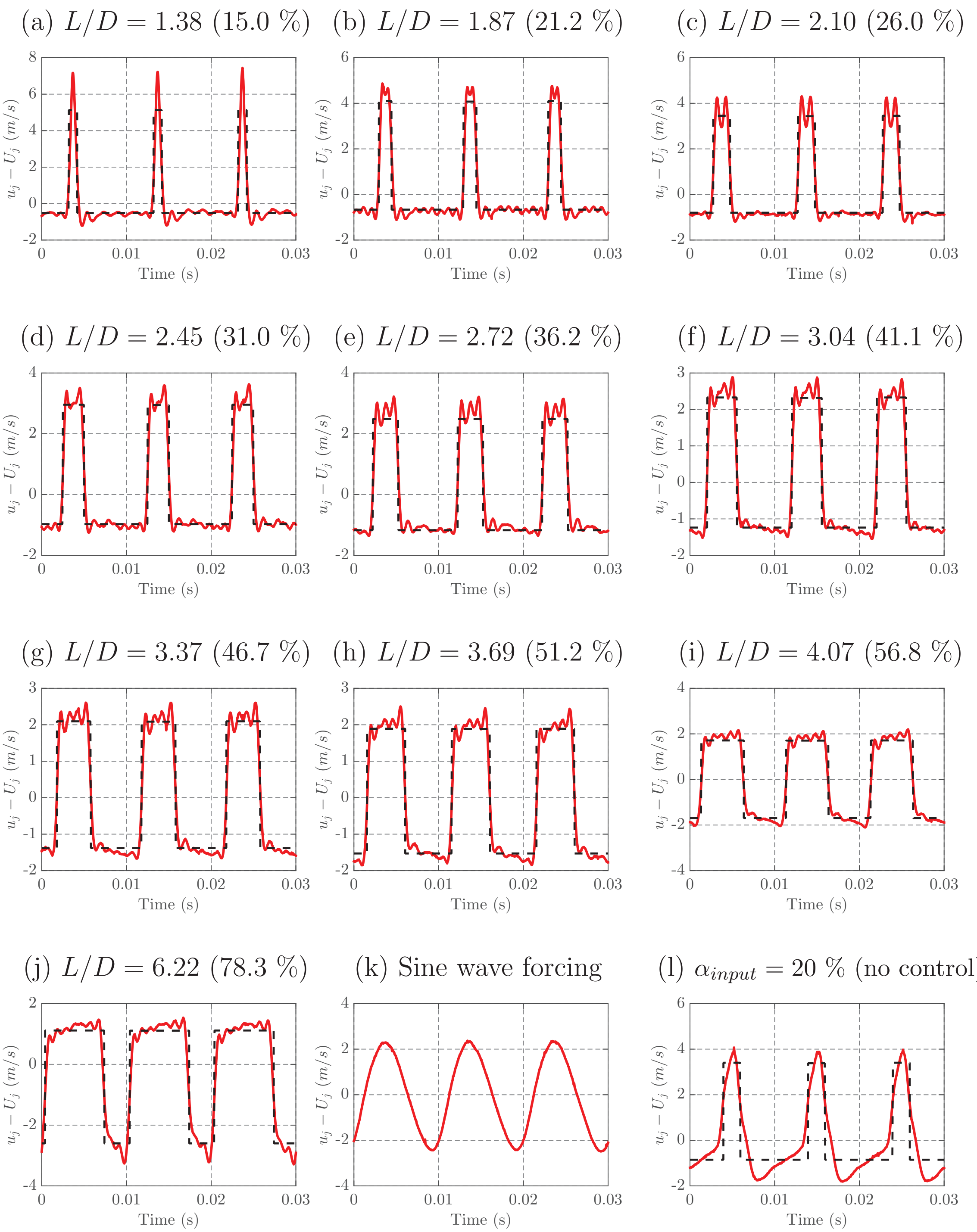

Figure C.9: For more figures and caption see next page.

(m) $\alpha_{input} = 50$ % (no control)

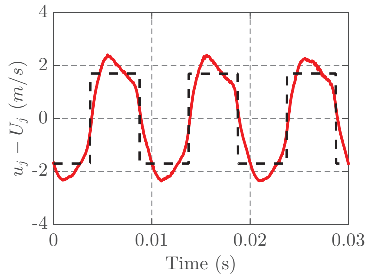

Figure C.9: Temporal mean-subtracted jet vertical velocity profiles $u_j - U_j$ (m/s) (—) with single-pulse square wave forcing measured via hotwire anemometry $0.2D$ above the jet exit plane at $S = 1.00$, and $J = 5$ ($f_f = 100$ Hz and $U'_{j,rms} = 1.7$ m/s) with seeded acetone. Ideal waveforms (- -) are also plotted for square wave forcing with and without control.

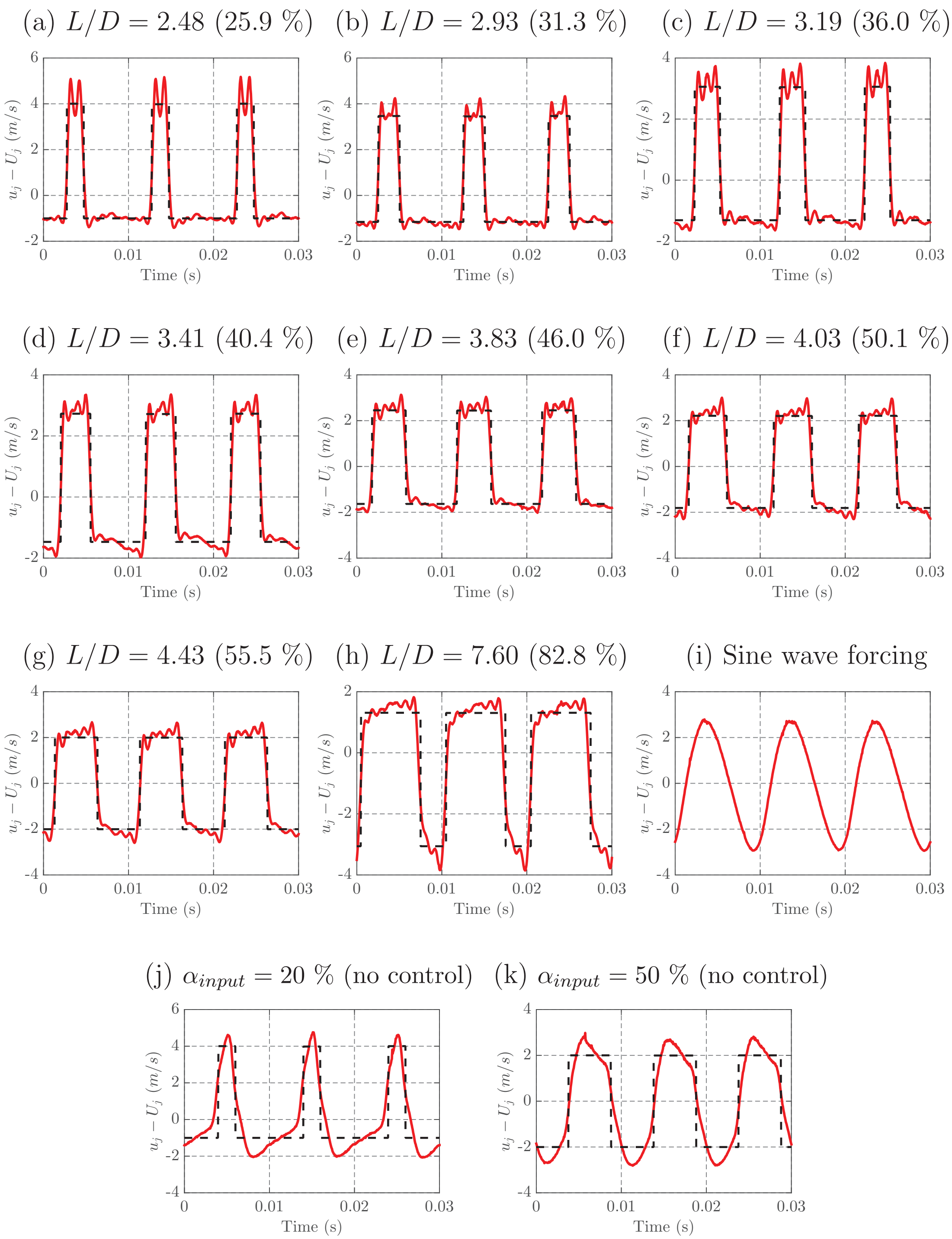

Figure C.10: Temporal mean-subtracted jet vertical velocity profiles $u_j - U_j$ (m/s) (—) with single-pulse square wave forcing measured via hotwire anemometry $0.2D$ above the jet exit plane at $S = 1.00$, and $J = 5$ ($f_f = 100$ Hz and $U'_{j,rms} = 2.0$ m/s) with seeded acetone. Ideal waveforms (- -) are also plotted for square wave forcing with and without control.

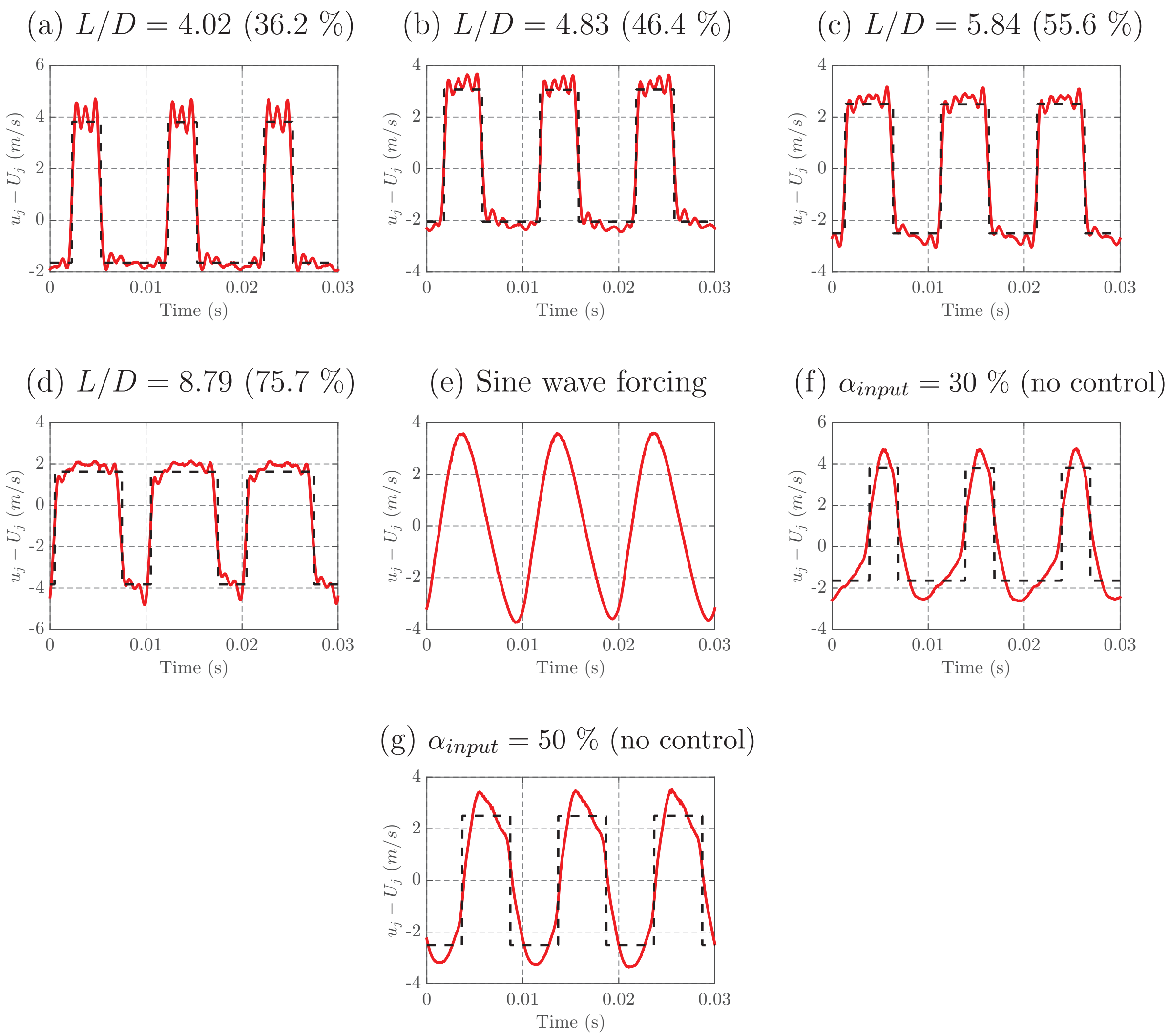

Figure C.11: Temporal mean-subtracted jet vertical velocity profiles $u_j - U_j$ (m/s) (—) with single-pulse square wave forcing measured via hotwire anemometry $0.2D$ above the jet exit plane at $S = 1.00$, and $J = 5$ ($f_f = 100$ Hz and $U'_{j,rms} = 2.5$ m/s) with seeded acetone. Ideal waveforms (--) are also plotted for square wave forcing with and without control.

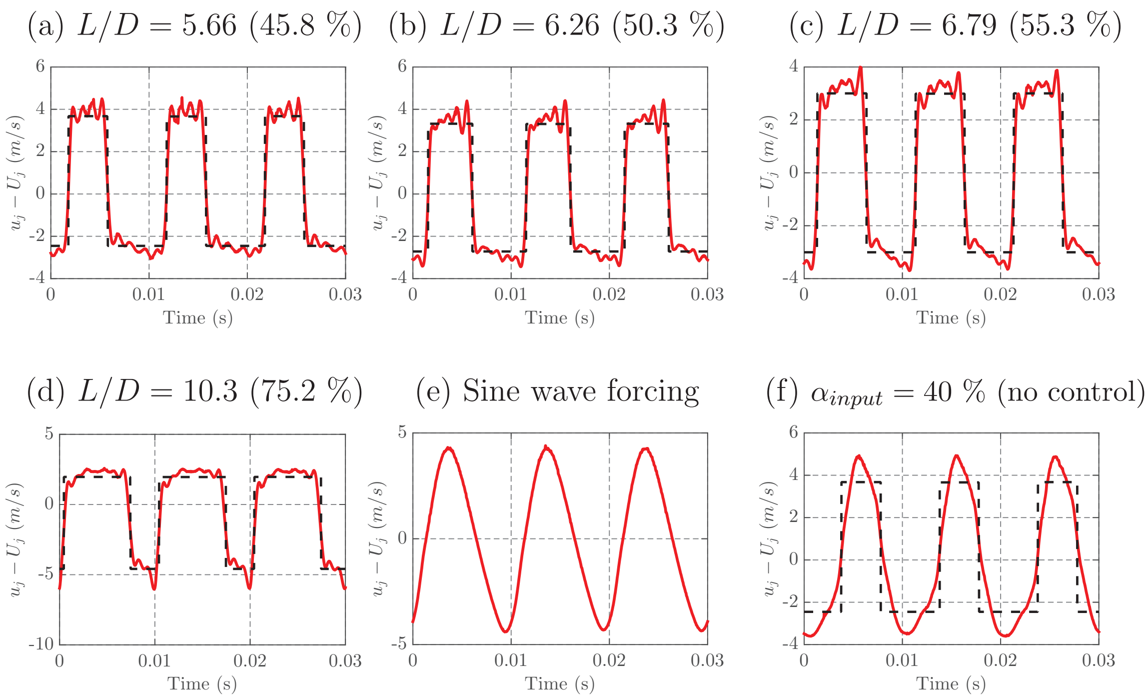

Figure C.12: Temporal mean-subtracted jet vertical velocity profiles $u_j - U_j$ (m/s) (—) with single-pulse square wave forcing measured via hotwire anemometry $0.2D$ above the jet exit plane at $S = 1.00$, and $J = 5$ ($f_f = 100$ Hz and $U'_{j,rms} = 3.0$ m/s) with seeded acetone. Ideal waveforms (--) are also plotted for square wave forcing with and without control.

C.3 Instantaneous and Mean Centerplane PLIF Images

This section represents instantaneous and mean centerplane PLIF images with single-pulse square wave forcing of the jet, which were not shown in Chapter 6. All mean images shown here are created by averaging 500 instantaneous images. Note that stroke ratio L/D with asterisk corresponds to the existence of deeply-penetrating puff-like vortical flow structures observed in instantaneous centerplane images.

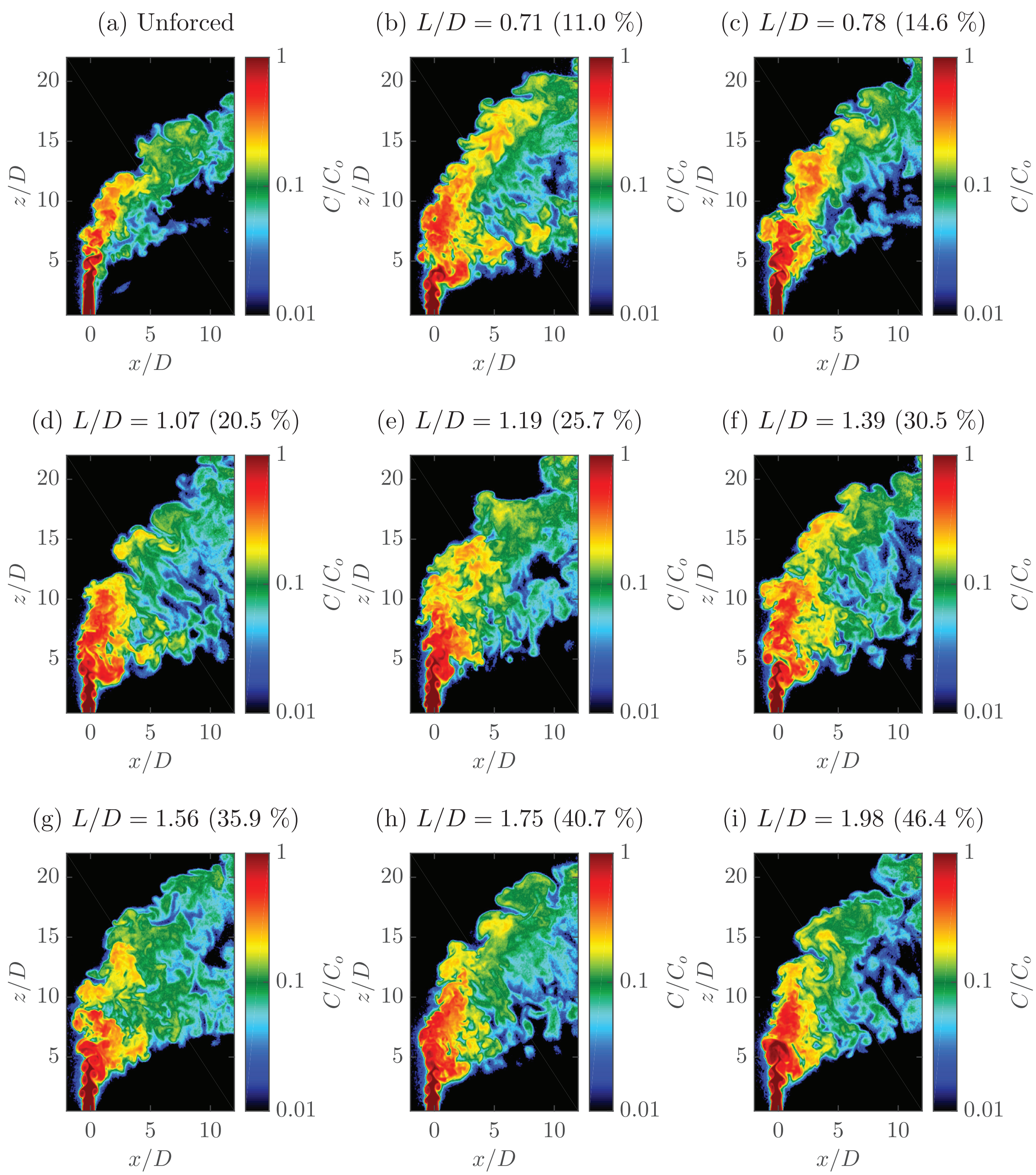

Figure C.13: For more figures and caption see next page.

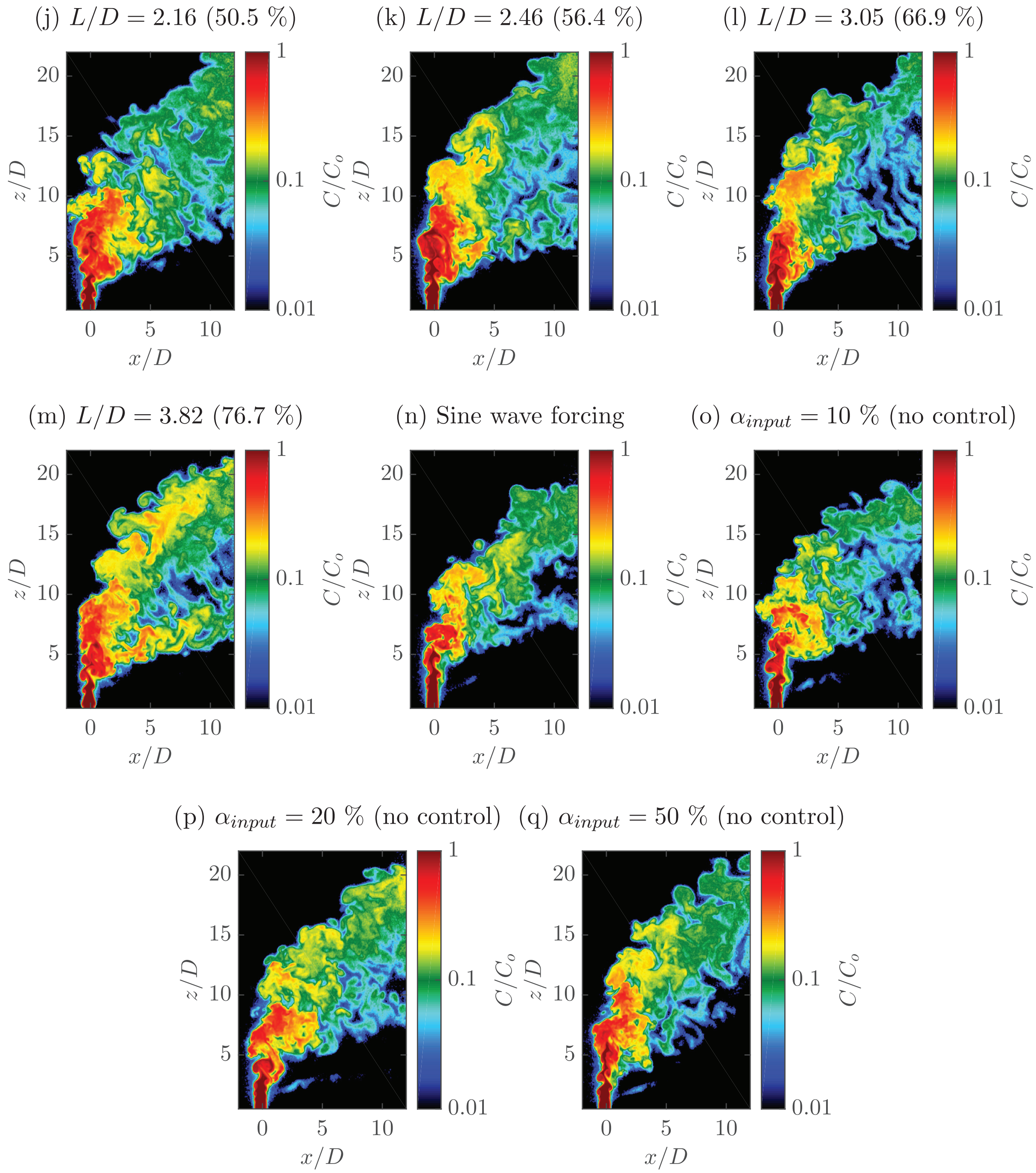

Figure C.13: Instantaneous centerplane PLIF images in the $x/D - z/D$ plane for the equidensity flush nozzle-injected JICF at $J = 41$ for (a) the unforced case, (b)-(m) the forced cases under single-pulse square wave forcing with control at stroke ratios ranging $L/D = 0.71 - 3.82$ (actual duty cycle α_{actual} (%) in parentheses), (n) under sine wave forcing, as well as (o)-(q) under single-pulse square wave forcing without control at $\alpha_{input} = 10 - 50$ %. All forcing conditions are at $f_f = 100$ Hz and $U'_{j,rms} = 1.0$ m/s (approximately 15 % of U_j).

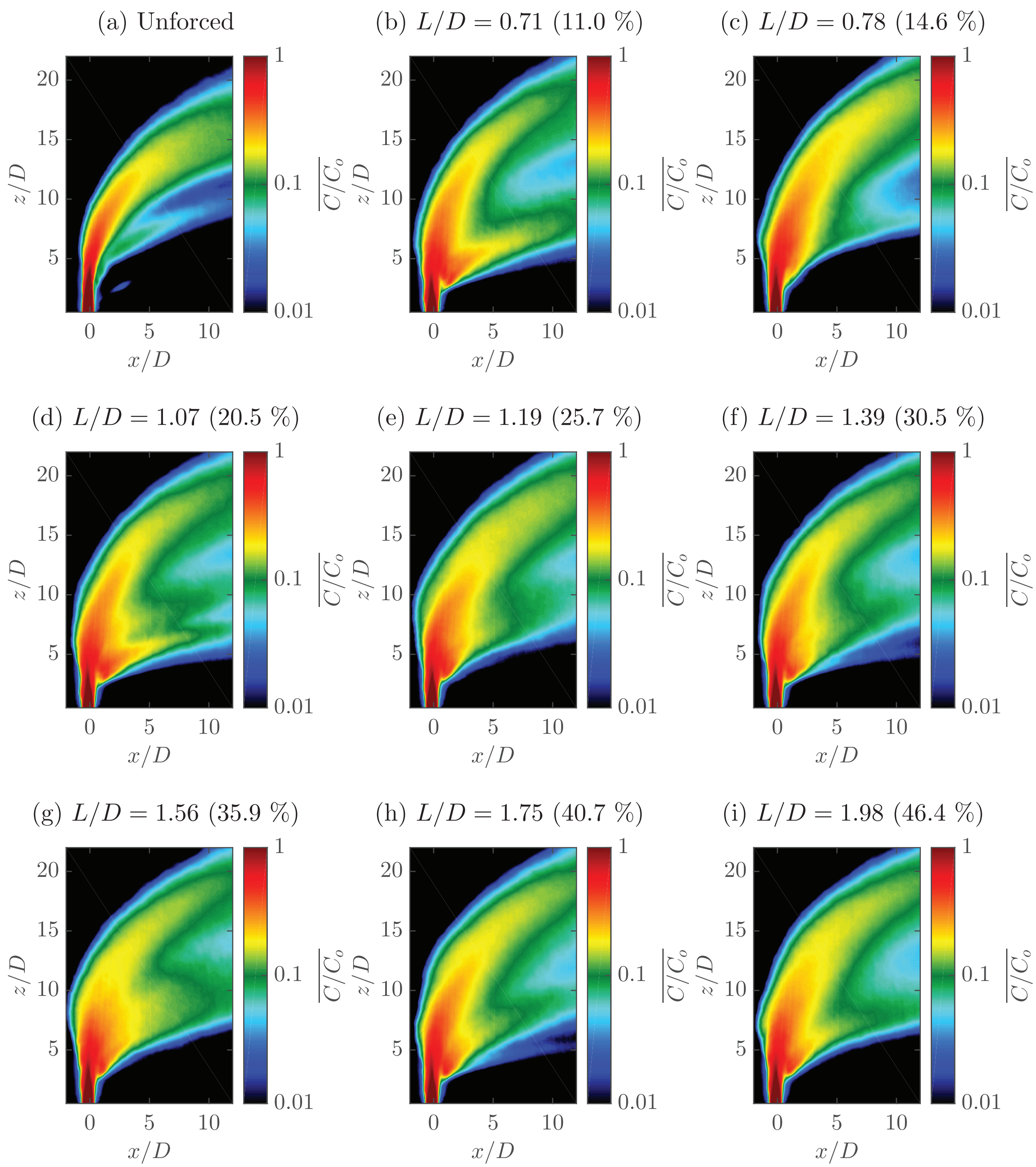

Figure C.14: For more figures and caption see next page.

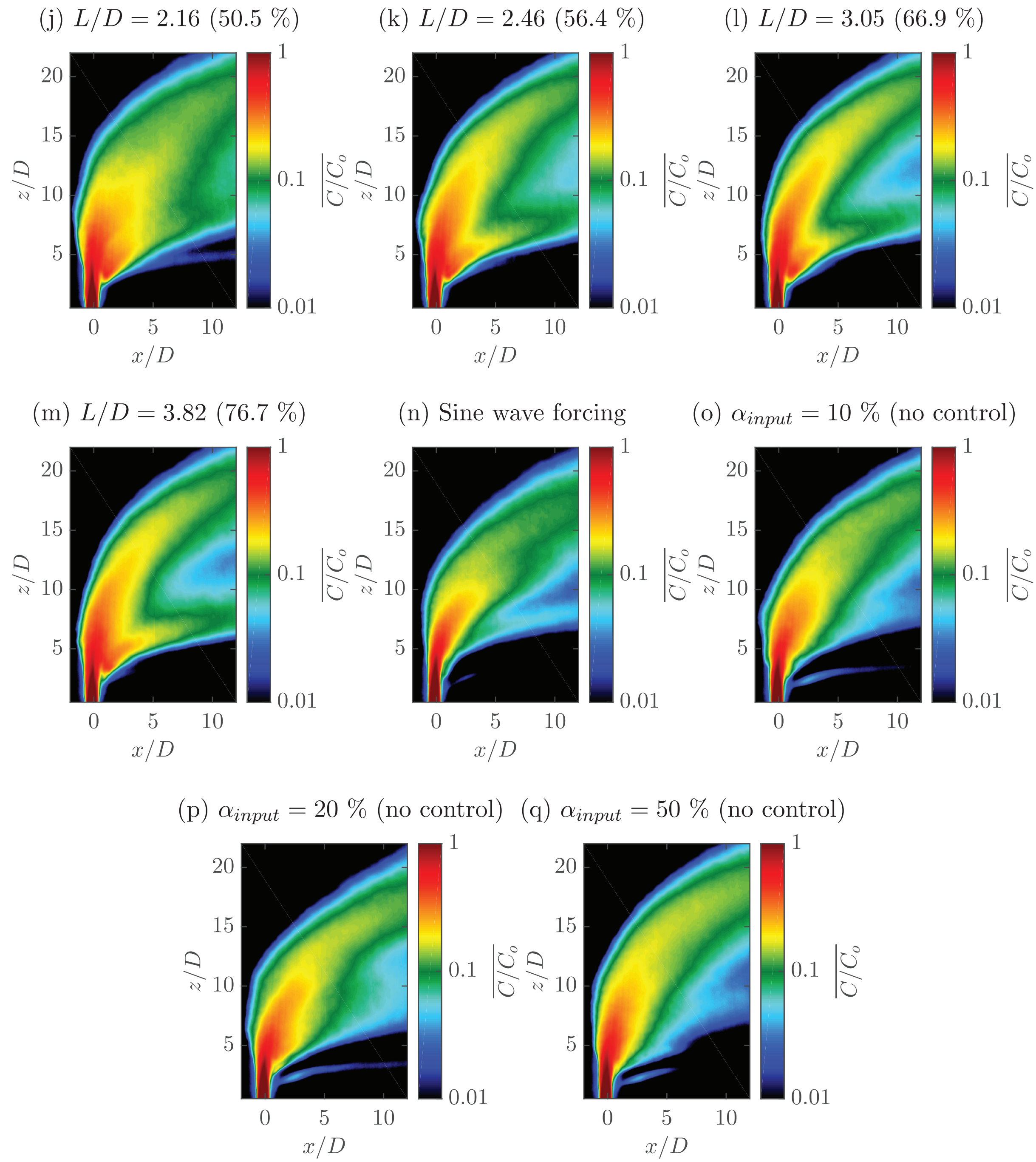

Figure C.14: Mean centerplane PLIF images in the $x/D - z/D$ plane for the equidensity flush nozzle-injected JICF at $J = 41$ for (a) the unforced case, (b)-(m) the forced cases under single-pulse square wave forcing with control at stroke ratios ranging $L/D = 0.71 - 3.82$ (actual duty cycle α_{actual} (%) in parentheses), (n) under sine wave forcing, as well as (o)-(q) under single-pulse square wave forcing without control at $\alpha_{input} = 10 - 50$ %. All forcing conditions are at $f_f = 100$ Hz and $U'_{j,rms} = 1.0$ m/s (approximately 15 % of U_j).

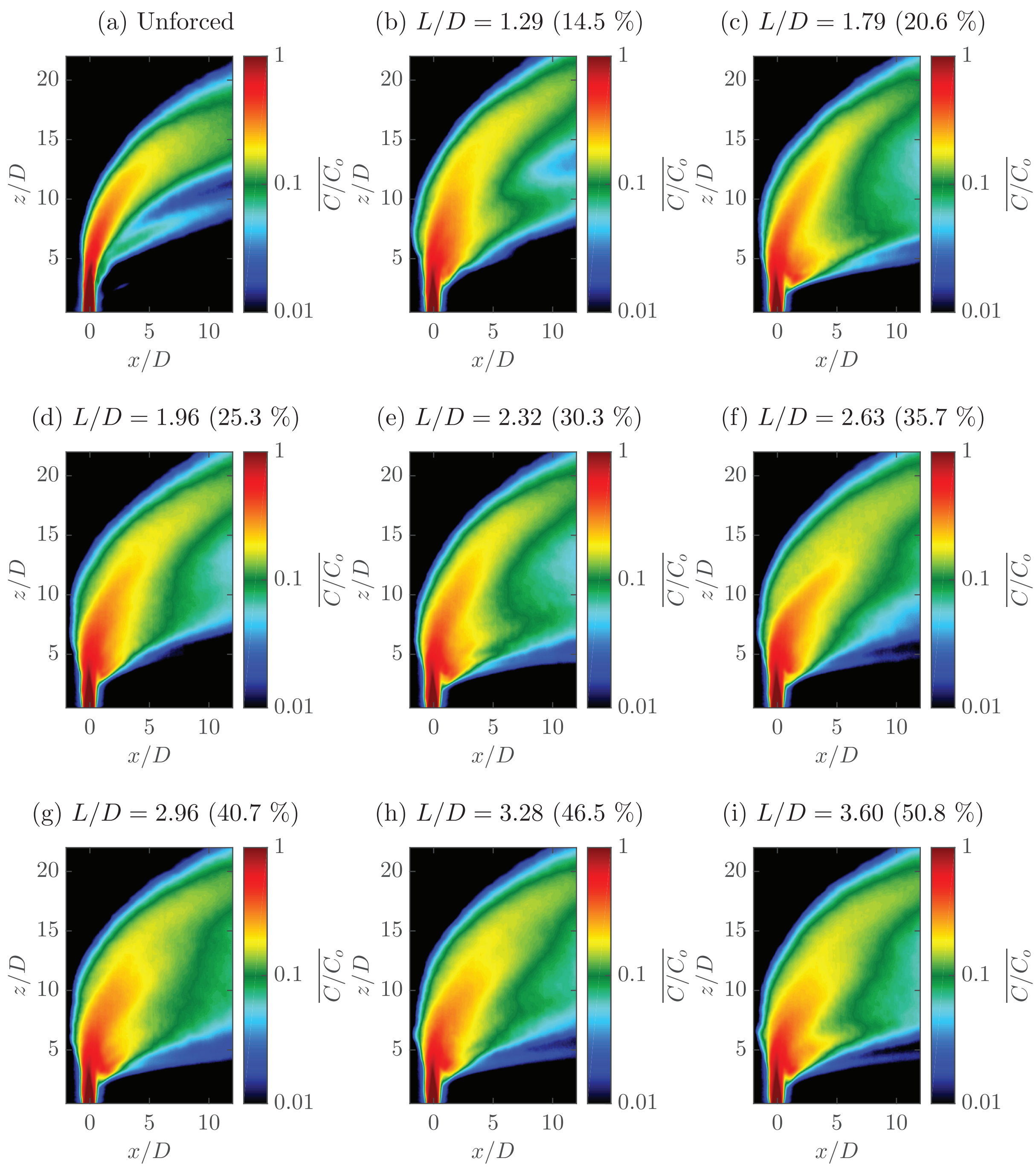

Figure C.15: For more figures and caption see next page.

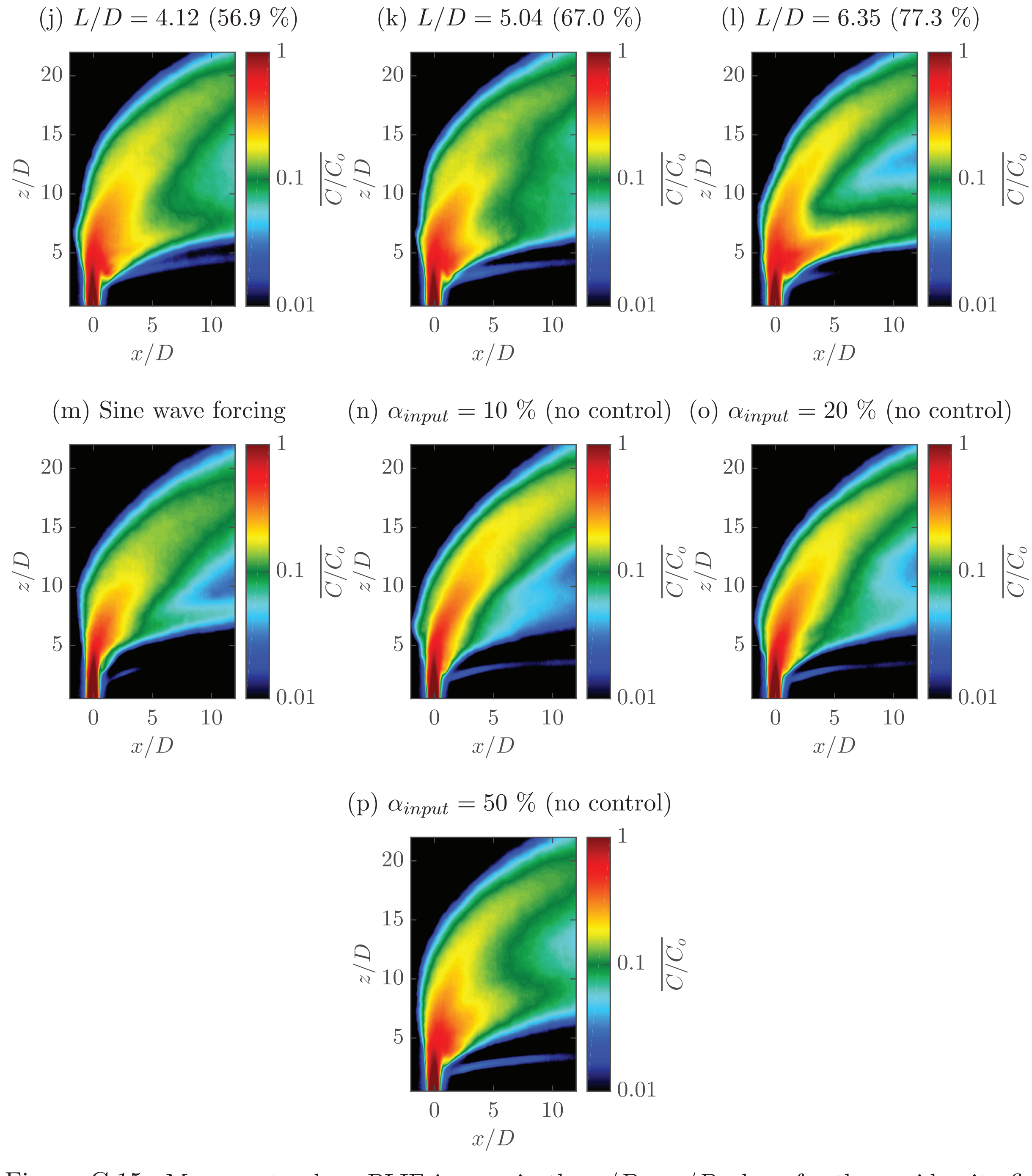

Figure C.15: Mean centerplane PLIF images in the $x/D - z/D$ plane for the equidensity flush nozzle-injected JICF at $J = 41$ for (a) the unforced case, (b)-(l) the forced cases under single-pulse square wave forcing with control at stroke ratios ranging $L/D = 1.29 - 6.35$ (actual duty cycle α_{actual} (%) in parentheses), (m) under sine wave forcing, as well as (n)-(p) under single-pulse square wave forcing without control at $\alpha_{input} = 10 - 50$ %. All forcing conditions are at $f_f = 100$ Hz and $U'_{j,rms} = 1.7$ m/s (approximately 26 % of U_j).

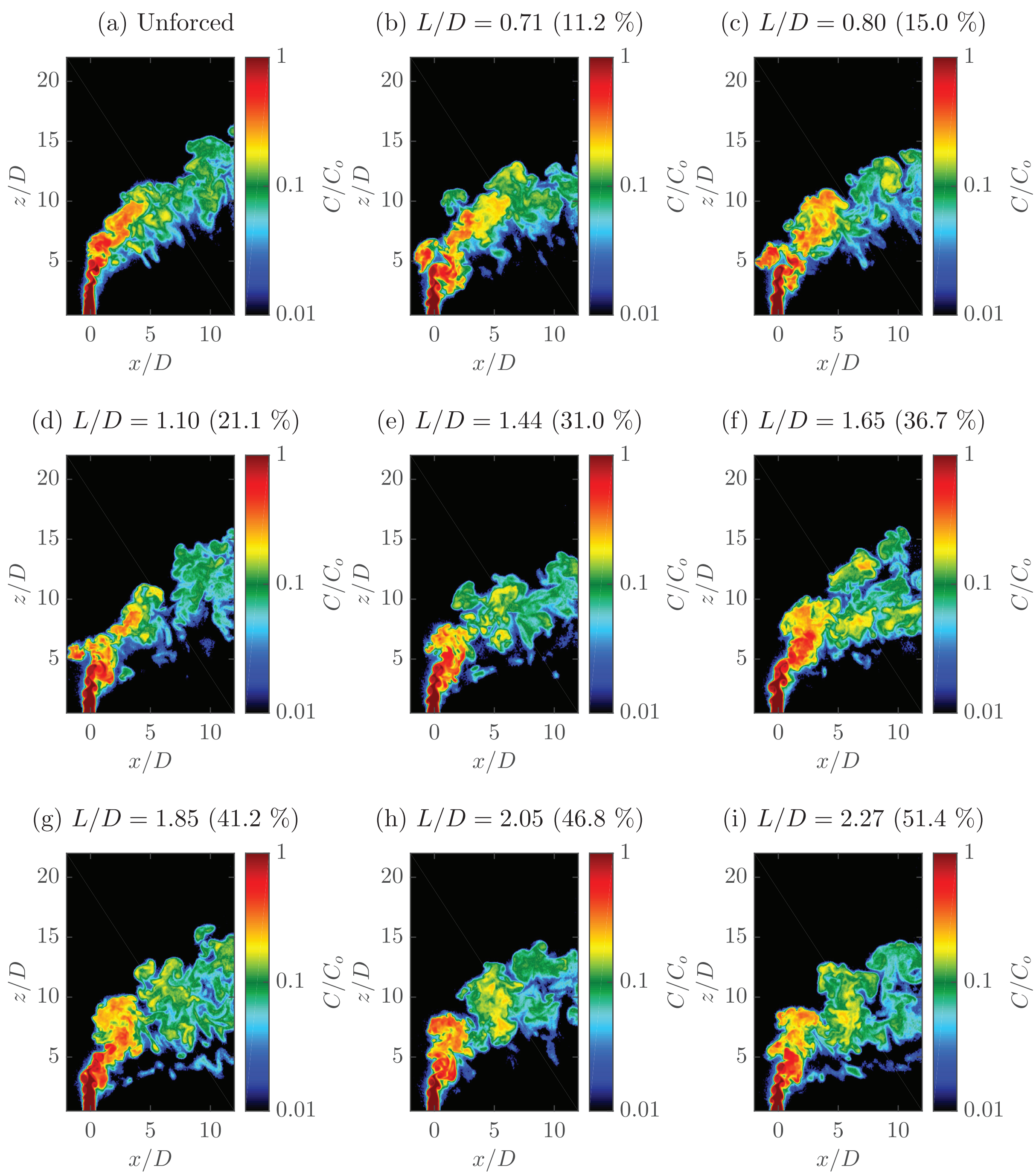

Figure C.16: For more figures and caption see next page.

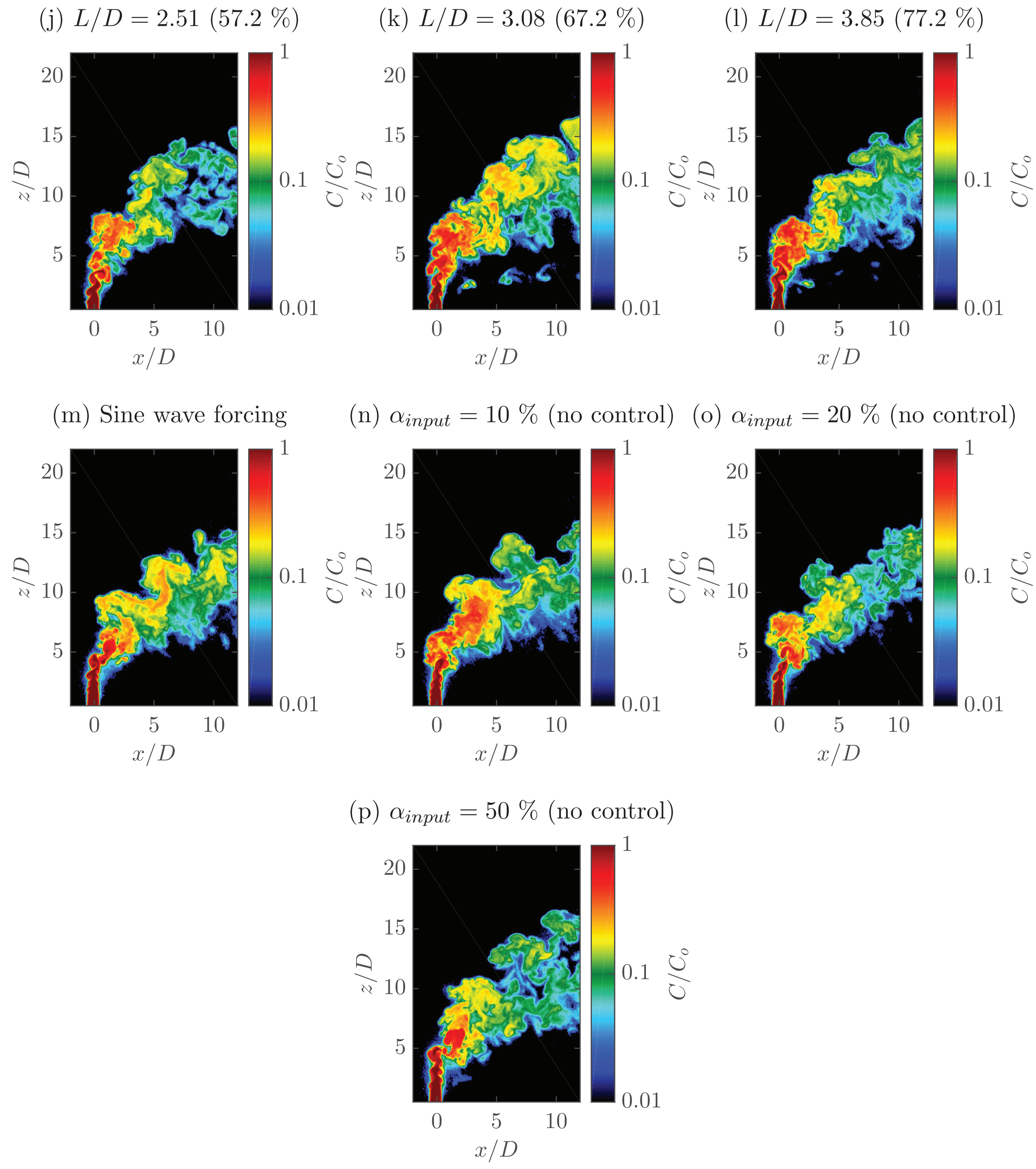

Figure C.16: Instantaneous centerplane PLIF images in the $x/D - z/D$ plane for the equidensity flush nozzle-injected JICF at $J = 20$ for (a) the unforced case, (b)-(l) the forced cases under single-pulse square wave forcing with control at stroke ratios ranging $L/D = 0.71 - 3.85$ (actual duty cycle α_{actual} (%) in parentheses), (m) under sine wave forcing, as well as (n)-(p) under single-pulse square wave forcing without control at $\alpha_{input} = 10 - 50$ %. All forcing conditions are at $f_f = 100$ Hz and $U'_{j,rms} = 1.0$ m/s (approximately 15 % of U_j).

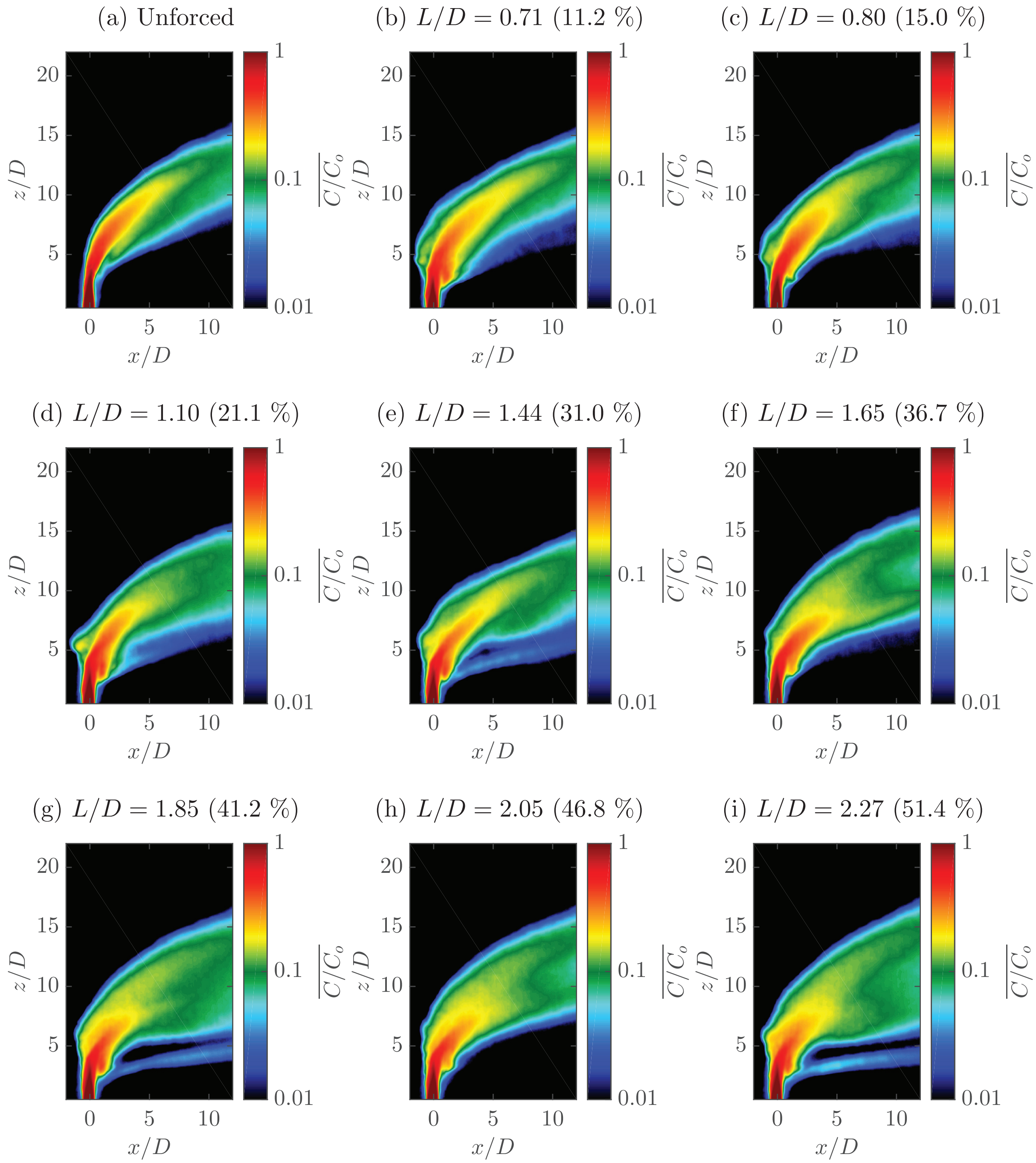

Figure C.17: For more figures and caption see next page.

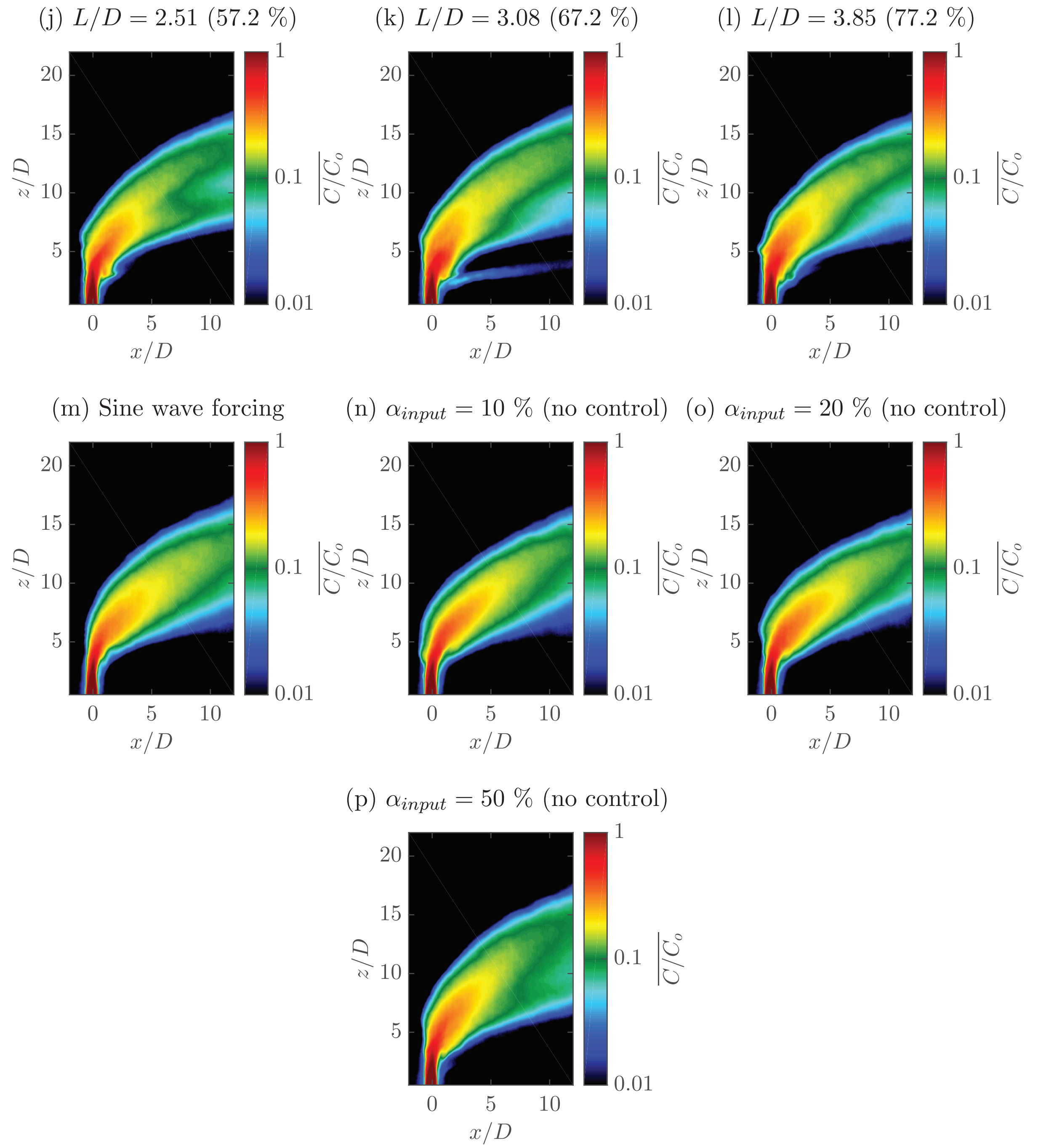

Figure C.17: Mean centerplane PLIF images in the $x/D - z/D$ plane for the equidensity flush nozzle-injected JICF at $J = 20$ for (a) the unforced case, (b)-(l) the forced cases under single-pulse square wave forcing with control at stroke ratios ranging $L/D = 0.71 - 3.85$ (actual duty cycle α_{actual} (%) in parentheses), (m) under sine wave forcing, as well as (n)-(p) under single-pulse square wave forcing without control at $\alpha_{input} = 10 - 50$ %. All forcing conditions are at $f_f = 100$ Hz and $U'_{j,rms} = 1.0$ m/s (approximately 15 % of U_j).

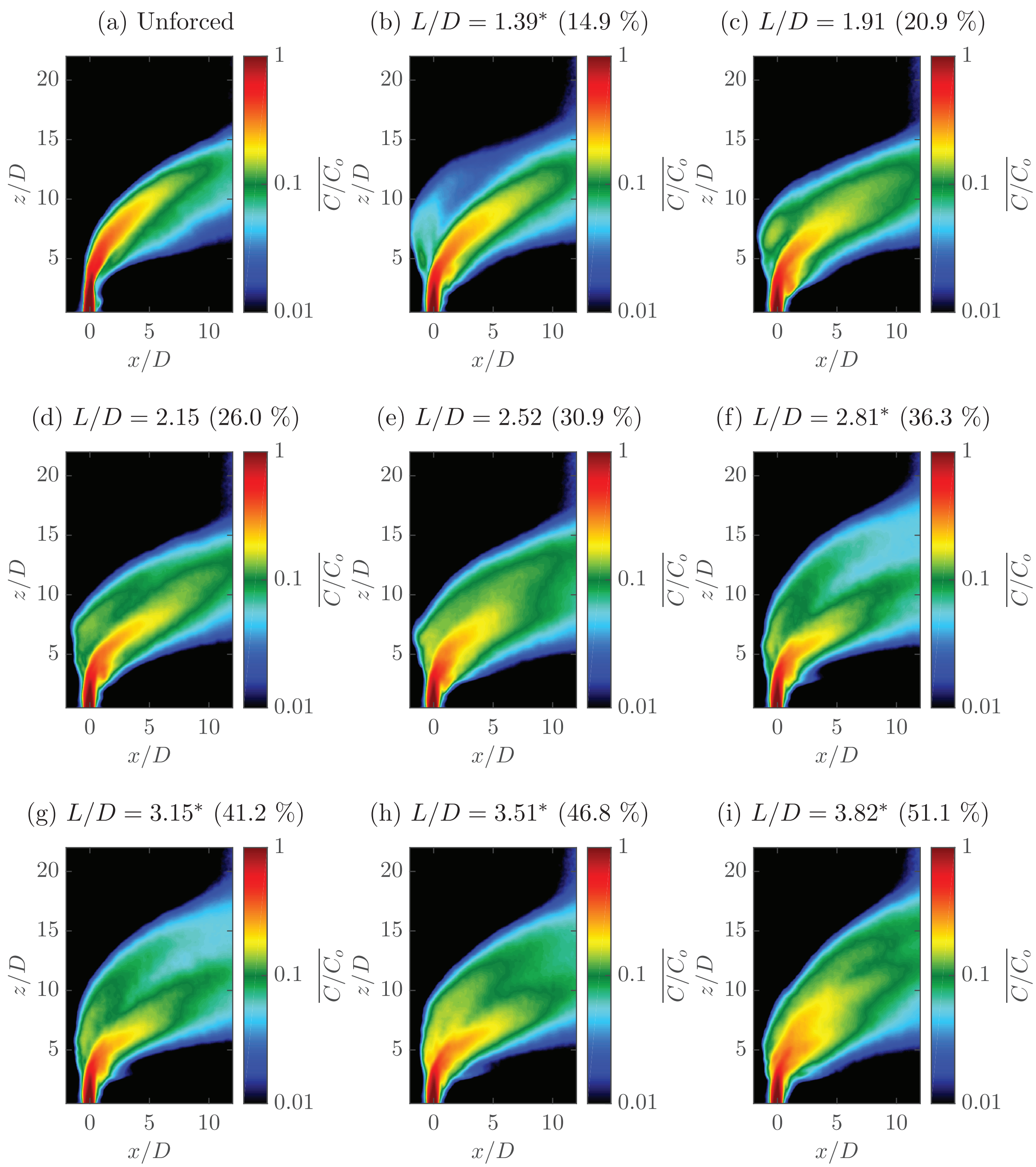

Figure C.18: For more figures and caption see next page.

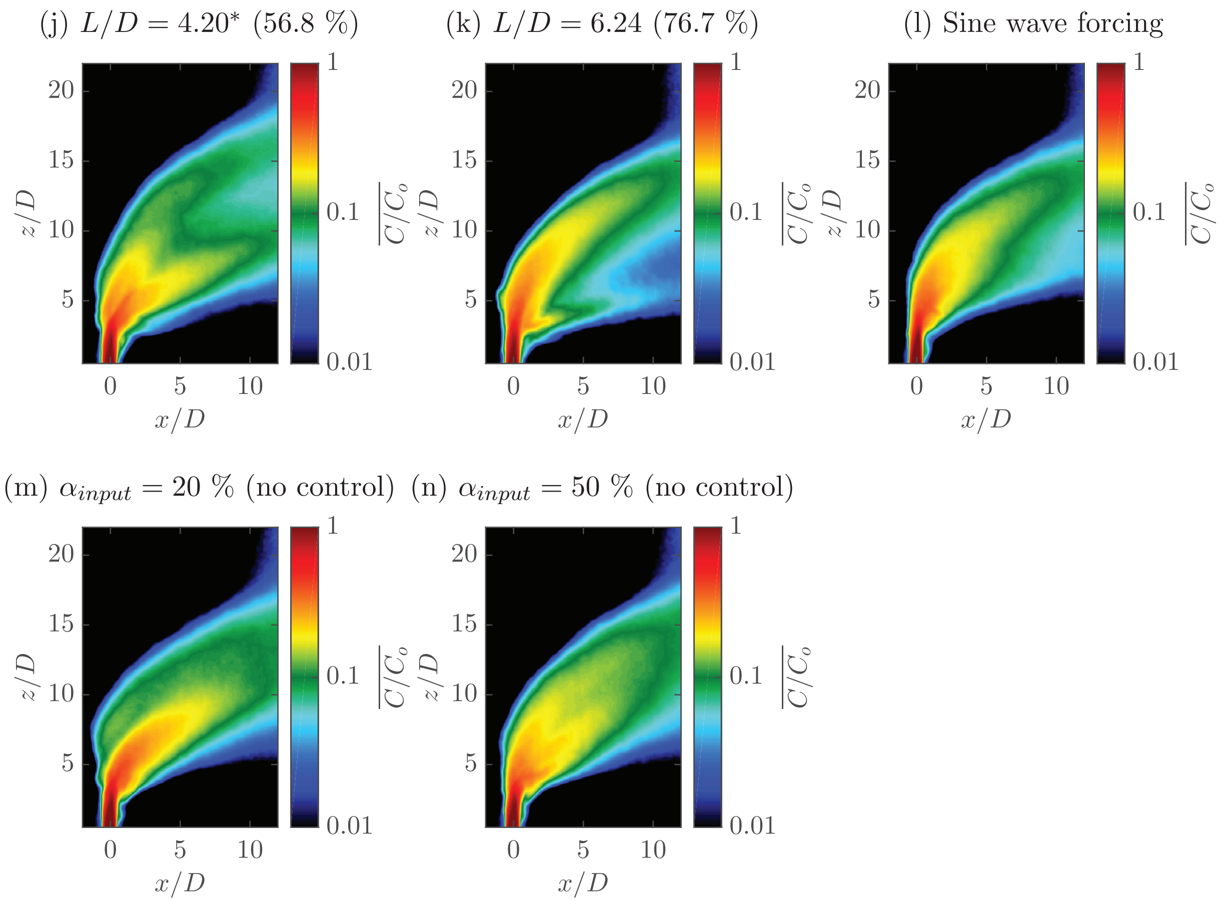

Figure C.18: Mean centerplane PLIF images in the $x/D - z/D$ plane for the equidensity flush nozzle-injected JICF at $J = 20$ for (a) the unforced case, (b)-(k) the forced cases under single-pulse square wave forcing with control at stroke ratios ranging $L/D = 1.39 - 6.24$ (actual duty cycle α_{actual} (%) in parentheses), (l) under sine wave forcing, as well as (m)-(n) under single-pulse square wave forcing without control at $\alpha_{input} = 20 - 50$ %. All forcing conditions are at $f_f = 100$ Hz and $U'_{j,rms} = 1.7$ m/s (approximately 26 % of U_j).

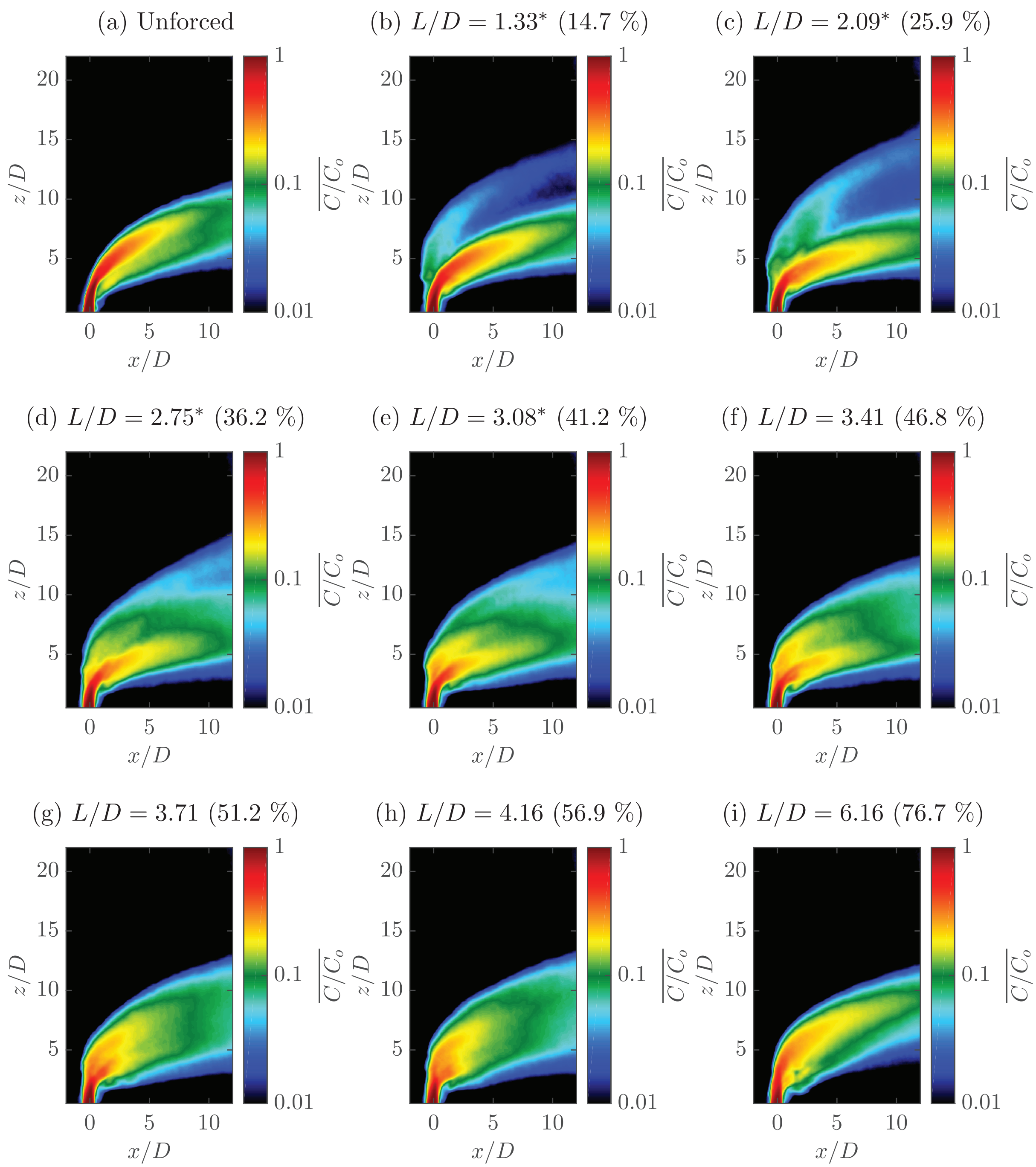

Figure C.19: For more figures and caption see next page.

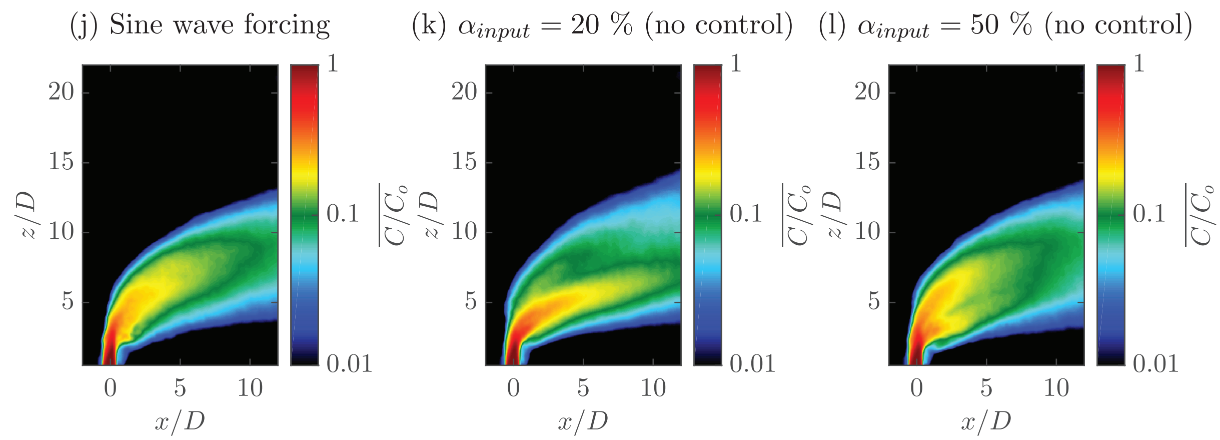

Figure C.19: Mean centerplane PLIF images in the $x/D - z/D$ plane for the equidensity flush nozzle-injected JICF at $J = 10$ for (a) the unforced case, (b)-(i) the forced cases under single-pulse square wave forcing with control at stroke ratios ranging $L/D = 1.33 - 6.16$ (actual duty cycle α_{actual} (%) in parentheses), (j) under sine wave forcing, as well as (k)-(l) under single-pulse square wave forcing without control at $\alpha_{input} = 20 - 50$ %. All forcing conditions are at $f_f = 100$ Hz and $U'_{j,rms} = 1.7$ m/s (approximately 26 % of U_j).

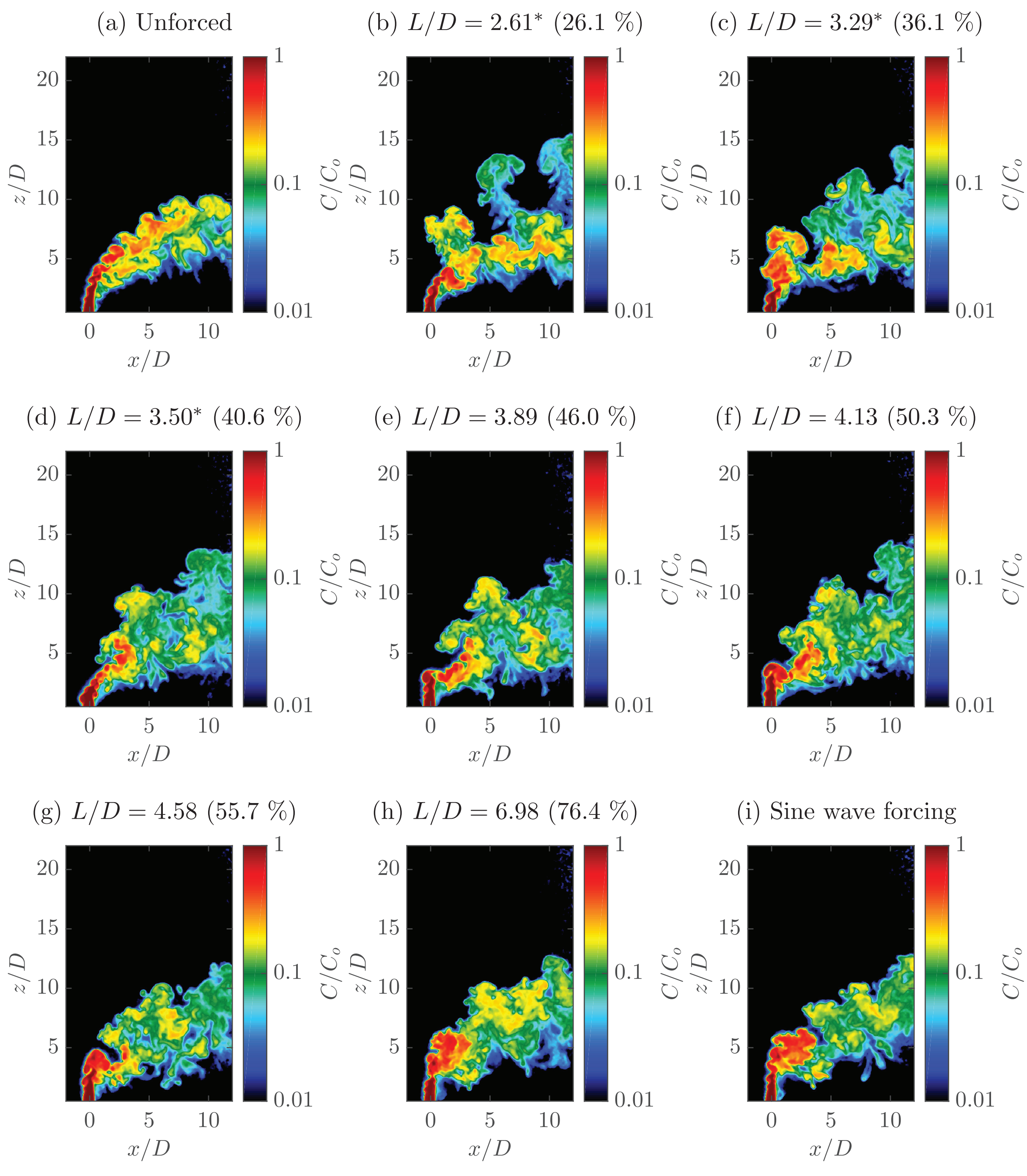

Figure C.20: For more figures and caption see next page.

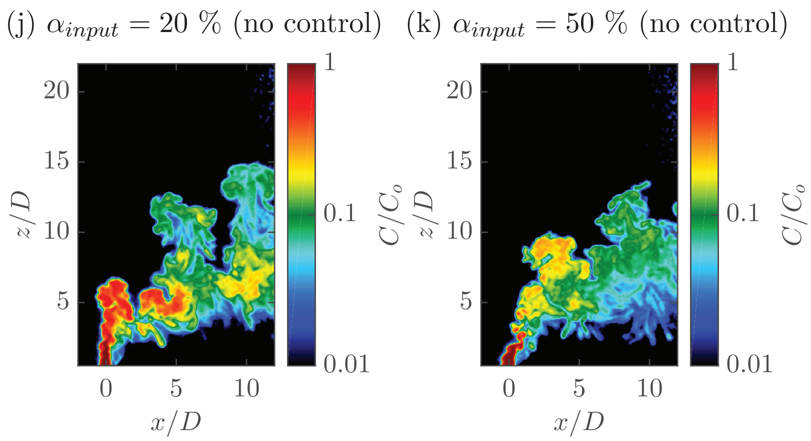

Figure C.20: Instantaneous centerplane PLIF images in the $x/D - z/D$ plane for the equidensity flush nozzle-injected JICF at $J = 10$ for (a) the unforced case, (b)-(h) the forced cases under single-pulse square wave forcing with control at stroke ratios ranging $L/D = 2.61 - 6.98$ (actual duty cycle α_{actual} (%) in parentheses), (i) under sine wave forcing, as well as (j)-(k) under single-pulse square wave forcing without control at $\alpha_{input} = 20 - 50$ %. All forcing conditions are at $f_f = 100$ Hz and $U'_{j,rms} = 2.0$ m/s (approximately 31 % of U_j).

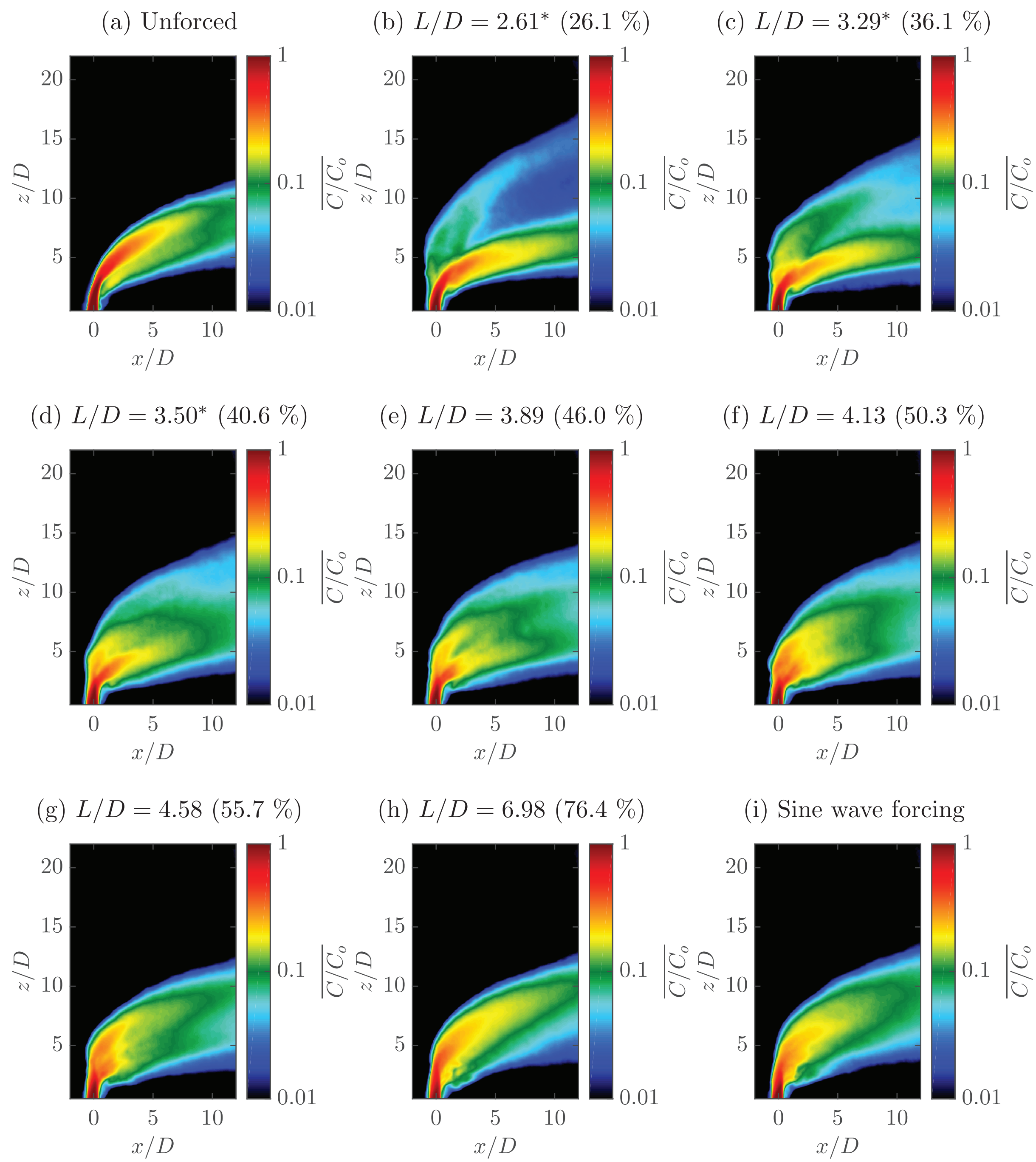

Figure C.21: For more figures and caption see next page.

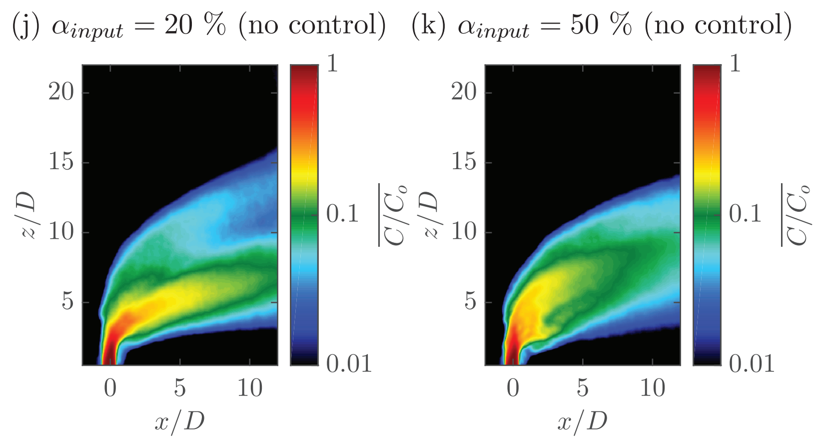

Figure C.21: Mean centerplane PLIF images in the $x/D - z/D$ plane for the equidensity flush nozzle-injected JICF at $J = 10$ for (a) the unforced case, (b)-(h) the forced cases under single-pulse square wave forcing with control at stroke ratios ranging $L/D = 2.61 - 6.98$ (actual duty cycle α_{actual} (%) in parentheses), (i) under sine wave forcing, as well as (j)-(k) under single-pulse square wave forcing without control at $\alpha_{input} = 20 - 50$ %. All forcing conditions are at $f_f = 100$ Hz and $U'_{j,rms} = 2.0$ m/s (approximately 31 % of U_j).

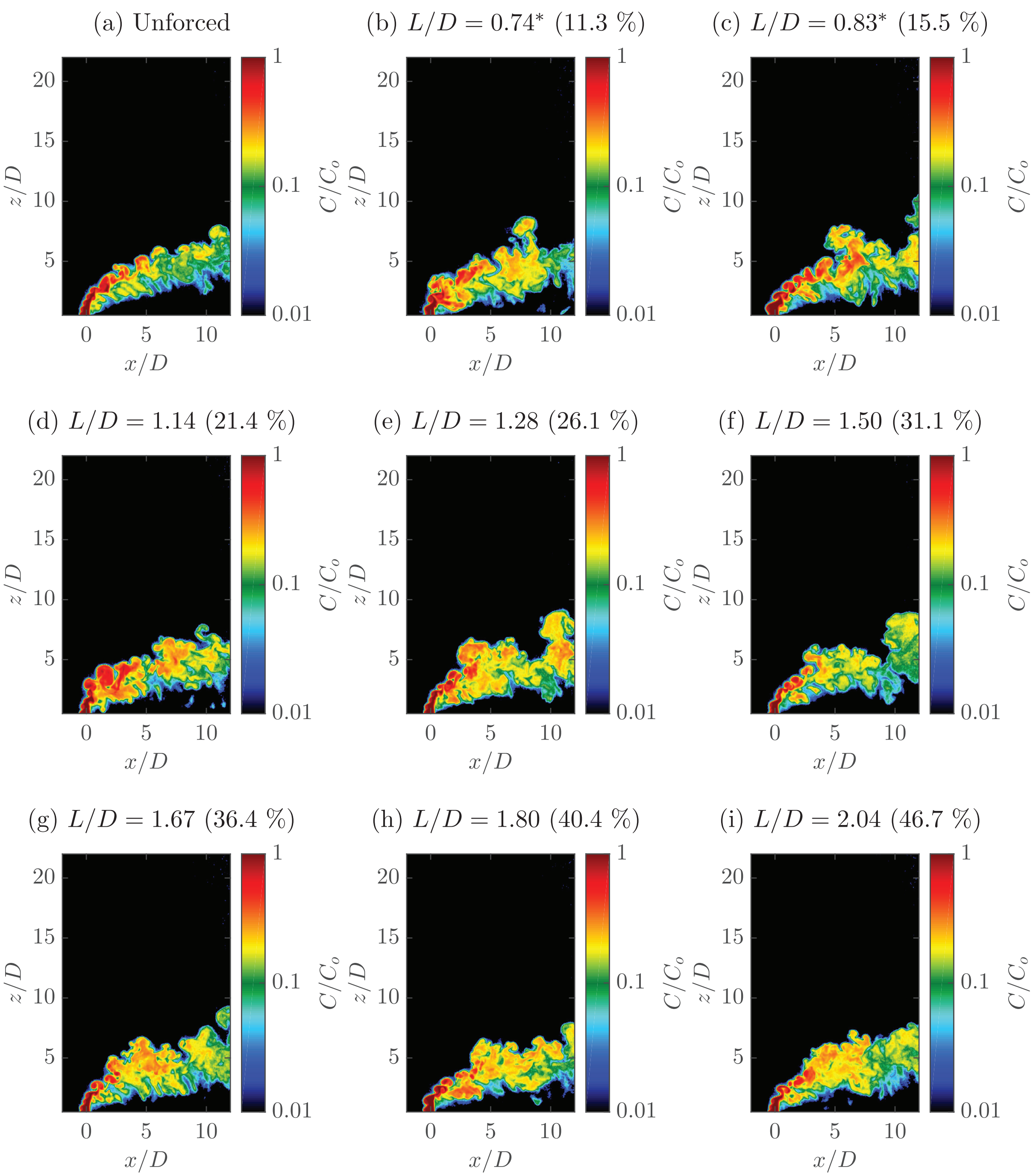

Figure C.22: For more figures and caption see next page.

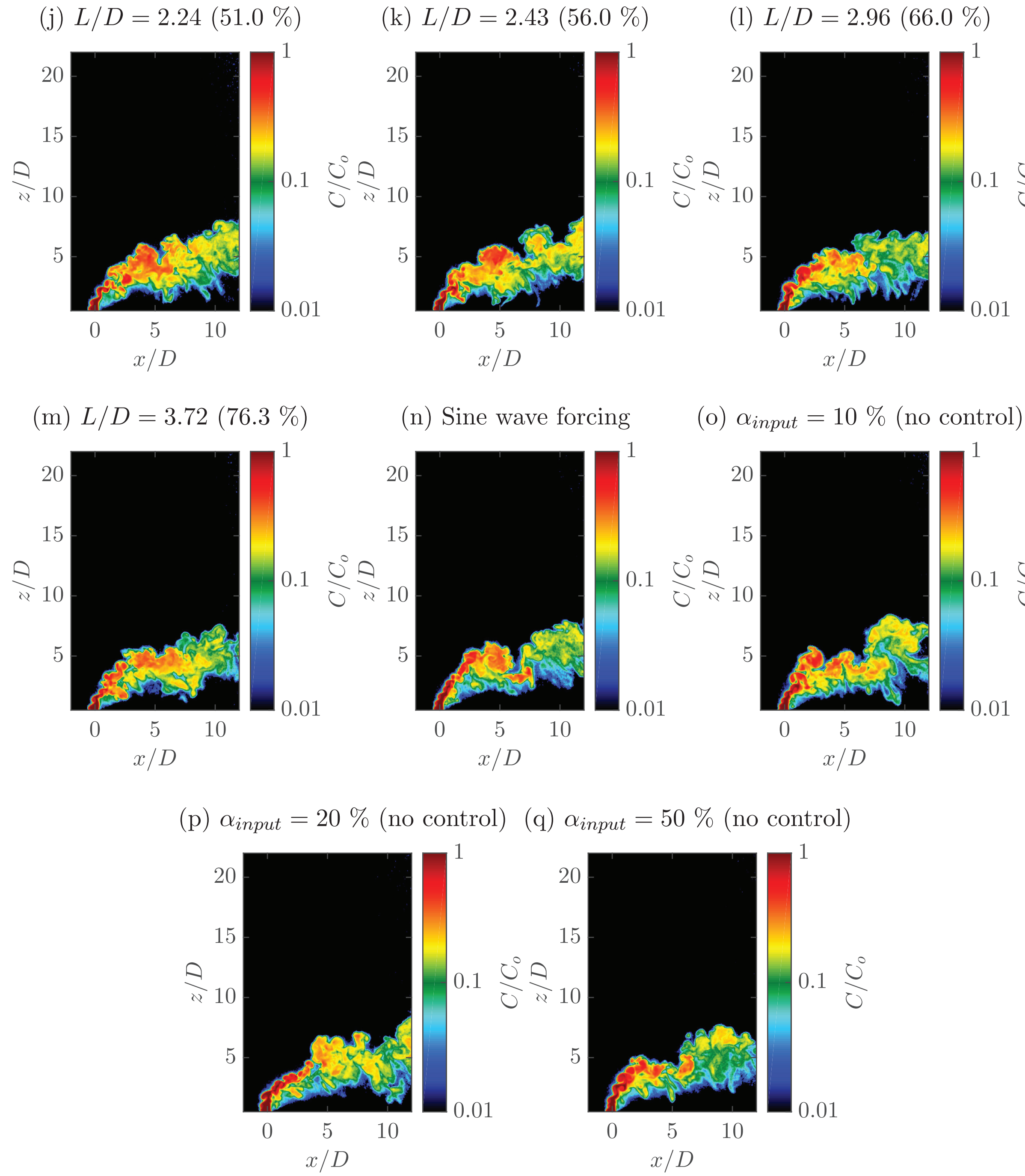

Figure C.22: Instantaneous centerplane PLIF images in the $x/D - z/D$ plane for the equidensity flush nozzle-injected JICF at $J = 5$ for (a) the unforced case, (b)-(m) the forced cases under single-pulse square wave forcing with control at stroke ratios ranging $L/D = 0.74 - 3.72$ (actual duty cycle α_{actual} (%) in parentheses), (n) under sine wave forcing, as well as (o)-(q) under single-pulse square wave forcing without control at $\alpha_{input} = 10 - 50$ %. All forcing conditions are at $f_f = 100$ Hz and $U'_{j,rms} = 1.0$ m/s (approximately 15 % of U_j).

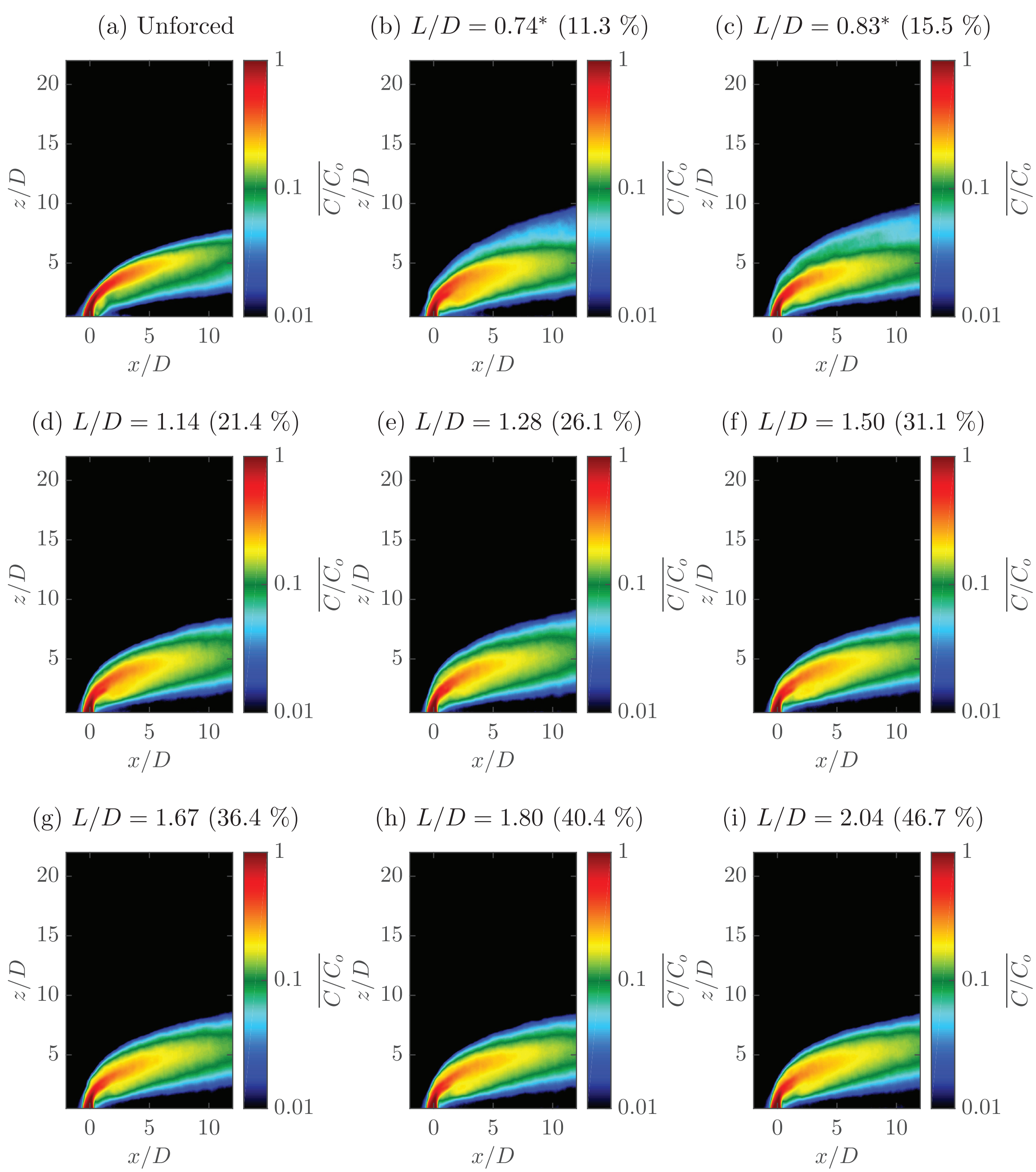

Figure C.23: For more figures and caption see next page.

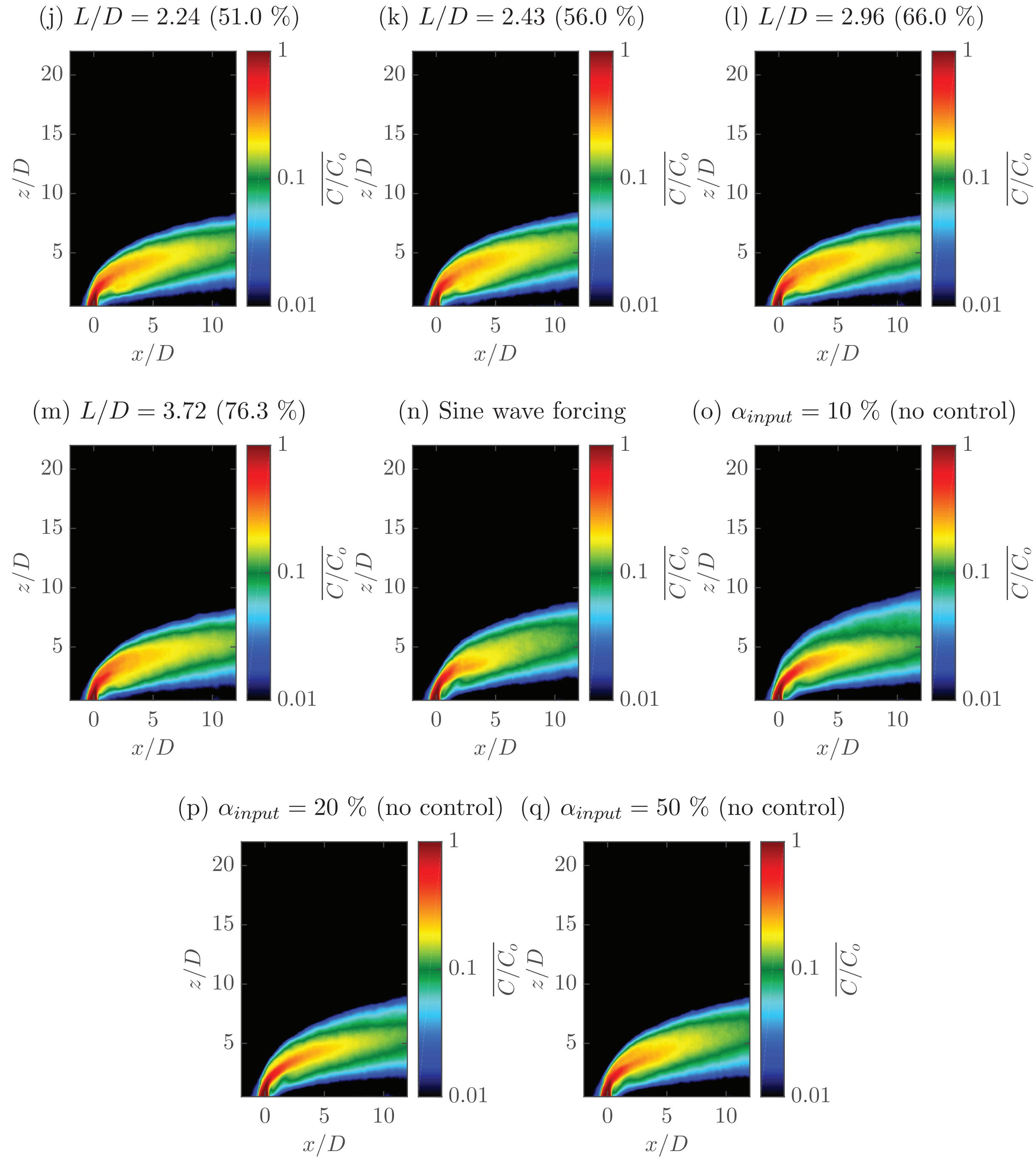

Figure C.23: Mean centerplane PLIF images in the $x/D - z/D$ plane for the equidensity flush nozzle-injected JICF at $J = 5$ for (a) the unforced case, (b)-(m) the forced cases under single-pulse square wave forcing with control at stroke ratios ranging $L/D = 0.74 - 3.72$ (actual duty cycle α_{actual} (%) in parentheses), (n) under sine wave forcing, as well as (o)-(q) under single-pulse square wave forcing without control at $\alpha_{input} = 10 - 50$ %. All forcing conditions are at $f_f = 100$ Hz and $U'_{j,rms} = 1.0$ m/s (approximately 15 % of U_j).

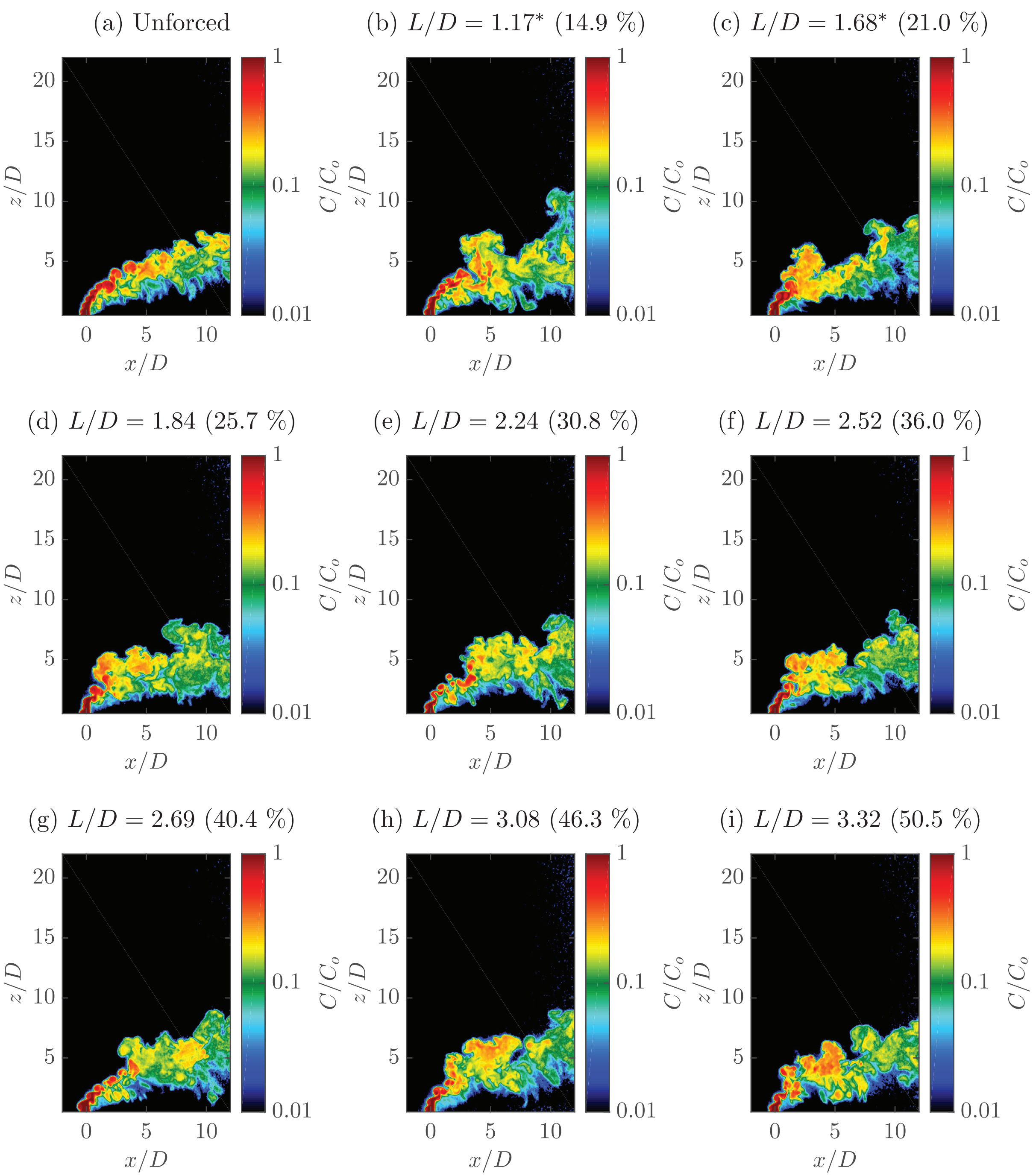

Figure C.24: For more figures and caption see next page.

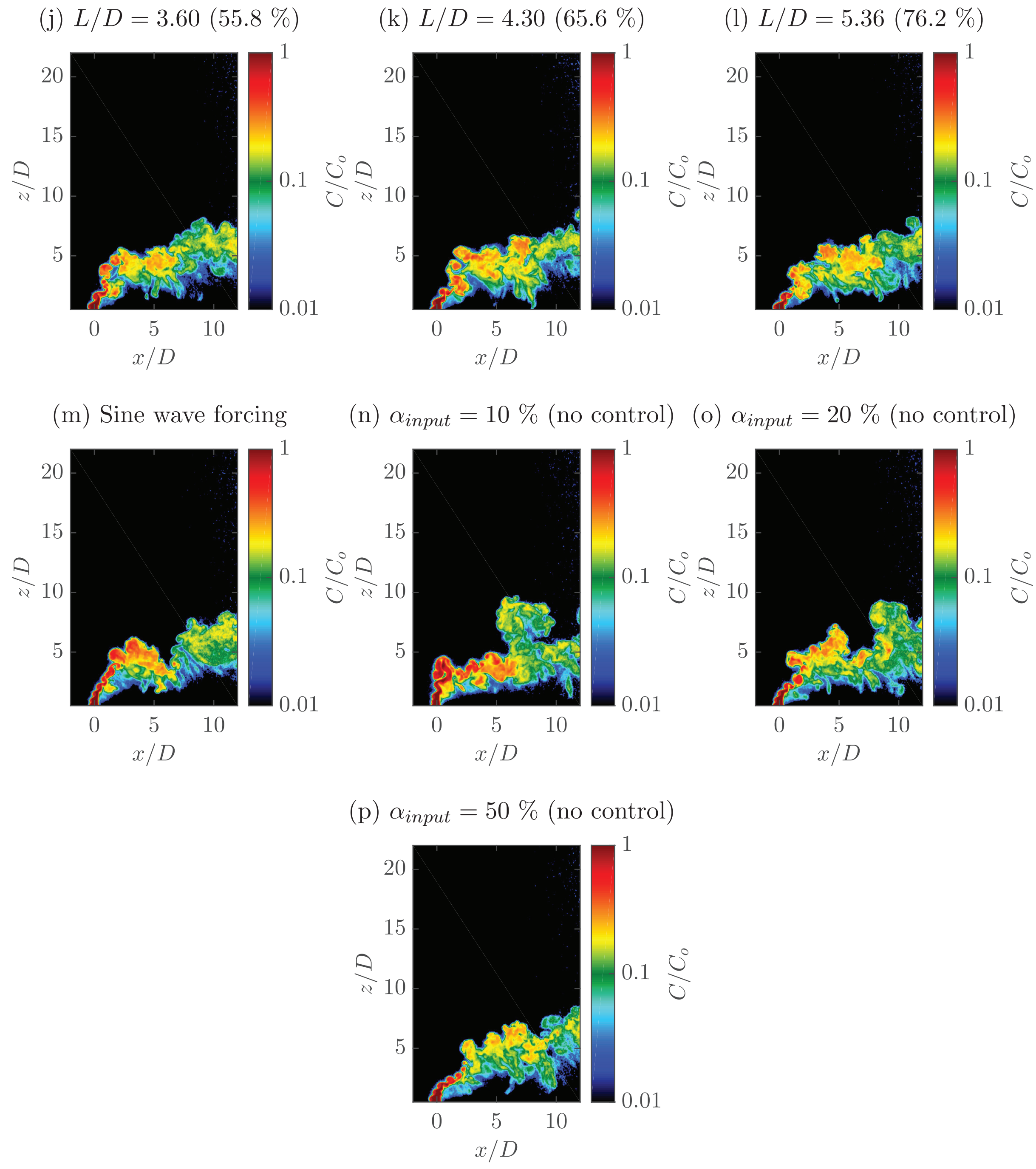

Figure C.24: Instantaneous centerplane PLIF images in the $x/D - z/D$ plane for the equidensity flush nozzle-injected JICF at $J = 5$ for (a) the unforced case, (b)-(l) the forced cases under single-pulse square wave forcing with control at stroke ratios ranging $L/D = 1.17 - 5.36$ (actual duty cycle α_{actual} (%) in parentheses), (m) under sine wave forcing, as well as (n)-(p) under single-pulse square wave forcing without control at $\alpha_{input} = 10 - 50$ %. All forcing conditions are at $f_f = 100$ Hz and $U'_{j,rms} = 1.5$ m/s (approximately 23 % of U_j).

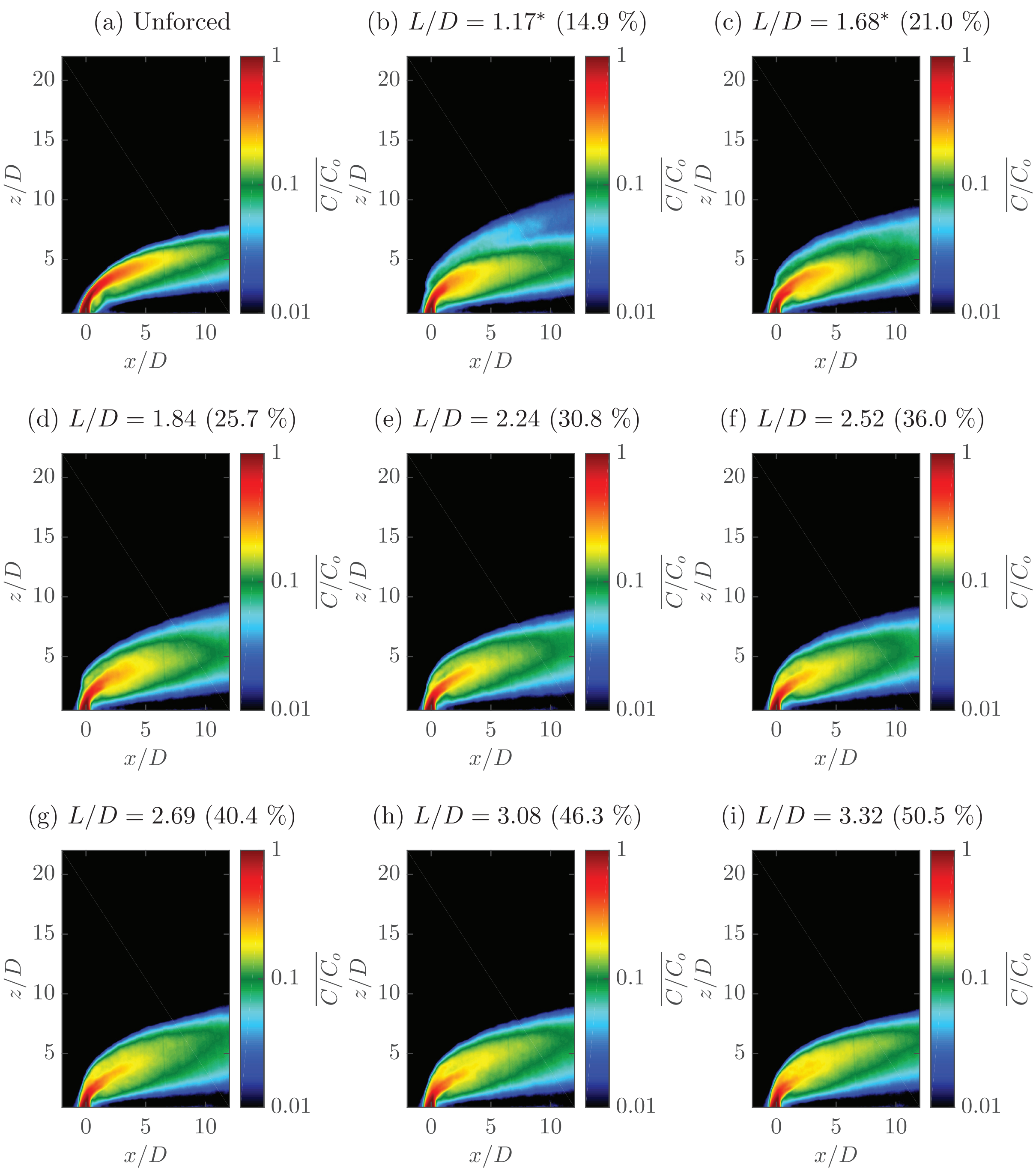

Figure C.25: For more figures and caption see next page.

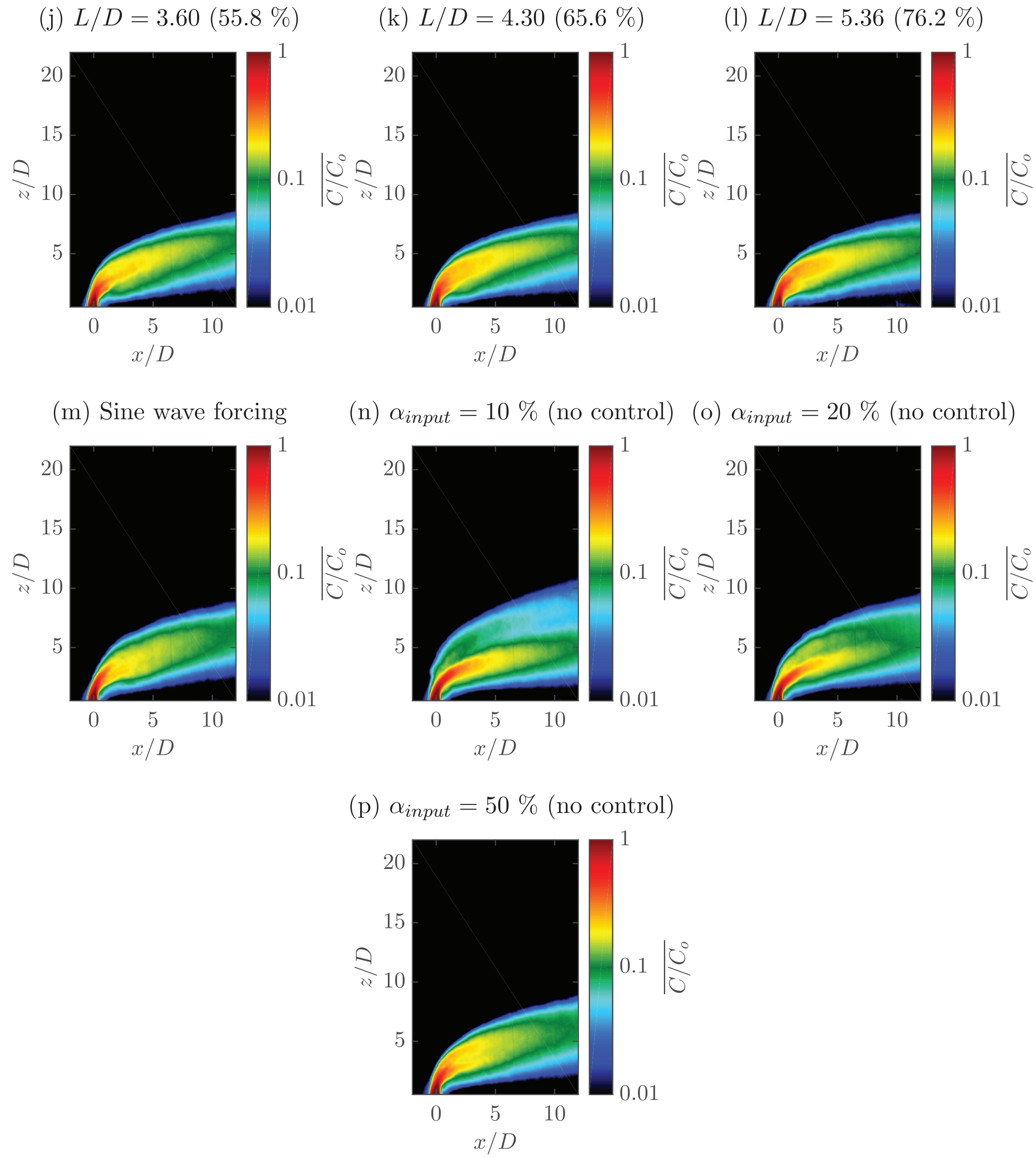

Figure C.25: Mean centerplane PLIF images in the $x/D - z/D$ plane for the equidensity flush nozzle-injected JICF at $J = 5$ for (a) the unforced case, (b)-(l) the forced cases under single-pulse square wave forcing with control at stroke ratios ranging $L/D = 1.17 - 5.36$ (actual duty cycle α_{actual} (%) in parentheses), (m) under sine wave forcing, as well as (n)-(p) under single-pulse square wave forcing without control at $\alpha_{input} = 10 - 50$ %. All forcing conditions are at $f_f = 100$ Hz and $U'_{j,rms} = 1.5$ m/s (approximately 23 % of U_j).

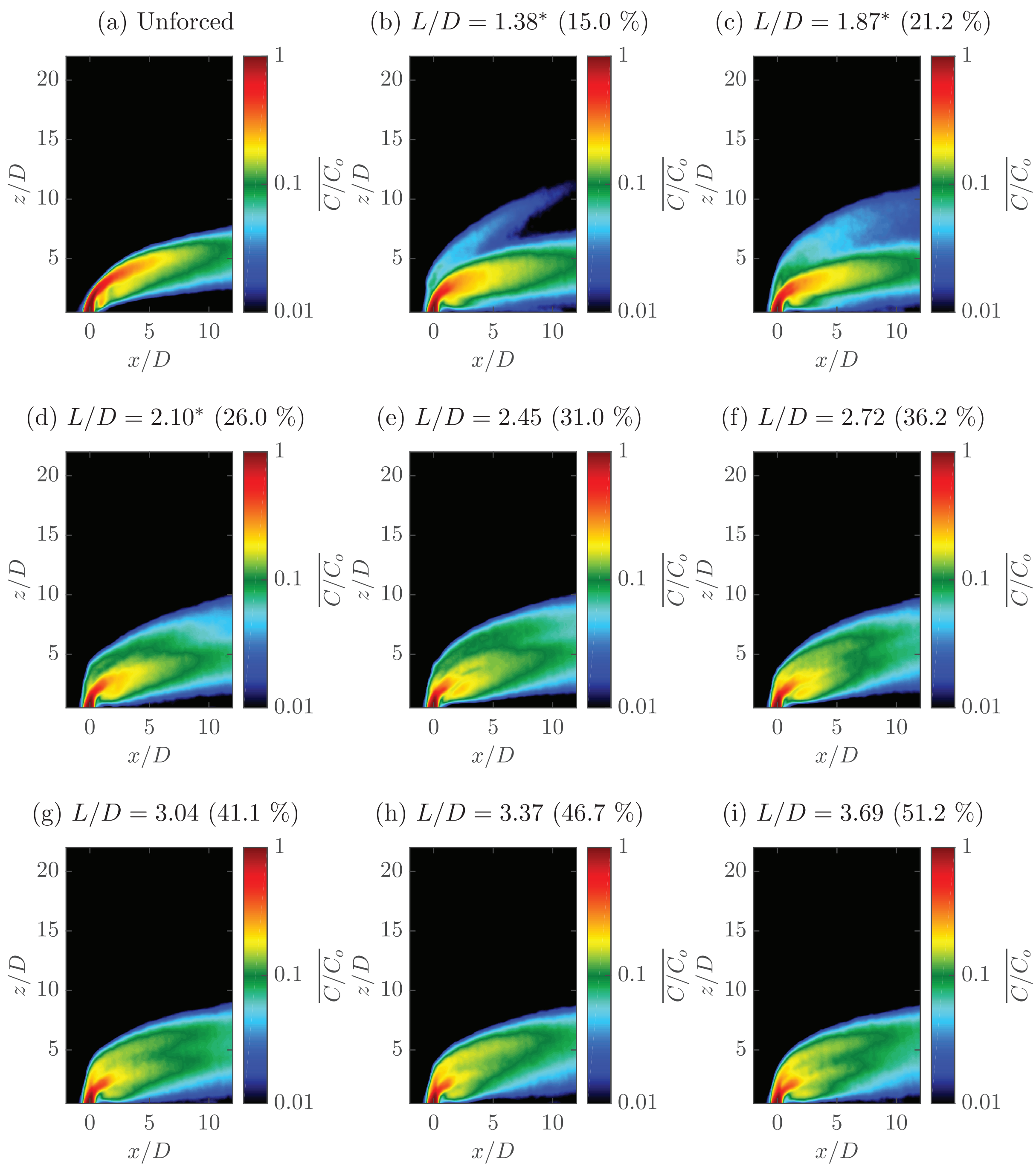

Figure C.26: For more figures and caption see next page.

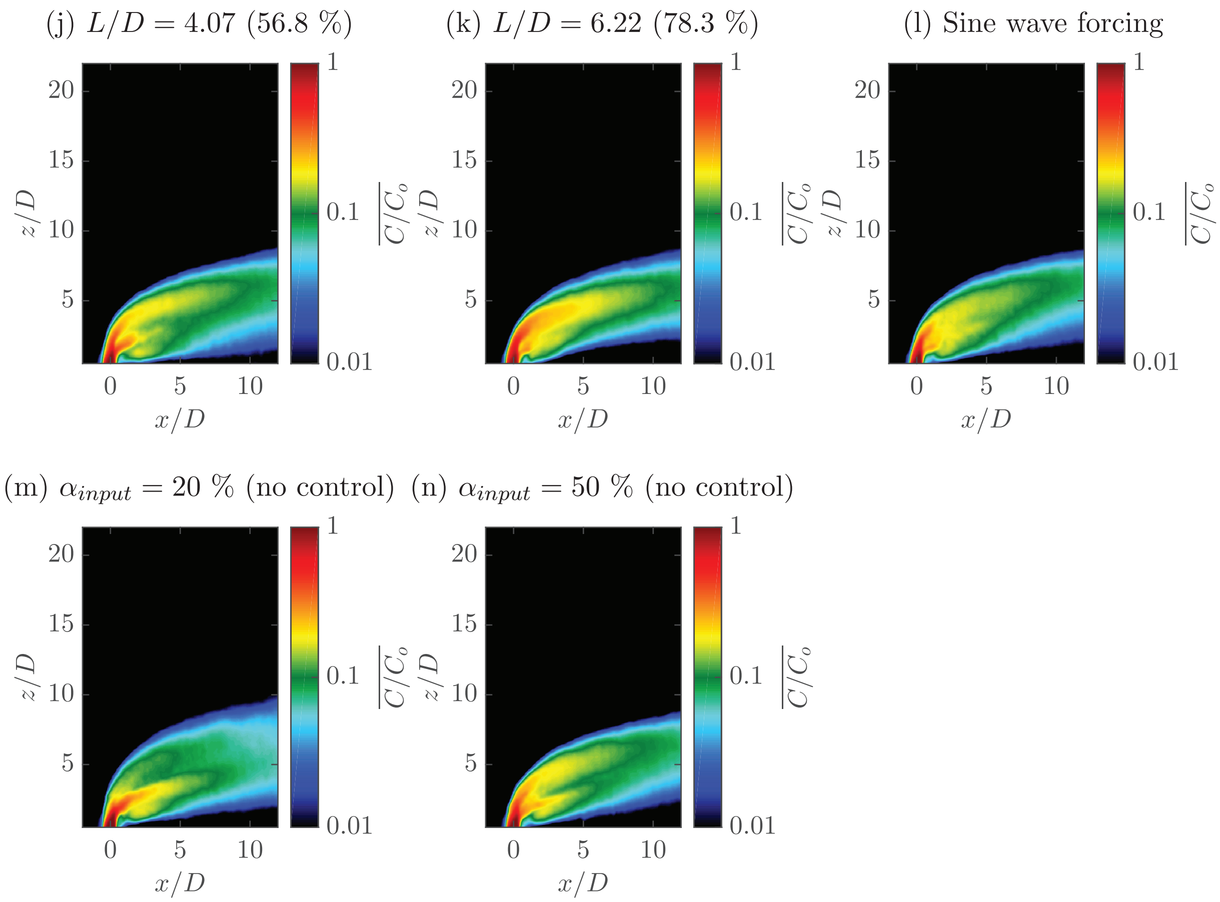

Figure C.26: Mean centerplane PLIF images in the $x/D - z/D$ plane for the equidensity flush nozzle-injected JICF at $J = 5$ for (a) the unforced case, (b)-(k) the forced cases under single-pulse square wave forcing with control at stroke ratios ranging $L/D = 1.38 - 6.22$ (actual duty cycle α_{actual} (%) in parentheses), (l) under sine wave forcing, as well as (m)-(n) under single-pulse square wave forcing without control at $\alpha_{input} = 20 - 50$ %. All forcing conditions are at $f_f = 100$ Hz and $U'_{j,rms} = 1.7$ m/s (approximately 26 % of U_j).

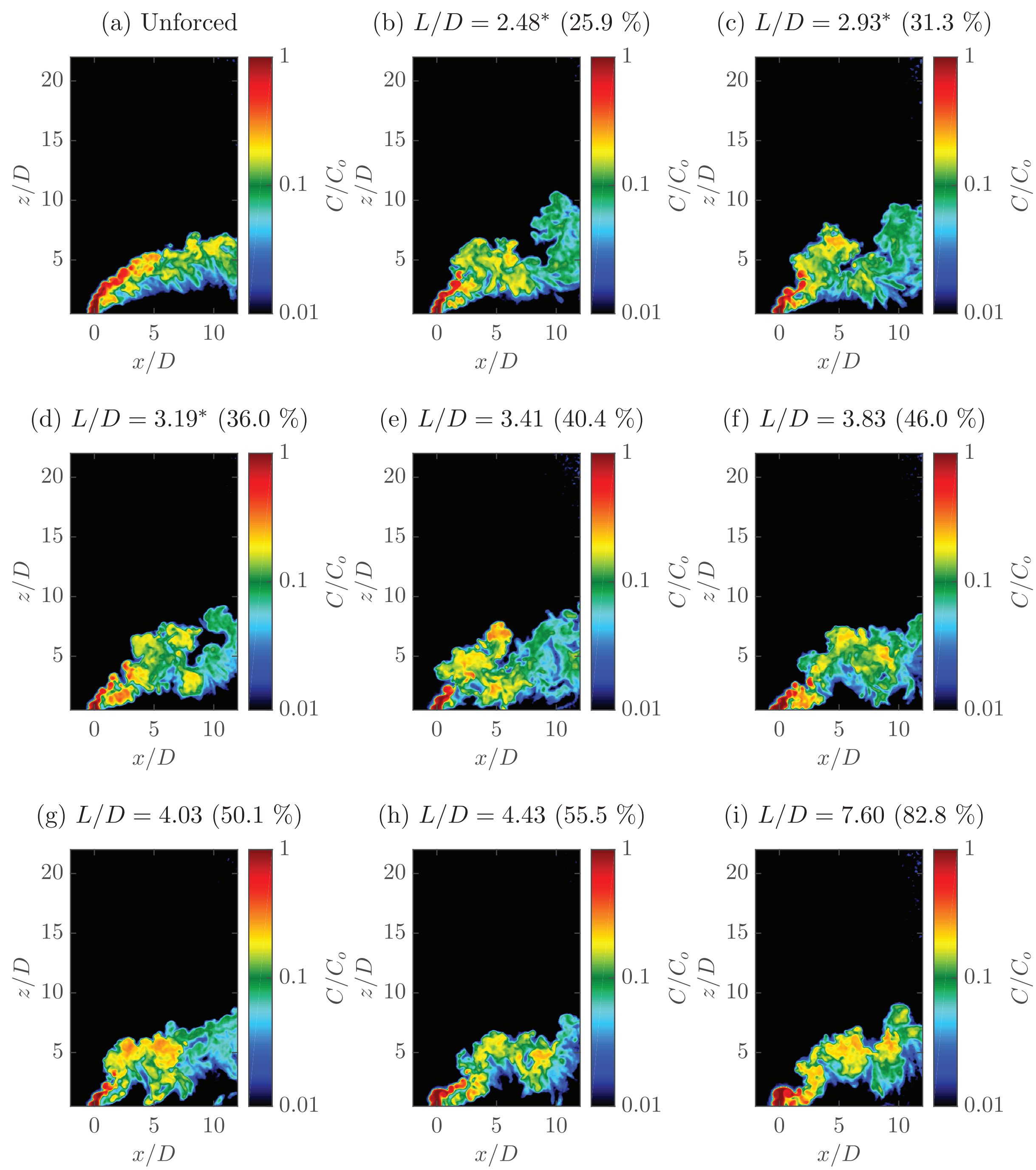

Figure C.27: For more figures and caption see next page.

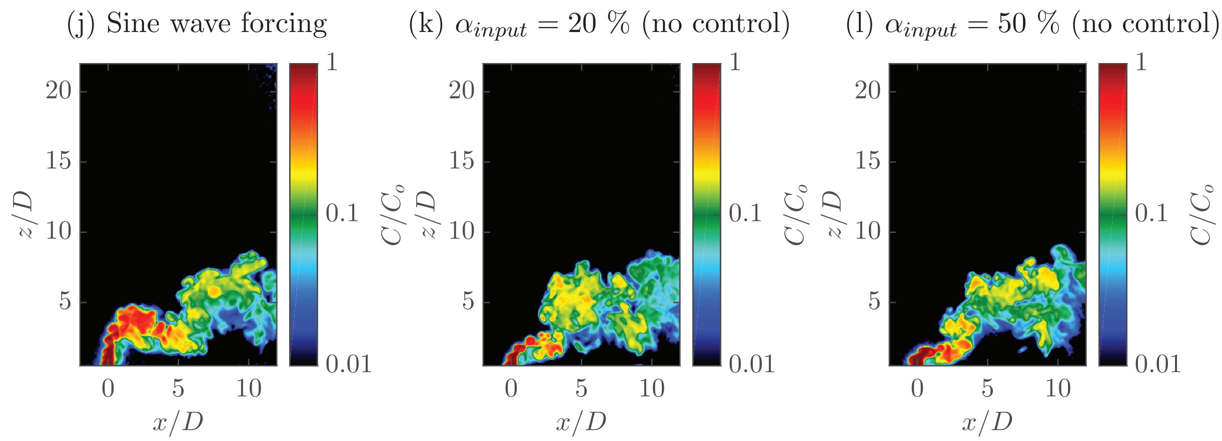

Figure C.27: Instantaneous centerplane PLIF images in the $x/D - z/D$ plane for the equidensity flush nozzle-injected JICF at $J = 5$ for (a) the unforced case, (b)-(i) the forced cases under single-pulse square wave forcing with control at stroke ratios ranging $L/D = 2.48 - 7.60$ (actual duty cycle α_{actual} (%) in parentheses), (j) under sine wave forcing, as well as (k)-(l) under single-pulse square wave forcing without control at $\alpha_{input} = 20 - 50$ %. All forcing conditions are at $f_f = 100$ Hz and $U'_{j,rms} = 2.0$ m/s (approximately 31 % of U_j).

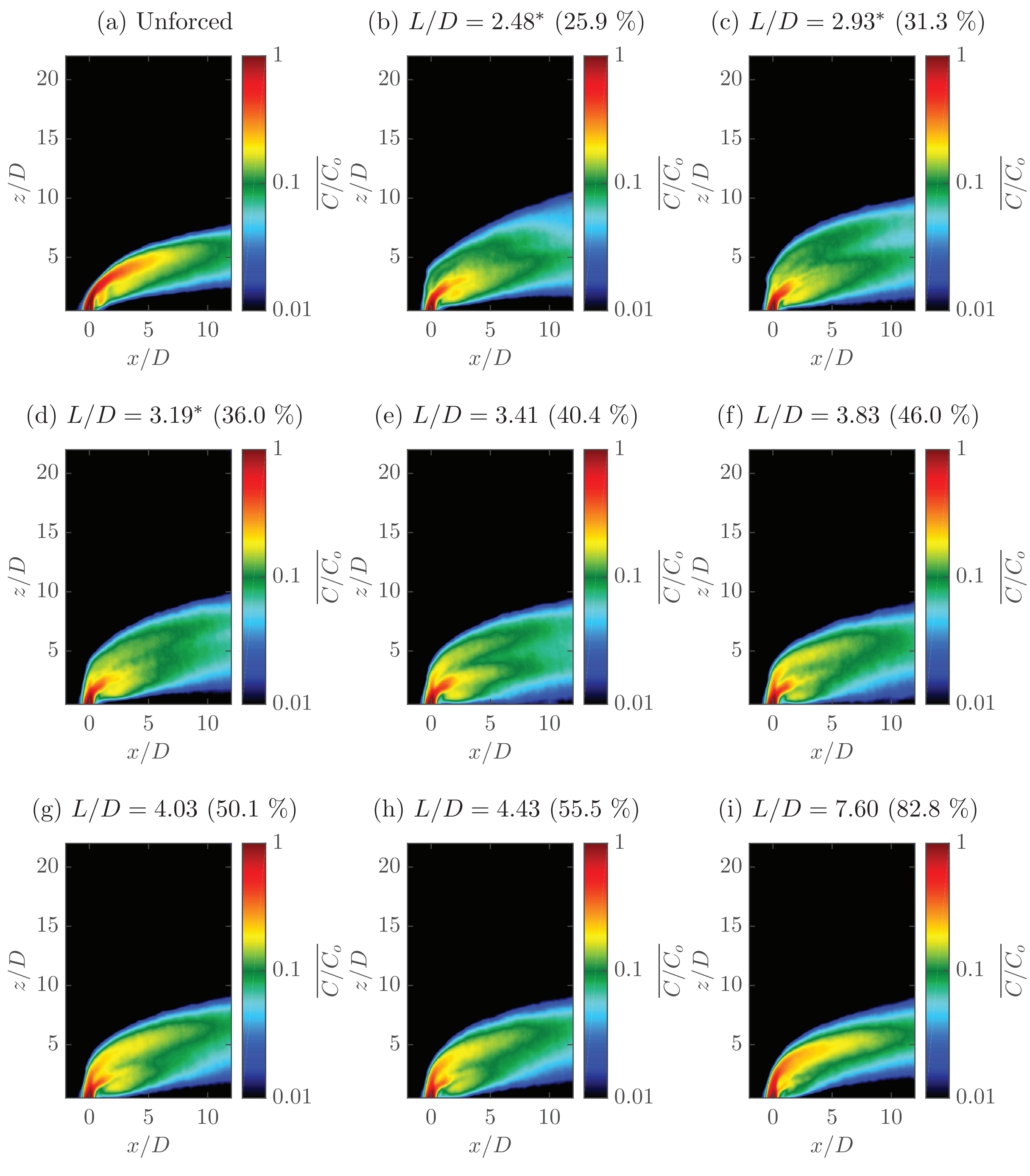

Figure C.28: For more figures and caption see next page.

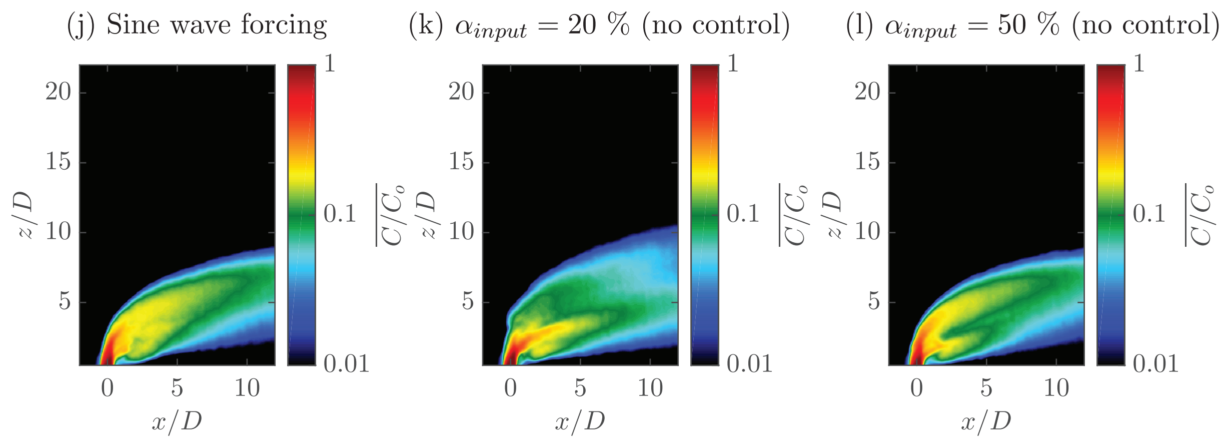

Figure C.28: Mean centerplane PLIF images in the $x/D - z/D$ plane for the equidensity flush nozzle-injected JICF at $J = 5$ for (a) the unforced case, (b)-(i) the forced cases under single-pulse square wave forcing with control at stroke ratios ranging $L/D = 2.48 - 7.60$ (actual duty cycle α_{actual} (%) in parentheses), (j) under sine wave forcing, as well as (k)-(l) under single-pulse square wave forcing without control at $\alpha_{input} = 20 - 50$ %. All forcing conditions are at $f_f = 100$ Hz and $U'_{j,rms} = 2.0$ m/s (approximately 31 % of U_j).

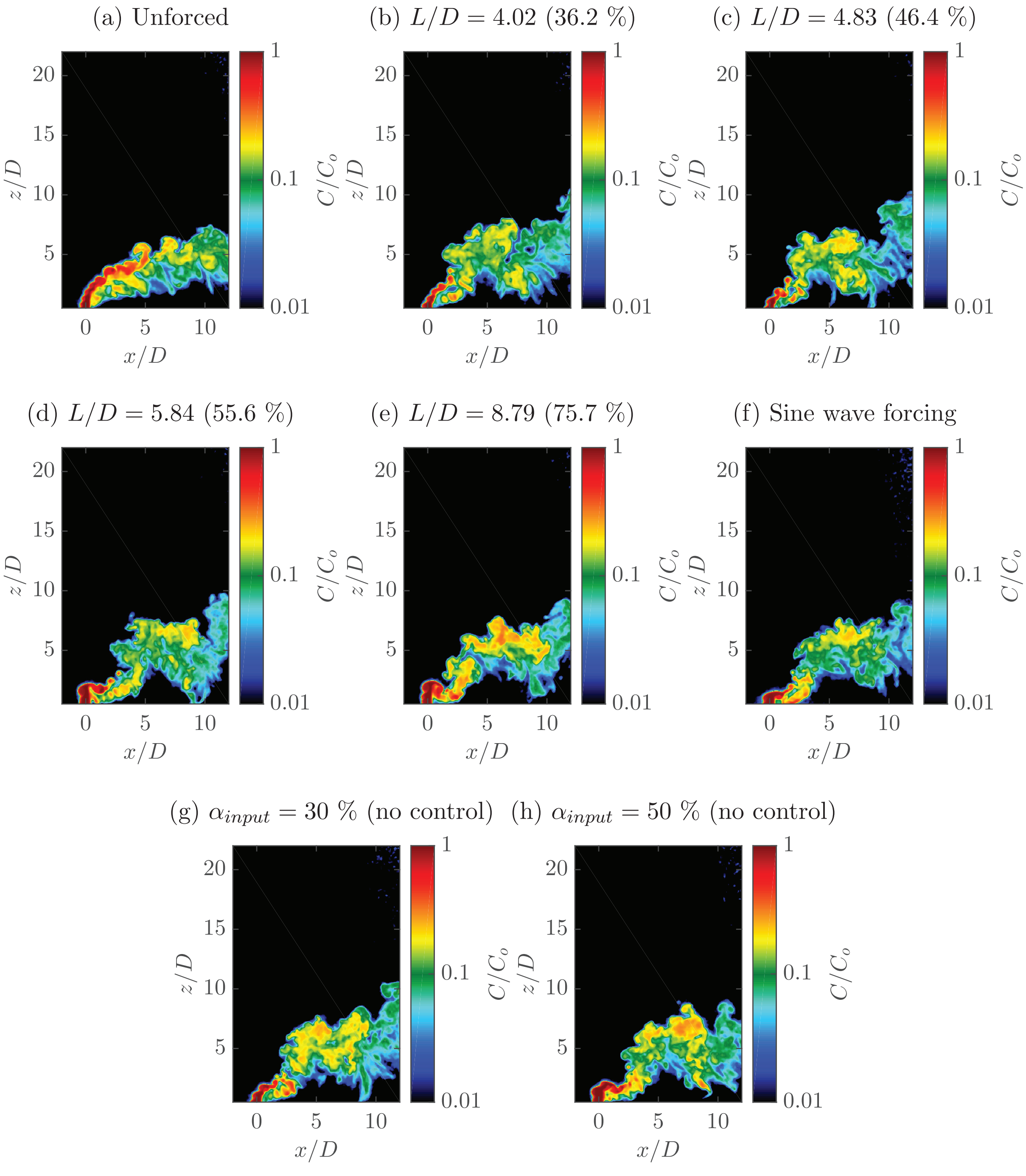

Figure C.29: Instantaneous centerplane PLIF images in the $x/D - z/D$ plane for the equidensity flush nozzle-injected JICF at $J = 5$ for (a) the unforced case, (b)-(e) the forced cases under single-pulse square wave forcing with control at stroke ratios ranging $L/D = 4.02 - 8.79$ (actual duty cycle α_{actual} (%) in parentheses), (f) under sine wave forcing, as well as (g)-(h) under single-pulse square wave forcing without control at $\alpha_{input} = 30 - 50$ %. All forcing conditions are at $f_f = 100$ Hz and $U'_{j,rms} = 2.5$ m/s (approximately 38 % of U_j).

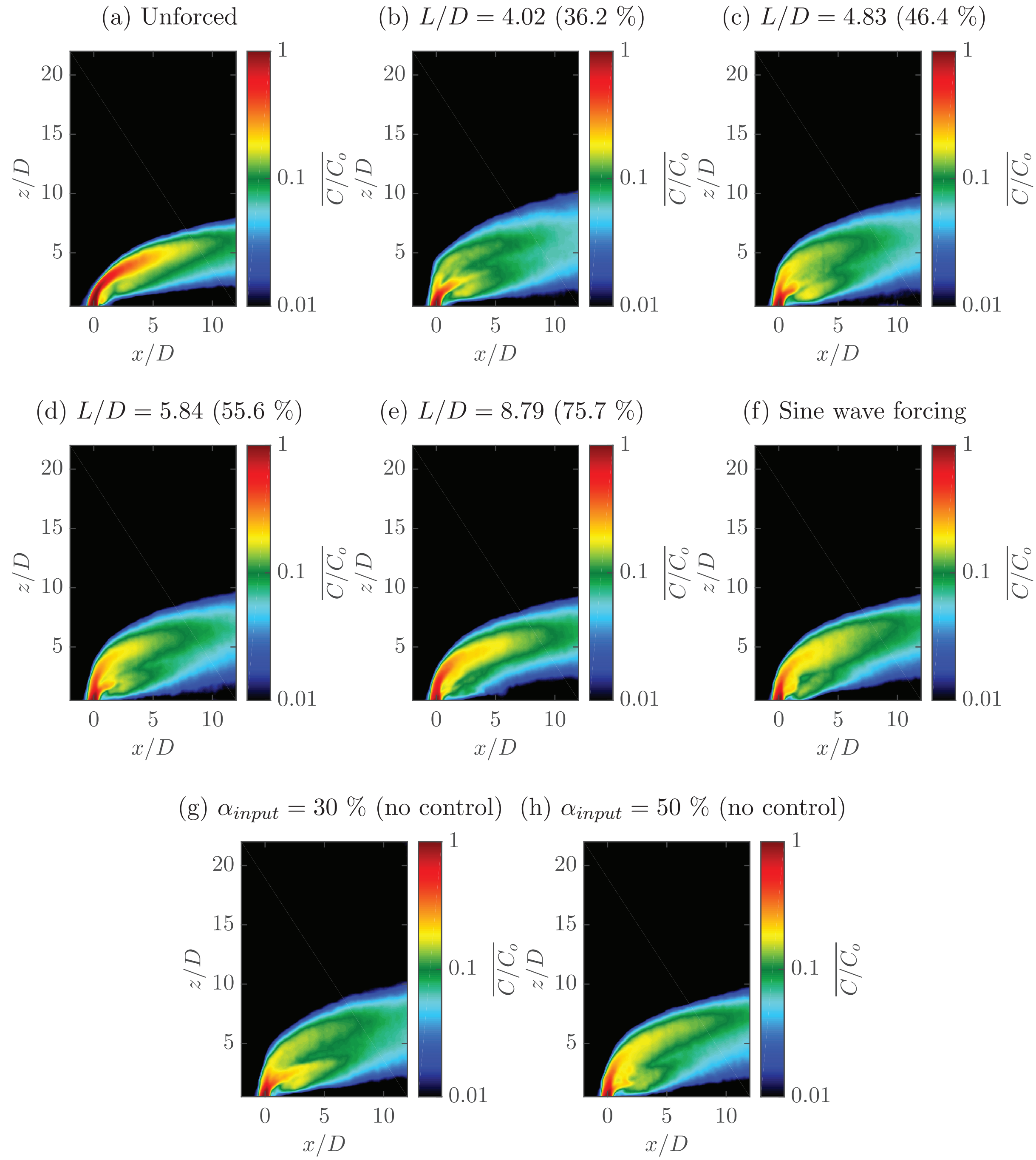

Figure C.30: Mean centerplane PLIF images in the $x/D - z/D$ plane for the equidensity flush nozzle-injected JICF at $J = 5$ for (a) the unforced case, (b)-(e) the forced cases under single-pulse square wave forcing with control at stroke ratios ranging $L/D = 4.02 - 8.79$ (actual duty cycle α_{actual} (%) in parentheses), (f) under sine wave forcing, as well as (g)-(h) under single-pulse square wave forcing without control at $\alpha_{input} = 30 - 50$ %. All forcing conditions are at $f_f = 100$ Hz and $U'_{j,rms} = 2.5$ m/s (approximately 38 % of U_j).

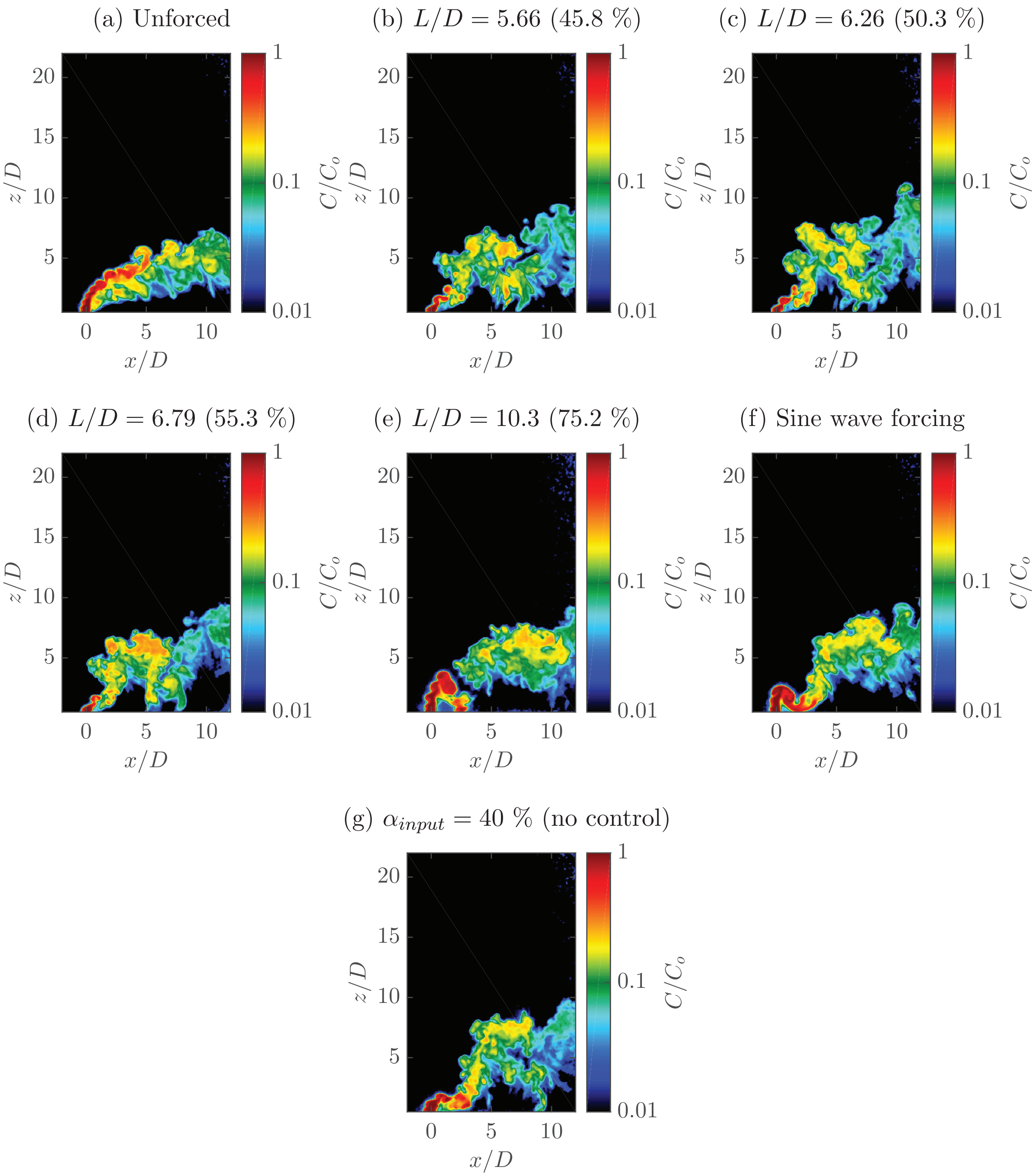

Figure C.31: Instantaneous centerplane PLIF images in the $x/D - z/D$ plane for the equidensity flush nozzle-injected JICF at $J = 5$ for (a) the unforced case, (b)-(e) the forced cases under single-pulse square wave forcing with control at stroke ratios ranging $L/D = 5.66 - 10.3$ (actual duty cycle α_{actual} (%) in parentheses), (f) under sine wave forcing, as well as (g) under single-pulse square wave forcing without control at $\alpha_{input} = 40$ %. All forcing conditions are at $f_f = 100$ Hz and $U'_{j,rms} = 3.0$ m/s (approximately 46 % of U_j).

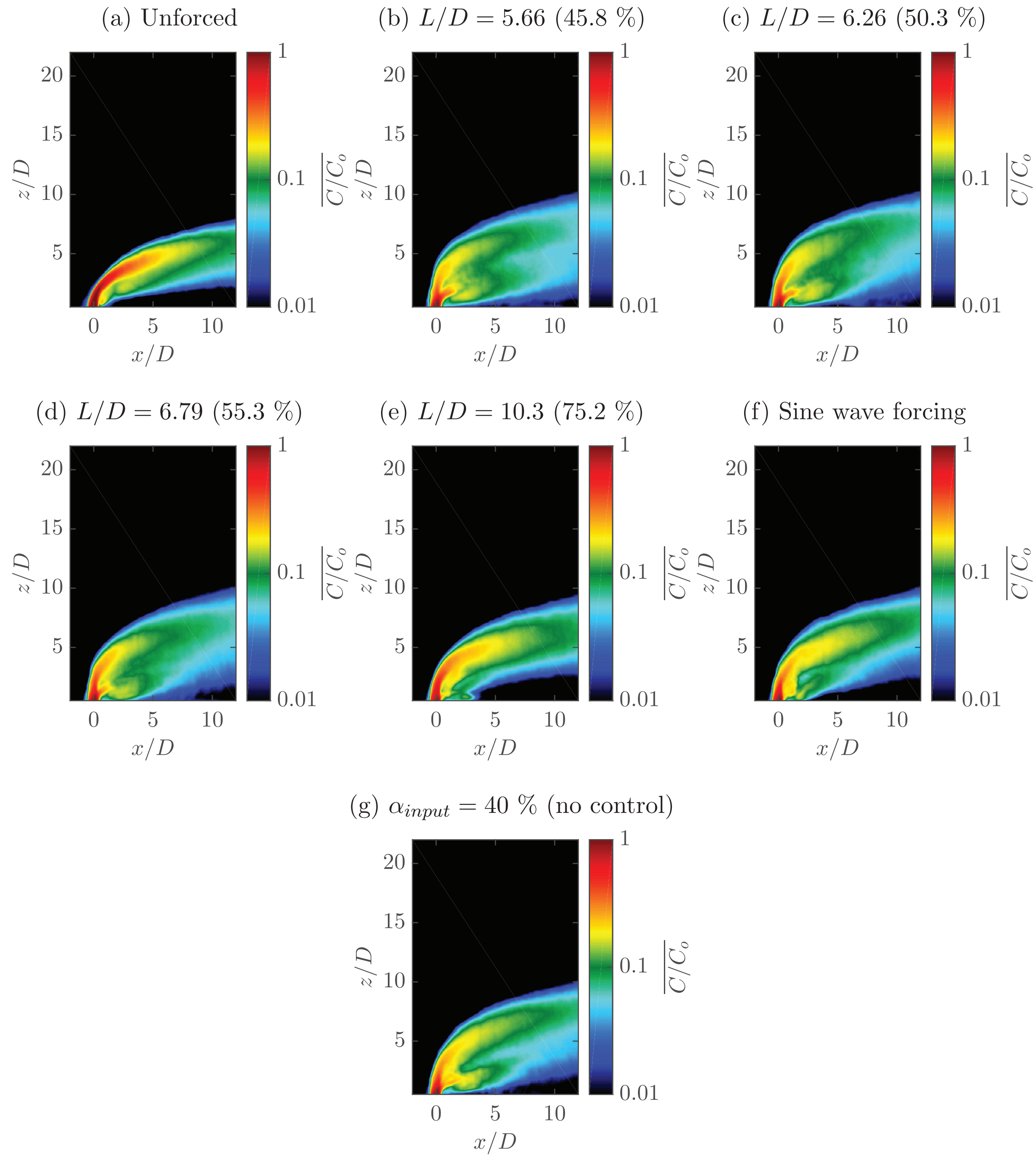

Figure C.32: Mean centerplane PLIF images in the $x/D - z/D$ plane for the equidensity flush nozzle-injected JICF at $J = 5$ for (a) the unforced case, (b)-(e) the forced cases under single-pulse square wave forcing with control at stroke ratios ranging $L/D = 5.66 - 10.3$ (actual duty cycle α_{actual} (%) in parentheses), (f) under sine wave forcing, as well as (g) under single-pulse square wave forcing without control at $\alpha_{input} = 40$ %. All forcing conditions are at $f_f = 100$ Hz and $U'_{j,rms} = 3.0$ m/s (approximately 46 % of U_j).

C.4 Mean Cross-Sectional PLIF Images

This section represents mean cross-sectional PLIF images with single-pulse square wave forcing of the jet, which were not shown in Chapter 6. All mean images shown here are created by averaging 500 instantaneous images. Again, stroke ratio L/D with asterisk corresponds to the existence of deeply-penetrating puff-like vortical flow structures observed in instantaneous centerplane images

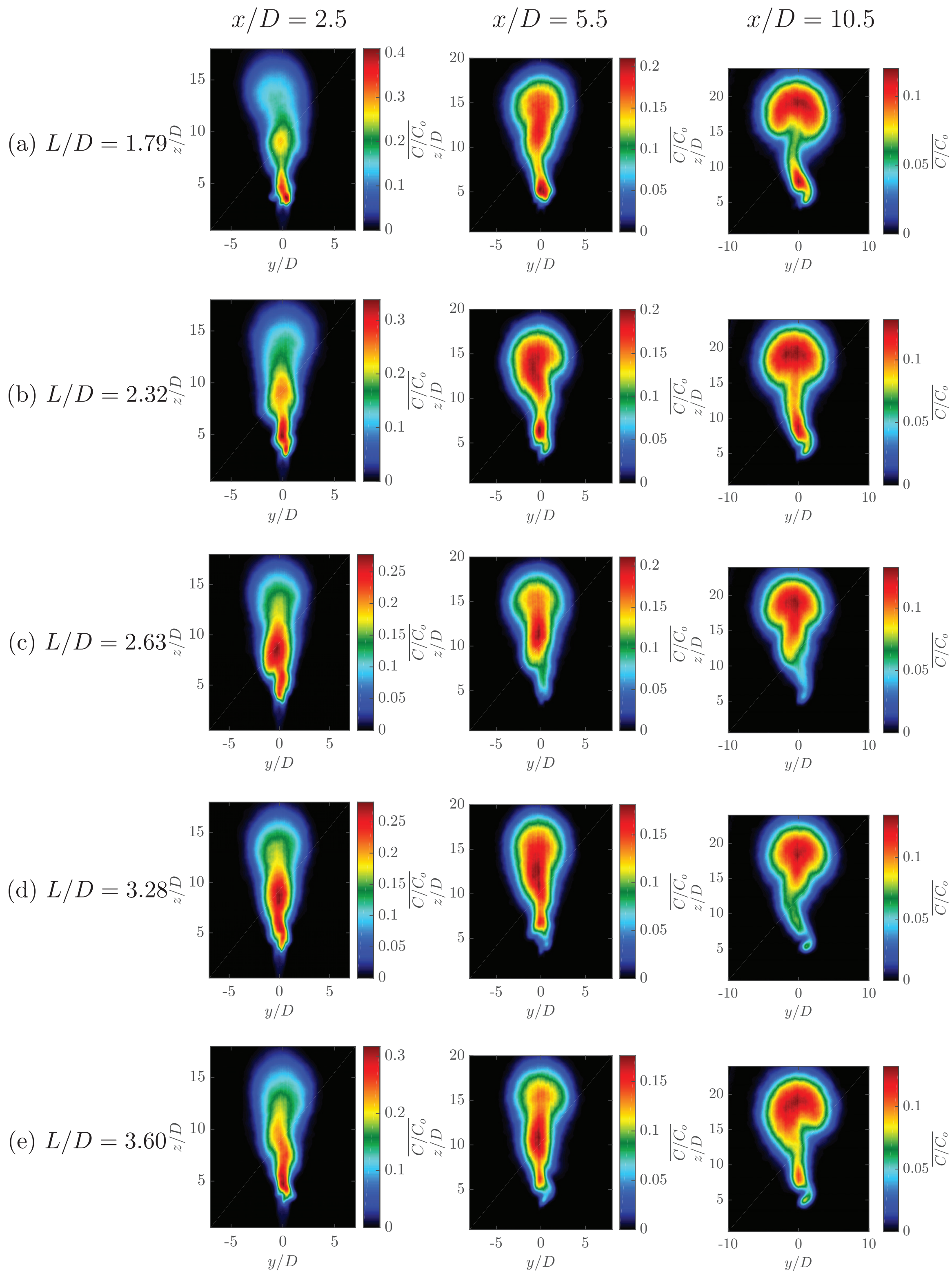

Figure C.33: For more figures and caption see next page.

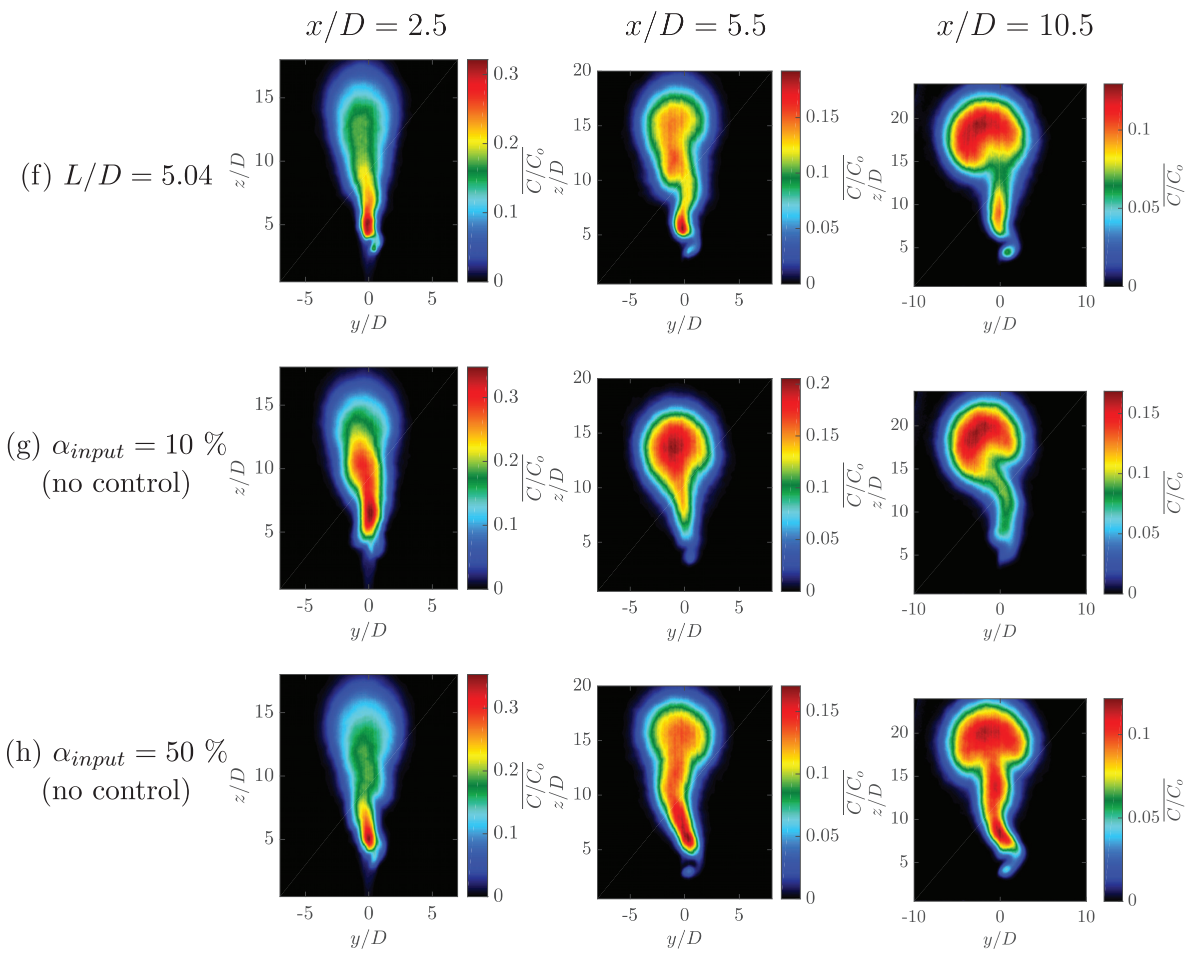

Figure C.33: Mean cross-sectional PLIF images in the $y/D - z/D$ plane for the equidensity flush nozzle-injected JICF at $J = 41$ for (a)-(f) the forced cases under single-pulse square wave forcing at stroke ratios ranging $L/D = 1.79 - 5.04$, and (g)-(h) under single-pulse square wave forcing without control at $\alpha_{input} = 10$ and 20 %. All forcing cases are at $f_f = 100$ Hz and $U'_{j,rms} = 1.7$ m/s (approximately 26 % of U_j).

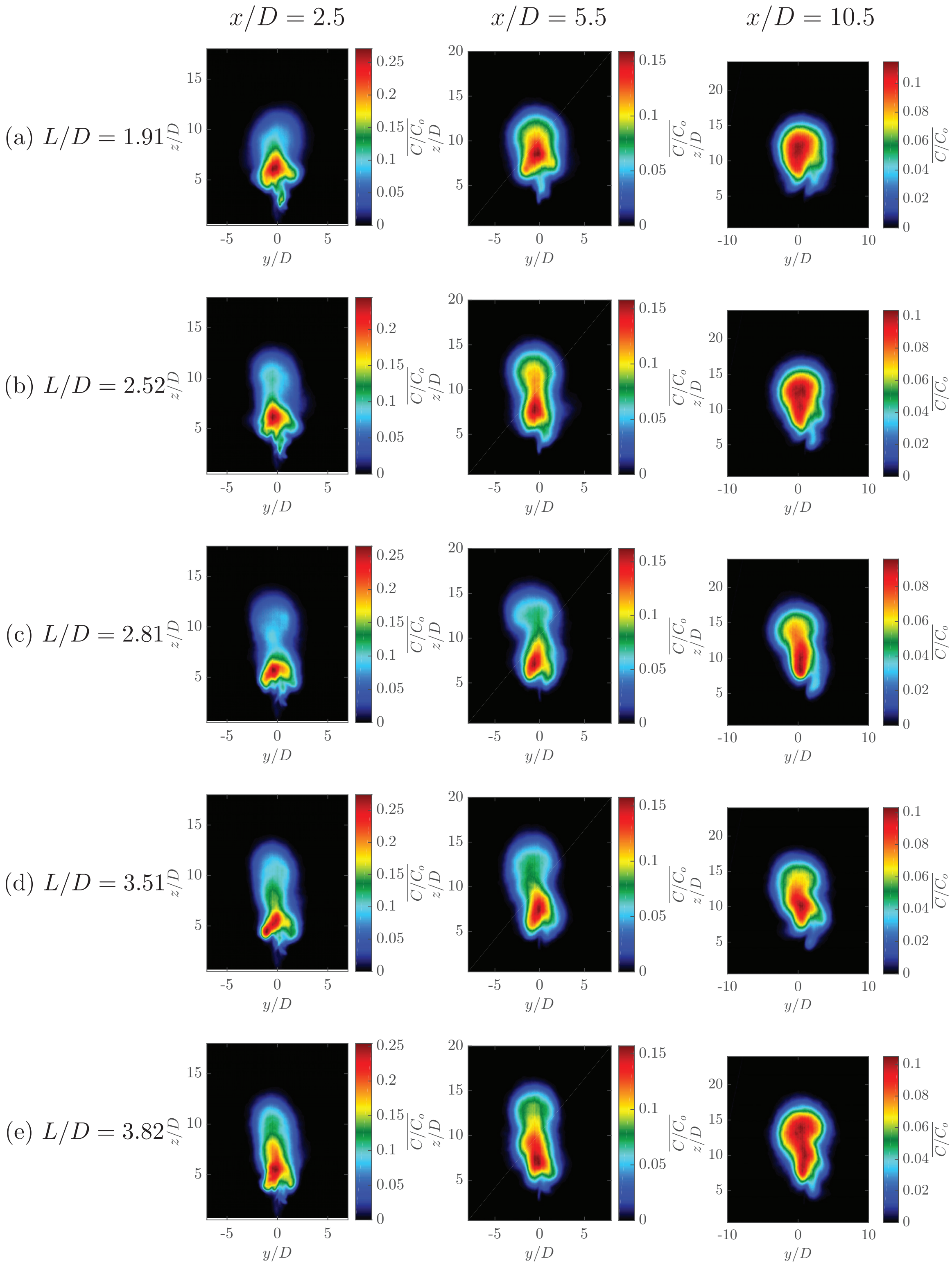

Figure C.34: For more figures and caption see next page.

(f) $\alpha_{input} = 50$ %
(no control)

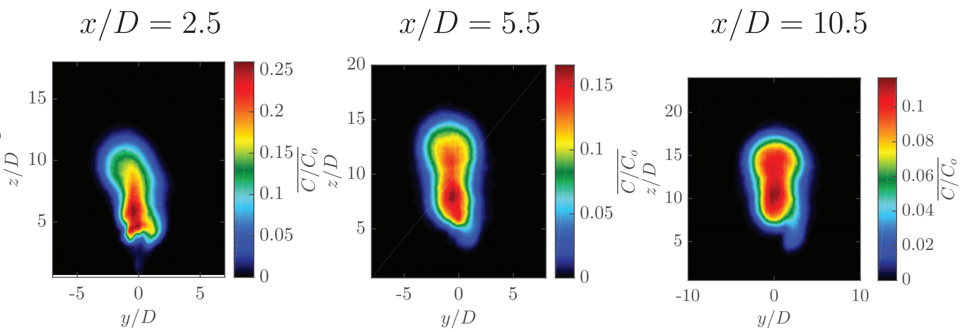

Figure C.34: Mean cross-sectional PLIF images in the $y/D - z/D$ plane for the equidensity flush nozzle-injected JICF at $J = 20$ for (a)-(e) the forced cases under single-pulse square wave forcing at stroke ratios ranging $L/D = 1.91 - 3.82$, and (f) under single-pulse square wave forcing without control at $\alpha_{input} = 50$ %. All forcing cases are at $f_f = 100$ Hz and $U'_{j,rms} = 1.7$ m/s (approximately 26 % of U_j).

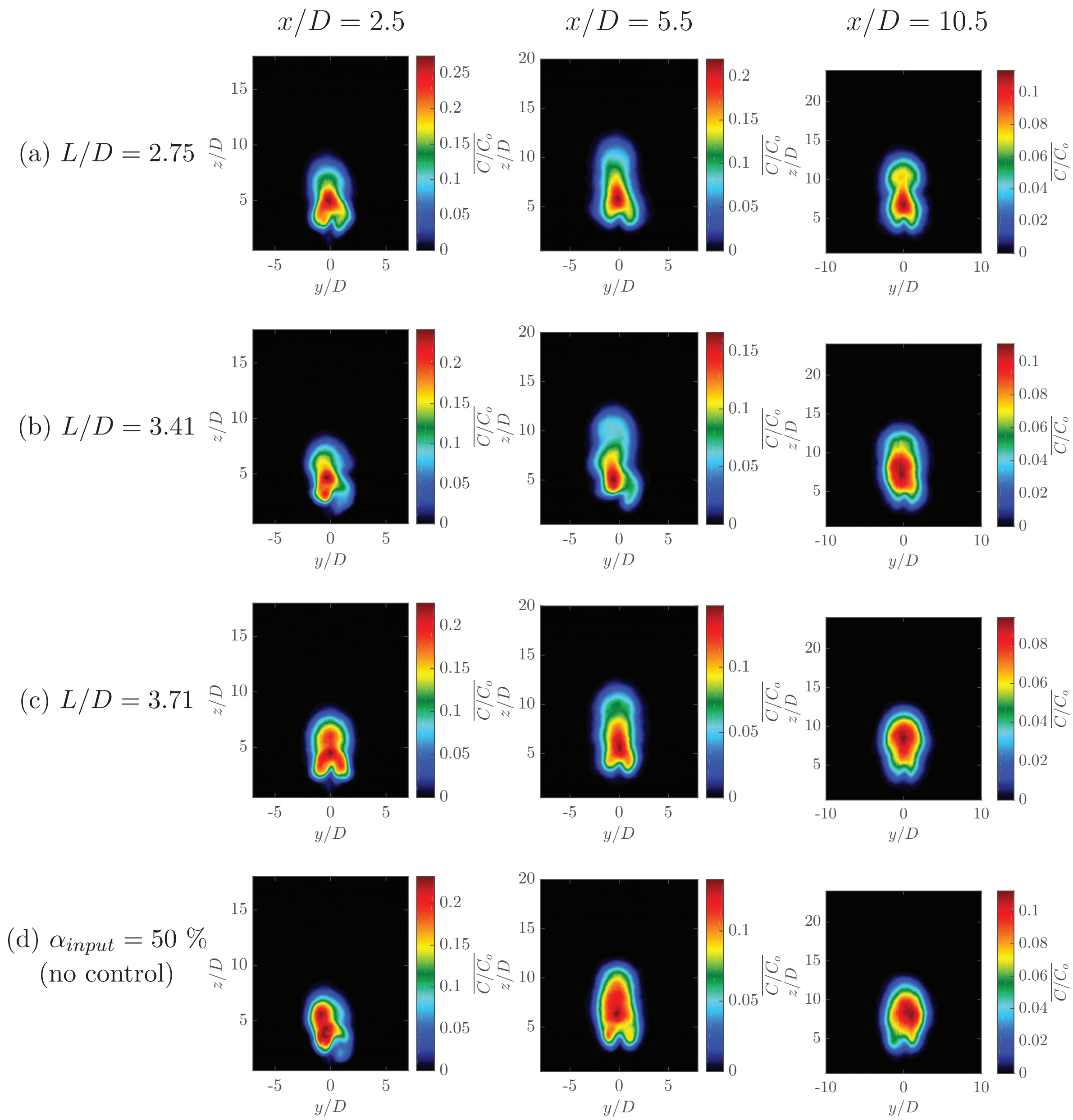

Figure C.35: Mean cross-sectional PLIF images in the $y/D - z/D$ plane for the equidensity flush nozzle-injected JICF at $J = 10$ for (a)-(c) the forced cases under single-pulse square wave forcing at stroke ratios ranging $L/D = 2.75 - 3.71$, and (d) under single-pulse square wave forcing without control at $\alpha_{input} = 50$ %. All forcing cases are at $f_f = 100$ Hz and $U'_{j,rms} = 1.7$ m/s (approximately 26 % of U_j).

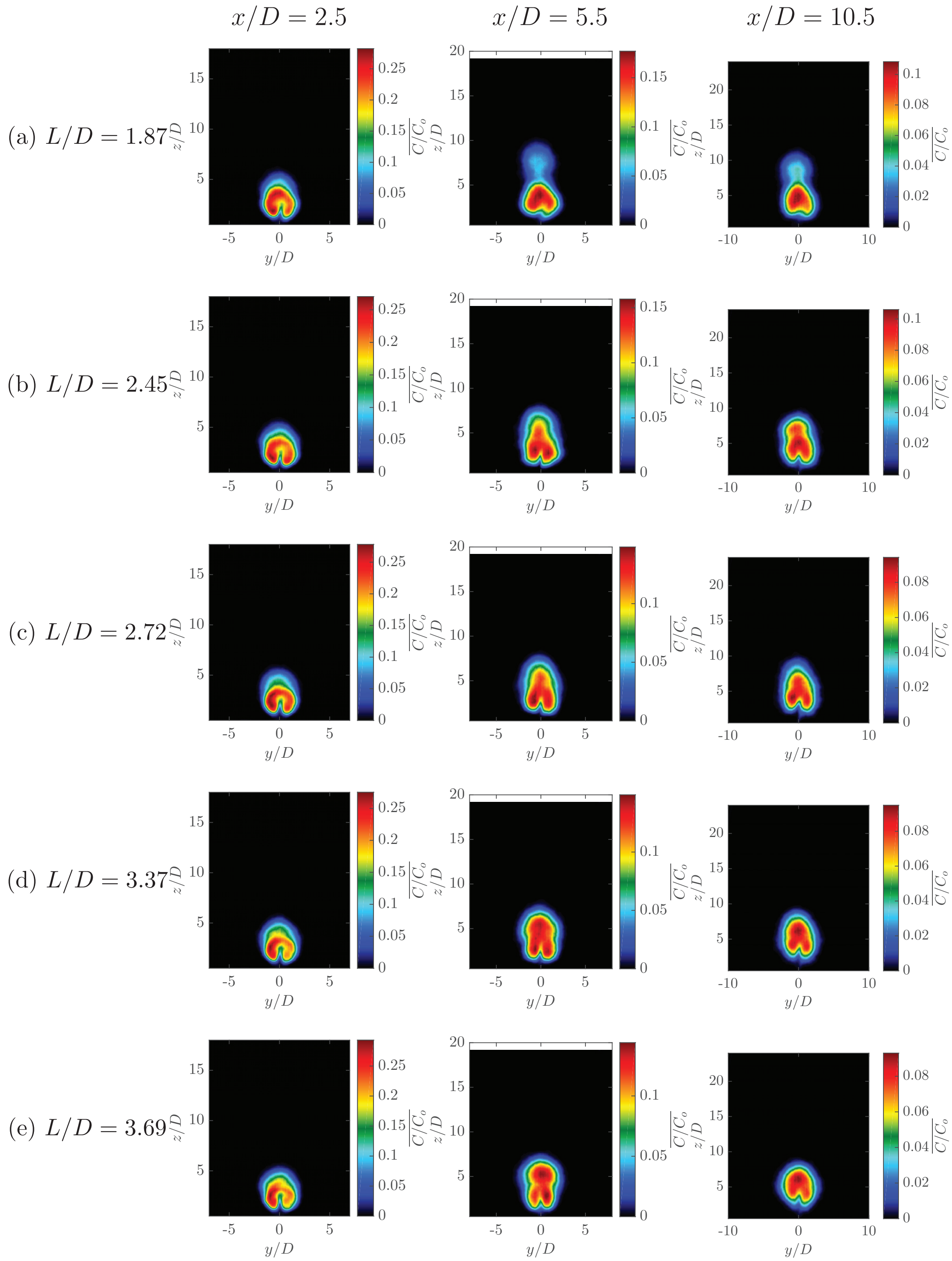

Figure C.36: For more figures and caption see next page.

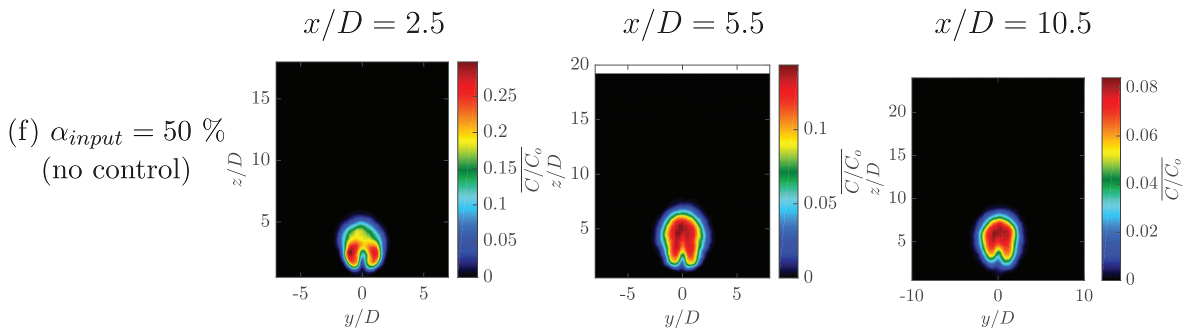

Figure C.36: Mean cross-sectional PLIF images in the $y/D - z/D$ plane for the equidensity flush nozzle-injected JICF at $J = 5$ for (a)-(e) the forced cases under single-pulse square wave forcing at stroke ratios ranging $L/D = 1.87 - 3.69$, and (f) under single-pulse square wave forcing without control at $\alpha_{input} = 50$ %. All forcing cases are at $f_f = 100$ Hz and $U'_{j,rms} = 1.7$ m/s (approximately 26 % of U_j).

C.5 Mixing Quantification for Forced JICF

This section represents the results of mixing quantification, which were not shown in Chapter 6.

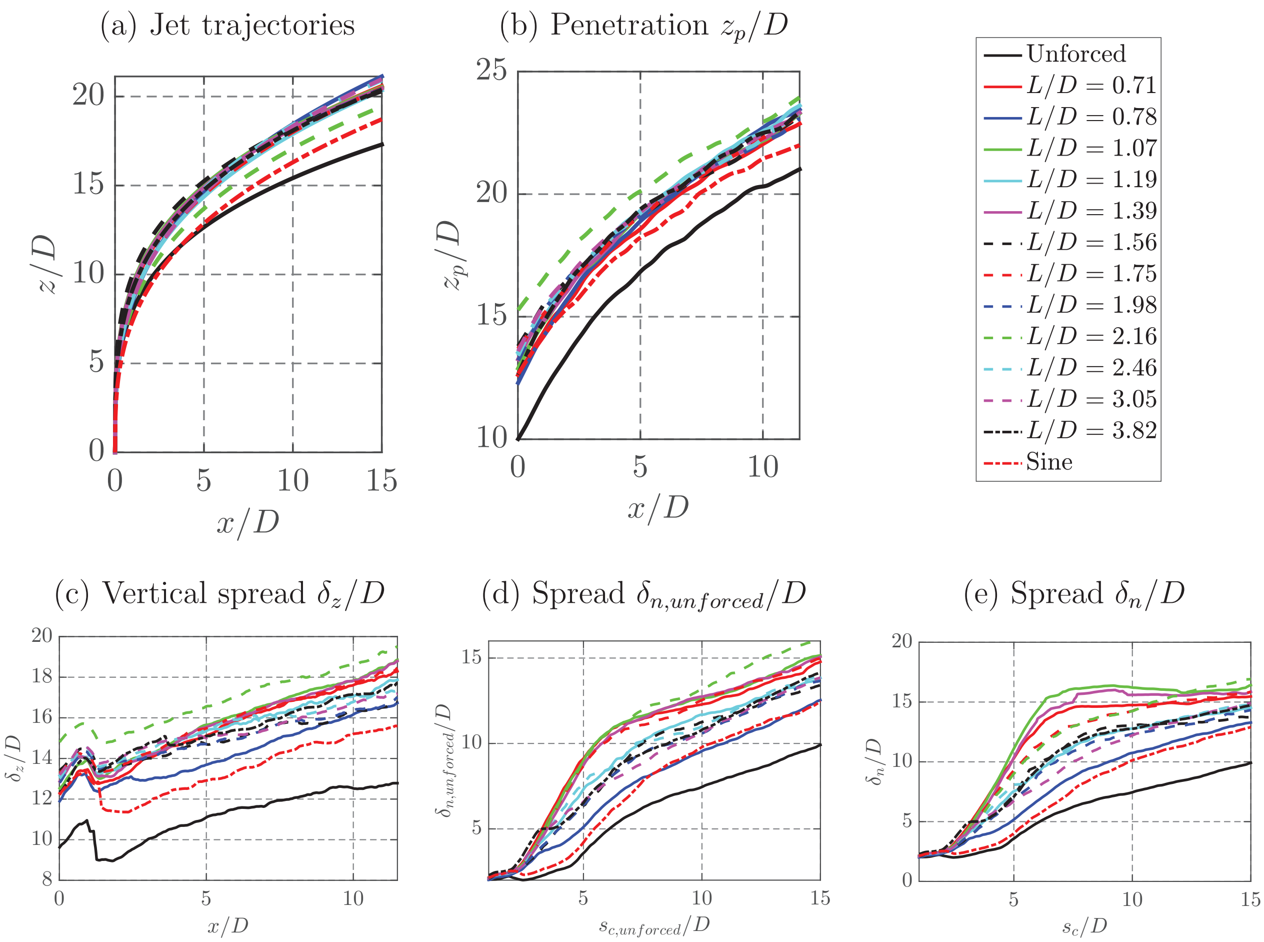

Figure C.37: Mean mixing metrics for the equidensity flush nozzle-injected JICF at $J = 41$ for the unforced case and forced cases under sine wave forcing as well as single-pulse square wave forcing with control ($0.71 \leq L/D \leq 3.82$) at $f_f = 100$ Hz and $U'_{j,rms} = 1.0$ m/s: (a) Jet trajectories, (b) jet penetration z_p/D, (c) jet vertical spread δ_z/D, (d) jet spread normal to the unforced jet trajectory $\delta_{n,unforced}/D$ and (e) jet spread normal to each jet trajectory in question δ_n/D.

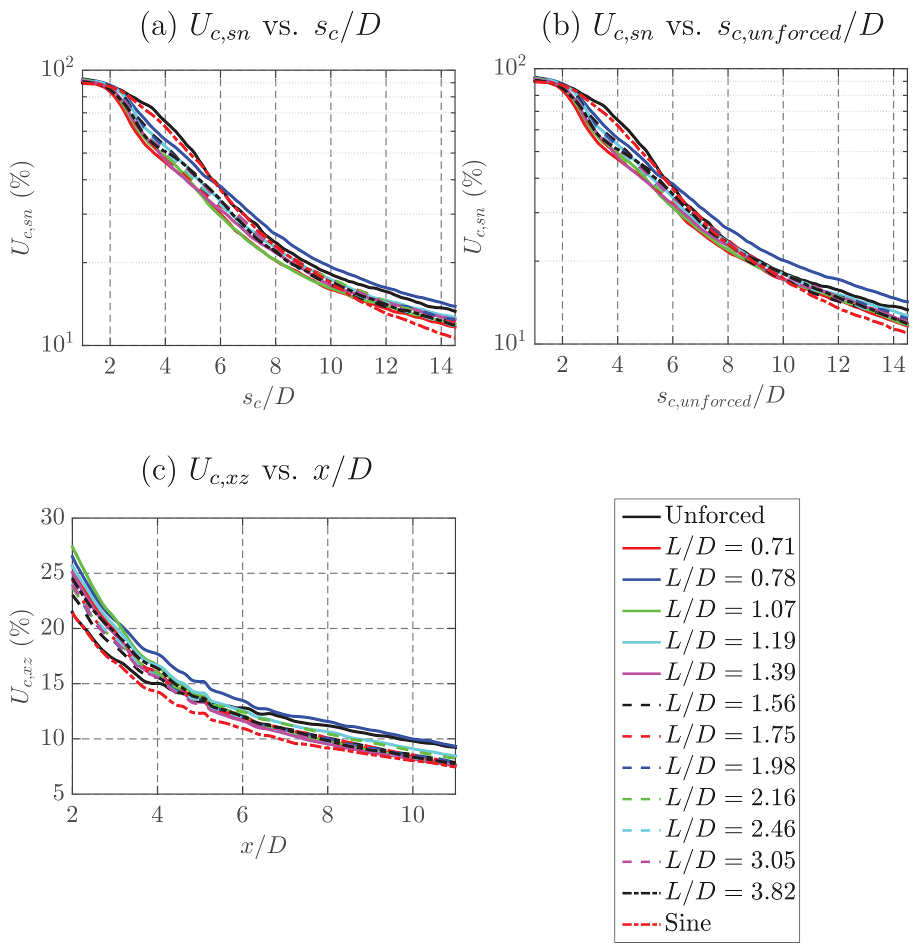

Figure C.38: Instantaneous mixing metrics for the equidensity flush nozzle-injected JICF at $J = 41$ for the unforced and forced cases under sine wave forcing as well as single-pulse square wave forcing with control ($0.71 \leq L/D \leq 3.82$) at $f_f = 100$ Hz and $U'_{j,rms} = 1.0$ m/s. Each figure represents (a) centerplane-based mean Unmixedness $U_{c,sn}$ along s_c/D, (b) $U_{c,sn}$ along $s_{c,unforced}/D$, and (c) centerplane-based mean Unmixedness $U_{c,xz}$ along x/D, respectively.

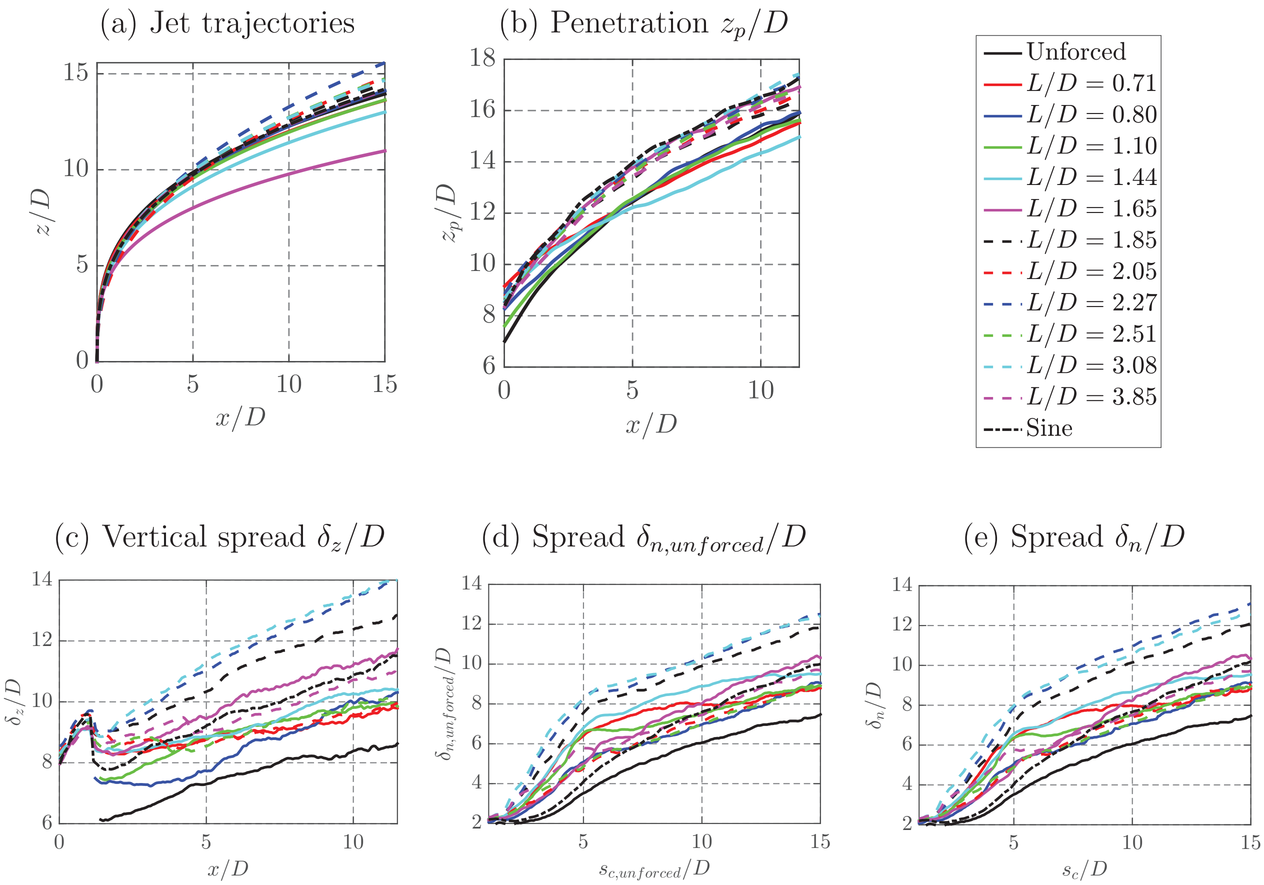

Figure C.39: Mean mixing metrics for the equidensity flush nozzle-injected JICF at $J = 20$ for the unforced case and forced cases under sine wave forcing as well as single-pulse square wave forcing with control ($0.71 \leq L/D \leq 3.85$) at $f_f = 100$ Hz and $U'_{j,rms} = 1.0$ m/s: (a) Jet trajectories, (b) jet penetration z_p/D, (c) jet vertical spread δ_z/D, (d) jet spread normal to the unforced jet trajectory $\delta_{n,unforced}/D$ and (e) jet spread normal to each jet trajectory in question δ_n/D.

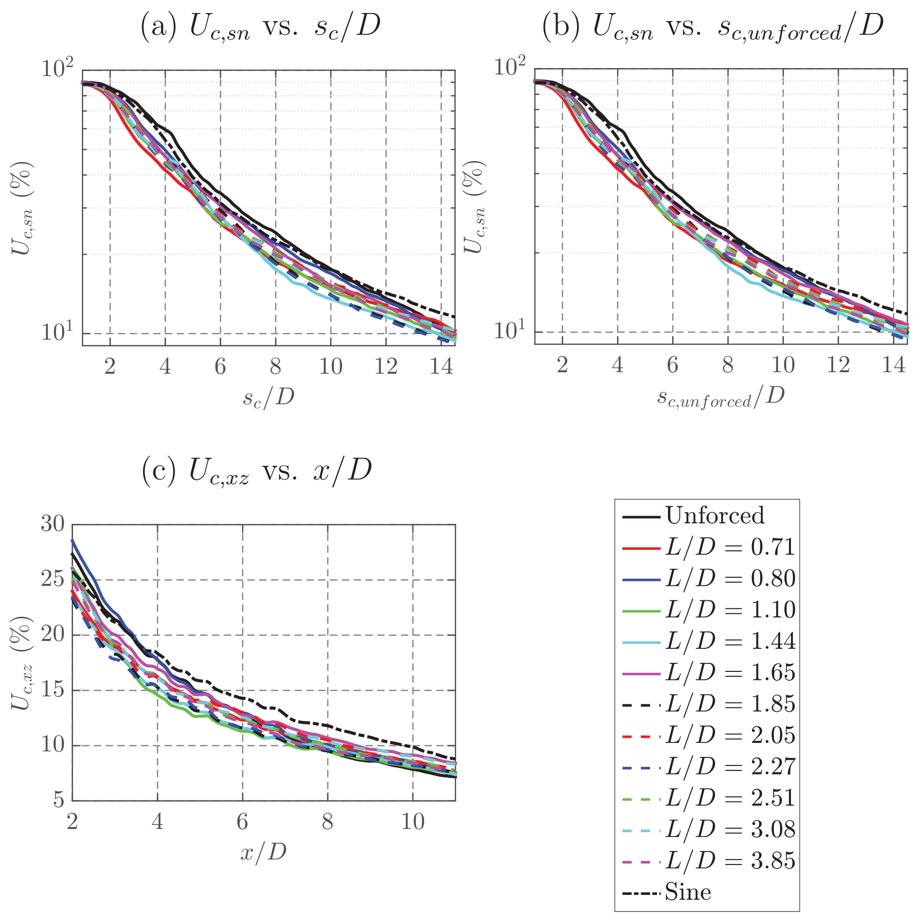

Figure C.40: Instantaneous mixing metrics for the equidensity flush nozzle-injected JICF at $J = 20$ for the unforced and forced cases under sine wave forcing as well as single-pulse square wave forcing with control ($0.71 \leq L/D \leq 3.85$) at $f_f = 100$ Hz and $U'_{j,rms} = 1.0$ m/s. Each figure represents (a) centerplane-based mean Unmixedness $U_{c,sn}$ along s_c/D, (b) $U_{c,sn}$ along $s_{c,unforced}/D$, and (c) centerplane-based mean Unmixedness $U_{c,xz}$ along x/D, respectively.

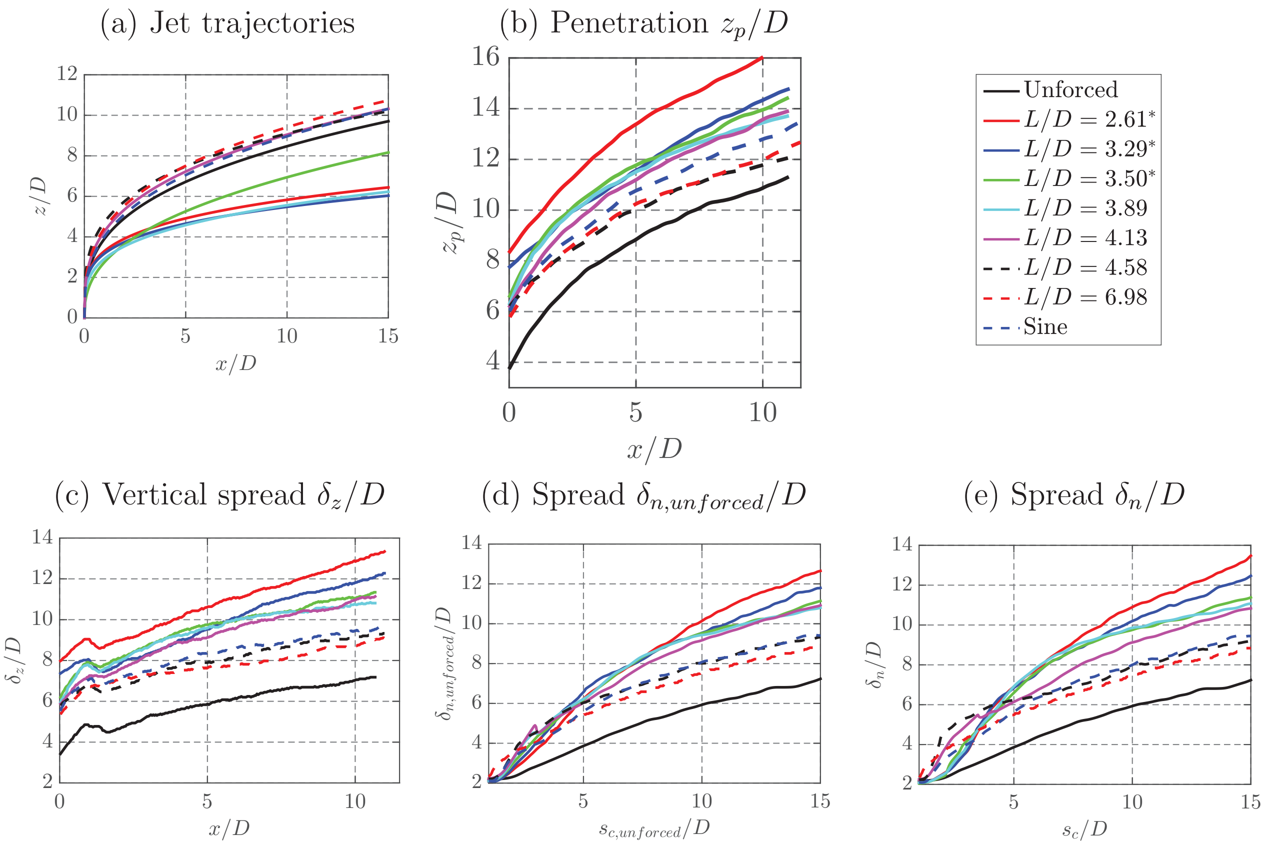

Figure C.41: Mean mixing metrics for the equidensity flush nozzle-injected JICF at $J = 10$ for the unforced case and forced cases under sine wave forcing as well as single-pulse square wave forcing with control ($2.61 \leq L/D \leq 6.98$) at $f_f = 100$ Hz and $U'_{j,rms} = 2.0$ m/s: (a) Jet trajectories, (b) jet penetration z_p/D, (c) jet vertical spread δ_z/D, (d) jet spread normal to the unforced jet trajectory $\delta_{n,unforced}/D$ and (e) jet spread normal to each jet trajectory in question δ_n/D.

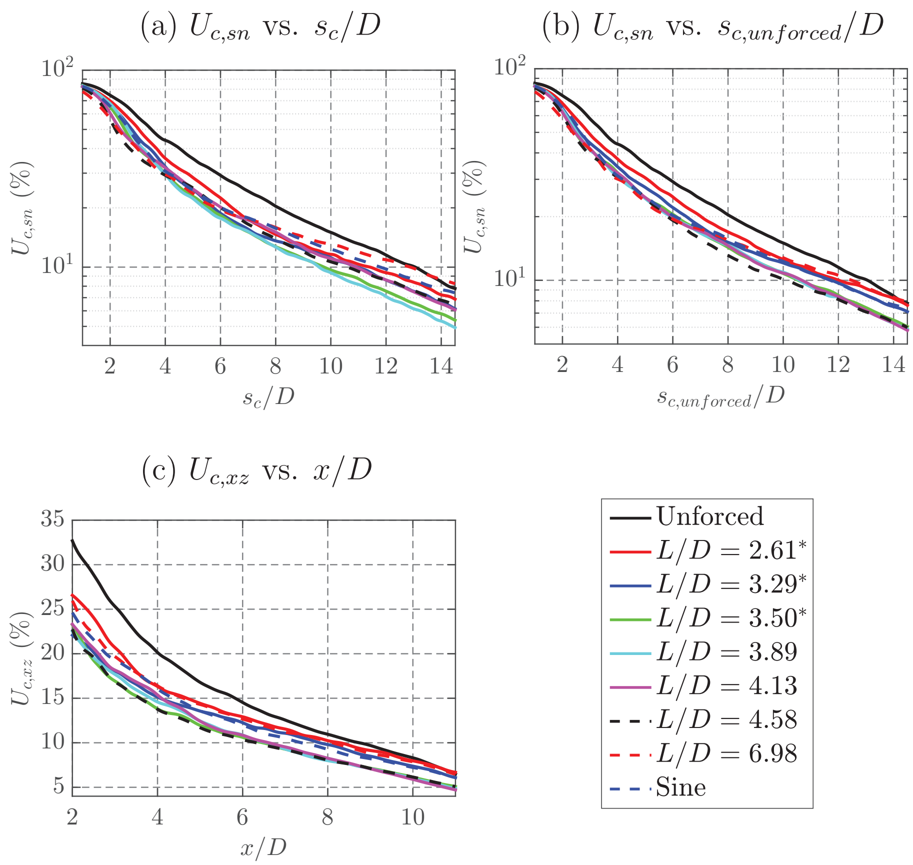

Figure C.42: Instantaneous mixing metrics for the equidensity flush nozzle-injected JICF at $J = 10$ for the unforced and forced cases under sine wave forcing as well as single-pulse square wave forcing with control ($2.61 \leq L/D \leq 6.98$) at $f_f = 100$ Hz and $U'_{j,rms} = 2.0$ m/s. Each figure represents (a) centerplane-based mean Unmixedness $U_{c,sn}$ along s_c/D, (b) $U_{c,sn}$ along $s_{c,unforced}/D$, and (c) centerplane-based mean Unmixedness $U_{c,xz}$ along x/D, respectively.

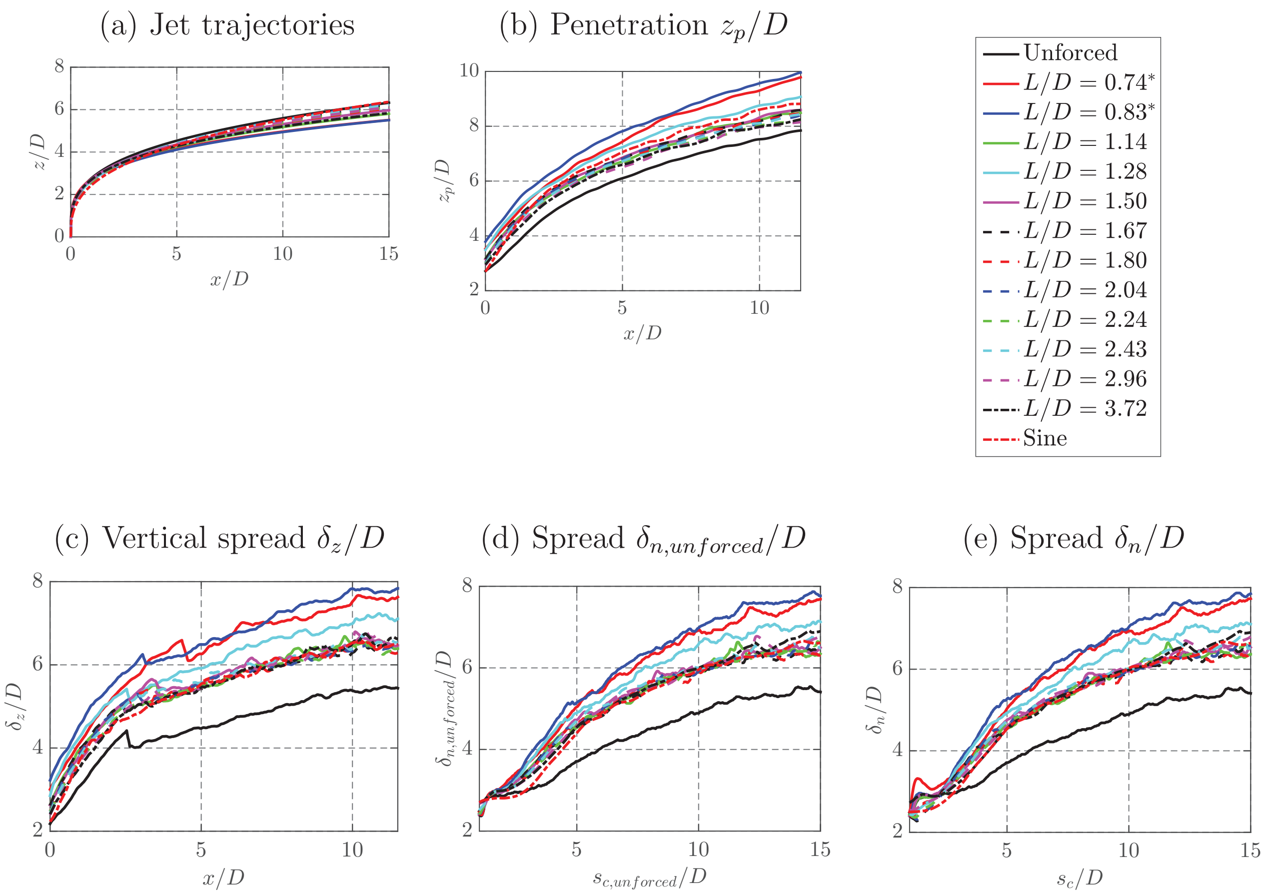

Figure C.43: Mean mixing metrics for the equidensity flush nozzle-injected JICF at $J = 5$ for the unforced case and forced cases under sine wave forcing as well as single-pulse square wave forcing with control ($0.74 \leq L/D \leq 3.72$) at $f_f = 100$ Hz and $U'_{j,rms} = 1.0$ m/s: (a) Jet trajectories, (b) jet penetration z_p/D, (c) jet vertical spread δ_z/D, (d) jet spread normal to the unforced jet trajectory $\delta_{n,unforced}/D$ and (e) jet spread normal to each jet trajectory in question δ_n/D.

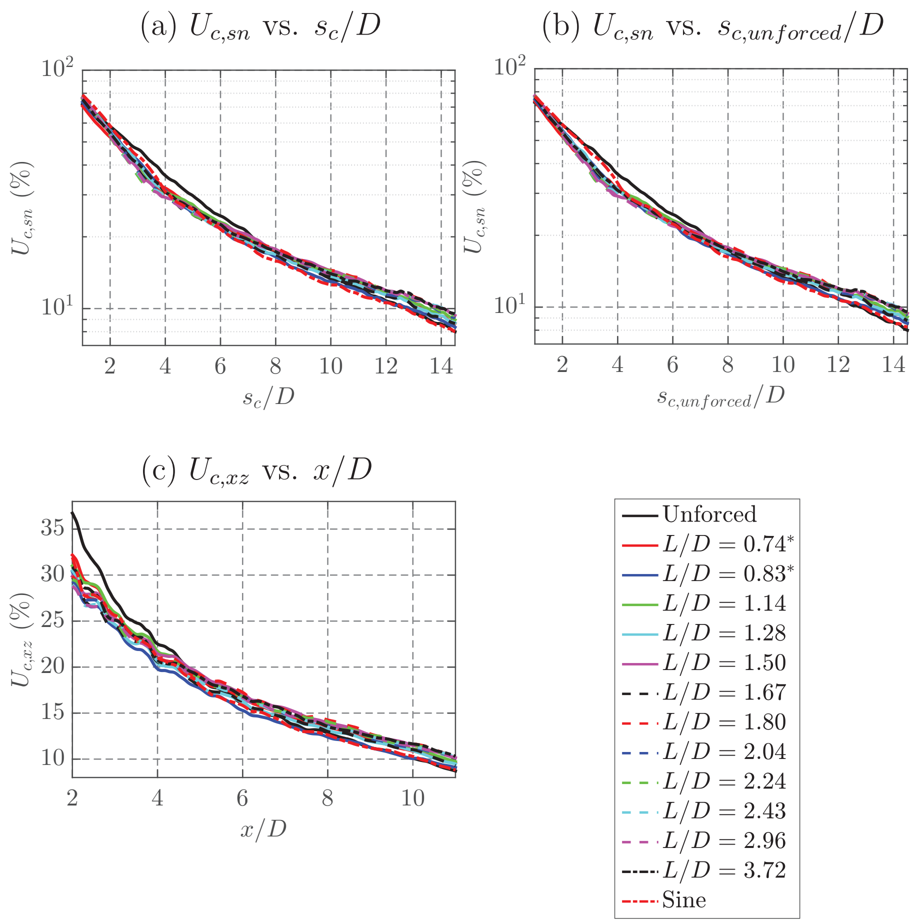

Figure C.44: Instantaneous mixing metrics for the equidensity flush nozzle-injected JICF at $J = 5$ for the unforced and forced cases under sine wave forcing as well as single-pulse square wave forcing with control ($0.74 \leq L/D \leq 3.72$) at $f_f = 100$ Hz and $U'_{j,rms} = 1.0$ m/s. Each figure represents (a) centerplane-based mean Unmixedness $U_{c,sn}$ along s_c/D, (b) $U_{c,sn}$ along $s_{c,unforced}/D$, and (c) centerplane-based mean Unmixedness $U_{c,xz}$ along x/D, respectively.

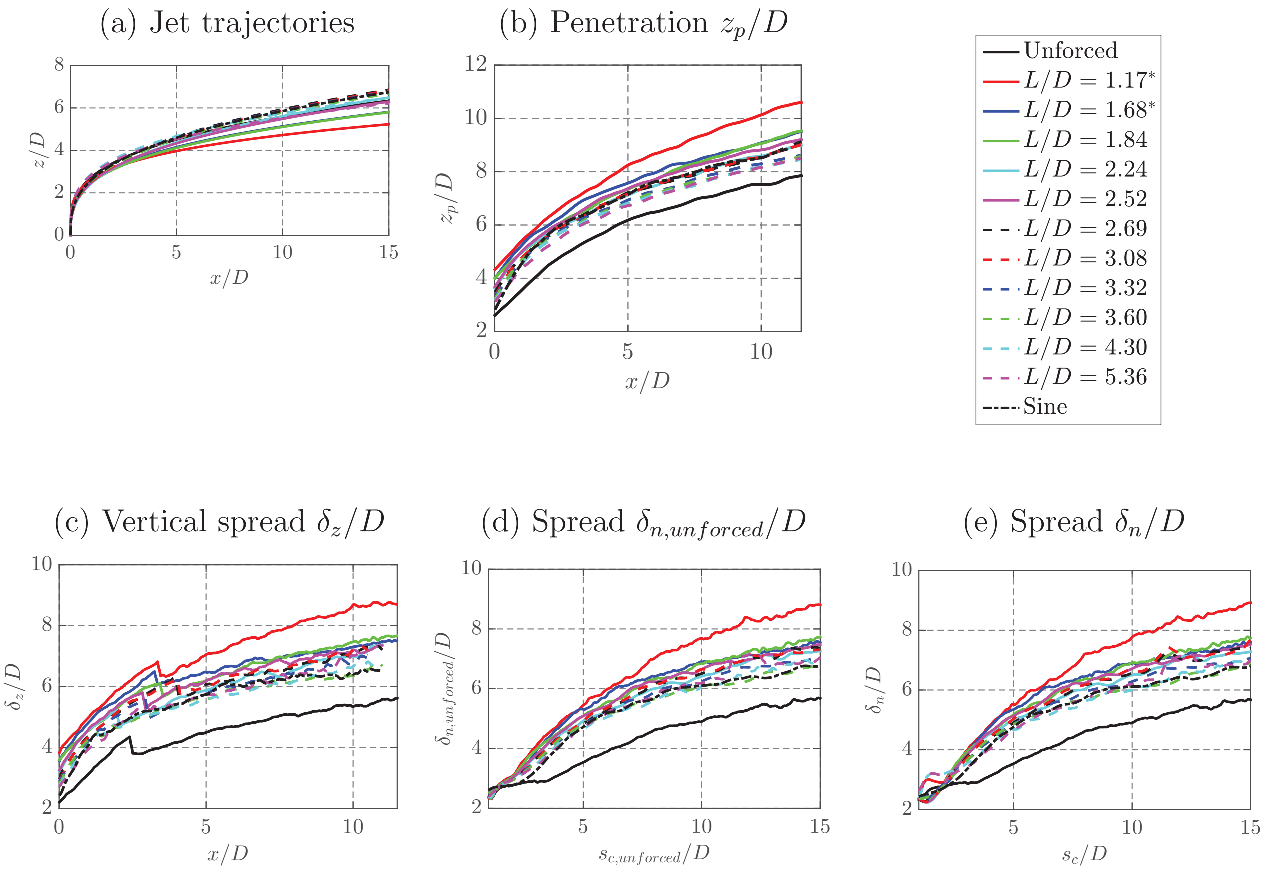

Figure C.45: Mean mixing metrics for the equidensity flush nozzle-injected JICF at $J = 5$ for the unforced case and forced cases under sine wave forcing as well as single-pulse square wave forcing with control ($1.17 \leq L/D \leq 5.36$) at $f_f = 100$ Hz and $U'_{j,rms} = 1.5$ m/s: (a) Jet trajectories, (b) jet penetration z_p/D, (c) jet vertical spread δ_z/D, (d) jet spread normal to the unforced jet trajectory $\delta_{n,unforced}/D$ and (e) jet spread normal to each jet trajectory in question δ_n/D.

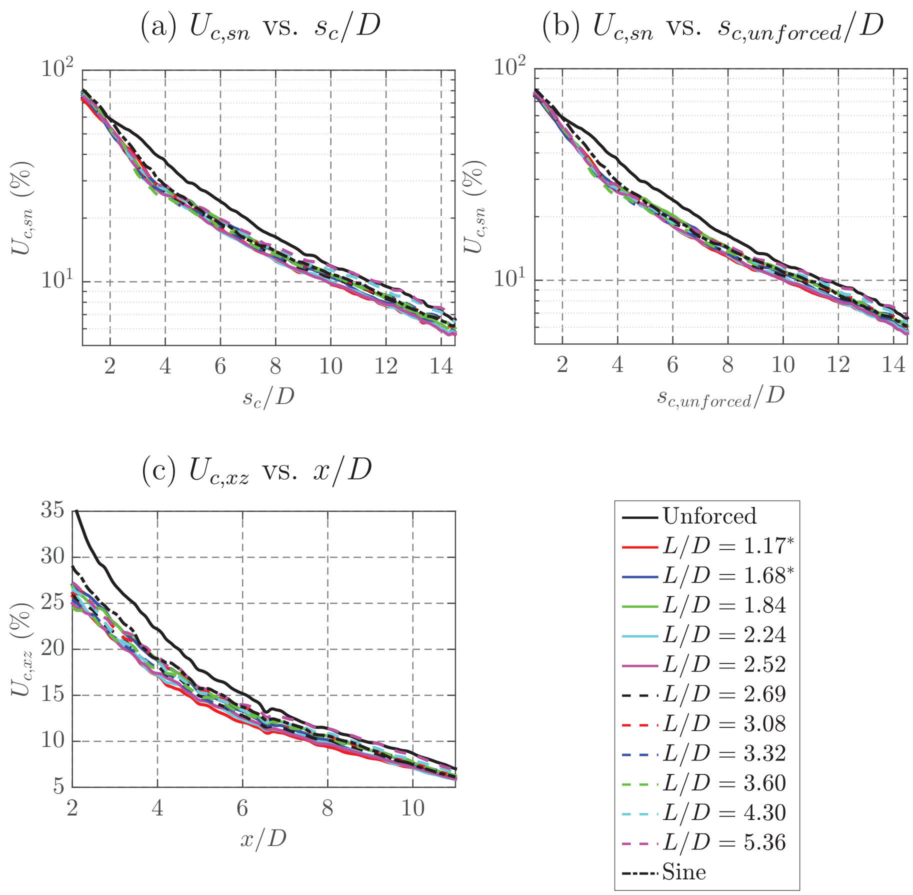

Figure C.46: Instantaneous mixing metrics for the equidensity flush nozzle-injected JICF at $J = 5$ for the unforced and forced cases under sine wave forcing as well as single-pulse square wave forcing with control ($1.17 \leq L/D \leq 5.36$) at $f_f = 100$ Hz and $U'_{j,rms} = 1.5$ m/s. Each figure represents (a) centerplane-based mean Unmixedness $U_{c,sn}$ along s_c/D, (b) $U_{c,sn}$ along $s_{c,unforced}/D$, and (c) centerplane-based mean Unmixedness $U_{c,xz}$ along x/D, respectively.

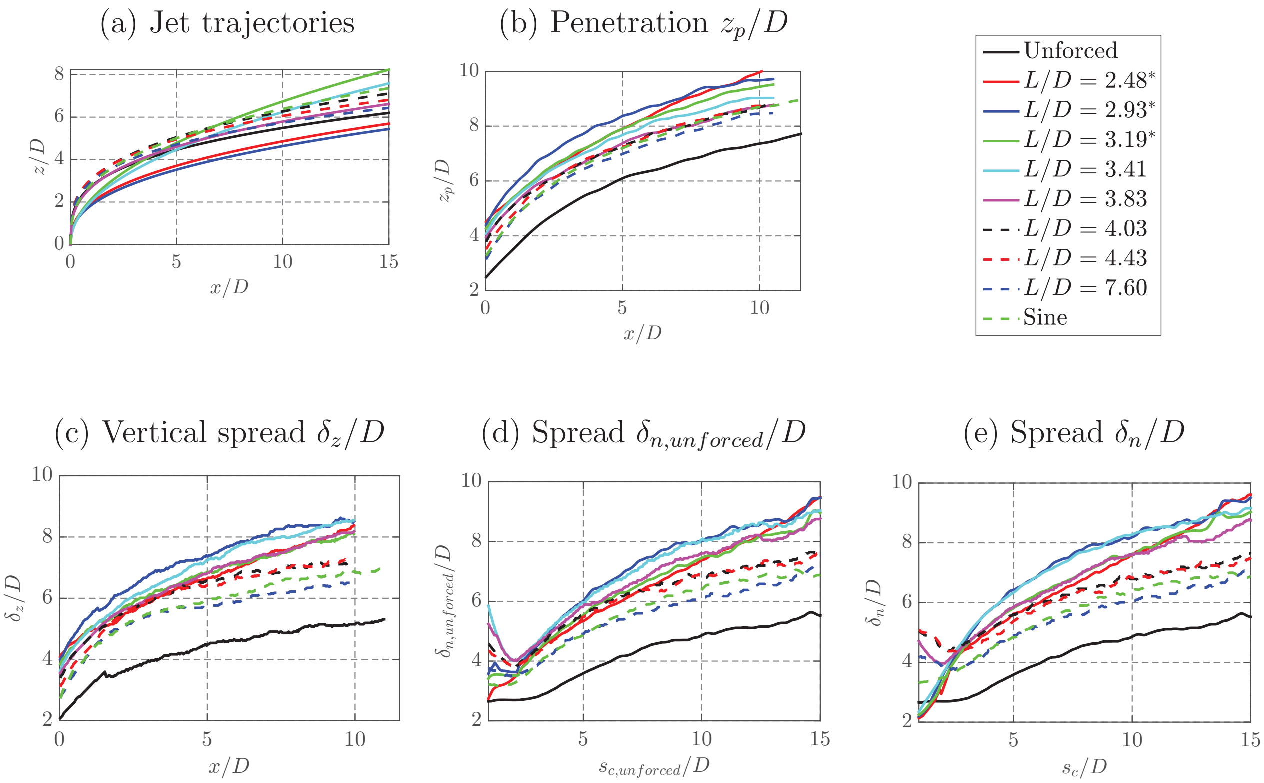

Figure C.47: Mean mixing metrics for the equidensity flush nozzle-injected JICF at $J = 5$ for the unforced case and forced cases under sine wave forcing as well as single-pulse square wave forcing with control ($2.48 \leq L/D \leq 7.60$) at $f_f = 100$ Hz and $U'_{j,rms} = 2.0$ m/s: (a) Jet trajectories, (b) jet penetration z_p/D, (c) jet vertical spread δ_z/D, (d) jet spread normal to the unforced jet trajectory $\delta_{n,unforced}/D$ and (e) jet spread normal to each jet trajectory in question δ_n/D.

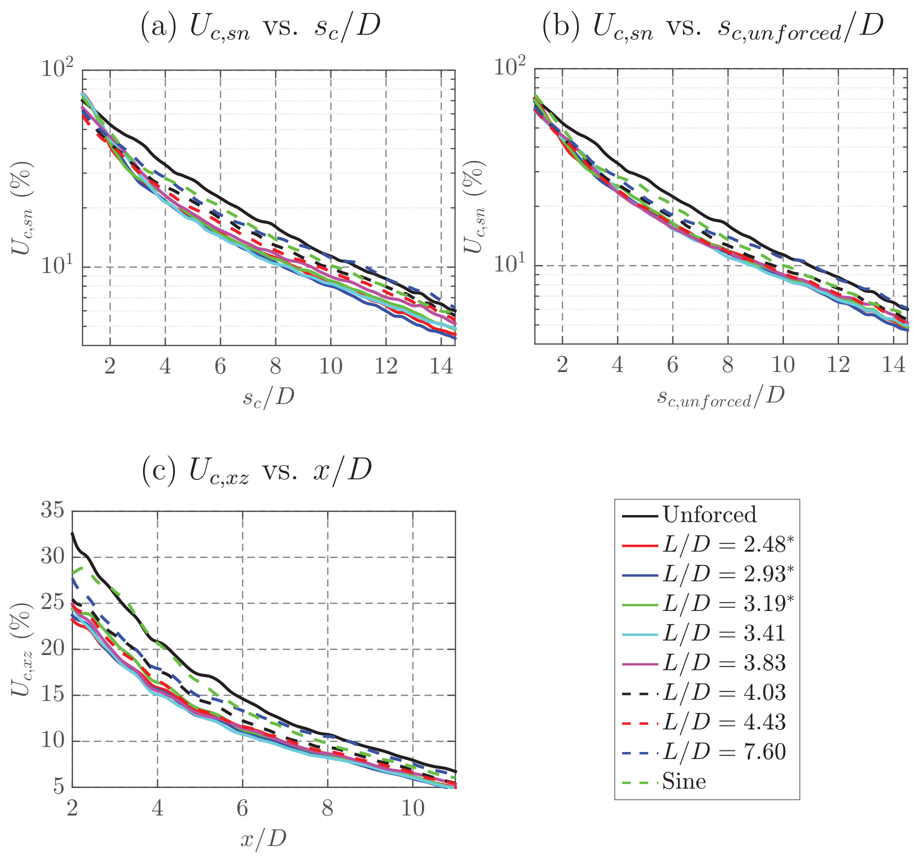

Figure C.48: Instantaneous mixing metrics for the equidensity flush nozzle-injected JICF at $J = 5$ for the unforced and forced cases under sine wave forcing as well as single-pulse square wave forcing with control ($2.48 \leq L/D \leq 7.60$) at $f_f = 100$ Hz and $U'_{j,rms} = 2.0$ m/s. Each figure represents (a) centerplane-based mean Unmixedness $U_{c,sn}$ along s_c/D, (b) $U_{c,sn}$ along $s_{c,unforced}/D$, and (c) centerplane-based mean Unmixedness $U_{c,xz}$ along x/D, respectively.

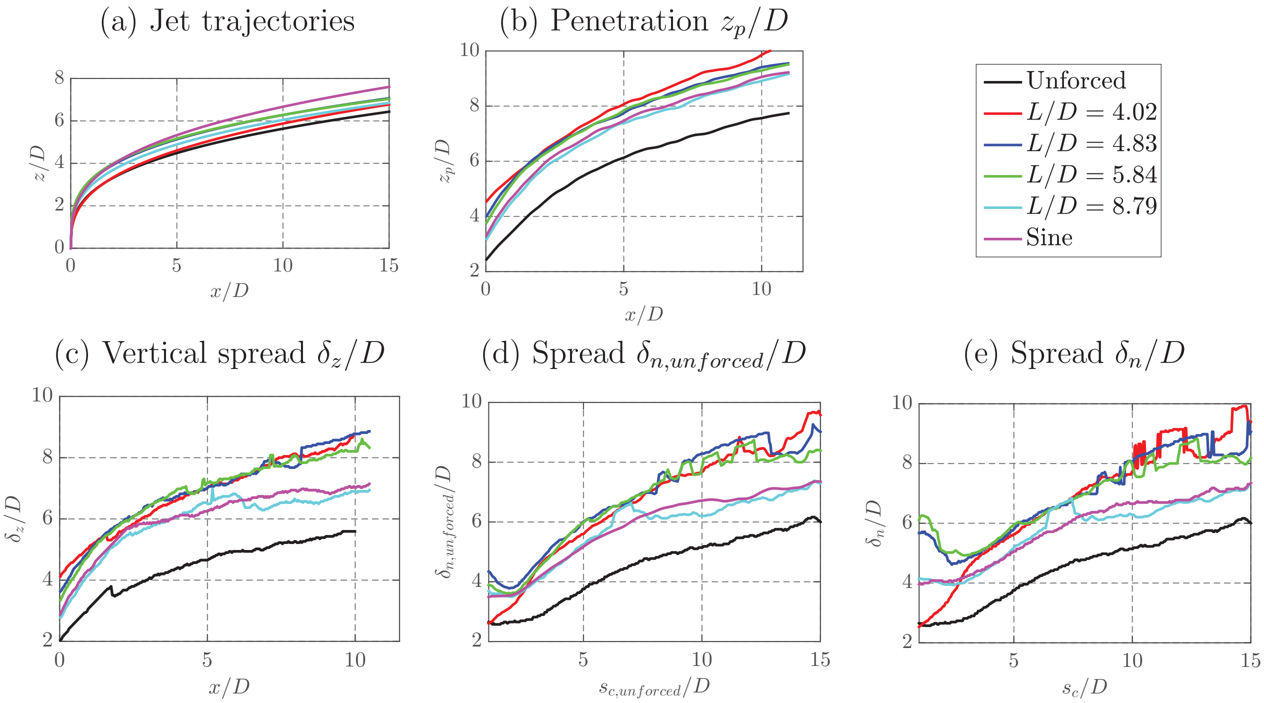

Figure C.49: Mean mixing metrics for the equidensity flush nozzle-injected JICF at $J = 5$ for the unforced case and forced cases under sine wave forcing as well as single-pulse square wave forcing with control ($4.02 \leq L/D \leq 8.79$) at $f_f = 100$ Hz and $U'_{j,rms} = 2.5$ m/s: (a) Jet trajectories, (b) jet penetration z_p/D, (c) jet vertical spread δ_z/D, (d) jet spread normal to the unforced jet trajectory $\delta_{n,unforced}/D$ and (e) jet spread normal to each jet trajectory in question δ_n/D.

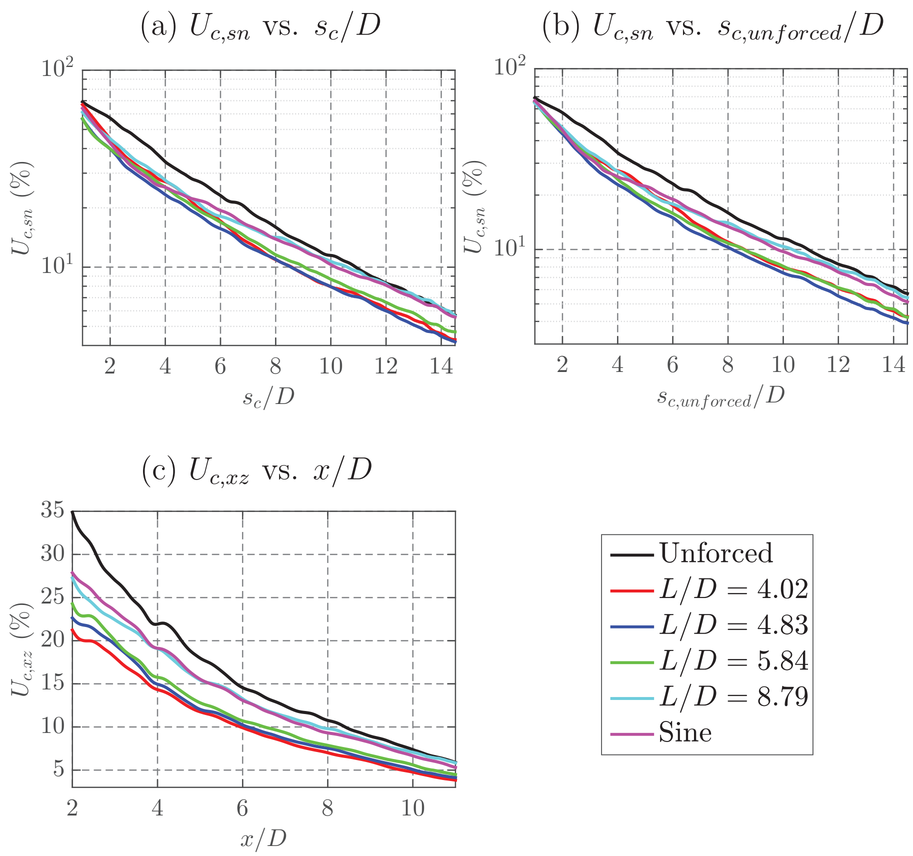

Figure C.50: Instantaneous mixing metrics for the equidensity flush nozzle-injected JICF at $J = 5$ for the unforced and forced cases under sine wave forcing as well as single-pulse square wave forcing with control ($4.02 \leq L/D \leq 8.79$) at $f_f = 100$ Hz and $U'_{j,rms} = 2.5$ m/s. Each figure represents (a) centerplane-based mean Unmixedness $U_{c,sn}$ along s_c/D, (b) $U_{c,sn}$ along $s_{c,unforced}/D$, and (c) centerplane-based mean Unmixedness $U_{c,xz}$ along x/D, respectively.

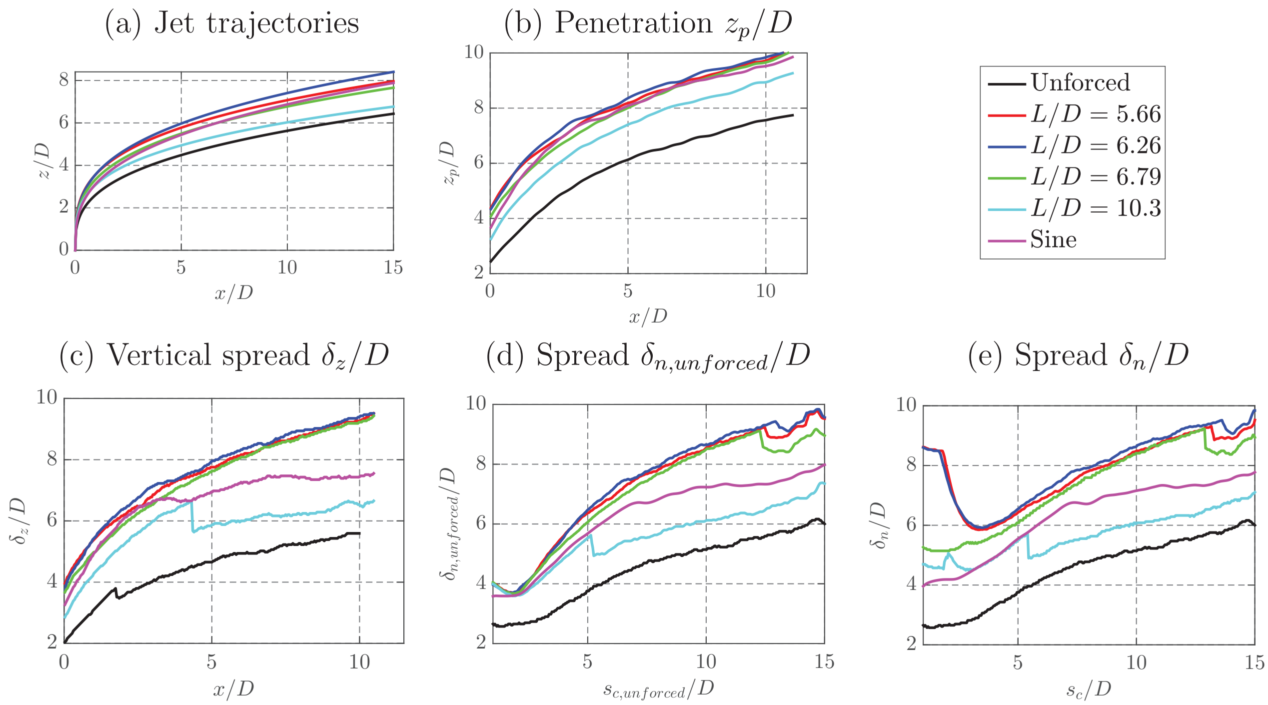

Figure C.51: Mean mixing metrics for the equidensity flush nozzle-injected JICF at $J = 5$ for the unforced case and forced cases under sine wave forcing as well as single-pulse square wave forcing with control ($5.66 \leq L/D \leq 10.3$) at $f_f = 100$ Hz and $U'_{j,rms} = 3.0$ m/s: (a) Jet trajectories, (b) jet penetration z_p/D, (c) jet vertical spread δ_z/D, (d) jet spread normal to the unforced jet trajectory $\delta_{n,unforced}/D$ and (e) jet spread normal to each jet trajectory in question δ_n/D.

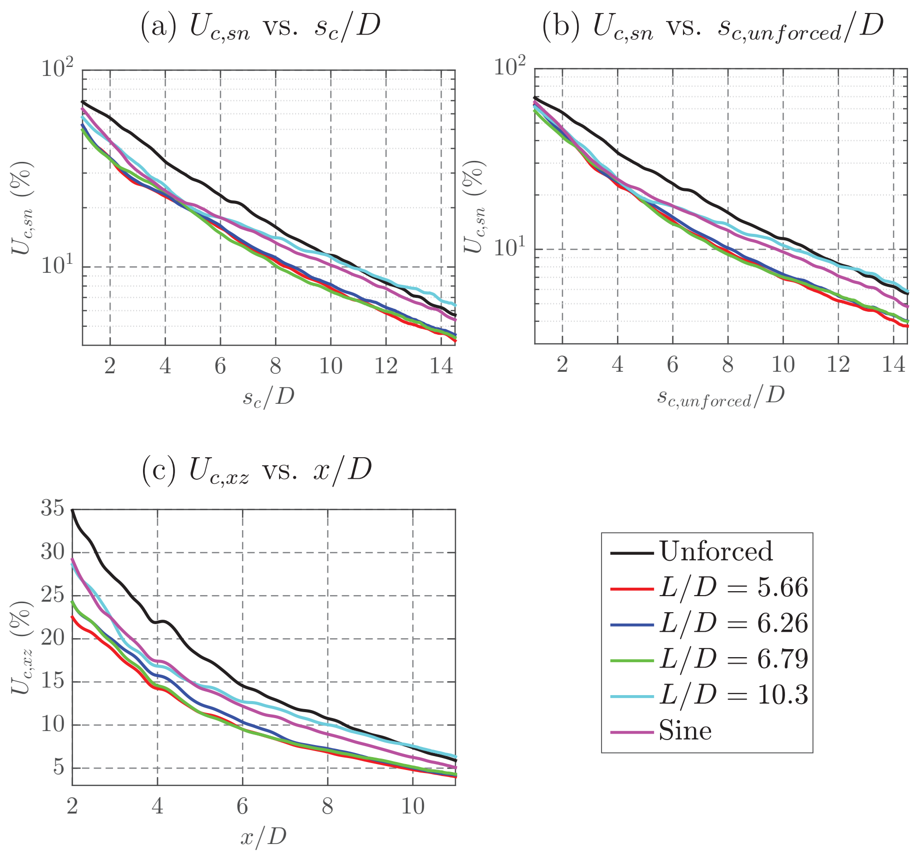

Figure C.52: Instantaneous mixing metrics for the equidensity flush nozzle-injected JICF at $J = 5$ for the unforced and forced cases under sine wave forcing as well as single-pulse square wave forcing with control ($5.66 \leq L/D \leq 10.3$) at $f_f = 100$ Hz and $U'_{j,rms} = 3.0$ m/s. Each figure represents (a) centerplane-based mean Unmixedness $U_{c,sn}$ along s_c/D, (b) $U_{c,sn}$ along $s_{c,unforced}/D$, and (c) centerplane-based mean Unmixedness $U_{c,xz}$ along x/D, respectively.

APPENDIX D

Double-Pulse Square Wave Forcing Data

The following results correspond to data associated with the study of double-pulse square wave forcing in Chapter 7.

D.1 Mean Centerplane PLIF Images

This section represents mean centerplane PLIF images for all data sets discussed in Chapter 7. All mean images shown here are created by averaging 500 instantaneous images.

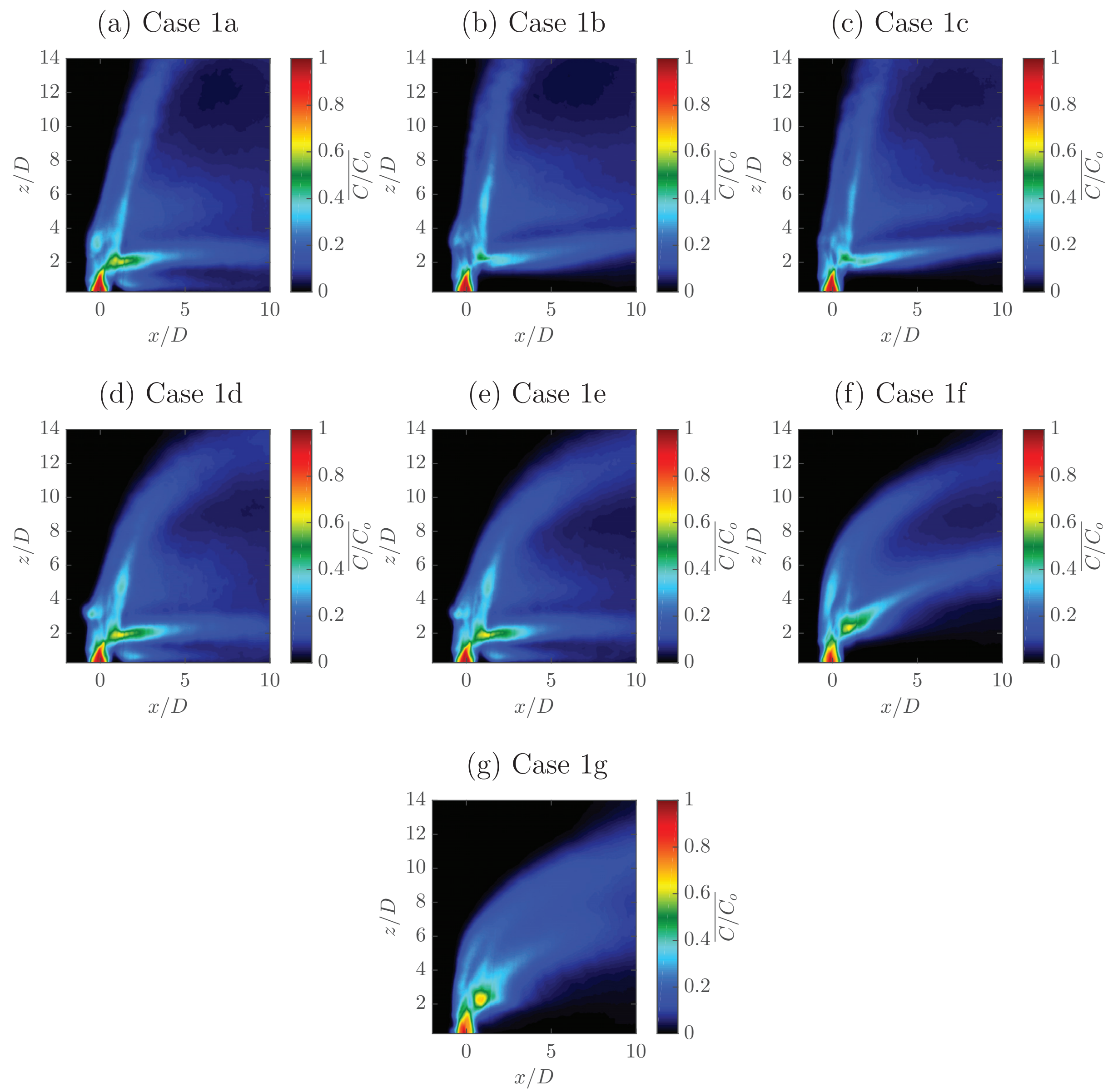

Figure D.1: Mean centerplane PLIF images (ensemble of 500 instantaneous images) under double-pulse square wave forcing (f_f = 55 Hz) for Cases 1a-1g with matching RMS of jet velocity perturbation at $U'_{j,rms}$ = 1.7 m/s (approximately 63 % of the mean jet velocity at the jet exit plane U_j = 2.7 m/s). These images were acquired at a recording rate of 5 Hz.

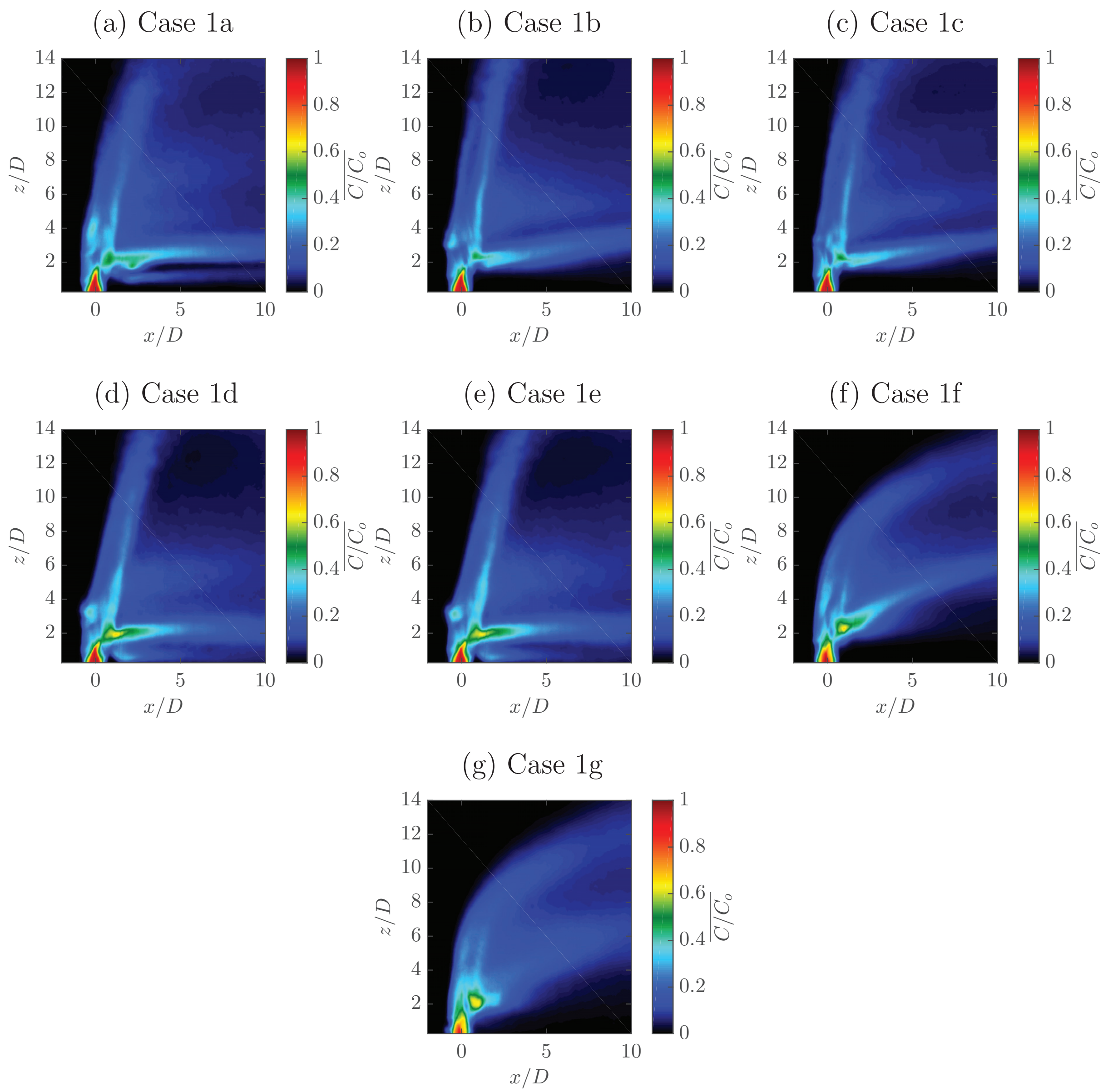

Figure D.2: Mean centerplane PLIF images (ensemble of 500 instantaneous images) under double-pulse square wave forcing ($f_f = 55$ Hz) for Cases 1a-1g with matching peak-to-peak jet velocity amplitude at $\Delta U_j \approx 4.3$ m/s. These images were acquired at a recording rate of 5 Hz.

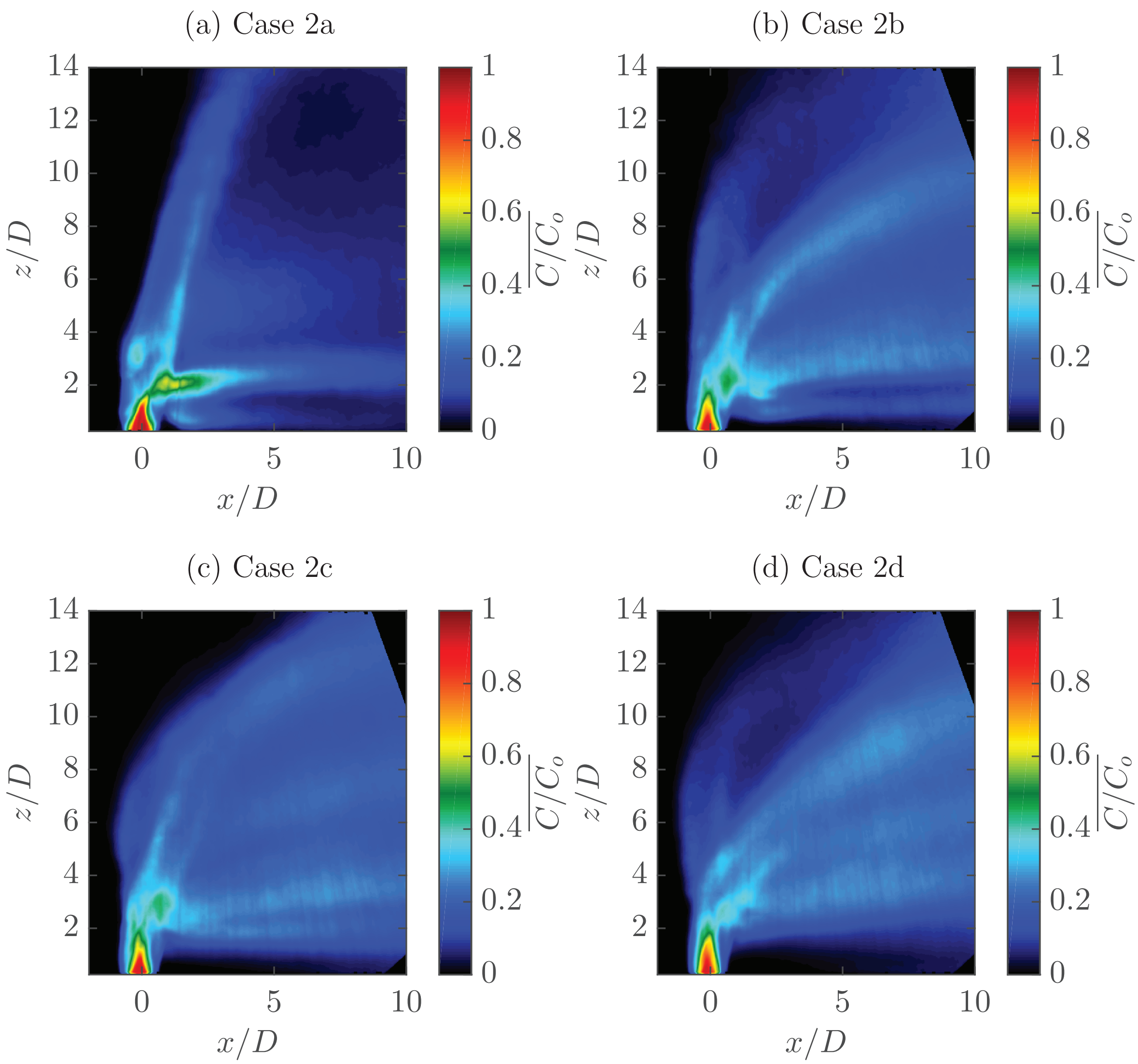

Figure D.3: Mean centerplane PLIF images (ensemble of 500 instantaneous images) under double-pulse square wave forcing ($f_f = 55$ Hz) without the improvements in the feedback controller for Cases 2a-2d with matching RMS of jet velocity perturbation at $U'_{j,rms} = 1.7$ m/s (approximately 63 % of the mean jet velocity at the jet exit plane $U_j = 2.7$ m/s). These images were acquired at a recording rate of 1 Hz.

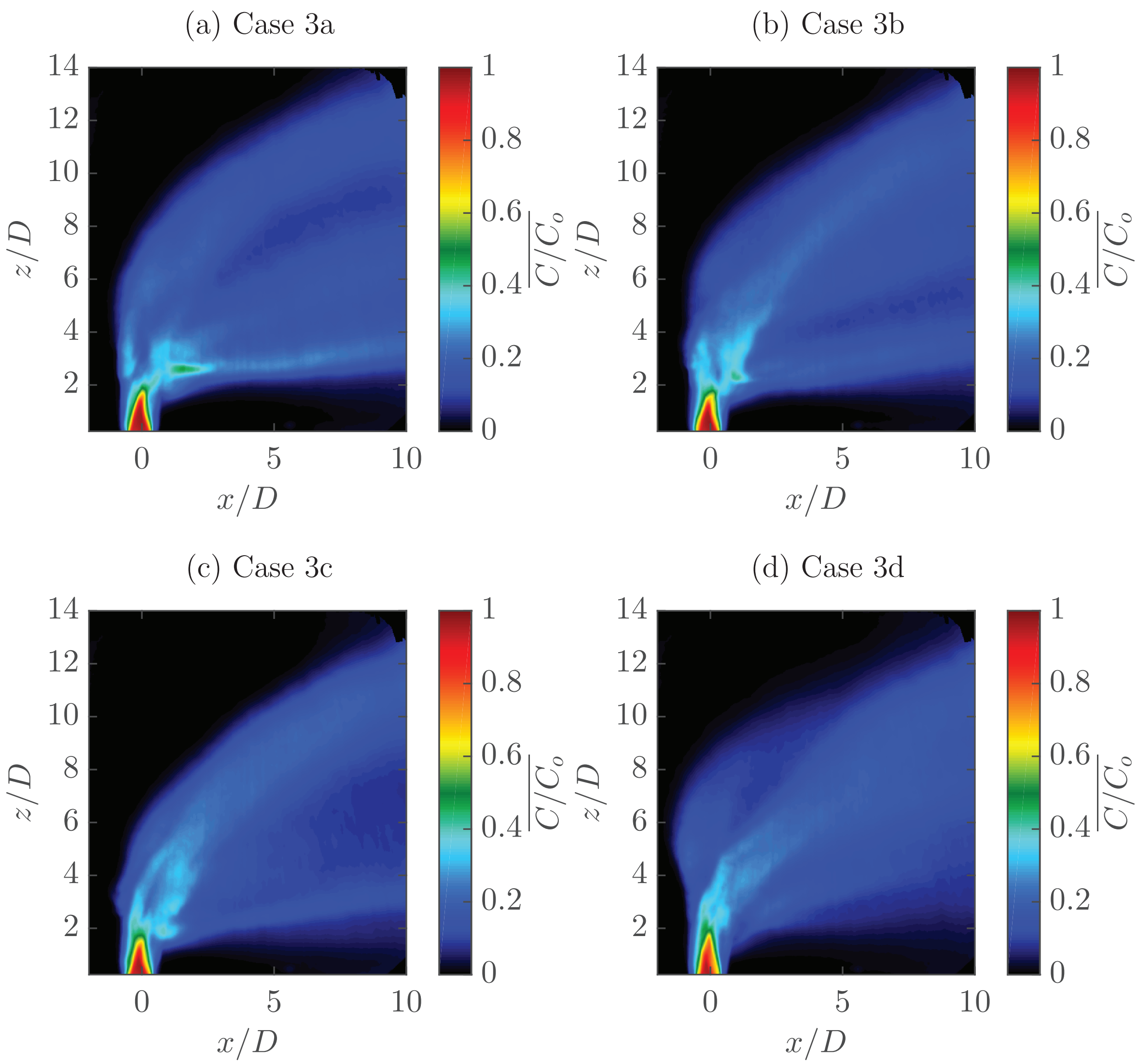

Figure D.4: Mean centerplane PLIF images (ensemble of 500 instantaneous images) under double-pulse square wave forcing (f_f = 55 Hz) without the improvements in the feedback controller for Cases 3a-3d with matching RMS of jet velocity perturbation at $U'_{j,rms}$ = 1.7 m/s (approximately 63 % of the mean jet velocity at the jet exit plane U_j = 2.7 m/s). These images were acquired at a recording rate of 1 Hz.

D.2 Instantaneous and Mean Cross-Sectional PLIF Images

This section represents instantaneous and mean cross-sectional PLIF images for Cases 3a-3d, which were not shown in Chapter 7. All mean images shown here are created by averaging 500 instantaneous images.

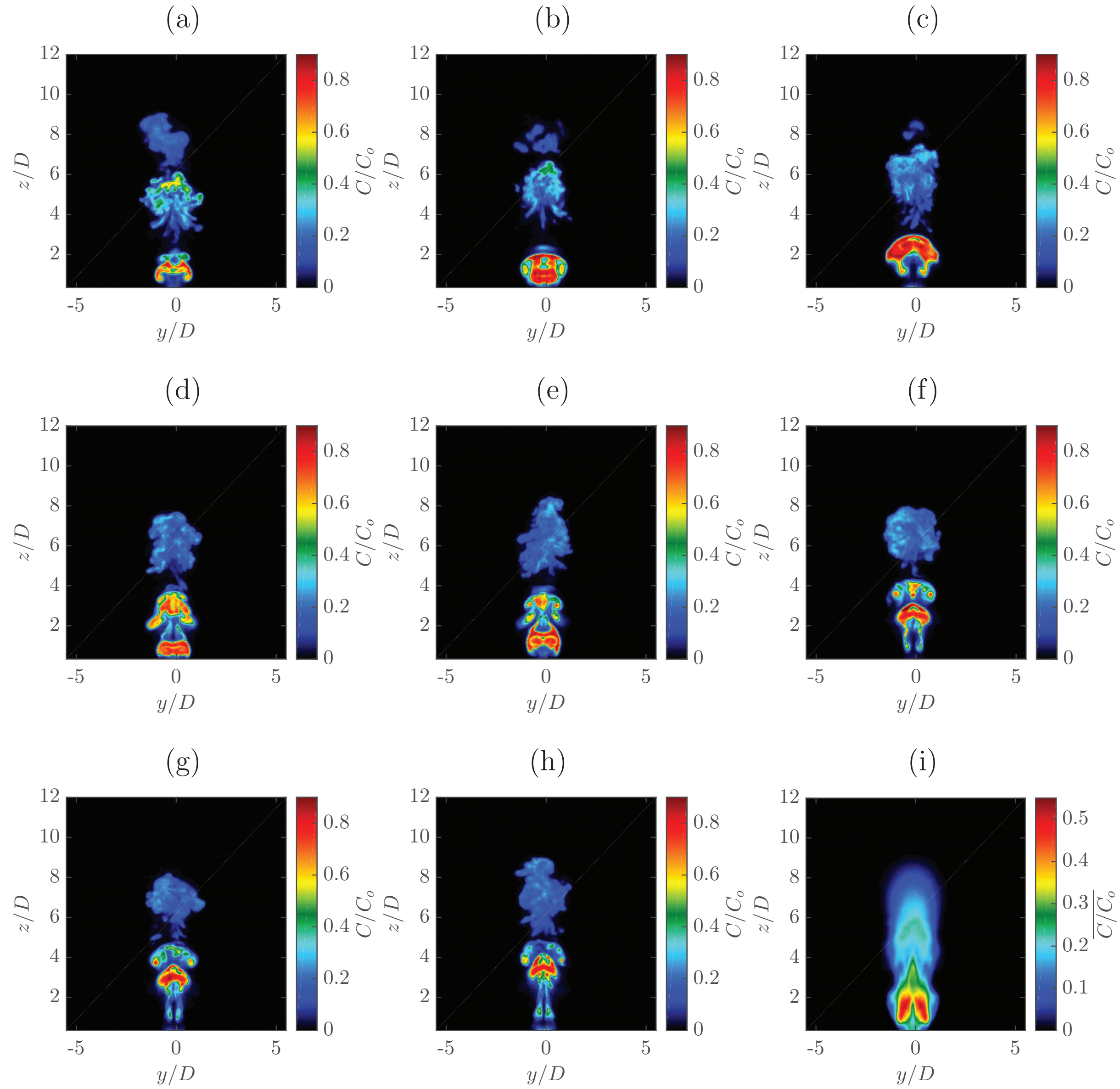

Figure D.5: (a)-(h) Sequential instantaneous and (i) mean cross-sectional PLIF images (ensemble of 500 instantaneous images) under double-pulse square wave forcing at $f_f = 55$ Hz and $U'_{j,rms} = 1.7$ m/s acquired at the downstream location of $x/D = 0.5$ (Case 3a). These images were acquired at a recording rate of 1 Hz.

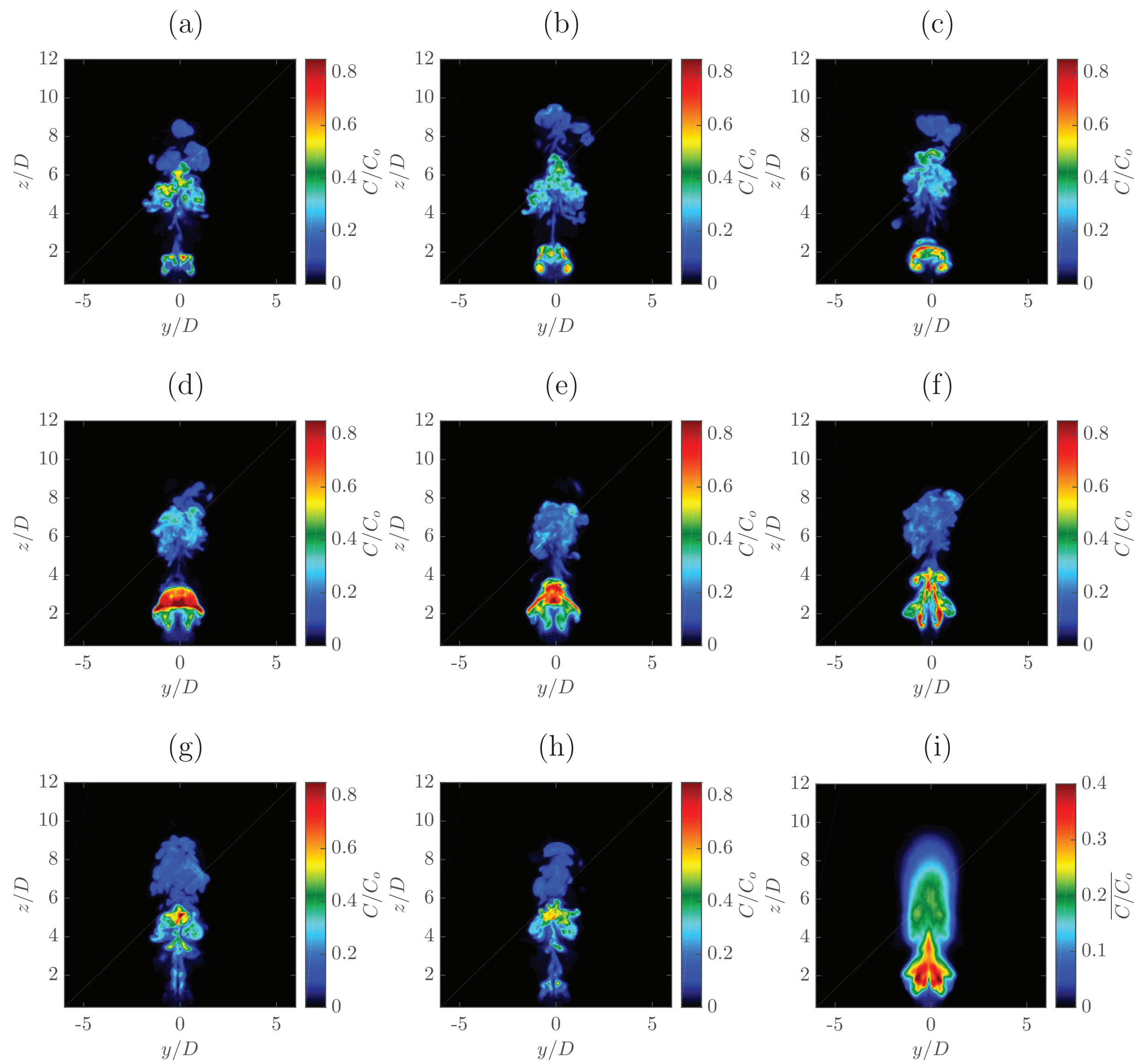

Figure D.6: (a)-(h) Sequential instantaneous and (i) mean cross-sectional PLIF images (ensemble of 500 instantaneous images) under double-pulse square wave forcing at $f_f = 55$ Hz and $U'_{j,rms} = 1.7$ m/s acquired at the downstream location of $x/D = 1.0$ (Case 3a). These images were acquired at a recording rate of 1 Hz.

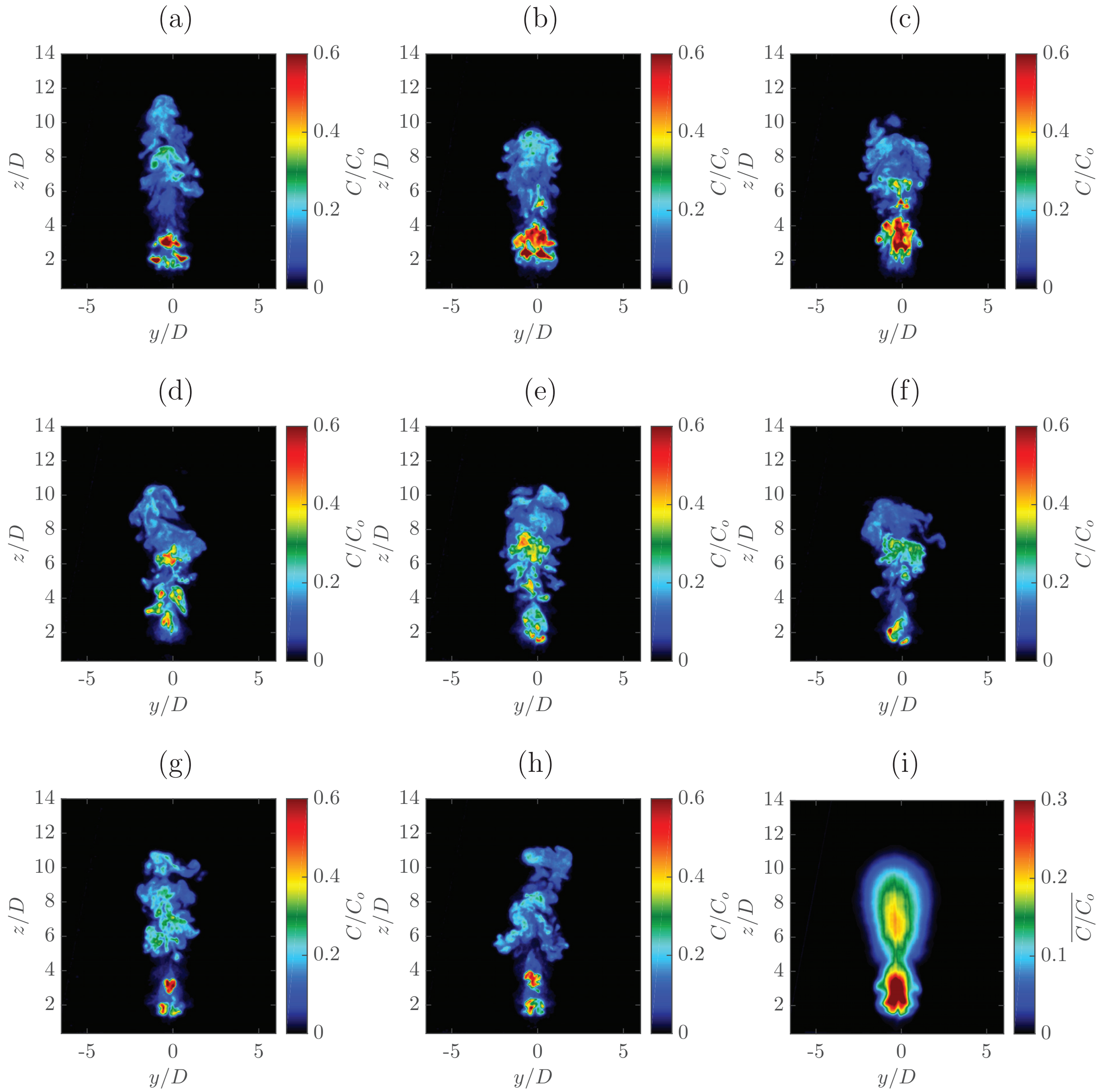

Figure D.7: (a)-(h) Sequential instantaneous and (i) mean cross-sectional PLIF images (ensemble of 500 instantaneous images) under double-pulse square wave forcing at $f_f = 55$ Hz and $U'_{j,rms} = 1.7$ m/s acquired at the downstream location of $x/D = 2.5$ (Case 3a). These images were acquired at a recording rate of 1 Hz.

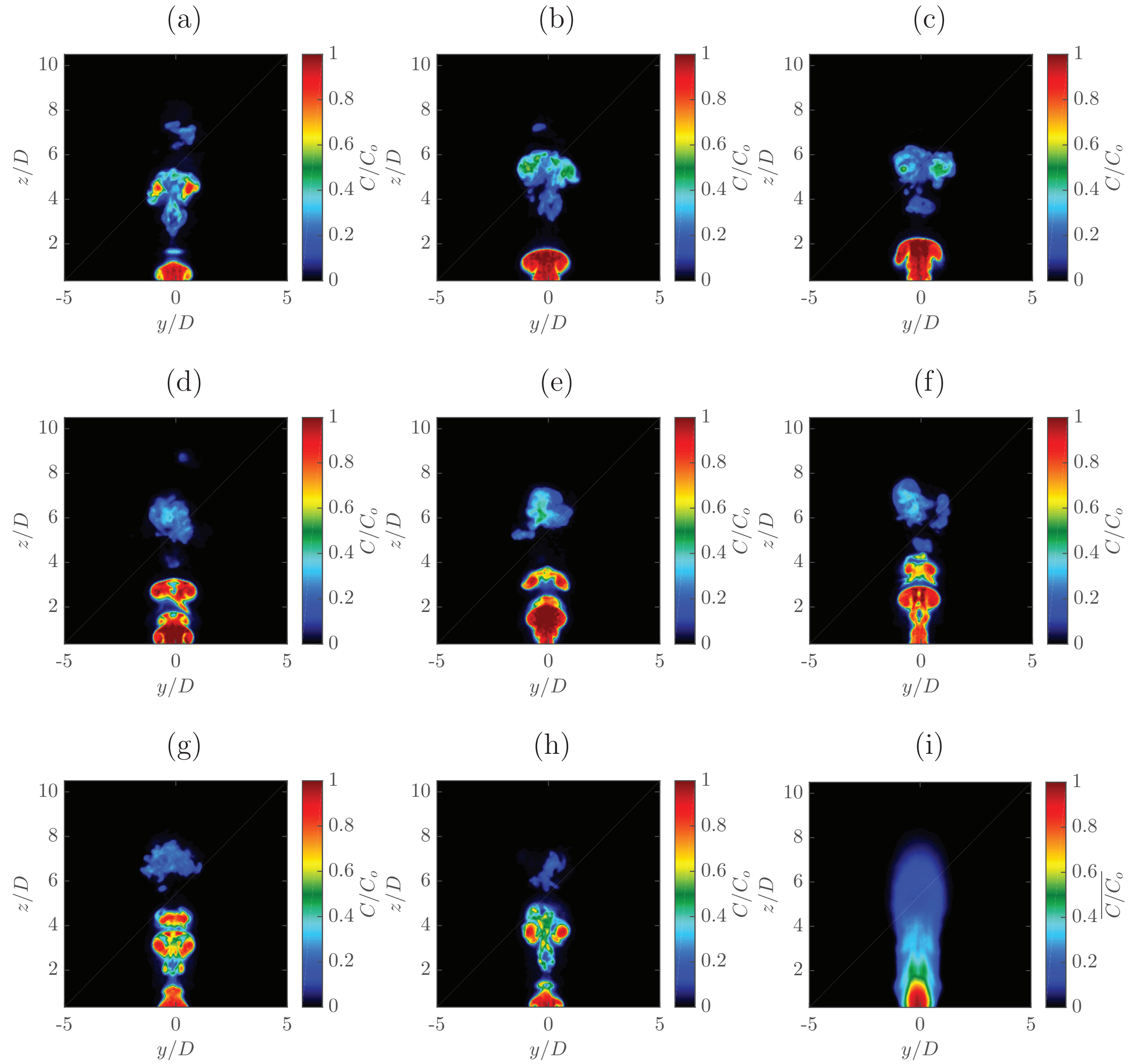

Figure D.8: (a)-(h) Sequential instantaneous and (i) mean cross-sectional PLIF images (ensemble of 500 instantaneous images) under double-pulse square wave forcing at $f_f = 55$ Hz and $U'_{j,rms} = 1.7$ m/s acquired at the downstream location of $x/D = 0$ (Case 3b). These images were acquired at a recording rate of 1 Hz.

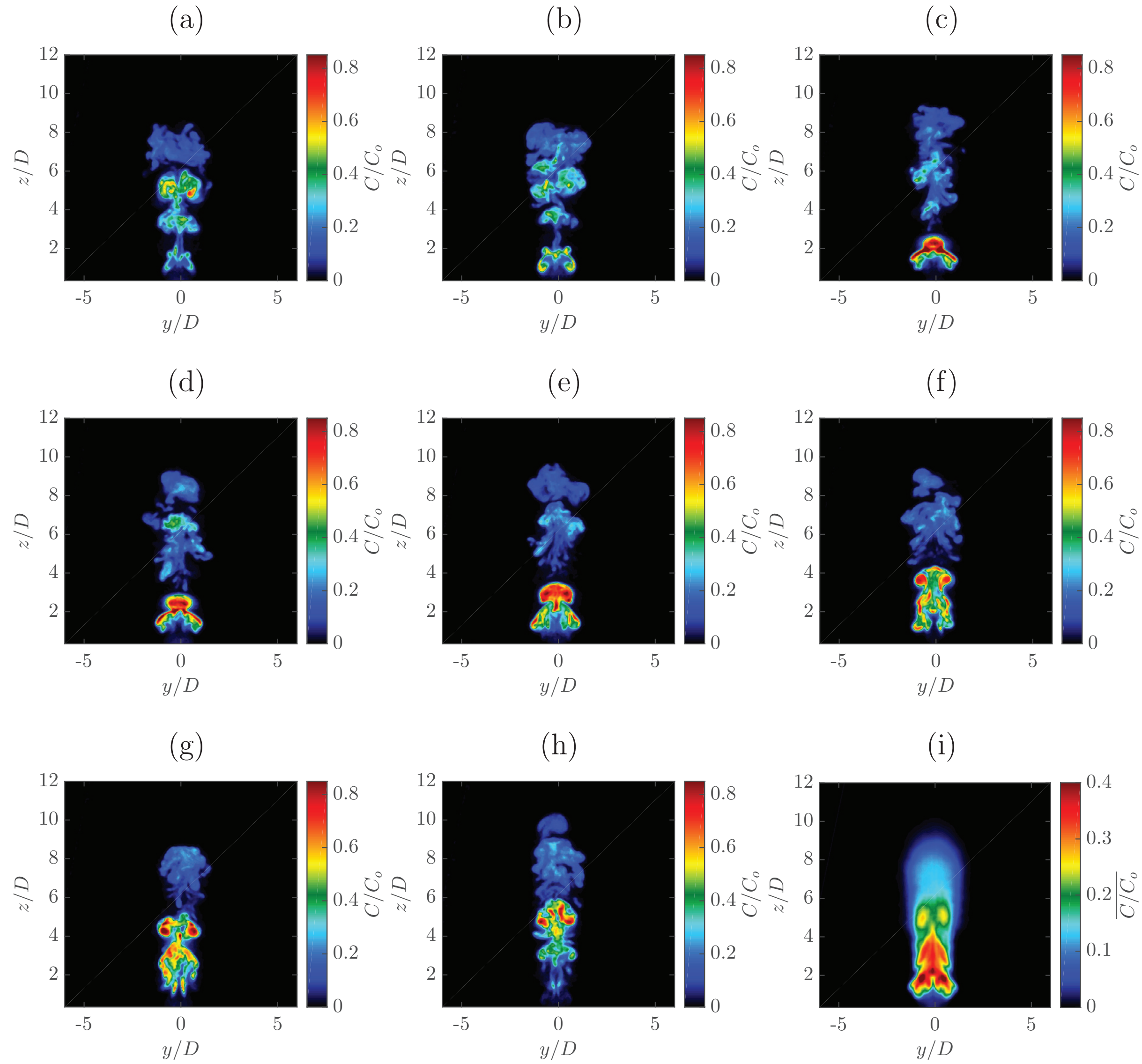

Figure D.9: (a)-(h) Sequential instantaneous and (i) mean cross-sectional PLIF images (ensemble of 500 instantaneous images) under double-pulse square wave forcing at $f_f = 55$ Hz and $U'_{j,rms} = 1.7$ m/s acquired at the downstream location of $x/D = 1.0$ (Case 3b). These images were acquired at a recording rate of 1 Hz.

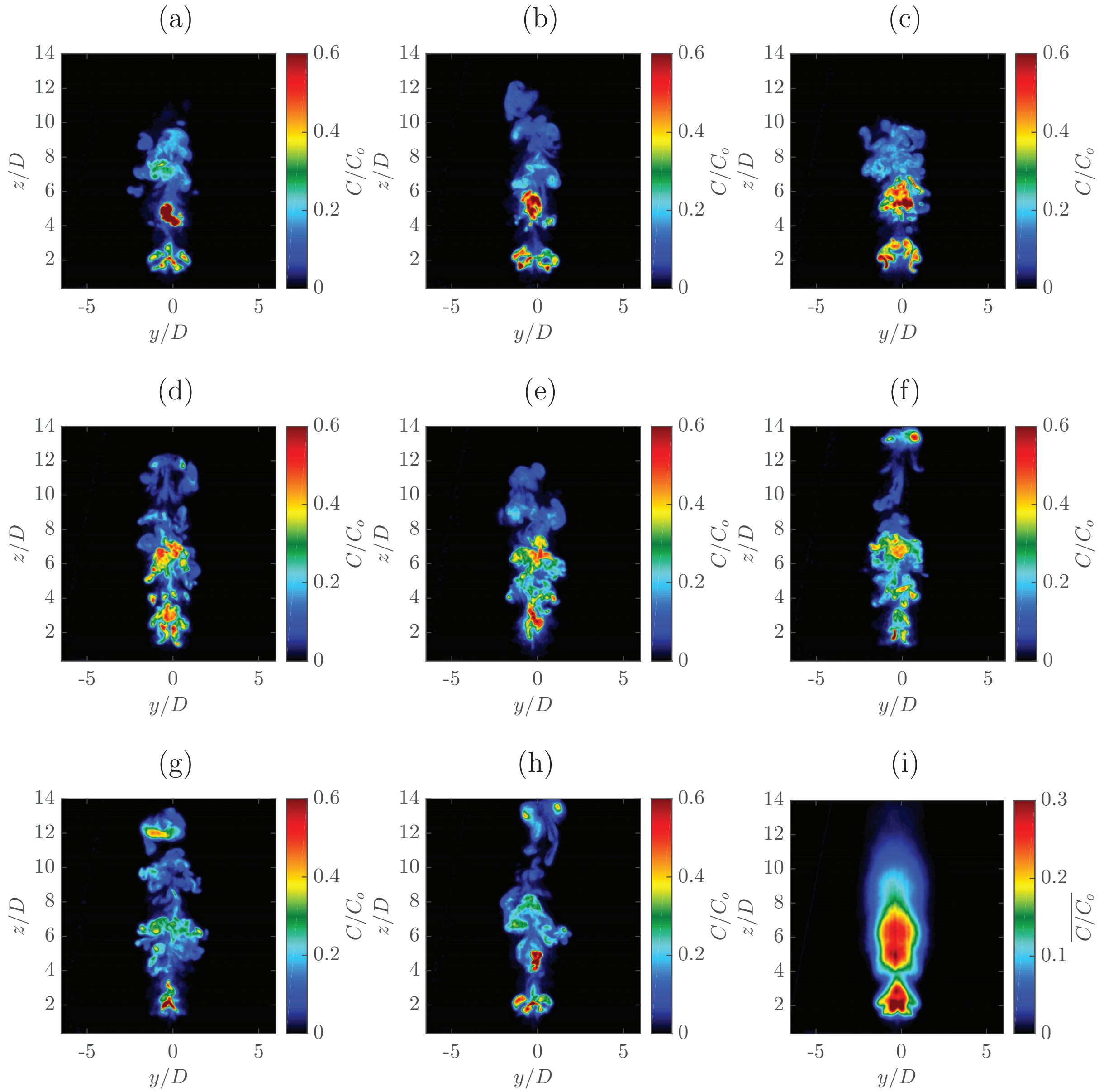

Figure D.10: (a)-(h) Sequential instantaneous and (i) mean cross-sectional PLIF images (ensemble of 500 instantaneous images) under double-pulse square wave forcing at $f_f = 55$ Hz and $U'_{j,rms} = 1.7$ m/s acquired at the downstream location of $x/D = 2.5$ (Case 3b). These images were acquired at a recording rate of 1 Hz.

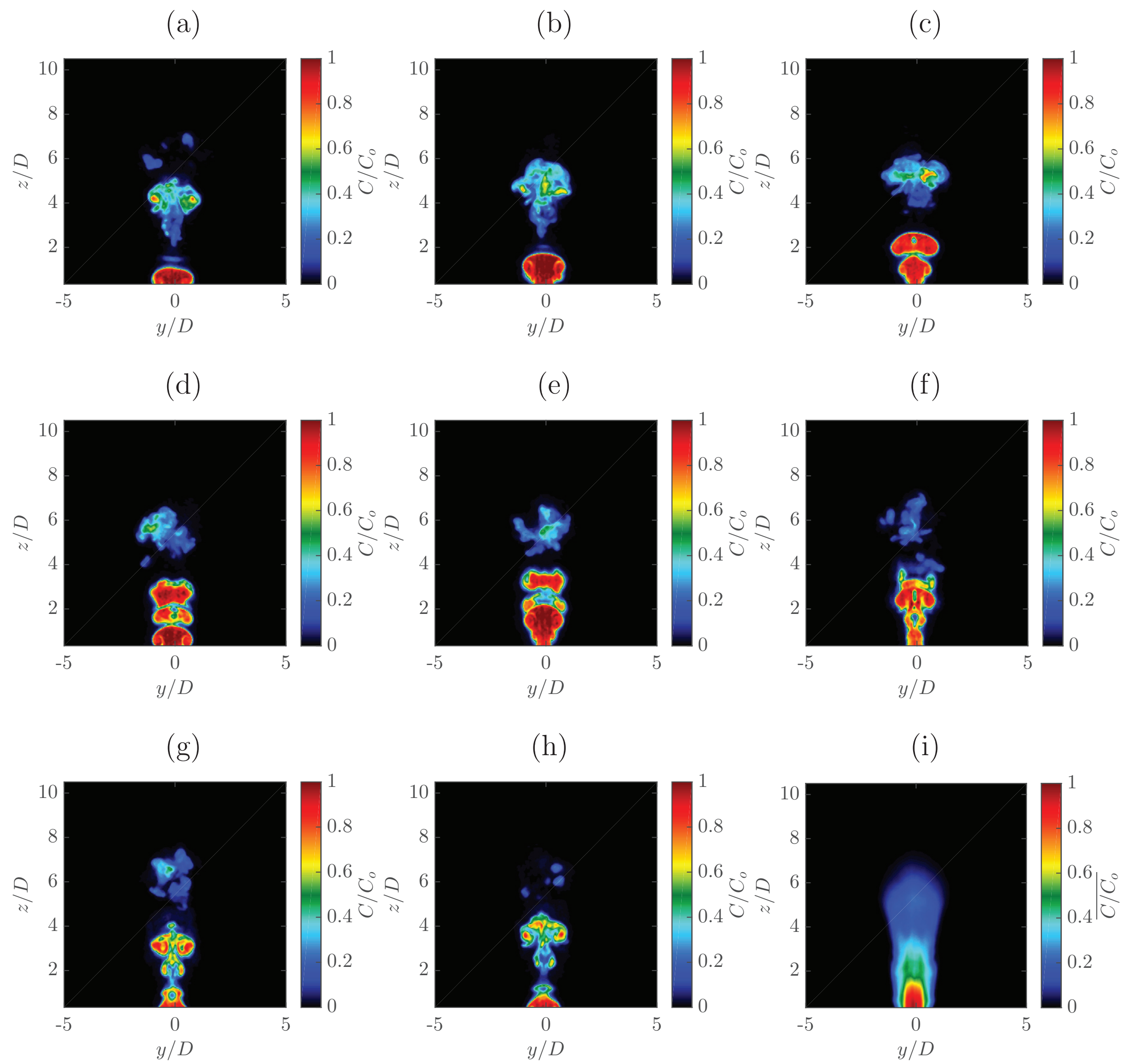

Figure D.11: (a)-(h) Sequential instantaneous and (i) mean cross-sectional PLIF images (ensemble of 500 instantaneous images) under double-pulse square wave forcing at $f_f = 55$ Hz and $U'_{j,rms} = 1.7$ m/s acquired at the downstream location of $x/D = 0$ (Case 3c). These images were acquired at a recording rate of 1 Hz.

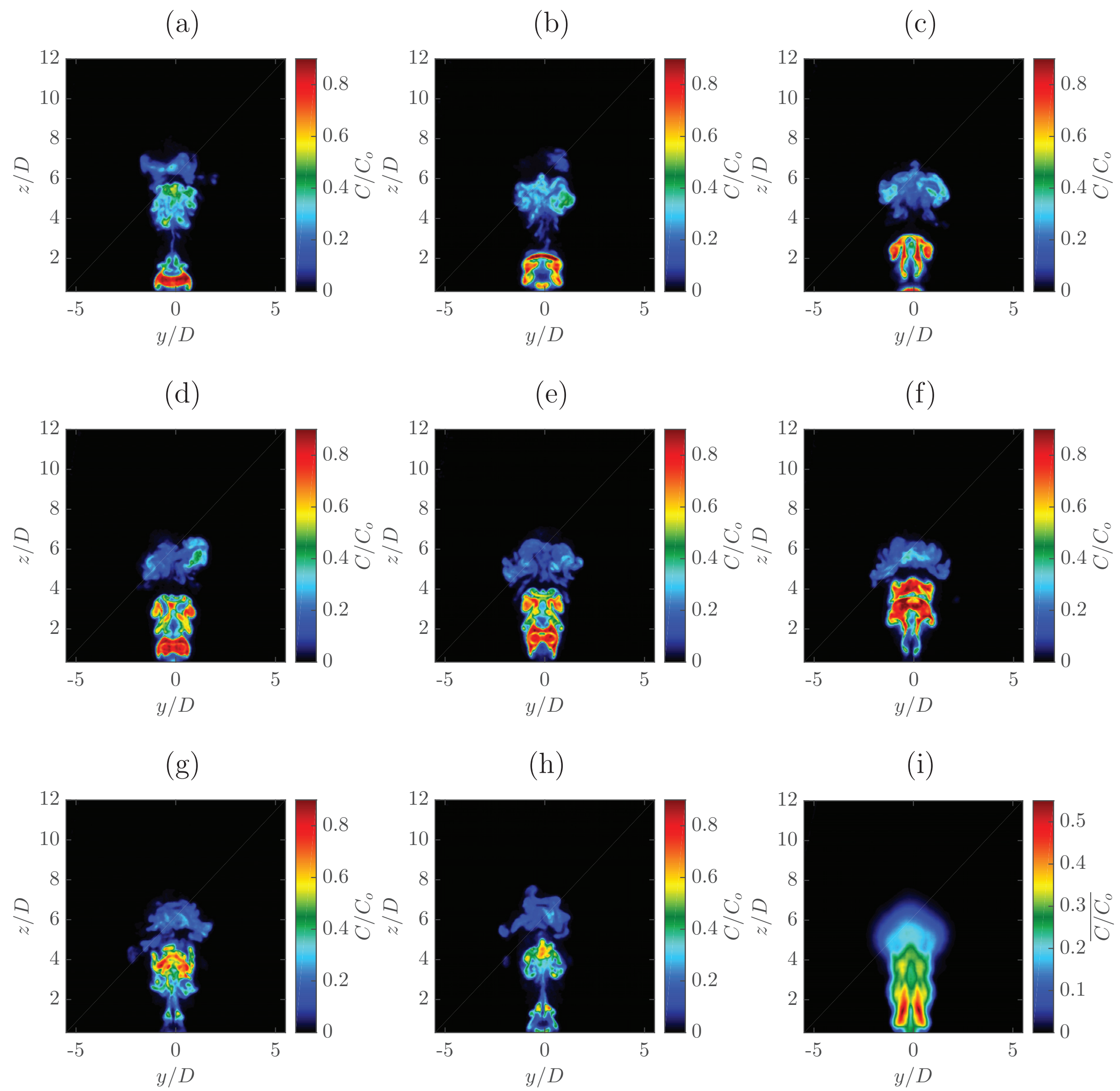

Figure D.12: (a)-(h) Sequential instantaneous and (i) mean cross-sectional PLIF images (ensemble of 500 instantaneous images) under double-pulse square wave forcing at $f_f = 55$ Hz and $U'_{j,rms} = 1.7$ m/s acquired at the downstream location of $x/D = 0.5$ (Case 3c). These images were acquired at a recording rate of 1 Hz.

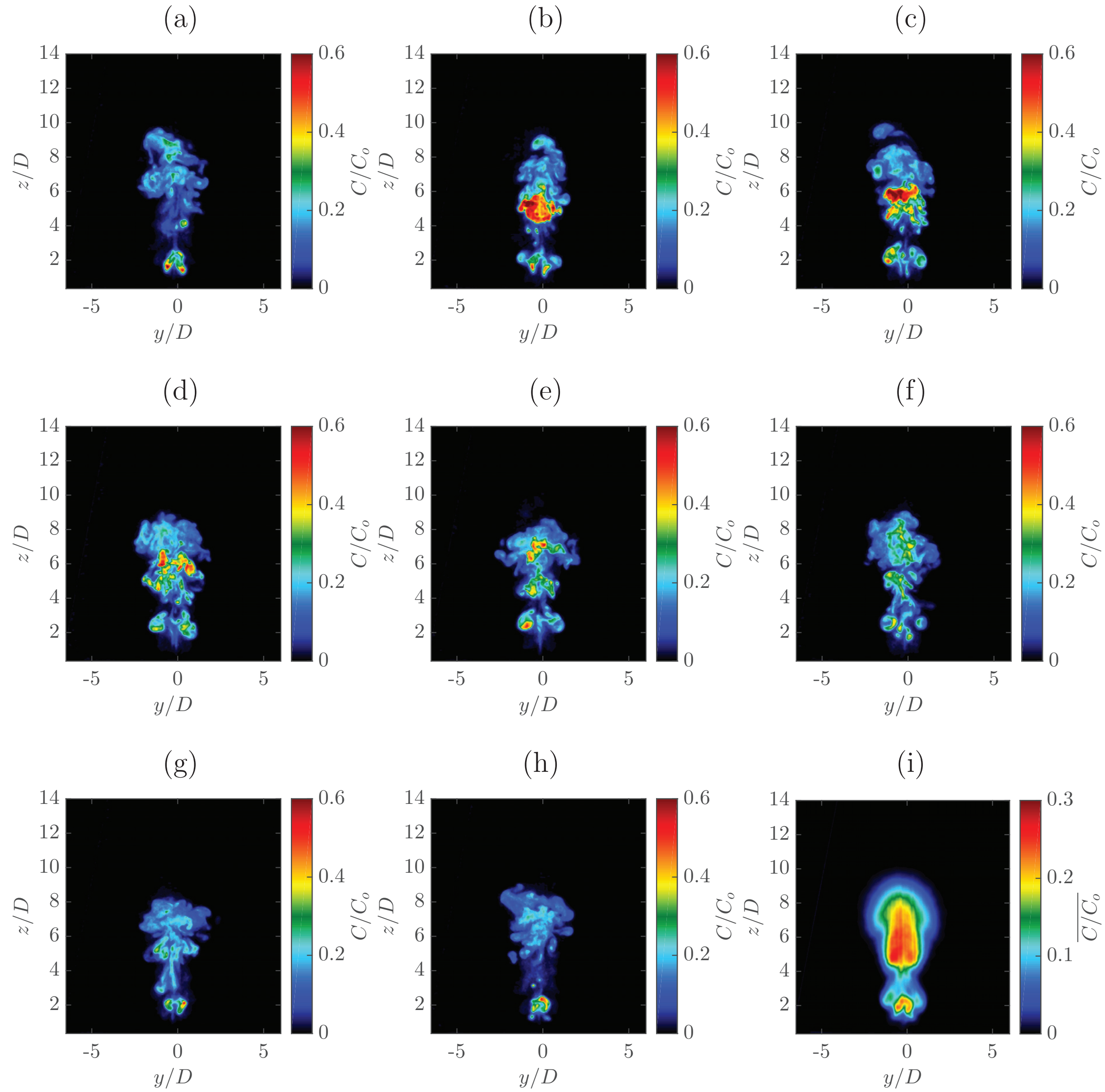

Figure D.13: (a)-(h) Sequential instantaneous and (i) mean cross-sectional PLIF images (ensemble of 500 instantaneous images) under double-pulse square wave forcing at $f_f = 55$ Hz and $U'_{j,rms} = 1.7$ m/s acquired at the downstream location of $x/D = 2.5$ (Case 3c). These images were acquired at a recording rate of 1 Hz.

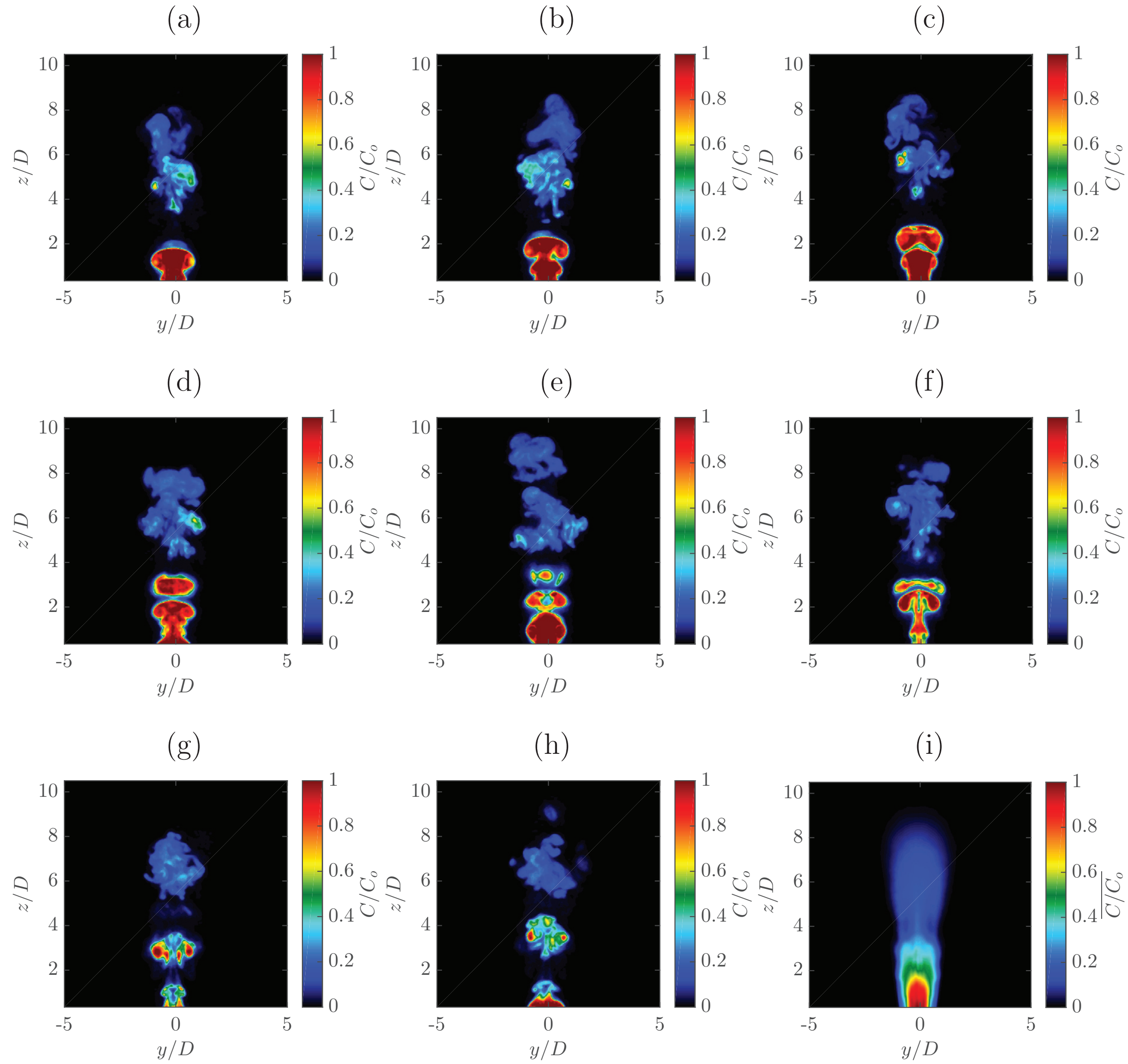

Figure D.14: (a)-(h) Sequential instantaneous and (i) mean cross-sectional PLIF images (ensemble of 500 instantaneous images) under double-pulse square wave forcing at $f_f = 55$ Hz and $U'_{j,rms} = 1.7$ m/s acquired at the downstream location of $x/D = 0$ (Case 3d). These images were acquired at a recording rate of 1 Hz.

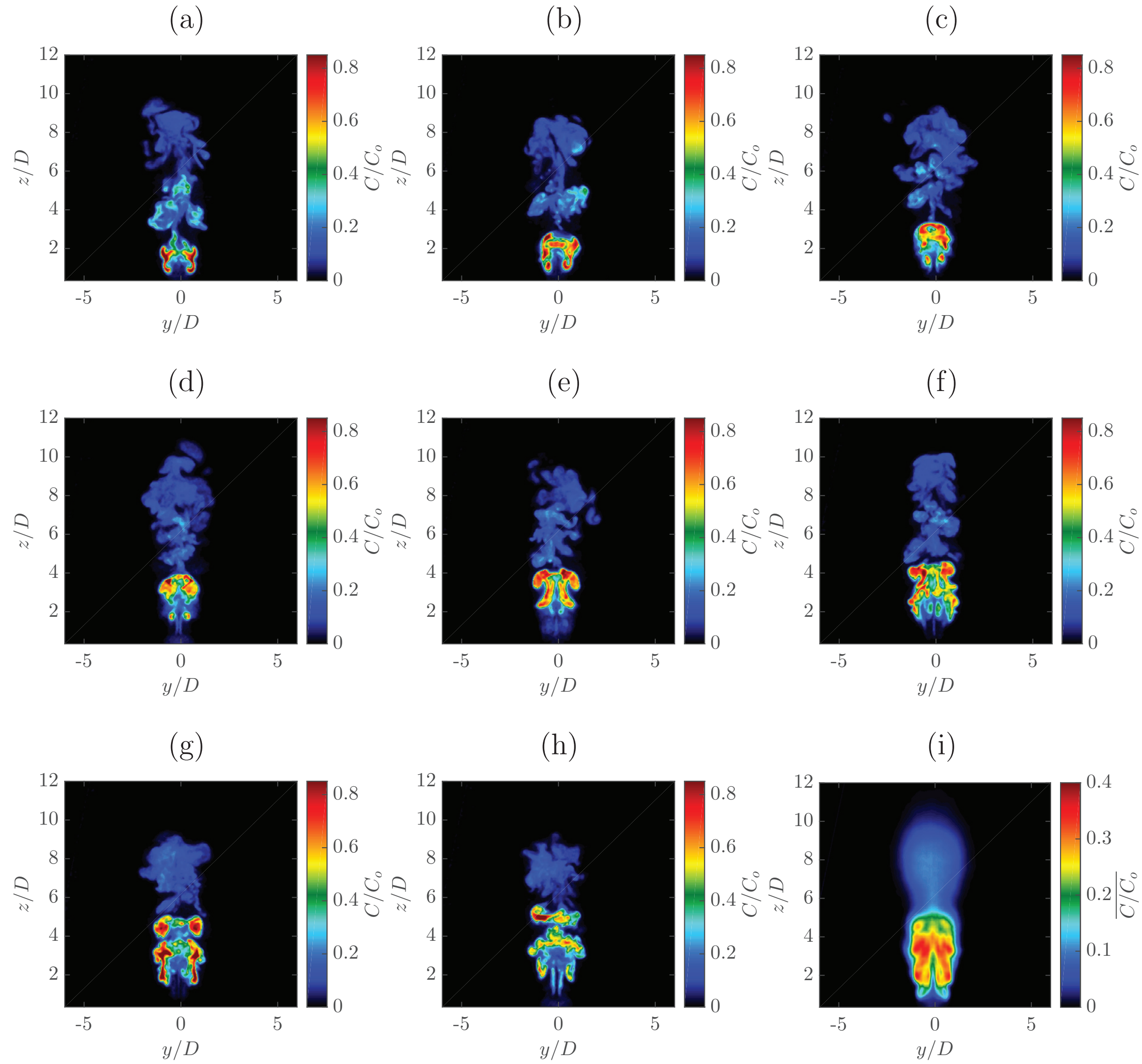

Figure D.15: (a)-(h) Sequential instantaneous and (i) mean cross-sectional PLIF images (ensemble of 500 instantaneous images) under double-pulse square wave forcing at $f_f = 55$ Hz and $U'_{j,rms} = 1.7$ m/s acquired at the downstream location of $x/D = 1.0$ (Case 3d). These images were acquired at a recording rate of 1 Hz.

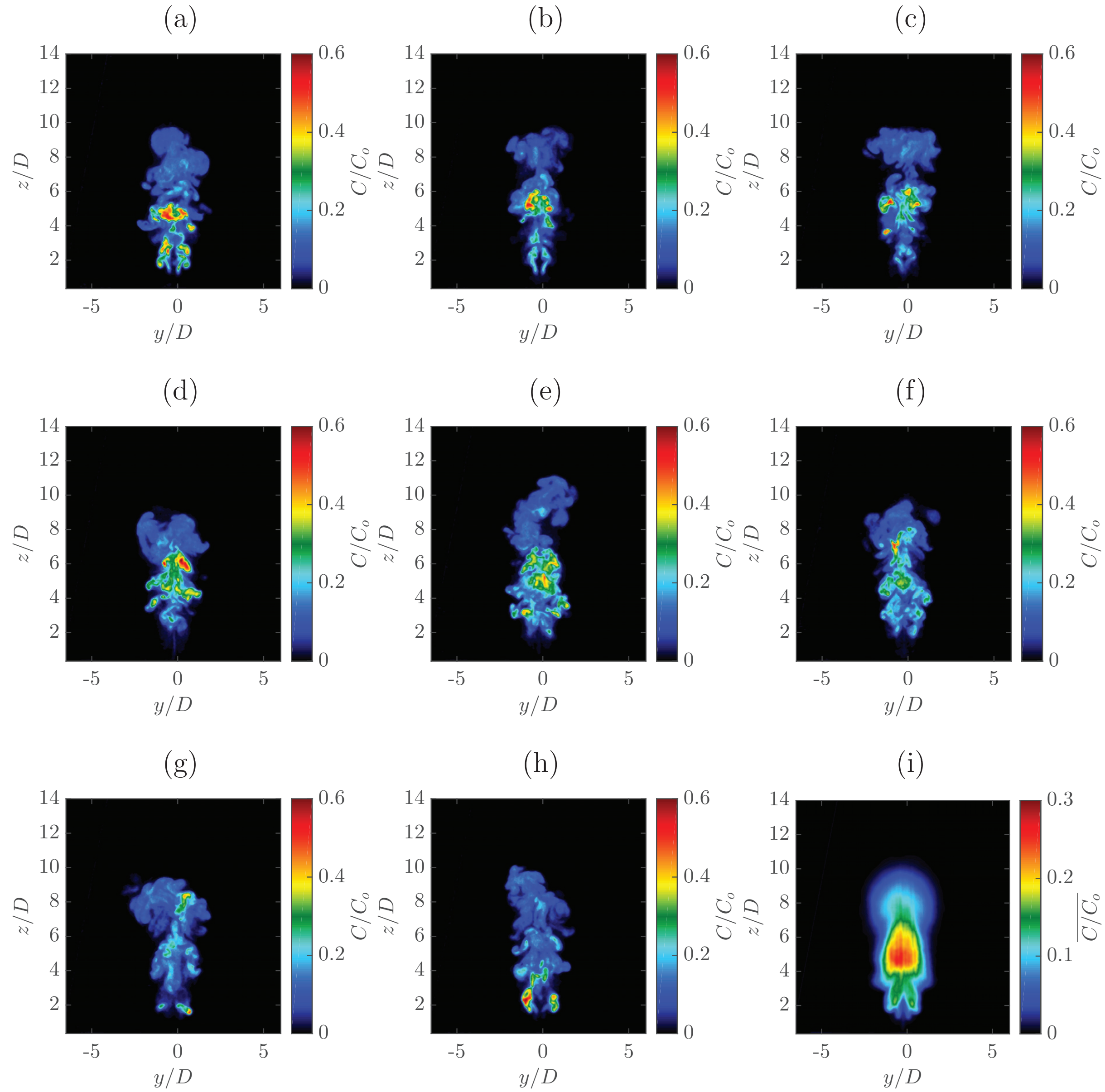

Figure D.16: (a)-(h) Sequential instantaneous and (i) mean cross-sectional PLIF images (ensemble of 500 instantaneous images) under double-pulse square wave forcing at $f_f = 55$ Hz and $U'_{j,rms} = 1.7$ m/s acquired at the downstream location of $x/D = 2.5$ (Case 3d). These images were acquired at a recording rate of 1 Hz.

D.3 Mixing Quantification for Forced JICF

This section represents mixing quantification of JICF for all data set, which were not shown in Chapter 7.

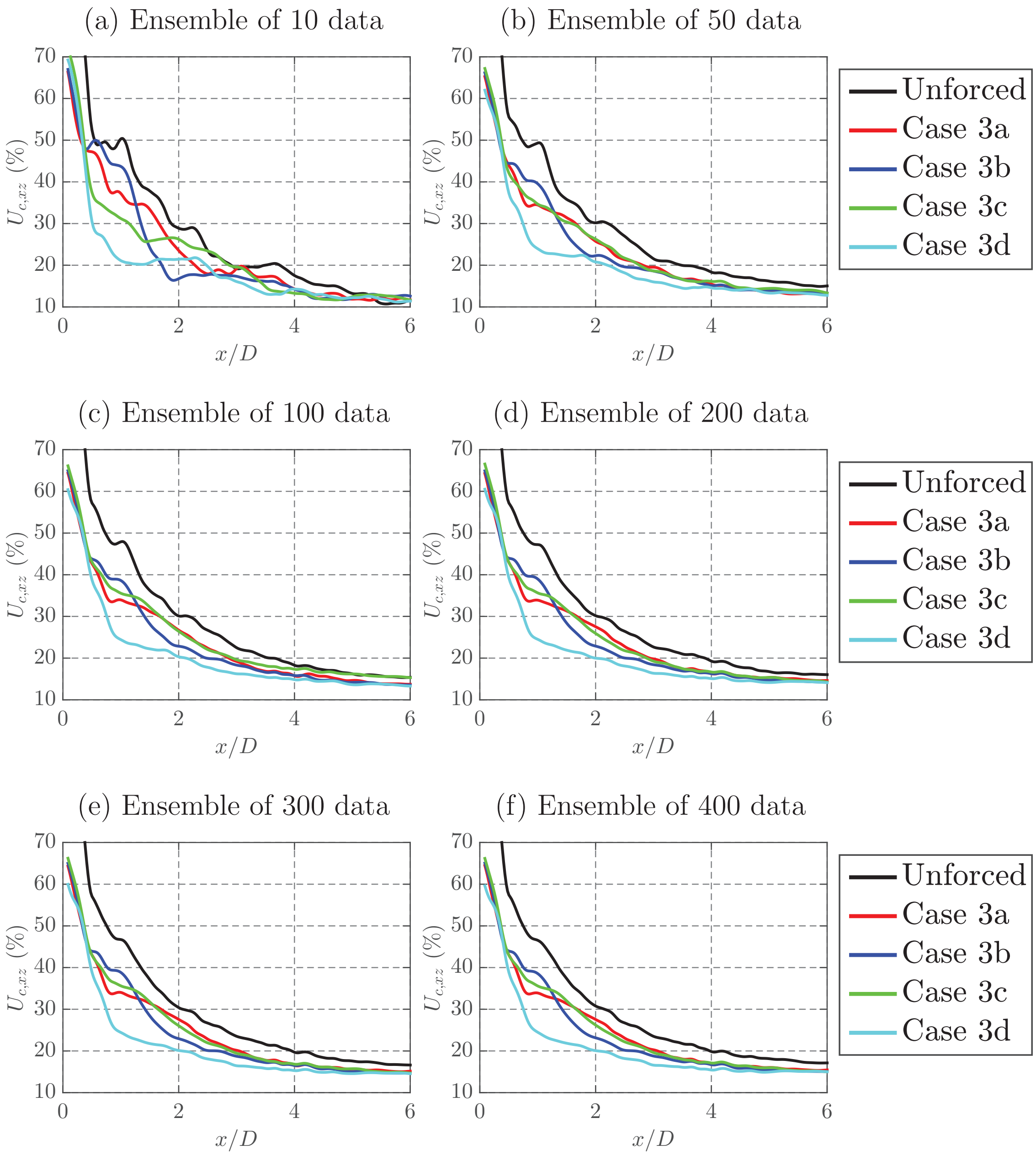

Figure D.17: Quantification of centerplane-based Unmixedness $U_{c,xz}$ along x/D for Cases 3a-3d with matching RMS of jet velocity perturbation at $U'_{j,rms} = 1.7$ m/s using an ensemble of (a) 10, (b) 50, (c) 100, (d) 200, (e) 300, and (f) 400 instantaneous images. The quantification is based on PLIF data acquired at a recording rate of 1 Hz.

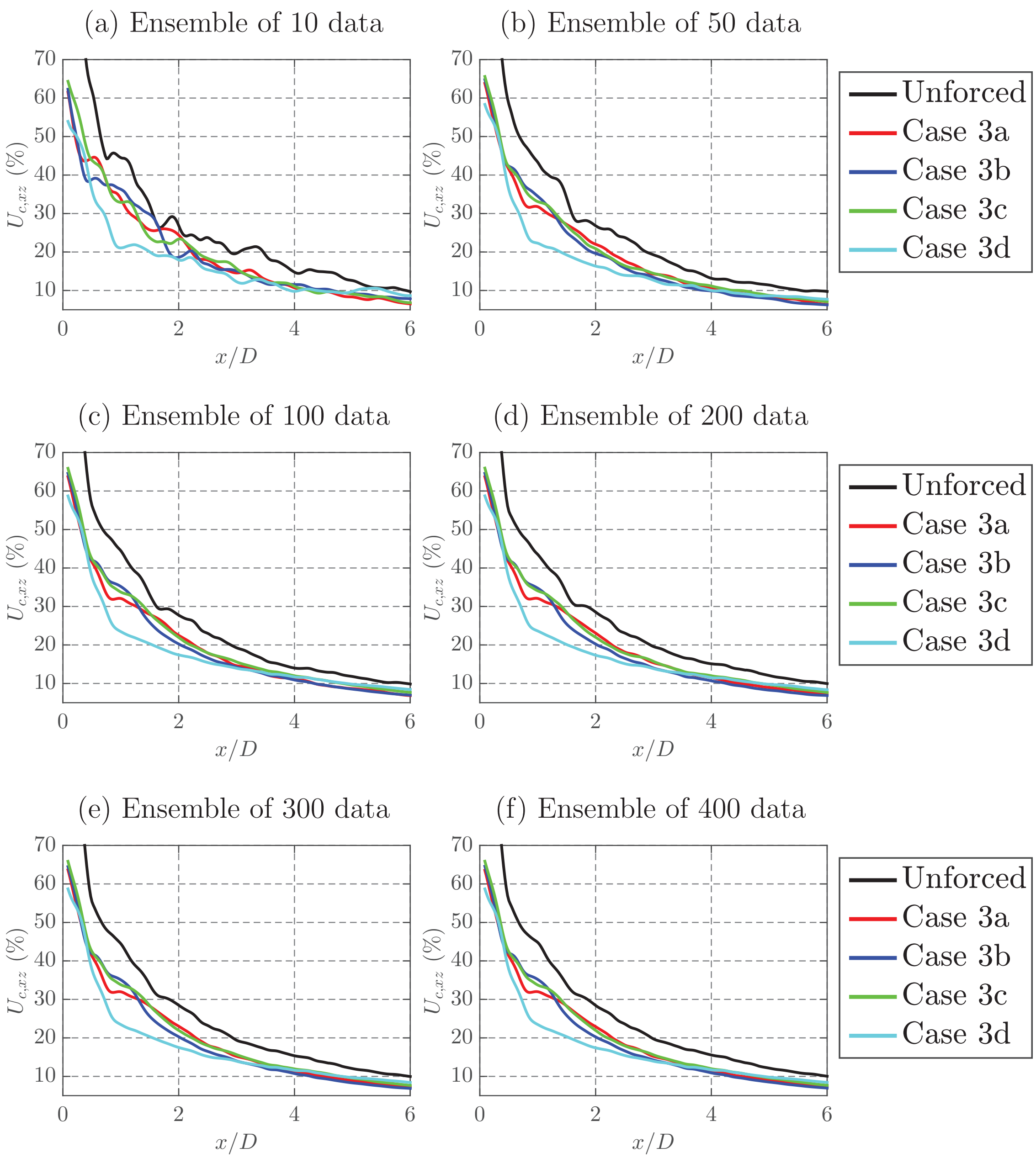

Figure D.18: Quantification of centerplane-based Unmixedness $U_{c,xz}$ along x/D for Cases 3a-3d with matching RMS of jet velocity perturbation at $U'_{j,rms} = 1.7$ m/s using an ensemble of (a) 10, (b) 50, (c) 100, (d) 200, (e) 300, and (f) 400 instantaneous images. The quantification is based on PLIF data acquired at a recording rate of 7.5 Hz.

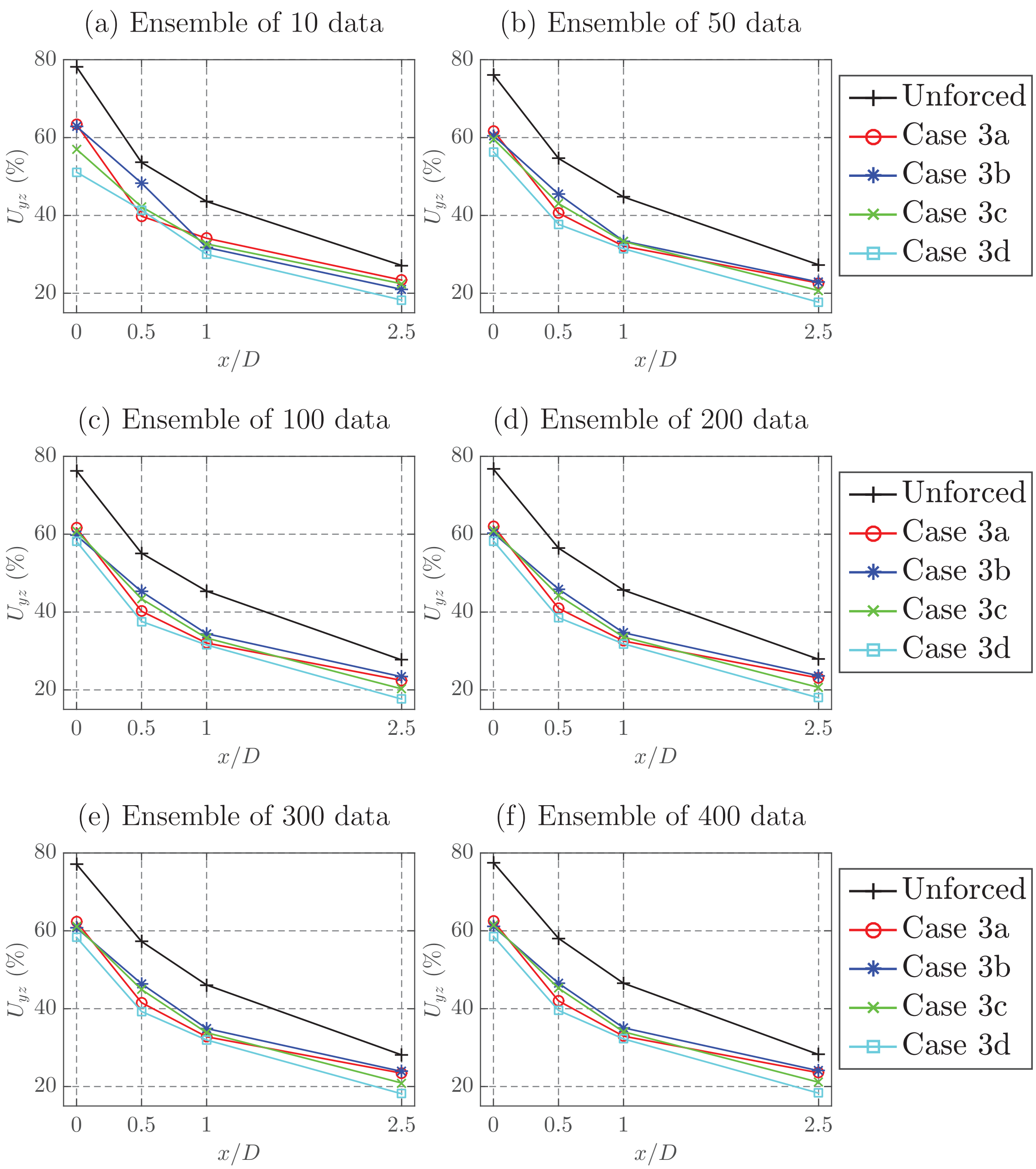

Figure D.19: Quantification of cross-section-based Unmixedness $U_{c,xz}$ along x/D for Cases 3a-3d with matching RMS of jet velocity perturbation at $U'_{j,rms} = 1.7$ m/s using an ensemble of (a) 10, (b) 50, (c) 100, (d) 200, (e) 300, and (f) 400 instantaneous images. The quantification is based on PLIF data acquired at a recording rate of 1 Hz.

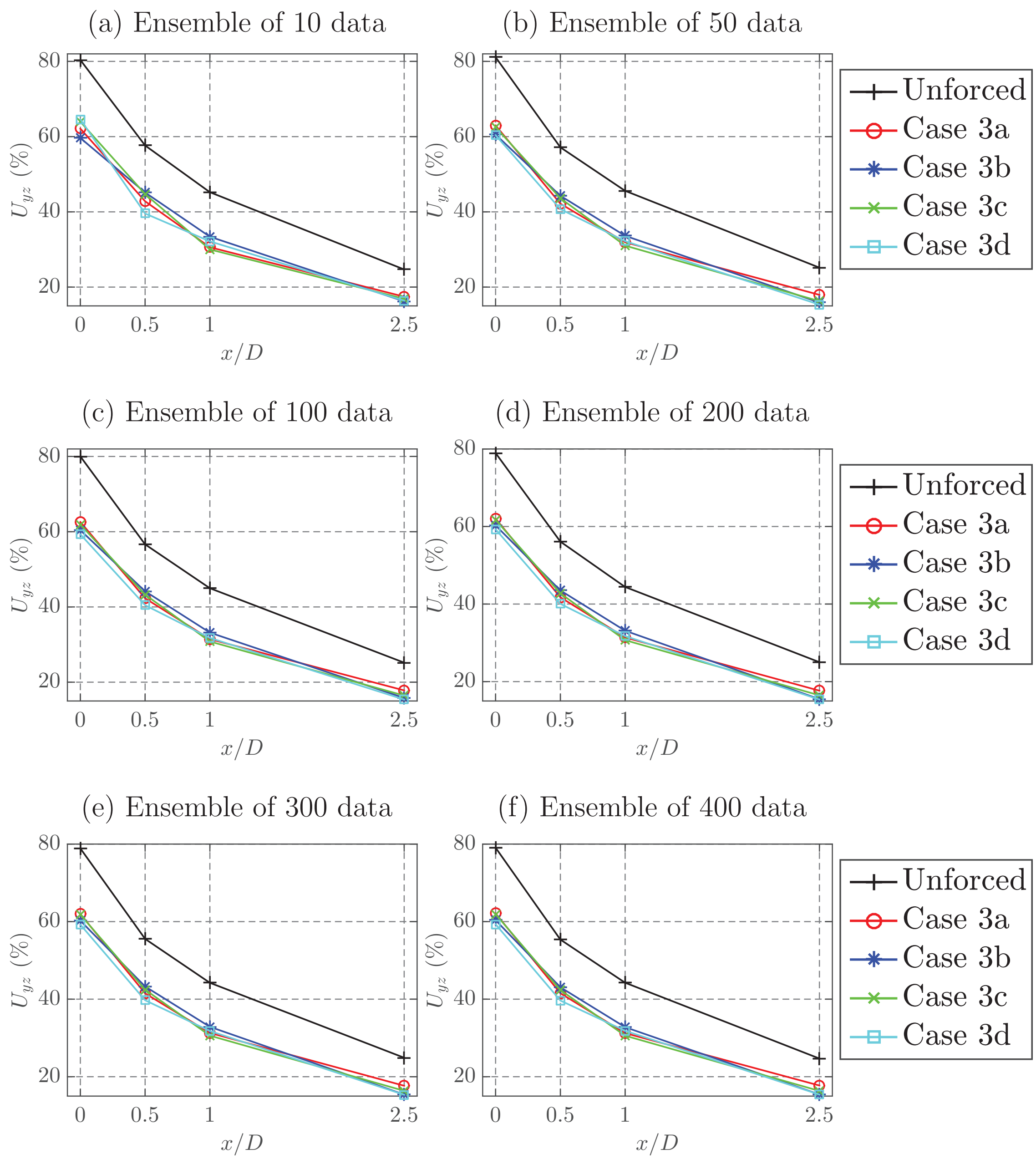

Figure D.20: Quantification of cross-section-based Unmixedness $U_{c,xz}$ along x/D for Cases 3a-3d with matching RMS of jet velocity perturbation at $U'_{j,rms} = 1.7$ m/s using an ensemble of (a) 10, (b) 50, (c) 100, (d) 200, (e) 300, and (f) 400 instantaneous images. The quantification is based on PLIF data acquired at a recording rate of 7.5 Hz.

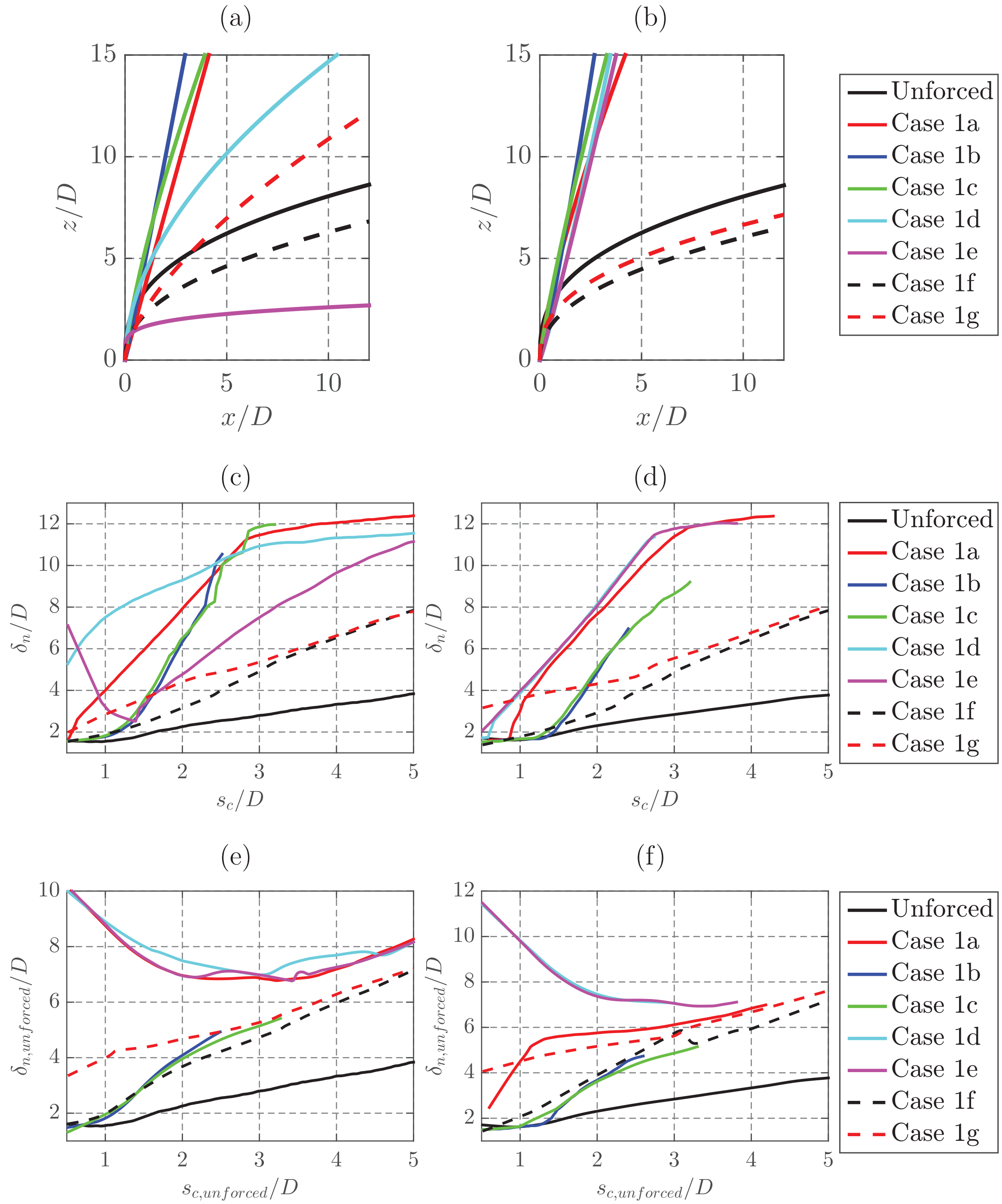

Figure D.21: Quantification of centerplane-based mean mixing metrics for Cases 1a-1g with (a,c,e) matching RMS of jet velocity perturbation at $U'_{j,rms} = 1.7$ m/s and (b,d,f) matching peak-to-peak jet velocity amplitude at $\Delta U_j \approx 4.3$ m/s: (a,b) jet centerline trajectories, (c,d) jet spread normal to each jet centerline trajectory in question, and (e,f) jet spread normal to the unforced jet centerline trajectory.

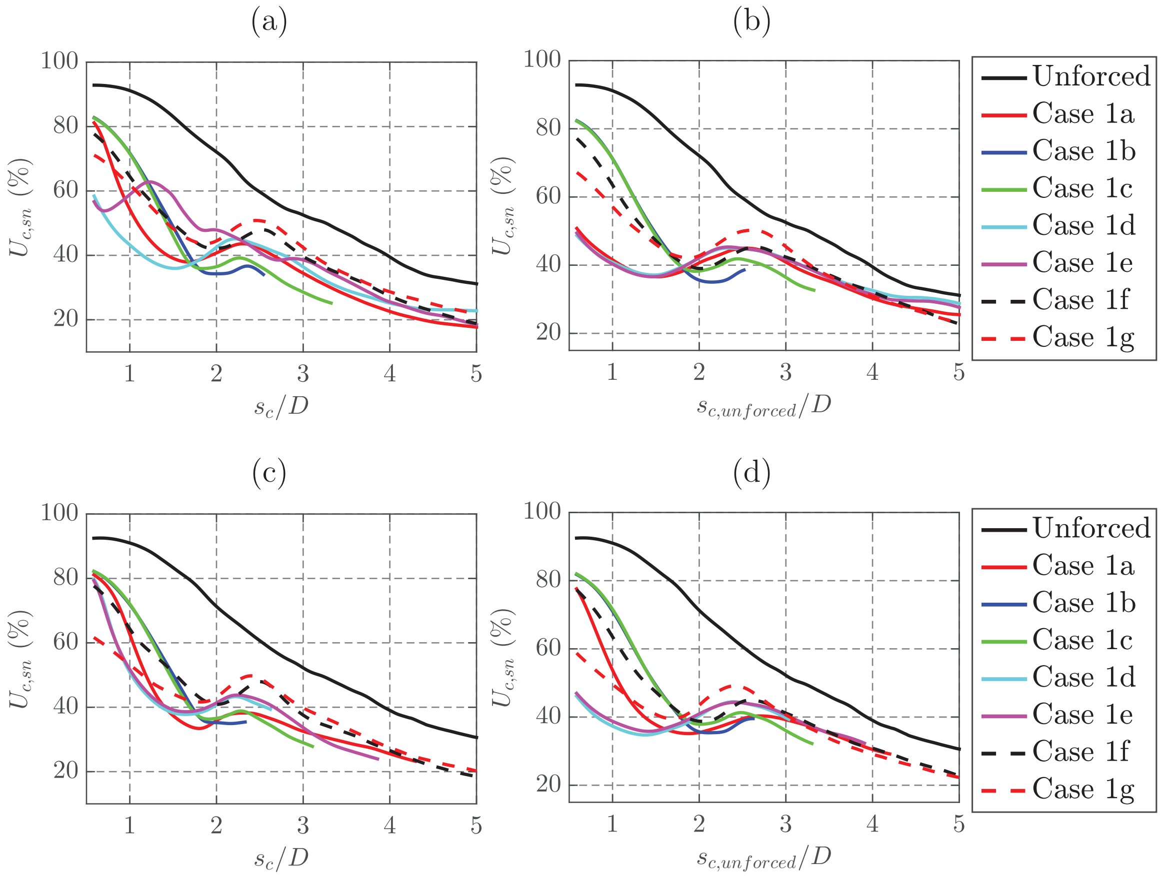

Figure D.22: Quantification of the centerplane-based Unmixedness for Cases 1a-1g with (a,b) matching RMS of jet velocity perturbation at $U'_{j,rms} = 1.7$ m/s and (c,d) matching peak-to-peak jet velocity amplitude at $\Delta U_j \approx 4.3$ m/s: (a,c) normal to each jet centerline trajectory in question, and (b,d) normal to the unforced jet centerline trajectory.

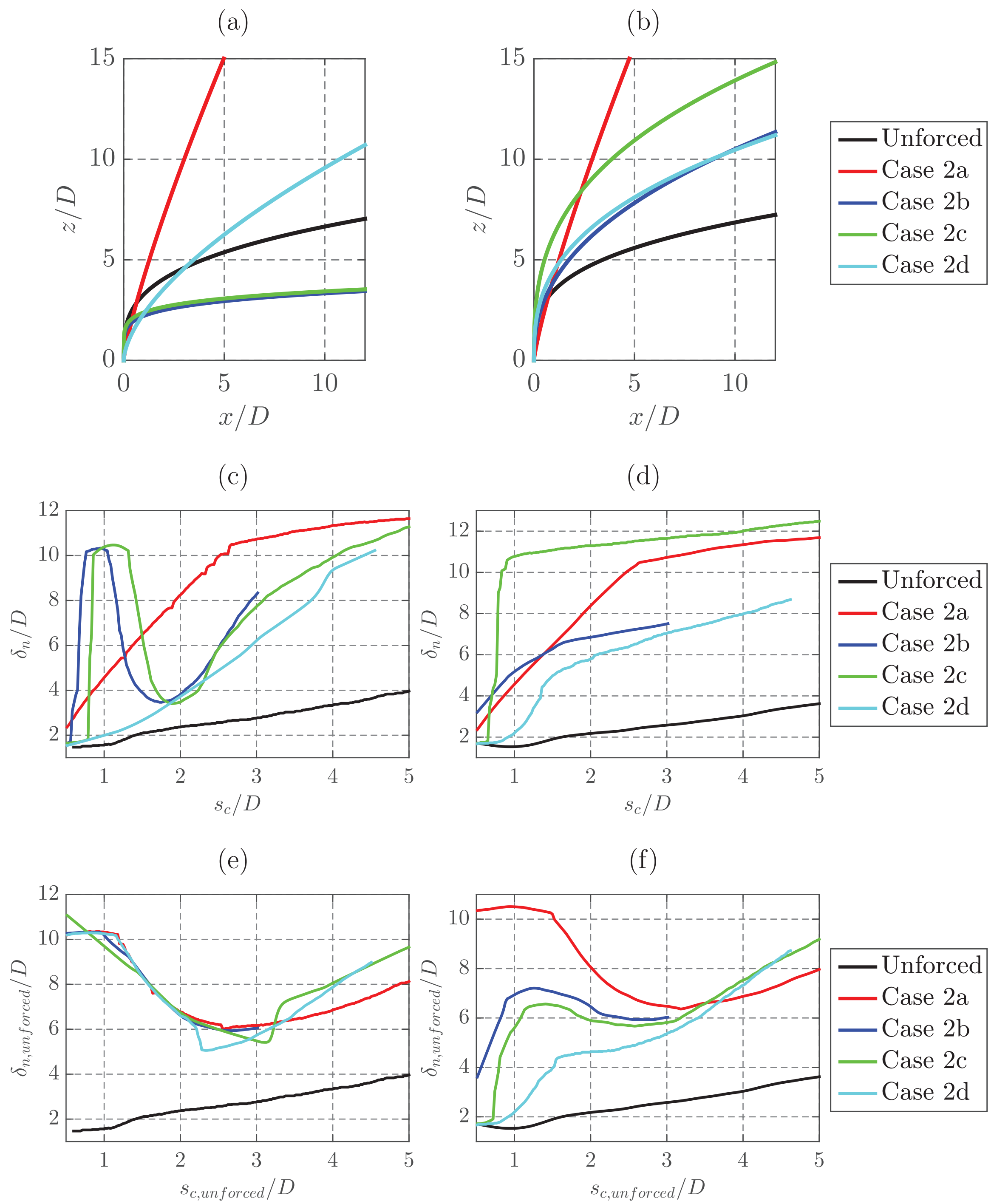

Figure D.23: Quantification of centerplane-based mean mixing metrics for Cases 2a-2d with matching RMS of jet velocity perturbation at $U'_{j,rms} = 1.7$ m/s based on PLIF data taken at (a,c,e) 1 Hz and (b,d,f) 7.5 Hz: (a,b) jet centerline trajectories, (c,d) jet spread normal to each jet centerline trajectory in question, and (e,f) jet spread normal to the unforced jet centerline trajectory.

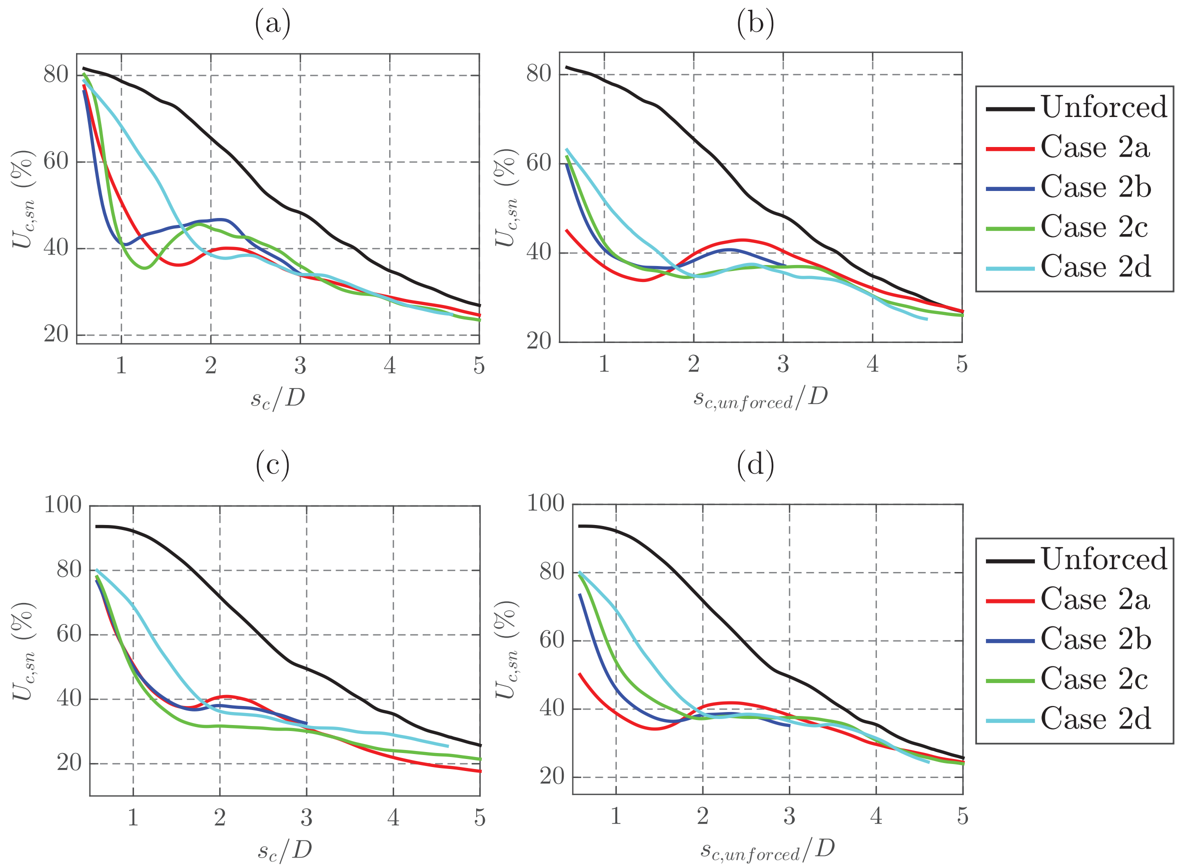

Figure D.24: Quantification of the centerplane-based Unmixedness for Cases 2a-2d with matching RMS of jet velocity perturbation at $U'_{j,rms} = 1.7$ m/s based on PLIF data taken at (a,b) 1 Hz and (c,d) 7.5 Hz: (a,c) normal to each jet centerline trajectory in question, and (b,d) normal to the unforced jet centerline trajectory.

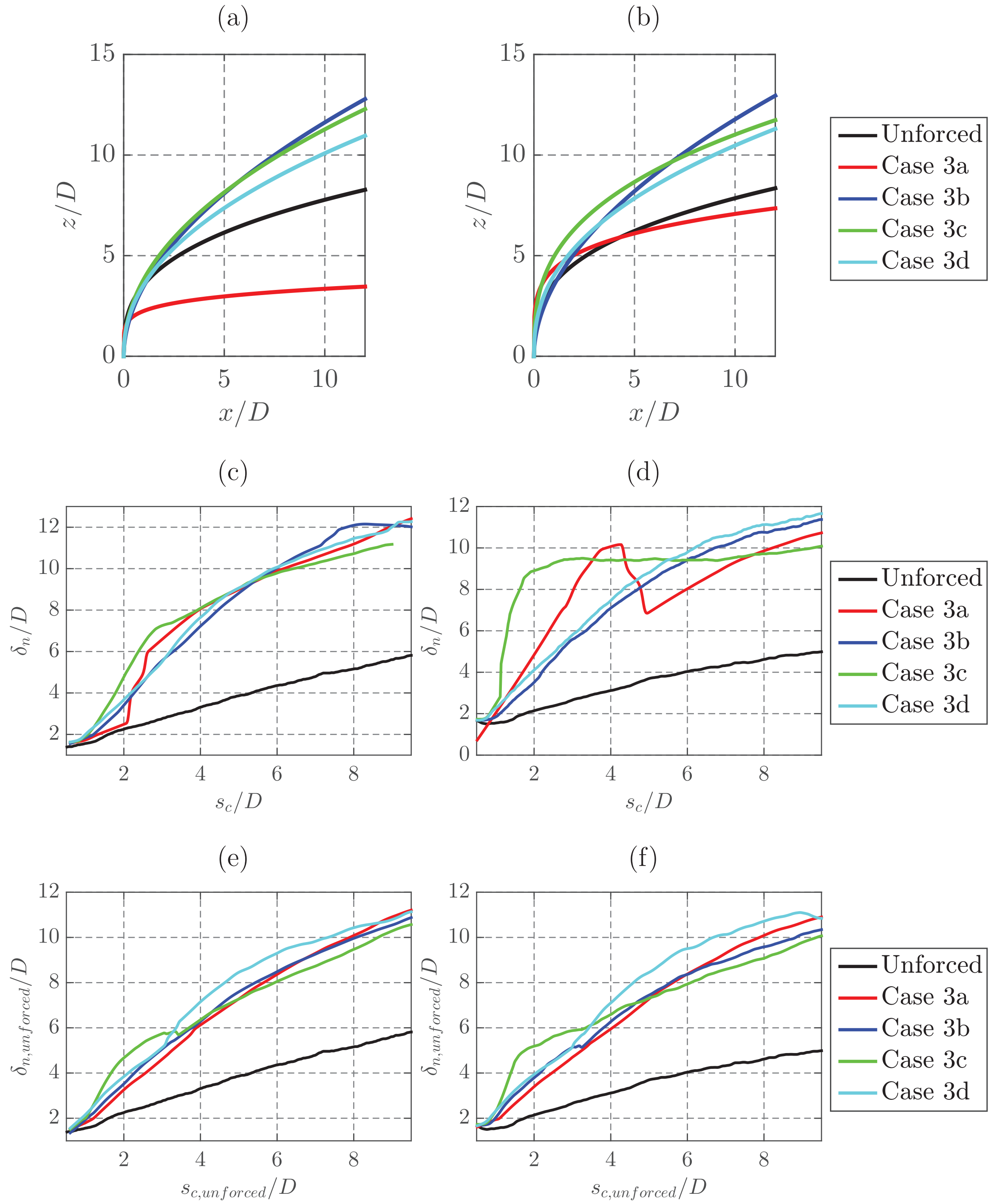

Figure D.25: Quantification of centerplane-based mean mixing metrics for Cases 3a-3d with matching RMS of jet velocity perturbation at $U'_{j,rms} = 1.7$ m/s based on PLIF data taken at (a,c,e) 1 Hz and (b,d,f) 7.5 Hz: (a,b) jet centerline trajectories, (c,d) jet spread normal to each jet centerline trajectory in question, and (e,f) jet spread normal to the unforced jet centerline trajectory.

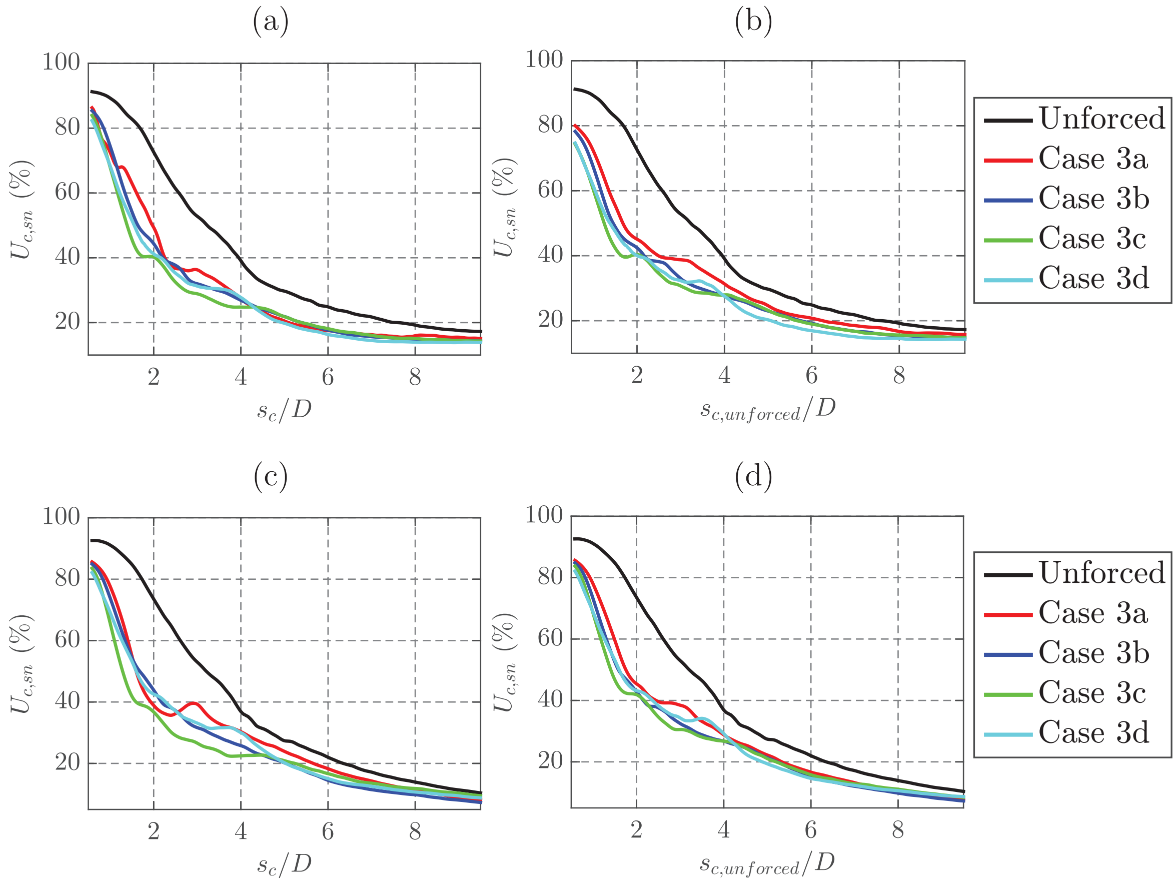

Figure D.26: Quantification of the centerplane-based Unmixedness for Cases 2a-2d with matching RMS of jet velocity perturbation at $U'_{j,rms} = 1.7$ m/s based on PLIF data taken at (a,b) 1 Hz and (c,d) 7.5 Hz: (a,c) normal to each jet centerline trajectory in question, and (b,d) normal to the unforced jet centerline trajectory.

Bibliography

R. J. Adrian and J. Westerweel. *Particle Image Velocimetry*. Cambridge University Press, New York, NY, 2011.

L. S. de B. Alves, R. E. Kelly, and A. R. Karagozian. Local stability analysis of an inviscid transverse jet. *Journal of Fluid Mechanics*, 581:401–418, 2007.

L. S. de B. Alves, R. E. Kelly, and A. R. Karagozian. Transverse-jet shear-layer instabilities. part 2. linear analysis for large jet-to-crossflow velocity ratio. *Journal of Fluid Mechanics*, 602:383–401, 2008.

J. Andreopoulos. On the structure of jets in a crossflow. *Journal of Fluid Mechanics*, 157: 163–197, 1985.

H. Aref. Stirring by chaotic advection. *Journal of Fluid Mechanics*, 143:1–21, 006 1984.

H. Aref. The development of chaotic advection. *Physics of Fluids*, 14(4):1315–1325, 2002.

J.B. Barlow, W.H. Rae Jr., and A. Pope. *Low-Speed Wind Tunnel Testing*. Wiley-Interscience, 1999.

G. K. Batchelor. *An Introduction to Fluid Dynamics*. Cambridge University Press, 1967.

A. Ben-Yakar, M. R. Kamel, C. I. Morris, and R. K. Hanson. Hypersonic combustion and mixing studies using simultaneous OH-PLIF and schlieren imaging. In *36th AIAA Aerospace Sciences Meeting & Exhibit*, January 1998. AIAA Paper 98-0940.

G. Berkooz, P. Holmes, and J. L. Lumley. The proper orthogonal decomposition in the analysis of turbulent flows. *Annual review of fluid mechanics*, 25:539–575, 1993.

R. B. Bird, W. E. Stewart, and E. N. Lightfoot. *Transport Phenomena*. John Wiley & Sons, Inc., New York, 1960.

E. S. Bish and W. J. A. Dahm. Strained dissipation and reaction layer analyses of nonequilibrium chemistry in turbulent reacting flows. *Combustion and Flame*, 100:457–464, 1995.

J. N. Blanchard, Y. Brunet, and A. Merlen. Influence of a counter rotating vortex pair on the stability of a jet in crossflow: an experimental study by flow visualizations. *Experiments in Fluids*, 26:63–74, 1999.

D. G. Bogard and K. A. Thole. Gas turbine file cooling. *Journal of Propulsion and Power*, 22(2):249–270, 2005.

J. P. Bons, R. Sondergaard, and R. B. Rivir. The fluid dynamics of lpt blade separation control using pulsed jets. *Journal of Turbomachinery*, 124(1):77–85, 2002.

C. T. Bowman. Control of combustion-generated nitrogen oxide emissions: Technology driven by regulation. *Twenty-Fourth Symposium on Combustion*, 24:859–878, 1992.

J. E. Broadwell and R. E. Breidenthal. Structure and mixing of a transverse jet in incompressible flow. *Journal of Fluid Mechanics*, 148:405–412, 1984.

K. A. Buch and W. J. A. Dahm. Experimental study of the fine-scale structure of conserved scalar mixing in turbulent shear flows. part 1. Sc$\gg$1. *Journal of Fluid Mechanics*, 317: 21–71, 1996.

K. A. Buch and W. J. A. Dahm. Experimental study of the fine-scale structure of conserved scalar mixing in turbulent shear flows. part 2. Sc$\approx$1. *Journal of Fluid Mechanics*, 364: 1–29, 1998.

R. Camussi, G. Guj, and A. Stella. Experimental study of a jet in a crossflow at very low reynolds number. *Journal of Fluid Mechanics*, 454:113–144, 2002.

M. S. Chong, A. E. Perry, and B. J. Cantwell. A general classification of three-dimensional flow fields. *Physics of Fluids A*, 2(5):765–777, 1990.

N. T. Clemens. Flow imaging. In *Hornank JP (ed) Encyclopedia of imaging science and technology*. John Wiley and Sons, 2002.

T. C. Corke, F. Shakib, and H. M. Nagib. Mode selection and resonant phase locking in unstable axisymmetric jets. *Journal of Fluids Mechanics*, 223:253–311, 1991.

L. Cortelezzi and A. R. Karagozian. On the formation of the counter-rotating vortex pair in transverse jets. *Journal of Fluid Mechanics*, 446:347–373, 2001.

A. Coussement, O. Gicquel, and G. Degrez. Large eddy simulation of a pulsed jet in cross-flow. *Journal of Fluid Mechanics*, 695:1–34, 2012.

S. C. Crow and F. H. Champagne. Orderly structure in jet turbulence. *Journal of Fluid Mechanics*, 48(3):547–591, 1971.

D. D'Alessandro, M. Dahleh, and I. Mezić. Control of mixing in fluid flow: a maximum entropy approach. *IEEE Transactions on Automatic Control*, 44(10):1852–1863, Oct 1999.

U. Dallmann. Topological structures of three-dimensional flow separation. *Deutsche Forschungs- und Versuchsanstalt für Luft- und Raumfahrt DFVLR-IB Report*, (221-82), 1983.

P. V. Danckwerts. The definition and measurement of some characteristics of mixtures. *Applied Science Research*, A3:279–296, 1952.

J. Davitian, D. Getsinger, C. Hendrickson, and A. R. Karagozian. Transition to global instability in transverse-jet shear layers. *Journal of Fluid Mechanics*, 661:294–315, 2010a.

J. Davitian, C. Hendrickson, D. Getsinger, R. T. M'Closkey, and A. R. Karagozian. Strategic control of transverse jet shear layer instabilities. *AIAA Journal*, 48(9):2145–2156, 2010b.

P. E. Dimotakis. Turbulent mixing. *Annual Review of Fluid Mechanics*, 37:329–356, 2005.

P. E. Dimotakis and P. L. Miller. Some consequences of the boundedness of scalar fluctuations. *Physics of Fluids A*, 2(11):1919–1920, 1990.

S. V. Ekkad, S. Ou, and R. B. Rivir. Effect of jet pulsation and duty cycle on film cooling from a single jet on a leading edge model. *Journal of Turbomachinery*, 128(3):564–571, 2006.

A. Eroglu and R. E. Breidenthal. Structure, penetration, and mixing of pulsed jets in crossflow. *AIAA Journal*, 39(3):417–423, 2001.

R. Fearn and R. Weston. Vorticity associated with a jet in a crossflow. *AIAA J*, 12:1666–1671, 1974.

M. J. Foust, D. Thomsen, R. Stickles, C. Cooper, and W. Dodds. Development of the GE aviation low emissions TAPS combustor for next generation aircraft engines. In *50th AIAA Aerospace Sciences Meeting Including the New Horizons Forum and Aerospace Exposition*, number AIAA 2012-0936, Nashville, Tennessee, January 2012.

T. F. Fric and A. Roshko. Vortical structure in the wake of a transverse jet. *Journal of Fluid Mechanics*, 279:1–47, 1994.

D. R. Getsinger. *Shear Layer Instabilities and Mixing in Variable Density Transverse Jet Flows*. PhD thesis, UCLA, 2012.

D. R. Getsinger, C. Hendrickson, and A. R. Karagozian. Shear layer instabilities in low-density transverse jets. *Experiments in Fluids*, 53:783–801, 2012.

D. R. Getsinger, L. Gevorkyan, O. I. Smith, and A. R. Karagozian. Structural and stablity characteristics of jets in crossflow. *Journal of Fluid Mechanics*, 760:342–367, 2014.

L. Gevorkyan. *Structure and Mixing Characterization of variable Density Transverse Jet Flows*. PhD thesis, University of California, Los Angeles, 2015.

L. Gevorkyan, T. Shoji, D. R. Getsinger, O. I. Smith, and A. R. Karagozian. Transverse jet mixing characteristics. *Journal of Fluid Mechanics*, 790:237–274, 2016.

L. Gevorkyan, T. Shoji, W. Y. Peng, and A. R. Karagozian. Influence of the velocity field on scalar transport in gaseous transverse jets. *submitted to Journal of Fluid Mechanics*, 2017.

M. Gharib, E. Rambod, and K. Shariff. A universal time scale for vortex ring formation. *Journal of Fluid Mechanics*, 360:121–141, 1998.

E. Gouillart, J-L. Thiffeault, and M. D. Finn. Topological mixing with ghost rods. *Phys. Rev. E*, 73:036311, Mar 2006.

M. Gruber, J. Donbar, C. Carter, and K-Y Hsu. Mixing and combustion studies using cavity-based flameholders in a supersonic flow. *Journal of Propulsion and Power*, 20:769–778, 2004.

O. Gubanov and L. Cortelezzi. Towards the design of an optimal mixer. *Journal of Fluid Mechanics*, 651:27–53, 2010.

M. P. Hallberg and P. J. Strykowski. On the universality of global modes in low-density axisymmetric jets. *Journal of Fluid Mechanics*, 569:493–507, 2006.

C. Hendrickson and R. M'Closkey. Phase compensation strategies for modulated-demodulated control with application to pulsed jet injection. *ASME Journal of Dynamic Systems, Measurement, and Control*, 134(011024), 2012. accepted for publication.

C. S. Hendrickson. *Identification and Control of the Jet in Crossflow*. PhD thesis, University of California, Los Angeles, Department of Mechanical and Aerospace Engineering, 2012.

J. D. Holdeman. Mixing of multiple jets in a confined subsonic crossflow. *Prog. Energy Comb. Sci.*, 19(1):31–70, 1993.

L. Howarth. Concerning the effect of compressibility on laminar boundary layers and their separation. *Proceedings of the Royal Society A*, 194(1036):16–42, July 1948.

P. Huerre. *Perspectives in Fluid Dynamics: A Collective Introduction to Current Research*. Cambridge University Press, 2000.

P. Huerre and P. A. Monkewitz. Local and global instabilities in spatially developing flows. *Annual Review of Fluid Mechanics*, 22:473–537, 1990.

A. J. Humber, E. W. Grandmaison, and A. Pollard. Mixing between a sharp-edged rectangular jet and a transverse cross flow. *International Journal of Heat and Mass Transfer*, 36(18):4307–4316, 1993.

J. C. R. Hunt, A. A. Wray, and P. Moin. Eddied, stream, and convergence zones in turbulent flows. *Center for Turbulence Research*, CTR-S88:193–208, 1988.

A. K. M. F. Hussain and K. B. M. Q. Zaman. The free shear layer tone phenomenon and probe interference. *Journal of Fluid Mechanics*, 87:349–383, 1978.

P. S. Iyer and K. Mahesh. A numerical study of shear layer characteristics of low-speed transverse jets. *Journal Fluid of Mechanics*, 790:275–307, 2016.

S. Jendoubi and P. J. Strykowski. Absolute and convective instability of axisymmetric jets with external flow. *Physics of Fluids*, 6:3000–3009, 1994.

M. H. Jensen, P. Bak, and T. Bohr. Complete devil's staircase, fractal dimension, and universality of mode- locking structure in the circle map. *Physical Review Letters*, 50: 1637–1639, 1983.

J. Jeong and F. Hussain. On the identification of a vortex. *Journal of Fluid Mechanics*, 285: 69–94, 1995.

H. Johari. Scaling of fully pulsed jets in crossflow. *AIAA Journal*, 44(11):2719–2725, 2006.

H. Johari, M. Pacheco-Tougas, and J. C. Hermanson. Penetration and mixing of fully modulated turbulent jets in crossflow. *AIAA Journal*, 37(7):842–850, 1999.

M. P. Juniper, L. K. B. Li, and J. W. Nichols. Forcing of self-excited round jet diffusion flames. *Proc. of the Combustion Institute*, 32:1191–1198, 2009.

Y. Kamotani and I. Greber. Experiments on a turbulent jet in a cross flow. *AIAA Journal*, 10(11):1425–1429, 1972.

A. R. Karagozian. An analytical model for the vorticity associated with a transverse jet. *AIAA Journal*, 24:429–436, 1986.

A. R. Karagozian. Transverse jets and their control. *Progress in Energy and Combustion Science*, 36:531–553, 2010.

A. R. Karagozian, K. C. Wang, A.-T. Le, and O. I. Smith. Transverse gas jet injection behind a rearward-facing step. *Journal of Propulsion and Power*, 12(6):1129–1136, 1996.

R. M. Kelso and A. J. Smits. Horseshoe vortex systems resulting from the interaction between a laminar boundary layer and a transverse jet. *Phys. Fluids*, 7:153–158, 1995.

R. M. Kelso, T. T. Lim, and A. E. Perry. An experimental study of round jets in cross-flow. *Journal of Fluid Mechanics*, 306:111–144, 1996.

S. Kida and H. Miura. Identification and analysis of vortical structures. *European Journal of Mechanics B/Fluids*, 17:471–488, 1998.

P.S. Kothnur and N. T. Clemens. Effects of unsteady strain rate on scalar dissipation structures in turbulent planar jets. *Physics of Fluids*, 17, 2005.

A. Krothapalli, L. Lourenco, and J. M. Buchlin. Separated flow upstream of a jet in a crossflow. *AIAA Journal*, 28(3):414–420, 1990.

A. Kukukova, J. Aubin, and S. M. Kresta. A new definition of mixing and segregation: Three dimensions of a key process variable. *Chemical Engineering Research and Design*, 87:633–647, 2009.

D. M. Kuzo. *An Experimental Study of the Turbulent Transverse Jet*. PhD thesis, California Institute of Technology, 1995.

D. M. Kyle and K. R. Sreenivasan. The instability and breakdown of a round variable-density jet. *Journal of Fluid Mechanics*, 249:619–664, 1993.

H. Lamb. *Hydrodynamics*. Cambridge University Press, 1895.

M. J. Landman and P. G. Saffman. The three-dimensional instability of strained vortices in a viscous fluid. *Physics of Fluids*, 30:2339–2342, 1987.

T. Lee and R. Budwig. Two improved methods for low-speed hot-wire calibration. *Measurement Science and Technology*, 2:643–646, 1991.

L. K. B. Li. *Forcing of GlGlobal Unstable Jets and Flames*. PhD thesis, University of Cambridge, 2011.

L. K. B. Li and M. P. Juniper. Lock-in and quasiperiodicity in a forced hydrodynamically self-excited jet. *Journal of Fluid Mechanics*, 726:624–655, 2013a.

L. K. B. Li and M. P. Juniper. Lock-in and quasiperiodicity in hydrodynamically self-excited flames: Experiments and modeling. *Proceedings of the Combustion Institute*, 34:947–954, 2013b.

D. S. Liscinsky, B. True, and J. D. Holdeman. Crossflow mixing of noncircular jets. *Journal of Propulsion and Power*, 12:225–230, 1996.

A. Lozano. *Laser-Excited Luminescent Tracers for Planar Concentration Measurements in Gaseous Jets*. PhD thesis, Stanford University, Department of Mechanical Engineering, 1992.

A. Lozano, B. Yip, and R. K. Hanson. Acetone: a tracer for concentration measurements in gaseous flows by planar laser-induced fluorescence. *Experiments in Fluids*, 13:369–376, 1992.

K. Mahesh. The interaction of jets with crossflow. *Annu. Rev. Fluid Mech.*, 2013.

F.E. Marble and J. E. Broadwell. The coherent flame model for turbulent chemical reactions. Technical report, Project Squid Technical Report TRW-9-PU, 1977.

R. J. Margason. Fifty years of jet in cross flow research. *AGARD-CP-534*, 1:1–141, 1993.

G. Mathew, I. Mezić, and L. Petzold. A multiscale measure for mixing and its application. In *42nd IEEE Conference on Decision and Control*, 2003.

G. Mathew, I. Mezić, R. Serban, and L. Petzold. Optimization of mixing in an active micromixing device. *Nano Science and Technology Institute - Nanotech 2004*, 1:300–303, 2004.

G. Mathew, I. Mezić, and L. Petzold. A multiscale measure for mixing. *Physicia D*, 211: 23–46, 2005.

G. Mathew, I. Mezić, S. Grivopoulos, U. Vaidya, and L. Petzold. Optimal control of mixing in Stokes fluid flows. *Journal of Fluid Mechanics*, 580:261–281, 2007.

R. T. M'Closkey, J. King, L. Cortelezzi, and A. R. Karagozian. The actively controlled jet in crossflow. *Journal of Fluid Mechanics*, 452:325–335, 2002.

S. Megerian, J. Davitian, L. S. de B. Alves, and A. R. Karagozian. Transverse-jet shear-layer instabilities. part 1. experimental studies. *Journal of Fluid Mechanics*, 593:93–129, 2007.

K.E. Meyer, J.M. Pedersen, and O. Özcan. A turbulent jet in crossflow analysed with proper orthogonal decomposition. *Journal of Fluid Mechanics*, 583:199–227, 2007.

D. N. Miller, P. J. Yagle, and J. W. Hamstra. Fluidic throat skewing for thrust vectoring in fixed-geometry nozzles. *AIAA P. 99-0365*, 1999.

M. G. Mitchell, L. L. Smith, A. R. Karagozian, and O. I. Smith. Burner emissions associated with lobed and non-lobed fuel injectors. In *Proceesings of the Combustion Institute*, volume 27, pages 1825–1831, 1998.

M. G. Mitchell, O. I. Smith, and A. R. Karagozian. Passive fuel-air mixing and emissions control via lobed injectors. *AIAA Journal*, 42(1):61–69, January 2004.

M. F. Modest. *Radiative Heat Transfer*. Academic Press, 3rd edition, 2013.

P. A. Monkewitz, D. W. Bechert, B. Barsikow, and B. Lehmann. Self-excited oscillations and mixing in a heated round jet. *Journal of Fluid Mechanics*, 213:611–639, 1990.

Z. M. Moussa, J. W. Trischka, and S. Eskinazi. The nearfield in the mixing of a round jet with a cross-stream. *Journal of Fluid Mechanics*, 80:49–80, 1977.

F. Muldoon and S. Acharya. Direct numerical simulation of pulsed jets in crossflow. *Computers & Fluids*, 39:1745–1773, 2010.

S. Muppidi and K. Mahesh. Study of trajectories of jets in crossflow using direct numerical simulations. *Journal of Fluid Mechanics*, 530:81–100, 2005.

S. Muppidi and K. Mahesh. Direct numerical simulation of round turbulent jets in crossflow. *Journal of Fluid Mechanics*, 574:59–84, 2007.

S. Narayanan, P. Barooah, and J. M. Cohen. Dynamics and control of an isolated jet in crossflow. *AIAA Journal*, 41(12):2316–2330, 2003.

T. H. New, T. T. Lim, and S. C. Luo. A flow field study of an elliptic jet in crossflow using dpiv technique. *Experiments in Fluids*, 36:604–618, 2004.

T. S. Oh and J. A. Schetz. Finite element simulation of complex jets in a crossflow for v/stol applications. *Journal of Aircraft*, 27:389–399, 1990.

Nobuyuki Otsu. A threshold selection method from gray-level histograms. *IEEE Transactions on Systems, Man, and Cybernetics*, SMC-7(1):62–66, 1979.

J. M. Ottino. *The kinematics of mixing: stretching, chaos, and transport*. Cambridge University Press, 1989.

A. Pearson, N. Shankland, and E. G. Salole. The molecular weight of liquid paraffin by cryoscopy. *International Journal of Pharmaceutics*, 34:185–186, 1986.

S. D. Peterson and M. W. Plesniak. Evolution of jets emanating from short holes into crossflow. *Journal of Fluid Mechanics*, 503:57–91, 2004.

M. W. Plesniak and D. M. Cusano. Scalar mixing in a confined rectangular jet in crossflow. *Journal of Fluid Mechanics*, 524:1–45, 2005.

B. E. Poling, J. M. Prausnitz, and J. P. O'Connell. *The Properties of Gases and Liquids*. McGraw-Hill, New York, 5^{th} edition, 2001.

A. K. Prasad. Stereoscopic particle image velocimetry. *Experiments in Fluids*, 29:103–116, 2000.

C. Priere, L. Y. M. Gicquel, P. Gajan, and A. Strzelecki. Experimental and numerical studies of dilution system for low-emission combustors. *AIAA Journal*, 43(8):1753–1766, 2005.

M. Provansal, C. Mathis, and L. Boyer. Benard-von karman instability: transient and forced regimes. *Journal of Fluid Mechanics*, 182:1–22, 1987.

W. C. Reynolds, D. E. Parekh, P. J. D. Juvet, and M. J. D Lee. Bifurcating and blooming jets. *Annual Reviews in Fluid Mechanics*, 35(1):295–315, 2003.

D. Rothstein, E. Henry, and J. P. Gollub. Persistent patterns in transient chaotic fluid mixing. *Nature*, 401(6755):770–772, October 1999.

S. Samuelsen. Rich Burn, Quick-Mix, Lean Burn (RQL) combustor. In *The Gas Turbine Handbook*, pages 227–233. National Energy Technology Laboratory, 2016.

R. Sau and K. Mahesh. Passive scalar mixing in vortex rings. *Journal of Fluid Mechanics*, 582:449–461, 2007.

R. Sau and K. Mahesh. Dynamics and mixing of vortex rings in crossflow. *Journal of Fluid Mechanics*, 604:389–409, 2008.

R. Sau and K. Mahesh. Optimization of pulsed jets in crossflow. *Journal of Fluid Mechanics*, 653:365–390, 2010.

P. Schlatter, S. Bagheri, and D.S. Henningson. Self-sustained global oscillations in a jet in crossflow. *Theoretical and Computational Fluid Dynamics*, 25:29–146, 2011.

J. Shan and P. Dimotakis. Reynolds-number effects and anisotropy in transverse-jet mixing. *Journal of Fluid Mechanics*, 566:47–96, 2006.

S. Shapiro, J. King, R. T. M'Closkey, and A. R. Karagozian. Optimization of controlled jets in crossflow. *AIAA Journal*, 44:1292–1298, 2006.

L Sirovich. Turbulence and the dynamics of coherent structures. *Quarterly of Applied Mathematics*, 45:561–590, 1987.

L. L. Smith, A. J. Majamaki, I. T. Lam, O. Delabroy, A. R. Karagozian, F. E. Marble, and O. I. Smith. Mixing enhancement in a lobed injector. *Physics of Fluids*, 9(3):667–678, March 1997.

S. H. Smith. *The Scalar Concentration Field of the Axisymmetric Jet in Crossflow*. PhD thesis, Stanford University, Department of Mechanical Engineering, 1996.

S. H. Smith and M. G. Mungal. Mixing, structure and scaling of the jet in crossflow. *Journal of Fluid Mechanics*, 357:83–122, 1998.

L. K. Su and N. T. Clemens. Planar measurements of the full three-dimensional scalar dissipation rate in gas-phase turbulent flows. *Experiments in Fluids*, 27:507–521, 1999.

L. K. Su and M. G. Mungal. Simultaneous measurements of scalar and velocity field evolution in turbulent crossflowing jets. *Journal of Fluid Mechanics*, 513:1–45, 2004.

R. Sullivan, B. Wilde, D. R. Noble, J. M. Seitzman, and T. C. Lieuwen. Time-averaged characteristics of a reacting fuel jet in vitiated cross-flow. *Combustion and Flame*, 161: 1792–1803, 2014.

M. C. Thurber, F. Grisch, B. J. Kirby, M. Votsmeier, and R. K. Hanson. Measurements and modeling of acetone laser-induced fluorescence with implications for temperature-imaging diagnostics. *Applied Optics*, 37:4963–4978, 1998.

S. Tomar, J. Arnaud, and J. Soria. Structure of a zero-net-mass-flux round jet in crossflow. In *15th Australasian Fluid Mechanics Conference*, 2004.

I. van Cruyningen. *Quantitative Imaging of Turbulent Gaseous Jets Using Planar Laser-Induced Fluorescence*. PhD thesis, Stanford University, Department of Mechanical Engineering, September 1990.

P. J. Vermeulen, J. Odgers, and V. Ramesh. Acoustic control of dilution-air mixing in a gas turbine combustor. *J. Eng. Gas Turbines Power*, 104(4):844–852, 1982.

P. J. Vermeulen, P. Grabinski, and V. Ramesh. Mixing of an acoustically excited air jet with a confined hot crossflow. *J. Engr. for Gas Turbines and Power, ASME Transactions*, 114: 46–54, 1992.

R. Vernet, L. Thomas, and L. David. Analysis and reconstruction of a pulsed jet in crossflow by multi-plane snapshot pod. *Experiments in Fluids*, 47:707–720, 2009.

H. Vollmers, H. P. Kreplin, and H. U. Meier. Separation and vortical-type flow around a prolate spheroid - evaluation of relevant parameters. In *Proceedings of the AGARD Symposium on Aerodynamics of Vortical Type Flows in Three Dimensions*, volume AGARDCP-342, pages 14–1 – 14–14, Rotterrdam, 1983.

J. A. Wagner, S. W. Grib, M. W. Renfro, and B. M. Cetegen. Flowfield measurement and flame stabilization of a premixed reacting jet in vitiated crossflow. *Combustion and Flame*, 2015.

G. H. Wang and N. T. Clemens. Effects of imaging system blur on measurements of flow scalars and scalar gradients. *Experiments in Fluids*, 37:194–205, 2004.

J. Westerweel. Fundamentals of digital particle image velocimetry. *Meas. Sci. Technol.*, 8: 1379–1392, 1997.

B. Wieneke. Stereo-piv using self-calibration on particle images. *Experiments in Fluids*, 39: 267–280, 2005.

P. J. Yagle, D. N. Miller, K. B. Ginn, and J. W. Hamstra. Demonstration of fluidic throat skewing for thrust vectoring in structurally fixed nozzles. *ASME Journal of Engineering for Gas Turbines and Power*, 123(3):502–507, 2001.

L. L. Yuan and R. L. Street. Trajectory and entrainment of a round jet in crossflow. *Phys. Fluids*, 10:2323–2335, 1998.

L. L. Yuan, R. L. Street, and J. H. Ferziger. Large-eddy simulations of a round jet in crossflow. *Journal of Fluid Mechanics*, 379:71–104, 1999.

K. B. M. Q. Zaman. Reduction of jet penetration in a cross-flow by using tabs. *34th AIAA/ASME/SAE/ASEE Joint Propulsion Conference & Exhibit*, 1998.

K. B. M. Q. Zaman and I. Milanovic. Control of a jet-in-crossflow by periodically oscillating tabs. *Physics of Fluids*, 24(5):055107, 2012.